UNIVERSITÉ DE GRENOBLE

THÈSE

Pour obtenir le grade de

DOCTEUR DE L'UNIVERSITÉ DE GRENOBLE

Spécialité : **Sciences de la Terre, de l'Univers, et de l'Environnement**

Arrêté ministérial : 7 août 2006

Présentée par

Morgane LEDEVIN

Thèse dirigée par **Alexandre Simionovici**
et codirigée par **Nicholas Arndt**

préparée au sein **Institut des Sciences de la Terre de Grenoble (ISTerre)**
et de **Ecole doctorale Terre Univers Environnement (TUE)**

Les cherts Archéens de la ceinture de roches vertes de Barberton (3.5-3.2Ga), Afrique du Sud.

Processus de formation et utilisation comme proxys paleo-environnementaux.

Thèse soutenue publiquement le **6 Juin 2013**,
devant le jury composé de :

Mr. Etienne Jaillard
Directeur de Recherche, Université de Grenoble, Président
Mme. Frances Westall
Directeur de Recherche, Université d'Orléans, Rapporteur
Mr. Donald Lowe
Professeur, University of Stanford, Rapporteur
Mr. Stephen Mojzsis
Professeur, University of Colorado, Examinateur
Mr. Kurt Konhauser
Professeur, University of Alberta, Examinateur
Mr. Alexandre Simionovici
Professeur, Université de Grenoble, Directeur de thèse
Mr. Nicholas Arndt
Professeur, Université de Grenoble, Co-Directeur de thèse

Rapport soumis aux rapporteurs, dans le but de sanctionner le
dossier pour l'obtention du grade de
Docteur en Sciences de la Terre, de l'Univers et de l'Environnement
de
l'Université de Grenoble

Les cherts Archéens de la ceinture de roches vertes de Barberton $(3.5 − 3.2Ga)$, Afrique du Sud.

Processus de formation et utilisation comme proxys paleo-environnementaux.

Morgane Ledevin, le Vendredi 12 Avril 2013

La Thèse sera soutenue publiquement devant le jury composé de :

Donald Lowe	Professeur, Univ. of Stanford, Californie, USA	(Rapporteur)
Frances Westall	Directeur de recherche, CBM, Orléans, France	(Rapporteur)
Etienne Jaillard	Directeur de recherche, Univ. de Grenoble, France	(Examinateur)
Stephen Mojzsis	Professeur, Univ. of Colorado, Boulder, USA	(Examinateur)
Kurt Konhauser	Professeur, Univ. of Alberta, Edmonton, USA	(Examinateur)
Nicholas Arndt	Professeur, Univ. de Grenoble, France	(Directeur)
Alexandre Simionovici	Professeur, Univ. de Grenoble, France	(Directeur)

A toi Grand-Père,
Toi qui ne disais mot,
mais n'en pensais pas moins.

Résumé

Les cherts archéens permettent de contraindre les environnements primitifs qui ont vu l'apparition et l'évolution de la vie sur Terre. Ces roches siliceuses se forment selon trois processus : les C-cherts (cherts primaires) se forment par précipitation chimique de silice océanique, soit sous la forme d'une boue siliceuse (ou gel) sur le plancher, soit en ciment dans les sédiments meubles à la surface ; les F-cherts (cherts de fracture) précipitent depuis les fluides circulant dans la croûte au sein de veines concordantes ou recoupant les unités en place ; les S-cherts (cherts secondaires) sont issus du métasomatisme (silicification) de roches préexistantes lors de la percolation de fluides enrichis en silice.

Ces processus sont largement acceptés mais des questions majeures subsistent : comment reconnaître ces différents types de chert ? Quelle est l'origine de la silice et sous quelle forme a-t-elle précipité ? Quel signal chimique est porté par les cherts et comment s'en servir pour les reconstructions paléo-environnementales ? Ces questions sont abordées ici à travers trois sites de la ceinture de roches vertes de Barberton, en Afrique du Sud, qui regroupent une variété de cherts mis en place dans des environnements très différents. L'approche adoptée combine l'analyse des structures sédimentaires et de déformation, de la pétrologie et de la composition chimique et isotopique de ces unités.

Dans ces sites, la formation des cherts est étroitement liée à l'environnement de mise en place. La sédimentation clastique est à l'origine des C-cherts de Komati River, déposés sous la forme d'une boue siliceuse visqueuse par adsorption sur les particules argileuses en suspension. En absence de contribution continentale, les alternances de cherts noirs et blancs (C-cherts) de Buck Reef sont interprétées comme issues de la précipitation chimique de silice océanique sous l'effet de variations climatiques saisonnières (chert noir), voire glaciaires/inter-glaciaires (chert blanc). Les cherts de fracture de Barite Valley sont liés à la précipitation de silice depuis une suspension colloïdale thixotrope remontant à travers la croûte.

La composition chimique des cherts est essentiellement contrôlée par leur environnement de mise en place, et représente un mélange entre une phase siliceuse et une phase contaminante, indépendamment des processus qui ont précipité la silice. Les C-cherts de Komati River et les F-cherts de Barite Valley sont enrichis en Al, K, Ti, HFSE et en REE (typiquement $\Sigma REE > 0.6 wt\%$), ce qui est attribué à la contamination de la matrice siliceuse par la présence de phyllosilicate. Une telle contribution clastique peut expliquer les larges gammes de $\delta^{30}Si$ dans les cherts de Komati River ($-0.69‰$ à $+3.89‰$), même si la majorité des valeurs positives est probablement liée à la contribution de l'eau de mer. Dans les dykes de Barite Valley, les $\delta^{30}Si$ très négatifs ($-4.5‰$ à $+0.22‰$) sont cohérents avec l'origine hydrothermale à basse température des fluides initiaux.

A Buck Reef, l'absence de contribution continentale s'exprime dans les cherts blancs par une minéralogie exclusivement microquartzitique et par des concentrations extrêmement faibles en éléments traces (i.e. $\Sigma HFSE$ et $\Sigma REE < 1 ppm$). Nous calculons que 2% de carbonates et 3-4% de matériel continental (e.g. argiles) suffisent à masquer le signal siliceux dans ces cherts purs. Nous ne pouvons conclure sur la présence d'un signal océanique dans ces cherts en raison du manque de fiabilité des proxys océaniques modernes (appauvrissement en LREE, enrichissement en La et Y). Reconnus à la fois dans des quartz océaniques, hydrothermaux, magmatiques et pegmatitiques, ces caractéristiques ne permettent pas d'identifier un signal d'eau de mer dans les cherts archéens. Les $\delta^{18}O$ de ces cherts indiquent la présence de circulations fluides secondaires à moins de $100°C$, et leurs $\delta^{30}Si$ négatifs ou positifs ($-2.23 \pm 0.29‰$ et $+1.13 \pm 0.28‰$ en moyenne) représentent la contribution de fluides d'origines différentes au moment de leur formation.

Le couplage des observations pétrologiques et de terrain semble être la seule approche fiable pour différencier les cherts et reconnaître leur mode de mise en place, tandis que leur composition chimique dépend plus des conditions environnementales que des caractéristiques du fluide initial.

Abstract

Archean cherts potentially constrain the primitive environment in which life emerged and evolved. These siliceous rocks formed by three processes : C-cherts (primary cherts) formed by the chemical precipitation of oceanic silica, either as a siliceous ooze (or silica gel) on the seabed, or as cement within still soft sediments at the surface ; F-cherts (fracture-filling cherts) precipitated from circulating fluids in concordant or crosscutting veins in the shallow crust ; S-cherts (secondary cherts) are the result of the metasomatism (silicification) of preexisting rocks during the percolation of silica-rich fluids.

These processes are generally accepted but major questions remain unsolved : how to recognize various chert types ? Where does the silica come from and how did it precipitate ? What chemical signal is hosted in cherts and how can it be used for paleo-environmental reconstructions ? These questions are addressed here using three sites in the Barberton Greenstone Belt, South Africa, which contain a variety of cherts deposited in very different environments. The approach combines field description of sedimentary and deformation structures, the characterization of various chert petrologies, and the study of their chemical and isotopic composition.

In these three sites, chert formation strongly depends on the environmental setting. Clastic sedimentation is directly linked to C-chert formation at Komati River, where the silica was deposited as a viscous, siliceous ooze by sorption process onto suspended clay particles. A continental contribution is absent at Buck Reef, and the black and white banded cherts (C-cherts) are interpreted to have formed by chemical precipitation of oceanic silica during seasonal (black chert) and maybe glacial/inter-glacial (white chert) climatic variations. The fracture-filling cherts from Barite Valley precipitated from a thixotropic colloidal suspension that migrated upward through the crust.

The chemical compositions of cherts from these three sites are essentially controlled by the environment of deposition, and represent mixtures of a siliceous and contaminant phases, independent from the silica precipitation mode. Komati River C-cherts and Barite Valley F-cherts are both enriched in Al, K, Ti, HFSE and REE (typically $\Sigma REE > 0.6wt\%$) which represents the contamination by phyllosilicates of the microquartzitic fabrics. Such a clastic contribution may account for the wide range of $\delta^{30}Si$ in Komati River cherts ($-0.69‰$ to $+3.89‰$) although the majority of positive values is attributed to seawater involvement. In the dykes, $\delta^{30}Si$ is strongly negative ($-4.5‰$ to $+0.22‰$) and is consistent with the low-temperature hydrothermal nature of these fluids.

At Buck Reef, the lack of continental contribution is expressed in the white cherts, by a mineralogy exclusively composed of microquartz, and by extremely low trace element contents, i.e. HFSE and REE below $1ppm$. We calculate that 2% of carbonates and 3-4% of clastic particles (i.e. clay, feldspar) would be enough to mask the silica composition in these high purity cherts. A marine signature was not recognized in their geochemistry because of the unreliability of commonly used modern proxys (i.e. LREE depletion, La and Y enrichment). These features were identified in oceanic, hydrothermal, magmatic and pegmatitic quartz and thus do not reliably identify an oceanic signal in Archean cherts. Because the $\delta^{18}O$ values in these white cherts indicates secondary fluid circulations at $<100°C$, their negative or positive $\delta^{30}Si$ values ($-2.23 \pm 0.29‰$ and $+1.13 \pm 0.28‰$ in average) most probably represent different fluid contributions at the time they formed.

The combination of field and petrological observations appears to be the most reliable approach to classify cherts and to deduce their origin, and we show here that their chemical composition depends more on the environmental conditions than on the primary fluid characteristics.

TABLE DES MATIÈRES

Introduction générale

1

———————————————————

1.1 Petit aperçu de l'environnement archéen.

1.1.1 Une atmosphère anoxique et riche en gaz à effets de serre.

L'un des grands paradoxes de la Terre primitive est celui dit du "soleil jeune" (Sagan et Mullen 1972, Gough 1981, Sagan et Chyba 1997, Kasting 2001). Il y a $3.5 - 3.2 Ga$ la luminosité solaire est estimée à $70 - 75\%$ de sa valeur actuelle (Newman et Rood 1977, Gilliland 1989), une puissance trop faible pour maintenir la température de surface de la Terre au dessus du point de congélation de l'eau, et ce jusqu'à environ $2 Ga$.

Pourtant, les traces d'un océan liquide à l'Archéen sont nombreuses, à commencer par la présence de roches sédimentaires dès $3.8 Ga$, préservées dans les ceintures de roches vertes (see Eriksson et al. 1998, for a review). A l'inverse les traces de glaciation sont rares, les plus anciennes reconnues à ce jour étant enregistrées à $3.0\text{-}2.9 Ga$ dans les unités du Pangola Supergroup et Witwatersand Supergroup, dans le craton sud-africain de Kaapvaal en Afrique du Sud (Wiebols 1955, Harland 1981, Von Brunn et Gold 1993). Mais l'interprétation de ces dépôts reste discutable et l'Archéen est généralement considéré libre de toute glaciation (Young et Gostin 1991)

Dans ces conditions, il devait exister des processus capables de contre-balancer le déficit solaire et de maintenir des températures clémentes à la surface de la Terre. Cette question, posée très tôt par Sagan et Mullen (1972), a occupé un bon nombre de chercheurs depuis près de $40 ans$, et a largement contribué à étendre nos connaissances sur l'environnement primitif. Un nombre croissant de modèles ont ainsi vu le jour, invoquant des thématiques scientifiques variées comme les caractéristiques océaniques et atmosphériques, l'activité mantellique et hydrothermale, la biosphère et les processus de surface au Précambrien (voir Kasting 1987; 1993; 2010, Goldblatt et Zahnle 2011, pour un résumé des travaux). Parmi ces modèles, une atmosphère archéenne riche en gaz à effet de serre semble faire consensus (voir cependant Rosing et al. 2010), bien que les gaz impliqués restent sujet à débat.

Le CO_2 est aujourd'hui toujours considéré comme étant la clé du paradoxe, et une P_{CO_2} 100 à 1000 fois supérieure aux valeurs actuelles aurait permis d'empêcher le développement de glaciations (*e.g.* Eugster 1966, Walker et al. 1981, Kasting 1987;

1993, Sugitani et al. 2003). Les concentrations atmosphériques ont pu être élevées en raison (1) d'un stockage limité par les carbonates, peu présents dans les enregistrements précambriens (Walker et al. 1981, Berner et al. 1983, Berner 2004), (2) d'un recyclage sédimentaire rapide (*e.g.* Viezer et Jansen 1985), et (3) d'un volcanisme intense lié à un manteau archéen plus chaud.

Les observations géologiques montrent cependant que les niveaux de CO_2 à l'Archéen étaient au moins 5 fois trop faibles pour produire un effet de serre suffisant (Rye et al. 1995, Pavlov et al. 2000, Hessler 2004), et une contribution significative du méthane (CH_4) viendrait alors compléter l'équation (Kiehl et Dickinson 1987, Sagan et Chyba 1997, Kasting 2005). Qu'il soit produit de manière abiologique par les émanations mantelliques aux sites de résurgence hydrothermales Pavlov et al. (2000), Kasting (2005), ou de manière biologique par l'apparition et le développement d'organismes méthanogènes (Rye et al. 1995, Kasting et Pavlov 2002, Ueno et al. 2006, Trainer 2006), le méthane a pu être présent en concentrations suffisantes à l'Archéen (Kasting et al. 1983, Pavlov et al. 2003) pour combiner ses effets au dioxyde de carbone et produire un effet de serre capable de résoudre le paradoxe (Kiehl et Dickinson 1987, Sagan et Chyba 1997). L'azote, enfin, a pu jouer un rôle indirect sous sa forme N_2, en augmentant de manière significative la pression atmosphérique, ce qui augmente en retour la quantité de radiation perçue et absorbée par le dioxyde de carbone et le méthane (Goldblatt et al. 2006).

D'autres facteurs ont pu jouer dans le maintient de températures clémentes à l'Archéen, comme un albédo plus faible (voir Rosing et al. 2010) : la Terre devait tourner plus vite à l'Archéen pour préserver le moment angulaire du système Terre-Lune ($\sim 14h/j$; Williams 1998), diminuant l'albédo en réduisant la quantité de nuages à la surface d'au moins 20% (Jenkins et al. 1993). D'un autre côté, la formation des nuages devait être favorisée par l'absence de larges surfaces continentales à l'émergence, rendant peu significatif l'effet d'une rotation terrestre accrue (Galer 1991, Jenkins 1995, Rosing et al. 2010).

L'abondance de gaz à effet de serre contraste avec l'absence d'oxygène libre à la surface de la Terre précambrienne. D'après le modèle de Kasting (1991), l'atmosphère terrestre a pu évoluer en trois étapes successives :

(1) une période réductrice, sans trace d'oxygène libre dans les océans et atmosphères.

(2) une période de transition, où de faibles niveaux d'oxygène sont présents dans l'atmosphère et à la surface des océans, mais pas dans les océans profonds.

(3) une période aérobique, où l'oxygène est présent dans l'ensemble du système hydrosphère-atmosphère.

L'Archéen représente la période réductrice et anoxique de ce schéma évolutif (Holland 1994; 2006). Certains organismes marins, les cyanobactéries, devaient pourtant produire une certaine quantité d'oxygène grâce à leur métabolisme photosynthétique. Cependant, cette production était largement contre-balancée par l'incorporation rapide de l'oxygène dans les formations de fer rubanés (*Banded-Iron Formations*, BIFs), ces roches emblématiques de la Terre primitive et formées par l'oxydation et la précipitation du fer réduit Fe^{2+} présent en solution.

Les preuves géologiques pour de faibles P_{O_2} archéennes reposent essentiellement sur la présence de paléosols réduits (Macfarlane et al. 1994, Rye et Holland 1998) et de minéraux qui n'ont pu se former que dans des conditions réductrices, comme la pyrite et l'uraninite (Rasmussen et Buick 1999, Krupp et al. 1994, Grandstaff 1980). En se basant sur le fractionnement indépendant de la masse des isotopes du soufre dans les sulfides et sulfates précambriens, Kasting (2001) et Pavlov et Kasting (2002) proposent une pression partielle en oxygène (P_{O_2}) 10^{-5} fois moins importante qu'aujourd'hui (voir aussi Farquhar et al. 2000, Ono et al. 2003, Farquhar et Wing 2003).

La disparition des dépôts d'uraninite après $2.2Ga$, l'apparition massive de minéraux oxydés au Protérozoïque (Rasmussen et Buick 1999, Farquhar et al. 2000, Pavlov et Kasting 2002, Holland 2006), et le développement croissant des premières cyanobactéries et organismes eucaryotes (organismes à métabolisme photosynthétique ; Hofmann 1976, Knoll 2006), sont autant de preuves géologiques avancées pour dater ce qu'on appelle le "*Great Oxidation Event*" (GOE) et le basculement vers un monde oxygéné dès $2.45Ga$. Cet évènement marque la fin de l'Archéen et le passage de concentrations en O_2 atmosphérique de 1%PAL (Holland 1994, Towe 1996) à 15%PAL en à peine quelques millions d'années (PAL = *Present Atmospheric Level*).

1.1.2   Un climat archéen chaud et agressif.

L'étude des caractéristiques chimiques et minéralogiques des sédiments clastiques archéens offrent une vision relativement homogène des conditions de surface à cette époque. Une compilation particulièrement exhaustive des processus de sédimentation à l'Archéen est proposée par Eriksson et al. (1998), et un aperçu de marqueurs paléo-climatiques typiques est présenté dans le tableau 2.1 (D'après Hessler et Lowe 2006).

En se basant sur les indices d'altération chimique dans des argiles noires (*black shale*) de différents âges, Condie et al. (2001) propose des conditions de surface relativement clémentes entre 3.5 et 3.0Ga. Les données isotopiques sur les précipités chimiques archéens offrent un panel de températures entre $\sim$ 30 et 85° en fonction des estimations (Knauth et Lowe 1978, De Ronde et de Wit 1994, Knauth et Lowe 2003, Knauth 2005, Robert et Chaussidon 2006, Van den Boorn et al. 2010, Marin et al. 2010), toutes indiquant des conditions relativement chaudes en accord avec la présence de dépôts évaporitiques et de carbonates stromatolitiques très tôt dans l'histoire archéenne.

De telles conditions favorisent l'évaporation à la surface des océans et permettent la mise en place de précipitations fortes sur les continents (Walker et al. 1981). La présence d'un réseau hydrographique actif est soutenue par la mise en place de grès et conglomérats typiques de systèmes fluviatiles continentaux (*e.g.* Mueller et Corcoran 1998). Des concentrations accrues en CO_2 atmosphérique pourraient favoriser des conditions relativement acides dans ces systèmes (Kasting 1993), expliquant ainsi le degré de maturation des sédiments clastiques (*i.e.* abondance de quartz détritique).

D'après Chandler (1988), Corcoran et al. (1998) et Donaldson et de Kemp (1998), l'abondance des arénites quartzitiques en particulier traduit des conditions d'altération proches des environnements tropicaux modernes. Le lessivage intense des cations les plus mobiles (Ca, Na, Sr) et les indices d'altération élevés dans l'ensemble des roches clastiques (*e.g.* arénites quartzitiques, grès, conglomérats, argiles) confirment un régime érosif intense en présence de précipitations fortes à l'Archéen (*e.g.* Fedo et al. 1996, Sugitani et al. 1996, Bhat et Gosh 2001, Tosca et al. 2012).

Study	Age (Ma)	Location	Rock type	Alteration	Weathering degree	Conclusions
Eriksson and Soegaard (1985)	3300	Moodies, S. Africa Pilbara, W. Australia	Braided alluvial	Unspecified	"Severe.tropical"	Relatively high Kspar over plagioclase; high Cr and Ni → concentrated during weathering
Eriksson and Soegaard (1985)	2700–3000	Wits, Pongola, S. Africa Fortescue, W. Australia	Braided fluvial to shallow marine	Unspecified	Severe, intense	Other paleosols show severe weathering; late Archean qtz-rich sandstone and low Ca, Na, K in paleosols → intense weathering
Sassano and Rocheleau (1987)	Archean	Otish, Mistassini Basins, Canada	qtz-, feld-sandstone	Unspecified	Acidic	Low pH needed to dissolve silica; Archean weathering by hydrolysis and acid rain
Wronkiewicz and Condie (1987)	2700	Witwatersrand, S. Africa	Shale			
Feng and Kerrich (1990)	2600–2700	Abitibi Belt, Canada	Volcano-sedimentary alluvial and turbiditic	Pumpellite-prehnite	Present	Positive relationship of K–Al, K–Rb, K–Ba, K–Cs, and decoupling of V from Cr and Ni → weathering
Camire et al. (1993)	2685	Pontiac subprovince, Canadian Shield	Turbiditic greywackes	Greenschist/amphibolite	Limited	Chemical weathering limited; Ca, Sr, Ba not leached; small variation of Cr/Ni
Cullers et al. (1993)	Early Archean	Panorama Fm, Pilbara, W. Australia	Volcaniclastics	Si, K metasomatism ($T<350C$)	"Lack of"	Immobility of REE → lack of weathering
Krupp et al. (1994)	<3200	Summary	Gold-bearing conglomerate	Varied	Unspecified	Detrital pyrite and uraninite → anoxic conditions
Legault and Keiko (1994)	Late Archean	Timiskaming Group, Abitibi Belt, Canada	Turbiditic clastics	None to low	Moderate to high	Fine sandstone and shale show CIA =68–77
Fedo et al. (1996)	3000	Buhwa Greenstone Belt, Zimbabwe	Cratonic shales	Regional greenschist	Intense	CIA =95–100; Ca, Na, Sr removed; nearly all plagioclase converted to clay; intense chemical weathering in S. Africa 3.0 Ga
Sugitani et al. (1996)	Early Archean	Pilbara, W. Australia	Clastics, carbonates	Greenschist	"Extensive", acidic	Al mobility → deep weathering of basalt; Al, Ti fractionation, mobile REEs → pH <4
Donaldson and de Kemp (1998)	2900–3000	Superior and Churchill provinces, Canada	Quartz arenite	Greenschist to granulite	Intense chemical weathering	Mineralogical maturity = intense weathering; textural maturity shows importance of sedimentary processes as well
Corcoran et al. (1999)	2600	Beaulieu Rapids Fmtn, Slave province, Canada	Coarse clastics	Greenschist	Intense, aggressive	Abundant quartz and clay, minor feldspar due to intense weathering → high CO2, rainfall, temps

TABLE 1.1 – *Compilation des études favorisant un climat chaud et agressif à l'Archéen, études essentiellement basées sur les compositions chimiques et caractéristiques minéralogiques des sédiments clastiques. Ce tableau est tiré de* Hessler et Lowe (2006).

L'altération chimique a pu être limitée par l'état dénudé des surfaces continentales : l'absence de couverture végétale augmente les taux d'érosion, mais diminue en contre-partie le temps de résidence des sédiments sur les continents, limitant leur altération avant enfouissement et retrait du cycle sédimentaire (Condie et al. 2001).

1.1.3   Des océans primitifs plutôt hospitaliers.

L'apparition et l'évolution des océans primitifs est étroitement liée à l'évolution même de l'atmosphère terrestre. Les océans se sont formés à la suite de différents épisodes de vaporisation/condensation liés aux grands impacts marquant l'histoire terrestre précoce (Nisbet et Sleep 2001), la dernière grande vaporisation ayant eu lieu vers $4.2Ga$ d'après Sleep et al. (1989). Dès $4.0Ga$, la dernière phase de condensation permet la mise en place de plus de 90% du volume des océans actuels (Condie 1997), recouvrant la majeur partie de la surface terrestre en absence de reliefs continentaux élevés (Zahnle et al. 2007).

Les plus anciens sédiments marins retrouvés à ce jour sont des unités de BIFs dans la ceinture de roches vertes Akilia (Groenland), datés à $3.8Ga$ (Nutman et al. 1997), et des sédiments pélagiques métamorphisés au sein de la ceinture d'Isua, et datés à $3.7Ga$ (Rosing et al. 1996). Les traces plus anciennes d'un océan liquide se limitent aux fameux zircons de Jack Hill et Mt Narryer, datés entre 4.28 et $4.40Ga$, et dont les compositions isotopiques en oxygènes traduisent l'implication d'eau de mer dans les processus magmatiques qui ont vu leur formation (Mojzsis et al. 2001, Peck et al. 2001, Wilde et al. 2001).

Quelques dizaines de millions d'années après leur formation, soit vers la fin de l'Hadéen, les océans ont acquis des conditions favorables à l'apparition de la vie sur Terre.

• *Température.* La température des océans primitifs a fait l'objet de nombreuses études essentiellement axées sur la composition isotopique des précipités chimiques anciens, tels que les cherts et les carbonates. Si Paris et al. (1985) et de Wit et al. (1987a) proposent des températures élevées de l'ordre de 90-160°C, la plupart des études convergent vers des températures un peu plus clémentes : *i.e.* $\sim 70°C$ d'après Knauth et Lowe (1978), Knauth (2005) et Robert et Chaussidon (2006), 55-

85°C d'après Knauth et Lowe (2003), 55°C d'après Van den Boorn et al. (2010) et plus récemment $\sim$ 37-52°C d'après Marin et al. (2010).

• **Acidité.** Les interactions et équilibrages entre les océans chauds et l'atmosphère riche en CO_2 suggèrent une certaine acidité pour l'eau de mer archéenne. A la fin de l'Hadéen, la condensation de l'atmosphère primitive a pu produire un océan initialement acide (pH< 7), enrichi en CO_2 et autres composés acides type sulfurique (H_2S) ou chlorhydrique (HCl). Cependant, les émanations volcaniques au niveau des résurgences hydrothermales sous marines, et le recyclage progressif de l'eau de mer à travers les rides médio-océaniques, ont du rapidement tamponner cet excès d'acidité, augmentant le pH vers des valeurs proches de la neutralité (pH $\sim$ 8-9) (Condie 1997).

• **Salinité.** D'après Knauth (2005), la salinité des fluides archéens devait être 1.5 à 2 fois supérieure aux valeurs modernes. Un hydrothermalisme accru à l'Archéen contribuait de manière significative aux flux de cations vers les océans, tandis que les processus d'évaporation favorisent leur précipitation sous forme de sels marins (type halite). Cependant, le manque de masse continentale suffisante pour retenir ces sédiments maintient des concentrations dissoutes anormalement élevées dans les océans.

• **Etat redox.** L'absence d'oxygène libre sur la Terre archéenne implique un environnement océanique essentiellement réducteur, une caractéristique largement soutenue par le dépôt massif des BIFs, qui nécessitent la présence de fer réduit dans les océans, et par la présence quasi-systématique d'un excès en cérium dans les sédiments anciens (*e.g.* Wright et al. 1987, Holser 1997, Shields et al. 1997, Bau et al. 1998, Yang et al. 1999). Dans les océans modernes, l'oxydation du cérium réduit considérablement sa solubilité et provoque un appauvrissement des fluides océaniques par le retrait de Ce^{4+} sur les oxyhydroxydes de fer qui précipitent (*i.e.* croûtes et nodules de fer-manganèse au niveau des résurgences hydrothermales) (Goldberg et al. 1963, Elderfield et Greaves 1981, Bau et al. 1996, De Carlo et al. 1998, Bau 1999, Bau et Koschinsky 2009). L'absence de tels précipités à l'Archéen, et l'excès de cérium dans les précipités chimiques océaniques, est l'un des arguments phare en faveur d'un milieu océanique globalement anoxique.

1.2   Les cherts, roches emblématiques de l'Archéen.

C'est dans ce monde primitif chaud, humide, riche en CO_2 et pauvre en O_2 que se sont développés les premiers organismes vivants. Selon certains auteurs, les microbes procaryotes font déjà partie intégrante de la Terre primitive à 3.5-3.8Ga (Schopf 1993, Mojzsis et al. 1996, Rosing 1999, Westall et al. 2001, Rosing et Frei 2004), probablement les premiers descendants des organismes hyperthermophiles soupçonnés à l'Hadéen. L'arrivée des organismes eucaryotes précèdera le GOE à 2.7Ga (Brocks et al. 1999), puis les métazoaires s'établiront vers 0.55Ga (Runnegar 1982).

Les cherts Archéens ont permis de préserver les plus anciens organismes primitifs jusqu'à ce jour, faisant de ces roches une cible scientifique majeure pour l'étude des conditions environnementales qui ont vu l'apparition de la vie sur Terre (*e.g.* Awramik et al. 1983, Schopf 1993, Schopf et al. 2007, Westall et al. 2001, Allwood 2006, Allwood et al. 2007, Hofmann et Bolhar 2007, van Kranendonk 2007, Wacey 2010). Ces roches hautement siliceuses (> 75-80%) sont présentes en abondance dans l'ensemble des cratons archéens, et traduisent des conditions physicochimiques très particulières dans les océans primitifs.

Sur la Terre moderne, les concentrations en silice océanique dissoute sont trop faibles pour permettre la précipitation massive de silice inorganique. Issue essentiellement de l'altération des silicates à la surface des continents (Piepgras et Wasseburg 1980, Andersson et al. 2008), la silice est rapidement consommée par les organismes marins constructeurs de tests siliceux, comme les diatomées, les radiolaires et les éponges à spicules siliceux. L'accumulation de ces organismes sur le plancher océanique constitue le principal mécanisme contrebalançant les flux de silice continentaux, maintenant les faibles concentrations et l'état de sous-saturation des océans modernes.

Une partie de la silice stockée dans la croûte océanique est remobilisée lors du recyclage de l'eau de mer : les fluides océaniques percolent à travers les fissures du plancher, se réchauffent et interagissent en profondeur avec les basaltes de la croûte, et s'enrichissent en silice (et en éléments traces) par ré-équilibrage chimique avec le quartz contenu dans ces roches (Norton 1984, Seyfried et al. 1998,

Elderfield et al. 1999, Shibuya et al. 2010). Cette eau de mer recyclée remonte vers la surface sous la forme de résurgences hydrothermales aux niveau des rides médio-océaniques pour former les fameuses fumeurs noires, ou en dehors des zones de ride pour former les fumeurs blanches (*e.g.* James et al. 1995, Haas et al. 1995, Gamo et al. 2001, Kelley et al. 2001, Wheat et al. 2002, Douville et al. 2002, Ludwig et al. 2006). Une large portion de silice est cependant perdue alors même que les fluides remontent vers la surface. La solubilité de la silice dépend essentiellement des paramètres physico-chimiques des fluides considérés, et la température en particulier fait partie des facteurs les plus sensibles (Fournier 1985, Herzig et al. 1988) : le gradient thermique extrême entre les fluides hydrothermaux ascendants et les fonds marins entraine une précipitation massive de la silice au coeur même du système hydrothermal, essentiellement par incorporation dans les roches encaissantes désormais silicifiées (*e.g.* Seyfried 1987). A la surface, le peu de silice restante est rapidement dilué en raison de l'état de sous-saturation des océans déjà établi par la balance efficace des flux continentaux et organismes marins.

Les contributions hydrothermales sont donc aujourd'hui négligeables, mais un tout autre schéma se dessine pour l'Archéen. La surface continentale à l'émergence était bien moindre qu'aujourd'hui, ne représentant probablement que 10-15% de la surface actuelle à $3.8 Ga$ (Taylor et McLennan 1995) et tout juste 20% il y a $2.8 Ga$ (Galer 1991, Jenkins 1995), limitant ainsi les flux de silice vers les océans primitifs. A l'inverse, les contributions hydrothermales étaient bien plus importantes qu'aujourd'hui : un manteau archéen plus chaud et des longueurs de rides océaniques plus grandes, entre des proto-plaques continentales plus petites, ont dû favoriser un hydrothermalisme intense sur la Terre primitive (*e.g.* Martin et al. 2006) et des flux majeurs de silice recyclée vers les océans. Un dernier facteur d'enrichissement est le climat chaud à l'Archéen, qui favorise une évaporation intense à la surface des océans et aide à maintenir des concentrations élevées en silice dissoute (*e.g.* Siever 1992, Maliva et al. 2005).

De l'autre côté de la balance, l'absence des organismes à test siliceux ne permet pas le stockage biologique de cette silice océanique, et seuls les processus abiologiques peuvent alors tamponner les concentrations (*e.g.* Siever 1992, Treguer et al. 1995, Perry et Lefticariu 2003, Maliva et al. 2005). La formation massive de cherts

à l'Archéen constitue ainsi la réponse de l'environnement à ces concentrations excessives.

La précipitation colossale de silice à cette période se traduit par la silicification quasi-systématique de toute roche sédimentaire ou magmatique en contact avec l'eau de mer, et par la formation massive de sédiments chimiques à la surface du plancher océanique (Duchac et Hanor 1987, Hanor et Duchac 1990, Knauth 1994, Lowe 1999, Perry et Lefticariu 2003, Hofmann et Wilson 2007, Orberger et al. 2006). Initialement précipitée sous une forme amorphe (type opale ou gel de silice), la conversion de la silice en quartz et autres formes cristallines pendant la diagenèse a permis de produire des roches hautement résistantes à l'altération et de les préserver jusqu'à nos jours dans l'ensemble des cratons archéens.

Dans ces conditions, le lien étroit entre les cherts et les eaux de surface font de ces roches un outil puissant pour comprendre quelles étaient ces conditions si favorables à l'émergence et à l'évolution de la vie sur Terre au Précambrien. La composition chimique et isotopique de ces roches est ainsi largement utilisée pour retrouver, entre autres, la température (*e.g.* Knauth et Lowe 1978, Paris et al. 1985, de Wit et al. 1987a, Knauth et Lowe 2003, Knauth 2005, Robert et Chaussidon 2006, Van den Boorn et al. 2010, Marin et al. 2010) et les caractéristiques géochimiques des océans archéens (*e.g.* Sugitani 1992, Murray et al. 1992b, Bolhar et al. 2004, Van den Boorn et al. 2007; 2010, Allwood et al. 2010), une approche basée sur le postulat que les cherts sont effectivement capables de retenir la composition chimique des fluides dont ils sont issus.

L'intérêt des cherts ne se limite pas aux processus océaniques et s'étend à la fois aux processus hydrothermaux et circulations fluides dans la croûte (*e.g.* Paris et al. 1985, Van Kranendonk et Pirajno 2004, de Vries et Touret 2007, Van den Boorn et al. 2007, Hofmann et Wilson 2007) et aux processus d'altération à la surface des continents (*e.g.* Sugitani et al. 1996; 1998) en lien étroit avec les conditions climatiques et atmosphériques (*e.g.* Knauth et Lowe 1978; 2003).

1.3 Contexte géologique et sites de l'étude.

Les cratons Archéens ($< 2.5Ga$) constituent les plus anciennes traces de la Terre primitive et échantillonnent des périodes remontant à $4Ga$ dans le Bouclier canadien (Craton Acasta), $3.8Ga$ au Groenland (Ceintures d'Isua, Akilia et Amitsoq) et $3.5Ga$ en Afrique du Sud (Craton de Kaapvaal) et au Nord-Ouest de l'Australie (Craton de Pilbara). Au coeur de ces cratons, les ceintures de roches vertes représentent les reliquats de la Terre primitive, préservés du recyclage tectonique et transmis jusqu'à nous sous la forme d'unités tectono-stratigraphiques, hautement déformées et entourées de terrains métamorphiques (orthogneiss) et plutons magmatiques.

La ceinture de Barberton fait partie des enregistrements Archéens les mieux préservés sur Terre et présente de nombreuses similitudes avec sa jumelle Australienne de Pilbara. Cet enregistrement volcano-sédimentaire, quasi-continu sur près de $12km$ d'épaisseur, s'est mis en place entre 3.55 et $3.22Ga$ (Krüner et al. 1991, Hofmann 2005, Hofmann et Harris 2008). La ceinture s'étend dans la direction NE-SW sur près de 100-150km pour une largeur d'à peine 50km. Elle se présente aujourd'hui sous la forme de terrains hautement déformés en une série de synclinaux et anticlinaux séparés par des zones de cisaillement.

Le contexte géologique et les sites de l'étude étant largement décrits dans les différents chapitres, je ne présente ici qu'un résumé rapide des grandes unités et des grands évènements qui ont marqué l'histoire de la ceinture.

Le groupe d'Onverwacht (3.55-3.26Ga ; Kröner et al. 1996, Byerly et al. 1996) représente la phase volcanique active de la ceinture et constitue une série épaisse caractérisée par plusieurs cycles volcano-sédimentaires. Chaque cycle se compose d'une base ultramafique (komatiites, basaltes komatiitiques, basaltes) évoluant vers des laves et dépôts volcanoclastiques felsiques (*e.g.* dacites), l'ensemble étant recouvert d'unités de cherts souvent lités et recoupées de dykes et fractures remplis également de matériel siliceux. Un environnement de type plateau océanique est envisagé pour expliquer la mise en place de ces unités en l'absence de laves acides et de séries sédimentaires clastiques épaisses. Le groupe de Fig Tree (3.26-3.23Ga)
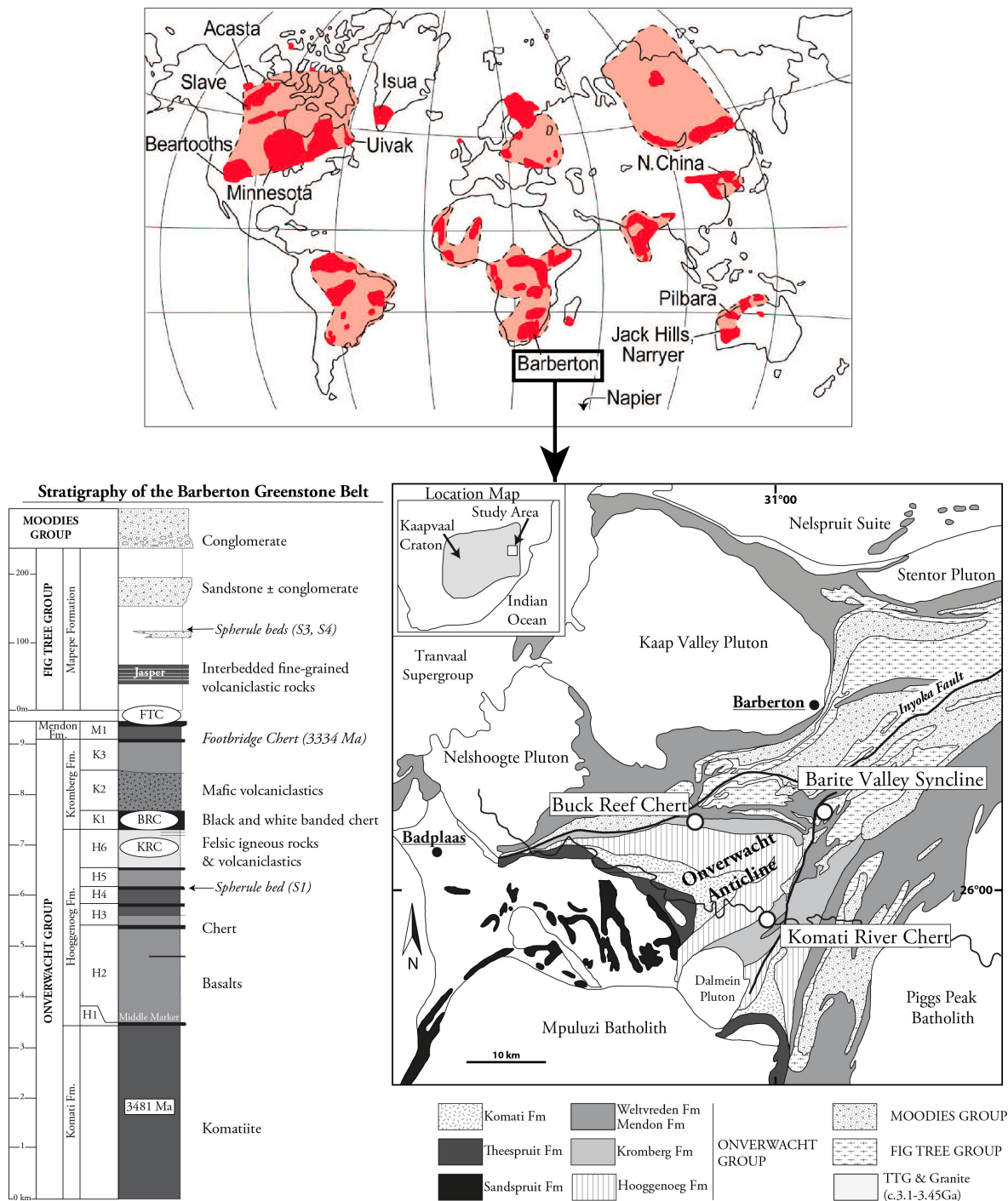
FIGURE 1.1 – *Carte géologique (d'après Hofmann 2005) et colonne stratigraphique simplifiée (d'après Lowe et al. 2003) de la ceinture de roches vertes de Barberton. La carte mondiale (Valley 2006) montre en rouge la répartition des terrains archéens. Les sites de Komati River (KRC), Buck Reef (BRC) et Barite Valley (FTC) sont localisés sur la carte et dans la colonne stratigraphique.*

marque une évolution vers un milieu de type arc insulaire et montre les prémices de l'histoire orogénique de la ceinture. Il se compose d'une série épaisse de sédiments siliciclastiques, issus du remaniement des unités sous-jacentes d'Onverwacht, et d'unités volcaniques essentiellement felsiques (Condie et al. 1970, Heinrichs 1980, Hofmann 2005). Le groupe de Moodies (3.22-3.21Ga) termine la séquence par une séquence de sédiments détritiques, grès quartzeux et conglomérats, déposés en conditions fluviatiles ou proche du continent.

Dans l'ensemble de ces unités, les roches sont faiblement métamorphisées et restent globalement dans le faciès schiste vert ($< 320°C$; Xie et al. 1997, Grosch et al. 2012), un métamorphisme qui peut atteindre le faciès amphibolite à proximité des fameux plutons TTG (tonalite-trondhjemite-granotiorite) qui bordent la ceinture (Hofmann et Harris 2008). Ces plutons se sont mis en place à la faveur de trois épisodes magmatiques majeurs à $3.45Ga$, $3.22Ga$ et $3.1Ga$ (Kamo et Davis 1994). L'histoire de la ceinture est également marquée par plusieurs impact météoritiques majeurs, révélés par le présence de niveaux à sphérules, et datés entre 3.47 et $3.24Ga$ (Byerly et al. 1996; 2002, Lowe et Byerly 2003).

Trois sites de la ceinture ont été choisis pour cette étude, un choix essentiellement basé sur un projet de forage mis en place en 2006, mais qui n'aura finalement vu le jour qu'en 2011, empêchant l'intégration de ces échantillons dans ces travaux. Les sites de Komati River, Buck Reef et Barite Valley sont localisés dans la Figure 2.2 et seront amplement détaillés dans les chapitres à venir. Ils représentent trois contextes géologiques et environnementaux très différents où se sont déposés des cherts d'origines variées. Ce panel d'échantillon forme la base de cette étude, dont les objectifs sont détaillés dans la section suivante.

1.4 Objectifs de la thèse et présentation du manuscrit.

Si la section 1.2 met en avant l'intérêt que peuvent représenter les cherts dans l'étude des conditions régnant sur la Terre primitive, elle ne reflète pas l'ambiguité de ces roches emblématiques de l'Archéen. Malgré la littérature extensive qui a vu le jour ces 50 dernières années, nombre de questions restent en suspend quant à l'origine de la silice et aux processus même de formation des cherts, des questions cruciales qui ont motivé cette étude.

J'ai choisi dans cette travaux d'aborder les questions suivantes :

Comment différencier les différents types de chert rencontrés à l'Archéen ?

Comment se sont-ils formés et à partir de quel(s) fluide(s) siliceux ?

Quel est le signal chimique contenu dans ces cherts et comment s'en servir pour les reconstructions paléo-environnementales ?

Afin de répondre à ces questions fondamentales, je propose une étude complète des cherts issus des sites de Komati River, Buck Reef et Barite Valley, représentatifs de contextes environnementaux variés :

• Les cherts de **Komati River** se présentent sous la forme d'horizons siliceux au sommet de niveaux turbiditiques. Ils se sont mis en place en conditions peu profondes, proches du continent et dans un environnement où les flux clastiques sont abondants.

• Le site de **Buck Reef** contient une série épaisse de cherts lités, formés d'alternance de cherts noirs et blancs déposés sur une plateforme continentale en subsidence, depuis des conditions évaporitiques et lagunaires jusqu'à des environnements plus profonds situés sous la limite d'action des vagues ($> 200m$). Ce site se caractérise en outre par une absence notable de flux clastiques.

• A **Barite Valley**, trois types de cherts sont rencontrés : des roches sédimentaires silicifiées qui constituent les unités principales du site, des niveaux de chert noir concordants et en intercalation dans ces unités sédimentaires, et des dykes de chert recoupant l'ensemble de ces formations. Les séries clastiques silicifiées traduisent un environnement d'abord marin et profond puis continental et fluviatile.

En me basant sur la littérature et sur les différents types de chert rencontrés dans ces différents sites, je propose une nouvelle nomenclature, basée sur les trois principaux processus de formation des cherts, et qui servira de fil rouge dans ce manuscrit.

(I) La première partie de ces travaux consiste à identifier l'origine des cherts de chacun des sites échantillonnés, leur contexte précis de mise en place (environnement, contexte géologique et tectonique) et leur mode de formation.

• **Le Chapitre 2** est dédié aux sites de Komati River et Buck Reef, contenant les meilleurs échantillons de cherts déposés à la surface du plancher océanique archéen. En combinant une approche de terrain et pétrologique, je propose des critères de reconnaissance pour distinguer ces cherts, en accord avec la nomenclature définie en premier lieu. Ces données me permettent de proposer différents modèles de formation pour les cherts de ces sites, en relation étroite avec les conditions environnementales qui ont vu leur formation.

• **Le Chapitre 3** est dédié aux cherts de fracture de Barite Valley. L'approche ici est la même, combinant observations de terrain et pétrologiques afin de caractériser les conditions de mise en place de ces fractures et la nature des fluides siliceux qui les ont remplies. Une attention très particulière est donnée ici à la rhéologie des cherts au moment de leur mise en place, une approche peu courante qui révèle une comportement très particulier dans ce contexte intra-crustal.

(2) La deuxième partie de ces travaux s'intéresse plus particulièrement à identifier ce qui contrôle la composition chimique des cherts et à déterminer quels types d'informations paléo-environnementales peuvent être préservées de ces compositions.

• **Le Chapitre 4** se base sur la comparaison entre la composition géochimique des cherts et celle des différentes phases minérales qui le constitue. Cette approche me permet d'identifier les différents signaux chimiques contenus dans les cherts des trois sites. Ayant caractérisé ces signatures, je teste les proxys géochimiques modernes couramment utilisés pour rechercher les traces d'un signal océanique dans les précipités chimiques anciens.

• **Le Chapitre 5** vient compléter ces données par l'analyse des compositions isotopiques en silicium et oxygène des grains individuels de microquartz constituant la majorité des cherts. Ces données me permettent de retracer l'origine de la silice et de tester ainsi l'ensemble des modèles proposés dans ces travaux et les critères de reconnaissance établis dans le premier chapitre.

ORIGINE DES CHERTS ET PROCESSUS DE FORMATION.

2

CE chapitre présente un premier article axé sur les observations de terrain et pétrologiques des cherts de Buck Reef et Komati River. Nous proposons une nouvelle nomenclature pour les cherts, de nouveaux modèles de formation et une ré-évaluation des contextes environnementaux archéens pour chaque site.

_____

THIS chapter presents a first article focused on field and petrological observations of Buck Reef and Komati River cherts. We offer a new nomenclature for cherts, new models of their formation and a re-evaluation of Archean environmental context for each area.

2.1   Article 1

Chert recognition and new insights in formation process based on field and petrological approaches : a case study from the Barberton Greenstone Belt, $3.5 - 3.2Ga$, South Africa.

Morgane Ledevin[1a], Nicholas Arndt[1], Alexandre Simionovici[1], Marc Ulrich[1]

[1] ISTerre, Maison des Géosciences, Grenoble, France
[a] Corresponding author : morgane.ledevin@ujf-grenoble.fr

Abstract

Field and petrological observations are used to investigate the nature, origin and formation of Komati River (3432Ma) and Buck Reef (3416Ma) cherts from the Barberton Greenstone Belt, South Africa. We first introduce a new nomenclature based on Archean chert formation process : C-cherts form by the chemical precipitation of silica at surface condition from oceanic fluids, either as silica gel (or siliceous ooze) or as cement in unconsolidated sediments ; F-cherts precipitate in discordant and concordant veins from circulating fluids ; S-cherts result of replacement by Si-metasomatism of pre-existing rocks by percolating fluids.

The Komati River cherts formed as C-chert at the surface of turbidite units. Their primary origin is evidenced by (1) the lack of secondary fluid circulation features, (2) the presence of sedimentary structures typical of surface conditions (i.e. flame structures, ripples, chert pebbles), (3) the chemical/physical preservation of turbidite clastic particles from Si-metasomatism and (4) the continuous evolution from silica-cemented siltstone to homogeneous chert. Komati River cherts deposited as a siliceous ooze during the waning stages of turbidite emplacement. The precipitation of silica is favored by efficient sorption on suspended clay particles. The chert originated from marine fluids with possible porosity fluid contribution from deeper part of the turbidite.

The Buck Reef cherts deposited at individual, massive black and white C-chert layers in a clastic-free, Si-saturated environment. (1) The sharp contact between both facies, (2) the presence of microbial mats soft-deformed at the interface, (3) the disruption of white layers as slabs in conglomerates and (4) the abundant soft deformation structures occurring at or close to the seabed (i.e. load cast, ball-and-pillow structures) are all evidence for their deposition on the seafloor. A microcrystalline fabrics mostly composed of microquartz is taken as representative of silica precipitation at surface conditions whereas void-filling and vein textures characterized by chalcedony and megaquartz are evidence for secondary fluid precipitations.

We propose a model decoupling the origin of the black and white facies. Micro-layers of carbonaceous matter and silica in black cherts are interpreted as seasonal variations where pure silica precipitate during winter and microbial community growth during summer. The high purity white layers may result from very rapid, dramatic silica precipitation with a possible periodicity of a few thousand years. We envisage the destabilization of the surface layer in a stratified water column and proposed several trigger mechanisms among which climatic variations at a glacial/inter-glacial scale seems the most likely. Another possibility is the involvement of Si-enriched, cold bottom seawater in an upwelling system and/or hydrothermal plume contribution from hydrothermal vents away from the continental platform.

Key Words - Archean environment ; Chert formation ; Recognition criteria.

2.1.1 Introduction

On the modern Earth, ever since the Proterozoic, both the silica cycle and the formation of cherts are controlled by biological activity ; during the Archean, however, the absence of skeleton-forming organism allowed only inorganic silica precipitation (*e.g.* Siever 1992, Treguer et al. 1995, Perry et Lefticariu 2003, Maliva et al. 2005). The massive deposits of cherts found in all Archaean greenstone belts are therefore interpreted to reflect the physico-chemical conditions of the eon, and particularly elevated concentrations of dissolved silica in the oceans (*e.g.* Siever 1992, Maliva et al. 2005). Like banded iron formations (BIFs), some Archaean cherts are considered to have precipitated from seawater, and their composition is regarded as representative of early ocean chemistry, making them among the most powerful tools to investigate early Earth environments (*e.g.* Derry et Jacobsen 1990, Sugitani et al. 1996; 1998, Knauth et Lowe 2003, Perry et Lefticariu 2003; 2006, Kato et Nakamura 2003, Bolhar et al. 2005, Robert et Chaussidon 2006, Jaffres et al. 2007).

There is, however, no consensus on the nomenclature, and even the definition, of chert. All authors agree that the silica content must exceed 75 to $80wt\%$, but differences emerge regarding the origin of cherts. In the most common models, most Archean cherts are considered to be the result of silicification of preexisting rocks, including (1) volcaniclastic and terrigenous debris (*e.g.* Lowe et Knauth 1977, Lowe 1980, Paris et al. 1985, de Vries 2004), (2) chemical sediments such as carbonates and evaporites (Knauth 1973, Lowe et Knauth 1977, Knauth et Lowe 1978, Lowe et Byerly 1986b, Weis et Wasserburg 1987, Lowe et Fisher Worrell 1999, Van Kranendonk et al. 2003) and (3) massive, layered volcanic rocks (Hofmann et Wilson 2007, Hofmann et Harris 2008). The silicification is thought to be triggered either by convective fluid circulation during hydrothermal activity (Knauth et Lowe 1978, de Wit 1982, Duchac et Hanor 1987, Paris et al. 1985, de Wit et Hart 1993, Knauth 1994, Perry et Lefticariu 2003, Hofmann 2005, Hofmann et Wilson 2007, Hofmann et Harris 2008), or by low-temperature seawater-rock interaction at or below the surface during early diagenesis (Knauth et Lowe 1978, de Wit 1982, Sugitani 1992, Lowe 1999, Lowe et Fisher Worrell 1999, Van Kranendonk et Pirajno 2004, Tice et Lowe 2006, Rouchon et Orberger 2008). Other proposed sources of silica could be the serpentinization of oceanic rocks (de Wit 1982) and the devitrification of vol-

caniclastic sediments (Paris et al. 1985) or volcanic glasses (Knauth 2005). Direct precipitation of silica from oceanic water is another model that was first proposed for jasper layers in banded iron formations, then extended to other siliceous deposits such as banded cherts. The silica can be precipitated from Si-oversaturated seawater (Knauth et Lowe 1978, Hesse 1989, Sugitani et al. 1998, Perry et Lefticariu 2003, Hofmann 2005, Tice et Lowe 2006), from hydrothermal vent fluids near volcanic, active settings (*e.g.* mid-oceanic ridges)(*e.g.* Sugitani 1992), or from a mixture of both (*e.g.* Derry et Jacobsen 1990, Frei et Polat 2007, Van den Boorn et al. 2007; 2010, Marin-Carbonne et al. 2012).

In addition to this long-standing debate, the absence of clear nomenclature that distinguishes different chert types renders difficult the comparison of various chert studies and hinders a better understanding of Archean cherts. Most of the previous commonly used nomenclatures are based on (1) chert color, with a large range of shades (*e.g.* light to dark grey, greenish grey to green, bluish to dark blue, etc.), (2) structure and outcrop organization (*e.g.* laminated, massive, vein, banded, etc.), and/or (3) minor component contents (*e.g.* carbonaceous, ferruginous, argillaceous, tuffaceous, etc.). Such terminologies, although useful for chert descriptions, provide no information on the chert formation process, and they vary widely from one author to another.

Van den Boorn et al. (2007) was among the first to propose a nomenclature based on chert formation process and we provide here a similar terminology for our classification (Fig.2.1). Primary cherts are defined as primary chemical precipitates which can be of two origins : (1) we conserve the term "C-chert" (*i.e.* chemical-chert) of Van den Boorn et al. (2007) for oceanic precipitates, perhaps of a silica-rich colloidal gel, directly on the ocean floor or as primary, early diagenetic cement in the uppermost sedimentary layers. (2) We introduce the term "F-chert" (*i.e.* fracture-filling-chert) for discordant and concordant chert precipitated in veins/fractures from fluids that circulated through the crust (*e.g.* hydrothermal fluids, diagenetic fluid escapement, shallow seawater circulation). (3) Secondary cherts are the result of replacement by Si-metasomatism of a sedimentary or volcanic protolith, either during percolation of low-temperature seawater or by circulation of low- to high-temperature silica-rich hydrothermal or diagenetic fluids. We also conserve here
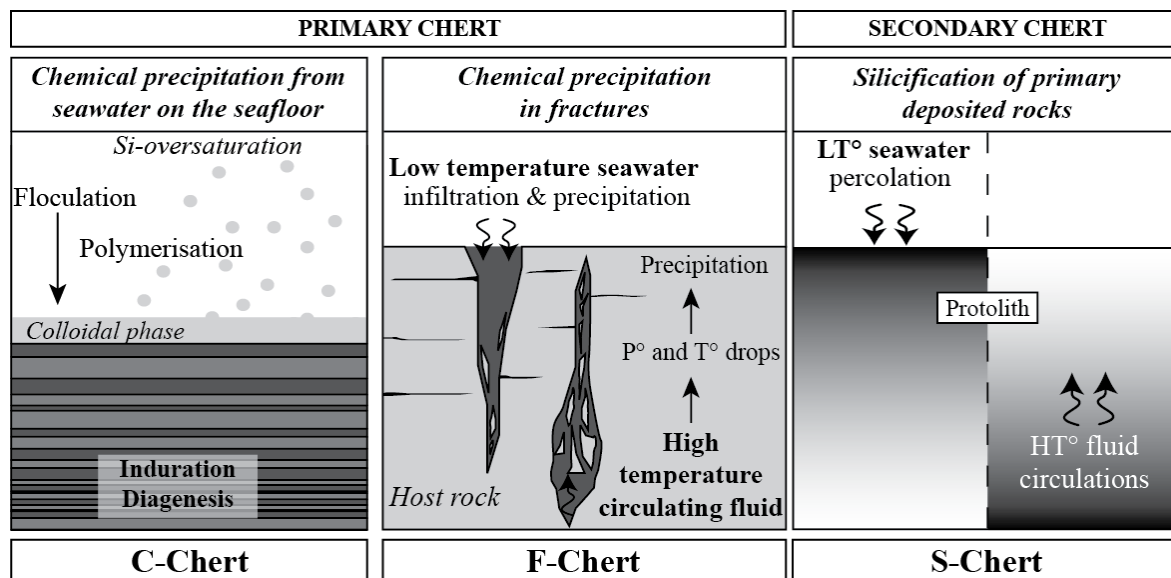
PRIMARY CHERT		SECONDARY CHERT
Chemical precipitation from seawater on the seafloor	*Chemical precipitation in fractures*	*Silicification of primary deposited rocks*

Si-oversaturation

Floculation

Polymerisation

Colloidal phase

Induration Diagenesis

C-Chert

Low temperature seawater infiltration & precipitation

Precipitation

P° and T° drops

High temperature circulating fluid

Host rock

F-Chert

LT° seawater percolation

Protolith

HT° fluid circulations

S-Chert

FIGURE 2.1 – *Schematic representation of the new nomenclature proposed for cherts based on their formation process. The nomenclature is modified from* Van den Boorn et al. (2007). *Primary cherts form by chemical precipitation of silica in aqueous environments oversaturated with respect to dissolved silica. They are divided into oceanic cherts (or C-chert), precipitated from low temperature seawater, and fracture-filling chert (or F-chert), precipitated in fractures or concordant veins, either from seawater or hydrothermal fluids. Secondary cherts (or S-chert) are the silicification product of sedimentary or volcanic protolith by low temperature seawater percolation or low to high temperature hydrothermal fluid circulations.*

the term S-chert of Van den Boorn et al. (2007). This nomenclature and associated formation processes are summarized in Figure 2.1.

C-cherts best represent the chemistry of ancient seawater and are a major target for all studies focused on early Earth environment and oceans. In the Archean Barberton Greenstone Belt ($3.5 - 3.2By$) in South Africa, the best candidates for primary cherts are found in banded chert sequences, *i.e.* black and white banded cherts, ferruginous banded cherts and banded iron formations, where bands of nearly pure, white or beige-colored silica alternate with darker bands of carbonaceous, iron-rich, carbon-rich siliceous or detrital sediment. As previously emphasized, opinion is divided concerning the origin of the pure white chert layers : depending on the author, they are supposed to be either secondary cherts (*e.g.* Lowe et Knauth 1977, Lowe et Fisher Worrell 1999, Walsh et Lowe 1999, Knauth et Lowe 2003, Hofmann 2005, Hofmann et Bolhar 2007), or of marine origin and formed during early diagenesis (Lowe 1999, Sugitani 1992, Tice et Lowe 2006), or
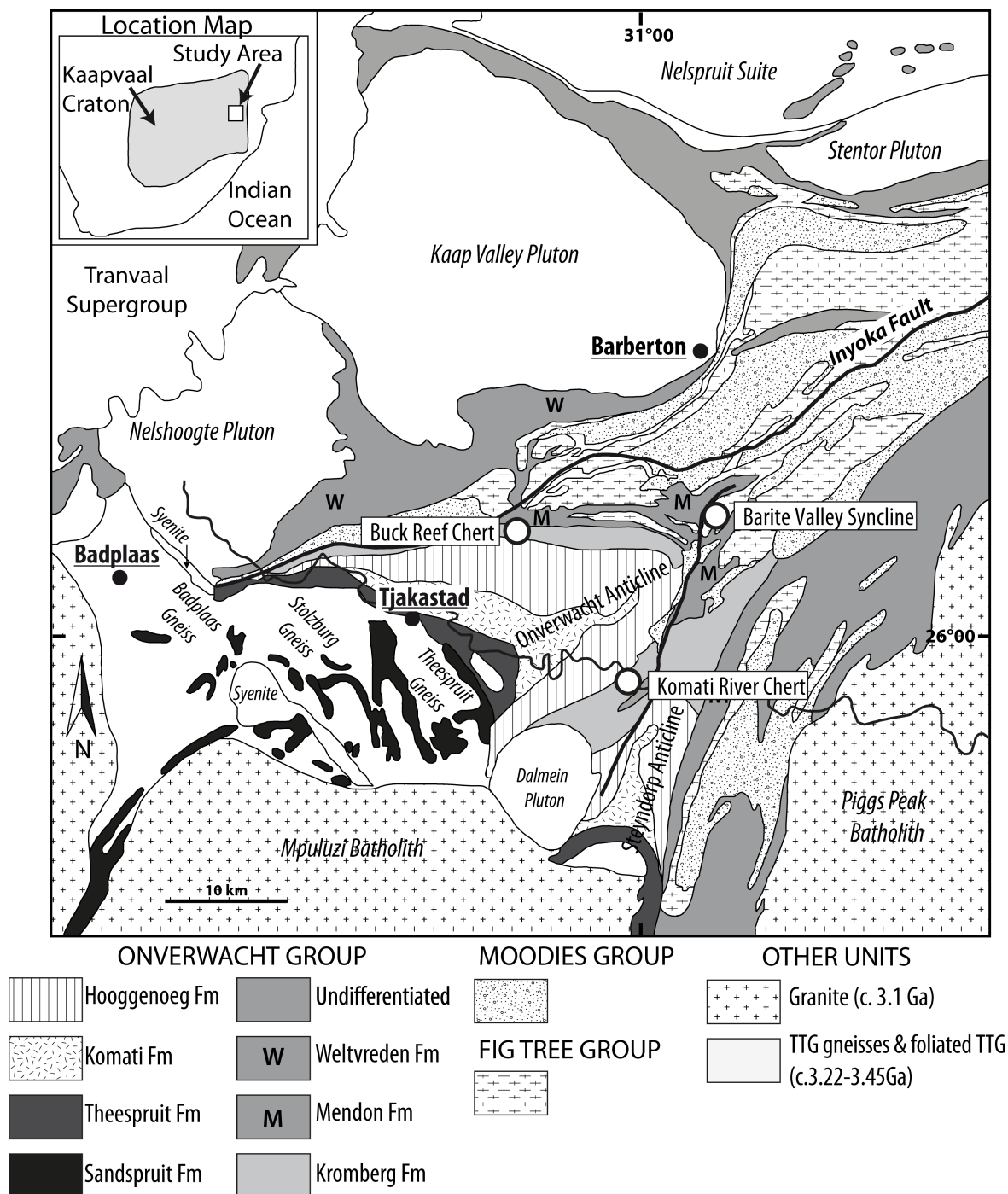
FIGURE 2.2 – *Geological map of the Barberton Greenstone Belt, 3.5 − 3.2By, South Africa, modified from Hofmann (2005). The Onverwacht, Fig Tree and Moodies Groups are a typical succession of volcanic and sedimentary rocks : the base is dominated by mafic and ultramafic rocks with minor sedimentary intercalation, and the top of the sequence is largely dominated by clastic sedimentary rocks with minor basaltic intercalations. These units form the core of the belt and are folded and tilted between major magmatic intrusions mainly made of TTG (Tonalite-Trondjemite-Granodiorite).*

of hydrothermal origin (Paris et al. 1985, Duchac et Hanor 1987, Sugitani 1992, Nijman et al. 1999, de Vries 2004, Lindsay et al. 2005, Orberger et al. 2006, Hofmann et Bolhar 2007, Hofmann et Wilson 2007).

Van den Boorn et al. (2007) interpreted C-cherts as orthochemical precipitates of silica and he envisaged their precipitation as colloidal gel that formed by flocculation/polymerization in silica-saturated seawater. Flocs of silica aggregate in the water column until a critical size is reached and settling occurs. The "gelling" (*i.e.* accumulation) of flocs on the seafloor leads to the formation of an amorphous silica precursor that may have totally dissolved before reprecipitating as microquartz to form the primary chert during the earliest stage of diagenesis (Hesse 1989, Knauth 1994, Marin et al. 2010, Marin-Carbonne et al. 2012). No traces of early gels remain because of such diagenetic (re-)crystallization processes but rheological and mineralogical evidence should be conserved.

Criteria for the recognition of the various chert types are ambiguous and none is able to distinguish such a primary oceanic precipitate from hydrothermal precipitates or secondary cherts. Criteria include field relations and sedimentary structures (*e.g.* Knauth et Lowe 2003, Maliva et al. 2005), petrological characteristics (*e.g.* Knauth 1994, Knauth et Lowe 2003), and trace element and/or isotopic composition (*e.g.* Kato et Nakamura 2003, Bolhar et al. 2005, Van den Boorn et al. 2007; 2010, Marin et al. 2010, Marin-Carbonne et al. 2011; 2012, and Chapter 4) of cherts, the latter being the most commonly used approaches.

To better understand the origin of Archean cherts, we conducted field, petrological and microanalytical studies of well-preserved examples from the $3.5 - 3.2 Ga$ Barberton Greenstone Belt in South Africa. We first review previous interpretation of the Archean environment in the studied areas, then propose and discuss a new model for chert formation. We also use this approach to develop new field and petrological criteria for chert type recognition, especially to distinguish C-cherts from S-cherts. Such criteria currently do not exist but need to be developed to avoid misinterpretation of the chemical composition of cherts. F-cherts will not be discussed as they are the subject of another paper (Chapter 3). We also conducted geochemical analyses with the aim of testing the chemical proxies commonly used

to identify oceanic signatures in chert compositions. This part of the project is the subject of a third paper (Chapter 4).

2.1.2   Geological context : the Barberton Greenstone belt

Archean rocks of the Barberton greenstone belt ($3.5 - 3.2By$) in South Africa (Fig.2.2) include a well-preserved volcano-sedimentary succession known as the Swaziland Supergroup or Barberton Supergroup (*e.g.* Viljoen et Viljoen 1969b, Lowe et Byerly 1999). Three main units are defined, with locations reported in Figure 2.2 and lithologies detailed in Figure 2.3. The Onverwacht Group ($3530 - 3334Ma$) (Viljoen et Viljoen 1969b;a, Armstrong et al. 1990, Kröner et al. 1991, Lowe et Byerly 1999, Hofmann 2005, Hofmann et Harris 2008) forms the base of the belt and is essentially composed of mafic to ultramafic igneous rocks, mainly komatiites, with minor sedimentary intercalations. It is divided into four subunits : the Komati, Hooggenoeg, Kromberg and Mendon Formations (*e.g.* Viljoen et Viljoen 1969c, Armstrong et al. 1990, Kröner et al. 1991, Kamo et Davis 1994, Byerly et al. 1996, Lowe et Byerly 1999). It evolves upward to the argillaceous Fig Tree Group ($3258 - 3226Ma$) (*e.g.* Kröner et al. 1991, Byerly et al. 1993, Hofmann 2005), in which sedimentary rocks become dominant. Minor felsic-siliciclastic tuffs, and various depositional environments are recorded, ranging from coastal to deep sea and deltaic to alluvial deposits (Lowe et Nocita 1999). The uppermost Moodies Group ($3230 - 3110Ma$) (Kröner et al. 1991, Kamo et Davis 1994) consists of arenaceous sedimentary rocks, with facies representative of alluvial to deep sea environments (see following authors for further stratigraphic details : Viljoen et Viljoen 1969a, Brandl et al. 2006, Lowe et Byerly 1999, Tice et Lowe 2004, Hofmann 2005, de Wit et al. 2011, Furnes et al. 2011).

During Archean tectonics, the Barberton units underwent strong deformation that folded and tilted most of the sequence to sub-vertical or vertical orientations. During their deposition, diagenesis and deformation, the rocks of the belt were altered and metasomatised, but in the sections we sampled the metamorphic grade did not exceed lower greenschist facies (Button 1973, Miyano et Beukes 1984, Ward 1995, Toulkeridis et al. 1998, Tice et al. 2004, Rouchon et Orberger 2008, Grosch et al. 2012).
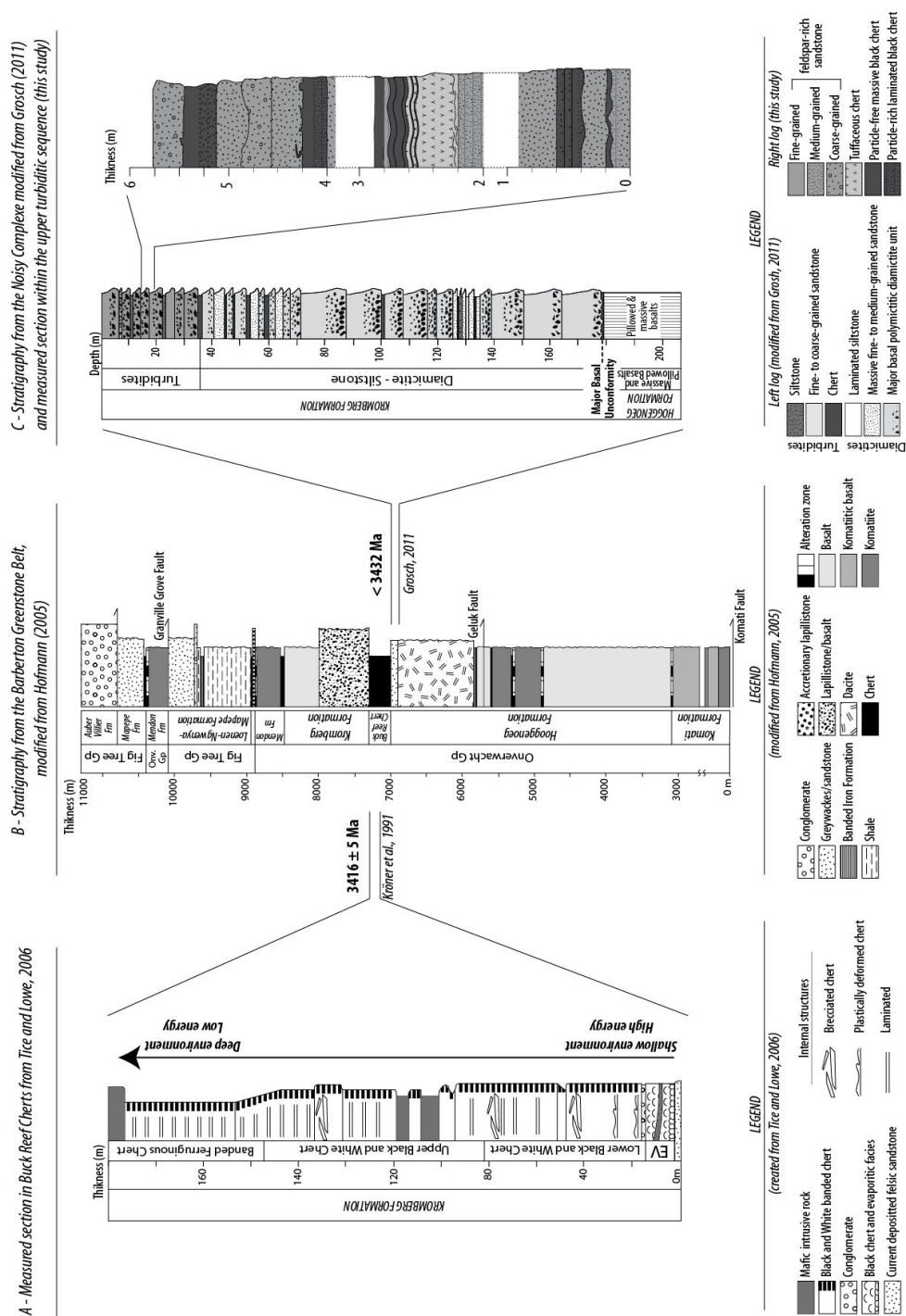
FIGURE 2.3 – *Stratigraphic columns of (B) the Barberton Greenstone Belt, (A) the Buck Reef area and (C) the Komati River area (C), modified from* Hofmann *(*2005*),* Tice et Lowe *(*2006*) and* Grosch *et al. (*2011*) respectively. The rightmost stratigraphic column is a measured section from this study realized along the Komati River banks. The global column from the whole Barberton belt (B) shows typical upward evolution of greenstones, from mafic to ultramafic rocks with few sedimentary units to thick clastic sedimentary units with few basaltic intercalations. The Buck Reef sequence (A) is a* 250 − 400m *thick unit of siliceous deposits mainly composed of black and white banded cherts with varying ferruginous alteration. The Komati River sequence (C) is a 200m thick clastic unit composed of diamictites and turbidites. The rightmost log is from this study and evidenced black chert intercalations within turbiditic units. Cherts are located at uppermost part of turbidite events with a gradational transition from turbidite to chert (see Figure* 2.4 *for details)*

A striking phenomenon is locally intense silicification (*e.g.* de Wit 1982, Lowe et Byerly 1986a, Hofmann et Wilson 2007, Hofmann et Harris 2008) and massive deposition of cherts, especially in the lower Onverwacht and Fig Tree Groups. They occur as individual bands, as massive sequences interbedded with other sedimentary or volcanic rocks, as cement within sedimentary rocks, as zones of silicification of pre-existing rocks, and as concordant or cross-cutting veins. For this study, we chose two sites of special interest in the Onverwacht Group : the Buck Reef Chert (BRC), located at the top of the Hooggenoeg Formation, and the Komati River Chert (KRC), located within the Kromberg Formation (Fig.2.3 - a,c).

2.1.3   The Komati River chert : cherts in clastic units.

Environmental context.

The Komati River cherts are located on the eastern limb of the Onverwacht anticline (see location in Figure 2.2 ; Studied area : $S26°01.520$-01.712 ; $E30°59.331$-59.353). They form part of the Kromberg Formation, in a unit referred to as the Noisy Complex by de Wit et al. (2011) and the Noisy Formation by Biggin et al. (2011). Along the banks of the Komati River, inside the Songimvelo Nature Reserve, a $200m$-thick sequence of well-bedded clastic sediments outcrops continuously and is essentially made of upward-fining diamictites, turbiditic sandstones and conglomerates (Fig.2.3 - c). This section has been widely studied to constrain the emplacement and origin of clastic deposits and to better understand local and regional tectonic processes (*e.g.* Viljoen et Viljoen 1969a, Lowe et Knauth 1977, de Wit et al. 1987a;b; 2011, Armstrong et al. 1990, Lowe et Byerly 1999). Grosch et al. (2011) used U-Pb zircon dating to obtain a minimum age of $3452Ma$ for the onset of deposition of this sedimentary sequence.

Clastic sediments overlie chert-veined massive basalts and deep-water pillowed basalts of the Hooggenoeg Formation with a well-defined unconformity that records massive erosion (up to $1200m$ of basalt) before clastic sedimentation (Grosch et al. 2009b;a; 2011, Furnes et al. 2011, de Wit et al. 2011). Above the unconformity, a $1m$-thick horizon of laminated carbonaceous black and grey cherts evolves upward
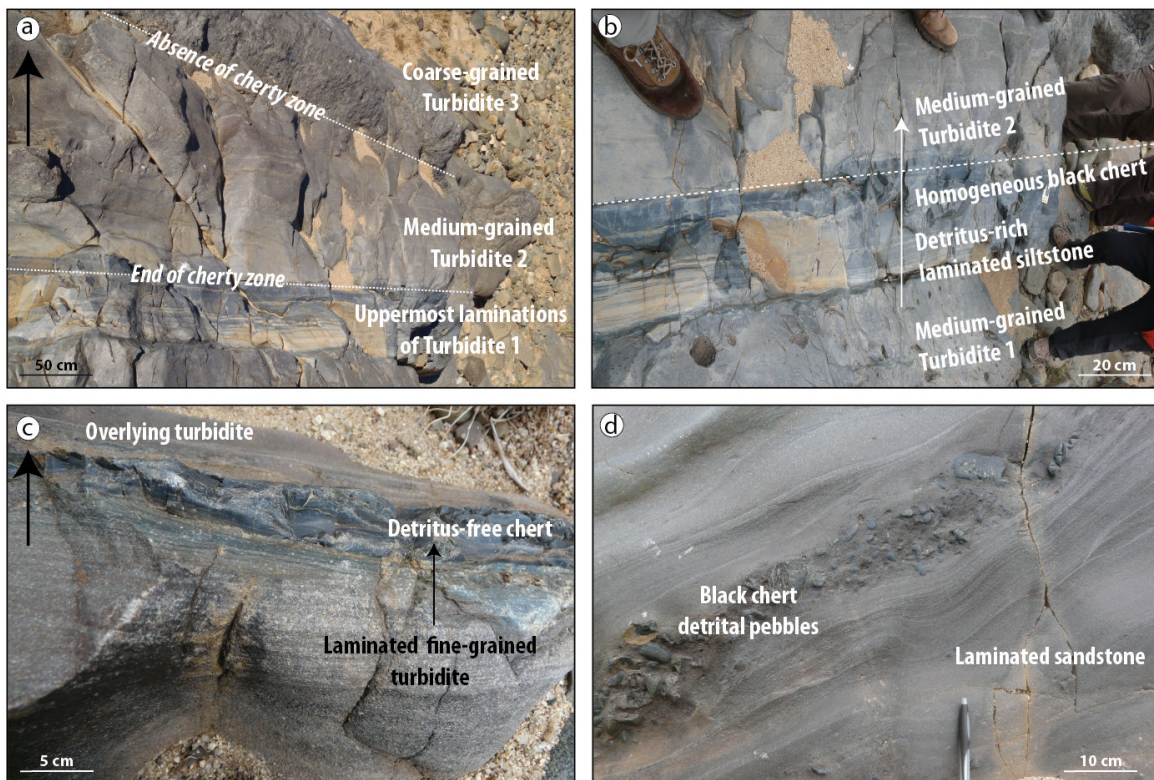
FIGURE 2.4 – *Typical turbiditic deposits showing gradational evolution from medium-grained clastic deposits to laminated fine-grained sediments. The uppermost part of several turbidite layers is made of detritus-free translucent black chert following a laminated, detritus-rich zone. (d) Black chert pebbles embedded in a finely laminated sandstone and produced by seafloor erosion and reworking under high energy current action (possibly during debris-flow).*

through the 170*m*-thick clastic sedimentary sequence shown in the stratigraphy column of Figure 2.3 - c.

The first clastic unit is a massive, poorly sorted conglomerate with clasts composed mainly of silicified dacitic volcanic rocks and grey to black cherts in a coarse-grained sandstone matrix. Overlying units include thick diamictite and laminated siltstone beds that evolve through normally graded massive beds of fine- to coarse-grained volcaniclastic sandstones (up to 5*m*-thick) (Grosch et al. 2011). They show features typical of debris-flow deposits such as cross-bedding, graded bedding, flame structures, and slumps. Lowe et Knauth (1977) interpreted these rocks as tuffs and felsic volcanics reworked as turbidites in a shallow marine environment. Grosch et al. (2011) confirmed this hypothesis through systematic dating of the various clastic facies. He argued for a bimodal source for detrital products, *i.e.* felsic
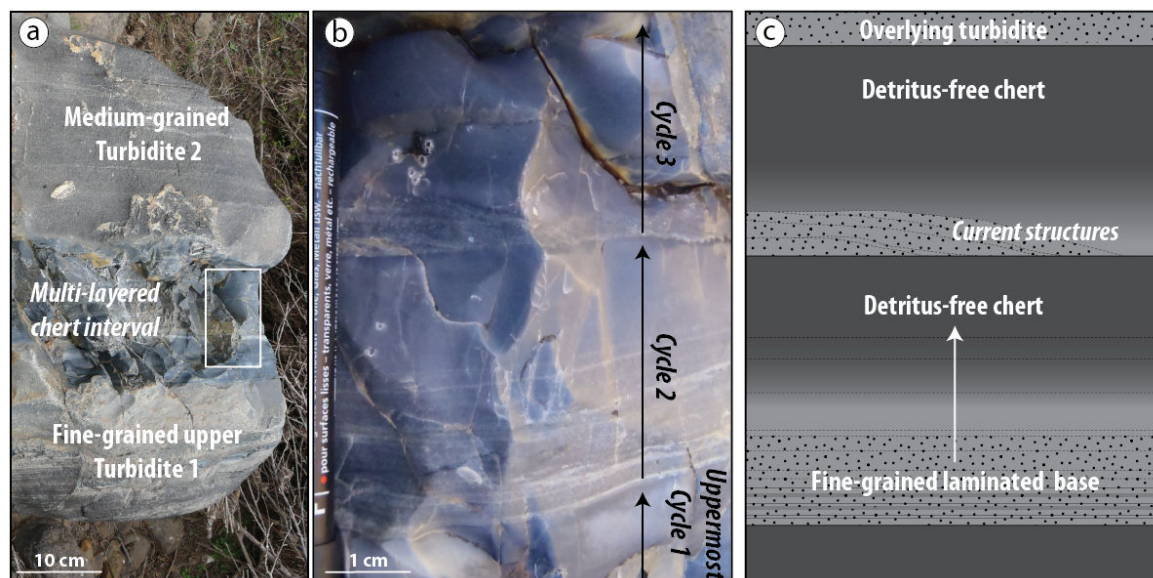
FIGURE 2.5 – *Multiple chert layers at the interface between two turbiditic events. Three cycles are defined by (1) a laminated, detrital-rich base often marked by current induced structures (e.g. ripple marks, cross bedding), (2) a gradational evolution with decreasing detrital content and increasing silica matrix and (3) an uppermost facies solely made of detrital-free, translucent black chert.*

volcanics, gneisses and a component from the Buck Ridge Volcano-Sedimentary Complex (see also de Vries et al. 2006, de Vries 2010), and proposes emplacement of the sedimentary rocks as fan-delta sequences "during tectonic uplift of an [...] oceanic basin, with turbidite deposition occurring during or after orogenic activity at 3.432*Ga* most likely in a shallow, intra-continental epieric sea".

Within the upper turbidite sequence, above the diamictite facies, several continuous layers of black chert are interbedded with detrital units and persistently located at the top of turbidite layers (Fig.2.4 and 2.5). Lowe (1999) and Rouchon et al. (2009) interpreted them as the final endmember of a Bouma-like sequence, being the silicified product of previously deposited shales during debris flow-driven sedimentation. In this study, we focus on a *6m*-thick sequence that contains the best outcrops of such layers (Fig.2.3 - c, rightmost log) in order to determine whether the cherty units are C-cherts or S-cherts, to identify the origin of silica in a detrital environment, and to investigate a possible hydrothermal contribution to the sequence. A model for chert emplacement is then proposed.

		Internal Structures	Detrital grain size	Matrix
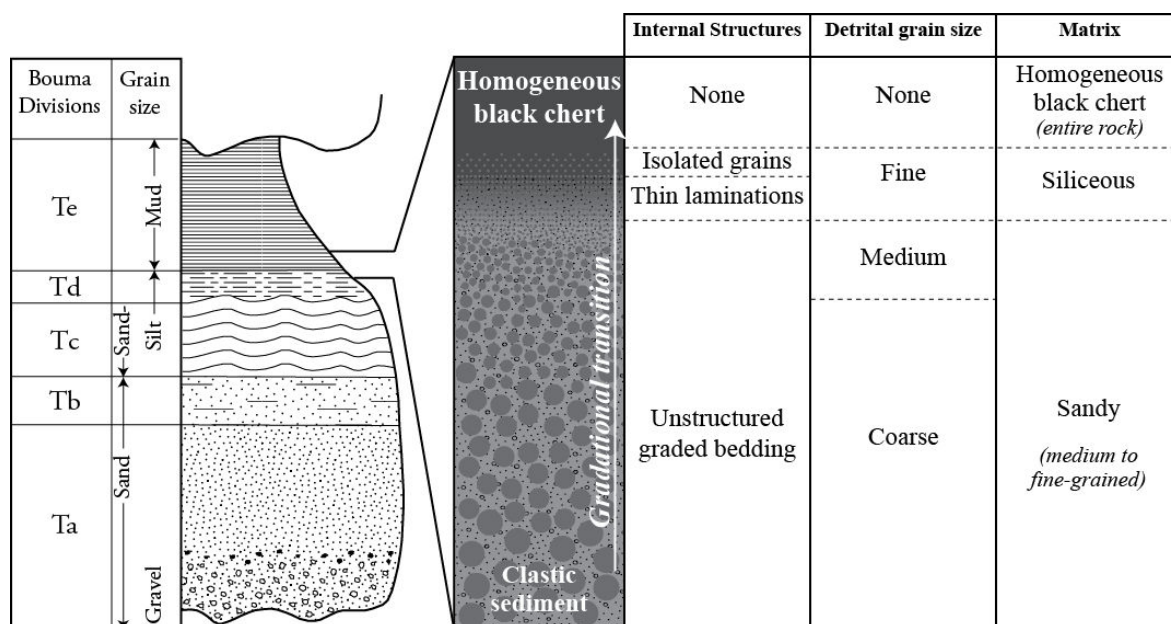
FIGURE 2.6 – *Schematic representation of a typical Bouma sequence (*Bouma 1962*) and upward evolution of uppermost turbiditic facies at Komati River. Laminations appear with decreasing detrital content and size before disappearance of clastic material. In the same time, the siliceous matrix content increases then forms the entire rock as homogeneous, detrital-free and translucent black chert.*

Field description.

Although the turbidites are not the primary objective of this study, we describe them in some detail because they help define the sedimentary context in which the cherts were deposited.

The turbidites form thick, 1 to $5m$ beds with internal organization typical of a Bouma sequence (Bouma 1962). They are well sorted, with systematic upward gradation from coarse- to medium-grained at the base (1 to $3mm$) to fine-grained and in some cases laminated at the top ($<1mm$) (Fig.2.4). The first $10cm$ of erosional bases often contain sub-angular to rounded clasts of dark chert ($2-8cm$ in size) as shown in Figure 2.4 - d. The laminated fine-grained upper part of many turbidite cycles evolves to black chert deposited either as single layers (2 to $25cm$ thick) or as several layers that can reach up to $20-30cm$ in total thickness (Fig.2.5).

The transition from turbidite to chert is either sharp or gradual. Where gradational, as shown in Figure 2.6 (see also Fig.2.4), we first observe a decrease in the abundance and size of detrital grains, from silt to clay, and the appearance of
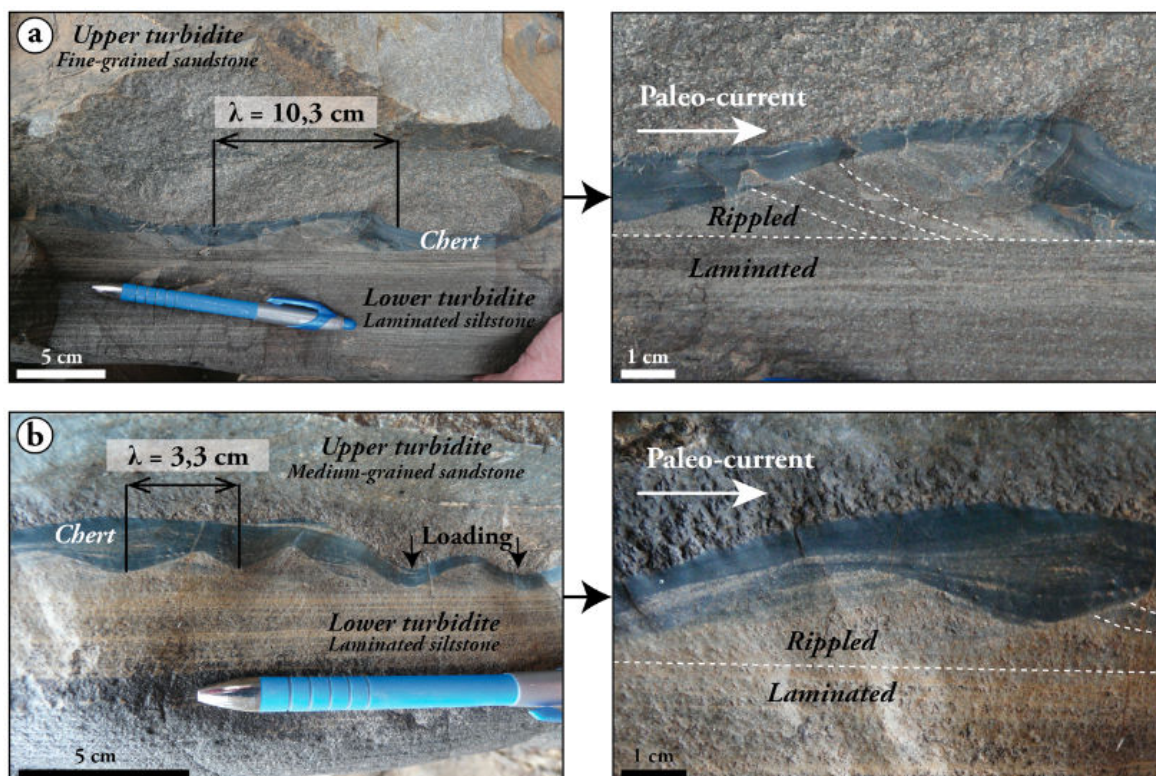
FIGURE 2.7 – *Rippled structures in black cherts at the interface with overlying turbidite layer. The ripples indicate paleo-current direction to the SW (modern direction).*

thin laminations over 2 to 3*cm*. Such laminations can be rippled or cross-bedded, providing evidence of current action during emplacement (Fig.2.7). At the same time, the matrix evolves from fine clay to chert, and, with the disappearance of the last detrital grains and laminations, the rock is transformed to homogeneous translucent black chert. The chert layers are commonly deformed at the interface with the overlying clastic deposit, to produce well-developed flame structures as shown in Figure 2.8 - b to d.

Between two turbiditic events, several cycles of chert deposition without massive clastic deposition can be observed, as shown in Figure 2.5. Each chert layer is less than 10*cm*-thick and shows the gradational transition described above : the basal part is composed of grey detrital grains, 0.3-0.5*mm* in size and comprising up to 90% of the rock, in a matrix of dark-blue-grey massive chert. The distribution of these grains defines thin laminations within the cherty matrix, often marked by sedimentary structures such as cross-bedding, ripple marks, and ascending strati-
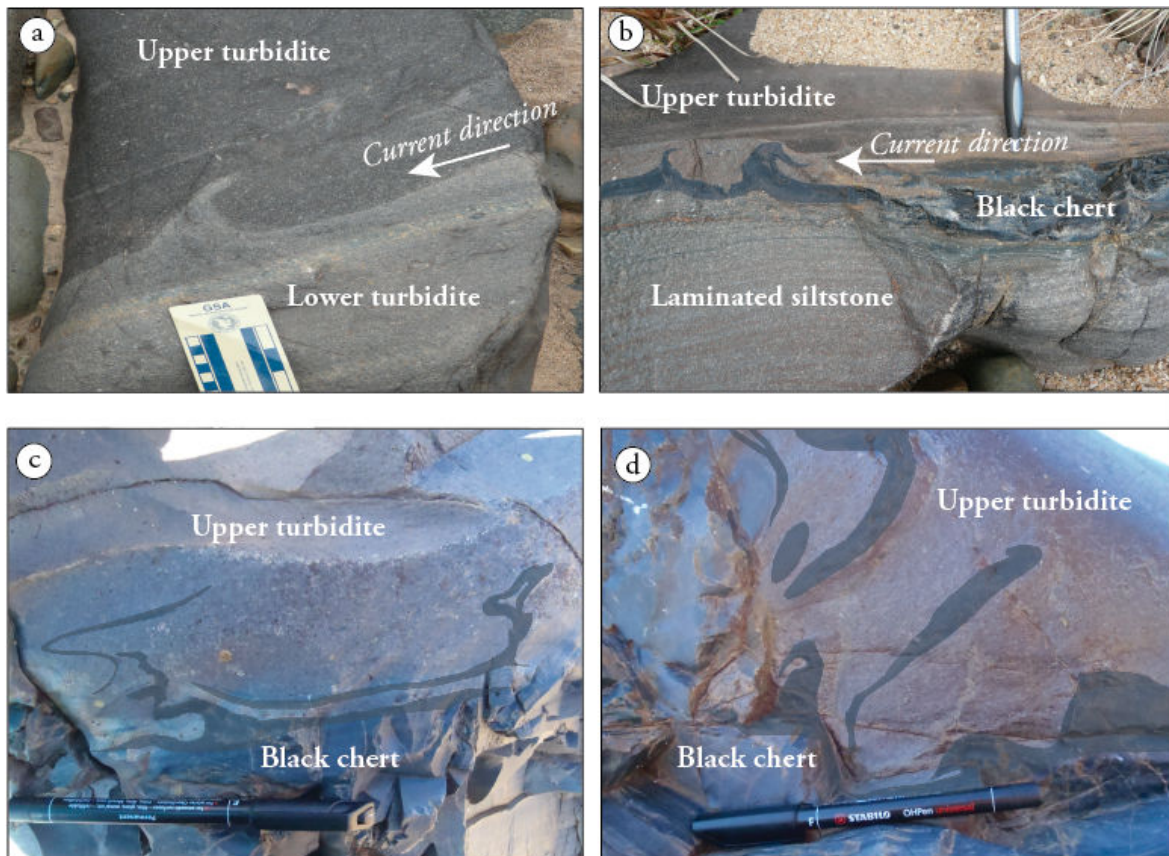
FIGURE 2.8 – *Photos of flame structures at the top of Komati River turbidites. Flames are well-preserved and observed in most of turbidite layers with (b, c, d) or without (a) a black chert horizon. These flame-like structures reveal the presence of still-soft black chert at the top of the sedimentary pile during turbidite emplacement.*

fications (Fig.2.5). The laminations persistently disappear upward after few centimeters leaving the homogeneous, translucent and particle-free blue-grey chert that comprises the upper portion of each chert layer. The contact with an overlying cycle is sharp, undeformed and marked by the abrupt reappearance of detrital grains.

In the central part of the section, a 1m-thick sedimentary sequence consists of very fine-grained siliceous and tuffaceous sediments (Fig.2.9). It abruptly overlies the laminated, fine-grained upper part of a turbidite unit. The lower part of this chert sequence is composed of greenish chert showing ascending stratifications, and it evolves upward through 20cm to a dark bluish chert with well-developed ripples. The transition is continuous and defined by an increase of a dark component within the chert, probably carbonaceous matter. The uppermost ripples of bluish chert facies are filled by the overlying very fine-grained ($<$0.3mm) laminated
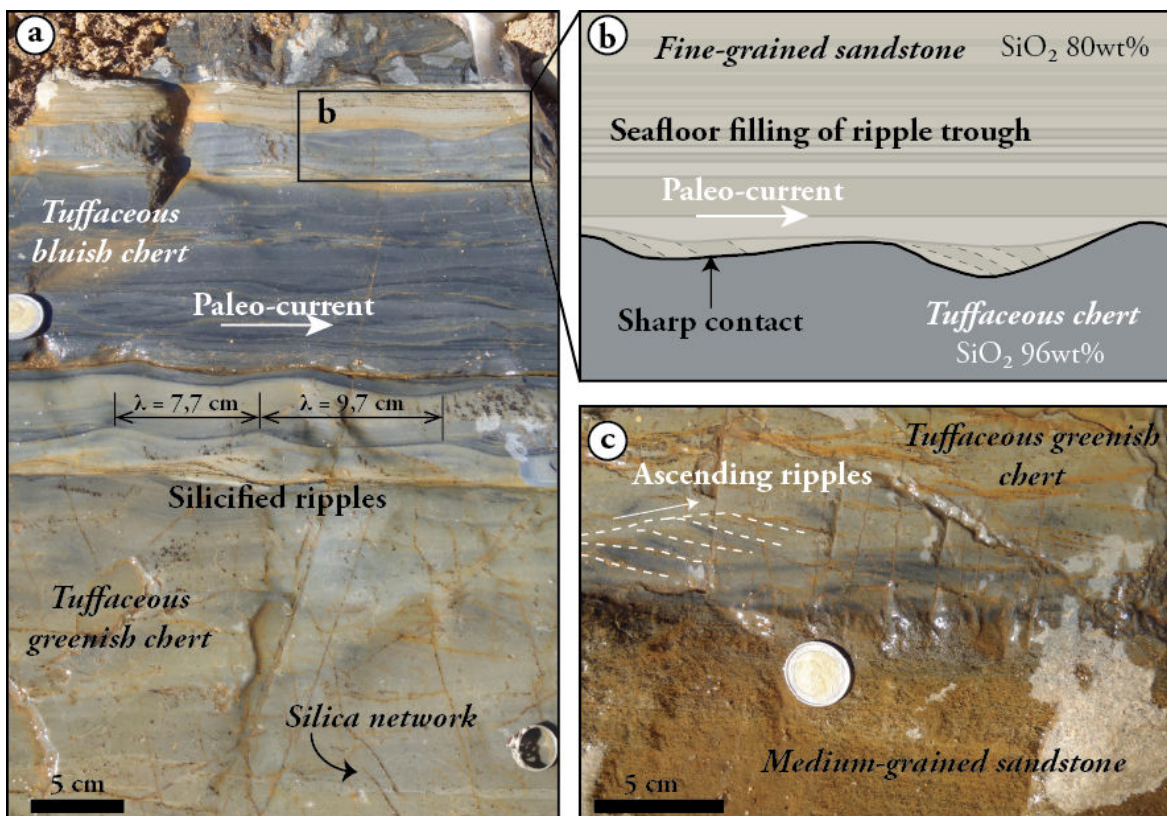
FIGURE 2.9 – *Photos and magnifications of a 1m-thick unit of greenish to bluish tuffaceous cherts embedded within two turbidites at Komati River. Ripples in this facies evolve from (b) climbing ripples, to (a) symmetric then flat ripples. (b) The sequence ends with a poorly silicified fine-grained siltstone with straight laminations. The silica network in the greenish facies is further described in Figure 2.10 and might represent a unique evidence of silica gel deposition directly at the surface during the Archean.*

siltstone. This material displays fan-like sedimentary structures and well-developed overlaps on trough edges within ripples. The sequence is capped by a massive, homogeneous particle-free black chert that cannot be followed upward due to lack of outcrop.

One intriguing structure is observed in the lower greenish facies and shown in Figure 2.10. It consists of a white, translucent silica network that can be followed all along a specific interval within the tuffaceous chert (see Fig.2.9 for location). The network is straight at its base while convex at its top, forming two generations of "ripples" if the shape is indeed inherited from current action. The structure is a spiderweb of milky, nearly translucent silica enclosing rounded packages of the greenish, tuffaceous material. We could not find any similar structure in the mo-
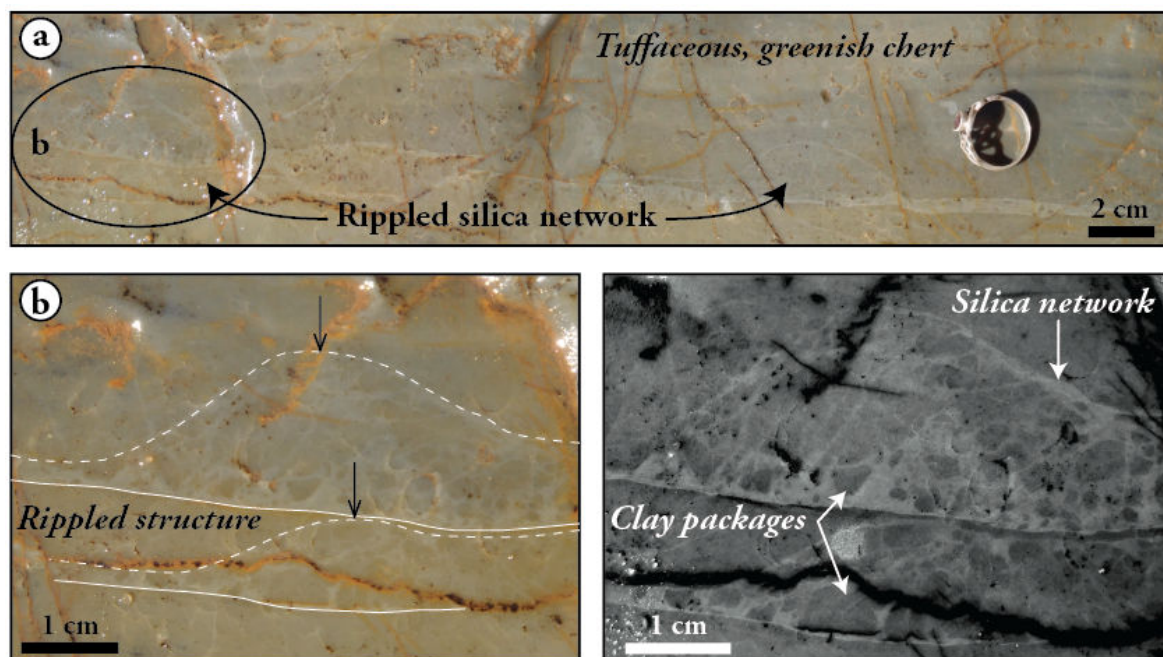
FIGURE 2.10 – *Magnification of the silica network localized in the tuffaceous unit of Figure 2.9. The structure is a spiderweb of translucent silica enclosing rounded packages of clay. It is straight at its base while convex at its top, which is very like ripple structures. Thus, the inferred silica gel might have been cohesive enough to be reworked without disruption while still at the surface (see text for further discussion).*

dern or ancient sedimentary record and drilling into the outcrops is now forbidden because of intense "geo-vandalism" in the area. The origin and possible formation of such structure will be discussed in a later section.

The current structures encountered in massive, well-sorted turbidites and particle-rich cherty transitions provide evidence of a low to medium energy, shallow environment of deposition where detrital inputs alternate between massive debris flow and classic detrital sedimentation. This is in good agreement with previous studies, especially that from Grosch et al. (2011), and demonstrates rapid seaward sedimentation in a shallow marine, near-shore setting during tectonic uplift of the basin.

Petrological characteristics

The Komati River chert samples chosen for petrological (this chapter) and geochemical (Chapter 4) study were taken from the uppermost $20cm$ of turbidite layers, covering the siltstone through to the cherty upper facies (named "black chert" in
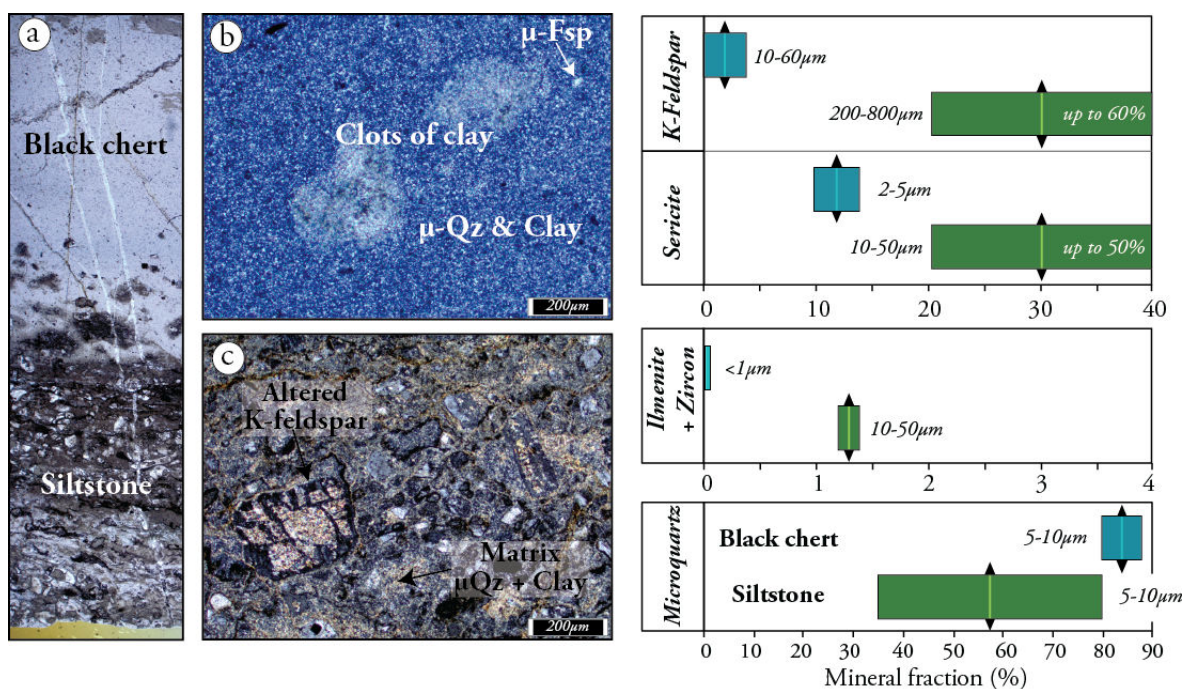
FIGURE 2.11 – *Mineralogy of the topmost part of turbidite layers with special emphasis to the distribution and size of the clastic fraction in both the siltstone (green) and upper chert facies (blue). (a) Rapid but gradual transition from the clastic-rich and laminated siltstone (base) through to the clastic-poor and homogeneous black chert (top). The transition is characterized by an increase of the siliceous content while the particle size and amount decreases. (b) Mineralogy of the upper black chert, entirely composed of cryptocrystalline microquartz with disseminated clays, minor angular micro-K-feldspar and rare clots of clays. (c) Mineralogy of underlying siltstone, composed of detrital K-feldspar and sericite in a matrix of microquartz and sericite.*

the following section) (Fig.2.4), and within the tuffaceous greenish chert illustrated in Figure 2.9. Petrological characteristics are shown in Figures 2.11 and 2.12.

At the top of turbidite layers, the gradational transition from the siltstone to the cherty facies is first marked by the disappearance of detrital grains, laminations and cross-bedding structures (Fig.2.11 - a and 2.12 - a, b). Detrital grains first represent up to 80% of the siltstone and are the finer counterpart of lower coarser material of turbidite events. These grains are fine to medium in size and mainly composed of feldspar ($200\mu m$-$800\mu m$) and clay ($10\mu m$-$50\mu m$) minerals in roughly equal proportions (Fig.2.11), associated with rare carbonate grains (<1%) (Fig.2.12 - e, f) and few heavy minerals (<2%) of less than $50\mu m$ in size, mostly Ti- and Fe-
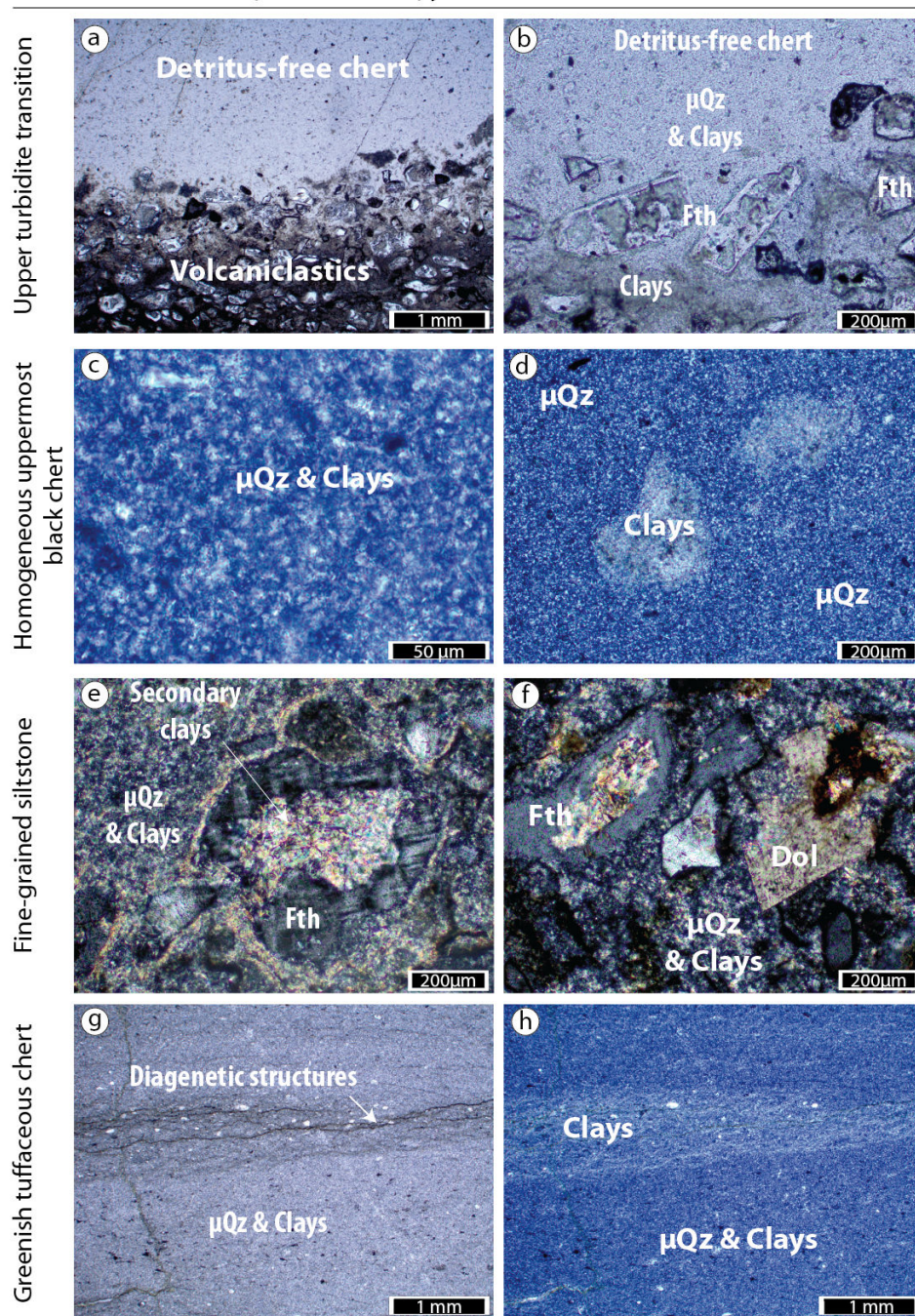
FIGURE 2.12 – *Optical microscopy pictures of Komati River chert samples. Qz = quartz; μ Qz = microquartz; Fth = feldspar; Dol = dolomite. Photos (a) and (b) (LPNA) are taken at the transition from detrital-rich turbidite facies to cherty uppermost turbidite facies. They both show the abruptness of the transition due to a rapid decrease in detrital grain size and content together with an increase in the abundance of the siliceous matrix. Photo (b) is a detail showing detrital feldspar grains enclosed in a microquartz matrix. (c) (LPA) The homogeneous black chert at the top of turbidite units is mainly composed of microquartz (< 5μm) in close relationship with clay minerals (<2μm). (d) (LPA) Rare clots of clays are preserved as isolated aggregates. (e) and (f) (LPA) The detrital particles are essentially composed of feldspars that preserve twins (here microcline in "e") despite strong alteration to clay minerals in embrayment and along boundaries. Few dolomite crystals are observed, slightly altered with sharp to diffuse edges. The matrix around detrital grains is a mixture of microquartz and clay minerals. The preservation of clays and feldspars, as well as the continuity between the siliceous matrix around detrital grains and the uppermost cherty zone, show the absence of secondary silicification and point to contemporaneous deposition of feldspar and silica.*

	- Standard - Orthoclase		KOMATI RIVER							
			Black Chert				Siltstone			
			Micro K-Feldspath		Quartz		K-Feldspath		Secondary Clay	
(wt%)	n = 12	Std. Dev.	n = 6	1σ	n = 12	1σ	n = 32	Std. Dev.	n = 6	1σ
SiO_2	65,0	0,21	65,2	0,68	98,7	0,50	65,1	0,51	48,7	0,52
Al_2O_3	18,5	0,07	18,0	0,28	0,33	0,27	18,2	0,37	34,5	0,48
K_2O	14,9	0,06	15,8	0,44	0,10	0,07	15,9	0,48	8,22	0,29
Na_2O	1,40	0,02	0,17	0,02	0,02	0,01	0,17	0,02	0,10	0,02
MgO	<0,02		0,01	0,01	0,01	0,01	0,00	0,00	1,66	0,08
CaO			0,00	0,01	0,00	0,01	0,00	0,00	0,01	0,01
FeO	0,03	0,02	0,03	0,02	0,03	0,01	0,02	0,02	0,85	0,03
MnO	0,01	0,01	0,01	0,01	0,00	0,00	0,00	0,00	0,00	0,00
TiO_2	<0,01		0,00	0,00	0,00	0,01	0,00	0,01	0,54	0,04
Total	100,0		99,3		99,2		99,4		94,6	

TABLE 2.1 – *Average composition of selected phases in the siltstone of turbidites and uppermost black chert facies. Data are obtained by high resolution microprobe single point analyses and given in weight per cent. 1σ is the deviation from average composition. "n" is the number of analyses.*

oxides. The surprising feature is the near absence of detrital quartz grains whereas they are more abundant lower in turbidite layers (*i.e.* in coarser sandstone with lithic fragments) (Rouchon et al. 2009).

Two families of detrital feldspar grains are present, in about equal proportions. The first are angular to sub-angular in shape and show well-defined sharp boundaries. The second are more rounded, with diffuse edges coated with iron oxides (Fig.2.12 - a, b). All feldspars are little altered and twinning is commonly preserved, either typical of orthoclase or microcline, as shown in Figure 2.12 - e, f. Embayments are filled with phyllosilicates less than $20\mu m$ in size. The smallest feldspar grains ($\sim 200\mu m$) usually are completely altered and only ghosts composed of clouds of clay minerals remain.

The matrix enclosing detrital grains is composed of microquartz ($<5\mu m$) in association with large amounts of fine-grained phyllosilicates, probably up to 30% (Fig.2.12 - e). Microquartz grain boundaries are well defined and because no trace of significant recrystallization is observed, the absence of propagating radial extinctions precludes the presence of an earlier chalcedony phase within the matrix. Phyllosilicates are heterogeneously distributed and form concentration zones in the matrix, often but not systematically located at feldspar boundaries.

X-ray diffraction and *in situ* microprobe analyses were performed to identify the detrital phases. The method is described in Annexe A.1 and A.2. Results are shown
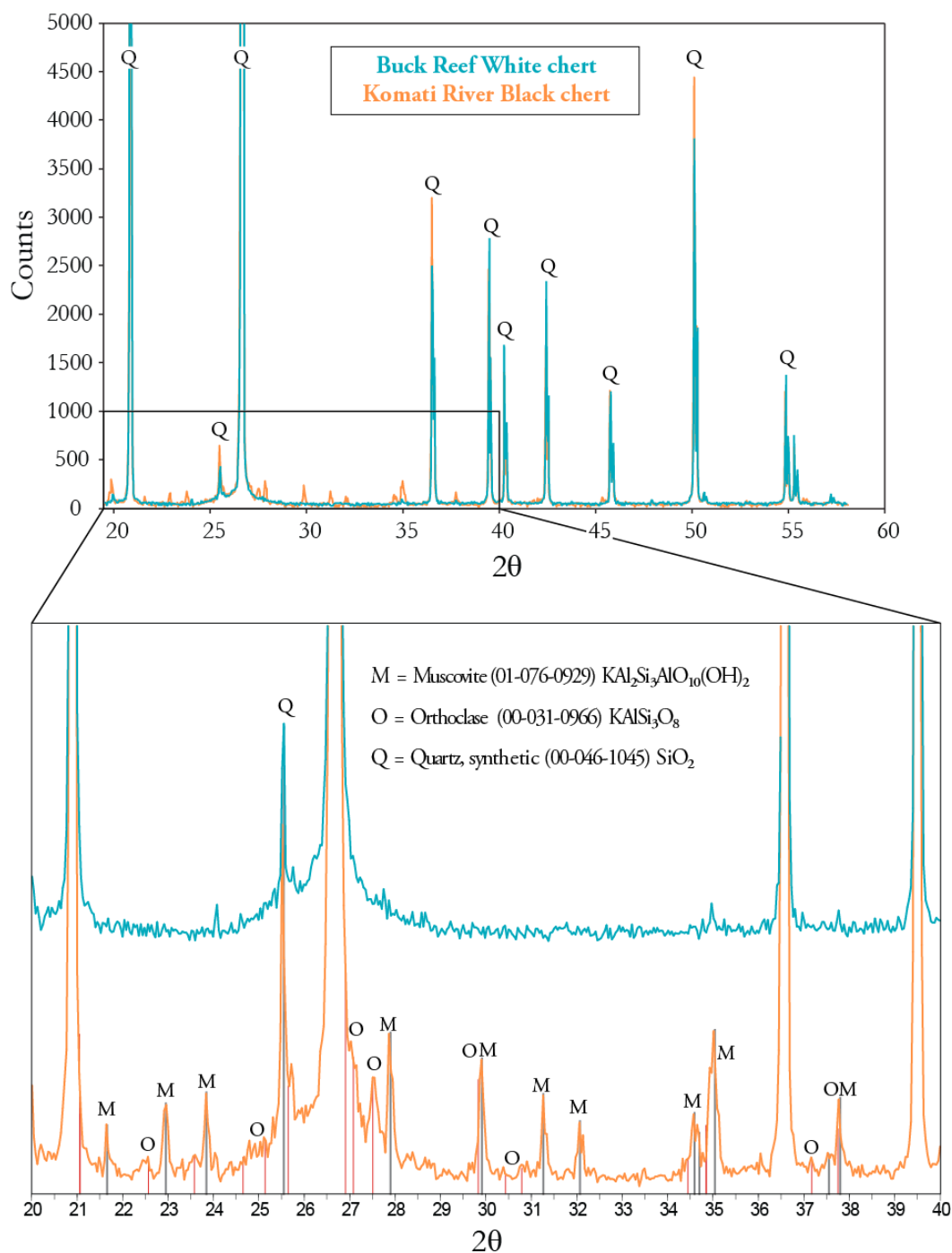
FIGURE 2.13 – *Diffraction spectra for Komati River chert and (orange) and Buck Reef white chert (blue). The Komati sample corresponds to a black chert at the top of a turbidite unit. Results for siltstones (not shown) are very similar but peaks attributed to detrital phases are higher, showing higher proportion of such material. The Buck reef white chert is exclusively composed of microquartz. O = orthoclase ; M = muscovite.*

in Figures 2.13 and Table 2.1 for diffraction and microprobe analyses respectively. Feldspars consist of orthoclase (70%, estimated by microscopy) and microcline (20%) and clay minerals are K-micas of sericite or muscovite composition.

Above the gradational contact, after the disappearance of detrital grains and internal laminations, the translucent black chert consists of a mixture of homogenous microcrystalline quartz ($<10\mu m$, $80 - 90\%$ of the chert), sericite ($<5\mu m$, $10 - 15\%$) and minor isolated, very fine-grained K-feldspars ($<60\mu m$) (Fig.2.11). Internal sedimentary structures are lacking (Fig.2.12 - c, d). Whereas the majority of clay minerals are homogeneously distributed, rare isolated clumps ($<500\mu m$ in total size) are found enclosed in the silica matrix, as shown in Figure 2.12 - d. In the BSE image of Figure 2.16 (see next section), isolated detrital feldspar grains are observed : they are $<50\mu m$ in size with angular shapes, preserved twinned and show no trace of alteration to clay. Near the contact with the underlying siltstone, isolated detrital feldspar grains are observed : they are coarser (up to $1mm$) and strongly resemble those in the siltstone facies, with preserved twins, minor alteration to clay and sharp/angular to diffuse/oxidized boundaries (Fig.2.12 - a, b).

In this transition zone, the evolution from the siltstone to upper black chert facies is abrupt but continuous (Fig.2.12 - a, b) : over a mere centimeter, the size and quantity of detrital particles decrease abruptly, coupled with a rapid increase of the siliceous matrix content and a decrease in clay content.

In the central part of the sequence, we sampled the $50cm$-thick very-fine grained greenish tuffaceous chert. In the thin sections shown in Figure 2.12 - g, h, the rock is homogeneous and entirely made of microquartz and very fine ($<5\mu m$), yellowish platy clay minerals. The latter are commonly oriented along thin internal laminations of the chert, and can be interpreted either as primary or secondary minerals. Minor rounded detrital quartz and feldspar grains ($<200\mu m$) can be observed where laminations are the best developed.

We consider two aspects of these rocks particularly important. The first is the presence of the isolated, unaltered detrital feldspars in the black chert facies (Fig.2.12 - e, f) ; the second is the appearance of the microquartz in the matrix of the uppermost detrital facies, well before it becomes the dominant phase in the
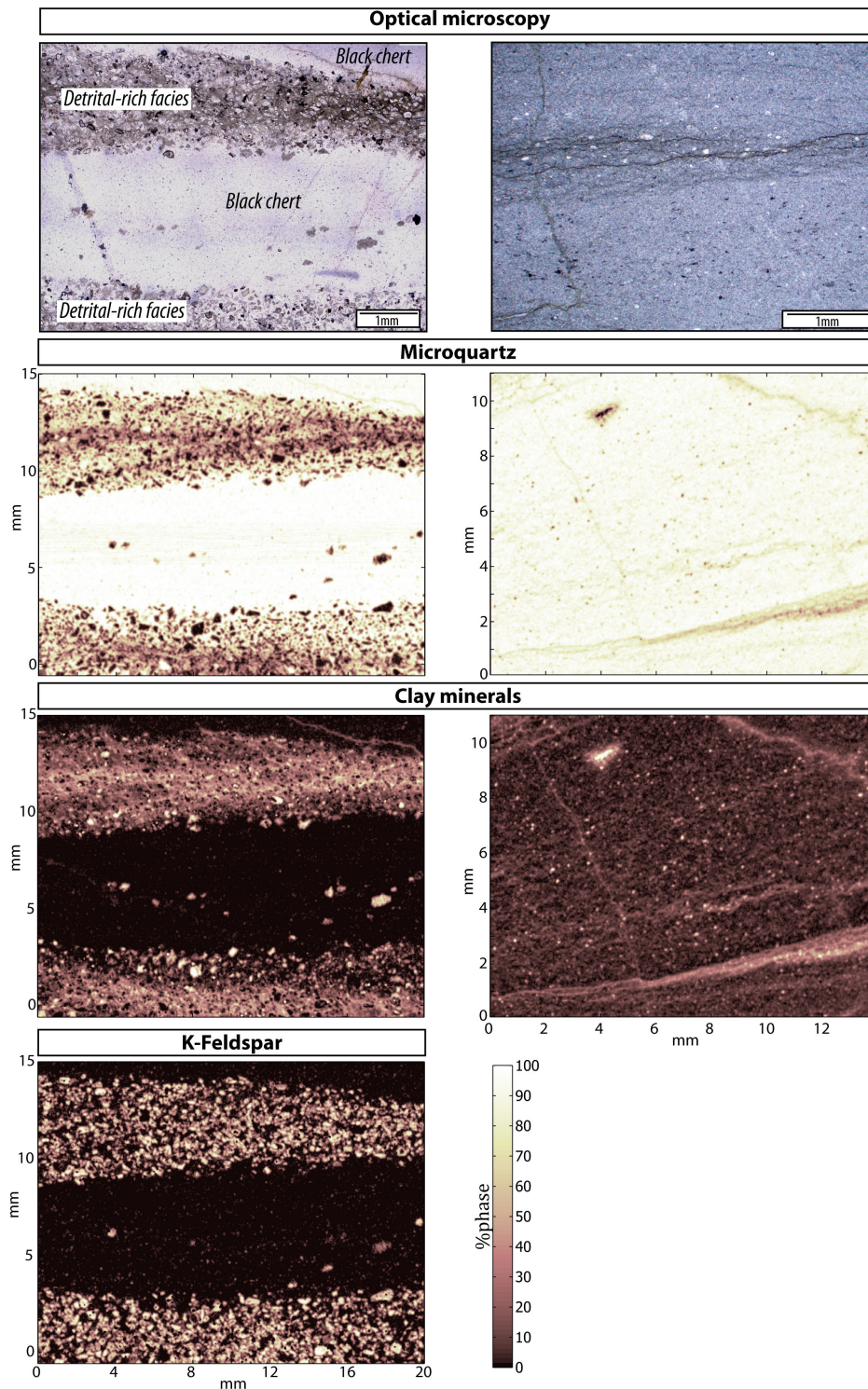
FIGURE 2.14 – *Mineral phase maps from microfluorescence analyses using the EAGLE III. Maps in the left column represent results from two cycles of detrital to homogeneous chert at the top of a turbidite layer. The detritus content decreases abruptly but continuously whereas the silica matrix increases until it forms the entire chert. Some isolated clots of clays are suspended within the black chert. Maps on the right maps are obtained for the greenish tuffaceous chert and show internal laminations defined by clay mineral alignment.*

overlying black chert layer (Fig.2.12 - a, b) . We will argue in a later section that these observations provide evidence that the silica is primary and was not introduced by silicification of preexisting fine-grained sediment.

Microprobe and microfluorescence analyses.

Selected polished thin sections were mapped using an EAGLE III X-Ray microfluorescence spectrometer at ISTerre (Grenoble, France). The data were processed using the Supermaps software developed by Ulrich et al. (submitted). In the procedure, the raw microfluorescence data, combined with optical microscopy, were used to define several pure phases in samples. Using the characteristics of pure phases, the software defines each pixel as a mixture of various constituents, thus producing individual phase maps for each sample. Figure 2.14 presents results for two samples : one is from the multiple chert layers of Figure 2.5 and shows two of these "siltstone to black chert" cycles, the other is from the greenish tuffaceous chert.

The microfluorescence map at the interface between black chert and lower detrital facies (Fig.2.14 - left) confirms the abrupt but gradational transition observed in optical microscopy. In the siltstone, detrital feldspars are readily visible and surrounded by microquartz and minor clay minerals. In this matrix, the clay content decreases through the contact whereas microquartz increases, leading to a black chert essentially composed of silica. In this facies, the small feldspar fragments are barely distinguishable from clays, both representing less than 15% of the rock. Isolated clumps of clay are only a minor constituent of the black chert.

Microprobe mapping produces higher spatial resolution maps and are used to characterize the various constituents of both the detrital-rich and black chert facies. In Figure 2.15, we focus on the detrital facies and show the excellent preservation of feldspars. They have sharp boundaries, and uniform internal compositions, marred only by partial alteration to clays. They are unsilicified, as revealed by chemical compositions typical of potassium feldspars : single point analyses give an average silica contents of $65.2wt\%$, and high potassium and aluminum concentrations ($18wt\%$ and $15.7wt\%$ respectively) (Table 2.1). The detrital clays, either in feldspars
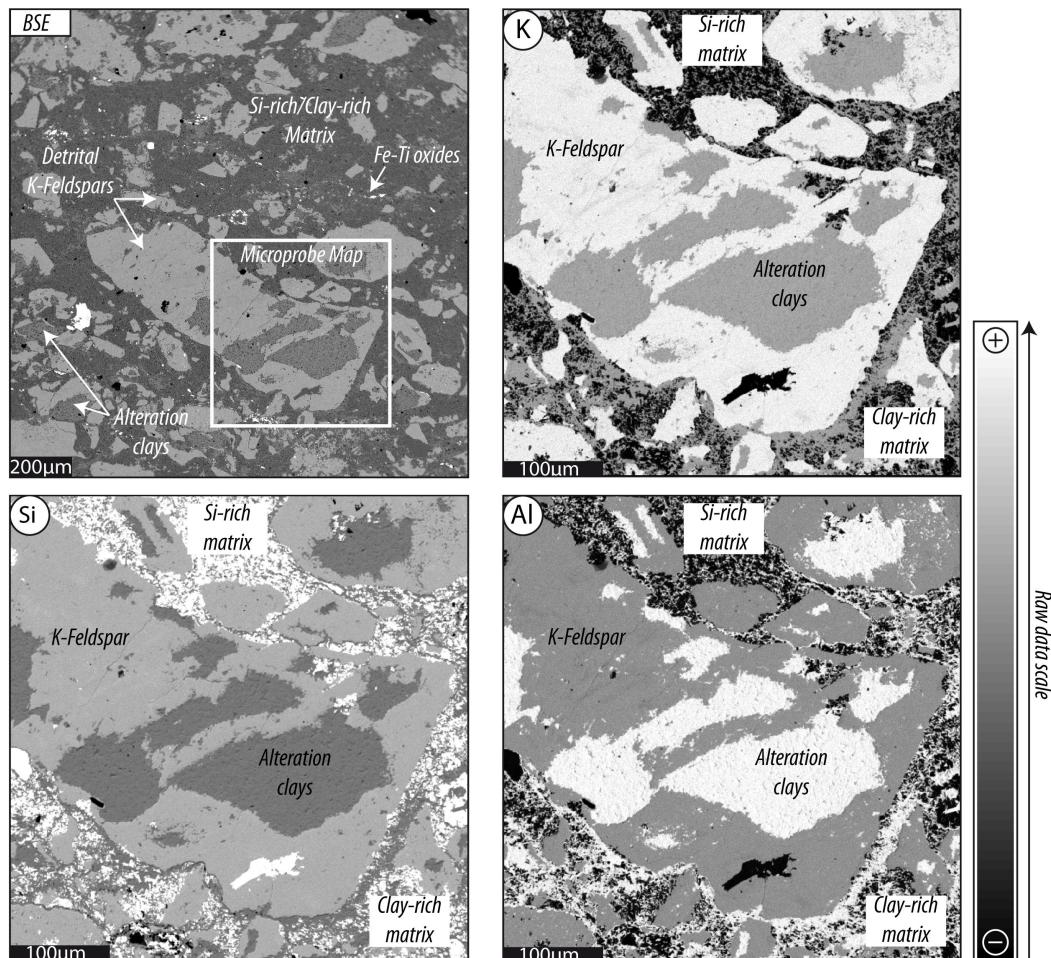
FIGURE 2.15 – *Microprobe BSE imaging (upper left) and in situ chemical maps of silicium, po-tassium and aluminum of detrital K-feldpars in the siltstone of upper turbidite layers. Results are given as raw data and represent relative chemical contents. Feldspars are unsilicified and partially altered to sericite. The surrounding matrix is essentially composed of silica with concentrations of potassium and aluminum representative of the sericite content.*

or in the surrounding matrix, are similarly unsilicified as shown by their typical SiO_2 content of $48.7wt\%$.

The clay component can be interpreted in four ways :

(1) as detrital feldspars transformed to sericite within the sedimentary pile, both within detrital grains and in the surrounding siliceous matrix.

(2) as feldspars that were altered to clay during weathering of the source rock, and were deposited as detrital particles after erosion and transport to the basin.

(3) as secondary minerals produced by the circulation of *Al*- and *K*-rich fluids within the sedimentary pile.
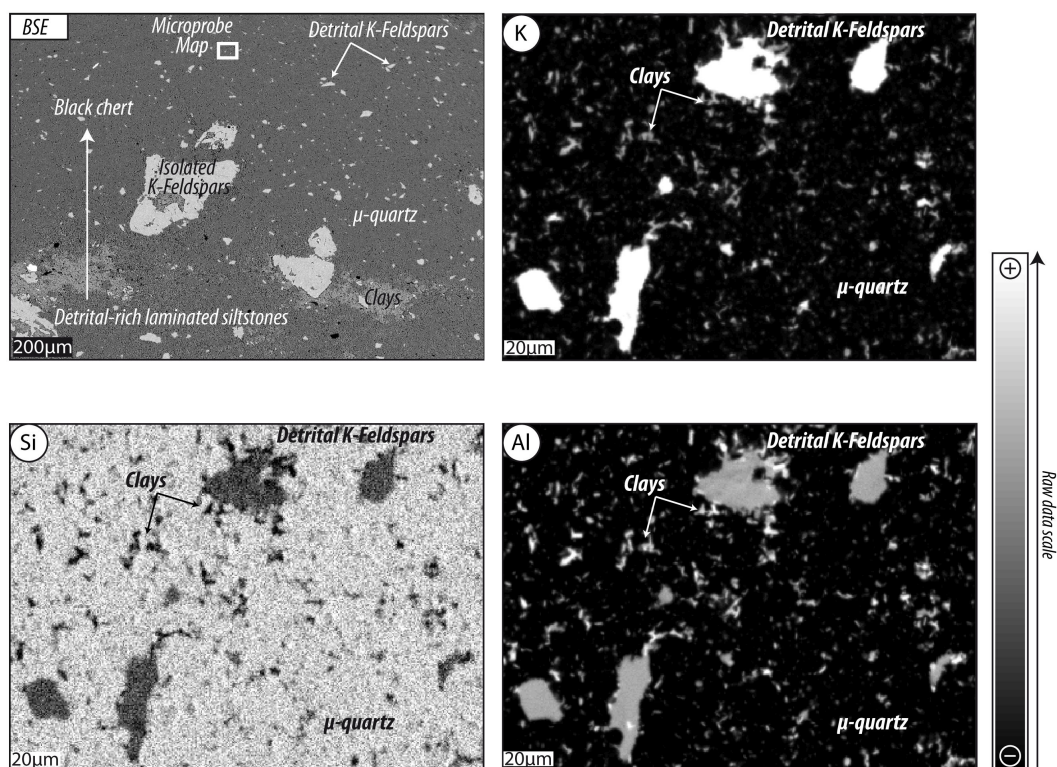
FIGURE 2.16 – *Microprobe BSE imaging (upper left) and in situ chemical maps of silicium, po-*
tassium and aluminum of upper black chert facies. Results are given as raw data and represent
relative chemical contents. Micrograins of feldspars are surrounded by pure silica grains. The quartz
boundaries are coated with aluminum and potassium, which reveals the presence of very small clay
particles (less than 5μm).

(4) as the product of recrystallization of *Al-* and *K*-rich sediment during diage-
nesis.

We favor the second hypothesis for the following reasons : firstly, feldspar edges
are sharp and only a minor proportion is coated by sericites, which is unlikely if
the clay minerals formed by *in situ* chemical disintegration of feldspars within
turbidites. Secondly, authigenic growth of sericite is unlikely because there is no
evidence of fluid circulation within turbidites, and because, if the basin itself were
enriched in *Al* and *K*, the sericites should be homogeneously distributed rather
than preferentially aggregated.

The Figure 2.16 represents high-resolution chemical maps of the upper black
chert facies. It highlights the presence of isolated, micrograins of feldspar that are

angular in shape and enveloped within the microquartzitic matrix. They are chemically undistinguishable from larger feldspars in the underlying detrital-rich facies and are unsilicified with average SiO_2 concentrations of 65.2wt%, Al_2O_3 of 18wt% and K_2O of 15.8wt% (Table 2.1). Minor amounts of very fine-grained sericite-like minerals (5μm) are located at microquartz boundaries. They are homogeneously distributed and not preferentially associated with feldspars. Microquartz is the main component of black chert layers. Microprobe analyses give average SiO_2 concentrations of 98.7wt% with minor amount of aluminum (0.33wt%). Because the sericites are very fine and barely visible, even in BSE imaging, the aluminum content can be attributed to clay coatings at microquartz grain boundaries.

Finally, microfluorescence maps were obtained in the greenish tuffaceous facies as shown in Figure 2.14 - right. Only microquartz and clays were identified in this facies. The clay minerals are either elongated and distributed along internal sedimentary structures, or homogeneously distributed through the sample as little clumps less than 50μm in size. One larger clump is visible at the top of the map. Clays are also the main phase within small veins that cross-cut the chert. On the microquartz distribution map, clays are characterized by darker zones, showing little to no silicification and chemical preservation. The microquartz is very abundant and comprises about 90% of the rock. Because clays are responsible of the observed sedimentary structures and seems to be unsilicified, we propose that they are of detrital origin and were deposited together with silica. However, we cannot exclude that some could be authigenic minerals, *i.e.* grown from Al- and K-rich fluids.

2.1.4 Summary and primary discussion on Komati River units.

The source of the clastic fraction.

The Komati River sedimentary section is interpreted as a series of thick clastic deposits emplaced as debris flows in a shallow intracontinental basin and produced by tectonic uplift of the adjacent protocontinent (Grosch et al. 2011). The numerous sedimentary structures preserved in the topmost fine-grained sedimentary rocks (*i.e.* cross-bedding, graded bedding, ripple marks and ascending stratifications) confirm shallow deposition with low to medium energy current activity. Grosch

et al. (2011) proposed several possible origins of the detrital content in turbidites, including the Buck Ridge volcano-sedimentary complex and the Theespruit Pluton, and Rouchon et al. (2009) considered the dacites of the Hooggenoeg Formation as the main source. However, the preponderance of orthoclase and the abundance of microclines are evidence for us for a significant granitic source to the sediment.

The surprising feature is a lack of abundant detrital quartz grains, which is unexpected for a granitic. Because quartz grains are more stable than feldspars in all terrestrial conditions, a preferential dissolution of these grains is unconceivable. They could have recrystallized as microquartz and be now part of the matrix, but it is also unlikely considering the excellent preservation of other detrital phases. Because the quartz content is slightly higher in the lower part of turbidites, we envisaged density-driven segregation of quartz over feldspars. However, such vertical process would have been accompanied by lateral segregation, yet no quartz-rich clastic rocks (*e.g.* quartzites, arkoses) are found in the Komati River and surrounding areas. Rest the possibility of a quartz-poor, K-feldspar-rich source to the turbidites.

In the Barberton Greenstone Belt, syenites are the best candidates and are found in the Granodiorite-Monzogranite-Syenite suite. The suite post-dates the TTG suite and intruded between 3.2 and $2.6Ga$ (Davies 1971, Hawkesworth 1975, Barton 1983). Earlier occurrences of potassic-rich granitic rocks are found in the form of detrital clasts in younger formations, with an age of $3570Ma$ for the oldest record (*e.g.* Kröner et Compston 1988, Diergaardt et al. 2011, Sanchez-Garrido et al. 2011). However, these K-rich granites were still too rich in quartz compared to our observations (*e.g.* Sanchez-Garrido et al. 2011) and no trace of syenite is recorded at the time of Komati River turbidite emplacement, leaving the "quartz depletion enigma" unsolved.

From the textures in the siltstone, the sericites are considered to be of detrital origin, *i.e.* neither authigenic, nor produced by the *in situ* destabilization of feldspars, nor attributed to secondary alteration during seafloor K-metasomatism (Rouchon et al. 2009). As shown in Figure 2.15, they are heterogeneously distributed in the microquartzitic matrix surrounding detrital grains and do not systematically concentrate at feldspar margins.

Clay minerals are formed even at low temperature in soils, and, in our case, sericite could have been formed by weathering at the land surface, with potassium furnished by magmatic K-feldspars desegregation. High atmospheric P_{CO_2}, an absence of vegetation, and a large proportion of potassium felspar over plagioclase (*i.e.* almost complete dissolution of plagioclases) are arguments previously used by Sugitani et al. (1996), Alfimova et Matrenichev (2006), Sleep et Hessler (2006) to propose severe weathering under acidic meteoric conditions during the Archean (review in Hessler et Lowe 2006), which could have been responsible for the seritization of igneous feldspars. However, the formation of K-mica may as well be a local phenomenon, inherited from the low-grade metamorphism recorded in the area (215 to $< 350°C$; Grosch et al. 2012).

Primary origin of the silica and seafloor deposition evidence.

After erosion, the detrital particles were transported to the basin and deposited by debris-flows. As shown in Figure 2.4, each turbidite layer forms a full Bouma sequence, with erosional bases marked by flame-like structures, then graded beds from coarse-grained sandstones rich in lithic fragments (*e.g.* chert, Fig.2.4) to fine-grained and commonly laminated siltstones with well-defined current-induced structures. In a normal modern sequence, the final member would be very-fine clays or muds, leading previous authors to argue that the cherty upper zone observed in Komati River turbidites represents the product of silicification during secondary Si-rich fluid circulation (Lowe 1999) or during early diagenetic silica cementation (Rouchon et al. 2009). However, we found several lines of evidence against this hypothesis : instead, we suggest that silica is not secondary but represents the final sedimentary component of the Bouma sequence.

(1) Absence of secondary hydrothermal fluid circulation. Through the whole turbidite sequence, macro and microscale evidence for hydrothermal fluid circulations is lacking : chert-filled concordant veins, cross-cutting fractures, and silicification fronts are rare or absent, even in the coarser basal part of turbidites, and detrital grains are preserved. However, evidence is found that upward migration of Si-enriched pore water may have contribute to the chert formation (*i.e.* not hydrothermal, but diagenetic fluids). In Figure 2.17, a thin black chert network marks
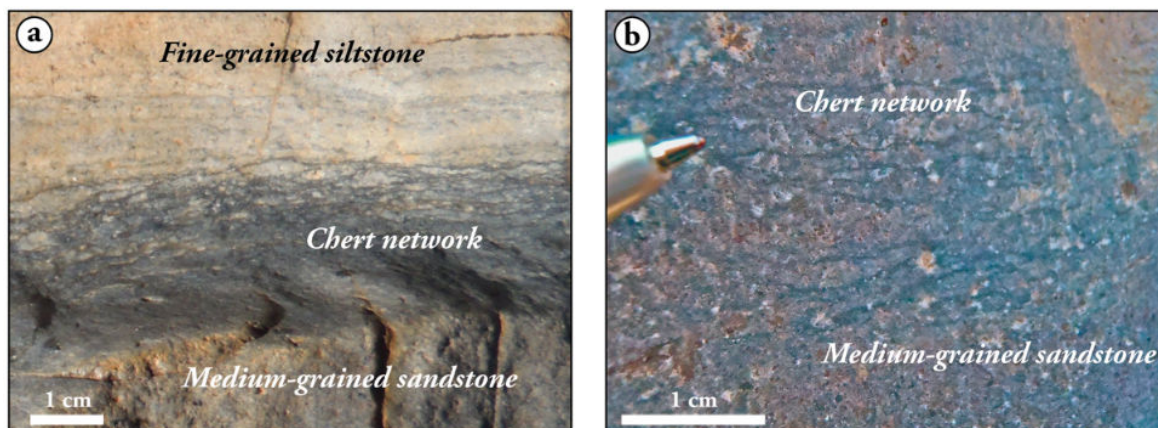
FIGURE 2.17 – *Possible evidence for porosity fluid migration at the interface between two clastic facies of contrasting granulometry. Such feature may indicate that part of the silica that form the chert was inherited from diagenetic fluid migrations.*

the base of fine clastic sediments. Silica concentrates around detrital particles and disappears upward, a feature that we interpret as porosity fluid migrations soon after deposition of the coarser, lower facies.

(2) Presence of chert at the seafloor. The presence of numerous chert pebbles in the basal erosional part of the turbidites indicates that partially indurated chert was already present at the top of the sedimentary pile when the next debris flow arrived (Fig.2.4 - d). Moreover, black cherts at the top of turbidites display numerous soft-sediment deformation structures, as illustrated in Figure 2.8. Although the flame structures could have been produced in muds that subsequently were silicified, the sharp contact between the chert and overlying rocks, the thinness of the structures, and the lack of any evidence of silicification of detrital grains in the turbidite, all lead us to favor a primary origin for the chert.

(3) Petrological and chemical preservation of detrital grains. The continuous evolution from detrital siltstone to homogeneous chert provides several additional arguments for primary silica deposition. The siliceous matrix appears within the siltstone well below the chert layer and persists, with the same characteristics and in continuity, from the siltstone through to the chert. Figures 2.11, 2.16 and 2.15 illustrate the identical characteristics of microquartz in the matrix and in homogeneous chert, suggesting a similar origin for both. Moreover, if the silica had been

introduced to the rock during secondary silicification, the detrital grains should have been affected, yet they are unsilicified, as shown by their optical characteristics (Fig.2.12) and chemical compositions which are typical of K-feldspars and sericite (Table 2.1). In the black chert facies, where the silica content is the highest, the floating micro grains of feldspars are also preserved from silica alteration.

These arguments lead us to propose that the chert was deposited as chemical sediment during the waning stages of deposition of detrital material from the debris flows. As the rate of clastic sedimentation declined, the accumulation of silica flocs first accompanied, then replaced the deposition of detrital grains. The presence of minor detrital sericite and micro-feldspar within the black chert suggests that the chemical sediment was probably deposited in the form of a siliceous ooze mixed with the finest clastic products, with sufficient viscosity to maintain the particles in suspension. The model for Komati River chert deposition is further discussed in a later section.

For the greenish to bluish tuffaceous chert, conclusions are less evident. Although significant traces of fluid circulation are lacking in this unit, the clays could have been authigenic, *i.e.* formed during diagenesis in a potassium- and aluminum-rich environment (*e.g.* precipitated from pervasive seawater or from pore fluids). However, because clays are aligned to define the internal sedimentary laminations, and because they have escaped silicification according to microfluorescence maps of Figure 2.14, we suggest that they too were deposited as primary detrital grains together with chemically precipitated silica.

2.1.5   The Buck Reef chert : clastic-free siliceous deposits.

Environmental context.

The Buck Reef Chert (3416*Ma*, Kröner et al. 1991) is a thick siliceous sedimentary unit located above shallow intrusive to possibly extrusive dacitic volcanic rocks and volcaniclastic units of the Hooggenoeg Formation defined by Lowe et Byerly (2007) (see Figure 2.2 for location) (Viljoen et Viljoen 1969a;c, de Vries et al. 2006, Lowe et Byerly 2007, de Vries 2010, de Wit et al. 2011, Furnes et al. 2011). The combined volcano-sedimentary sequence was called the Buck Ridge complex (BR-vsc)

by de Vries (2004) and de Vries et al. (2006) (see also de Vries 2010). It was emplaced during extensional tectonic activity as revealed by numerous listric normal faults (de Vries et al. 2006). Volcaniclastic units, composed of dacite-derived conglomerate and sandstones, are interpreted by Lowe et Fisher Worrell (1999) as coastal or braidplan deposits formed during the erosion of the Hooggenoeg Formation. They are the local equivalents of previously-described turbiditic sandstones of Komati River (Lowe et Fisher Worrell 1999, Lowe et Byerly 2007).

The Buck Reef Chert is a 250-400m-thick sequence of black and white banded cherts and minor ferruginous or shale units that outcrops continuously for more than 30km along the west limb of the Onverwacht anticline and discontinuously along its eastern limb (Lowe et Fisher Worrell 1999, Tice et Lowe 2006). On the eastern limb, the Buck Reef Chert has been stratigraphically linked to chert layers interbedded with ultramafic lapillistones and pillow basalts overlying the clastic sequence of Komati River Chert (Lowe et Byerly 2007). We focus on the western limb area, where the Buck Reef Chert is the thickest and best exposed.

The base of the unit is an evaporitic facies (EV) composed of silicified sandstones, cherts and nahcolite ($NaHCO_3$) pseudmorphs, as shown in Figure 2.3. The lithologies and sedimentary structures of this lower unit indicate a shallow-water lagunal environment (Tice et Lowe 2006). The following 200-300m of the sequence record a gradational transition from the lower facies (LBC in Figure 2.3), composed of detritus-rich B&W banded cherts and marked by medium- to low-energy current structures, to the upper facies (UBC), composed of continuous, finely-laminated B&W cherts recording deeper deposition, away from coastal turbulences. These banded carbonaceous cherts evolve upward through a highly ferruginous, altered cherty zone named banded ferruginous chert (BFC) in Figure 2.3, and reappear in the last 50m below the overlying Kromberg basalts.

There are two schools of thought on the origin and paleoenvironment of the Buck Reef Chert. de Vries (2004) and de Vries et al. (2006) regard the banded chert sequence as the uppermost silicified endmember of an arc-like succession of basaltic and felsic rock : based on the observation of chert veins, hydraulic breccias and quartz-filled cavities, they interpret the silicification as a result of strong hydrothermal involvement during felsic magmatism that controlled both sedimentation and

extensional tectonic activity. On the other hand, Lowe et Byerly (1999) and Tice et Lowe (2006) envisage deposition of cherts on a subsiding open-marine platform previously formed by the erosional products of an adjacent felsic volcanic edifice, now represented by the underlying Hooggenoeg Formation. According to these authors, the banded chert sequence formed without hydrothermal contribution by normal marine sedimentation of a carbonaceous, organic-matter-rich siliceous mixture from hot, Si-supersaturated seawater. An intermediate model was proposed by Hofmann et Bolhar (2007) and Hofmann et Harris (2008) who advocate hydrothermalism at least during the deposition of the lower evaporitic facies. Following silicification, this unit may have acted as a barrier to hydrothermal fluid circulation. Upon the cessation of hydrothermal activity, and thanks to the chert barrier, the upper part of the sequence was protected from hot fluid circulation and is probably composed of precipitated oceanic silica.

The presence of microfossils and microbial mats in the Buck Reef Chert (Walsh 1992, Tice et Lowe 2004; 2006, Westall 2005), and the unusual thickness of the banded chert sequence make this area of special interest. We focus here on the B&W banded chert facies and part of the lower evaporitic facies to better constrain the origin of cherts and silica, and to investigate chert formation in a detritus-free, open-marine setting.

Field description.

The first facies of clastic sediments is located within the lower evaporitic unit (Fig.2.3) and consists of 10 to 30cm-thick siltstone layers with contrasting characteristics. Homogeneous white layers, marked by a 2 to 3cm-thick dark black zone at the base, alternate with uniform, rusty-weathering layers (Fig.2.18 - a). In the lowermost part of this unit, the white layers are commonly discontinued and form Si-rich nodules with contorted shapes within the rusty facies (Fig.2.18-d). Variations in weathering colors are interpreted to reflect different silica and iron contents. Contacts between layers are sharp and commonly soft deformed : the top and/or base of white layers are undulating and often form contorted masses (Fig.2.18 - a, b). Internal thin laminations (1mm-thick in average) are observed in rusty layers and defined by fine-grained grey particles (Fig.2.18 - c).
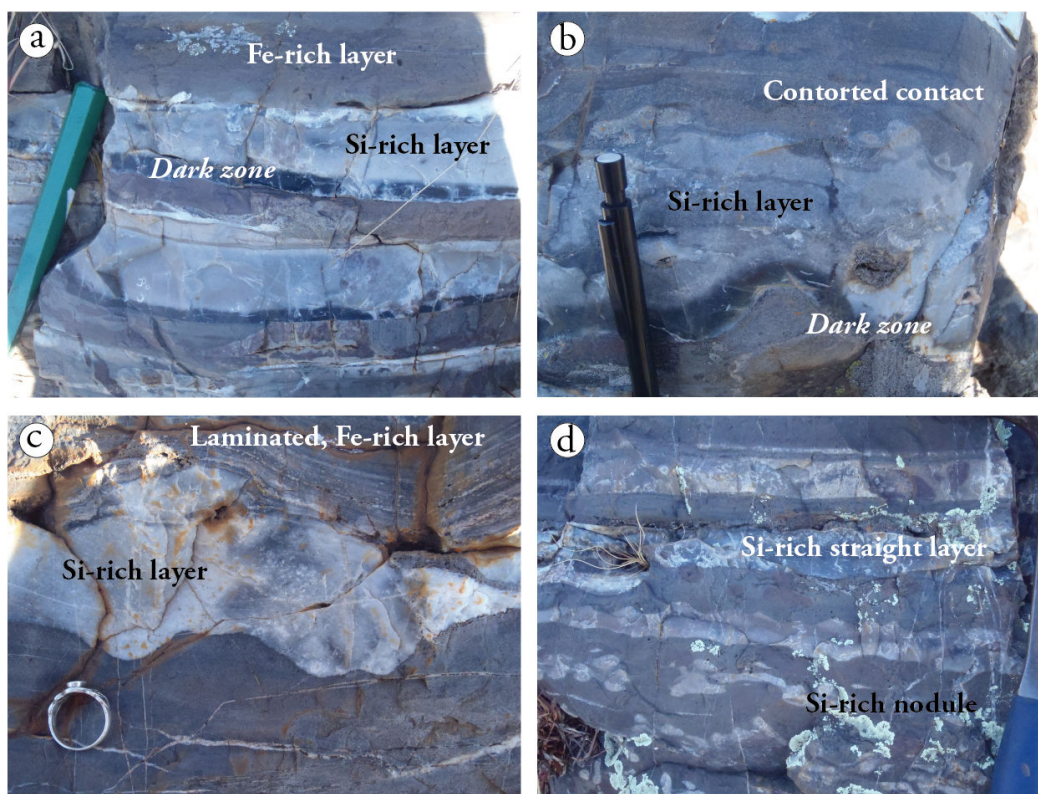
FIGURE 2.18 – *Selected photos of banded siltstone at the base of the Buck Reef Chert sequence (lower, evaporitic unit). (a) Alternations consist of white-weathered and rusty-weathered fine-grained siltstones where color changes are attributed to varying silica and iron contents. The white-weathered layers commonly have darker bases in diffuse contact with the white part. Photos (b) and (c) represent typical undulating, sharp contacts between both facies. (d) Part of the lowermost white siltstone form disseminated nodules instead of straight layers.*

The lower and upper sequences (LBC and UBC) are composed of alternating and equally common black carbonaceous chert and white translucent chert, as shown in Figure 2.19. The bands decreases in thickness from base to top, from 4-20*cm*-thick to 2-4*cm*-thick in average. All rocks have high silica contents, as revealed by the nearly translucent aspect of most of the layers.

The black chert layers preserve thin laminations and current-induced structures, such as ripple marks and cross-laminations. They contain light-grey, fine-grained particles ($< 1mm$ in average) which lie in a siliceous translucent matrix, especially in the LBC. The uppermost layers of the sequence contain fewer particles, with little to no sedimentary structures, and have slight rusty-weathering colors revealing the presence of ferruginous components. White chert layers lack obvious detrital grains and sedimentary structures, and are almost entirely composed of massive, homogeneous, finely crystallized silica (Fig.2.19). The weathering color is white
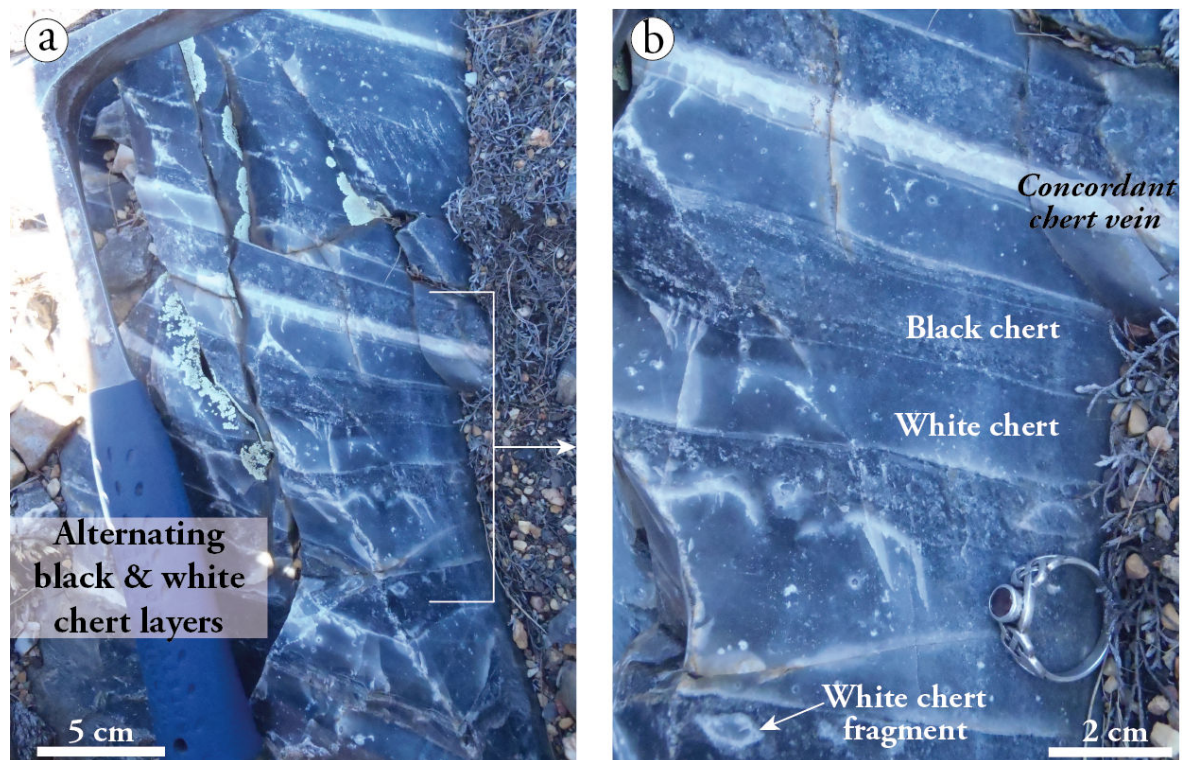
FIGURE 2.19 – *Typical banded black and white cherts facies. Regular alternation of particle-rich, thinly laminated black chert and particle-free, translucent white chert are shown. One layer at the top of the sequence is crystallized with colloform structures and is interpreted as concordant silica vein. White layers may be soft deformed on top (b) and rounded white fragments are commonly found isolated in the black facies.*

and milky, often preserving the translucent aspect of the chert. The absence of pink-, rust- or red-weathering colors is evidence for the absence of iron or other impurities.

Soft deformation structures are abundant in white cherts and typical examples are shown in Figure 2.20. Contacts with surrounding black cherts are sharp and frequently undulating (Fig. 2.20 - a,b). In photo (b), the laminations in the overlying black facies are disturbed close to the undulating contact but become regular and undeformed within 1-3cm of the contact. Undulation troughs lack evident onlaps or fan-like sedimentary structures, indicating that the deformation was not syn-sedimentary but rather occurred at very shallow burial, just after emplacement of the black chert and while the white chert was still soft and deformable. In photos (c) and (d) of the same figure, the deformation is still in the ductile field, but occurred in the opposite direction. The white layer is planar at its upper contact but strongly
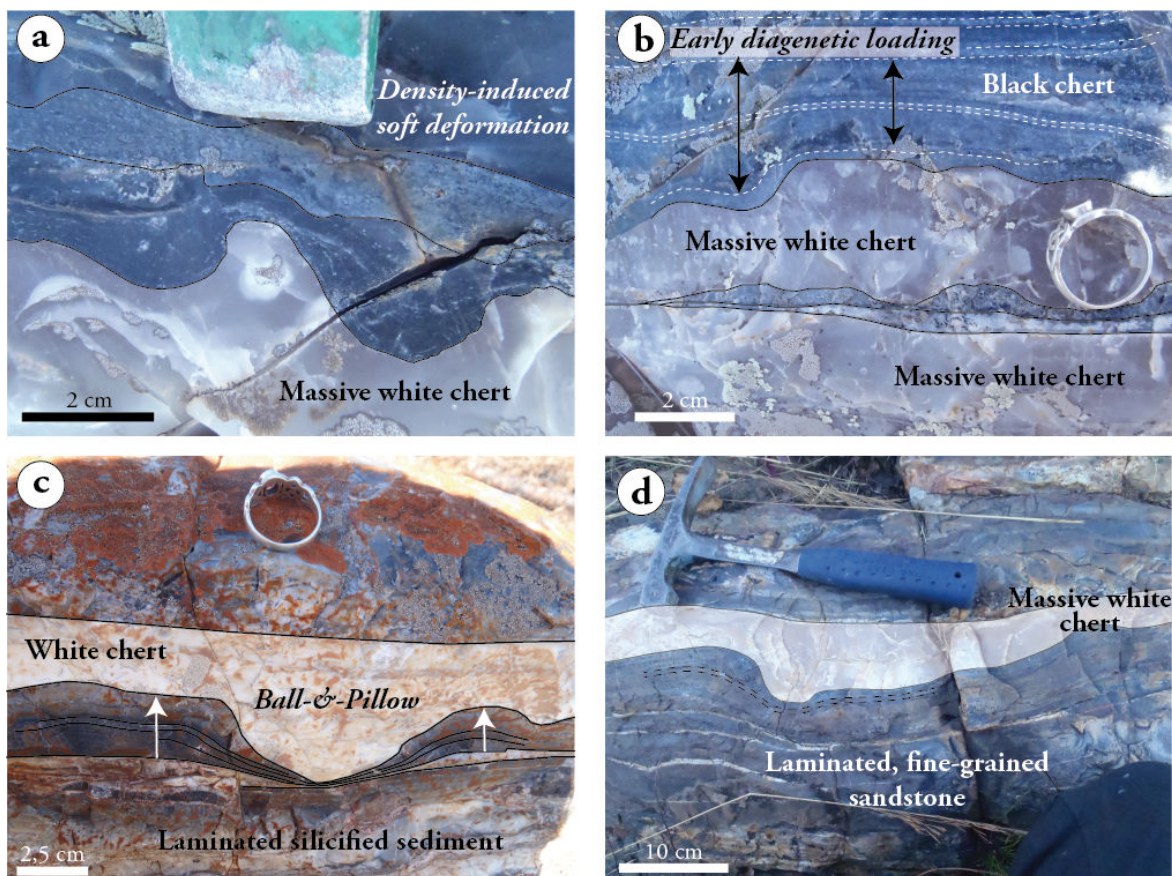
FIGURE 2.20 – *Photos of Buck Reef cherts showing the rheological evolution of the white facies through diagenesis, from (a & b) soft but cohesive near the seabed, developing load cast structures at the interface with the denser, upper black chert, to (c & d) denser than surrounding units during the early stages of diagenesis as shown by the sinking of the overlying white chert into the underlying laminated sediment.*

deformed at its base, pointing to the downward penetration of the chert into the underlying laminated sediment. The sediment lamination are strongly deformed and their convex-shape is characteristic of ball-&-pillow structures.

Both these types of deformations are characteristic of density inversions (*e.g.* Potter et Pettijohn 1963, Owen 1996, Pope et al. 1997, Obermeier 1998, Obermeier et Pond 1999, McLaughlin et Brett 2006), and the second type probably occurred at slightly deeper conditions as the white chert became denser during diagenesis.

A different type of soft deformation is shown in Figure 2.21. The outcrop consists of alternating black and white chert layers capped by a conglomeratic unit. Below the conglomerate, the black chert is homogeneous thorougout while the white layers are elongated and disrupted along the bedding. Such boudinage
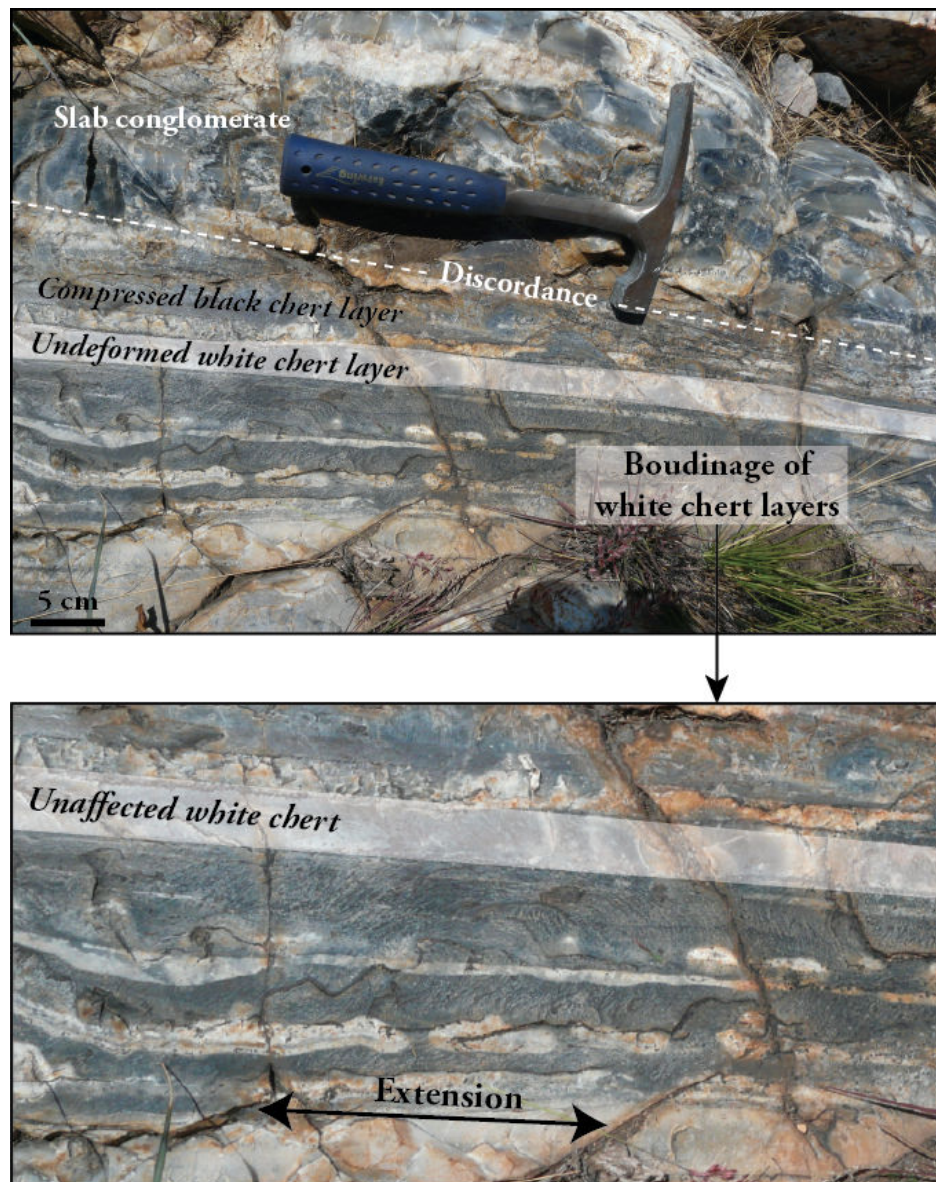
FIGURE 2.21 – *Succession of banded black and white chert layers ending with a conglomerate unit on top. Below the discordance (base of conglomerate), the white layers are elongated and softly disrupted along the bedding while the black facies remains homogeneous thorough. The "boudinage" of white cherts within undeformed black material is evidence for its faster induration and plastic behavior at the time of deformation.*
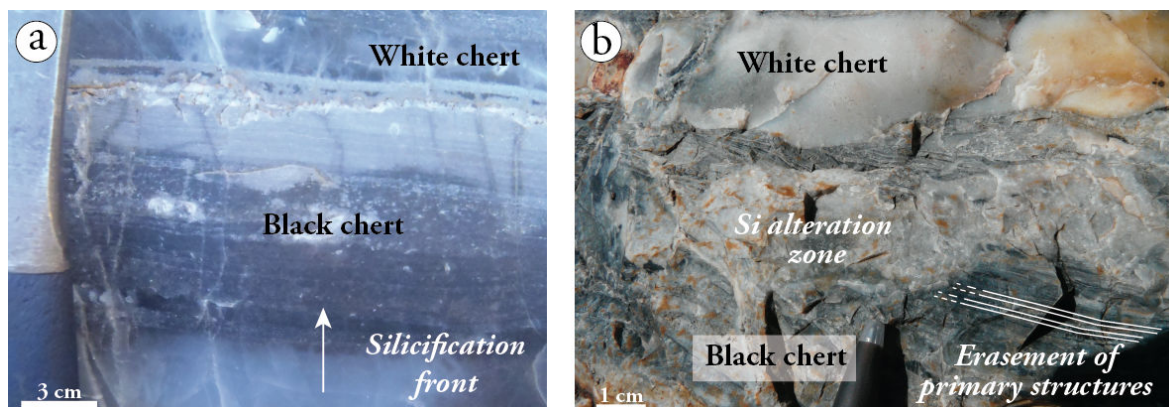
FIGURE 2.22 – *Silicification and fluid circulation structures within the Buck Reef Chert. (a) A thinly laminated, black to light grey chert presents diffuse silica intrusion from its base to its top, leading to disappearance of internal structures and giving rise to a white, semi-translucent color. (b) Example of a white chert vein intruded parallel to the bedding. The vein is filled by well-crystallized quartz contrasting with the particle-free, white, translucent chert it intruded. The lower part of the picture represents Fe-rich, very fine-grained siltstones with seafloor soft deformation structure.*

develops when a competent horizon is enclosed within two less competent layers. The elongated and contorted shape of each boudin suggests that the white chert was plastic at the time of deformation but less competent than the black chert (Goscombe et al. 2004).

Some white chert layers appear to have formed as veins or fractures that cut across surrounding units, commonly at very low angles, and can be traced only over small distances along outcrops. They are generally well-crystallized and coarser grained than the white chert layers. They typically preserve colloform structures and vary in thickness from $<1mm$ to $20cm$. One example of concordant chert vein is shown in Figure 2.19. Other traces of Si-rich fluid circulations are the presence of abundant silicification fronts that can strongly affect internal structures of black cherts. In Figure 2.22 - a, the front is pervasive and migrated perpendicularly to the bedding whereas in photo (b) of the same figure the silicification is much more heterogeneous and cuts across the black chert layering. These structures, together with the abundant silica veins, are evidence that strong silicification affected the Buck Reef cherts after their deposition.

Distinctive "slab conglomeratic" layers alternate with the regular black and white banded cherts (Fig.2.23). They can reach 1 to $2m$ in thickness (generally
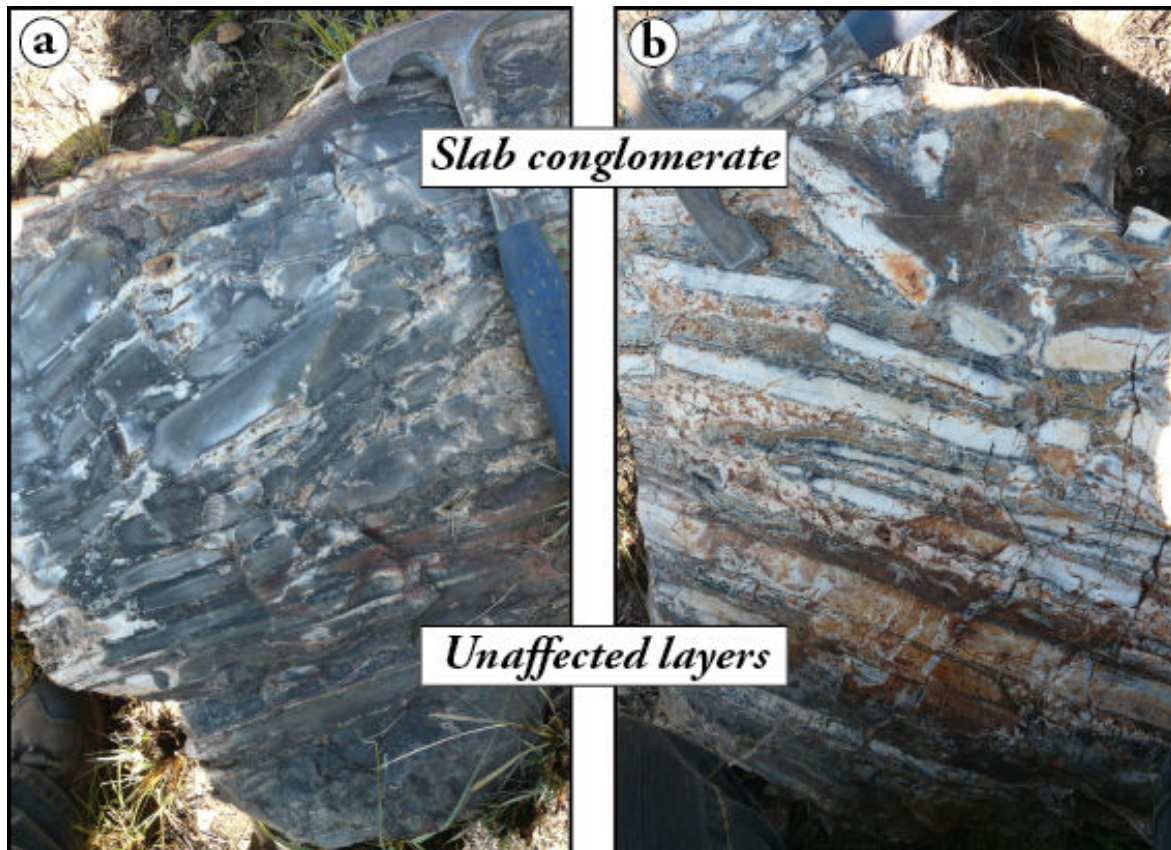
FIGURE 2.23 – *(a) and (b) Photos of slab conglomerates from the Buck Reef site. Each layer is characterized by an abrupt transition from undisrupted to disrupted white chert layers. The slabs are parallel at first to the bedding, then they become inclined and more rounded through the top of the unit. The white chert slabs are the disrupted equivalent of massive white layers and were reworked and redeposited in a still soft black chert matrix. Undisrupted white chert layers mark the lower limit of the sliding zone.*

$<50cm$) and often disappear laterally after a few meters. These conglomerates consist of elongated, angular to sub-rounded slabs of white chert, typically 2 to 50cm-long and 1 to 10cm-thick, in a matrix of grey to black chert. None of the conglomerate unit is made of black chert slabs in a white chert matrix. The slabs are generally oriented sub-parallel to bedding, but in places they are strongly disrupted and oriented at high angles.

The upper contacts of conglomerate beds are irregular due to the disposition of the slabs, and overlying detritus-rich black chert fill troughs with typical fan structures, as shown in Figure 2.24 - b. At the lower contact (photo a), fluid-escape structures are often observed and point to conglomerate deposition onto a still soft
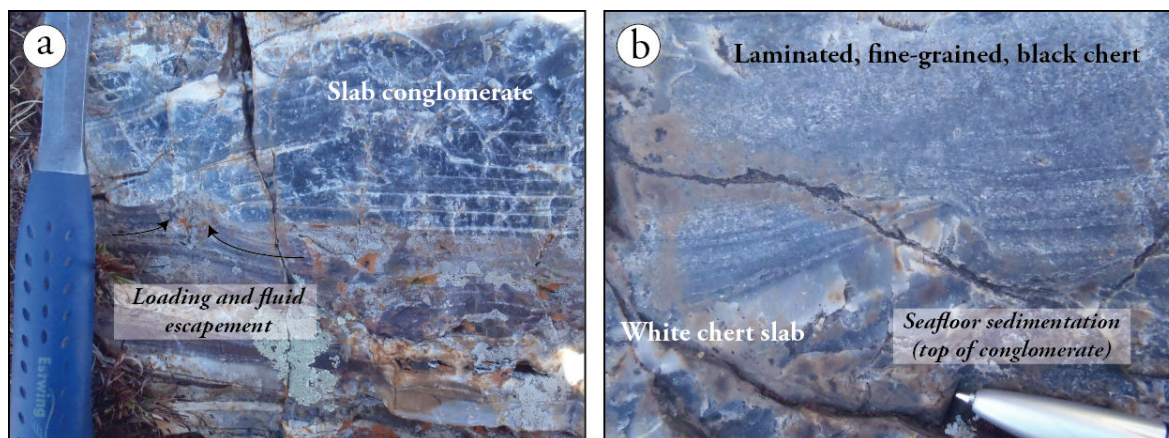
FIGURE 2.24 – *Seafloor deposition evidence for slab conglomerates. (a) The surface of conglomerates is dependent of slab geometry during deposition. The irregular surface is filled during by upper thinly laminated, particle-rich black chert with fan sedimentation and onlap structures. (b) At bottom contact, underlying laminated, iron-rich siltstone shows well-developed fluid escapement structure induced by slab conglomerate emplacement.*

and hydrated substratum. These observations indicate that the slab conglomerates form an integral part of the sedimentary sequence.

The slabs are lithologically similar to undisrupted white chert layers, being composed of homogeneous and translucent finely crystallized silica. Typical examples are shown in Figure 2.25. A few rusty-colored slabs have been found in the lowermost part of the LBC which is thought to reflect the local higher iron content in the form of minor impurities within the chert. Slabs commonly develop rims of well-crystallized quartz (up to 1*cm*-thick) in sharp contact with surrounding matrix (Fig.2.25 - e). The matrix is either homogeneous or thinly laminated and composed of light-grey detrital particles in a black siliceous matrix. In places, large cavities (up to 5*cm*-long and 1-3*cm*-large) are left between chert slabs and filled by well-crystallized, commonly colloform silica (Fig.2.25 - d).

Deformation structures are common in both slabs and matrix, and each component behaved differently. The slabs generally maintained an elongated, angular to sub-angular shape, indicating they were rigid at the time they were disrupted (Fig.2.25). In contrast, the matrix shows plastic deformation highlighted by flowage of the detrital content around chert fragments (Fig.2.25 - c). We interpret those features as evidence that the slabs were silicified and indurated early while still at the
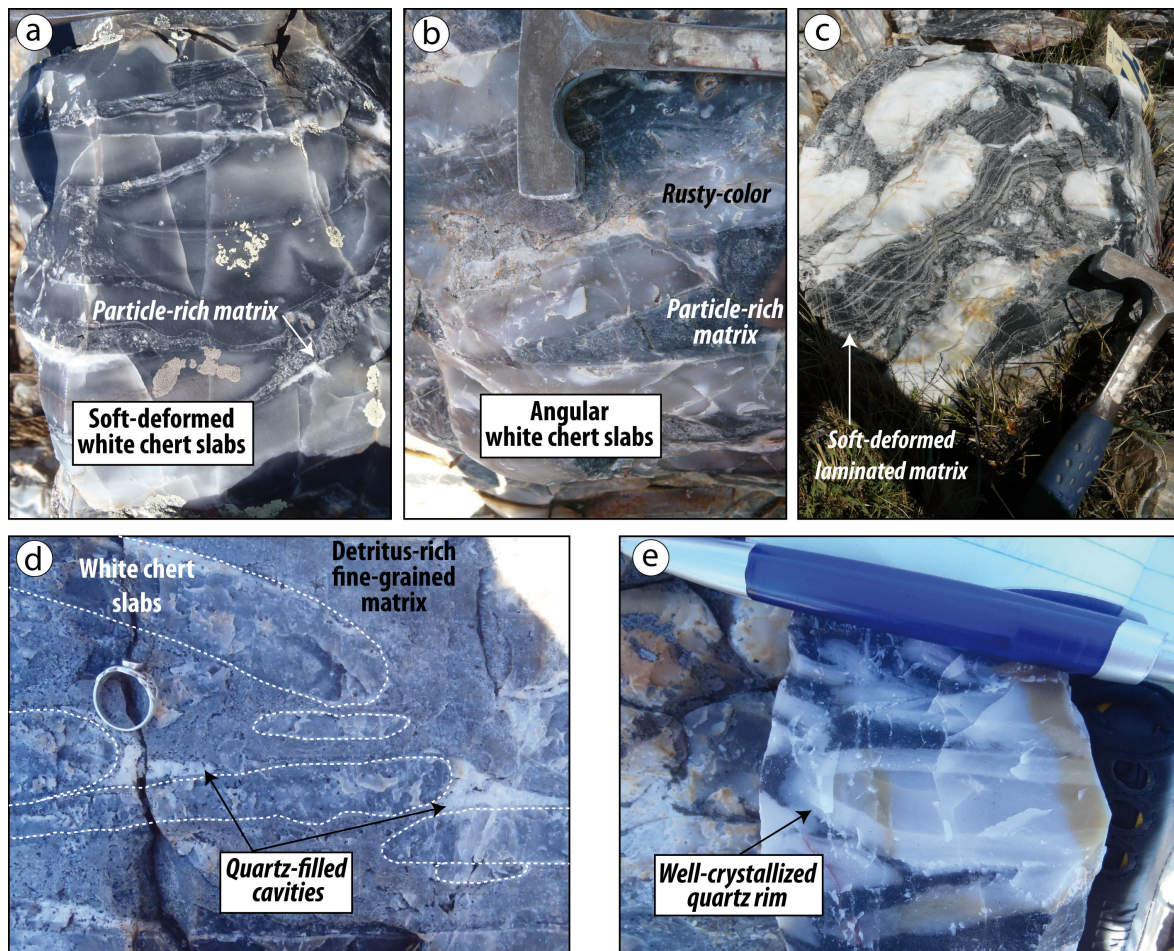
FIGURE 2.25 – *Selected photos of white chert slabs in conglomerate layers showing the range of shape, size and organization of such fragments. They are angular to sub-rounded, range in size from cm- to several dm-long and have or not well-crystallized siliceous aureoles. The matrix is invariably composed of black chert with soft-deformation structures (c) and void-filling silica is common in this facies.*

seafloor, then disrupted, probably during major storms, before being redeposited as fragments in a soft, detritus-rich siliceous matrix. Rare fragments show irregular undulating edges, and their sharp contacts with surrounding matrix point to very early disruption before complete induration on the seafloor rather than secondary dissolution after deposition (Fig.2.25 - a, c). Preservation of such soft-deformation structures enclosing brittle deformed, more rigid slabs of white chert, is another indication for very rapid induration of the fragments at the surface.
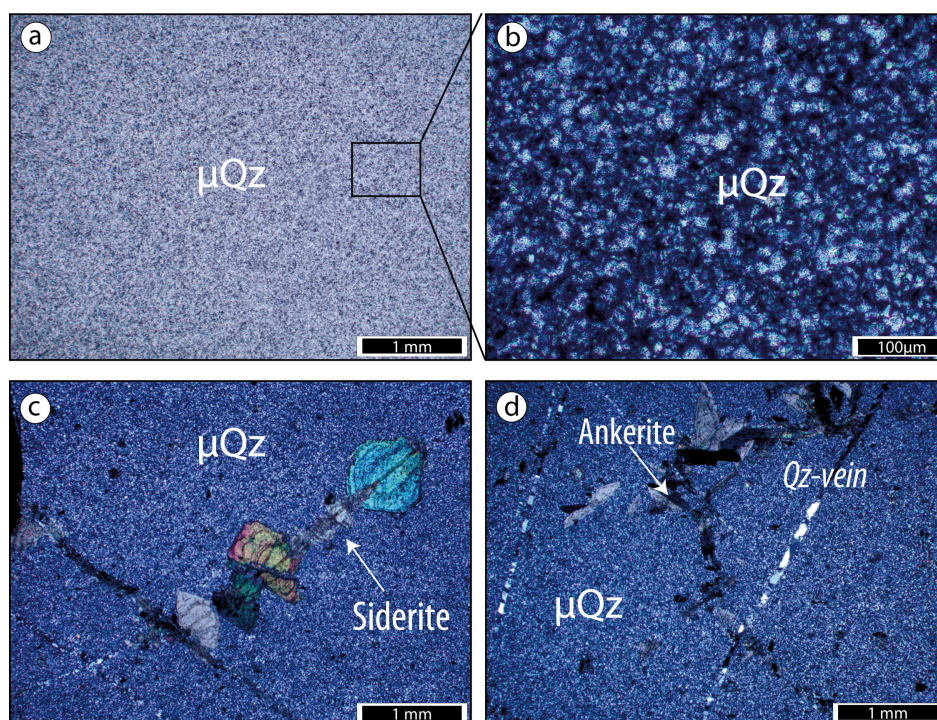
FIGURE 2.26 – *Optical microscopy for massive white chert samples. µQz = microquartz, Qz = Quartz. (a) and (b) show the purity and homogeneity of massive white chert. They are entirely composed of microquartz of 5µm in average. (c) and (d) All layers are cross-cut by thin quartz-filled veins (< 0.5mm) that can be associated with siderite (c) and ankerite (d) secondary minerals.*

Petrological characteristics

As the white, detritus-free chert layers are most likely to represent primary precipitates, we collected 5 samples at the interface with surrounding black cherts. An additional 15 samples were taken from massive black chert layers, white chert veins, and slab conglomerates.

Massive translucent white chert bands are homogeneous throughout the whole banded sequence. As shown in Figure 2.26, they are entirely composed of micro-crystalline α-quartz (>99%) as confirmed by the X-ray diffraction spectra from the previous section, Figure 2.13. The texture is equigranular and individual quartz grains are small, < 5-10μm in size (*i.e.* microquartz). They show irregular, crenulate boundaries and have sweeping extinctions (Fig.2.26 - a, b). Through the breadth of each band, grain size remains constant without internal sedimentary structures and the closely intergrown framework contains little porosity. Minor iron oxides (*e.g.* hematite), siderite and stilpnomelane are seen in white cherts from the upper,
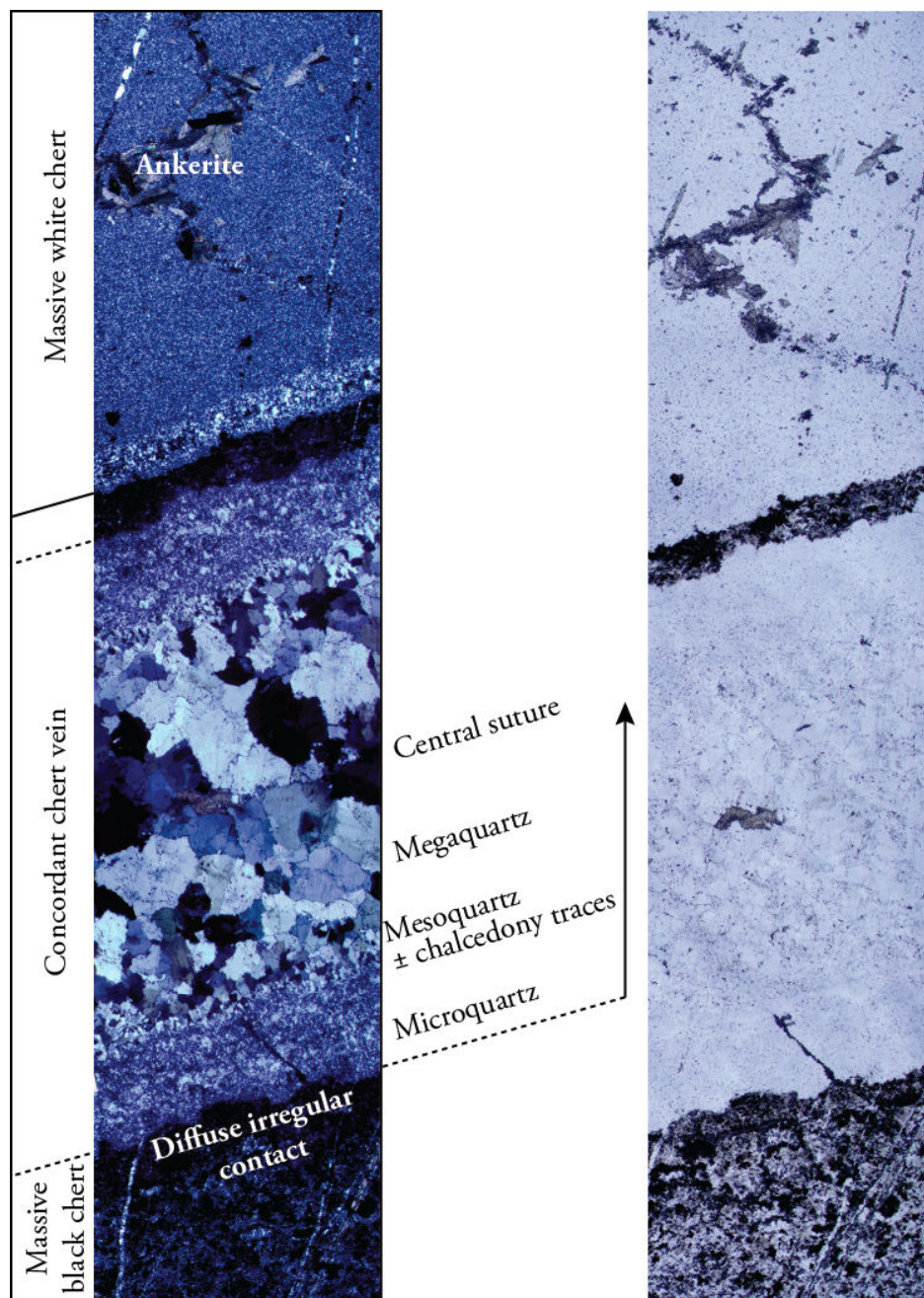
FIGURE 2.27 – *Natural (right) and polarized (left) photomicrographs showing the petrologic evolution from a massive black chert (base) to massive white chert (top) with an intermediate concordant quartz-filled vein. The contact of the vein is irregular with surrounding black chert and a specific internal organization : at the contact the vein is composed of microquartz that evolves to mesoquartz and megaquartz when going through the center. The micro to megaquartz transition is abrupt aver less than 0.2mm. Traces of chalcedony may be preserved in the microquartz facies in the form of radial twinning within neighboring quartz packages.*
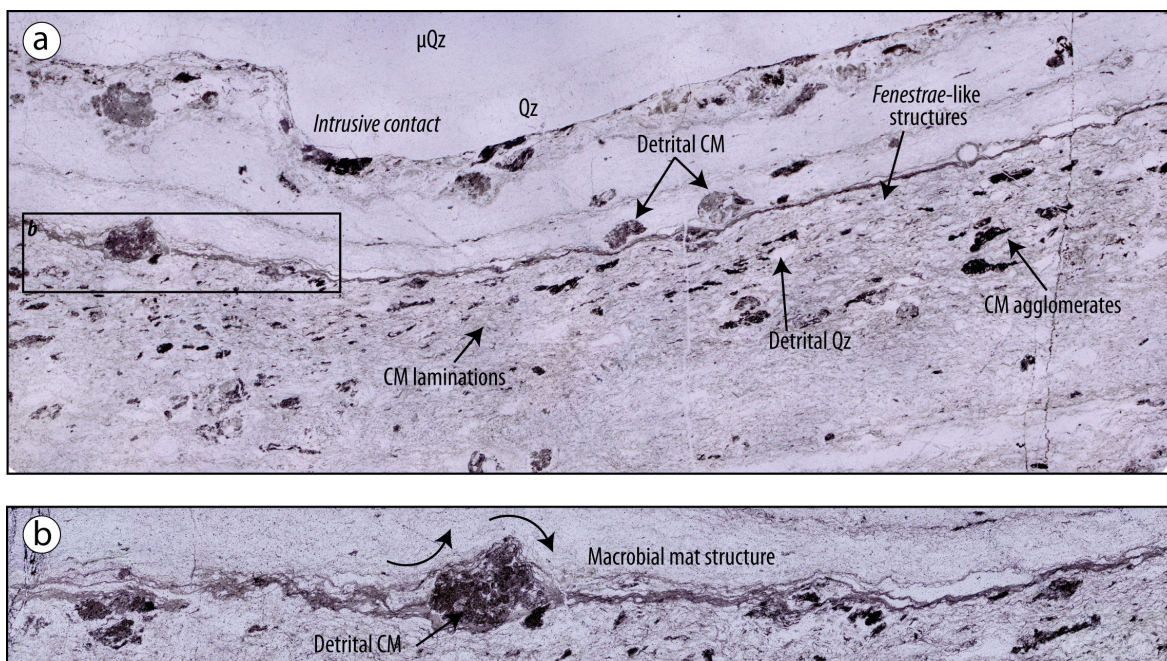
FIGURE 2.28 – *Massive black chert layer at the interface with a white chert vein. CM = Carbonaceous matter, μQz = microquartz, Qz = Quartz. (b) is a detail of (a). The chert contains all three carbonaceous matter facies : detrital rounded grains, elongated agglomerates and thin laminations. Laminations drape detrital grains (b) and may be microbial mat. They are irregular and define fenestrae that are representative of microbial activity. The contact with overlying chert vein cross-cuts black chert internal structures.*

ferruginous part of the sequence. Some grains appear to have grown on the microquartzitic matrix and are interpreted as secondary minerals ; others are located within thin cross-cutting chert veins as in Figures 2.26 - c, d.

In contrast, the white chert veins, independent of their thickness (from less than $1cm$ to $10cm$), show features that distinguish them from the massive white cherts. Their contacts with surrounding rocks are either diffuse and irregular, as shown in Figure 2.27, or sharp, as shown in Figure 2.28, and commonly cross-cut surrounding chert layers. Thin veins ($<1mm$-thick) often root in the main vein and penetrate perpendicularly the host-rock. From the smallest to largest veins, a typical internal organization is illustrated in Figure 2.27 : they have inhomogeneous quartzitic compositions and distinctive grading from margin to centre. A thin zone of microquartz (grain size $<5\mu m$) lines the contact with surrounding units, in places marked by a colloform structure, *i.e.* a fine concentric banding enveloping undulations at the contact. This fine-grained zone is followed inward by crystals of
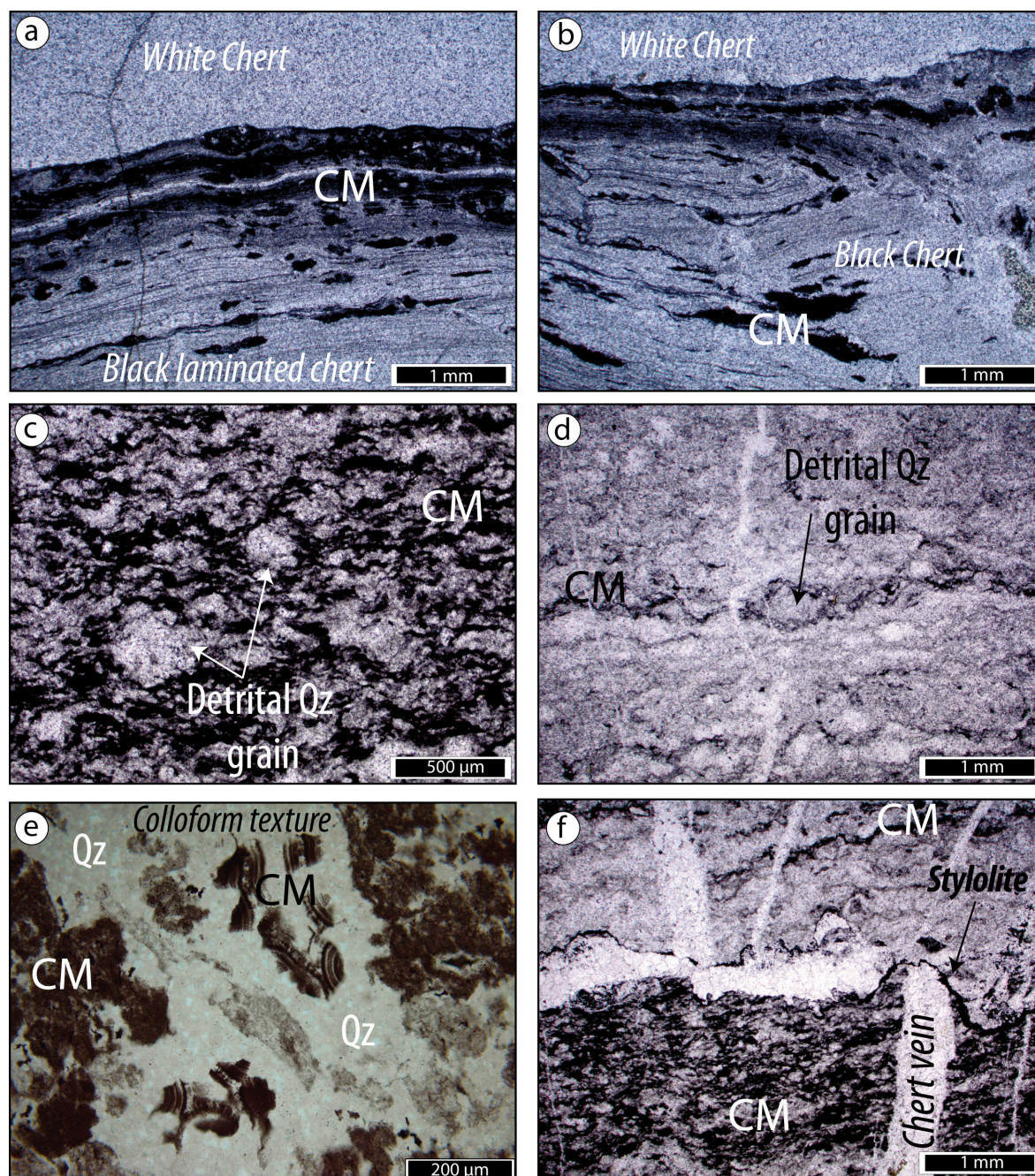
FIGURE 2.29 – *Photomicrographs for massive black chert samples. CM = Carbonaceous matter, µQz = microquartz, Qz = Quartz. (a) and (b) show the sharp and regular contact with overlying massive white chert layers. Black facies contain significant amount of carbonaceous matter in the form of small particle agglomerates (a, b), homogeneous grains (e) and thin laminations (a to d). (c) and (d) Detrital quartz grains are embedded within carbonaceous layers. They are rounded with diffuse edges and are recrystallized as microquartz so that only ghosts and shapes are conserved. (e) Carbonaceous matter can be more diffuse and highlight internal textures induced by silica migration within layers (colloform texture in this case). (f) Stylolites monitor a pressure-dissolution process during deep burial of cherts. They disturb chert vein and reveal silica redistribution during late diagenetic processes.*

megaquartz, up to $1mm$-long and commonly aligned perpendicular to the contact. The central parts of these veins often contains siderite or ankerite grains that are intergrown with macroquartz crystals and could represent the final crystallization product.

The black chert layers contain abundant and morphologically diverse types of carbonaceous matter, as shown in Figures 2.28 and 2.29, in association with variable quantities of sand-sized particles : the latter are interpreted as rounded detrital quartz grains that are almost entirely replaced by microquartz (Fig.2.29 - c, d). Carbonaceous matter occurs as (1) rounded agglomerates (up to $1mm$) of small particles, (2) elongated homogeneous grains ($<0,5mm$), and (3) thin laminations within the silicified sediments ($<10\mu m$ thick) (Fig.2.28). The agglomerates are generally rounded and undeformed with well-defined boundaries whereas the homogeneous grains are often elongated parallel to the laminations. Carbonaceous matter makes up to 10% of the black chert, the rest being microcrystalline quartz ($<5\mu m$).

The thin carbonaceous laminations are very common in black chert bands. They are commonly deformed by current action, especially in the lower part of the sequence. Several samples showed irregular, undulating shapes resembling microbial mats. The Figure 2.28 represents one of these organic-rich samples. The thin carbonaceous laminations can be followed laterally and are characterized by irregular undulations and local detachments that give way to fenestrae filled by microquartz. Such structures are considered to be fossil traces of fluid and gas circulations related to microbial activity of mat. Carbonaceous grains and agglomerates are commonly trapped within and draped by the thin layers of the biogenic structure (Fig.2.28 - b), which is interpreted to represent microbial growth in a detrital-rich environment. When such microbial mats are observed, they are systematically interbedded at a micrometer scale with pure, finely crystallized silica layers $<10\mu m$ in thickness.

The characteristics of the contacts between black and white cherts, and the contrasting features in each type of band, may be the key to understanding the origin of the banding in the Buck Reef Chert. Internal structures in black cherts, which are either biogenic laminations or abiological structures, generally follow
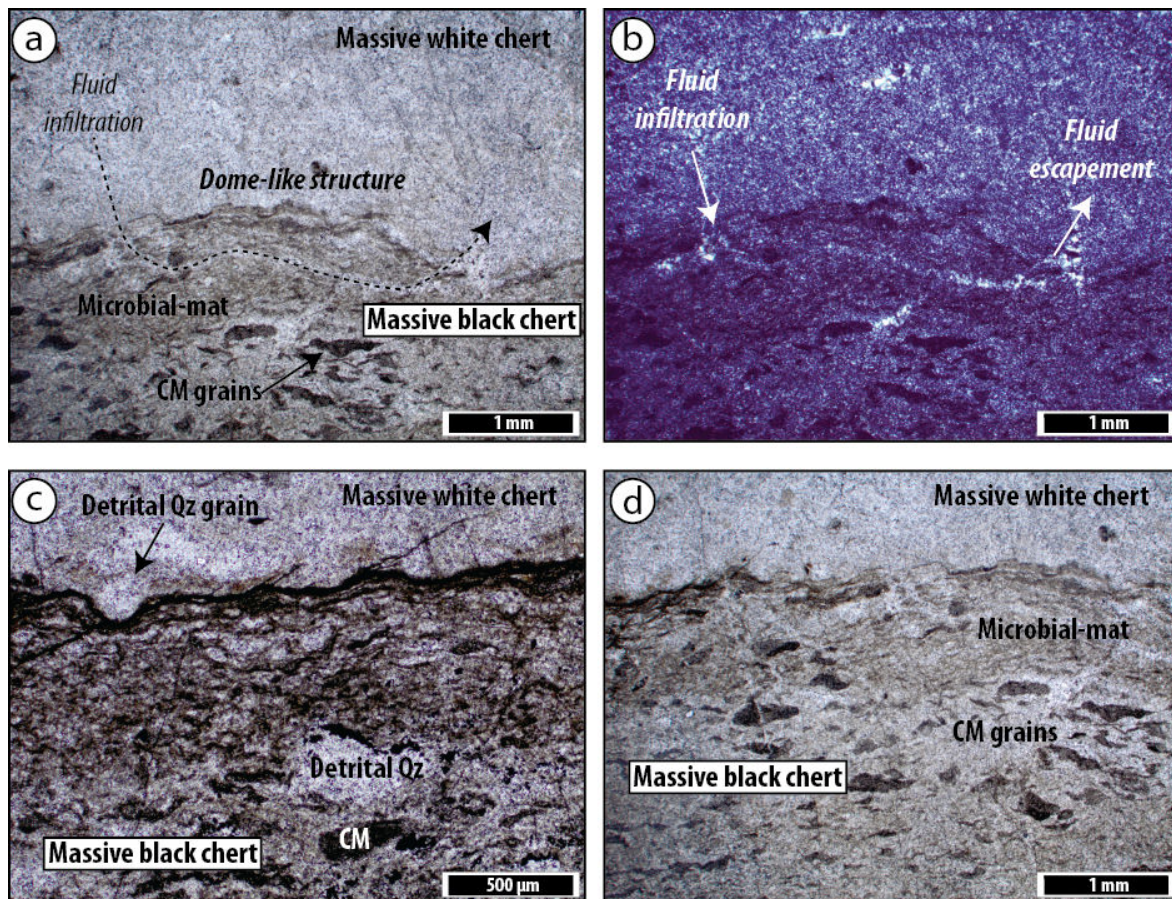
FIGURE 2.30 – *Optical microscopy of massive black and white cherts. CM = Carbonaceous matter, Qz = quartz. (a) and (b) The black chert has carbonaceous laminations typical of microbial mats. Perpendicular cracks connected within the black facies by a thin quartz-filled vein are interpreted as silica infiltration during white chert emplacement when the mat was still alive. (c) Sharp and irregular contact with small-scale load-cast structure induced by small, recrystallized detrital quartz grain. Carbonaceous matter is concentrated at the interface during compaction. (d) Microbial mat at the top of black chert partially erased by diffuse silica concentrations.*

the contact with surrounding white chert layers (Fig.2.30 - a, d). The contact is sharp with small-scale irregularities that are commonly associated with indentations from detrital particles from the overlying material, (*i.e.* small-scale load cast structures) (Fig.2.30 - c), or with the presence of microbial mats below (or above) the contact (Fig.2.30 - a, d). Both resemble soft-deformation structures that developed during sedimentation.

In Figure 2.30 - a and b, infiltration structures can be observed : the uppermost laminations of the mat are cut by fine fractures perpendicular to the general orientation, and the thin veins ,now filled by microquartz ($< 20\mu m$), appear to have
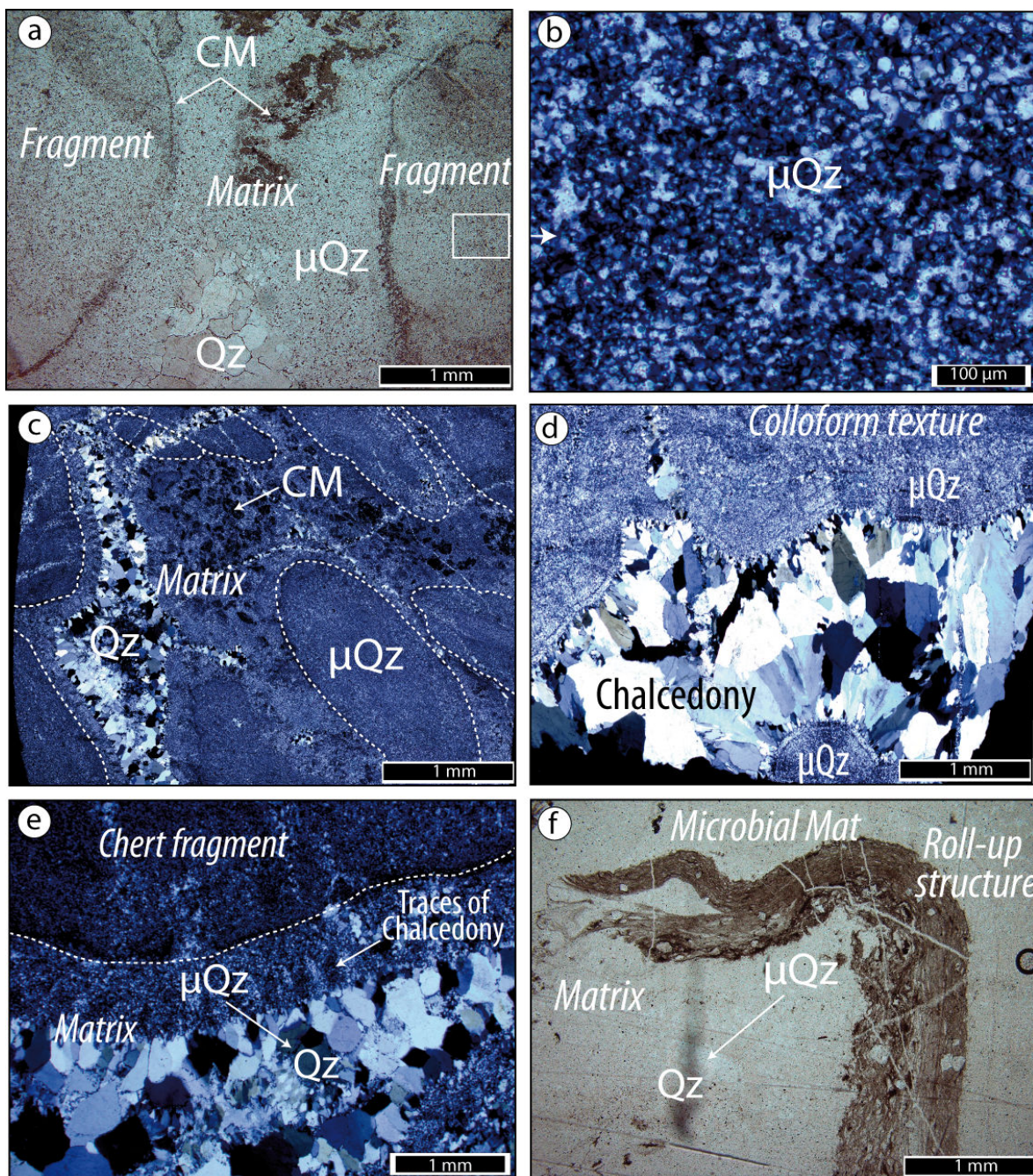
FIGURE 2.31 – *Optical microscopy in slab conglomerate samples. CM = Carbonaceous matter, µQz = Microquartz, Qz = quartz. Slabs are highlighted by white dotted lined. (a) and (c) show the internal matrix-supported structure of slab conglomerates. Slabs are elongated and sub-rounded with carbonaceous matter concentrated in their rim (a) at the contact with the matrix. (b) Chert fragments are entirely composed of quartz with sizes varying from $<2µm$ to $< 20µm$. (d) and (e) Part of the matrix has a cavity-filling texture, with microquartz at the contact with slabs that may conserve traces of chalcedony. It sharply evolves through macroquartz when going away from chert fragments. (d) This texture is often better developed with well-preserved large chalcedony crystals (up to 1mm). Is is associated with microquartz that design colloform textures. (a) and (c) highlight that if carbonaceous matter is present in the matrix, it precludes cavity-filling texture to develop and the matrix as microquartzitic composition. (f) Rare microbial mat fragments can be observed : here a surprisingly well-preserved mat is softly deformed with roll-up structure and local detachment, showing reworking when still alive.*

migrated along the mat, and to have generated a new, thin perpendicular crack. Such structures are interpreted as desiccation cracks that formed during the deposition of white chert onto living microbial communities.

The contact can also show anomalous concentrations of carbonaceous matter as in Figure 2.30 - c. Because underlying laminations are undeformed, and because there is no evidence of silica infiltrations between both facies, we suggest that this structure developed during the early compaction of underlying, carbonaceous-rich, black chert during white chert deposition on the seafloor.

Multiple generations of silicification can be observed, and especially in the black chert facies. Part of the contact with surrounding white chert layers may be erased by diffuse silica enrichment in the first $<0.2mm$, as shown in Figure 2.30 - d. Because the silica seems not to penetrate deeper in the black chert, we attribute this type of structure to very small-scale, pervasive silica diffusion during white chert precipitation onto previously deposited black chert. In places, pervasive silica can enter deeper into the underlying chert layer. Figure 2.29 - e shows that penetrating fluids locally redistribute carbonaceous matter, then concentrate it at crystal edges during precipitation of silica minerals. Thanks to carbonaceous matter concentrations, the very early colloform texture of the primary crystallization phase is preserved, despite secondary recrystallization. Such pervasive textures and diffusive contacts indicate that this silicification occurred at a very early stage of chert deposition, while it was not fully lithified, at or near the surface. Additional silicification occurred while the chert was indurated, as revealed by numerous generations of chert veins that cross-cut massive layers (Fig.2.29 - d, f). Finally, the presence of abundant stylolites (Fig.2.29 - f) deep in the sequence provides evidence of late remobilization of silica due to pressure-dissolution process. They affect the earlier chert veins and are thus the final stage of secondary silica migration. Despite the significant silicification of the sequence, we note that sedimentary structures are generally well preserved in the black facies. The lack of internal structures and carbonaceous content in white layers renders difficult the observation of possible secondary silicification, and chert veins being the most common evidence of this process.

In conglomeratic layers, the slabs consist entirely of homogeneous quartz that

varies little in grain size, from microquartz $<5\mu m$ to mesoquartz up to 20-30μm (Fig.2.31 - b). Carbonaceous matter is nearly absent within fragments but is commonly concentrated in well-crystallized rims (Fig.2.31 - a), located essentially at microquartz boundaries leading to a spiderweb aspect. When well-developed rims are observed (typically $>3mm$), they are composed of mesoquartz with grain sizes varying between 50 and 100μm.

The matrix around slabs is mainly composed of quartz and carbonaceous matter that produces the black color in outcrops (Fig.2.31 - a, c). Two facies are observed :

(1) When carbonaceous matter is abundant, either in the form of detrital rounded particles or carbonaceous aggregates, the surrounding matrix is very similar to massive black cherts, being essentially composed of microquartz ($<5\mu m$). Rare pieces of microbial mats may be present in the form of thin discontinuous and disrupted laminations. Figure 2.31 - f shows a remarkably well-preserved mat fragment with a roll-up structure and internal detachments typical of reworking of living biofilms.

(2) In part of the matrix, a coarser facies has characteristics similar to white chert veins (Fig.2.31 - c, e). At the contact with chert fragments, the matrix is finely crystallized to microquartz ($<5\mu m$) and traces of chalcedony are often preserved in the form of radial extinction patterns in juxtaposed quartz packages. This texture defines a $<0.5mm$-thick aureole around chert fragments. Moving away from slabs, the crystal size abruptly increases to that of megaquartz (up to 1mm). When secondary recrystallization is nearly absent, large chalcedony grains (up to 2mm) are preserved and colloform textures can remain (Fig.2.31 - d). This part of the matrix is free of carbonaceous matter and attributed to precipitation in cavities between slabs from circulating fluids. As in massive chert layers, numerous chert veins ($<1mm$-thick) cross cut conglomerates and affect both the slabs and matrix (Fig.2.31 - c), reflecting secondary fluid infiltration during early and/or late diagenesis processes.

X-ray microfluorescence analyses.

Using the methods described in Section 2.1.3, we produce X-Ray microfluorescence maps for two samples located at the interface between massive black and
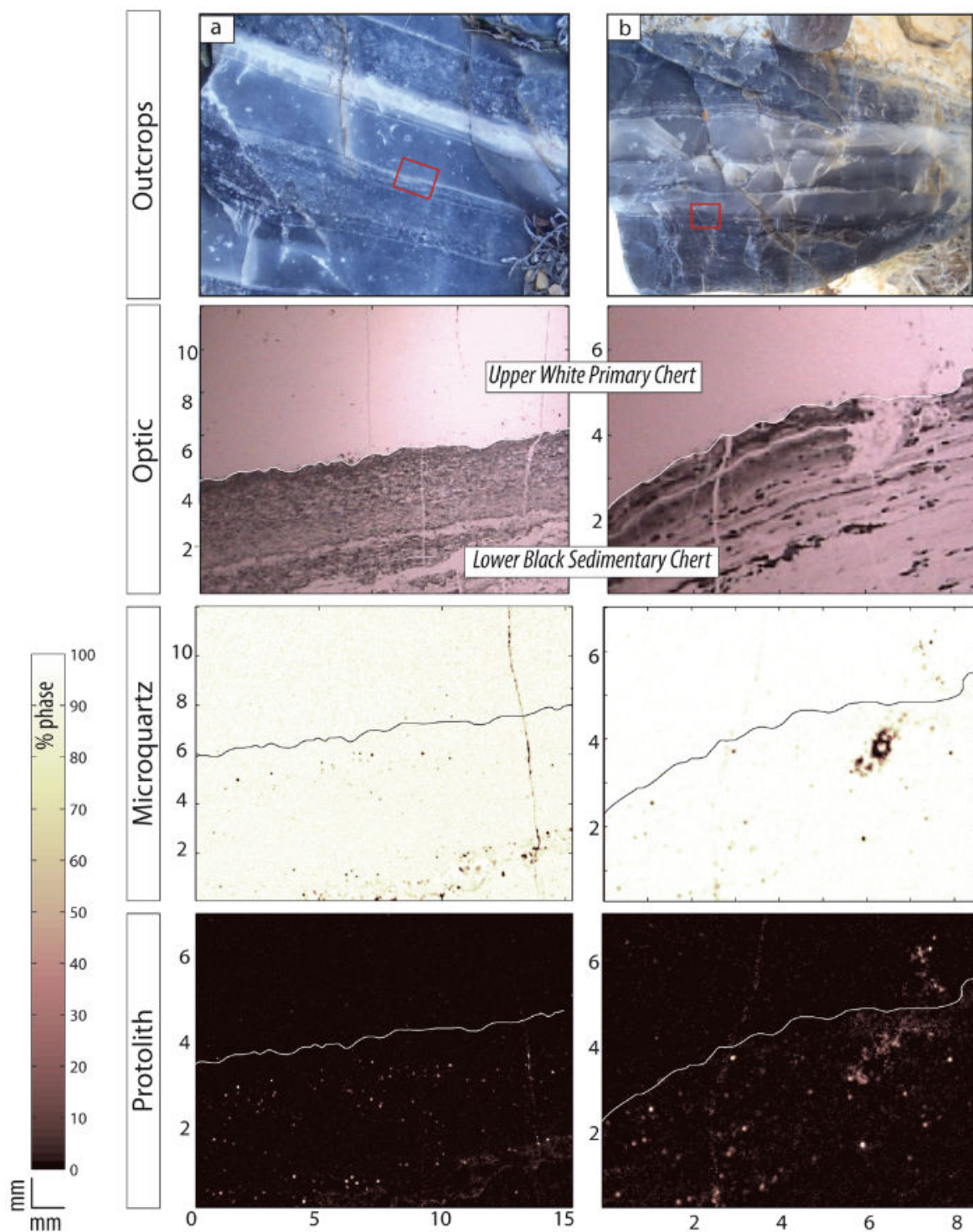
FIGURE 2.32 – *X-ray microfluorescence maps of phases distribution at the interface between massive black (base) and white (top) chert layers. The contact is highlighted with the solid white line. Two phases are described : a microquartz phase that is present in high amount in both facies, and a "protolith" phase restricted to the black chert facies. The reference for the protolith phase is obtained by choosing pixels with the highest amount of aluminum, potassium and iron according to the method described in section 2.1.3. The nature of the protolith could not be recognized due to the very low overall major element concentration.*

white chert layers. The results are shown in Figure 2.32. As the overall concentrations of major elements are very low compared to the silica content (SiO_2 is around $100wt\%$ for all samples), we chose zones with the highest aluminum, potassium and iron contents in order to identify traces of any putative protolith. The intense silicification process complicates the recognition of the protolith with this technique, but the resulting map highlights zones where possible minor detrital-like components are located. Geochemical whole rock analyses are the subject of Chapterchap4.

The high silica content is easily visible on maps of Figure 2.32 where the microquartz is the dominant phase in both black and white chert layers. However, black cherts show significant proportion of the "protolith" phase, expressed as lighter dots dispersed within the rock. The dispersion, scarcity and rounded shapes of protolith traces suggest that the phase represents isolated, very fine grained detrital particles now mostly silicified to microquartz.

2.1.6   Summary and primary discussion on Buck Reef Cherts.

The Buck Reef Chert is a thick siliceous sedimentary sequence deposited under evolutive conditions, from coastal lagunal at the base to deeper conditions at the top. Lowe et Fisher Worrell (1999) and Tice et Lowe (2006) proposed normal open-marine sedimentation on a subsiding platform, based on the abundance of current-induced sedimentary structures in the lower facies (*i.e.* ripples, cross-laminations, storm-induced conglomerates), their disappearance in the upper facies, and the thinning of the bedding through the top.

The origin of Buck Reef Chert is strongly debated. Lowe (1999), Westall et al. (2001) interpreted the sequence as being composed of silicified sediments with variable precursor types, either evaporites, microfossils, carbonates, felsic or komatiitic volcaniclastic sandstones. On the contrary, Lowe et Fisher Worrell (1999) and Tice et Lowe (2006) argued that the sequence was deposited as a mixture of a gelatinous silica and organic- and detritus-rich material, before being silicified. All advocate intense post-formation silicification of Buck Reef Chert, but disagree on the source of silicification : some proposed hydrothermal fluid circulation (*e.g.* de Wit 1982, de Vries 2004, de Vries et al. 2006) while others propose seawater-

seafloor interaction at or near the surface (Lowe et Fisher Worrell 1999, Knauth et Lowe 2003, Tice et Lowe 2006). The final element of controversy concerns the origin of the banding : whether it is inherited from the protolith of the result of diagenetic processes. Lowe et Fisher Worrell (1999) and Tice et Lowe (2006) argue for the segregation and migration of pure silica from the primary siliceous-rich, carbonaceous mixture during diagenesis. In the following section, we build the case for an alternative origin in which all elements of the sequence were originally deposited as banded sediments, some with detrital, volcanic or organic component, and others almost entirely chemical.

The situation is complicated in the Buck Reef sequence by the strong secondary silicification that pervades most of the sequence. In contrast to the Komati River sequence, the Buck Reef Chert is dominated by siliceous sediments, without a significant clastic contribution, and contains abundant traces of fluid circulation. Evidence for secondary, early to late, silica mobilization and fluid circulation is provided by the abundance of micro- to macro-scale quartz-filled veins (Fig.2.22 - b and 2.29 - d, f), the local alteration of internal sedimentary structures across well-defined silicification fronts (Fig.2.22 and 2.29 - e), and common replacement or cavity-filling textures in the slab conglomerate matrix (Fig.2.31 - c, d, e). The youngest structures are stylolites that pervade the sequence and represent pressure-driven dissolution during compaction of the sediment pile.

Despite the strong silicification, primary textures and sedimentary structures are generally well-preserved, particularly in the black chert, and we found abundant evidence for primary sedimentation of both black and white chert facies.

(1) The frequent occurrence of microbial mats in black cherts. Thin carbonaceous laminations alternate with silica micro-bands (both $<15\mu m$) in black cherts, which are interpreted as microbial structures. The shape, lateral continuity and good preservation of the carbonaceous laminations record microbial growth on the underlying surface rather than reworking of previously deposited material. This is further supported by the presence of detrital grains (either quartz or carbonaceous aggregates) enclosed in the structure : they deform the carbonaceous layers on which they were deposited and are draped by new growth structures, showing that the mat was gro-

wing as clastic particles were being deposited. When found at the lower part of a
bed, *i.e.* in contact with underlying massive white chert layers, the microbial mat is
modeled on the interface and is often deformed by millimeter-scale load cast struc-
tures (Fig. 2.30 - c). We interpret these structures to indicate deposition of silica
on a still soft and living microbial colony. The deposition of chert may have killed
the biota, as shown by the desiccation and silica-infiltration structures of Figure
2.30 - a,b. The contact is partially affected in places by small-scale silica migration
(Fig.2.30 - d), but is generally sharp and resembles a normal sedimentary contact.

(2) Syn-sedimentary soft-deformation structures. The contacts between white and
black chert layers are sharp and frequently marked by large- and small-scale de-
formation structures typical of seafloor sedimentation and early diagenetic den-
sity inversions. In outcrop, undulating white chert surfaces are deformed along
syn-sedimentary structures. Figure 2.20 shows lateral thickness variations of the
overlying black chert detritus-rich laminations (*i.e.* fan sedimentation), that are at-
tributed to accumulating load on the still soft underlying white chert shortly after
sedimentation. Additional evidence comes from the boudinage structure of Figure
2.21 that requires the presence of still competent, white chert layers close to the
seawater-sediment interface. In thin sections, the sharpness of the contact (Fig.2.29
and 2.30) and the occurrence of small-scale load cast structures provide additio-
nal support for our interpretation of seafloor sedimentation of both the black and
white cherts.

(3) Slab conglomerates. The texture and mineralogy of white chert slabs in conglo-
merates are very like that of undisrupted white chert layers (Fig.2.26 and 2.31) :
this likeness suggests a similar origin and similar physico-chemical conditions du-
ring precipitation of both chert facies. The slabs are thus interpreted to have once
been part of white chert layers that had been deposited on the seafloor before they
were disrupted and reworked by sedimentary processes. The brecciation, rewor-
king and redeposition of the conglomerate layers occurred at the surface, as shown
by fan sedimentation at their top (Fig.2.24). We believe that the fluid-escape struc-
tures shown in Figure 2.24 further support seafloor emplacement, although one can
argue that these are diagenetic features. If these not entirely convincing, the pre-

sence of the microbial mat with roll-up structure in Figure 2.31 - f constitutes solid evidence for the seafloor deposition of conglomerates because such structures imply that the mat was still alive at the time it was enclosed within the black, siliceous matrix. The resulting slabs were redeposited onto still-soft sediments, probably a mixture of primary silica, detrital grains and organic matter that now forms the matrix of the conglomerates. Plastic deformation of the matrix is highlighted by the flowage of the detrital components around chert fragments, as shown in Figure 2.25 - c. The reworking of slabs left large cavities that are now filled with microquartz, megaquartz and fibrous quartz, commonly with colloform textures, as shown in Figure 2.31 : the mineralogy and textures of this material strongly resemble that of fracture-filling cherts. The presence of large, well-preserved, fibrous quartz crystals is taken as evidence for the circulation of low temperature hydrothermal or seawater fluids (Cady et al. 1998) in the shallowest part of the sediment pile.

(4) Mineralogical homogeneity of silica phases and absence of protolith relicts. We previously emphasized that, even in a setting where some of the cherts were subject to strong silicification, the black cherts preserve internal structures (*e.g.* microbial mats and detrital grains), as shown in Figures 2.29 and 2.28, as well as protolith relicts in the form of particulate impurities, as shown in the chemical maps of Figure 2.32. Thus, because white cherts are entirely composed of microquartz, with no particular structure or contaminant phases (Fig.2.26), we argue that they precipitated from a Si-rich fluid rather than being replacement products. Moreover, as we showed that slabs in conglomerates are the disrupted equivalent of white chert layers, we use the pure, microquartzitic composition as evidence for silica deposition at Archean surface conditions.

2.1.7   Rheological considerations.

From the deformation structures observed in both the Komati River and Buck Reef site, several constraints can be proposed for the early behavior of chert during or just after deposition.

(1) Flame structures at Komati River. As previously described, flame structures are common features at the interface between the upper black chert facies and the next, overlying turbidite unit. From Figure 2.8, two types of flames are recognized : those of photos (c) and (d) penetrate up to 5-7*cm* the overlying sediment in various directions while those of photo (a) are tilted to the right. Because such structures are also common in modern, sedimentary equivalents, we can infer that the chert was deformed following similar processes during the Archean.

Flame structures are very common load-induced, antiform features that generally affect fine- to very-fine grained sediments (*e.g.* mud) (*e.g.* Mills 1983, Maltman et Bolton 2003, Oliveira et al. 2011). They are related to the vertical compression induced by the rapid sedimentation of a denser material onto a still-soft and water-rich substratum. The deformation is triggered by the density and rheology contrasts between the two superposed materials (*e.g.* sand over shales, shales over mud or salt) and to the buoyancy capacity of the lighter material (McKee et Goldberg 1969, Bishop 1977). The static, vertical loading (orthogonal to bedding) increases the pore pressure within the lower fine sediment and induces its liquefaction (Lowe 1975, Allen 1982, Owen 1987, Nichols 1955, Maltman et Bolton 2003). Porosity fluids are thus free to escape and start to migrate upward through the overlying, coarser sediment to form flame structures. In the case of turbidites, the basal motion of the debris flow brings an additional shear component (orthogonal shear ; Oliveira et al. 2011) that models the shape of the flame : the bottom part of the flow locally sinks into the underlying soft-sediment, and the narrowing top of the flame thus indicates the opposite direction of the turbidite emplacement (*e.g.* Myrow et al. 2002).

Because we showed that Komati River cherts formed at the surface and because we believe that the silica precipitated as a mixture with fine grained, clay minerals, we propose that such primary siliceous ooze must have behaved in a similar way

to mud-like sediments, meaning it was able to liquefy under vertical compressions and shear stress. Such rheological behavior is characteristic of thixotropic fluids such as colloidal suspensions of clay, mud and silica (Ambrose et Loomis 1933, Perret et al. 1996, Barnes 1997, Pignon et al. 1998, Besq et al. 2000, Coussot et al. 2002, Labanda et Llorens 2006), a property that may have had the siliceous ooze at Komati River.

As reported by Oliveira et al. (2011) (see also Oliveira et al. 2009), such deformation occurs at, or just below the seabed, thus supporting the marine origin of the black chert horizon. We cannot exclude that diagenetic fluids expelled from turbidites contributed to the silica enrichment at their top, but the significant lack of dewatering features (*e.g.* Marr et al. 2001, Tanner et Lucas 2010) indicates that such contribution was probably minor and diluted by the marine component.

(2) Silica gel in the tuffaceous chert unit ? The siliceous, translucent network of Figure 2.10 is one of the most intriguing feature we encountered in the Komati River site, and in any other site studied in this thesis. We failed to find a modern equivalent for such structure and can only hypothesize on its origin. We strongly believe that the planar bottom shape and ripple-like upper shape correspond to current induced deformation structures : (1) the silica network is concordant with the bedding, (2) two generations of such "ripples" are superposed, (3) several ripples are encountered along the same interval of silica network, and (4) such ripples are consistent with the current-induced ripples found in the surrounding tuffaceous chert.

Thus, we tentatively propose that such structure might have been produced at the surface, when an almost pure gel of silica was partially reworked under low-energy current activity. So doing, the gel enclosed packages of still-soft tuffaceous material, now forming isolated rounded masses within the siliceous structure.

(3) Soft-deformations at Buck Reef. The load-cast and ball-and-pillow structures of Figure 2.20 and the boudinage structure of Figure 2.21 are taken as evidence for the presence of soft (*i.e.* plastic) white chert layers just below the seabed, and for their high induration rate compared to the surrounding black units. The load structures are interpreted as density inversion features similar to those found in

modern setting, where denser sediments overly lighter material (*e.g.* shale/mud, siltstone/shale, etc.) (*e.g.* Potter et Pettijohn 1963, Owen 1996, Pope et al. 1997, Obermeier 1998, Obermeier et Pond 1999, McLaughlin et Brett 2006). It implies that the white chert was, at first, less dense than the black chert to produce the load structure of Figure 2.20-a,b. The black facies thus migrated into the underlying soft and deformable, pure siliceous deposit while the white chert migrated upward as a response of both its higher buoyancy and the excess material influx. The ball-and-pillow structure occurred in the opposite direction, with the white facies sinking into the underlying laminated sediment. Thus, we propose that these two structures represent two stages of the white chert diagenesis with a rapid evolution from soft and light siliceous material to more plastic and dense, partially indurated chert.

The boudinage structure provides further evidence for the contrasting induration rate of both the black and white chert facies. Indeed, the limited stretching of the white layers implies they were more competent than the surrounding black layers. The compressive stress provoked by the sedimentary loading transformed into tensile stress in the competent layer, leading to its disruption along the bedding (*e.g.* Ramberg 1955, Sanderson 1974, Smith 1975; 1977). As previously noted, the boudin shape, being elongated along the bedding and showing rounded edges, suggest a plastic behavior of the white, siliceous material at the time of deformation.

(4) Slab conglomerates and brittle deformation. As discussed in the previous section, slab conglomerates are composed of disrupted white chert layers deposited in a plastic black, siliceous matrix that was present at at the surface. Because the slabs have angular to sub-angular shapes, we argue that they were rigid at the time of disruption, an idea already proposed by Lowe et Knauth (1977).

The formation of slab conglomerates, also referred to as "flat-pebble conglomerates", have been investigated by numerous workers in modern and ancient settings. They recognized four principal mechanisms : (1) subaerial exposure, desiccation and reworking during subsequent emersion (Braun et Friedman 1969, James 1984) ; (2) Slope instability by ongoing sediment accumulation and formation of debris flows, mud flows or slump sheets (Szulczewski 1968, Bialik et al. 1972, Cook

et Mullins 1983) ; (3) Combination effects of flow, storms and active waves (Jansa et Fischbuch 1974, Jones et Dixon 1976, Seilacher 1991, Sepkoski Jr et al. 1991, Kozub 1997) ; (4) Seismic events and related fluctuating sea level and tsunamis (Kullberg et al. 2001, Myrow et al. 2004).

According to the structures described in these studies, the Buck Reef conglomerates best corresponds to reworked sediments under strong wave action. The recognition criteria we use are the angular shape of chert slabs (Szulczewski 1968, Vierek 2010), the lack of desiccation structures (*e.g.* mud cracks, fenestrae ; Braun et Friedman 1969), the horizontally of the slabs (Myrow et al. 2004) and the absence of typical tsunami features (*e.g* erosion features, channeling, injectites, cyclic sedimentation and seismic cracks ; Dawson et al. 1991, Kullberg et al. 2001, Pratt 2002).

According to this model, the cyclic shear stress induced by storm waves is capable to destabilized the upper part of the banded, siliceous sedimentary pile by increasing the pore fluid pressure in the least compacted materials and, consequently, lowering their strength (Myrow et al. 2004). Kazmierczak et Goldring (1978) described a "loosening along less cohesive laminae", which in our case corresponds to the cabonaceous-rich black chert intervals that now forms the black matrix. According to Myrow et al. (2004), a viscous flow dominated by laminar shear can account for the transport of the sediment-chert mixture and for the slab horizontality. If the carbonaceous-rich material was indeed able to flow, the white cherts behaved differently according to their higher degrees of lithification. Because large portions of chert slabs are preserved (up to several tens of centimeters), we advocate a short transport of chert layers that were close to the surface prior to reworking.

According to this model, and in good agreement with the previous observations, we further support the idea of rapidly indurated pure siliceous precipitates at or near the surface, whereas black, carbonaceous material remain soft and deformable even after some burial.

2.1.8   New models for chert formation

Komati River Chert

In the Komati River site, environmental conditions were very different from those of Buck Reef Chert : the basin is epicontinental according to Grosch et al. (2011) and was subject to very strong and rapid detrital inputs. The debris flows that deposited turbidites are short, gravitationally- and/or tectonically-induced events, with declining sedimentation rates from base to top of each flow emplacement : at first, the sedimentation rate is high as the coarsest and heaviest particles and lithic fragments are deposited, then the settling velocity declines with decreasing detrital grain size. This evolution produces the so-called Bouma sequence (Bouma 1962) within which the finest material comprises the uppermost part of turbiditic layers, generally in the form of fine-grained clay and mud deposits.

In Komati River turbidites, our observations show that, as the deposition rate decreased, the sedimentation mode evolved from clastic deposition to chemical precipitation of silica, first as cement between detrital grains, then as amorphous phase mixed with minor amount of clay minerals and minor, very fine grains of detrital feldspar. In the previous sections, we argued for inorganic chemical precipitation rather that secondary hydrothermal advection, and we admitted a possible contribution of diagenetic fluids : we now discuss the origin of the silica and its deposition mode and propose a new process for the formation of Komati River cherts.

Considering here a small Archean basin, as proposed by Grosch et al. (2011), the seawater chemistry must thus have been significantly enriched in dissolved silica. We favor continental silica fluxes exceeding possible hydrothermal contributions given the large quantities of erosional products and clastic sediments deposited here, whereas hydrothermal features are lacking (*e.g.* dykes, veins, chimneys, etc.). Indeed, during weathering, the K-feldspar to phyllosilicate transformation produces significant amount of dissolved silica, following the equation 2.1, which is then transported to the basin by rivers and contributes to the Si-enrichment of seawater.

$$3KAlSiO_3O_8 + 2H^+ + 12H_2O \leftrightarrow KAl_3Si_3O_{10}(OH)_2 + 6H_4SiO_4^0 + 2K^+ \qquad (2.1)$$
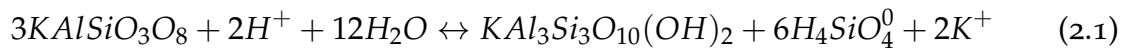
K-feldspar + Water ↔ Muscovite (Sericite) + Dissolved silica and potassium

Moreover, the limited area of the basin, due to its intracontinental position, could have enhanced the rate of evaporation and resulted in additional silica enrichment (*e.g.* Siever 1992, Maliva et al. 2005). However, as the amount of deposited chert at Komati River is low compared to other clastic-rich sites of the Barberton Belt, *e.g.* in the lower Fig Tree Group (see Chapter 3), such evaporative contribution to the local silica enrichment is not required. Our model thus assumes that the marine conditions were favorable enough to allow the chemical precipitation of silica in the water column.

During turbidite emplacement, the clastic sedimentation was initially rapid and overwhelmed the chemical sedimentation. The clastic deposition rate rapidly declined as the finest detrital particles deposited through the top of the Bouma sequence, while the silica precipitation became more significant, probably triggered by the high sorption capacity of detrital clay (Rouchon et Orberger 2008, Rouchon et al. 2009, Rimstidt et Barnes 1980, Williams et al. 1985, Williams et Crerar 1985). The precipitated silica initially constituted the turbidite cement, then became dominant to constitute the entire rock.

Because we lack the average time interval between turbidite events, we cannot constrain accurately the rate of chert deposition. A simple calculation shows that, if the basin were permanently saturated (or close to saturation), and if black chert layers do not exceed $30cm$ in thickness, the maximum rate of deposition ranges from 30 to $3mm/yr$ assuming typical modern intervals of 100 or 1000 years between debris flows. These values are significantly higher than previous estimations in BIFs, for which deposition rates of 0.03 to $1mm/yr$ have been proposed (Barley et al. 1997, Pickard 2002, Konhauser et al. 2005). Because the basin was subject to large detrital inputs, it is inconceivable that nothing else but silica and clays were deposited between two turbiditic events. Thus, because the internal organization of black cherts is homogeneous and continuous, without significant detrital contribu-

tion, we suggest that permanent Si-oversaturation of the basin water is unlikely and envisage short-term enhanced chemical precipitation triggered by the clay content.

The discontinuous inputs of debris flows is thus thought to be responsible for local and episodic precipitation of silica. During turbidite emplacement, large amounts of suspended particles are rapidly introduced to the basin and trigger heterogeneous nucleation and precipitation of silica. Siever et Woodford (1973), Williams et al. (1985), Williams et Crerar (1985), Gehlen et Van Raaphorst (2002) and Grenne et Slack (2003) described how such particles act as nuclei that concentrate dissolved silica via a sorption process controlled by the nature and specific area of particulate matter and by the dissolved silica concentration, cation content and pH of the solution. Accordingly, the weak silica addition to the coarser part of turbidites and its upward increasing content is best explain by the higher sorption capacity of clay minerals : their higher surface/volume ratio compared to coarser particles allow significant amount of silica to be sorbed.

Rouchon et al. (2009) calculated that $1g$ of shale take up about $35mmol$ of silica, whereas coarser sediments such as fine pebble conglomerates take up only $4.5mmol$. The sorption takes place either at the seawater-sediment interface, or directly in the water column during particle settling, with the low settling velocity of phyllosilicates ($<0.1mm/s$, value for silt-size particles ; Gibbs et al. 1971) that enhances the quantity of sorbed silica. Although silica precipitates primarily together with clays, it also forms the majority of the cement in the final chert and underlying siltstone, pointing to additional silica nucleation in the fine porosity of the sediment and/or to diagenetic fluid contribution at this stage of the model. Despite the very high silica content in this clastic environment, detrital particles are physically and chemically preserved, which could be used as a criteria for the recognition of primary silica precipitation from low temperature oceanic fluids. Nevertheless, such criterion requires that we can be confident of the non-authigenic origin of the observed phases.

In our study, we showed that the majority of sericites represent detrital particles inherited from granitic and dacitic rocks, and are thus neither neoformed nor autigenic minerals. Adapting the model of Rouchon et Orberger (2008), we propose that the sorption of silica onto the clastic particle within the Si-rich water column,

and the subsequent settling of these flocs to the seafloor, resulted in the deposition of a gelatinous phase mixed with detrital clays and micro-feldspars at the top of turbidite layers. We depart from their interpretation by suggesting that (1) sericites are continent-derived detritus and not locally produced, (2) the silica sorption does not affect detrital-particle chemistry, (3) the transformation of K-feldspar to sericite in the source occurred during weathering at the land surface rather than during seafloor K-metasomatism, and (4) the source of the detrital particles must be a mixture of dacitic and granitic rocks to account for the presence of orthoclase and microclines in the turbidites.

In Chapter 4, the Si and O isotopic compositions of Komati River siltstones and cherts are used to provide further constraints to our model.

Buck Reef Chert

The Buck Reef black and white cherts were deposited in a very different setting in which continental-derived, detrital inputs were minor, thus favoring chemical sedimentation driven by oceanic processes. In the previous sections, we provided evidence that the bedding represents periodic sedimentation of alternating pure siliceous deposits and carbonaceous-matter rich siliceous mixtures in a shallow subsiding basin. Here, we review and discuss several hypotheses and possible trigger mechanisms for the deposition of such a massive banded chert sequence.

(1) The diagenetic hypothesis. Lowe et Fisher Worrell (1999) and Tice et Lowe (2006) proposed an early diagenetic origin for the banding. They argued that at first a mixture of chemical sediment, detrital particles and organic matter, was deposited on the seafloor, then the silica segregated to form the white chert bands, the rest forming the black chert layers. Such hypothesis has also been proposed for the similar structures in banded iron formations (BIFs) (*e.g.* Krapez et al. 2003, Lascelles 2007). However, we prefer wholly a sedimentary origin for the bedding, based on the following observations :

(1) The upper and lower contacts of white chert layers with surrounding black units are sharp, and local diffusion of silica is rare and limited to the very first 1mm of the transition, as shown by the pervasive structures of Figure 2.30 - d.

(2) The microbial mat structures are very well preserved. Upward migration of

silica during early diagenesis would have resulted in disturbance, and probably disruption and flattening of carbonaceous laminations, which is not the case, as shown in Figure 2.28.

(3) Each black and white chert layer maintains a uniform lateral thickness over several tens of meters in outcrop : such regularity is unlikely to be preserved if the layers formed by the segregation of the white phase.

(4) One may expect that each black chert/white chert couplet will have a rather constant thickness ratio through the sequence if the white facies were produced by the dewatering/re-precipitation of a primary mixture. Although both facies are concomitantly thinning upward as the basin depth increased, such ratio is not respected and strongly varies from one couplet to another, a typical example of which is shown in Figure 2.19.

(5) In the sandstones and siltstones from the lower part of the Buck Reef sequence (Fig.2.18), white layers alternate with rusty-weathered layers with the palest color being associated with the highest silica content. If silica segregation was a major process for the banding, it is barely conceivable that the highly porous, silica-rich siltstones did not produce pure white chert layers at their tops.

(6) Arguments against a diagenetic origin also emerged from geochemical analyzes, and are pointed out in Chapter 4. These arguments are essentially based on the strong differences in composition between black and white layers sampled next to each other. Especially their mobile element content is very contrasting which is barely conceivable if both facies were genetically related.

We thus favor a sedimentary origin for the bedding, which implies cyclic variations of the physicochemical characteristics of local seawater that triggered the precipitation mode of silica, either as a pure phase (*i.e.* white chert), or mixed with carbonaceous matter and detrital particles (*i.e.* black chert). The following paragraphs thus focus on the possible cyclic variations that may have occurred in the paleo-basin.

(2) The hydrothermal hypothesis.

Models of early Earth evolution suggest higher heat production and faster seafloor spreading rate during the Archean (*e.g.* McKenzie et Weiss 1975, Abbott

et Hoffman 1984). Moreover, enhanced hydrothermalism has been evidenced based on specific chemical characteristics of marine precipitates (carbonates, iron-formations and cherts), including very common, black-smoker fluid-like, positive europium anomalies, low, mantle-like Sr isotopic values and radiogenic Nd isotopic ratios (*e.g.* Fryer et al. 1979, Veizer et al. 1989, Derry et Jacobsen 1990, Danielson et al. 1992, Kamber et Webb 2001, Eglington et al. 2003).

Hydrothermal fluids may thus have significantly contributed to the Archean seawater chemistry, and several models propose their involvement in the formation of marine precipitates, especially for banded iron-formations (BIFs) (*e.g.* Holland 1973, Dymek et Klein 1988, Kato et al. 1998, Van Kranendonk et al. 2003, Bolhar et al. 2005) : these rocks are composed of alternating Si-rich and Fe-rich layers, the former being precipitated during normal chemical sedimentation and the latter produced under active hydrothermal inputs to the basin. Although this model is not unique (*e.g.* Alibert et McCulloch 1993, Hamade et al. 2003, Posth et al. 2008), a similar process can be proposed for the deposition of the Buck Reef Chert : white chert layers could have precipitated from Si-rich, high-temperature fluids during enhanced hydrothermal activity at the vent (de Wit 1982, Paris et al. 1985, Brasier et al. 2002), while the black chert layers could represent quiescence periods and "normal", oceanic sedimentation of silica and carbonaceous matter, with varying detrital inputs (Tice et Lowe 2006).

Although significant secondary fluid circulations were evidenced in this study, we agree with the observations of Tice et Lowe (2006) that the Buck Reef units lack relicts of hydrothermal-derived plumbing structures, such as vent mounds, chimney or dikes, and that no identifiable heat source could have triggered widespread hydrothermalism in the area. Moreover, hydrothermal venting cannot account for the remarkable regularity of the banding and periodicity of white chert layers. It would require a very regular and cyclic activity in which chimneys released equal amount of silica during each pulse, and pulses would be equally spaced in time, which seems unlikely for hydrothermal systems (Tice et Lowe 2006), even in the Archean.

However, such considerations are not sufficient to rule out the hydrothermal hypothesis because the source of the fluids can be far from the deposition site.

Upwelling currents or hydrothermal plumes can transport deep hydrothermal waters onto the continental shelf, the latter which may expend up to $10km$ from their source (*e.g.* Lupton et al. 1985, Baker et al. 1985, Baker et Massoth 1986, Baker et al. 1987, Klein et Beukes 1989, Baker 1990, Dymond et Roth 1988, Feely et al. 1994b;a, Isley 1995, Feely et al. 1996). In such a model, hydrothermal activity would have driven the silica influx and saturation state of the local oceanic fluids at Buck Reef.

Tice et Lowe (2006) ruled out such contribution on the basis of the absence of hydrothermally-derived metal enrichment in the Buck Reef cherts. Such observation relies on the comparison with modern hydrothermal fluids characteristics, especially black-smoker-like fluids that vent at mid-oceanic ridges. However, Shibuya et al. (2010) recently used thermodynamical calculations to suggest that Archean hydrothermal fluids could have been significantly different from modern analogues, thus questioning the relevance of modern comparisons.

As will be discussed in Chapter 4, geochemical analyses fail to distinguish oceanic *vs.* hydrothermal contribution, even when using the highly immobile rare-earth elements. However, some trace element features, such as Ba, Pb, Cr and Ni enrichments, could be attributed to specific marine conditions in which hydrothermal fluids might have been part of the chemical budget of the Buck Reef paleo-basin. The Si and O isotopic data (Chapter 5) are ambiguous and appear to indicate a marine contribution in one white chert layer, whereas another layer taken less than $5m$ above has a strong hydrothermal signal.

Thus, although we prefer a strong seawater contribution to both the primary cherts and the subsequent silicification of the sequence, we do not exclude the possible contribution of hydrothermal fluids, but we still require a trigger mechanism for the massive precipitation of the silica. The following paragraphs deal with what we call the "Oceanic hypothesis" which is a discussion of possible parameters that could have led to cyclic oversaturation of seawater with respect to dissolved silica.

(3) Seasonal variations.

The base of the Buck Reef Chert has been dated at $3416 \pm 5Ma$ (Kröner et al. 1991), but we lack an upper limit to constrain the span of time that saw the deposition of the 200-450m-thick siliceous units. The next age determination corresponds

to the Footbridge Cherts, dated at $3334Ma \pm 3$ and located at about $1200m$ above the present unit. It is probable that the errors are larger than the ± 5 and $\pm 3Ma$, but we assume for the purpose of this exercise that the interval was no more than $90Ma$. Thus, we can assume a reasonable time of deposition of about $15 \pm 5Ma$ for the Buck Reef cherts.

Using a maximum thickness of $400m$ for the sequence and an average $2cm$ for each chert layer, a simple calculation shows that the Buck Reef cherts would have formed in about $10,000$ years if each white/black chert couplet represented a seasonal deposition of silica. Moreover, such a calculation gives a minimum sedimentation rate of $4cm/yr$, which is far greater than the 0.03 to $1mm/yr$ proposed for Precambrian BIFs (Barley et al. 1997, Pickard 2002, Konhauser et al. 2005).

We thus envisage an alternative model in which the massive black layers represent "normal" sedimentary conditions whereas the white layers were produced under abnormal conditions as described later in the section.

In the black chert facies, the microbial mats occur as a mixture of silica and carbonaceous detrital components that could have served as substrate for the community growth. The laminations constitutive of the mat are intercalated with thin silica bands, both of which are 5 to $10\mu m$-thick in average (Fig.2.28 and 2.30).

Such structures are observed in modern siliceous sinters and has been interpreted in two ways. Walter et al. (1972) and Berelson et al. (2011) both proposed a daily cycle in sinter deposits of Yellowstone, and interpreted microbial laminations of tens of micrometer-thickness as produced by biological activity during the day that balances the abiologic precipitation of silica, while at night quiescence of microbes allows inorganic silica precipitation. This daily growth is unlikely in our case because the Buck Reef cherts would have been deposited in more than $400My$. Konhauser et al. (2001) focused on the microbial-silica interaction in modern sinters from Iceland and prefer a seasonal microbial activity, with active growth during summer onto a silica-rich substratum, followed by a quiescence period during winter when abiological silica precipitation exceeds the bacteria growth capacity.

Considering the seasonal hypothesis, and assuming a maximum thickness of $200m$ for the black units, $2cm$ for each layer, and $10\mu m$ for the microlayers, then the whole black chert sequence would have been deposited within $\sim 10Ma$, which

is consistent with the proposed estimation of the timing of deposition of the Buck Reef Chert. Moreover, such calculation gives an average sedimentation rate of $\sim$ $0.2mm/yr$, which is within the range of BIFs estimates (Barley et al. 1997, Pickard 2002, Konhauser et al. 2005).

Thus we suggest that the black cherts represent the common type of sedimentation in the Buck Reef basin, within which are recognized seasonal cycles of silica precipitation *vs.* microbial growth similar to those reported by Konhauser et al. (2001) in Iceland. However, the origin of the white chert layers remains unsolved : because white cherts are entirely composed of cryptocristalline silica without detrital content or microbial communities, they must have been deposited in a very short period of time. Thus, we envisage a catastrophic precipitation process for such layer, triggered by one or another parameter that cyclically varies and allowed periodically the water column to pass through its saturation limit with respect to dissolved silica. Following the same logic as the above calculations, the periodicity of the white chert deposition would be around $10,000$ years.

(4) The climate forcing hypothesis

A first possible explanation involves climatic changes to account for the banding. We envisage the presence of a stratified ocean where a surface layer, *e.g.* above the thermocline, is progressively enriched in dissolved silica during high evaporation periods. Then, several factors could have caused the concentrations to exceed the sursaturation level, which, as a consequence, could induce rapid and massive pure silica precipitation and an drastic lowering of dissolved silica contents in the water column. Then, a new evaporative period would allow the recharge in dissolved silica of the surface layer until the next perturbation occurs.

Glacial/interglacial transitions could be an interesting option as they could fit the inferred thousand years periodicity for the white chert deposition. Such a model is proposed in Figure 2.33. During inter-glacial periods, the environment could have been warm enough to favor the colonization of the seafloor by microorganisms and high evaporation rates could account for permanent silica precipitation from Si-saturated surface water (*e.g.* Siever 1992). Such conditions would favor the formation of a Si-saturated layer at the surface of Archean oceans, especially in the
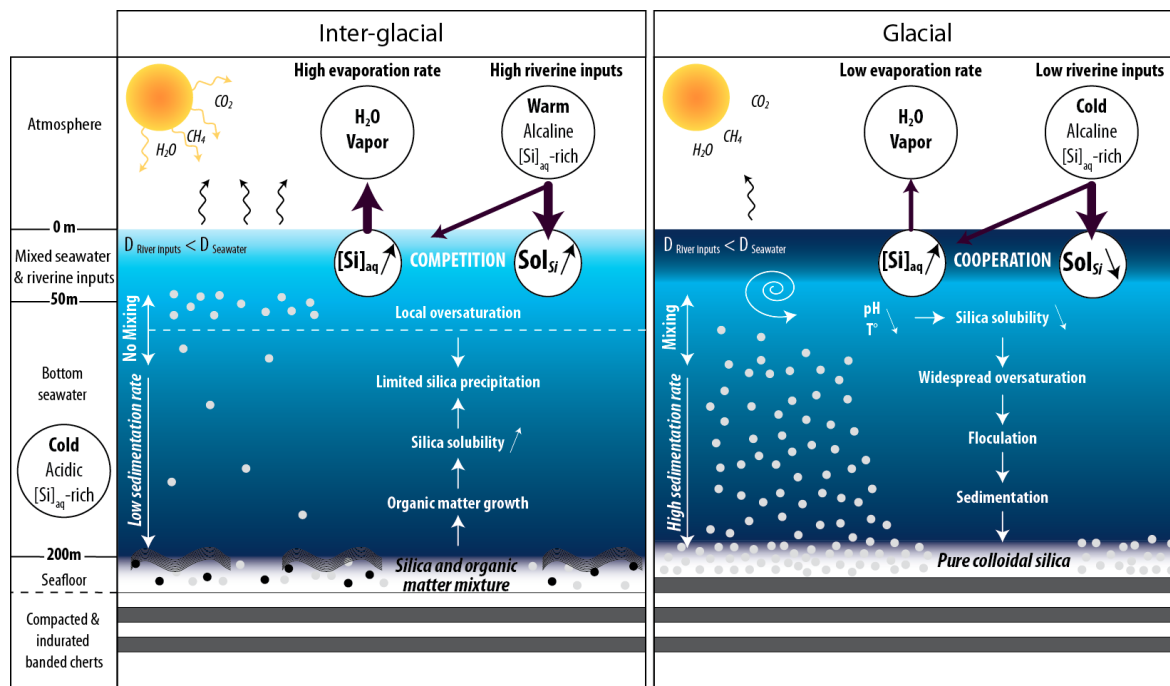
FIGURE 2.33 – *Theoretical model for the formation of Buck Reef black and white banded cherts, with special emphasize to the white chert formation. According to the model, inter-glacial periods are marked by strong evaporation and high riverine inputs that have competitive influence on the silica solubility. Surface water is maintained close to the saturation with respect to dissolved silica and permanent precipitation of silica is accompanied by the colonization of the seafloor by microbial communities. During glacial periods, the evaporation rate is low, the seawater temperature drops and the pH is lowered. These factors cooperate to allow the destabilization of the surface water and the precipitation of massive and translucent silica by flocculation/sedimentation process.*

Buck Reef case where the water depth is low. The presence of evaporitic deposits at the base of the sequence also sustains such warm and favorable conditions for high silica precipitation. Hydrothermal contributions are still envisaged in this model and could have contributed to the Si enrichment of ambient fluid, but are not responsible for the banding.

Continental influxes are known to be a significant source of silica to Precambrian oceans (*e.g.* Cloud 1973, Laschet 1984, Hamade et al. 2003, Basile-Doelsch et al. 2005, Alexander et al. 2008; 2009). The alkalinity of river waters may have promoted the dissolution of silica in the water column as the silica solubility is enhanced under high pH conditions (typically for pH>9 ; Knauss et Wolery 1988, Brady et Walther 1990, Bennett 1991, Dove 1994). Thus, high evaporation rates at the ocean-atmosphere interface and significant riverine contribution during inter-

glacial periods could maintain the water basin close to the silica saturation and would have been able to produce the siliceous and carbonaceous-matter rich mixture at the origin of the black cherts. A permanent settling of silica flocs in the water column or its permanent uptake at the sediment-water interface by the living biota can thus account for the black chert formation.

During glacial periods, the temperature drops, riverine inputs are insignificant and the pH may be lowered to more acidic conditions. These factors would cooperate to destabilize the now strongly enriched surface water, leading to sudden and dramatic precipitation of pure silica from this layer and its settling down through the water column as silica flocs. In the same time, the biota would have entered a quiescent period of a thousand years, leaving the environment free of anything but silica.

Such a model fits well (1) with the regularity of the banding and its homogeneous lateral extent, (2) with the thickness decrease up-section as deeper marine conditions dilute the silica concentrations, (3) with the purity of the white cherts, *i.e.* their lack of continental inputs and living biota, (4) with the varying isotopic composition in this facies, as hydrothermal and marine contributions are not incompatible with the climatic-triggered silica precipitation, and (5) with the time constraint of a few thousand years for the periodicity of white chert deposition.

This model brought into questions when considering the extensive literature dedicated to the Archean climate, which is believed to have been warm and humid based on numerous geological evidence, including the presence of evaporitic deposits and stromatolitic carbonates (Hofmann 1999, Van Kranendonk et al. 2003, Allwood 2006, Tice et Lowe 2006, Allwood et al. 2007, Lowe et Tice 2007, Allwood et al. 2010), the abundance of fluvial sandstones and conglomerates (*e.g.* Mueller et Corcoran 1998, Eriksson et al. 1998, Lowe et Fisher Worrell 1999, Sugitani et al. 2003), the low Ca, Na and Sr content in Archean shales (Eriksson et al. 1998), high weathering indexes in clastic rocks (see Hessler et Lowe 2006, for a review), the Si and O isotopic compositions of cherts (*e.g.* Knauth et Lowe 1978; 2003, Robert et Chaussidon 2006) as well as thermodynamic models involving high contents of greenhouse gases in the atmosphere to solve the Faint Young Sun Paradox (*e.g.* Lowe et Tice 2004, Ohmoto 2004, Shaw 2008).

The oldest glaciation is recorded at 3.0-2.9Ga in the Pangola Supergroup in South Africa, and followed a long term cooling of Precambrian surface conditions (Von Brunn et Gold 1993). Archean glaciogenic deposits, essentially found in South Africa, are limited to diamictites in the Witwatersand Supergroup (3-2.7Ga; Wiebols 1955, Harland 1981) and glaciaclastic strata in the Pangola Supergroup (3.1-2.8Ga; Von Brunn et Gold 1993). Apart from these rare and questionable traces, most of the Archean appears to have been non-glaciated according to Young et Gostin (1991). However, glacial/inter-glacial periods, in our sense, do not necessary involve ice sheet development/destruction, but could have well be expressed as strong variations of mean surface temperatures during the Archean. We believe that the shorter Milankovitch cycle of $\sim 20,000$ years, resulting from the periodic axial precession of the Earth, can account for the substantial temperature drops and rises proposed in our model, and could explain the Buck Reef black and white banding. Such natural temperature variations have also been advocated by Posth et al. (2008) to explain the layering in BIFs, although no time constrain has been proposed.

(5) The water mass mixing hypothesis

An alternative model to the climate forcing involves water mass mixings due to upwelling systems and/or hydrothermal plume formation in the Archean oceans. Both these types of water currents were proposed in some models for BIFs formation to account for the supply of iron in shallow marine, near continental settings (*e.g.* Drever 1974, Degens et Stoffers 1976, Ewers et Morris 1981, Ewers 1983, Morris et Horwitz 1983, Klein et Beukes 1989, James 1992, Morris 1993).

The lack of significant iron, or other component but silica, in the major part of the Buck Reef Chert requires specific water masses enriched solely in dissolved silica and lacking particulate matter, an assumption that may be supported by the recent thermodynamic model proposed by Shibuya et al. (2010). Based on the fact that Archean seawater was significantly different from modern oceans, *i.e.* near-neutral to slightly acidic and enriched in CO_2, they proposed that fluid-rock interactions in hydrothermal systems may have differ from modern settings, leading to the production of hydrothermal fluids with specific composition that departs from

present day acidic and iron-rich vent fluids. Their model proposes the emanation of high-temperature, alkaline and silica-rich buoyant plumes from basalt-hosted plumbing systems. Such alkaline emanations have been similarly proposed for the Hadean (Russell et al. 1993, Martin et al. 2008) and for Archean, Al-depleted komatiite hosted hydrothermal systems (Wang et al. 2009). The modern Lost City field, a hydrothermal system off the Mid-Atlantic Ridge, also provide evidence that alkaline fluids can be produced in ultramafic hosted plumbing systems((Kelley et al. 2001).

Because modern plumes can extent several thousands of kilometers away from their vent (Lupton et al. 1985, Lupton 1995), the Si-rich plume hypothesis can reconcile the large amount of silica deposition at Buck Reef and the lack of hydrothermal plumbing evidence in the area. It is also consistent with the thinning upward of chert layers as the plume would be more diluted in deeper waters. The minute iron oxides and chromites found disseminated in the white chert microquartzitic fabrics could also have been brought by such a fluid and could have act as nuclei for the precipitation of silica. However, the regularity of the bedding requires that plumes were highly periodical features, a requirement we still doubt of.

Upwelling currents could as well be an option for the silica addition to the Buck Reef paleo-basin and subsequent precipitation as massive siliceous deposits. Decadal upwelling currents were early proposed by Klein et Beukes (1989) to account for the formation of iron-formations in shallow platform settings. The deep, bottom seawater of Precambrian oceans could have been significantly enriched in hydrothermal-derived components, such as silica, and the mixing of such cold water with the warm Buck Reef oceanic fluids, already enriched in silica by evaporation, could account for the massive precipitation of the white cherts. More recently, Dezileau et al. (2004) recognized in a past, coastal upwelling systems a strong correlation between vertical rain rates of biogenic opal and organic carbon and the well-known precessional cycles of about 20000 years. These authors showed that the silica productivity triples as a result of such cycles, although their study focused on biogenic processes, thus providing a time constrain consistent with that inferred for the Buck Reef periodicity. However, Wefer et al. (1998) pointed out that upwelling waters generally carry significant particulate matter, such

as clay, silt and phosphorite, eroded from the continental slope on their way up. They also observed that sediments close to upwelling systems are subject to intense chemical activity, with the common formation of authigenic minerals such as dolomite, phosphorite and iron sulfides. All these features are lacking in the pure and massive white cherts at Buck Reef.

2.1.9 Conclusions

In this study, we first introduce a new nomenclature based on Archean chert formation process : C-cherts formed by the chemical precipitation of silica at surface condition from ambient oceanic fluids, either as silica gel (or siliceous ooze) or as cement in unconsolidated sediments ; F-cherts were chemically precipitated in discordant and concordant veins from circulating fluids ; S-cherts resulted of replacement by Si-metasomatism of pre-existing rocks by percolating fluids.

The Komati River and Buck Reef sites from the Barberton Greenstone Belt were selected as a case study for Archean chert investigations. Field and petrological observations are used (1) to recognize depositional settings, (2) to identify the origin of cherts and (3) to propose recognition criteria as well as (4) new model for chert formation.

The Komati River cherts formed as C-chert at the surface of turbidite units by clastic-triggered, chemical precipitation of silica. The recognition criteria we used are : the lack of secondary fluid circulation evidence, the deformation structures typical of surface conditions (*i.e.* flame structures, ripples, chert pebbles), the chemical/physical preservation of clastic particles from Si-metasomatism and the continuous evolution from silica-cemented siltstone to homogeneous chert.

We propose that the chert deposited as a siliceous ooze during the waning stages of turbidite emplacement and marked a transition from clastic to chemical sedimentation. The precipitation of silica is favored by efficient sorption on suspended clay particles. The amount of deposited chert is low and does not require a high Si-saturation of ambient fluids, mostly of oceanic origin with possible porosity fluid contribution from deeper in the turbidite.

The Buck Reef cherts deposited on the seafloor, as individual black and white chemical precipitates in a clastic-free, Si-saturated environment where secondary

Si-rich fluid circulations were abundant. The recognition criteria we used are : the sharp contact between both facies, the presence of microbial mats soft-deformed at the interface and soft deformation structures at or close to the seabed (*i.e.* load cast, ball-and-pillow structures). Petrological evidence is the pure, microcrystalline fabrics of massive cherts, representative of seafloor silica precipitation whereas void-filling and vein textures characterized by chalcedony and megaquartz are evidence for secondary fluid precipitations. Slabs in conglomerates are interpreted as the disrupted equivalent of massive white layers and are additional evidence for the presence of white cherts at the surface as well as for their very rapid induration just after deposition.

We argue that the bedding is neither of diagenetic origin, nor representative of periodic hydrothermal activity within the area. We propose a model decoupling the origin of the black and white facies. The micro-layering in black cherts (*i.e.* carbonaceous matter/silica laminations) is interpreted as seasonal variations with pure silica precipitation during winter and microbial community growth during summer. The high purity white layers are thought to result from very rapid, dramatic silica precipitation with a possible periodicity of a few thousand years. We envisage the destabilization of the surface layer in a stratified water column and proposed several trigger mechanisms among which climatic variations at a glacial/inter-glacial scale seems the most likely. Another possibility is the involvement of Si-enriched, cold bottom seawater in an upwelling system and/or hydrothermal plume contribution from hydrothermal vents away from the continental platform.

Acknowledgments

Comportement rhéologique des cherts de fracture.

<div style="text-align: right">3</div>

Ce chapitre est consacré à l'étude des dykes de chert du synclinal de Barite Valley et au comportement rhéologique des cherts en conditions de sub-surface.

—————————————————————

In this chapter, we focus on the rheological behavior of carbonaceous cherts in large dykes from the Barite Valley syncline.

3.1   Avant-propos

Le chapitre précédent a permis de mettre en avant l'intérêt du couplage entre des observations de terrain et la caractérisation pétrologique des cherts. Une telle approche apparaît comme un outil indispensable pour reconnaître l'environnement de mise en place des cherts, mais surtout leur mode de formation. J'ai pu mettre en place plusieurs critères de reconnaissance permettant notamment de distinguer des cherts océaniques (C-chert) de cherts secondaires (S-chert) et révélant ainsi la nature primaire des cherts de Komati River et de Buck Reef.

Un aspect relativement peu exploré dans les travaux consacrées aux cherts en général, concerne l'étude des structures sédimentaires et de déformation. Dans ce premier chapitre, j'ai montré comment, sur la base des observations de terrain, de telles structures peuvent être utilisées pour contraindre la forme sous laquelle a précipité la silice. Cette approche me permet en outre de comprendre le comportement rhéologique qu'avait le précurseur siliceux à l'origine des cherts, à la fois sur le plancher et dans les premiers stades de diagenèse.

Dans ce chapitre, je présente un article consacré à l'étude des cherts de fracture de Barite Valley. La rhéologie est au coeur de cette étude, où je m'attache à décrite les structures de déformation, en l'occurrence les structures de fracturation, afin de comprendre comment ce sont formés les dykes et quel était le comportement rhéologique des fluides siliceux qui les ont remplis.

Deux aspects sont essentiels dans l'approche proposée ici : la description des structures à l'échelle macroscopique, et l'observation des caractéristiques microscopiques du chert. La combinaison de ces données montre que les structures internes du chert sont étroitement corrélées à son comportement initial, à savoir un comportement à viscosité variable rarement, si ce n'est jamais, observé ni décrit dans les dykes de la ceinture de Barberton.

Cette caractéristique thixotropique des cherts de fracture est attribuée ici à la capacité de la silice à former des polymères en solution, parfois jusqu'à un stade de gélification avancé en absence de contrainte, et maintenant une viscosité élevée

dans la solution colloidale. A l'inverse, sous l'effet de contraintes cisaillantes, la polymérisation est inhibée et la viscosité reste suffisamment faible pour provoquer le fluage du matériau initial. Un tel comportement pourrait s'appliquer aux cherts déposés sur le plancher océanique, et l'étude systématique des structures de déformation dans les C-cherts devrait apporter de nouvelles perspectives quant à la nature de la phase siliceuse précipitant depuis l'eau de mer dans des environnements très variés (*e.g.* gel de silice, silice amorphe, boue siliceuse).

3.2   Article 2

The rheology of fracture-filling cherts : evidence for thixotropic fluid infiltrations.

Morgane Ledevin[1a]**, Nicholas Arndt**[1]**, Alexandre Simionovici**[1]

[1] ISTerre, Maison des Géosciences, Grenoble, France

[a] Corresponding author : morgane.ledevin@ujf-grenoble.fr

Abstract

The transition from the Mendon to Mapepe Formations ($\sim 3260Ma$) in the Barberton Greenstone Belt, South Africa, is marked by a $\sim 100m$-thick complex of black carbonaceous chert dykes that cut through silicified volcanogenic units. The fracturation was intense in this area, as shown by the width of the dykes ($<1m$ in average, up to 8m-thick) and by the abundance of completely shattered rocks. The dyke-and-sill organization of part of the plumbing system and the upward narrowing of some of the large veins indicates that at least part of the fluid originated from below and migrated upward.

Abundant angular fragments, either eroded from adjacent country rocks or brecciated in situ during fluid infiltration, are suspended and uniformly distributed within the larger dykes. The lack of closure of the veins below eroded blocks proves that the fragments did not settled to the lower part of fractures. This is taken as evidence that overpressured fluids were involved in the formation of the fractures : following the model of Hofmann et Bolhar (2007), we believe that hydraulic fracturation was at the origin of the dykes.

The most important finding of this study is that the material at the origin of the fracture-filling black chert was thixotropic. The presence of black chert in networks filling extremely fine fractures is evidence for a low viscosity at the time of injection, but the apparent suspension of large blocks of country rock within larger veins indicates a high viscosity. The inference is that the viscosity of the injected fluid changed from low to high.

Such rheological behavior is characteristic of media composed of solid particles suspended in a fluid. The presence of abundant fine-grained (i.e. clay-sized) particles of silica and carbonaceous matter, the relatively high proportion of siliceous matrix and the capacity of colloidal silica to form cohesive 3D networks, can account for the viscosity variations and thixotropic behavior of the fluid that filled the veins. When it was injected, the stirring and shearing of the fluid imparted a low viscosity by lowering internal particle interactions, but as the rate of movement decreased, it became highly viscous as the inter-particulate bonds were reconstituted.

Key Words - Fracture-filling cherts ; Thixotropy ; Viscosity ; Fracturation ; Hydrothermalism.

3.2.1 Introduction

In the previous chapter, we focused essentially on the petrological characteristics of Archean cherts with special emphasis given to their identification as either seafloor chemical precipitates, replacement chert of fracture-filling chert. We proposed several mechanisms for their respective formation and gave new insights on the rheological behavior of C-cherts from their deposition at the surface to shallow and deep burial conditions.

In this chapter, we focus on the fracture-filling cherts found in the Barite Valley Syncline. These black carbonaceous cherts are found filling large dykes that mark the transition from the Onverwacht to Fig Tree Group. They are part of a volcano-sedimentary complex very similar to those found in other parts of the Barberton Greenstone Belt, as well as in other Archean terranes (Lowe et Knauth 1977, Nijman et al. 1998, Lowe et Byerly 2003, Lowe et al. 2003, de Vries et al. 2006, de Wit et al. 2011).

The origin of the widespread shattering of preliminary deposited, and probably already silicified, sedimentary units is controversial, and thus the origin of the cherts itself needs to be clarified. Two important papers are considered together with the present study : Hofmann et Bolhar (2007) and Lowe (in press.). These authors provided extensive field work in the area and proposed contrasting theories for the origin of dykes.

In the present study, we would like to fill a gap that concerns the rheology of the material which precipitated to form the now fracture-filling black cherts. Through descriptions of the field relations and dyke geometry, and the macro- and microscopic characteristics of the chert, we will demonstrate that the fluids from which they formed had unusual thixotropic behavior, a characteristic already proposed for seafloor-deposited cherts in the previous chapter. Although the discussion of the mechanism of dyke formation is beyond the scope of this study, the theories proposed by Hofmann et Bolhar (2007) and Lowe (in press.) will be briefly reviewed to better constrain the origin of the fracture-filling cherts.
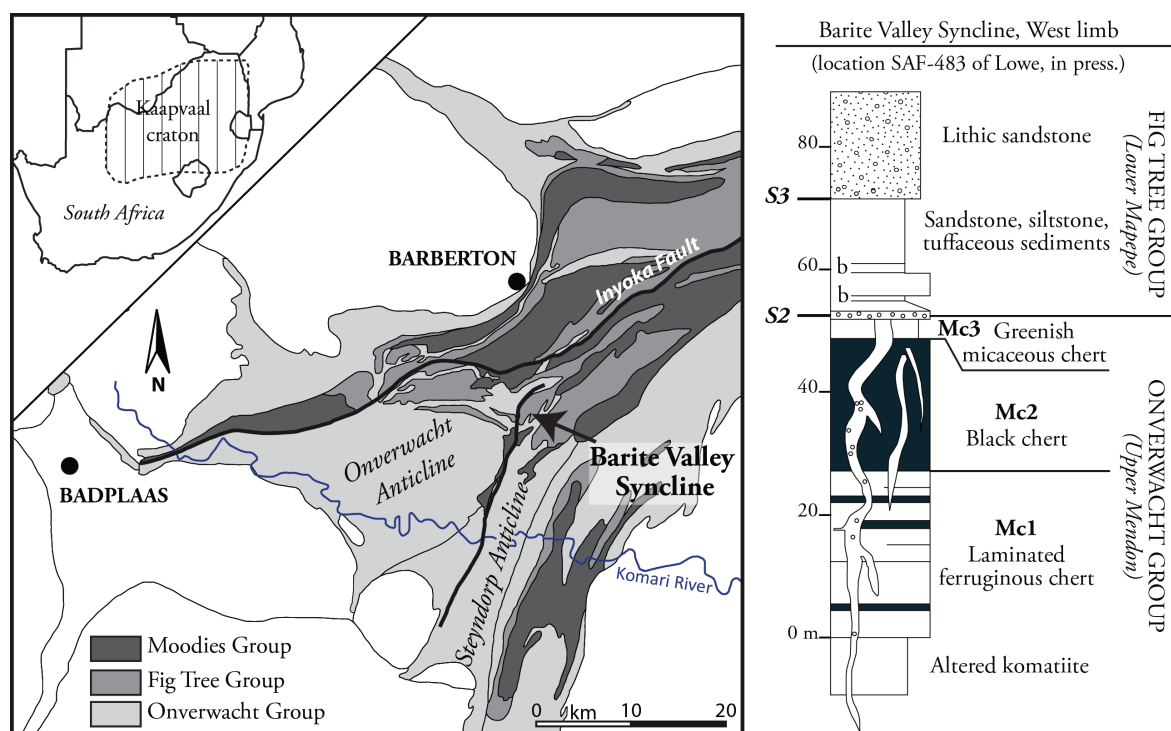
FIGURE 3.1 – *Simplified geological map of the Barberton Greenstone Belt and location of the Barite Valley Syncline north-east to the Onverwacht Anticline. The stratigraphy is modified from Lowe (in press.) and corresponds to the western limb of the Barite Valley (location SAF-483 of Lowe (in press.)). The Onverwacht to Fig Tree transition is marked by the spherule bed S2 (Lowe et Byerly 1986b) below which is found the dyke complex of this study. The dykes begin in the sedimentary units M3c and M2c, cut through M1c and extent down to the Si-metasomatised komatiitic flows.*

3.2.2   Geological context and location of studied dykes

The Barberton Greenstone Belt is a 3.5-3.2Ga volcano-sedimentary sequence typical of Archean greenstone belts, beginning with the thick, magmatic-dominated Onverwacht Group at its base (3530-3334Ma ; Viljoen et Viljoen 1969b;a, Armstrong et al. 1990, Kröner et al. 1991, Lowe et Byerly 1999, Hofmann 2005, Hofmann et Harris 2008), essentially composed of ultramafic rocks with few sedimentary intercalations. It is further divided into the Komati, Hooggenoeg, Kromberg and Mendon Formations (*e.g.* Viljoen et Viljoen 1969c, Armstrong et al. 1990, Kröner et al. 1991, Kamo et Davis 1994, Byerly et al. 1996, Lowe et Byerly 1999). The overlying Fig Tree Group marks an evolution to more felsic rocks with increasing sediment contributions in the form of clastic or chemical deposits (3258-3226Ma ; *e.g.* Kröner et al. 1991, Byerly et al. 1993, Lowe et Nocita 1999, Hofmann 2005). The sequence
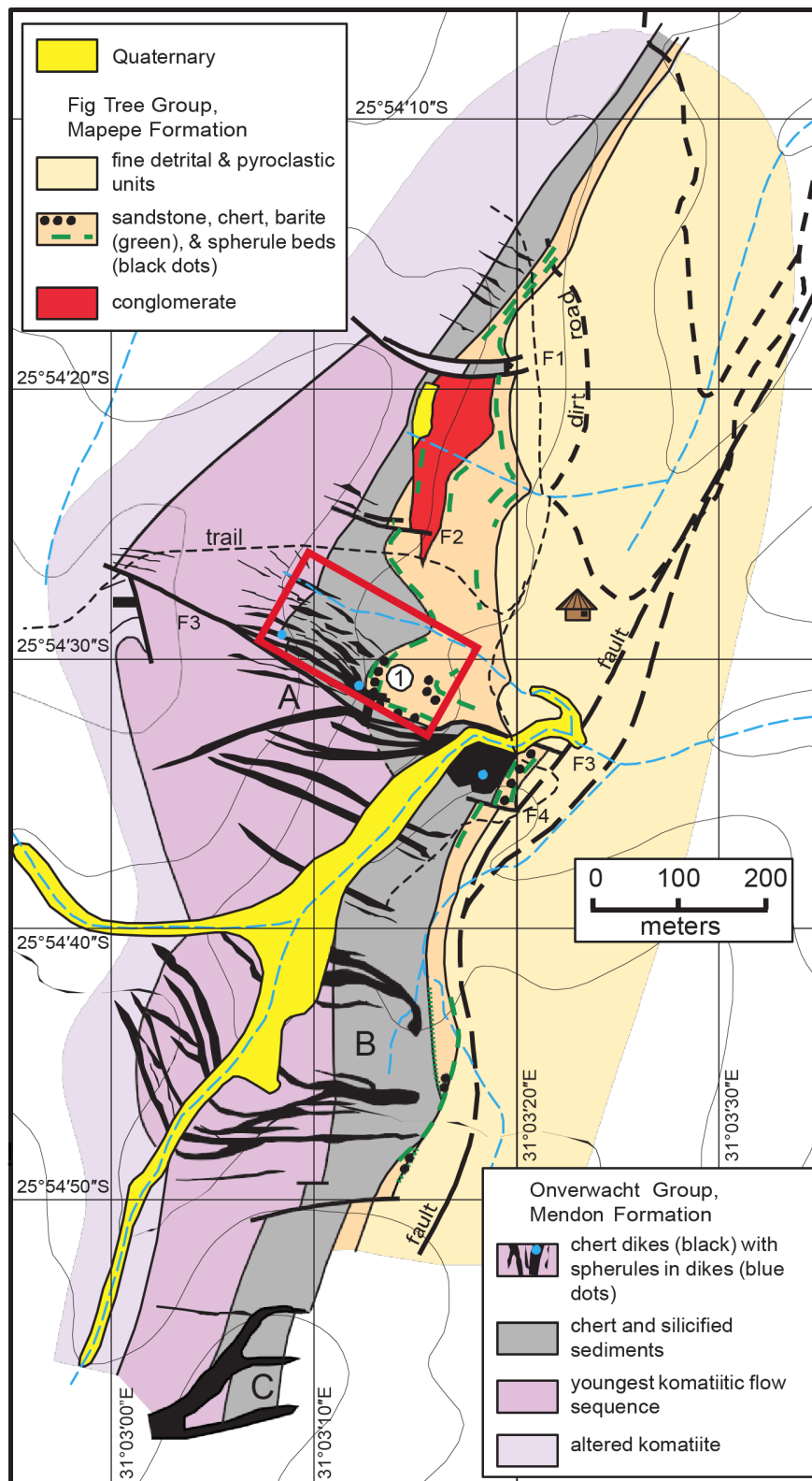
FIGURE 3.2 – *Geological map of the Barite Valley site from* Lowe *(*in press.*) showing the repartition of the dykes. They start at the top of the Mendon Formation (grey) and extent downward through to the komatiitic units (pink). The red rectangle represents the studied area.*

ends with the thick, clastic-dominated Moodies Group (3230-3110Ma; *e.g.* Kröner et al. 1991, Kamo et Davis 1994), essentially composed of the erosional products of previously deposited Fig Tree and Onverwacht Groups.

The Barite Valley site is located North-East of the Onverwacht anticline (Fig.3.1), where the uppermost units of the Mendon Formation (3335-3260Ma; Kröner et al. 1991, Byerly et al. 1993; 1996) are conformably overlain by the lowermost units of the Mapepe Formation (3260-3225Ma; Armstrong et al. 1990, Byerly et al. 1996) (Fig.3.2). The Onverwacht to Fig Tree transition is well-exposed on the western limb of the Barite Valley syncline (Studied area : $S25°54.509 - 54.535$; $E30°03.185 - 03.236$; Fig.3.2).

Here, the Mendon Formation comprises a series of komatiite flows (Fig.3.1) with silicified upper parts (Duchac et Hanor 1987, Hanor et Duchac 1990, Hofmann et Harris 2008), which evolves to a $\sim 100m-$thick unit of thinly laminated ferruginous cherts (Mc1), massive bedded black cherts (Mc2) then greenish micaceous cherts (Mc3), all deposited in quiet, probably deep, subaqueous environments (Lowe in press.). The series contain concordant layers of seafloor-deposited cherts briefly described in Chapter 2 and recognized as marine, chemical precipitates.

These units are conformably overlain by the felsic volcanogenic sediments of the Mapepe Formation (Fig.3.1) which comprise intervals of lithic sandstone, slab conglomerate, barite and minor chert and jasper layers (Heinrichs 1980, Lowe 1999, Lowe et Nocita 1999). They represent clastic sedimentation in shallower environments, evolving from fan-delta to alluvial and shallow marine conditions (Lowe et Nocita 1999, Lowe in press.). Part of the detritus, especially the chert clasts in conglomerates, was derived from the underlying Mendon Formation (Lowe in press.).

The sedimentary units are folded and steeply deep to the S-SE ($\sim 60°$; Fig.3.3-a). At the top of Mendon Formation, they are cut by numerous veins and fractures filled with black, carbonaceous chert (Fig.3.2) (Lowe et Nocita 1999, Lowe et Braunstein 2003, Lowe et al. 2003, Lowe in press.). The nature and origin of the veins and of the filling material are the focus of this chapter. The veins terminate below the spherule bed S2 of the overlying Mapepe unit (Lowe et Byerly 1986b).
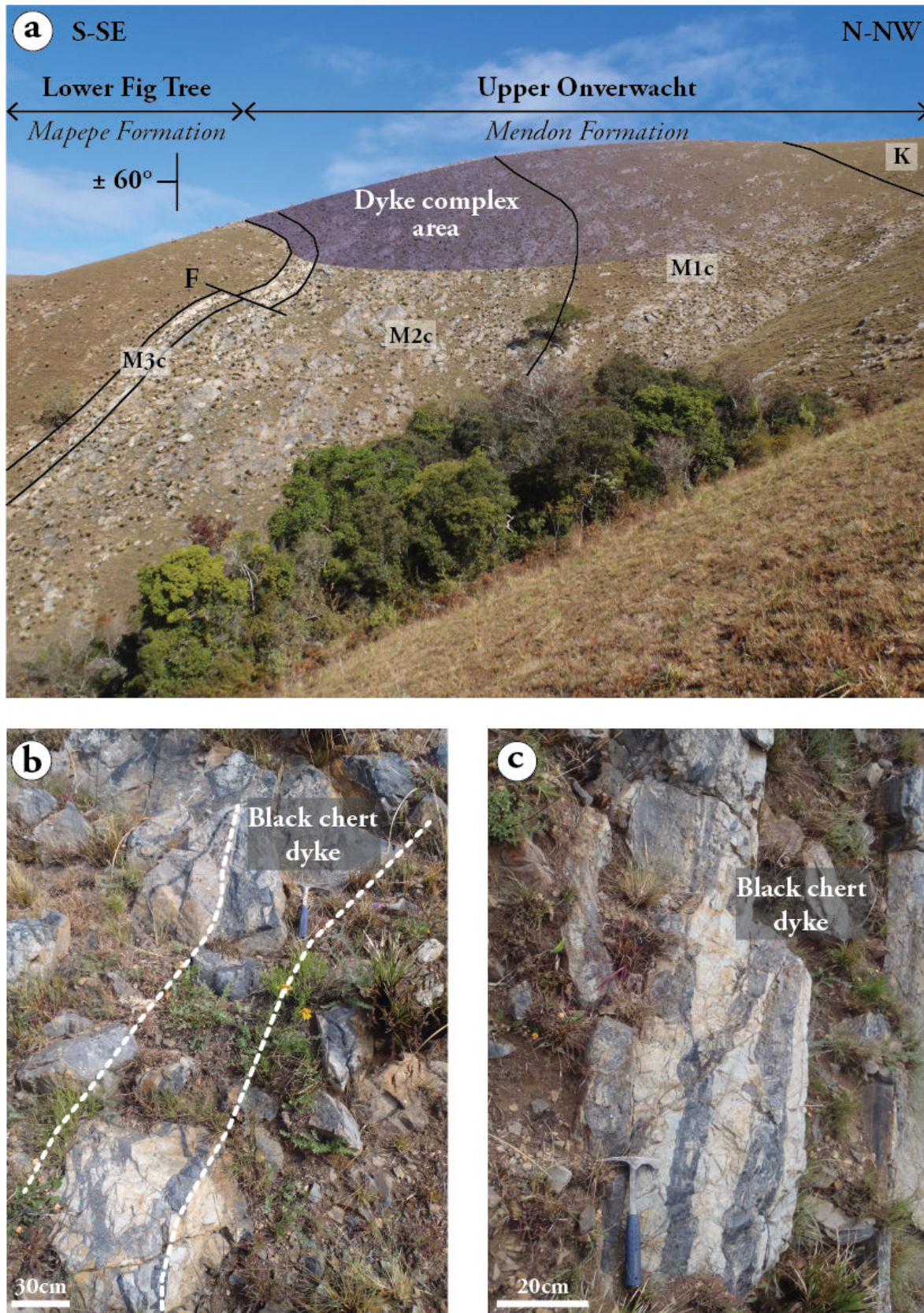
FIGURE 3.3 – *(a) Photo of the Barite Valley area (NE side of the hill) showing the main limits of Mendon and Mapepe Formations. The series young to the S-SE and steeply deep at ~ 60° in the same direction. The main dyke complex area begins in the sedimentary units M3c and M2c, cuts through M1c and extends down to the Si-metasomatised komatiitic flows (K). The stratigraphy is shown in Figure 3.1. Photos (b) and (c) are examples of black chert dykes cross-cutting the volcaniclastic rocks of the upper Mendon formation.*

Geometry of black chert dykes
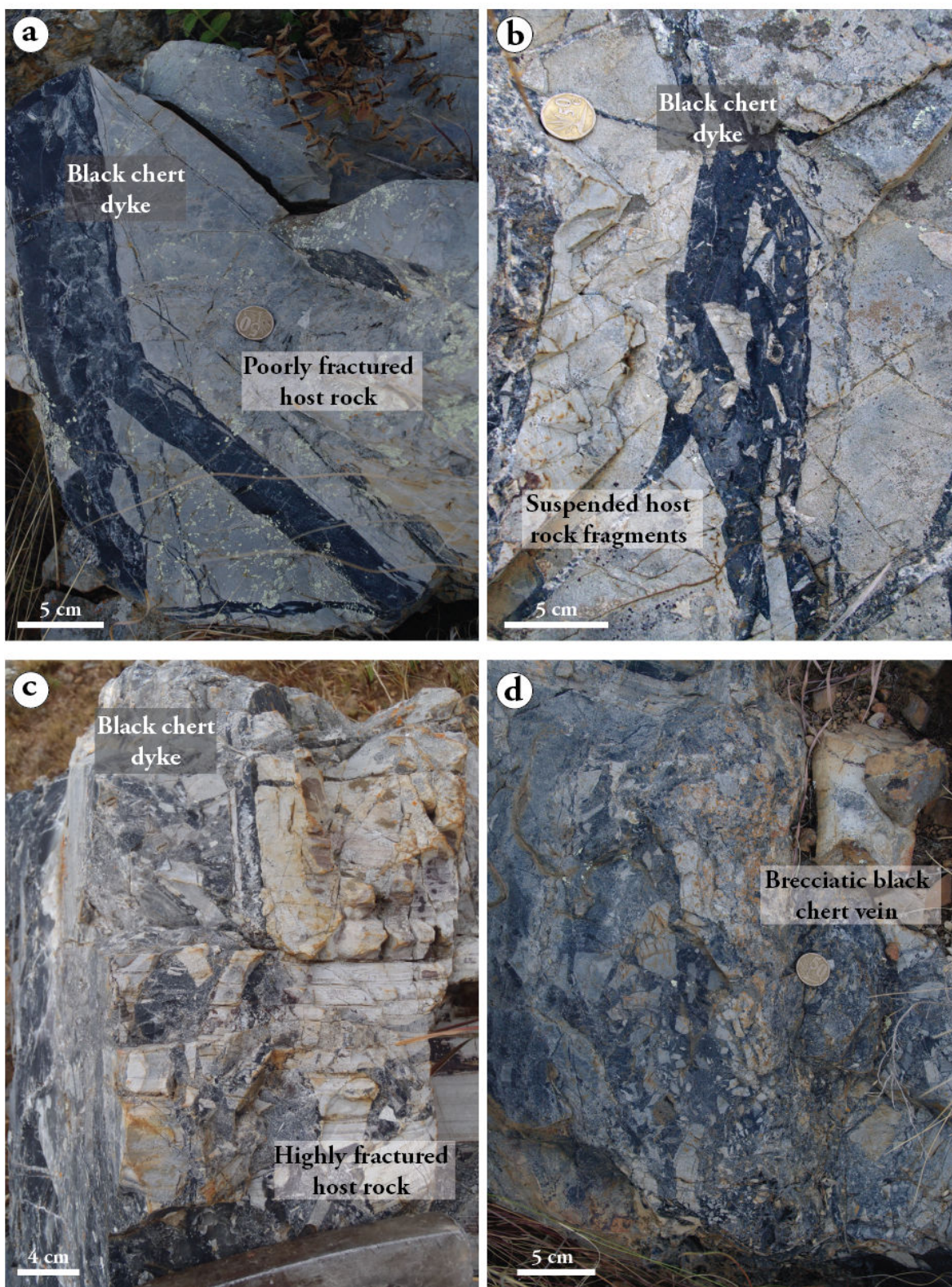
FIGURE 3.4 – *Main types of dykes encountered in the Barite Valley syncline with degree of fracturation increasing from photo (a) to (d). The fractures have straight and sharp (a) to irregular boundaries (c). They contain variable amount of country rock fragments embedded in the black chert matrix, leading to clast-supported (c,d) or matrix-supported (b) textures in outcrop. Fragments are most commonly angular in shape and preserve primary laminations.*

Some fractures are parallel to the bedding and commonly root in larger and discordant dykes that can be followed down into the underlying Mendon units.Typical examples are illustrated in Figure 3.3 - b & c.

3.2.3   Discordant dykes

Geometry of fractures

As shown in Figures 3.1 and 3.3, the dyke complex starts in the greenish micaceous cherts and black cherts of units Mc3 and Mc2 at the top of the Mendon Formation, as described by Lowe (in press.). They can be followed several tens of meters through to the underlying laminated, ferruginous cherts of M1c unit and can extend up to $100m$ into the underlying, komatiitic volcanic units Lowe (in press.). In average, the fractures become narrower with depth in the Mendon formation. The dykes are oriented to the W-NW and cut across the sedimentary rocks at high angle, commonly at 60 to 90° to the bedding although Lowe (in press.) reported values down to 20-40°.

The fractures display a wide range of shapes, widths and fracturation intensities as presented in Figure 3.4. They vary in thickness from a few centimeters to several meters (max. $8m$; $<1m$ in average) and have complex structures with numerous mm-thick veins that branch out from the main part of intrusions. From photo (a) to (d), the shape evolves from straight dykes to irregular fractures, the intermediate shapes (b) and (c) being the most common type encountered in the area.

The fractures are in sharp contact with surrounding host rocks and contain variable amounts of host rock fragments embedded within a black chert matrix. The fragments are most commonly angular in shape, although sub-rounded to rounded grains can be observed (see next section and Fig.3.7 and 3.8 for description). The resulting structure is either matrix-supported (Fig. 3.4 - b) or clast-supported (Fig. 3.4 - c) depending on the clast/matrix ratio and degree of fracturation.

Intense cases of fracturation are illustrated by the clast-supported fracture of Figure 3.5. The structure consists of little displaced, minimally rotated, sub-angular to angular clasts of fine-grained country rock separated by $< 1mm$ to cm-thick veins of black chert. All clasts are elongated thorough the same direction due to the sub-parrallel orientation of most of the chert veins, and the fragments form a

«Jigsaw-puzzle» Structure

a - Upper zone   *b - Bottom zone*

Fracture-filling black chert

Light grey, fine tuffaceous chert *(Country rock)*

Highly altered zones (Coarse
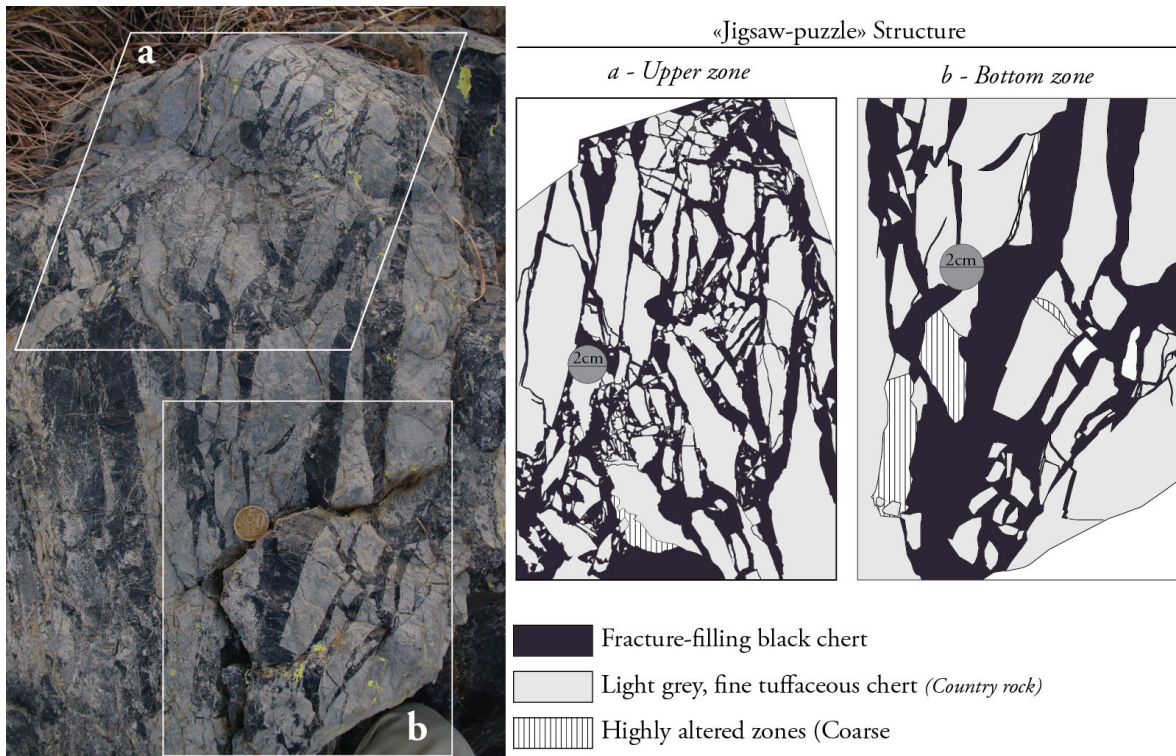
FIGURE 3.5 – *Highly brecciated zone composed of long and angular host rock fragments with jigsaw fits separated by mm- to cm-thick black chert veins. The structures are more easily visible on sketches (a) and (b) corresponding to the upper and bottom parts of the structure respectively. (a) Rocks are fragmented in small blocks separated by thin black chert veins (<1mm-2cm). Each block is minimally displaced. (b) This part of the outcrop is less fragmented and the black chert veins are thicker, reaching 4-5cm. Note that the blocks present in the chert did not settle to the bottom part of the jigsaw structure. Instead, they look suspended in the siliceous matrix, at least in the two-dimension view of the outcrop.*

"jigsaw-puzzle" texture. The fracturation was more intense in the upper part of the structure (Fig.3.5-a) as shown by the abundance of small-size fragments (typically <5mm). When moving through the bottom, black chert veins are larger and country rock fragments are bigger. These fragments look suspended in the siliceous matrix, at least in the two-dimensional view of the outcrop.

Other examples of highly fractured zones are shown in Figure 3.6. In photo (a), the texture resembles the previous jigsaw-puzzle although the fragments are slightly more rounded. The black chert veins are abundant and range in size from <1mm to ∼ 5mm. Photo (b) differs from (a) by showing multiple directions of veins which spread out at 360° from a highly fractured central zone.

Highly fractured zones
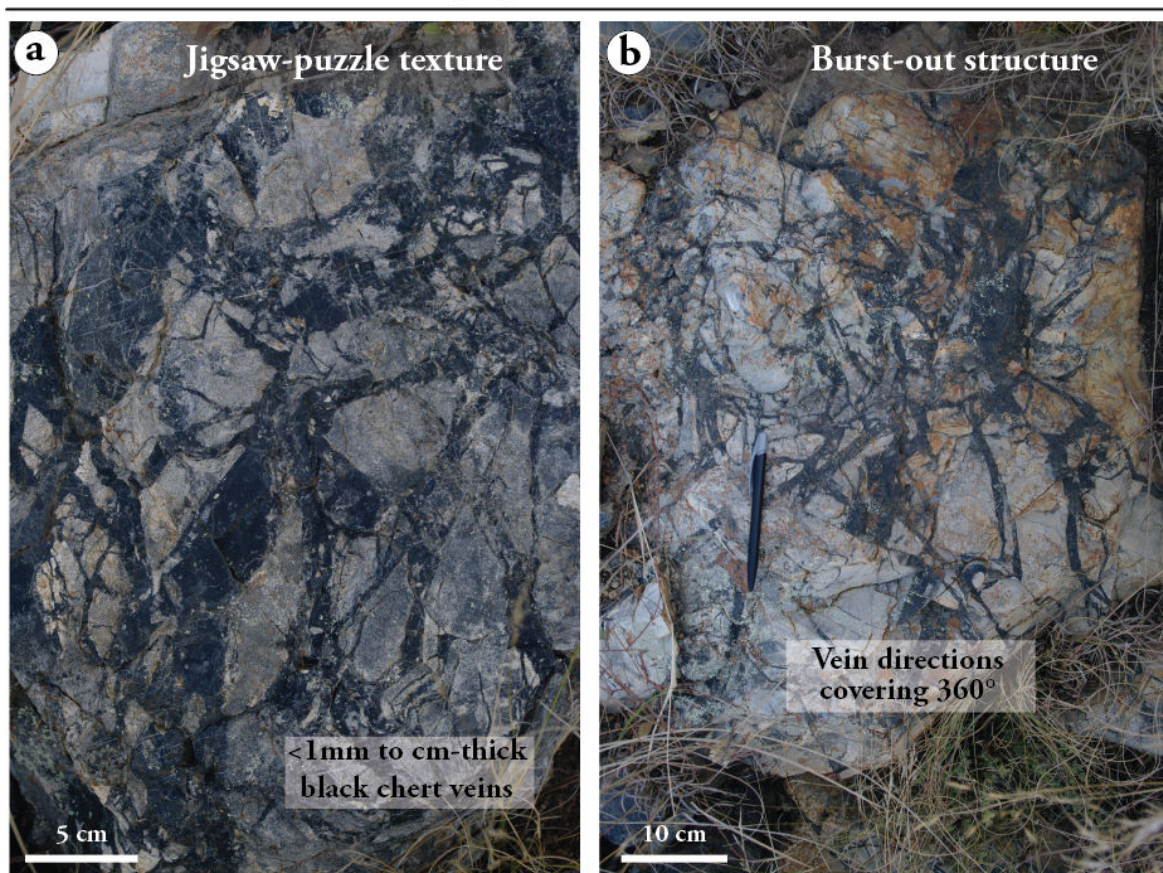
FIGURE 3.6 – *Hydraulic-fracturation features in Barite Valley dykes. (a) Jigsaw-puzzle texture : angular and long-shaped country rock fragments little displaced and separated by cm-thick black chert veins. (b) Burst-out texture : radiating black chert veins at 360° around a central, highly fractured zone.*

Internal structures

Although some of the dykes are filled entirely with homogeneous, translucent black chert (see Fig.3.4-a), most are charged with fragments originating from the silicified country rocks. As shown by the multiple examples in Figure 3.7, fragments have polyhedral shapes covering the whole range between sub-rounded (a) and cobble (c) clasts. They range in size from $\sim 1cm$ to 40-$50cm$ ($<10cm$ in average) (see also Fig.3.4 b to d) and are uniformly distributed within the dyke with their long dimension commonly sub-parallel to the fracture walls (Fig. 3.7 - b,d), especially when close to the contact.

Geometry of country rock fragments (1)
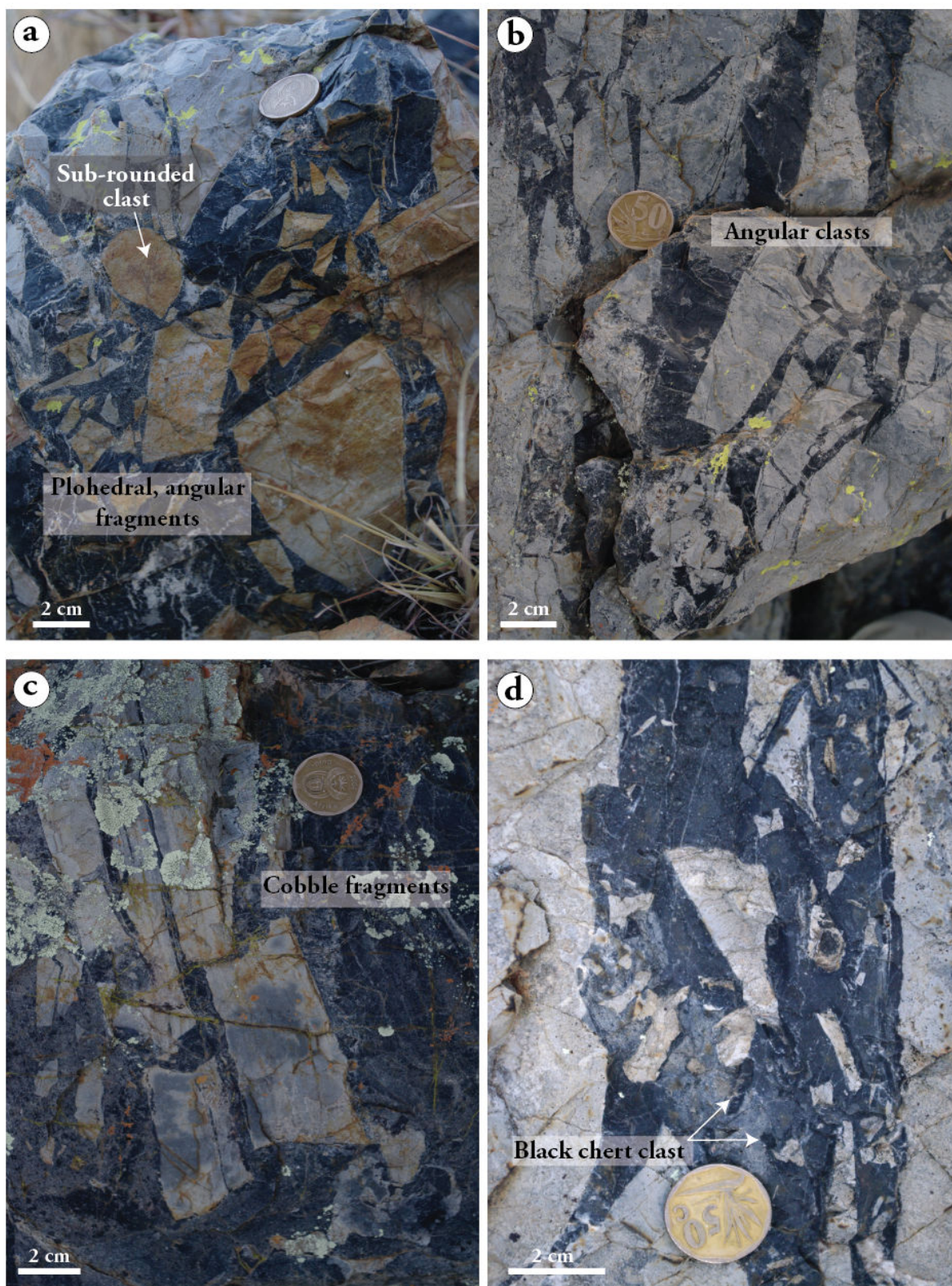
FIGURE 3.7 – *Selection of dykes showing the most common shapes of country rock fragments. They range in size from ~ 1cm to 40-50cm (<10cm in average) and show a wide range of polyhedral shapes, from (a) sub-rounded to (c) cobble-like. They are most commonly irregular as in (b) and (c). More than 90% of embedded fragments are from the surrounding host rock. The rest consists essentially of clasts eroded from older veins.*

Geometry of country rock fragments (2)
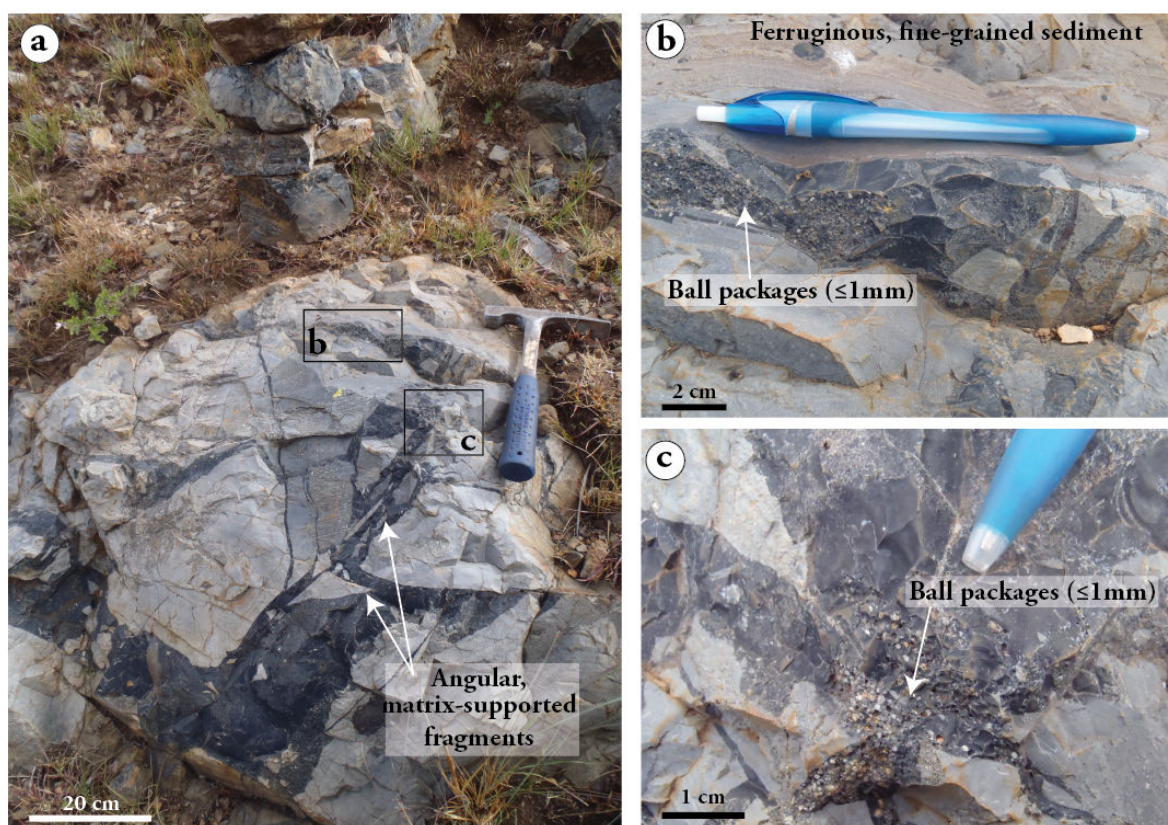
FIGURE 3.8 – *(a) Homogeneous dyke essentially filled of black chert with low amount angular country rock fragments. Photos (b) and (c) are located in photo (a) and show agglomerates of small balls of translucent silica (<1mm). More than half of the balls were eroded during weathering and part of the remaining holes are now filled with modern zeolite. The packages are found (b) at the bottom part of a black chert sill or (c) between suspended fragments in the main, vertical channel.*

The finest and roundest particles we found are shown in Figure 3.8. They form dense packages at the bottom of a sill (b) or between suspended fragments in the main channel (c). The rounded particles are less than $1mm$ in diameter and composed of pure, translucent silica and highly weathered grains of unidentified origin. Such aggregates are rare and most of the fragments less than $1cm$ in size display sub-rounded to sharp edges similar to larger clasts (*e.g.* Fig.3.4-d).

The origin of eroded blocks is easily determined thanks to their resemblance with surrounding units in terms of color, grain size, structure and texture. We estimate that more than 90% of the clasts are derived from the adjacent units. The laminations of the source rock are generally preserved (*e.g.* Fig.3.4-d), except in the

most intense cases of silicification. In Figure 3.7-c, the darker zones show signs of interaction with the primary siliceous fluid and partial disappearance of primary structures.

The distribution of country rock fragments varies from one dyke to another. The jigsaw structures, previously shown in Figure 3.6-a, have the highest clast to matrix ratio and all the fragments are close to one another, being separated only by thin veins of black chert. These clasts are much longer than large, and preserve typical spindle-shape edges representative of their minimal displacement. They comprise more than 60-70% of the fractured zone whereas the black chert is restricted to thin veins typically less than $1mm$.

In larger dykes, the proportion of clasts is more variable. The transition from clast- to matrix-supported is not particularly obvious, being limited by the two-dimension of outcrops, but a typical example of matrix-supported dyke is shown in Figure 3.7, photo (d) (see also Fig.3.4-b for a larger view). In this fracture, pale grey blocks eroded from the country rock are suspended in the black chert matrix. Multiple cobble clasts of translucent black chert (Fig.3.7-d) are seen in some veins : these may have been inherited from an older vein given the lack of black chert horizons in surrounding units. In other examples of matrix-supported dykes, the black chert matrix appears homogeneous and free of macroscopic fragments, like in the previous Figure 3.4-a.

3.2.4   Microscopic observations

The petrography of two representative fracture-filling cherts are shown in Figure 4.12 (FTC4 and FTC9). These samples were taken in matrix-supported fractures that cut through pale grey, tuffaceous cherts essentially composed of sericite and microquartz with variable amount of Fe-carbonates.

The apparent homogeneity of the chert in outcrop does not apply at a microscopic scale. Sample FTC9 (Fig.4.12-a) consists of rounded silica and carbonaceous matter grains in a microquartzitic matrix. The proportion of matrix is difficult to determine but is estimated between 20 and 30%. The carbonaceous matter grains

Sample FTC9
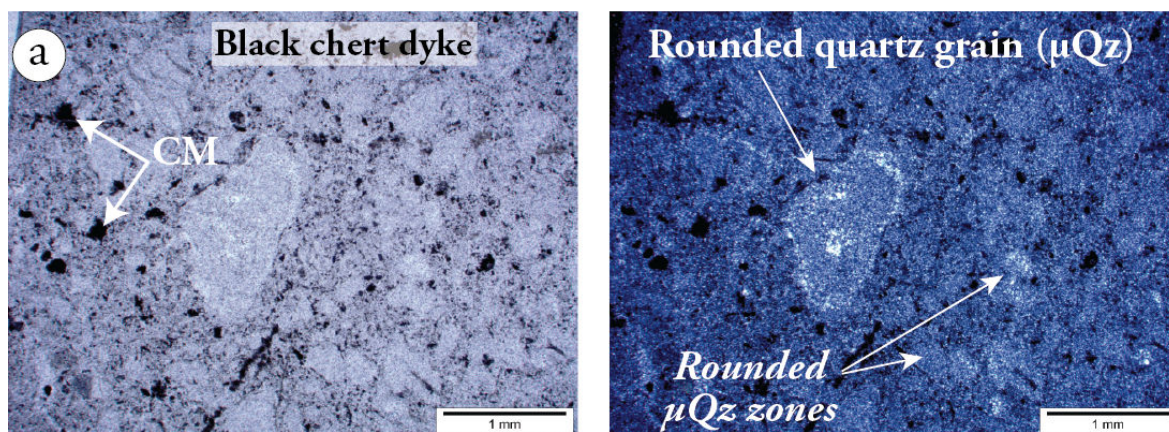
Sample FTC4
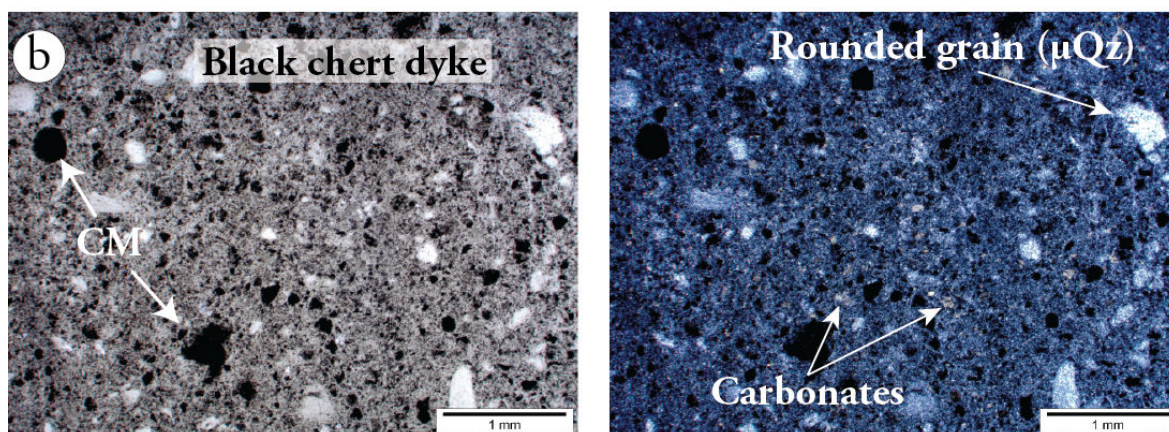
FIGURE 3.9 – *Photomicrographs of fracture-filling black chert samples FTC9 (a) and FTC4 (b). CM = carbonaceous matter ; μQz = microquartz. (a) Sample FTC9 is composed of rounded particles of silica and carbonaceous matter in a matrix of microquartz. The grains are 100-200μm in average. Silica grains are composed of microquartz similar to surrounding matrix leading to diffusive contact between both phases. Carbonaceous grains are aggregates of smaller particles. (b) Sample FTC4 is composed of rounded particles of silica (50% of the particulate fraction), carbonaceous matter (50%) and carbonate (< 2-%) in a matrix of microquartz (up to 50-60% of the chert).*

represent a few percent of the rock. The grains are rounded in shape, consist of fine particles aggregates and are less than $100\mu m$ in size, with rare, larger grains reaching 500-600μm. On the other hand, the amount of silica grains is much more abundant and comprises the majority of the chert. Each grain is in close contact to one another and all are composed of pure microquartz very similar to the surrounding matrix. These silica grains are characterized by sub-rounded to very well-rounded shapes and have typical size of 200-300μm with minor occurrences of mm-sized particles.

The sample FTC4 (Fig.4.12-b) is similarly organized and comprises a mixture of small rounded grains of silica, carbonaceous matter and carbonate in a very fine microquartzitic matrix. This sample differs from the previous one by showing higher matrix content (up to 50-60%) whose dark color is due to the presence of diffuse carbonaceous matter. The grains of carbonaceous material comprises half of the particulate fraction. They have near-rounded shapes and range in size from 10 to 500μm (100μm in average). Silica grains form the rest of the particulate fraction and display rounded shapes similar to the carbonaceous grains. They are composed of almost pure microquartz ($<$5-10μm) in either sharp or diffusive contact with the surrounding matrix. Carbonates are a minor component ($<$5%) and found as isolated, rounded grains no larger than 50μm.

3.2.5   Discussion

Two main theories have been proposed to explain the intense fracturation observed in the Barite Valley Syncline.

The "*hydraulic fracturation hypothesis*" was proposed by Hofmann et Bolhar (2007) who argue that the sedimentary units of Upper Mendon Formation were silicified early at the surface, during or just after deposition, by the pervasive and diffuse venting of low temperature hydrothermal fluids through the seafloor. The resulting impermeable cap of chert would have acted like the seal of a pressure cooker, increasing the pressure of trapped fluids from the paleo-hydrothermal system and leading to extensive fracturation and dyke formation.

The "*impact hypothesis*" was first proposed by Lowe et Byerly (2003) who believe that a large meteorite or asteroid impact and subsequent seismic activity supplied

sufficient energy to produce intense fracturing of the Archean seafloor and the development of open fractures. More recently, Lowe (in press.) described the most accurate field work ever done on the Barite Valley dykes and put together various lines of evidence that favor the fracturation of the primitive oceanic crust by one or multiple impactors. He proposes a model that includes contemporaneous crustal fracturing and tectonic activity leading to local block displacement, dyke formation and tsunami generation, all related to the impact spherule bed described by Lowe et Byerly (1986b).

The following sections focuses on the rheology of the infilling material at the origin of the fracture-filling black chert. Complete discussion of the mechanism of dyke formation is beyond the scope of this study, but both the above hypotheses need to be considered and will be briefly discussed as the fracturation must be strongly related to the circulating fluid properties.

Filling of the fractures : from below or from above ?

Although the *Hydraulic* and *Impact* hypotheses invoke different the trigger mechanism of fracturation, they concur on the following point : the fractures are filled from above, by the downward migration of unconsolidated carbonaceous sediments of the Mc2 and Mc3 divisions (Fig.3.1). According to Hofmann et Bolhar (2007) and Lowe (in press.), these sediments were present on the seafloor at the time of dyke formation and migrated toward, then into the newly formed, open fractures in the form of soft and/or liquefied material. The main arguments advocated by Lowe (in press.) are (1) the presence of rock fragments in dykes that come from higher stratigraphic levels and the lack of fragments from lower stratigraphic levels, (2) the downward displacement of blocks eroded from adjacent country rocks and (3) the geometry of the dyke complex that is $50m$ wide on top and extend as individual dykes downward through to the Mendon volcanic units.

However, the Figure 3.10 shows evidence of (pene-)contemporaneous upward fluid migration for some of the studied dykes. The photo (a) shows a dyke-and-sill structure similar to those observed in magmatic plumbing systems. The main, vertical channel spreads out laterally at specific sedimentary intervals (*i.e.* weaker plans) to form horizontal veins (or sills) concordant with host rock bedding. The

Upward flow evidence
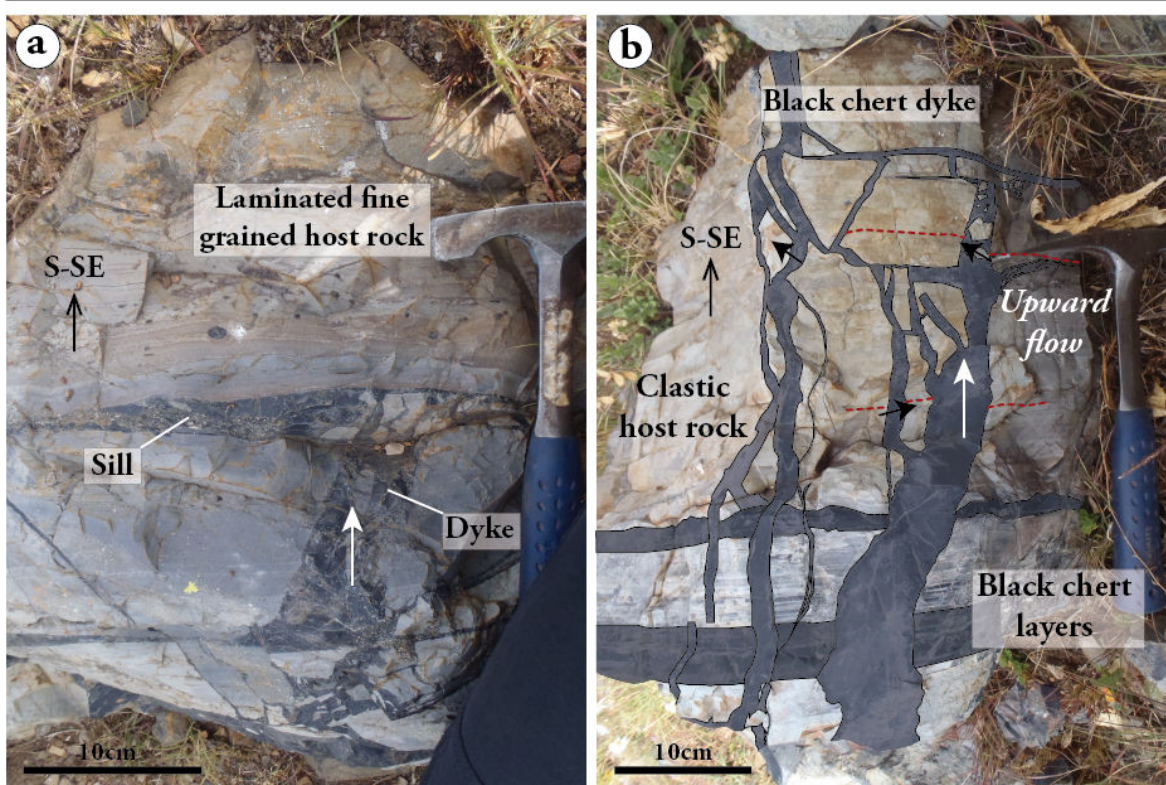
FIGURE 3.10 – *(a) Dyke-and-sill structure : a central, vertical channel spread out laterally along weaker sedimentary plane to produce sills concordant with country rock bedding. The structure ends in the younging direction by a final, <40cm-thick sill. (b) Vertical dyke narrowing in the younging direction. both photos are evidence for the migration of fluids from below contrarily to the majority of the dykes that show emplacement from above.*

structure does not persist upward as the fluid lost its fracturation capacity, and ends with a final sill of limited lateral extent (<40cm). Another example comes from the multi-branch dyke of photo (b) where the main channel, or feeder channel, is larger at the base and narrower when cutting through younger units. The central part of the dyke has suspended host rock fragments that are little displaced (1cm) toward the top of the structure.

Both these structures are evidence that some fluids came from below. However, we will show in the following section 3.2.5 that upward fluid migrations are not incompatible with the downward flows observed by Lowe (in press.).

Behavior of the circulating fluids.

Arguably the most important finding of this study centres on the physical characteristics of the fluid that filled the fractures. In section 3.2.3, we showed several examples where the black chert occupies a network of extremely fine fractures (*e.g.* jigsaw textures of Fig.3.5), which is evidence for us that the chert had a low viscosity at the time it was injected. In contrast, very soon after injection, it must had acquired a viscosity high enough to suspend large blocks of country rock.

Such a capacity to change viscosity refers to the concept of thixotropy (*e.g.* Bauer et Collins 1967, Barnes 1997, Mewis et Wagner 2009). When the fluid was injected, the stirring and shearing imparted a low viscosity but, as the rate of movement decreased, it became highly viscous.

The fact that blocks of country rock are distributed uniformly through the volumes of chert in the large "matrix-supported" dykes (e.g. Fig.3.4-a) indicates that the transition from low to high viscosity was rapid; sufficiently rapid that the blocks did not have the time to migrate towards the lower part of the fracture. This is especially noticeable in the jigsaw zones, where the veins are wider in the bottom part of the structure and much thinner at the top (Fig.3.5). The lack of vein closure through the lower zone indicates that the blocks of country rock did not settle downwards and suggests again that the transition from low to high viscosity was rapid.

The cause of thixotropic behavior

Inspection of thin sections shows that the fracture-filling black chert is not uniform but consists of an assemblage of fine particles in a siliceous medium (Fig.4.12). The significance of this finding is made clear by consultation of the extensive literature on thixotropic systems.

From the recent reviews of Barnes (1997) and Mewis et Wagner (2009) (and reference therein), it is obvious that thixotropy is typical of colloidal suspensions or any other system in which solid particles are suspended in a fluid. Examples of such materials are abundant in the everyday life, including food products (*e.g.* yoghurt, mayonnaise, ketchup), pharmaceutical and personal care products, adhesives, paints, coatings, printing inks and so on (see references in Barnes 1997, Mewis

et Wagner 2009). From the mining industry, evidence is shown that mineral slurries, such as clay (bentonite, montmorillonite) and silicate suspensions, are strongly thixotrope (*e.g.* Nguyen et Boger 1985, Besq et al. 2000, de Kretser et Boger 2001, Klein et Hallbom 2002, Oleksy et al. 2007).

In the geological world, it has been shown by Boswell (1948) that all unconsolidated sediments can exhibit thixotropy to a greater or lesser extent. The degree of thixotropy depends on a variety of factors according to authors, among which are of major importance the (1) size and shape of suspended particles, (2) the loose packing and water content of the system, and (3) the presence of adequate electrolytes such as seawater salts.

The geometry of the grains are particularly important : Freundlich (1935), a pioneer of thixotropy, pointed out that a substantial proportion of fine-grained particles, characterized by small size and platy shapes, will promote viscosity drops under shear stress. He also recognized that rounded shapes or significant amount of silt and/or sand in the particulate fraction does not inhibit the development of thixotropic behavior, although it lowers its efficiency. Thus, we propose that the thixotropy of the fluid at the origin of Barite Valley fracture-filling cherts can be linked directly to the presence of the small rounded particles randomly distributed in the siliceous matrix. The thixotropy is especially enhanced by the presence of fine clay particles (Boswell 1948) eroded from the surrounding silicified tuffaceous country rocks and by the abundance of carbonaceous matter of organic origin (Boswell 1948, Hofmann et Bolhar 2007, Lowe in press.).

The mechanism of viscosity variations is still poorly constrained, but it is broadly accepted that the competition between(1) break-down of microstructures under flow stresses and (2) build-up due to in-flow collisions and Brownian motion drives the rheological behavior of the particulate (or colloidal) suspensions (Boswell 1948, Barnes 1997, Mewis et Wagner 2009). In other words, when the slurry is stirred and critical shear stress is reached, the attraction between particles is lowered and the viscosity drops to a minimum, but as movement decreases the attraction becomes more important and the slurry more viscous.

Barnes (1997) reported that, at rest, the only forces that favor the re-formation of inter-particle bonds are the Brownian forces whereas the nature of inter-particle

bonds must control the rapidity of the build-up process. From the petrology of the fracture-filling cherts, we propose that the siliceous matrix had the best chance to account for the rapid recovery of a viscous state soon after the injection of the primary material. In siliceous colloidal suspensions, such as those produced at hydrothermal vents (*e.g.* Guidry et Chafetz 2002; 2003, Channing et al. 2004, Tobler et al. 2008), the polymerization of small (nm) to large (*μm*) silica flocs have the capacity to form coherent 3D networks, or gel-like structures (Iler 1979, Williams et Crerar 1985, Bergna 1994, Channing et al. 2004). The polymerization is enhanced when nuclei are available (Rimstidt et Barnes 1980, Williams et al. 1985, Williams et Crerar 1985, Rouchon et Orberger 2008), a role that we attribute to the abundant rounded, clay-sized grains present in the primary injected mixture.

However, the timing of network formation, the timing of viscosity recovery, and the strength of the newly formed network remain uncertain and depend on several factors affecting the silica polymerization, which includes (1) the temperature, supersaturation state and acidity of the fluid (Iler 1979, Chen et Marshall 1982, Rimstidt et Cole 1983, Fournier 1985, Renaut et al. 2002, Renaut et Jones 2003), (2) the current state of the material and the amount of previously underwent aggregation/disaggregation processes (Stade et Wicker 1971, Dietzel 2000, Chanson et al. 2006), and (3) the presence of activated complexes such as salts (Marshall et Warakomski 1980, Marshall et Chen 1982, Dandurand et al. 1982, Yates et al. 1998) that will help balancing the negatively charges silica colloids, especially in near-neutral and alkaline media (Grenne et Slack 2003, Channing et al. 2004).

The timing and mechanism of dyke formation.

In this section we focus on the linkage between the process that produced the fractures and the process that introduced the chert. We remain undecided about the exact trigger mechanism that shattered the rock at first, but for reasons outlined above and developed below, we favor hydraulic fracturing.

The key argument centres on our inference that the time between the development of the fractures and their in-filling with chert was very short. The lack of settling of matrix-supported blocks and the lack of closure of fracture networks even in the bottom part of the fractures points to rapid influx of the initial low-

viscosity fluid that was able to invade the entire fracture network. We suggest that unless the fractures were kept open by overpressured fluid, or perhaps by the presence of sufficient amount of particles in the fluid (in the manner of sand injected during hydraulic fracturing for shale gas extraction), the fractures would close.

In our opinion, such rapid influx of fluid is inconsistent with the models of Lowe (in press.). He suggests that the fractures remained open for a certain amount of time based on their observation of cavity-filling textures (*i.e.* botryoidal precipitative silica on cavity edges that grades into coarser quartz crystals through to the center) and sediment accumulation features on fracture edges. He argued that the lower part of the largest fractures remained open for a longer time compared to their upper part, and that the soft sediments that are supposed to have descended into the dyke took some time to reach the deepest levels of the fractures.

In our opinion, the formation of impact-triggered open fractures from on the seafloor fails to explain the lack of clast settling and their suspension in the black chert, the maintaining of fracture thicknesses in bottom part of highly fractured zones and the confined bursting of country rocks inferred from both the jigsaw structures (Fig.3.5) and the apparent 360° spreading out of some vein networks (Fig.3.6).

For these reasons we propose that the fluid that deposited the chert in fractures was the same as that which shattered the rock. We support the model of Hofmann et Bolhar (2007) who suggested that the development of layered silicified rocks formed a impermeable cap that allowed the pressure to build up in the confined fluids that pervaded the substrate from below. Once the pressure exceeded their strength limit, the rock was shattered, opening passageways into which a slurry of fine abraded particles of country rock in colloidal solution was injected. Overpressure in the fluid kept open the fractures until the flow velocity decreased and the viscosity increased to a value sufficient to suspend the fractured blocks. Relaxation of the system, soon after its emplacement and before its complete induration, allowed the collapse of surface sediments that were still soft and capable to liquefied in their way toward and into the newly formed fractures.

3.2.6 Conclusions

Based on the geometry of Barite Valley dykes and on the petrology of the fracture-filling black cherts, several conclusions were reached concerning both the mechanism of fracture formation and the nature and behavior of the pervasive fluid.

(1) Part of, if not all, the fractures originated from hydraulic fracturation as overpressured fluids are required to maintain opened the veins and prevent the settling of clasts eroded from adjacent units.

(2) Such process can account for the intense *in situ* brecciation of the country rocks and requires the confining of fluids below impermeable series of rocks silicified early on the seafloor. Such model is similar to that proposed by Hofmann et Bolhar (2007).

(3) The fluid that provoked the fracturation had a thixotropic behavior, being fluid during flow and viscous early after the filling stopped. The presence of fine particles (clay size) mixed with the Si-rich fluid and the capacity of silica to form cohesive 3D networks at rest can account for the viscosity variations.

(4) The relaxation of the siliceous plumbing system allowed the collapse and downward migration of unconsolidated material present at the surface.

Among the above concluding remarks, the thixotropy of fracture-filling cherts at the time they formed is an important take-home message as such behavior may be a characteristic common to other chert types, including seafloor-deposited cherts (marine precipitates) as briefly discussed in Ledevin et al. (in prep.a), Chapter 2.

Acknowledgments

La géochimie des cherts et les proxys paleo-environnementaux.

<div style="text-align: right">4</div>

Dans ce chapitre, le but est de comprendre ce qui contrôle la composition chimique des cherts afin de tester leur fiabilité en tant que proxys paléo-environnementaux.

_____

In this chapter, I aim to understand what controls the chert geochemistry in order to test their reliability as paleo-environment recorders.

4.1 Avant-propos.

Dans les chapitres précédents, nous avons vu que l'approche de terrain, la pétrologie et l'étude des structures sédimentaires et de déformation offrent des indices précieux et indispensables dans la reconnaissance des différents types de cherts et de leur processus de formation. Ces approches sont pourtant trop souvent négligées et nombre de travaux leur préfèrent une approche géochimique, essentielle pour les études paléo-environnementales.

L'utilisation des précipités océaniques, tels que les carbonates, les BIFs et les cherts, repose sur le fait (ou la supposition) qu'ils enregistrent la composition du fluide à partir duquel ils précipitent. Dès lors, ils peuvent être considérés comme de véritables fenêtres sur les conditions océaniques à l'Archéen. Mais avant même d'interpréter la chimie de telles roches, encore faut-il être capable de distinguer un signal océanique parmi toute autre contribution. Interviennent alors les proxys océaniques, critères de reconnaissances basés sur les caractéristiques chimiques des océans modernes.

Dans ce chapitre, je présente le troisième article de ces travaux de thèse, destiné à être soumis à la revue scientifique *Precambrian Research*. Je teste ici la fiabilité des cherts Archéens en tant que traceurs paléo-environnementaux grâce aux analyses géochimiques des échantillons identifiés comme précipités océaniques dans le Chapitre 3.

En premier lieu, je cherche à comprendre ce qui contrôle la chimie de ces cherts en distinguant les éléments majeurs et traces portés par la *silice* de ceux portés par ce que j'appelle les *phases contaminantes*, *i.e.* les phases détritiques, carbonatées ou organiques que peuvent contenir les cherts. Cette approche me permet de sélectionner les échantillons les plus à même de représenter la chimie du fluide à partir duquel ils ont précipité, et de tester les proxys océaniques couramment utilisés dans l'étude des précipités anciens (*e.g.* carbonates, cherts et BIFs).

Grâce à cette approche, je montre que la chimie des cherts est dominée par la composition du contaminant qu'ils contiennent et que le signal porté par la silice

est inaccessible. Seules des concentrations extrêmement faibles sont garantes de la pureté du chert et ce critère est une condition *sinequanone* pour étudier la composition des cherts comme traceurs paléo-environnementaux. Je montre également que l'utilisation des proxys océaniques modernes sur les cherts Archéen n'est pas une approche fiable, quoique toujours potentiellement applicable aux roches carbonatées.

Dans cet article, je présente ainsi la première quantification réelle du pouvoir contaminant de différentes phases minérales sur la chimie des cherts. Il en résulte que les carbonates sont les plus à même d'obscurcir le signal siliceux, que les argiles ont également un fort pouvoir contaminant, et que la matière carbonée a un effet moindre.

4.2   Article 3

Archean cherts : are they reliable paleo-seawater proxies ?

Morgane Ledevin[1a], Nicholas Arndt[1], Alexandre Simionovici[1]

[1] ISTerre, Maison des Géosciences, Grenoble, France

[a] Corresponding author : morgane.ledevin@ujf-grenoble.fr

Abstract

Archean cherts represent some of the oldest sedimentary rocks on Earth. It is commonly thought that they could be useful paleo-environment indicators, assuming that the silica phase retained the composition of the fluid from which it precipitated. In this study, we conducted major and trace element analyses of three types of cherts (seawater-derived precipitates, fracture-filling cherts and silicified sediments) from the Komati River, Barite Valley and Buck Reef sites of the Barberton greenstone belt (3.5-3.2Gy), South Africa, in order to test their reliability for paleo-environment studies.

We show that Archean cherts are a mixture of (1) a silica phase that has extremely low concentrations of trace elements and contributes only SiO_2 to the bulk composition, and (2) another phase that dominates the trace element composition and varies from site to site. We encountered three types of contaminants and calculated that 3-4% of phyllosilicate, 20% of carbonaceous matter and only 2% of carbonate is enough to control the chert chemistry and mask the silica composition. Carbonate-rich cherts could be of interest because this phase has long been known to retain oceanic fluid chemistry. However, caution must be taken because carbonates could be secondary phases produced under much more recent conditions.

Because the silica phase is easily contaminated, the use of cherts for paleo-environment reconstructions is seriously limited and requires high purity precipitates. Massive white chert layers at Buck Reef have SiO_2 close to $100wt\%$ and extremely low concentrations in all the trace elements. We argue that these chemical features are the sole reliable criteria available for now to recognize a pure precipitate, i.e. one that lacks continental contributions, but that they are not sufficient to rule out a possible hydrothermal contribution. Otherwise, only systematic field and petrographic studies can help to distinguish the various chert types, as their composition does not depend on the formation process.

The high purity white cherts from Buck Reef display strong LREE depletions, positive La anomalies and superchondritic Y/Ho ratios that resemble modern seawater. They lack significant Ce-anomalies and have europium enrichments typical of Archean sediments. However, these commonly used proxies for the recognition of seawater-derived precipitates fail to distinguish the origin of the silica, these characteristics being similar to those found in hydrothermal, metamorphic and pegmatitic quartz. An unusual feature is the strong positive Sm-anomalies of these samples which have never been observed in any other terrestrial rock. To solve this problem and to further test the reliability of cherts as paleo-environment recorders, we need to improve our understanding of element partitioning during the precipitation of the siliceous phase.

Key Words - Archean chert composition ; Oceanic proxies ; Primitive environment ; Sm anomaly.

4.2.1 Introduction

The reconstruction of the composition of Archean oceans is motivated by our need to understand the habitat in which life first emerged then evolved. Precambrian hydrogenous sediments are of particular interest as they preserve the oldest fossils on Earth (*e.g.* Awramik et al. 1983, Schopf 1993, Schopf et al. 2007, Westall et al. 2001, Allwood 2006, Allwood et al. 2007, Hofmann et Bolhar 2007, van Kranendonk 2007, Wacey 2010) and may have retained the chemistry of Archean seawater (*e.g.* Sugitani 1992, Murray et al. 1992b, Allwood et al. 2010). A common approach is to use modern seawater rare-earth element characteristics as a proxy of an oceanic signatures in ancient chemical precipitates such as carbonates, cherts and banded-iron formations (see Bolhar et al. 2004, for a review).

In this study, we test the reliability of cherts as paelo-environment recorders. Archean cherts, an important component of the Precambrian sedimentary record, formed by three different processes (Van den Boorn et al. 2010, Ledevin et al. in prep.a, and Chapter 2) : direct precipitation of silica at or near the surface from ocean water (C-chert), secondary silicification of magmatic or sedimentary protoliths (S-chert), and precipitation of silica in fractures or veins within the crust (F-chert). They precipitated from oceanic, diagenetic and/or hydrothermal fluids in a variety of environments, thus constituting a major target for paleo-environment reconstructions. Perry et Lefticariu (2003) argued that "chert can retain a chemical/isotopic signature of surface processes because of its genetic relation to surface water bodies" (*i.e.* ocean and/or shallow groundwater) (see also Schopf 1993, Pinti et al. 2009). However, we still know very little about the way cherts formed and the origin of the silica is still controversial (*e.g.* Lowe et Byerly 1986a, Duchac et Hanor 1987, Hanor et Duchac 1990, Buick et Dunlop 1990, Lowe 1999, Lowe et Fisher Worrell 1999, Nijman et al. 1999, Kato et Nakamura 2003, Knauth et Lowe 2003, van Kranendonk 2006, Van den Boorn et al. 2007).

In Chapter 2 (Ledevin et al. in prep.a), we used field and petrographic criteria to recognize various chert types from different paleo-environments in the Barberton Belt. In this paper, we present major and trace element analyses of the same sample set, which includes oceanic and fracture-filling cherts, and discuss seve-

ral geochemical constraints that seriously compromise the use of these rocks for paleo-environment reconstructions.

4.2.2   Modern oceanic proxies : a brief review.

Modern ocean compositions are controlled firstly, by the various inputs to the basin, *i.e.* terrestrial *vs.* hydrothermal sources, and secondly, by the particle-solution interactions and the predictable behavior of the rare-earth elements (REE) in solution (Wood 1990, Bau et al. 1995; 1996, Bau 1999). Whereas the former mostly depend on the geological setting, the latter are strongly influenced by the environment, including the water depth, temperature, salinity and redox state of seawater (Elderfield et al. 1988).

Hydrothermal fluids are one to three orders of magnitude enriched compared to oceanic fluids (Michard et Albarède 1986, Michard 1989), but their contribution to the chemical budget of seawater is limited by the rapid incorporation of REE in Fe-Mn oxides that precipitate near hydrothermal vents (Bau et al. 1996, Bau 1999, Bau et Koschinsky 2009, and references therein). This efficient scavenging maintain low concentrations in seawater and hydrothermal activity is thus regarded as a sink and not a source for the REE budget of oceans (Olivarez et Owen 1989, Elderfield et Schultz 1996). The major source of REE is continental influx (Piepgras et Wasseburg 1980, Andersson et al. 2008) which are enriched during the weathering of silicate minerals on the land surface. Continent-ocean transition zones, *i.e.* deltas and estuaries, act as filters in which complexation reactions greatly modify the original composition of river waters to produce the well-known composition of modern oceans (Elderfield et al. 1990, Zhang et Nozaki 1998, Bau et al. 2000, Lawrence et Kamber 2006).

The following paragraphs briefly describe the REE characteristics common to all modern oceans, their origin in terms of complexation reactions and the way they are used as proxies for the recognition of seawater signals in ancient sediments. Typical modern oceanic fluid compositions are shown in Figure 4.1.

(1) Highly fractionated rare-earth element patterns with strong LREE depletion
The well-known contraction effect of lanthanides facilitates the complexation of
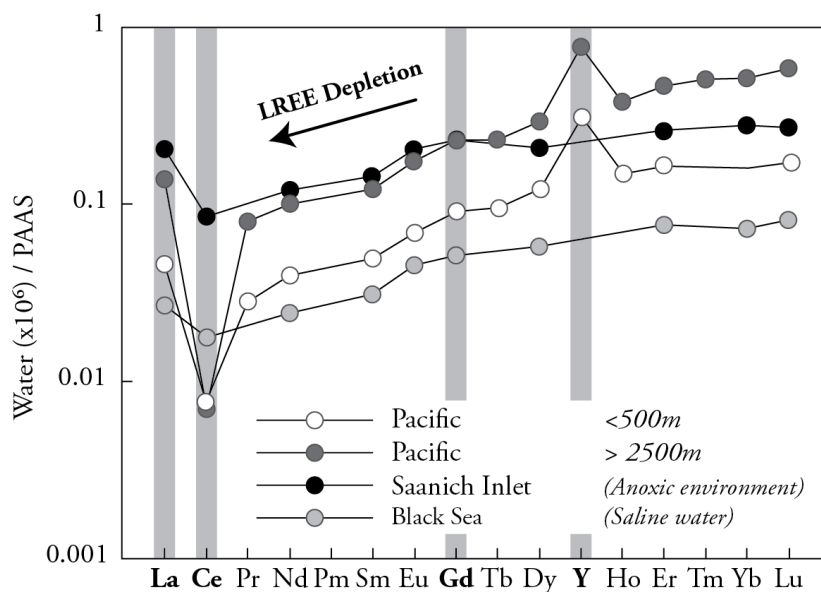
FIGURE 4.1 – *PAAS-normalized REE+Y patterns of various modern oceanic fluids : the surface and deep waters of Pacific Ocean (Alibo et Nozaki 1999), the hyper-saline and periodically anoxic waters of the Black Sea (German et al. 1991) and the anoxic waters from Saanich Inlet (German et Elderfield 1989). Concentrations are normalized to the Post-Archean Australian Shales (Taylor et McLennan 1985) and are multiplied by* 10^6*. Oxygenic waters have characteristic La and Y enrichments and Ce and LREE depletions. Anoxic water lack a Ce anomaly and have lower La enrichment.*

the heavy REE (HREE : Tb to Lu, including Y) with dissolved carbonates whereas the light (LREE : La to Gd) tend to associate with particulate matter (Sholkovitz et al. 1994, Byrne et Kim 1990, Lee et Byrne 1992, Byrne et Lee 1993, Bolhar et al. 2004). The LREE are thus preferentially removed in deltas and estuaries (Goldstein et Jacobsen 1987, Elderfield et al. 1990, Lawrence et Kamber 2006, Kulaksiz et Bau 2007) leading to their depletion away from the mixing zone and in all modern oceans (Fig.4.1) (De Baar et al. 1985, Goldstein et Jacobsen 1987, Elderfield et al. 1988, Byrne et Kim 1990, Elderfield et al. 1990, Sholkovitz et al. 1994, Lee et Byrne 1992, Byrne et Lee 1993, Bolhar et al. 2004, Lawrence et Kamber 2006, Kulaksiz et Bau 2007).

The LREE depletion is quantified using the ratio Pr/Nd_{SN*} (SN=shale-normalized). This value represents the slope of the REE patterns and is below unity in the case of modern oceans. The use of Pr is unusual for most geochemists, but necessary for marine considerations as the commonly used lanthanum is subject to strong enrichment in modern oceans (Zhang et Nozaki 1996, De Baar et al. 1985, Alibo et Nozaki 1999) and cerium is highly variable due to its redox-sensitive

behavior (*e.g.* Liu et al. 1988, Braun et al. 1990, Bau et al. 1996, Shields et Stille 2001, Bau et Koschinsky 2009).

(2) Positive La anomaly   The empty $4f$ electronic shell of lanthanum confers to this element a higher stability in solution compared to other LREE. As a result, it is less affected by the "estuarine removal effect" and becomes enriched in modern oceans (Fig.4.1) (Zhang et Nozaki 1996, De Baar et al. 1985). The end-position of La in the lanthanide series renders difficult the quantification of the anomaly by the common approach, a difficulty bypassed by the Equation /refLa/La initially proposed by Bau et Dulski (1996). Here, the anomaly corresponds to the ratio between the measured La concentration and the concentration expected from the slope defined by the neighbors Pr and Nd. Cerium cannot be used due to the anomalies it develops under specific redox conditions (*e.g.* Elderfield et Greaves 1981, Liu et al. 1988, Braun et al. 1990, De Baar 1991, Bau et Dulski 1992, Bau et al. 1997, Shields et Stille 2001, Bau et Koschinsky 2009).

$$La/La^* = [La/(3Pr - 2Nd)]_{SN} > 1 \qquad (4.1)$$

(3) Superchondritic Y/Ho ratio   Yttrium and holmium have very similar chemical behavior thanks to their similar ionic radii and trivalent oxidation states (Shannon 1976), which results in very constant Y/Ho ratio, near chondritic values, in terrestrial rocks ($\backsim 26 - 28$ Pack et al. 2007). However, their behaviors differ in aqueous solution, leading to significant fractionation of these elements and superchondritic Y/Ho, typically above 50-60 in modern oceans, (Fig.4.1) (e.g. Hogdahl et al. 1968, De Baar et al. 1991, Byrne et Lee 1993, Sholkovitz et al. 1994, Nozaki et al. 1997, Bau 1999, Bau et al. 2000, Webb et Kamber 2000, Shields et Webb 2004). Several explanations have been proposed for the fractionation, including (1) element mobility during continental weathering (Bau et al. 1995), (2) higher stability of Y-phosphates compared to Ho-phosphates (Bau et al. 1995), (3) scavenging by particulate matter (Zhang et al. 1994, Nozaki et al. 1997), or (4) weaker absorption of Y in Fe-oxyhydroxides near high-temperature hydrothermal vents (Bau et al. 1996).
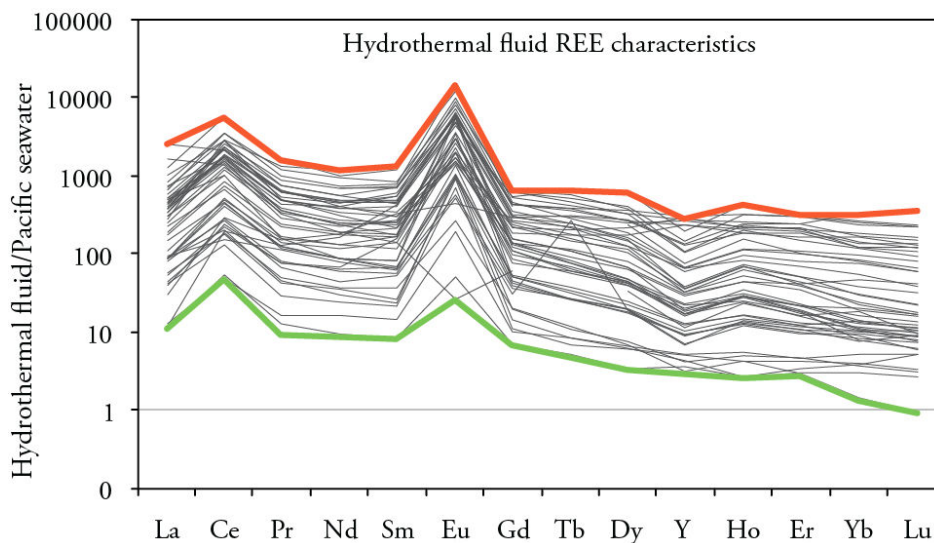
FIGURE 4.2 – *REE composition of hydrothermal fluids normalized to Pacific seawater (Alibo et Nozaki 1999). Data are compiled from James et al. (1995), Mills et Elderfield (1995), Douville et al. (1999), Hongo et al. (2007) and Bao et al. (2008). Hydrothermal fluids are characterized by HREE, Ce and Eu enrichment and Y depletion compared to modern seawater.*

(4) Negative Ce anomaly   Modern oceans are strongly depleted in cerium because of its specific redox-sensitive behavior. In its oxidized form, the tetravalent cerium (Ce^{4+}) is much less soluble and incorporated into Fe-Mn oxyhydroxides. The scavenging occurs either on the seabed into Fe-Mn crusts and nodules (Goldberg et al. 1963, Elderfield et Greaves 1981, Bau et al. 1996, Bau 1999, Bau et Koschinsky 2009) or directly in the water column by the suspended iron oxides (De Carlo et al. 1998). The lack of cerium anomaly or positive anomalies in ancient sediment (as in modern anoxic waters, Fig.4.1) is thus thought to represent anoxic marine conditions at the time of deposition (*e.g.* Wright et al. 1987, Holser 1997, Shields et al. 1997, Bau et al. 1998, Yang et al. 1999). The extent of Ce enrichment or depletion is calculated from Equation 4.2 (Bau et Dulski 1996).

$$Ce/Ce^* = [Ce/(2Pr - Nd)]_{SN} < 1 \tag{4.2}$$

(5) Lack of Eu anomaly   Whereas modern oceans lack an europium anomaly, Archean sediments are almost systematically enriched in this element (Fryer et al. 1979, Klein et Beukes 1989, Shimizu et al. 1990, Derry et Jacobsen 1990, Danielson et al. 1992, Kamber et Webb 2001). Because Eu is also enriched in high tempe-

rature hydrothermal fluids (Fig.4.2) (T°>250°C ; Bau et Möller 1993, Pichler et al. 1999, Wheat et al. 2002), the Eu anomaly, quantified from Equation 4.3, is generally included in the proxies used for paleo-environmental reconstructions (Derry et Jacobsen 1990, Danielson et al. 1992, Bau et Möller 1993, Alibert et McCulloch 1993).

$$Eu/Eu^* = [Eu/(Sm.Gd)^{1/2}]_{SN} > 1 \qquad (4.3)$$

All the above proxies are commonly used to try to extract the composition of ancient marine fluids from the composition of chemical precipitates. Seawater-like signatures have been retrieved in chemical precipitates with a wide range of ages and in a variety of marine hydrogenous sediments, supporting the reliability of the approach. Archean banded iron formations, stromatolitic carbonates and limestones, evaporites, Phanerozoic reef carbonates and Holocene microbialites, all appeared to record primary oceanic compositions (*e.g.* Derry et Jacobsen 1990, Sugitani 1992, Alibert et McCulloch 1993, Bau et Möller 1993, Webb et Kamber 2000, Kamber et Webb 2001, Van Kranendonk et al. 2003, Bolhar et al. 2004, Nothdurft et al. 2004, Alexander et al. 2008).

The use of proxies has been much debated (see Johannesson et al. 2006, for a review). Advocated arguments that cast doubt on the reliability of the method are (1) the post-diagenetic remobilization of REE, (2) the fractionation of REE during precipitation, (3) the common contamination of precipitates which have extremely low trace element contents, and (4) the occurrence of seawater-like signatures even in terrestrial waters (*i.e.* river water and groundwater) (*e.g.* Palmer 1985, Elderfield et Pagett 1986, Palmer et Elderfield 1986, Murray et al. 1992a, Sholkovitz et Shen 1995, Bau 1996, Reynard et al. 1999, Shields et Stille 2001, Shields et Webb 2004, Johannesson et al. 2006).

However, Bau (1991), Bau et Möller (1993), Murray et al. (1991; 1992a), Panahi et al. (2000) and many others reported that REE mobility is insignificant and that REE proportions remain unchanged to a certain extent during secondary processes (*i.e.* alteration, weathering, diagenesis, metamorphism). In this study, we focus on just one of the questions which is the capacity of cherts to have record the composition of the fluid from which they formed. More specifically, we investigate the

extent to which the presence of detrital or other non-silicate phases in the chert can mask the chemical signature of seawater. Our results provide several geochemical constraints that seriously limit the use of cherts for paleo-environment reconstructions.

4.2.3   New approach and aims of the study.

In Chapter 2, we used the petrology and sedimentary structures of various Archean cherts from the Barberton Belt to unravel their origin and mode of deposition. The studied sites, shown in Figure 4.3, correspond to various depositional environments (summarized in Table 4.1).

(1) The Komati River site contains a thick unit of turbidites characterized by black chert tops, both deposited in a fan-delta, shallow marine and near-continental setting Grosch et al. (*e.g.* 2011). According to Chapter 2, the chert most probably formed at first by the sorption of dissolved silica onto the suspended clays and other fine-grained detrital phases that represents the last-deposited particles at the end of turbidite Bouma sequences (Chapter 2). The silica might have been supplied either by ambient marine fluids, or by diagenetic fluids extracted through the surface and enriched in Si during the alteration of the silicate minerals of the turbidites.

(2) The Barite Valley site contains fine-grained, volcanogenic sediments now silicified to chert (S-chert) and deposited in settings ranging from quiet and probably deep conditions to fan-delta, alluvial and shallow marine conditions (Lowe et Nocita 1999, Lowe in press.). Minor conformable black chert interlayers are found in the deepest facies which comprises reddish ferruginous and light grey laminated shales. This type of chert is homogeneous and is believed to have formed by the direct precipitation of silica on the seafloor (Chapter 2), but the origin of the silica remains unclear : either oceanic or hydrothermal sources may have contributed to the basin chemistry in the area. Another type of chert corresponds to black cherts found filling large dykes that cross-cut the sedimentary sequences. These dykes were the object of Chapter 4 (Ledevin et al. in prep.b) in which we discussed both the physical behavior and the origin of the siliceous fluids.
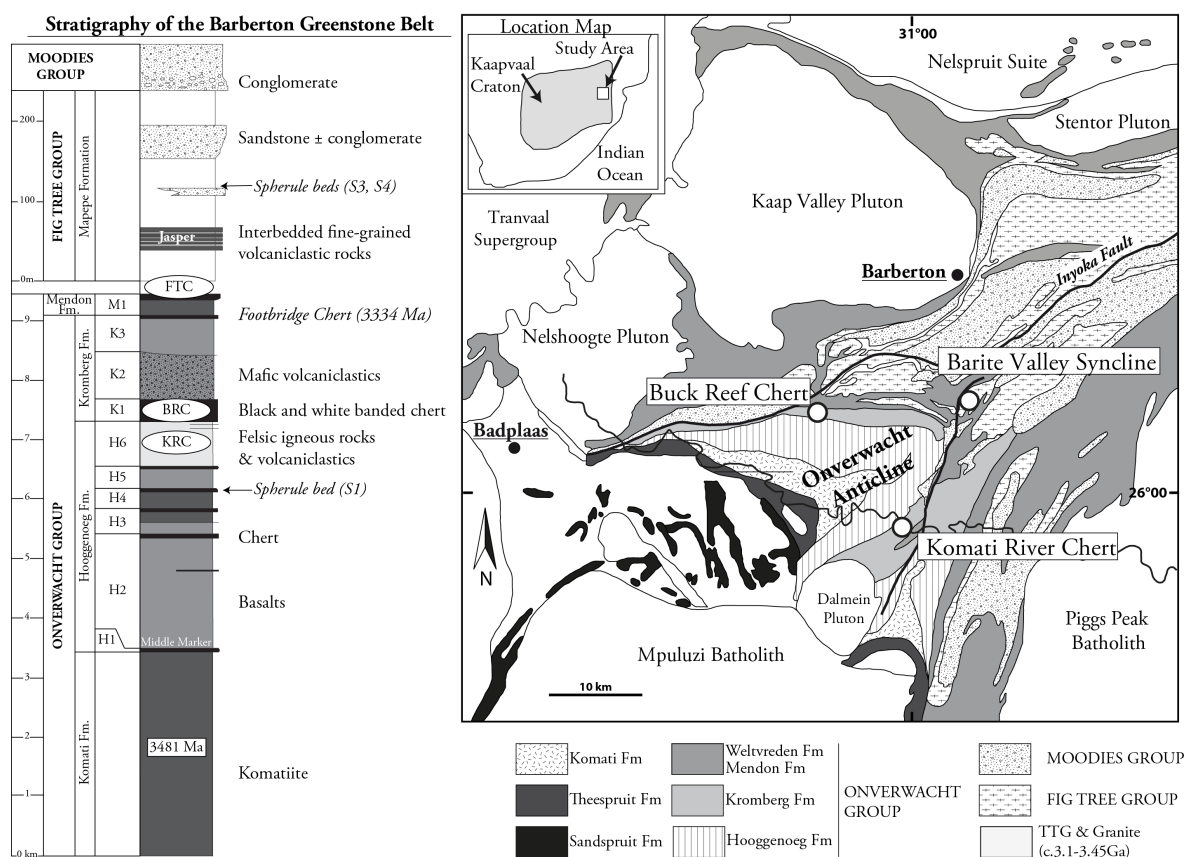
FIGURE 4.3 – *Geological map and simplified stratigraphy of the Barberton Greenstone Belt, South Africa. The map and stratigraphy column are modified from* Hofmann *(2005) and* Lowe et al. *(2003) respectively. The belt is NE-SW elongated and subdivided into the northern and southern domain along the Inyoka fault that represents a major suture. It contains three major units named the Onverwacht, Fig Tree and Moodies Groups. The three studied sites are shown on the map and stratigraphy column. KRC=Komati River Chert ; BRC=Buck Reef Chert ; FTC=Fig Tree Chert (Barite Valley).*

(3) The Buck Reef site lacks significant continental inputs and is characterized by a thick siliceous unit of black and white banded cherts deposited in lagunal to shallow ($<200m$) then slightly deeper ($>200m$) conditions onto a subsiding platform (Lowe 1999, Tice et Lowe 2006). Both facies were identified as chemically precipitated (Chapter 2) and are distinguished essentially by the contrasting purity of the white cherts and enrichment in carbonaceous matter of the black cherts. The origin of the silica and the conditions of deposition of these cherts remain uncertain.

The following sections are organized in three parts. Part I deals with the cherts that were deposited at or near the seafloor (C-cherts) in all the three sites whereas Part II is dedicated to the fracture-filling cherts (F-chert) of the Barite Valley locality. In Part III, we discuss the results and present several constraints for the use of geochemistry on Archean cherts.

The approach we used in Part I and II is the same for C-cherts and F-chert. The three sites are described to define what controls the geochemistry of the cherts. Special emphasize is given to their mineralogy : we use the major element composition of the various components (obtained by microprobe analyses) to estimate their contribution to the bulk, major element composition of cherts. This approach allows us to interpret the trace element patterns in terms of mineral phase contributions and to investigate the chemical signal specifically hosted in the silica phase.

In the final Part III, all phases that are not SiO_2 (*quartz, microquartz, chalcedony*) are considered as contaminants : *i.e.* clastic particles (K-feldspar and clay) at Komati River, carbonates and clays at Barite Valley and carbonaceous matter at Buck Reef (Table 4.1). Using the purest sample we have (*i.e.* the white cherts from Buck Reef, see Section 4.2.7), we estimate the capacity of these phases to dominate the composition of a chert : *i.e.* their capacity to obscure the chemical signal hosted by the silica phase.

The mineralogical to geochemical linkage used in this Chapter is not a common approach and such a quantification of the contamination effect has never been done. In the last section, we discuss the implications of such contamination on the

Locality	Environment	Rock type	Structure	Chert type	Silica phase	"Contaminant"	% of cont.
Buck Reef Chert *S25°55.433 to 55.886 E30°53.364 to 55.581*	Shallow to deep facies deposited onto a subsiding plateau	White chert	Alternating cm to dm scale layers of black and white cherts; Minor chert-slab conglomerates	**C-Chert**	Almost entirely composed of pure microquartz	Fe-oxide (µm) Chromite (µm)	<0,3%
		Black chert		**C-Chert**	Majoritary composed of pure microquartz	Fe-oxide (µm) Chromite (µm) Carbonaceous matter	<0,3% <10%
Komati River *S26°01.520 to 01.712 E30°59.331 to 59.353*	Shallow, nearcoastal turbidite deposits during protocontinent acretion and tectonic uplift of an epieric basin	Turbiditic siltstone	Graded, often laminated, fine-grained layers near the top of turbidite massive body	**C-Chert**	Variable proportions of microquartzitic matrix surrounding detrital grains	K-feldspar Sericite Ti-, Fe-oxide and other accessory minerals Minor carbonates	50% 50% <1% <1%
		Black chert	Final endmember of Bouma sequences at the top of turbidites; lack of internal structure	**C-Chert**	Majoritary composed of pure microquartz	K-feldspar Sericite	<1% <10%
S26°01.712 E30°59.416	Sedimentary interval within ultramafic rocks	Carbonate layer	5cm-thick rusty layer above the turbiditic section	**Undefined**	Matrix of microquartz	Ankerite	>50-60%
Barite Valley *S25°54.509 to 54.535 E30°03.185 to 03.236*	Deep- to shallow-water deposition of thich siliciclastic units during the orogenic phase of the belt	Massive black chert	Massive layer of black chert showing syn-sedimentary deformation structures *(loadcast structures up to diapir-like deformation)*	**C-Chert**	Almost entirely composed of pure microquartz	Isolated carbonate rhombs	<5%
		Silicified shales	Laminated, fine-grained layers of chert that resemble silicified shales in outcrop.	**S-Chert** *(C-Chert?)*	Siliceous mud as the shale matrix Ghosts of detrital quartz grains (minor)	Ba-sericite Carbonate	<10-20%
		Fracture-filling black chert	Large dykes (up to 1m-thick) filled with black chert and hostrock fragments	**F-Chert**	Matrix of microquartz	Hostrock fragments (clays) Dolomite Carbonaceous matter	Variable

TABLE 4.1 – *Summary of the studied cherts showing their locality and depositional environment. Coordinates represent the studied area for each site. The structure and petrology of the cherts are shown. Each phase that is not silica is considered as a contaminant whose percentages (% cont.) are estimated from optical microscopy and mixing calculations (see text).*

use of cherts as paleo-environment recorders. Special attention is given to the use and reliability of modern seawater proxies.

4.2.4 Analytical methods

Geochemical analyses were performed at ISTerre, Grenoble (France) using a Perkin Elmer Optima 3000 DV ICP-AES for the measurement of major element compositions, and an Agilent 7500ce ICP-MS for trace elements (See Annexe A.3). Chert samples are primarily crushed into powder using agate grinders to prevent contamination, and the following analytical procedure is adapted from Chauvel et al. (2011). Accuracy and precision of the data are evaluated using international rock reference materials as part of the sample set (Annexe A.3). Results are shown in Table 4.2.

Major element analyses. A portion of the powder is precisely weighed ($50mg$) and mixed in closed Savillex beakers with $2mL$ of nitric acid ($[HNO_3]=14mol.L^{-1}$) and 15 drops of hydrofluoric acid ($[HF]=24mol.L^{-1}$). Samples are entirely dissolved after 7 days onto a hotplate at $90°C$. After cooling, $20mL$ of boric acid ($[H_3BO_3]=20g.L^{-1}$) is added to neutralise the excess HF and the solution is further diluted by the addition of $250mL$ of Milli-Q water. The complete neutralisation of HF by H_3BO_3 is further guaranteed by two days of storage in refrigerators for the solutions, and analyses are performed within the following week. The calibration of the signal is obtained using a blank and mixed solutions containing pure elements : the solutions are prepared using five different dilutions to mimic and calibrate the major element composition of the samples. In the Buck Reef Chert samples, the silica content is so high that none of the dilution was able to mimic the real SiO_2 content, resulting in anomalously high concentrations as shown in Table 4.2. Other elements are not affected by this analytical bias. The volatile content, express as the loss on ignition (LOI), is estimated by heating samples at $1000°C$ for $1h$. The concentrations of the analysed reference materials are generally within 5% of the published values, and the uncertainties on the measurement (1s) varies from less than 0.01% to 1.23%, showing the very good reproducibility of our data.

Trace element analyses. A portion of the powder is precisely weighed ($100mg$) and mixed with perchloric acid ($HClO_4$) and high purity hydrofluoric acid ($[HF]$=24$mol.L^{-1}$). Samples are cooked in steel Paar bombs during 7 days to allow for the complete dissolution of heavy minerals such as zircons, and the use of $HClO_4$ is justified by the common presence of organic matter in our samples. The solution is then evaporated using hotplates to obtain a dry residue. The residue is diluted in concentrated HNO_3 for one day before being evaporated again, then diluted in about $40mL$ of $7mol.L^{-1}$ HNO_3. A weighed aliquot of this mother solution is sampled and diluted in 2% v/v HNO_3 with HF traces to produce a daughter solution with variable dilution factors according to sample specificities. For the detritus-rich samples and reference materials, best results are obtain for a 2500 dilution whereas the composition of almost pure silica samples (*i.e.* Buck Reef Chert) is best estimated for a dilution of 500. With such values, we minimise the matrix effects while maintaining sufficient signal for all measured elements. The daughter solution is finally mixed with a spike containing five elements (Be, Ge, In, Tm, Bi) before being analysed within the day of preparation. The international standard $BHVO_2$, diluted at 5000, is used for the calibration of the ICP-MS signal. The reference material DTS_2 is used to estimate the accuracy and precision of our measurement for the least concentrated samples.

X-ray micro-fluorescence analyses. X-ray micro-fluorescence analyses are realized on the EDAX Eagle III equipment at ISTerre, Grenoble (France) (See Annexe A.1). Major element maps are obtained using a beam of $30\mu m$ in diameter ($25kV$, $400\mu A$) and a counting time of $1s$ per pixel. Analyses are realized onto polished thin sections in order to avoid diffraction artifacts produced by rough surfaces. However, we systematically encountered Bragg peaks at specific energies (*i.e.* $4260eV$, $4800eV$, $5180eV$, $5500eV$) and recognized that these are similar to the diffraction spectra of international quartz reference $00-046-1045$ described par Kern et Eysel (1993). Thus, the Bragg peaks are inherited from the diffraction produced by the microquartzitic fabric in the chert. Such effect implies that the quartz is less than $5\mu m$ in size. The raw data are treated in two steps following the method described in Ulrich et al. (submitted). The first step uses the composition and X-ray micro-

fluorescence spectra of various internal standards to quantify the major element concentrations across the analysed area. The precision is about $5wt\%$. Then we use the composition of pixels representative of each pure mineral phases (microquartz, sericite and Fe-carbonate) to reconstruct the mineralogical map of the chert. Each pixel is thus expressed as a mixture of pure mineral phases, resulting in the RGB map of Figure 4.29.

Microprobe analyses. The microprobe maps and single-point analyses are realized on the JEOL JXA-8230 equipment at ISTerre, Grenoble (France) (See Annexe A.2). Polished and metallized thin sections are scanned using a beam of $<5\mu m$ in diameter ($15kV$) to obtain the best spatial resolution. The chemical maps are expressed in raw data, *i.e.* number of counts, which is sufficient as we are interested by the relative proportion of each elements. Results are given in Figures 4.25. Single-point analyses are given in weight percent in Table 4.3, calculated using internal standard compositions. Silica especially needs to be corrected because, at the time the analyses were made, the spectrometer gave anomalous and systematic $\pm 2wt\%$ deviations from expected concentrations whereas other elements were unaffected. With the correction, results are precise at $\pm 2\text{-}3wt\%$ in average, generally less than $1wt\%$.

BUCK REEF CHERT

(wt%)	Massive white chert layers				White chert slabs (conglomerates)				
	BRC20-WC	BRC21-WC	BRC22-WC1	BRC22-WC2	Slab-15	Slab-1	Slab-4	Slab-5	Slab-6
SiO_2	100,00	100,00	100,00	100,00	100,00	100,00	100,00	100,00	100,71
TiO_2									
Al_2O_3									0,11
Fe_2O_3 t	0,23	0,33	0,22	0,24	0,20				
MnO									
MgO									
CaO									
Na_2O									
K_2O									
P_2O_5									
Cr_2O_3									
NiO									
LOI		0,19	0,00	0,00	0,00	0,29	0,33	0,13	0,16
Somme	100,23	100,52	100,22	100,24	100,20	100,29	100,33	100,13	100,99
(ppm)									
Cs	0,058	0,060	0,053	0,040	0,039	0,020	0,027	0,029	0,064
Rb	0,397	0,488	0,244	0,212	0,105	0,162	0,065	0,233	0,416
Ba	9,82	14,5	10,9	7,48	3,44	5,09	1,73	3,76	13,9
Th	0,005	0,011	0,006	0,005	0,002	0,010	0,007	0,025	0,050
U	0,008	0,018	0,008	0,009	0,010	0,023	0,041	0,015	0,130
Nb	0,046	0,056	0,042	0,044	0,039	0,009	0,007	0,029	0,080
Ta			0,001	0,001				0,003	0,008
Pb	0,28	0,29	7,18	0,346	0,153	0,419	0,109	0,133	0,849
Sr	0,75	0,917	0,461	0,495	0,356	0,654	0,401	0,659	3,51
Zr	0,161	0,396	0,18	0,213	0,099		0,147		2,16
Hf	0,003	0,009	0,006	0,003					0,022
Ti	2,04	3,5	1,5	1,63	0,742	1,99	0,862		6,97
Li	0,338	0,343	0,376	0,287	0,27	0,115	0,084		0,237
Sc		0,093	0,043						0,263
V	1,16	1,44	0,75	0,855	0,762	0,052	0,030	0,271	1,39
Cr	230	270	168	199	170		0,231	1,02	2,67
Co	0,464	1,02	0,333	0,399	0,387	0,063	0,022	0,090	0,044
Ni	4,53	8,14	3,03	3,44	3,13	0,745	0,493	1,14	1,01
Cu	1,24	1,58	0,651	3,82	0,992	3,09	0,863	1,53	2,77
Zn	1,05	1,25	1,08	1,04		2,51		1,37	2,41
As	0,605	2,68	0,215	0,538	0,107	0,144	0,0452	0,713	2,94
La	0,018	0,040	0,133	0,033	0,007	0,063	0,014	0,138	0,520
Ce	0,034	0,078	0,24	0,065	0,016	0,081	0,0256	0,249	0,692
Pr	0,004	0,010	0,031	0,008	0,001	0,009	0,002	0,028	0,070
Nd	0,013	0,033	0,101	0,029	0,006	0,029	0,010	0,094	0,199
Sm	0,031	0,030	0,076	0,051	0,020	0,005	0,003	0,023	0,042
Eu	0,002	0,005	0,010	0,005	0,001	0,002	0,001	0,007	0,026
Gd	0,005	0,013	0,028	0,019	0,003	0,004	0,003	0,027	0,056
Tb	0,001	0,003	0,005	0,004				0,003	0,012
Dy	0,006	0,018	0,037	0,032	0,004	0,004	0,003	0,025	0,079
Ho	0,001	0,004	0,008	0,008				0,006	0,018
Y	0,044	0,152	0,205	0,227	0,0279	0,028	0,0242	0,212	0,674
Er	0,004	0,013	0,026	0,025	0,003	0,002	0,002	0,017	0,059
Yb	0,004	0,015	0,026	0,023	0,004	0,002	0,002	0,013	0,062
Lu		0,002	0,004	0,004				0,002	0,010
ΣREE	0,17	0,42	0,93	0,53	0,09	0,23	0,09	0,84	2,52
ΣHFSE	0,25	0,61	0,43	0,49	0,17	0,04	0,18	0,24	2,94
ΣLILE	10,3	15,0	11,2	7,73	3,58	5,27	1,82	4,02	14,4
Zr/Hf	54,03	43,33	27,73	71,24					100,00
Ti/Zr	12,67	8,84	8,33	7,65	7,51		5,86		3,23
Cr/Ni	50,77	33,17	55,45	57,85	54,31		0,47	0,89	2,64
Th/Sc		0,11	0,13						0,19
Pr/Yb $_{SN}$	0,30	0,20	0,37	0,10	0,11	1,54	0,33	0,66	0,35
Y/Ho	34,8	36,6	25,1	29,9				33,4	36,6
La/La*	1,12	0,92	0,87	1,14	2,61	1,45	2,26	1,00	1,24
Ce/Ce*	1,03	0,88	0,81	1,00	1,90	0,95	1,57	0,92	0,92
Eu/Eu*	0,86	1,29	1,05	0,82	0,65	1,87	2,31	1,38	2,51
Sm/Sm*	7,77	2,77	2,88	3,73	9,97	0,96	1,08	0,93	0,76

TABLE 4.2 – *Major and trace element composition of Buck Reef, Komati River and Barite Valley samples. Empty fields are for concentrations below the detection limit (or for unanalyzed samples). ΣREE = sum of concentrations from La to Lu including Y ; ΣHFSE- sum of Zr, Hf, Nb, Ta and Y ; ΣLILE=sum of Cs, Rb, Ba. See text for the calculation of REE anomalies.*

(continued) BUCK REEF CHERT

	Massive black chert layers					Black chert matrix (conglomerates)				
(wt%)	BRC20-BC	BRC21-BC	BRC22-BC	BRC2-BC1	BRC2-BC1	Mtx-4	Mtx-1	Mtx-5	Mtx-6	Mtx-15
SiO_2	100,00	100,00	100,00			100,00	100,94	100,84	100,23	99,99
TiO_2										
Al_2O_3	0,16	0,20	0,15				0,19		0,18	
Fe_2O_3 t	0,21	0,29	0,23				0,15		0,15	0,27
MnO										
MgO										
CaO										
Na_2O										
K_2O	0,06	0,05					0,07			
P_2O_5										
Cr_2O_3										
NiO										
LOI		0,33	0,05			0,35	0,49	0,37	0,24	
Somme	100,43	100,88	100,43			100,35	101,84	101,21	100,79	100,25
(ppm)										
Cs	0,129	0,131	0,074	0,076	0,075	0,040	0,057	0,070	0,067	0,076
Rb	0,855	0,824	0,454	0,196	0,268	0,059	0,995	0,183	0,801	0,209
Ba	19,8	20,3	11,5	19,3	19	0,799	22,7	4,61	15,6	7,32
Th	0,070	0,136	0,035	0,162	0,154	0,008	0,118	0,071	0,164	0,031
U	0,067	0,166	0,032	0,107	0,088	0,057	0,28	0,20	0,312	0,109
Nb	0,123	0,217	0,081	0,244	0,141	0,008	0,151	0,262	0,271	0,096
Ta	0,009	0,015	0,004	0,015	0,009		0,007	0,008	0,015	0,005
Pb	0,452	0,319	0,406	0,939	0,518	0,136	1,42	0,421	1,23	0,092
Sr	2,73	3,39	0,802	4,09	4,84	0,379	4,49	1,00	4,29	1,01
Zr	0,894	2,82	0,413	1,74	1,47	0,185	2,39	1,88	6,17	0,444
Hf	0,022	0,070	0,012	0,035	0,029		0,046	0,033	0,074	0,008
Ti	23,9	39,8	7,79	33,7	18,1	0,883	36,6	30,1	32,3	5,65
Li	0,574	0,941	3,140	0,376	0,220	0,159	1,19		0,402	0,436
Sc	0,226	0,258	0,064					0,176	0,578	0,016
V	2,65	2,39	0,787	1,54	0,466	0,078	0,654	1,61	4,50	0,937
Cr	171	210	159	2,62	2,41	0,877	2,54	6,74	6,49	205
Co	1,72	4,22	0,549	0,496	0,677	0,048	0,489	0,15	0,128	1,76
Ni	8,48	26,1	4,11	8,44	5,64	0,896	6,17	4,93	2,22	11,3
Cu	5,22	2,76	2,14	4,02	3,2	2,49	1,85	4,29	2,53	1,69
Zn	2,08		1,48	2,89	2,91	2,71	2,94	4,18	1,81	
As	15	7,82	1,89	15,2	6,14	0,099	1,89	1,15	11,7	1,16
La	0,211	0,495	1,11	0,31	0,338	0,004	0,635	0,162	0,422	0,051
Ce	0,424	1,03	2,16	0,465	0,546	0,010	0,967	0,277	0,616	0,107
Pr	0,047	0,122	0,251	0,045	0,042		0,094	0,028	0,059	0,011
Nd	0,166	0,485	0,928	0,139	0,103	0,004	0,314	0,096	0,208	0,046
Sm	0,035	0,103	0,165	0,020	0,011	0,002	0,054	0,027	0,074	0,024
Eu	0,011	0,038	0,067	0,011	0,005	0,001	0,021	0,009	0,053	0,014
Gd	0,024	0,091	0,162	0,021	0,012	0,003	0,054	0,038	0,176	0,040
Tb	0,004	0,015	0,027	0,003	0,002		0,011	0,008	0,038	0,009
Dy	0,028	0,104	0,19	0,029	0,019	0,004	0,064	0,059	0,286	0,071
Ho	0,006	0,026	0,040	0,007	0,005		0,011	0,012	0,063	0,016
Y	0,154	0,769	1,01	0,269	0,17	0,030	0,519	0,358	2,17	0,48
Er	0,021	0,087	0,124	0,027	0,016	0,003	0,037	0,035	0,185	0,049
Yb	0,027	0,104	0,125	0,025	0,020	0,003	0,030	0,044	0,189	0,045
Lu	0,005	0,017	0,018	0,004	0,003		0,004	0,006	0,029	0,007
ΣREE	1,16	3,48	6,38	1,37	1,29	0,06	2,82	1,16	4,57	0,97
$\Sigma HFSE$	1,20	3,89	1,52	2,30	1,82	0,22	3,11	2,54	8,70	1,03
$\Sigma LILE$	20,8	21,3	12,0	19,6	19,3	0,90	23,8	4,86	16,5	7,61
Zr/Hf	40,45	40,46	34,42	49,57	50,69		52,07	56,80	83,72	54,28
Ti/Zr	26,73	14,11	18,86	19,37	12,31	4,77	15,31	16,01	5,24	12,73
Cr/Ni	20,17	8,05	38,69	0,31	0,43	0,98	0,41	1,37	2,92	18,14
Th/Sc	0,31	0,53	0,55					0,41	0,28	1,90
Pr/Yb $_{SN}$	0,54	0,37	0,63	0,58	0,65		1,00	0,20	0,10	0,08
Y/Ho	24,7	29,9	25,0	38,6	35,8		45,9	30,6	34,3	29,6
La/La*	1,01	1,20	1,10	1,26	1,15		1,37	1,24	1,64	1,42
Ce/Ce*	0,98	1,05	0,99	1,01	1,10		1,06	1,05	1,15	1,21
Eu/Eu*	1,83	1,85	1,91	2,43	1,88	2,40	1,82	1,36	2,14	2,18
Sm/Sm*	1,18	1,11	0,94	0,73	0,53		0,88	0,85	0,60	0,86

(continued) KOMATI RIVER

		Turbidite layers										Reference Carbonate
	Upper black chert facies				Greenish	Bluish	Laminated siltstone				Light grey	
(wt%)	KRC1A-BC	KRC8-BC	KRC11-BC	KRC1B-BC	Tuff-12-1	Tuff-13	KRC8-Sed1	KRC8-Sed2	KRC10-Sed	KRC11-Sed	Tuff-12-2	KRC5
SiO_2	89,12	95,10	91,71	85,22	96,50	93,87	69,74	88,33	81,51	88,82	80,60	17,94
TiO_2	0,09	0,07		0,24		0,09	0,52	0,17		0,19	0,34	0,15
Al_2O_3	4,41	3,33	4,59	7,67	3,92	5,21	17,85	6,52		7,34	11,56	4,19
Fe_2O_3 t			0,31		0,30	0,33	0,38		0,39	0,36	0,35	13,38
MnO									0,01			0,76
MgO						0,14	0,52		0,25	0,13	0,29	7,71
CaO									0,65			26,95
Na_2O	0,03			0,04			0,04	0,03	0,03		0,02	0,03
K_2O	1,94	1,22	1,73	3,60	1,77	1,84	7,23	2,71	5,95	3,23	5,19	1,47
P_2O_5												
Cr_2O_3												0,05
NiO												0,01
LOI	0,79	0,76	0,66	0,77	0,50	0,81	2,62	0,78	1,36	0,87	1,34	30,81
Somme	96,37	100,48	99,00	97,54	102,98	102,29	98,89	98,55	90,15	100,95	99,68	103,45
(ppm)												
Cs	0,442	0,319	0,386	0,664	0,342	0,342	1,37	0,547	0,798	0,598	0,89	0,819
Rb	36,1	33,7	32,5	62,2	30,1	32,7	163	47,8	79	43	69,9	45,8
Ba	40,8	17,9	34,2	61,4	38,6	25,9	56,6	31,8	47,4	42,6	30,4	84,7
Th	2,25	2,42	2,55	2,22	3,45	3,84	2,46	2,34	1,43	1,2	0,855	0,25
U	0,67	0,375	0,555	0,604	1,06	0,746	0,577	0,478	0,642	0,551	0,462	0,193
Nb	2,1	3,07	2,91	3,18	2,86	3,5	10,3	2,9	6,55	4	7,85	0,81
Ta	0,221	0,265	0,295	0,283	0,322	0,382	0,667	0,287	0,462	0,338	0,655	0,049
Pb	5,06	1,16	1,62	1,92	2,41	1,17	1,03	1,14	1,72	1,69	1,39	3,63
Sr	2,19	1,18	0,902	2,05	1,5	0,953	1,74	1,27	1,55	0,861	0,646	42,8
Zr	48,8	38,1	43,3	88,4	39,5	60,4	192	63,7	175	82	141	9,33
Hf	1,29	0,889	1,31	1,98	1,08	1,65	4,32	1,6	3,91	2,05	3,87	0,278
Ti	518	555	531	1354	491	546	3424	989	2559	1133	1897	1067
Li	1,69	2,22	1,56	2,67	1,87	3,88	10,4	3,71	4,36	2,25	5,86	4,68
Sc	1,4	0,884	0,93	1,83	0,849	1,75	4,16	1,49	2,95	0,935	1,16	15,1
V	12,8	11,8	15,9	17,4	6,58	20,8	36,1	13,3	22,5	17,6	11,6	69
Cr	8,48	12,2	246	21,7	207	186	64,9	17,2	189	226	111	387
Co	21,2	0,578	1,66	31,9	1,67	0,972	1,5	24	2,7	1,2	1,15	33,2
Ni	6,25	5,84	8,31	6,29	9,68	10,8	20,5	8,23	9,81	8,63	18,1	121
Cu	3,26	3,46	8,09	17,8	15,3	3,53	5,85	4,14	18,1	4,91	56,6	28,2
Zn	5,57	4,88	2,45	7,25	19,9	2,36	12,6	7,93	3,95	3,73	57,7	176
As	1,18	0,705	1,21	1,17	1,2	0,46	1,46	1,09	2,32	0,912	9,75	6,6
La	6,49	5,02	6,21	6,55	13,5	13,2	5,16	6,33	6,64	2,34	2,1	2,58
Ce	13,7	10,7	13,7	15,4	24,6	27,9	10,5	13,9	30,3	14,5	7,6	5,29
Pr	1,41	1,07	1,32	1,49	2,45	2,5	1,11	1,4	1,67	0,526	0,437	0,683
Nd	5,12	3,88	4,82	5,46	8,35	8,7	4,17	5,05	6,67	2,01	1,59	2,96
Sm	0,963	0,677	0,894	1,03	1,39	1,49	0,801	0,915	1,47	0,422	0,297	0,833
Eu	0,312	0,204	0,308	0,343	0,337	0,404	0,249	0,278	0,454	0,149	0,070	0,440
Gd	0,769	0,484	0,679	0,844	0,97	1,1	0,696	0,703	1,3	0,401	0,261	1,270
Tb	0,123	0,072	0,105	0,127	0,133	0,159	0,115	0,092	0,186	0,066	0,039	0,222
Dy	0,814	0,427	0,682	0,725	0,766	0,978	0,73	0,569	1,13	0,443	0,237	1,660
Ho	0,179	0,076	0,14	0,149	0,146	0,196	0,146	0,113	0,232	0,096	0,048	0,395
Y	4,84	2,62	3,68	4,08	4,18	5,5	4,87	3,05	6,81	2,62	1,37	12,7
Er	0,55	0,205	0,428	0,425	0,409	0,58	0,412	0,3	0,683	0,3	0,144	1,24
Yb	0,614	0,16	0,446	0,412	0,369	0,578	0,347	0,244	0,668	0,334	0,157	1,16
Lu	0,092	0,022	0,066	0,060	0,053	0,083	0,052	0,036	0,101	0,049	0,025	0,183
ΣREE	35,98	25,62	33,48	37,10	57,65	63,37	29,36	32,98	58,31	24,26	14,38	31,62
ΣHFSE	57,25	44,94	51,50	97,92	47,94	71,43	212,16	71,54	192,73	91,01	154,75	23,17
ΣLILE	77,3	51,9	67,1	124,3	69,0	58,9	221,0	80,1	127,2	86,2	101,2	131
Zr/Hf	37,83	42,86	33,05	44,65	36,57	36,61	44,44	39,81	44,76	40,00	36,43	33,56
Ti/Zr	10,61	14,57	12,26	15,32	12,43	9,04	17,83	15,53	14,62	13,82	13,45	114,36
Cr/Ni	1,36	2,09	29,60	3,45	21,38	17,22	3,17	2,09	19,27	26,19	6,13	3,20
Th/Sc	1,61	2,74	2,74	1,21	4,06	2,19	0,59	1,57	0,48	1,28	0,74	0,02
Pr/Yb_{SN}	0,72	2,10	0,93	1,14	2,09	1,36	1,01	1,81	0,79	0,50	0,88	0,19
Y/Ho	27,0	34,6	26,3	27,4	28,6	28,1	33,4	27,0	29,4	27,3	28,5	32,2
La/La*	1,10	1,12	1,14	1,07	1,17	1,16	1,20	1,07	1,20	1,19	1,15	1,50
Ce/Ce*	1,09	1,12	1,17	1,17	1,06	1,20	1,10	1,11	2,27	3,27	1,96	1,08
Eu/Eu*	1,69	1,66	1,84	1,72	1,35	1,47	1,56	1,62	1,53	1,69	1,18	2,00
Sm/Sm*	1,07	1,08	1,09	1,06	1,03	1,03	1,05	1,06	1,13	1,04	1,01	0,86

(continued) BARITE VALLEY

	Black chert							Silicified country rock							
	Dyke in Sericite-shale			Dyke in Carbonate-shale		Concordant layers		Sericite-shales					Carbonate-shales		
(wt%)	FTC2-BC	FTC9-BC	FTC4-BC	FTC14-BC	FTC15-BC	FTC18-BC	FTC18-BC2	FTC1-Fgt	FTC2-Fgt	FTC9-Fgt	FTC4-Fgt1	FTC4-Fgt2	FTC4-Sh	FTC15-Sh	FTC18-Sh
SiO_2	97,80		97,07						96,19		91,47	90,74			
TiO_2									0,07		0,13	0,12			
Al_2O_3	1,24		0,83						2,38		3,86	3,69			
Fe_2O_3 t	0,22		0,23						0,65		0,36	0,35			
MnO			0,01												
MgO															
CaO			0,25												
Na_2O			0,02								0,04	0,04			
K_2O	0,26		0,21						0,44		0,84	0,80			
P_2O_5															
Cr_2O_3											0,01	0,01			
NiO															
LOI	0,67		1,15						0,66		0,98	0,98			
Somme	100,19		99,78						100,39		97,68	96,74			
(ppm)															
Cs	0,355	0,31	0,443	0,512	0,538	0,146	0,146	0,33	0,376	0,414	0,635	0,625	0,232	0,26	0,248
Rb	12,2	5,51	7,24	12,2	9,54	0,494	0,493	15,5	23,1	23	34,9	34,1	7,72	10,4	4,65
Ba	1817	736	728	1310	1023	101	101	2148	2442	3537	4466	4356	836	1092	812
Th	0,704	0,36	0,583	0,856	0,698	0,014	0,016	1,07	1,37	1,91	2,76	2,67	0,539	0,745	0,339
U	0,249	0,151	0,201	0,319	0,249	0,027	0,026	0,25	0,368	0,44	0,718	0,684	0,138	0,196	0,090
Nb	1,06	0,468	0,621	1,01	0,844	0,024	0,027	0,995	2,05	2,24	3,04	2,97	0,543	0,767	0,333
Ta	0,071	0,034	0,073	0,077	0,060			0,079	0,163	0,198	0,273	0,261	0,053	0,050	0,042
Pb	1,55	0,517	1,38	1,04	0,798	3,65	3,68	1,06	2,13	2,12	1,29	1,26	0,613	1,19	0,493
Sr	10	3,28	6,17	5,94	8,94	2,46	2,48	5,1	7,22	16,4	4,89	4,8	1,59	1,9	6,58
Zr	13,5	6,18	7,33	12,2	9,7	0,38	0,381	13,5	27,1	25,7	34,2	33,4	6,99	8,99	4,05
Hf	0,282	0,146	0,184	0,311	0,234			0,332	0,573	0,609	0,838	0,844	0,183	0,238	0,107
Ti	333	158	206	294	227	3,66	3,83	244	542	541	749	738	159	211	79,3
Li	0,72	0,342	0,829	0,71	1,25	0,167	0,170	0,933	1,83	1,78	1,75	1,74	0,554	0,679	0,855
Sc	1,38	0,62	1,01	1,26	0,939			4,67	2,51	2,03	3,44	3,34	1,1	1,52	0,846
V	13,1	6,76	7,03	8,25	6,34	0,42	0,396	20	20,3	16	24,2	24,2	5,99	8,49	6,45
Cr	76,5	26,6	29,2	43,9	53,2	27,1	26,8	64,7	98,2	94,3	107	106	43,2	42,8	32
Co	4,06	2,92	65,5	4,36	5,58	8,29	8,17	2,38	1,56	3,11	17	16,8	6,59	8,92	4,01
Ni	22,6	20,4	18,6	21,7	26,1	14,6	14,5	70,8	21,1	22,5	21,8	21,5	46,5	44,4	74,5
Cu	17,4	5	4,35	6,27	6,56	2,33	2,34	4,36	12,3	4,17	5,61	5,59	6,2	8,03	7,9
Zn	13,9		4,27					5,39	8,6		6,67	6,53			
As	10,4	3,14	9,24	2,72	2,86	60,3	60,1	5,17	17,2	3,2	17,8	17,4	3,92	6,39	1,54
La	5,17	1,2	1,59	4,26	2,21	0,047	0,042	5,47	7,68	8,74	7,94	7,7	0,971	2,27	0,573
Ce	5,88	2,21	3,06	6,84	4,26	0,082	0,080	5,56	9,18	11,4	12,9	12,6	1,64	3,5	1,1
Pr	1,08	0,268	0,379	0,866	0,479	0,011	0,010	1,44	1,56	1,49	1,7	1,62	0,195	0,424	0,121
Nd	3,31	0,946	1,41	3,1	1,88	0,040	0,042	4,93	4,82	4,75	5,78	5,57	0,705	1,52	0,474
Sm	0,507	0,164	0,286	0,585	0,363	0,019		0,801	0,817	0,765	0,915	0,884	0,17	0,265	0,097
Eu	0,105	0,046	0,073	0,178	0,107	0,008	0,008	0,199	0,187	0,209	0,273	0,256	0,065	0,097	0,027
Gd	0,386	0,171	0,342	0,478	0,354	0,038	0,031	0,698	0,656	0,747	0,987	0,919	0,234	0,299	0,18
Tb	0,052	0,023	0,046	0,070	0,044	0,006	0,008	0,102	0,095	0,102	0,134	0,13	0,044	0,049	0,034
Dy	0,297	0,139	0,284	0,443	0,286	0,059	0,065	0,661	0,649	0,663	0,867	0,797	0,317	0,36	0,267
Ho	0,058	0,028	0,056	0,085	0,059	0,013	0,013	0,136	0,126	0,132	0,173	0,169	0,069	0,077	0,058
Y	1,93	0,898	1,79	2,73	1,91	0,494	0,495	4,64	4,4	4,13	4,87	4,76	2,25	2,55	1,97
Er	0,154	0,08	0,17	0,236	0,174	0,038	0,033	0,394	0,381	0,369	0,528	0,501	0,214	0,239	0,19
Yb	0,151	0,073	0,178	0,217	0,16	0,034	0,035	0,376	0,345	0,355	0,559	0,539	0,208	0,244	0,188
Lu	0,021	0,011	0,025	0,031	0,024	0,005	0,005	0,057	0,052	0,052	0,078	0,079	0,031	0,038	0,029
ΣREE	19,10	6,26	9,69	20,12	12,31	0,89	0,87	25,46	30,95	33,90	37,70	36,52	7,11	11,93	5,31
ΣHFSE	16,84	7,73	10,00	16,33	12,75	0,90	0,90	19,55	34,29	32,88	43,22	42,24	10,02	12,59	6,50
ΣLILE	1830	742	736	1323	1033	102	102	2164	2465	3560	4502	4391	844	1103	817
Zr/Hf	47,87	42,33	39,84	39,23	41,45			40,66	47,29	42,20	40,81	39,57	38,20	37,77	37,85
Ti/Zr	24,67	25,57	28,10	24,10	23,40	9,63	10,05	18,07	20,00	21,05	21,90	22,10	22,75	23,47	19,58
Cr/Ni	3,38	1,30	1,57	2,02	2,04	1,86	1,85	0,91	4,65	4,19	4,91	4,93	0,93	0,96	0,43
Th/Sc	0,51	0,58	0,58	0,68	0,74			0,23	0,55	0,94	0,80	0,80	0,49	0,49	0,40
Pr/Yb_{SN}	2,25	1,16	0,67	1,26	0,94	0,10	0,09	1,20	1,42	1,32	0,96	0,95	0,29	0,55	0,20
Y/Ho	33,2	32,7	31,9	32,2	32,5	36,9	38,4	34,1	34,9	31,3	28,2	28,2	32,7	33,0	33,9
La/La*	0,87	1,01	1,06	1,14	1,32	0,96	1,87	0,81	0,90	1,12	0,99	1,02	1,18	1,25	1,35
Ce/Ce*	0,53	0,90	0,93	0,87	1,09	0,80	1,20	0,41	0,57	0,76	0,80	0,83	0,94	0,92	1,11
Eu/Eu*	1,11	1,29	1,09	1,57	1,39	1,32		1,24	1,19	1,29	1,34	1,32	1,51	1,61	0,95
Sm/Sm*	0,89	0,88	0,89	1,05	1,00	0,71		0,92	0,93	0,84	0,81	0,84	0,85	0,85	0,67

| (wt%) | Standard - Orthoclase | | Black Chert facies | | | | Detritus-rich zone facies | | | |
| | | | K-Feldspar | | Quartz | | K-Feldspar | | Sericite | |
	n = 12	Std. Dev.	n = 6	Std. Dev.	n = 12	Std. Dev.	n = 32	Std. Dev.	n = 6	Std. Dev.
SiO_2	65,0	0,21	65,2	0,68	98,7	0,50	65,1	0,51	48,7	0,52
TiO_2	<0,01		0,00	0,00	0,00	0,01	0,00	0,01	0,54	0,04
Al_2O_3	18,5	0,07	18,0	0,28	0,33	0,27	18,2	0,37	34,5	0,48
FeO	0,03	0,02	0,03	0,02	0,03	0,01	0,02	0,02	0,85	0,03
MnO	0,01	0,01	0,01	0,01	0,00	0,00	0,00	0,00	0,00	0,00
MgO	<0,02		0,01	0,01	0,01	0,01	0,00	0,00	1,66	0,08
CaO			0,00	0,01	0,00	0,01	0,00	0,00	0,01	0,01
Na_2O	1,40	0,02	0,17	0,02	0,02	0,01	0,17	0,02	0,10	0,02
K_2O	14,9	0,06	15,8	0,44	0,10	0,07	15,9	0,48	8,22	0,29
P_2O_5	0,01	0,01								
Cr_2O_3	0,00	0,01								
NiO	0,01	0,01								
BaO	0,18	0,02								
Total	100,0		99,3		99,2		99,4		94,6	

KOMATI RIVER CHERTS

| (wt%) | Black vein | | Shale (host rock) | | | | | | | |
| | Quartz | | Carbonate | | Sericite (Core) | | Sericite (Rim) | | Quartz | |
	n = 40	Std. Dev.	n = 22	Std. Dev.	n = 6	Std. Dev.	n = 5	Std. Dev.	n = 7	Std. Dev.
SiO_2	99,1	0,57	1,84	2,27	50,2	4,75	47,6	2,08	98,2	2,22
TiO_2	0,01	0,03	0,03		0,20	0,07	0,29	0,07	0,02	
Al_2O_3	0,16		0,05		34,2		32,4		0,25	
FeO	0,03	0,02	6,97	1,47	1,04	0,61	1,24	0,91	0,40	0,96
MnO	0,01	0,01	0,88	0,70	0,01	0,01	0,01	0,01	<0,02	
MgO	0,00	0,01	16,5	1,31	1,01	0,37	1,55	0,23	<0,02	
CaO	0,01	0,01	27,9	0,58	<0,01		<0,01		<0,02	
Na_2O	0,01	0,01	0,01	0,01	0,37	0,33	0,09	0,01	<0,01	
K_2O	0,02	0,03	0,01	0,01	7,64	1,25	7,04	0,65	0,04	0,03
P_2O_5	0,01	0,01	0,02	0,02	0,01	0,01	0,02	0,02	<0,01	
Cr_2O_3	0,01	0,01	0,01	0,01	0,07	0,04	0,14	0,02	0,01	0,02
NiO	0,00	0,01	0,01	0,01	0,01	0,01	0,01	0,02	0,01	0,02
BaO	0,07		0,06		0,68		4,07		0,09	
C			7,07	0,68						
Total	99,5		61,4		95,5		94,4		99,0	

BARITE VALLEY

TABLE 4.3 – *Major element compositions (wt%) of various mineral phases encountered in Komati River and Barite Valley samples, obtained using in situ microprobe analyses. Std.Dev.=Standard deviation.*

PART I
-
The geochemistry of seafloor-deposited cherts

4.2.5   Komati River : the clastic contaminant.

The Komati River site (Grosch et al. 2011) belongs to the Kromberg Formation and is located on the east limb of the Onverwacht anticline, in the Songimvelo Nature Reserve (Fig.4.3). The outcrop is distributed along the Komati River banks and comprises a $180m-$thick unit of well-bedded, fining-upward diamictites and turbiditic, clastic deposits. Grosch et al. (2011) proposed that the turbidites were deposited as fan-delta sequences with a minimum age of $3432Ma$ in a shallow, intra-continental epieric sea.

Cherts in this area form the uppermost parts of turbidite units (Fig.5.13-a) and represent the endmembers of Archean Bouma sequences. Because the "normal" endmember of a Bouma sequence in modern settings is very fine shale and/or mud, Lowe et Knauth (1977), Lowe (1999) and Rouchon et al. (2009) have inter- preted the upper black chert facies as the silicification product of such material, probably induced by pervasive seawater infiltration, hydrothermal fluid circula- tion, or early diagenetis. However, based on field and petrological observations, we proposed in Chapter 2 that the black cherts are seafloor-deposited and precipitated as a siliceous ooze, a primary mixture of gelatinous silica containing minor detrital sericite and micro feldspar grains (Chap.2 ; Ledevin et al. in prep.a).

Our samples were taken from the black chert layers and the immediately under- lying siltstones. We did not sample the coarser-grained sediments from the lower parts of the turbidite units.

Chert characteristics.

The turbidites were deposited as 1 to $5m$-thick layers characterized by well- defined Bouma sequences (Bouma 1962) : the facies evolves from coarse-grained bases (Bouma division T_a) in erosive contact with the underlying layer, to medium- grained, then laminated and fine-grained silicified siltstone near the top (Bouma division T_d). Black chert horizons are commonly, but not always, found at the tops of the sequences.

In the siltstones immediately below the chert layers, detrital grains of angular to sub-angular, K-feldspar (orthoclase and microcline) comprises the majority
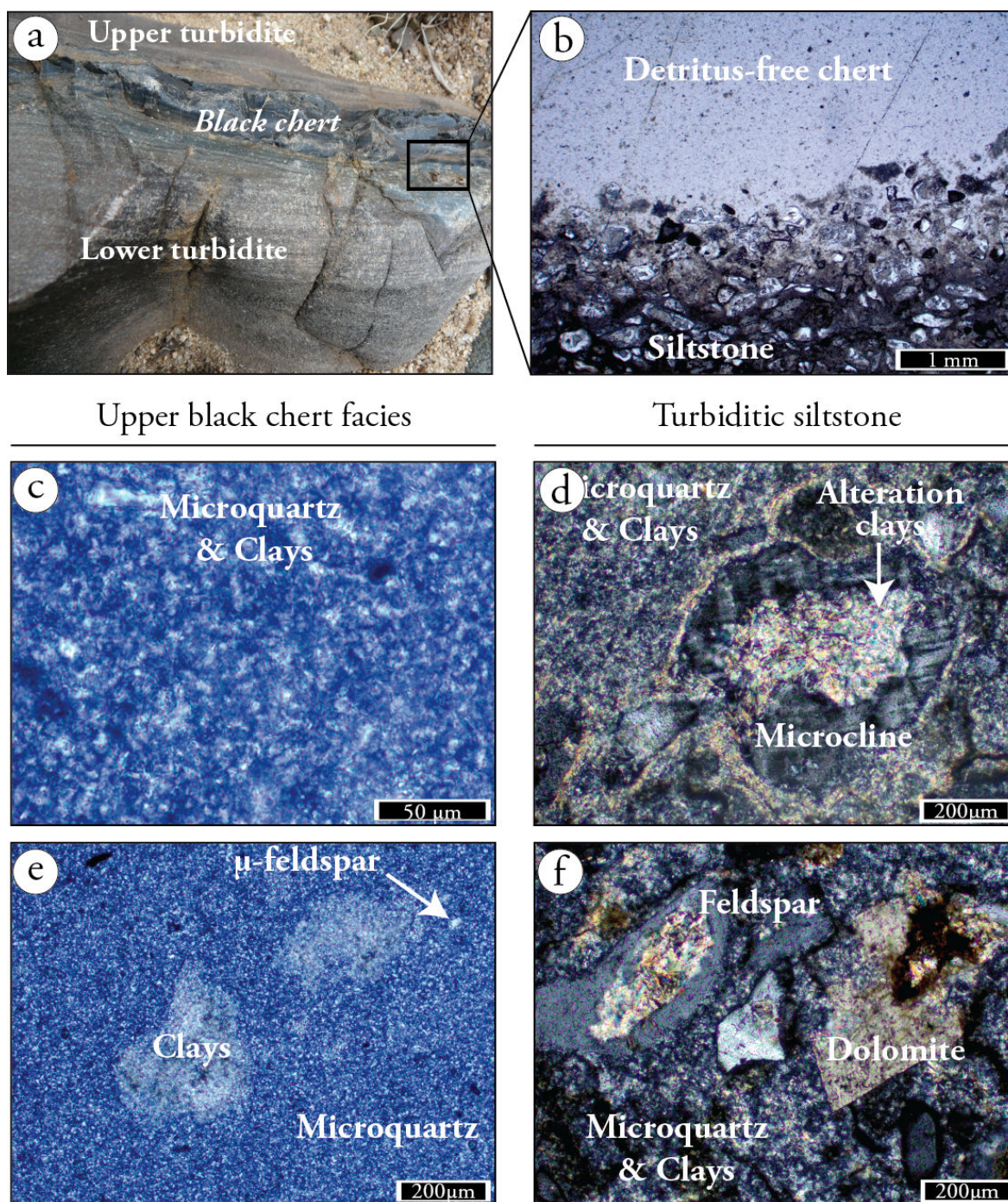
FIGURE 4.4 – *Petrological characteristics of Komati River turbiditic siltstone and above chert. Photo (a) shows a turbidite layer that contains a black chert horizon on top. Photo (b) shows the sharp transition between both facies : (c) and (e) highlight the homogeneous microquartzitic and clay fabrics in black cherts, with rare clots of clays found as isolated packages ; (d) and (f) show the detrital particles in siltstones, essentially composed of K-feldspar (orthoclase and microcline) partially altered to sericite, embedded in a matrix of microquartz and sericite. Rare dolomite crystals are preserved and detrital quartz grains are absent.*

of the detritus (Fig.5.13-d, f). They are partially altered to phyllosilicates and are embedded in a matrix of microquartz and clays. Minor heavy minerals (*i.e.* Ti-oxide, zircon) and rare carbonate and detrital quartz grains are observed. Over an interval of less than 5*mm*, the laminations disappear as the detrital content sharply decreases, and the siliceous matrix increases in abundance until it is forming the entire uppermost, homogeneous black chert layer (Fig.5.13-b). The chert is entirely composed of microquartz, with a small amount of clay (<10%) homogeneously distributed at quartz grain boundaries (Fig. 5.13-c), as well as rare clots of clay and micro feldspar grains found isolated in this siliceous matrix (Fig. 5.13-e).

In Chapter 2, we combined X-ray diffraction and microprobe analyses to identified the nature of the mineral phases : feldspars are typical orthoclases ; clays are K-micas showing muscovite or sericite characteristics ; the rest of the rock consists exclusively of microquartz. The K-micas are inherited from the low-grade metamorphism recorded in the area (215 to $<350°C$; Grosch et al. 2012). The X-ray diffraction spectra are shown in Figure A.3 (same as in Chapter 2) and chemical composition (microprobe analyses) are shown in Table 4.3.

Major element composition.

As shown in Figure 4.6, the black cherts from Komati River turbidites are enriched in Al_2O_3, $Fe_2O_{3(tot)}$, K_2O and TiO_2 compared to other sites (see also Table 4.2), which is consistent with the abundance of detrital particles in these samples.

The SiO_2 contents of both the chert (up to 92wt%) and siltstone (>69.7wt%) are higher than those of normal shales (Average Archean shales ; SiO_2=∼ 61wt% Condie 1993) due to the presence of microquartz in their matrix. In Figure 4.6, their composition lies on mixing lines between a pure silica component and the composition of K-mica and K-feldspar minerals. The gain of silica with decreasing major element concentrations is interpreted as an increase in the siliceous over detrital fraction from the siltstone through to the chert. Thus, the silica acts as a diluent while other major elements are controlled by the detrital fraction.

In Figure 4.7, well-defined positive correlation curves are observed between the continent-derived elements Al, K and Ti (and Zr, not shown) (r^2=0.92-0.99). The

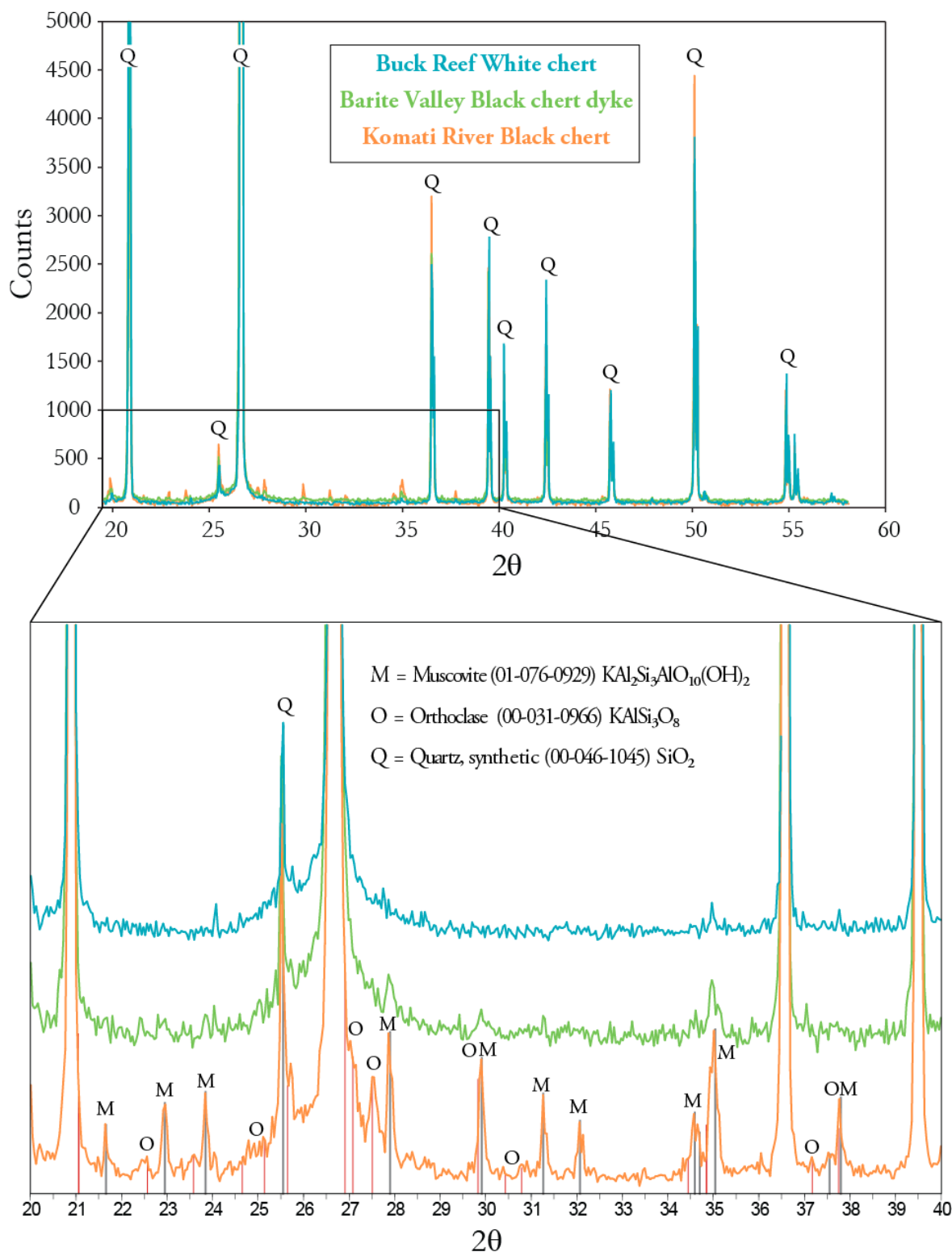FIGURE 4.5 – *X-ray diffraction spectra for Komati River siltstone, Barite Valley fracture-filling chert and Buck Reef white chert. Komati river siltstones are essentially composed of microquartz with significant amount of orthoclase and K-micas preserved from silicification. Barite Valley fracture-filling cherts are almost pure microquartz with low muscovite content. Buck Reef white cherts exclusively consist of microquartz.*
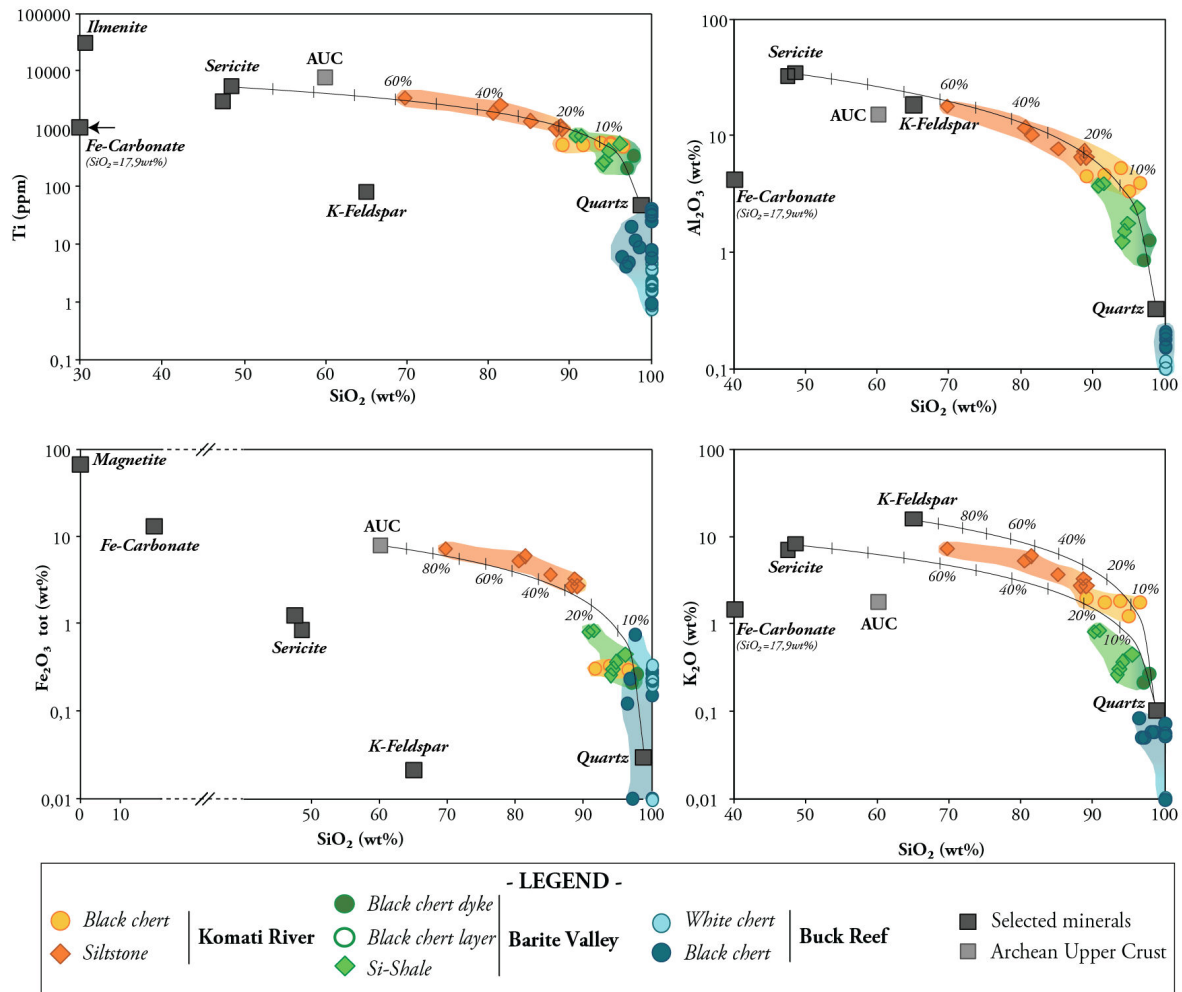
FIGURE 4.6 – *SiO₂ vs. major element diagrams. Solid lines represent mixing curves between quartz and sericite, feldspar or AUC. Note the Y-axis is in log scale. Symbols used for the various sites are similar in all incoming figures. Quartz, K-feldspar and sericite compositions were obtained using in situ microprobe analyzes (Table 4.3). Fe-carbonate is from Komati River ankerite layer (Samples KRC5 ; ICP-AES analyzes ; Table 4.2). AUC = Archean Upper Crust (Condie 1993).*

linear trends are best defined by the siltstone samples whereas the cherts plot close to each other near the quartz end-member. The consistency across the siltstones suggests that the composition of the detrital fraction does not vary from one turbidite layer to another, although it is affected by variable dilution effects of silica.

Using the *in situ* microprobe analyses of the silicate phases (Table.4.3), we are able to model the composition of the detrital fraction in absence of siliceous matrix. Because the siltstones come from the uppermost ∼ 10*cm* of *m*-scale units, such composition is not exactly representative of the average detrital influx that produced the turbidites, but still approach the composition of the eroded source.

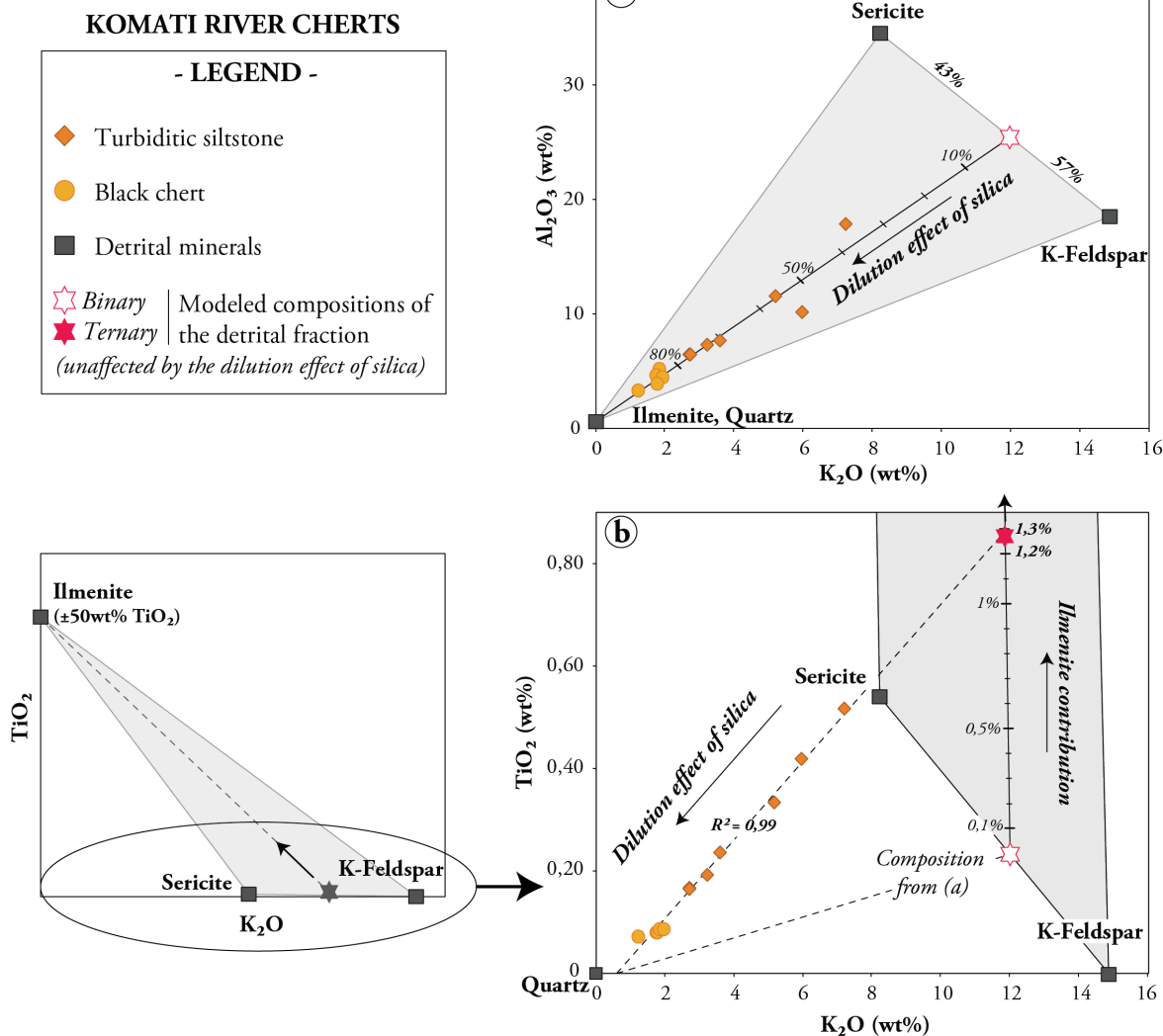FIGURE 4.7 – *Selected major element correlation diagrams for Komati River samples. Solid lines correspond to mixing curves involving two mineral species and dotted lines are correlation curves obtained from our samples. The composition of Komati River cherts and siltstones can be expressed as a mixture of feldspar and sericite in roughly equal proportion with ∼ 1% of ilmenite and diluted by the amount of siliceous matrix.*

From the mineralogy (X-ray diffraction and microprobe data), we can assume that K-feldspar and sericite host potassium and aluminum, whereas heavy minerals such as zircon and ilmenite grains must control zirconium and titanium contents. The composition of our samples can be expressed as a mixture of these minerals using the correlation curves of Figure 4.7. Calculations are based on siltstone curves as the cherts plot all close to each other and are thus less reliable. The dominant component in siltstones is microquartz, which, from Figure 4.7-a, comprises more than 50% of the rock, although one sample has only 35%. Sericite and feldspar comprise together the major rest of the rock and are present in roughly equal proportions. The Ti/Zr ratio of siltstones ranges from 13.3 to 17.8, which is very close to the average 15.2 ratio of ilmenite and far from the 0.10 value of zircon (Garçon et al. 2011). Thus, both the Ti and Zr contents in these samples are probably controlled by ilmenite, whose contribution is estimated at 1.2-1.3% from Figure 4.7-b.

To summarize, the major element composition of Komati River siltstones from the upper part of the turbidite units is consistent with a mixture of 43% sericite, 56% K-feldspars, $\sim$ 1% of ilmenite, and a fraction of silica that varies from about 35% in these samples to 85-97% in the overlying cherts.

Trace elements and the mineral sorting effect.

In Figure 4.8 are shown the trace element patterns of the Komati River cherts and siltstones (normalized to PAAS; Taylor et McLennan 1985), which are similar to some extent. They show relatively flat patterns with strong Rb, Zr and Hf enrichment, Sr and Li depletion, and a large range of trace metal compositions. To illustrate the main differences between both facies, and above all to monitor the chemical effect of higher silica content in the cherts, we use the lower graph of Figure 4.8 which represents the compositions of black cherts normalized to that of the siltstone from the same turbidite bed.

Compared to siltstones, the cherts are depleted in the *Large Ion Lithophile Elements* (LILE, Cs, Rb, Ba, K), as well as in Ti, Nb, Zr and Hf, whereas Th, U and the LREE are enriched. These features allow us to highlight what we call the *"mineral sorting effect"*. As the turbiditic cloud sedimented, the segregation of mineral spe-
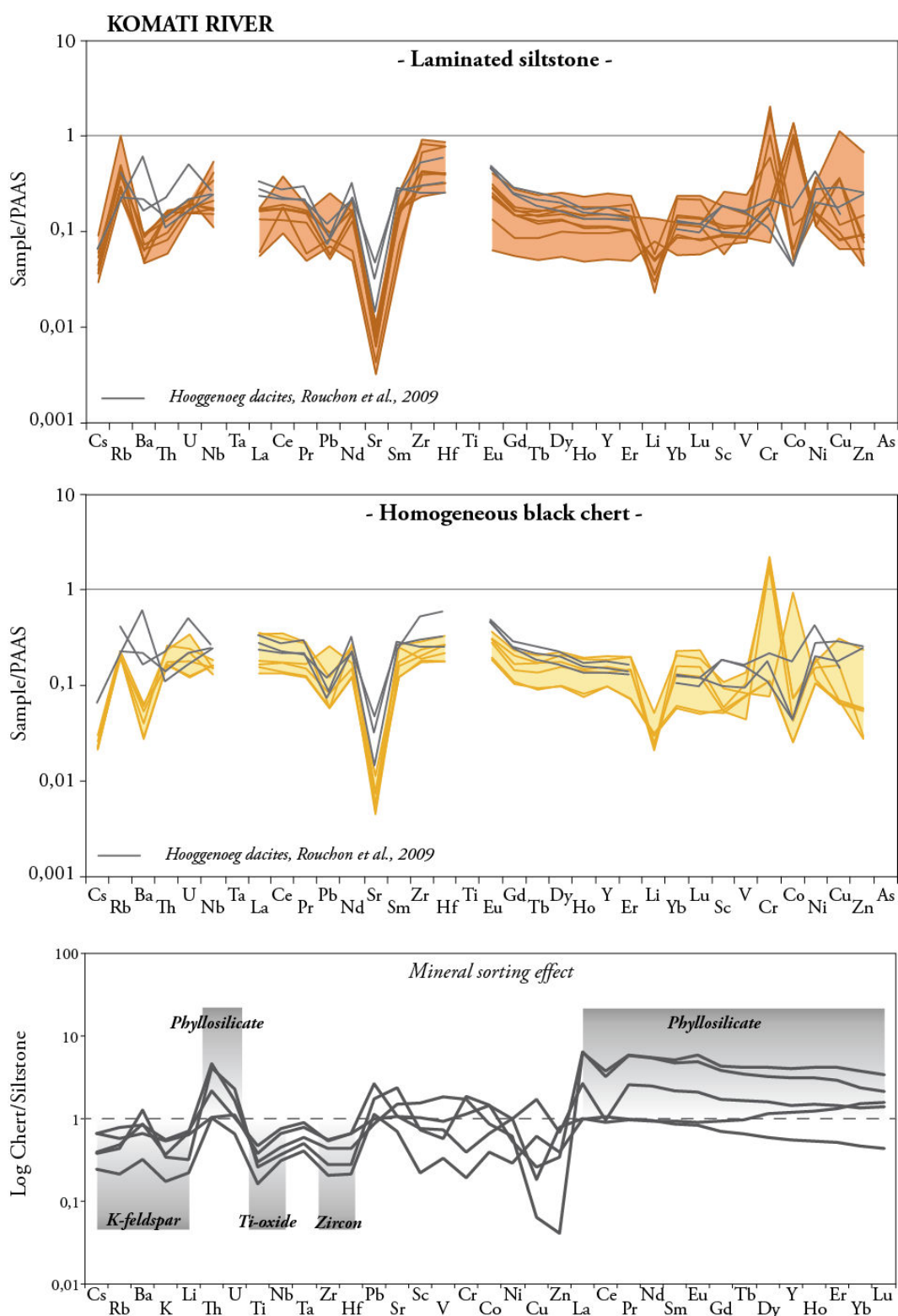
FIGURE 4.8 – *PAAS-normalized trace element patterns (PAAS = Post-Archean Australian Shales ; Taylor et McLennan 1985) for Komati River siltstones (top) and black cherts (middle) sharing some characteristics with the Hooggenoeg dacite from Rouchon et al. (2009) (dark grey line). The bottom diagram corresponds to the composition of black cherts normalized to the siltstone from the same turbidite layer : main differences are due to the mineral sorting effect as discussed in the text.*

cies according to their density resulted in their repartition between the siltstone and the chert, leading to the observed chemical differences : the siltstones are enriched in the densest phases, whereas the chert is enriched in clay which, because of its platy habit, settles more slowly (*e.g.* Gibbs et al. 1971).

The LILE depletion in cherts can be explained by the higher clay to feldspar ratio in these sample. Both clay and K-feldspar are enriched in LILE (Nesbitt et al. 1980), but the lack of coarse feldspar grains in the cherts most probably account for their apparent depletions in Cs, Rb and K. Barium is less depleted due to its preferential retention in phyllosilicates (Eylem et al. 1990, Göktürk et al. 1995, Shahwan et al. 2000), which constitute the majority of the clastic fraction in these samples.

Heavy minerals such as Ti- and Fe-oxides, as well as accessory minerals such as zircon, monazite and apatite are major hosts for the HFSE and REE in terrestrial rocks. Zircon especially is considered as the main reservoir for Zr and Hf, whereas Ti-oxides, such as ilmenite ($FeTiO_3$), have a large control on Ti and Nb-Ta (Hoskin et Schaltegger 2003, Klemme et al. 2006, Garçon et al. 2011, and reference therein). Thus, the lack of such phases in the chert can account for their significant depletion in Zr, Hf, Ti and Nb (Fig. 4.8).

Similarly, Th, U and the LREE are typically enriched in monazites (($La, Ce, Nd)PO_4$) and may contribute to the enrichment of the cherts (Kamineni et al. 1991, Ayres et Harris 1997, Zhu et O'Nions 1999, Nagy et al. 2002, Thöni et al. 2008, Radulescu et al. 2009, Garçon et al. 2011). However, the petrographic observations did not reveal the presence of such phase, and the abundant clay fraction is most probably responsible for the Th, U and LREE enrichment in the cherts (Götze et Lewis 1994, Coppin et al. 2002).

REE and the detrital signal.

Because the REE are supposed to be immobile during secondary processes (*e.g.* alteration, diagenesis) (*e.g.* Bau et Möller 1993, Bau et Dulski 1996, Webb et Kamber 2000, Shields et Stille 2001, Shields et Webb 2004, Nothdurft et al. 2004, Bolhar et al. 2004), and because no *in situ* silicification is observed (Chapter 2), the REE patterns should preserve the primary signature of the source rock.

Although we identified Komati River black cherts as seawater-derived precipi-
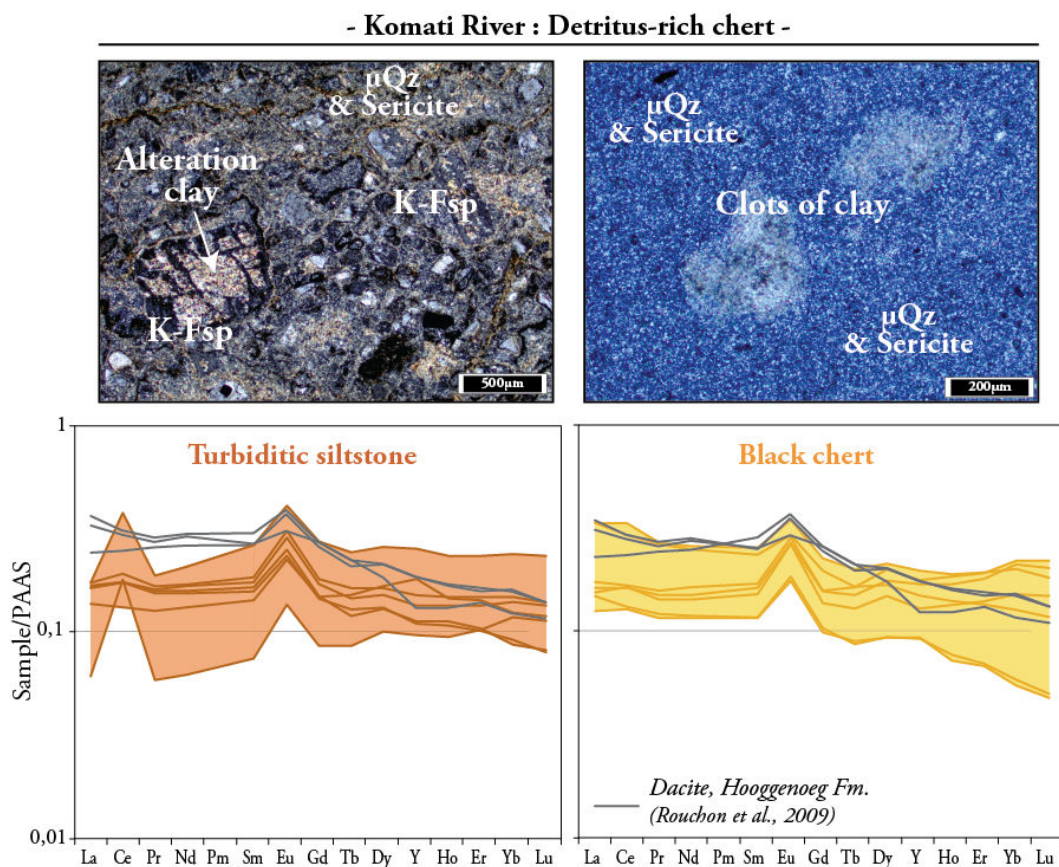
FIGURE 4.9 – *PAAS-normalized REE+Y patterns for Komati River black cherts and siltstones in relation with their respective mineralogy. Both the chert and siltstone have REE pattern consistent with their clastic contaminant. Hooggenoeg dacites from Rouchon et al. (2009) are shown form comparison. Note that Pm was not measured and is here estimated from its neighbors.*

tates, none of their REE characteristics is consistent with their deposition as chemical sediment from oceanic fluids. As shown in Figures 4.9 and 4.10, they have weakly to strongly fractionated REE patterns, with part of the samples showing large HREE depletions. All patterns have significant europium enrichment and lack cerium and lanthanum anomalies (Fig.4.10 and 4.11). The Y/Ho ratio is low in average and remains close to chondritic values (Pack et al. 2007).

Thus, as for the major and trace elements, the REE composition most probably represent a mixture of the various detrital phases, whose relative proportions vary according to the mineral sorting during deposition. We consider that phyllosilicates must dominate the composition of the chert layers because (1) zircon and ilmenite are lacking , (2) K-feldspars are only present as microphases and (3) clays are preferentially enriched in REE during efficient complexation and sorption processes
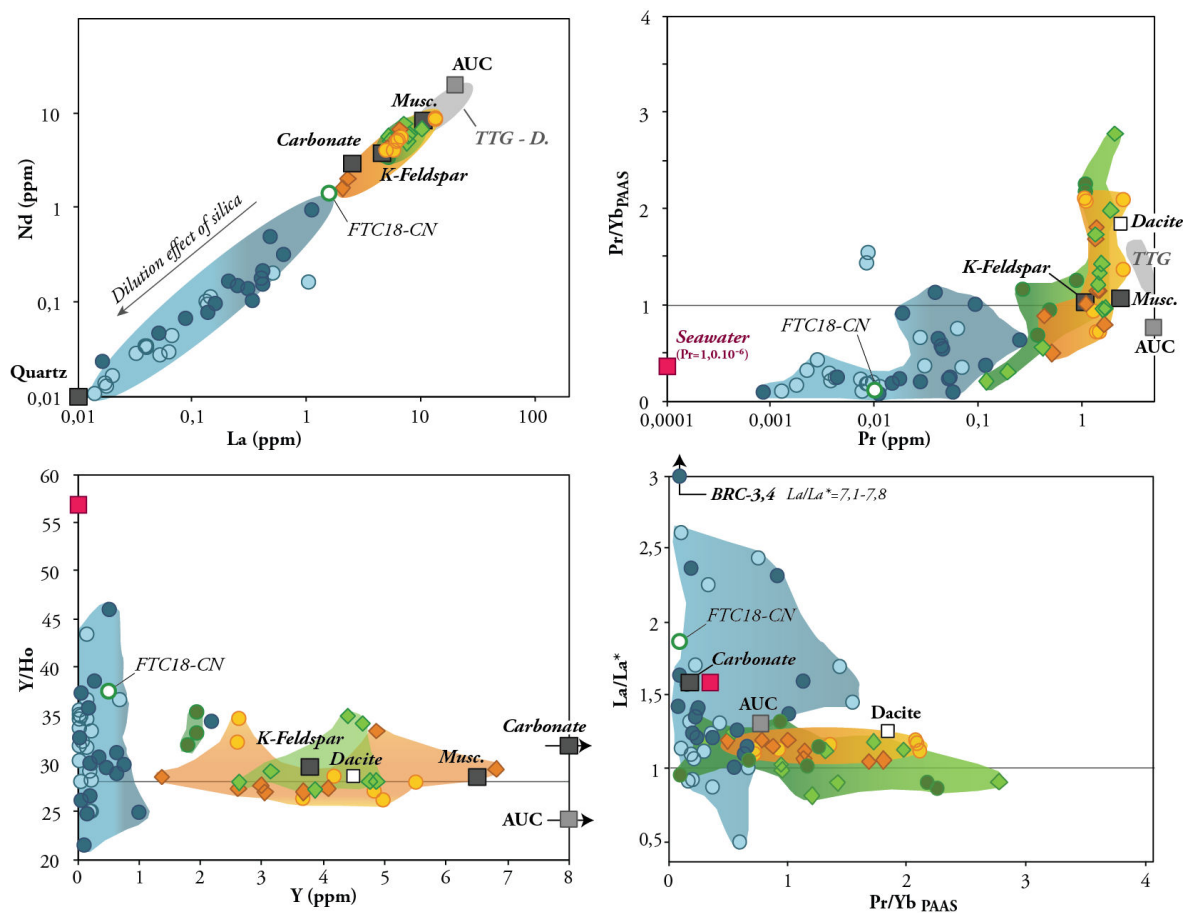
FIGURE 4.10 – *REE and anomaly diagrams for Komati River (orange), Barite Valley (green) and Buck Reef (blue) cherts. Symbols are detailed in Fig.4.6. Horizontal lines represent an absence of anomaly. Archean Upper Crust (AUC) is from Condie (1993) ; Dacite (D.) from Hofmann et Harris (2008) ; Modern Pacific seawater from Alibo et Nozaki (1999). Mineral compositions are from Garçon et al. (2011).*

in aqueous systems (*e.g.* Siever et Woodford 1973, Eylem et al. 1990, Götze et Lewis 1994, Coppin et al. 2002).

Origin of the detrital fraction

This section deals with the source of the detrital fraction. Rouchon et al. (2009) proposed that the dacitic volcanic rocks of the Hooggenoeg Formation represent the source of the detrital material in the turbidites. These rocks stratigraphically underly the Komati River section and outcrop farther to the north-east, below the Buck Reef site (Fig.4.3). Their composition has been plotted for comparison in all the Figures presented so far (From Fig.4.6 to 4.11).
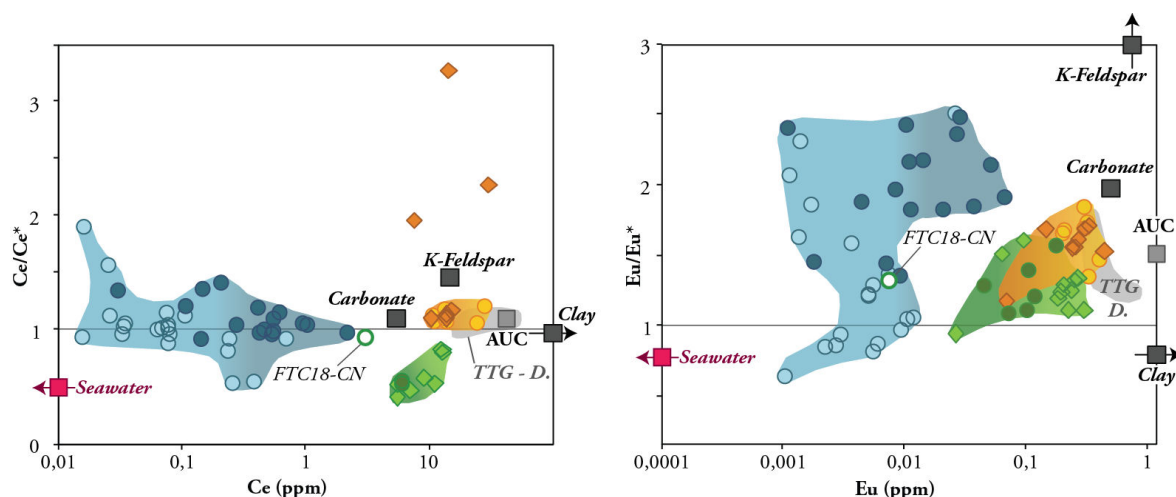
FIGURE 4.11 – *Diagrams representative of the Eu and Ce anomalies ; Legend similar to Fig.4.10.*

The trace element patterns of Figure 4.8 (upper diagram) shows some characteristics shared by the dacites and Komati River cherts, including the flat slope of the spectra, the strong depletion in Sr and similar enrichments in Zr and Hf. However, in the following ways the composition of the cherts and dacites are different.

(1) In Figure 4.6, one siltstone displays higher K_2O, Al_2O_3, and TiO_2 contents and lower SiO_2 than the dacite.

(2) In Figure 4.8 , the concentration of a number of trace elements in cherts exceeds those measured in the dacites : in particular the trace metals Cr and Co can be 10 times enriched compared to the dacite.

(3) In Figure 4.9, rare-earth elements are very different from dacites in both cherts and siltstones, being less fractionated with lower LREE enrichment and weaker HREE depletion.

(4) The presence of microcline in the detrital fraction (Fig.5.13-d) is inconsistent with a dacitic source because this mineral crystallizes only in slowly-cooled plutonic rocks (*e.g.* Deer et al. 1966).

Thus, the detrital fraction in Komati River turbidites best represents a mixing between different continental sources, probably a mixture of Hooggenoeg dacites and an unidentified granitic source.

4.2.6   Barite Valley : the carbonate contaminant.

The Barite Valley site, or Barite Syncline, is located at the north-east of the On-verwacht anticline (Fig.4.3). Here we focus on the western limb of the syncline and especially on the lower units that correspond to the Mendon Formation (3335-3260 *Ma* ; Kröner et al. 1991, Byerly et al. 1993; 1996). The series evolves upward from finely laminated, reddish shales (Fig. 4.12-a) to very fine-grained, light grey shales (Fig. 4.12-c) with homogeneous black chert interlayers, all deposited in quiet, probably deep, subaqueous environments (Lowe in press.).

The black chert layers range in thickness from millimeter-thick intercalations up to 30 *cm*-thick concordant layers ($\sim$ 5 *cm* in average). They were identified in Chapter 2 as seafloor-deposited, chemical precipitates although the origin of the silica remains ambiguous. Fracture-filling cherts from the area, found in large, cross-cutting dykes, will be described in Part II of this Chapter.

Chert characteristics.

As shown in Figure 4.12-e,f, the Barite Valley C-chert lacks detrital particles and internal structures, and is exclusively composed of cryptocrystalline micro-quartz with carbonate grains found as isolated packages (<2-5%). These grains are rhombohedral in shape with sharp to partially altered boundaries and show well-developed internal zoning. Such carbonates are probably early diagenetic products as they commonly fill thin veins cross-cutting the chert (Fig.4.12-e).

The laminated, ferruginous shales are composed of Si-rich (black) and Fe-rich (red) laminations (Fig.4.12-b) that correspond to alternating microquartz and iron oxide concentration zones. The light grey to yellowish shales lack significant iron but are characterized by abundant carbonates in a matrix of microquartz, carbonaceous matter and minor sericite (Fig.4.12-d). Both these shale types are now silicified to chert, a metasomatism that might have occurred during the earliest stages of diagenesis, as will be discussed in Part II (Section 4.2.8).

From the mineralogy, we can infer that the whole rock chemistry of the chert will should be a mixture of carbonate and silica compositions. At this point, we need to introduce a new sample that we consider representative of typical Archean carbonate. It corresponds to a carbonate layer (sample KRC5) sampled in the Ko-

- Silicified shales -
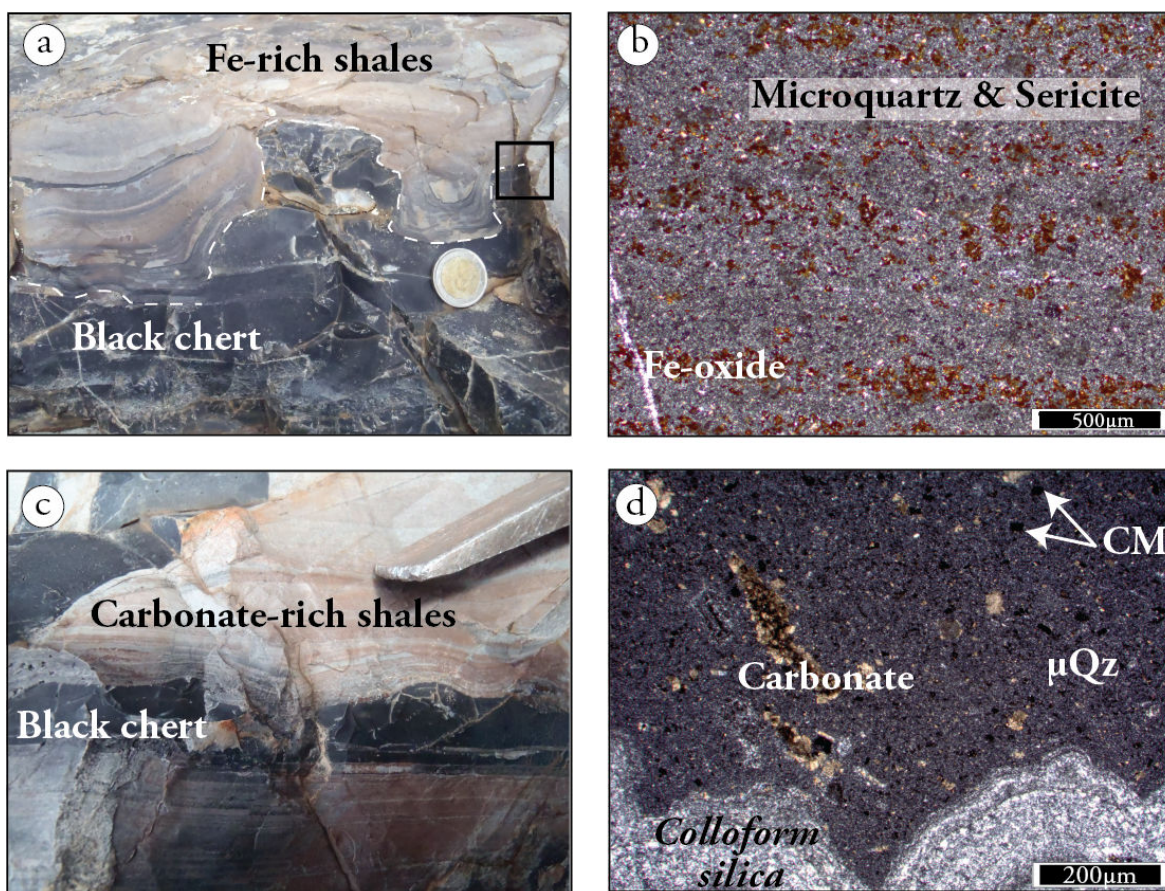
- Black chert -
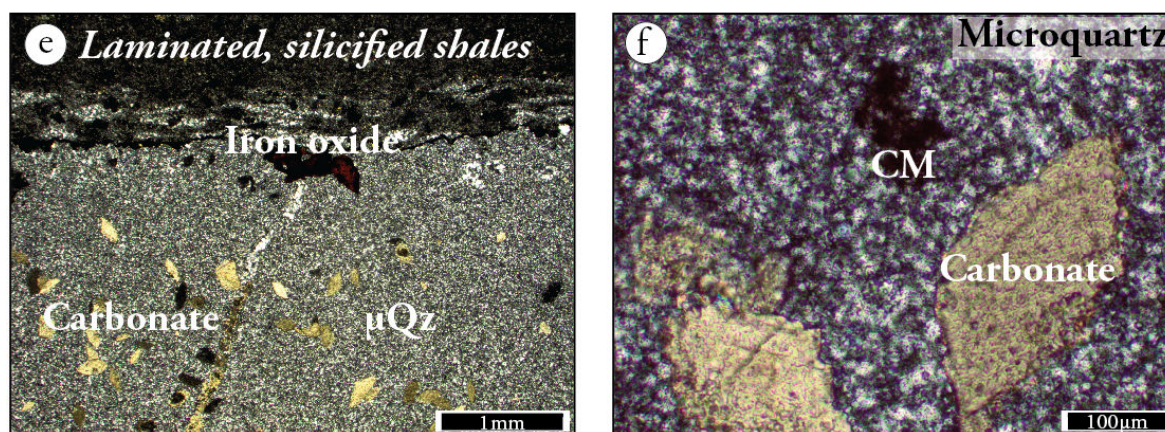
FIGURE 4.12 – *Field (a,c) and microscope photos of Barite Valley C-cherts (e,f) and adjacent shale units (b,d). The shales are of two types : (b) laminated, ferruginous shales characterized by alternating quartz-rich/Fe-oxide-rich layers ; (b) laminated, light grey shales composed of abundant carbonate and carbonaceous matter grains in a microquartzitic matrix. The black chert (e,c) is exclusively composed of microquartz in which are disseminated carbonate grains. Note the soft deformation of black chert layers at their upper interface with shales. µQz = microquartz ; CM = carbonaceous matter.*
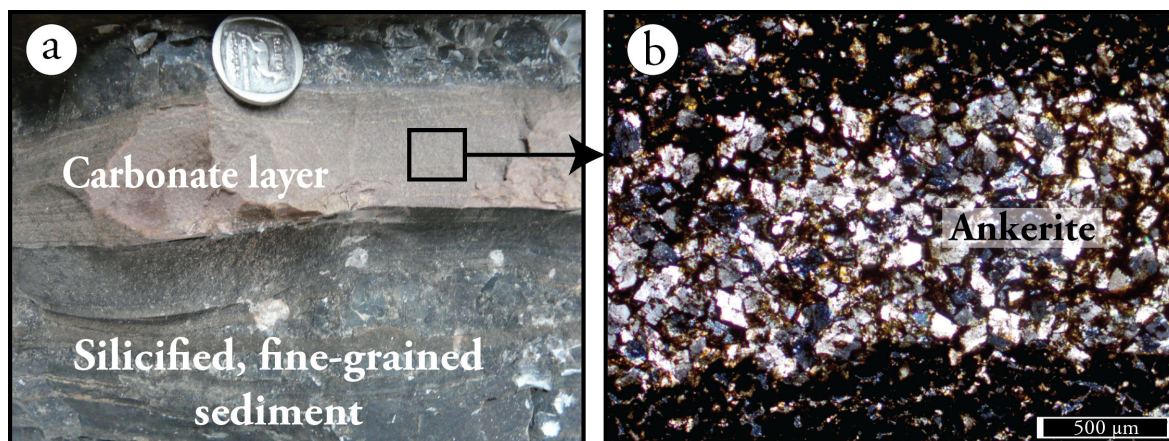
FIGURE 4.13 – *Field (a) and optical (b) photos of the carbonate layer found above the turbiditic units at Komati River (Sample KRC5). Carbonates have ankerite composition according to Table 4.2.*

mati River site and located above the turbiditic sequence (Fig.4.13-a). The layer is $\sim 3cm$-thick and confined between carbonaceous black chert layers close to ultramafic rocks. As shown in Table 4.2, the carbonate has a major element composition close to ankerite (Deer et al. 1966) but has an excess silica with a SiO_2 content of $17.9wt\%$. Because carbonate grains are well preserved in Figure 4.13-b, the silica enrichment is attributed to the presence of significant amount of siliceous matrix around carbonates. The carbonate layer lacks detrital particles which prevent any continental contribution to its bulk chemistry.

Accordingly, in the following sections this layer is used as a reference material for Archean carbonates and helps unraveling such contribution to the trace element composition of Barite Valley cherts.

Trace elements and possible origin of the fluid.

As shown in Figure 4.14, both the black chert and carbonate layers from the Barite Valley site have REE, HFSE (Zr, Hf, Nb, Ta, Y) and LILE (Cs, Rb, Ba) concentrations well below those of Komati River samples, which is consistent with the detritus-free mineralogy of these samples.

We can estimate the dilution effect of the silica matrix on the carbonate layer composition. In this facies, the excess $\sim 18wt\%$ SiO_2 reduces the REE and HFSE concentrations by about $1/5^{th}$, taking an initial SiO_2 for carbonates of $0wt\%$. Ac-
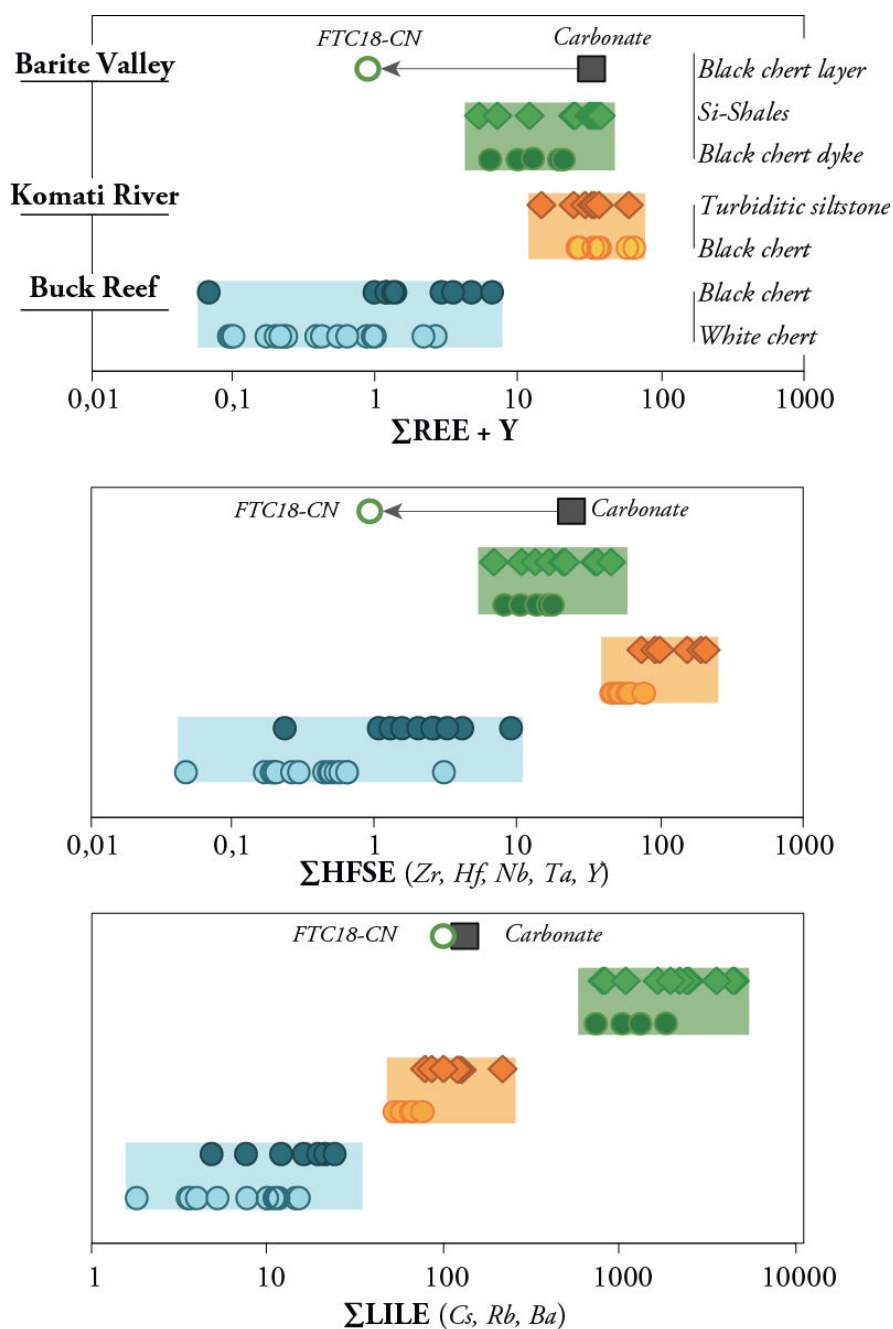
FIGURE 4.14 – *Concentration diagrams (Log scale) for the total REE+Y, HFSE (Zr, Hf, Nb, Ta, Y) and LILE (Cs, Rb, Ba) in Barite Valley, Komati River and Buck Reef samples. Buck Reef Chert samples, especially the white chert facies, are systematically lower than any other rock type. Sample FTC18-CN, the black chert layer from Barite Valley, is compared to the carbonate layer (KRC5) from Komati River.*
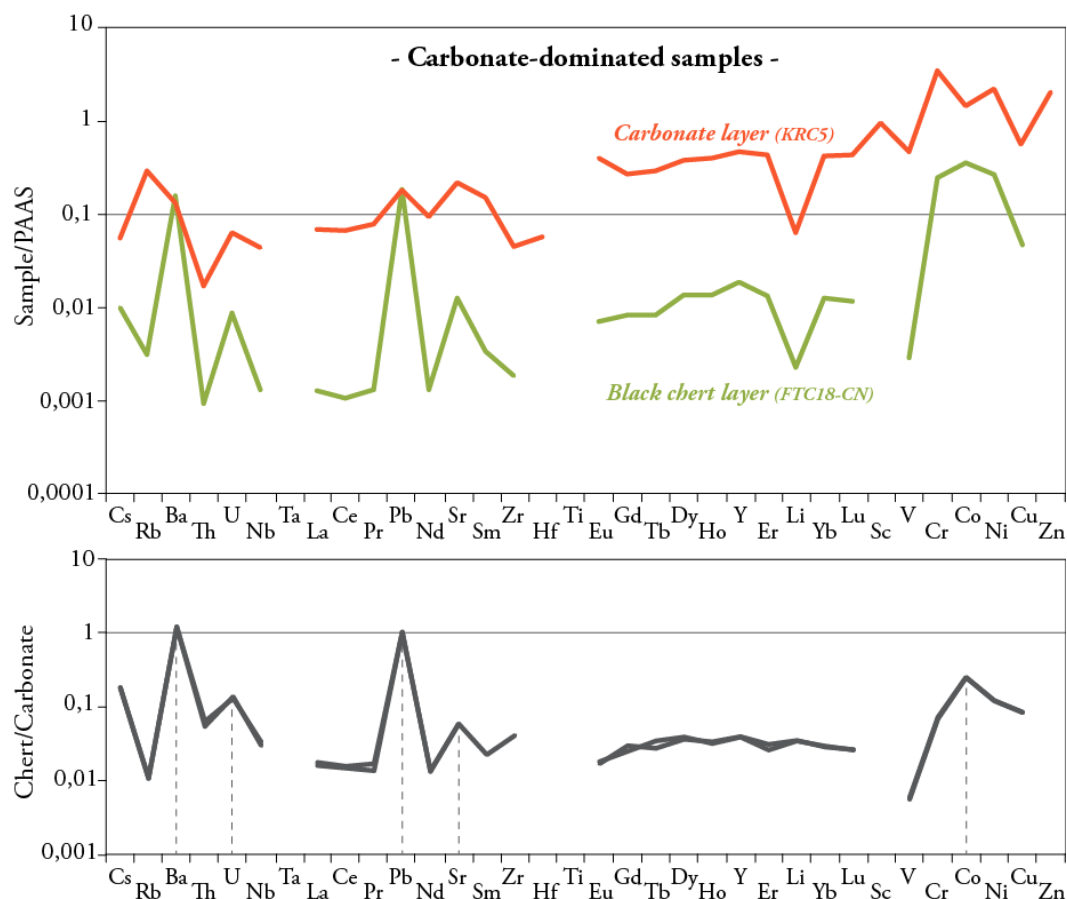
FIGURE 4.15 – *PAAS-normalized trace element patterns of the reference carbonate (Komati River, sample KRC5) and the black chert layer (Barite Valley, FTC18-CN). The lower graph corresponds to the chert composition normalized to the carbonate. Enrichments in Ba, U, Pb, Sr and in the transition metals Cr, Co and Ni in the chert are attributed to hydrothermally-influenced oceanic fluids (see text for discussion). The flat REE show that they are controlled by the carbonate fraction. Note that the LILE content for Barite Valley samples are essentially controlled by the barium enrichment in the area (see Tale 4.2).*

cordingly, the initial REE and HFSE contents would be 37.5*ppm* and 25*ppm* respectively instead of the present 30*ppm* and 20*ppm* values. The dilution is thus negligible in the carbonate, which is certainly not the case in the chert where the REE and HFSE remain below 1*ppm*.

The trace element patterns of these samples are shown in Figure 4.15. We retrieve from this graph the very low concentrations in Barite Valley cherts, whose pattern is characterized by strong enrichment in Ba, Pb and to a lesser extent U and Sr compared to other trace elements. The transition metal Cr, Co and Ni are similarly enriched in this sample. The carbonate layer displays higher concentrations and lacks major enrichment in one or another of the trace elements, although Rb,

Pb, Sr and the transition metals are slightly enriched. Lithium is depleted in both the carbonate and chert.

To allow for comparison, the chert is normalized to the carbonate layer in the bottom graph of Figure 4.15. Although differences are observed for the majority of trace elements (see below), the REE display a flat shape that indicates a chert composition very similar to the composition of the carbonate (see also Fig.4.16). Such consistency is evidence for us that the REE content of the Barite Valley chert is controlled by its carbonate fraction in a way similar to that observed in Komati River cherts, with the silica content acting again as a diluent.

The significant enrichment in Ba, U, Pb, Sr and in the trace metal Cr, Co and Ni in the chert remain to be explained. Because carbonates are known to record the chemistry of the fluid from which they precipitated (Veizer et al. 1989, Lee et Byrne 1992, Kamber et Webb 2001, Van Kranendonk et al. 2003, Nothdurft et al. 2004, Allwood et al. 2010), we believe that these differences may be inherited from specific conditions that prevailed in the Barite Valley paleo-basins.

Because the Barite Valley chert was found interbedded with deep sea shales, it is thought to have been deposited on the seafloor, in the deep ocean, where only very fine-grained sediments were transported and deposited. Thus, the fluid from which it precipitated could have been hydrothermally-influenced, which can account for the barium enrichment as already proposed by Heinrichs et Reimer (1977), Lowe et Knauth (1977) and Bao et al. (2007) for barite deposits commonly found in the area. The significant concentrations in Pb, U, Co and Cu are consistent with such a depositional setting as these elements are characteristic of modern hydrothermal fluids (*e.g.* Klinkhammer et al. 1994, Bau et Dulski 1999, Frei et Polat 2007).

REE contents and seawater proxies.

According to their REE+Y patterns (Fig. 4.16), the carbonate layer from Komati River is characterized by a seawater-like signature as described in Section 4.2.2. The carbonate is strongly depleted in LREE, with a Pr/Yb_{SN} ratio as low as 0.19, and displays a slight positive lanthanum anomaly (La/La^*=1.50). The HREE are relatively flat and only disturbed by a slight positive Y anomaly that gives a Y/Ho ratio of 32.2. This value is far from that of modern oceanic fluids (Y/Ho=50-60 in
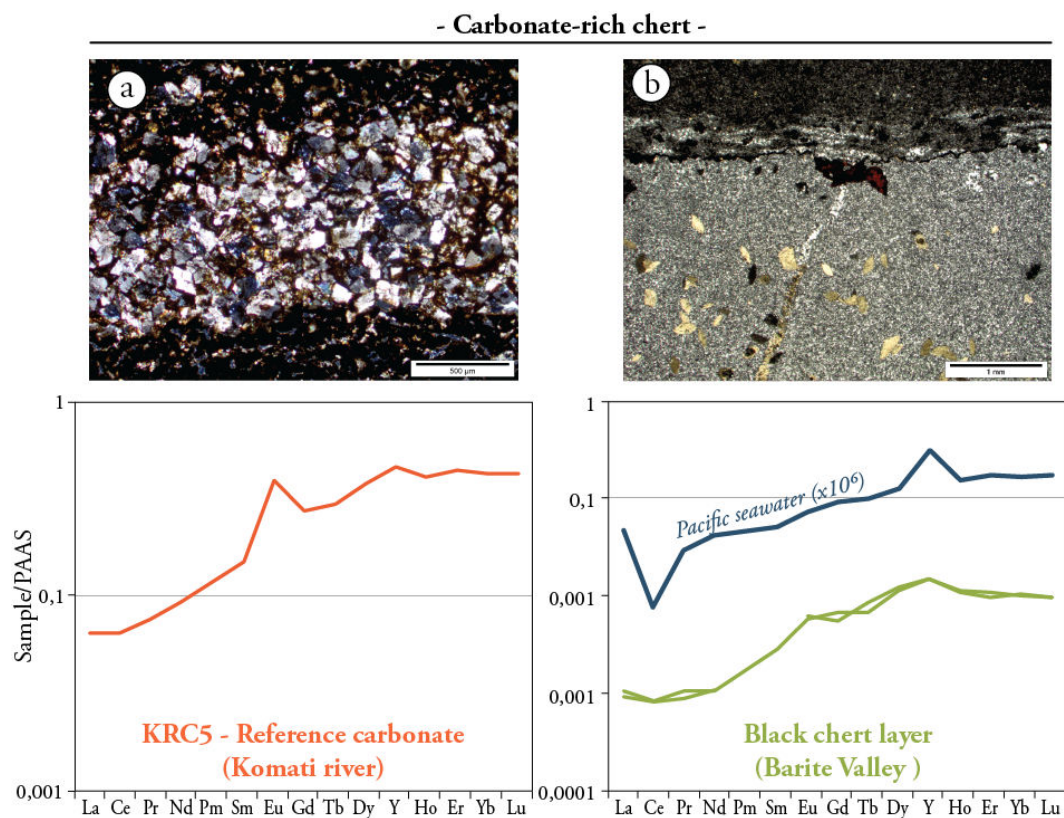
FIGURE 4.16 – *PAAS-normalized REE+Y patterns for the reference carbonate (Komati River, samples KRC5) and the black chert layer from Barite Valley (FTC18-CN). Both samples display seawater-like characteristics, including strong LREE depletion and Y enrichment. Note the different scales and the very low concentration of the chert.*

average ; *e.g.* Nozaki et al. 1997, Bau et al. 2000), but significantly exceeds the chondritic values of modern terrestrial rocks (Y/Ho=26-28 ; Pack et al. 2007). Despite these similarities, the carbonate layer differs from modern equivalents (*e.g.* Webb et Kamber 2000) by lacking a negative cerium anomaly (Ce/Ce^*=1.08) and showing strong europium enrichment ($Eu/Eu^* \sim 2$).

The REE pattern of Barite Valley black cherts is very similar to that of the Komati River carbonate. It displays strong LREE depletion ($Pr/Yb_{SN} = 0.10$) and slight lanthanum enrichment ($La/La^* = 1.32$), whereas the HREE are relatively flat. The Y/Ho ratio is superchondritic with a value of 36.9. The europium anomaly is positive ($Eu/Eu^* = 1.39$) but lower than in the Komati River carbonate, and cerium is slightly depleted with a Ce/Ce^* of 0.8. Slight samarium and gadolinium enrichment is observed when compared to KRC5.

Thus, the Barite Valley C-chert displays a well-defined seawater-like, chemical

composition, but its similarity with the ankerite layer suggests that the oceanic signal is hosted by the carbonate fraction and not by the silica fraction. As for the Komati River detritus-rich samples, the silica only contributes SiO_2 to the bulk chemistry and acts as a diluent to produce the very low concentrations found in FTC18-CN compared to KRC5.

Positive europium anomalies are a common feature of Archean chemical precipitates and have been previously attributed to primitive environments (*e.g.* Fryer 1977, De Baar 1991, Olivarez et Owen 1991, Danielson et al. 1992, Alibo et Nozaki 1998, Shields et Stille 2001, Hayashi et al. 2004, Bau et Koschinsky 2009). The Eu enrichment in modern hydrothermal systems (*e.g.* Von Damm 1990, Butterfield et al. 1997, Wheat et al. 2002, Seyfried Jr. et al. 2003, Bao et al. 2008) suggests the contribution of such fluids to both the chert and carbonates deposited at Komati River and Barite Valley. On the other hand, the slight negative cerium anomaly could be inherited from slightly oxidizing conditions in the Barite Valley site, although the anomaly is much lower than that observed in modern oxygenic oceans (see Fig.4.1).

4.2.7   Buck Reef : carbonaceous and high purity cherts.

The Buck Reef site is stratigraphically above Komati River units (Fig.4.3) and belongs to the Kromberg Formation (3.416Ga, Kröner et al. 1991). It is well exposed on the western limb of Onverwacht anticline and comprises a 250 to 400m-thick unit of banded siliceous sediments, *i.e.* black and white banded chert, overlying dacitic volcanic rocks and associated volcaniclastics of the Hooggenoeg Formation (Lowe et Byerly 2007).

The sequence is subdivided into three units, and grades from siltstones and evaporites to black and white banded cherts, with the upward disappearance of sedimentary structures and thinning of the beds. According to (Lowe 1999, Tice et Lowe 2006), it represents evolving marine conditions, from shallow, lagunal to deep, open-ocean settings. We focus here on the banded chert sequence whose origin remains ambiguous (*e.g.* Lowe et Knauth 1977, Walsh 1992, Lowe 1999, Westall et al. 2001, Westall 2005, Tice et al. 2004, de Vries 2004, Tice et Lowe 2006, de Vries et al. 2006). In Chapter 2, we identified both the black and white facies (Fig.4.17

- a) as oceanic chemical precipitates, probably deposited as soft and gelatinous amorphous silica.

The lower half of the sequence contains several slab conglomerate layers representative of occasional high-energy currents on the continental platform setting (Lower Banded Chert facies, Tice et Lowe 2006, Ledevin et al. in prep.a). In the conglomerates (Fig.4.17 - b), slabs are elongated and angular to sub-angular in shape and were produced by the disruption of massive white chert layers, whereas the surrounding matrix is similar to the massive black chert facies.

Chert characteristics.

The petrology of both the black and white cherts is consistent thorough the whole sequence (Fig.4.17). In conglomerates, the slabs have compositions similar to white chert and the matrix to black chert (4.17-d,f).

(1) Massive white cherts are almost entirely composed of homogeneous microquartz ($<5\mu m$) and lack obvious detrital grains or internal structures (Fig.4.17-c,d ; see also diffraction spectra of Fig.A.3). Rare ankerite and siderite grains are observed as secondary phases, grown within mm- to μm-thick silica-veins that cross-cut the chert. Minute grains ($<1\mu m$) of chromite and iron oxide are commonly found disseminated within the microquartzitic fabrics (only visible using high resolution imaging).

(2) Massive black cherts show higher petrological variability : they contain abundant carbonaceous matter in variable forms, including rounded agglomerates and elongated, homogeneous grains, mostly of detrital origin (Fig.4.17-e,f). Thin carbonaceous laminations are intercalated with silica layers, both $<10\mu m$ in thickness, and were interpreted as microbial mats by Tice et Lowe (2006) and in Chapter 2. Sand-size detrital particles, either ghosts of rounded grains now recrystallized to microquartz or carbonaceous grains, are commonly trapped within microbial laminations.

Throughout the whole sequence there is evidence of silicification, as revealed by numerous quartz-filled veins, pervasive silicification fronts and the partial disappearance of primary textures (Chapter 2. It is difficult to judge the extent of this process, but we estimate that it affects about 10-30% of the outcrop. Samples

Massive chert layer
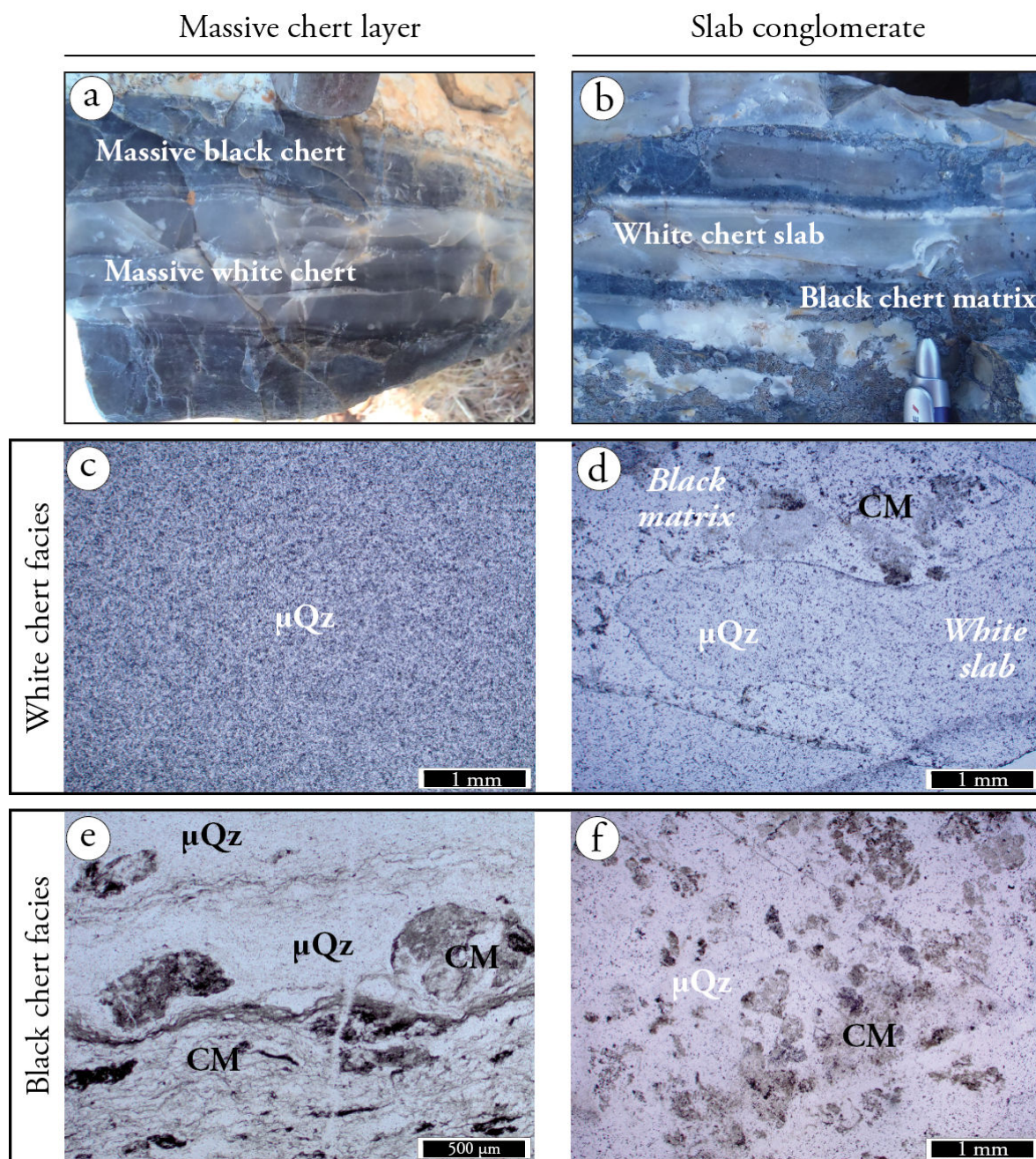
Slab conglomerate

FIGURE 4.17 – *Field (a & b) and microscope (c to f) photos of Buck Reef black and white chert samples. Massive white chert layers (c) and white chert slabs in conglomerates (d) have similar mineralogy, entirely composed of microquartz with disseminated chromites and iron oxides (<2µm). Massive black chert layers (e) and black matrix in conglomerates (f) are similarly composed of microquartz but display abundant carbonaceous matter contents, either as microbial mats, thin laminations, or rounded agglomerates. Rare ghosts of rounded detrital grains can be observed although they are recrystallized to microquartz.*
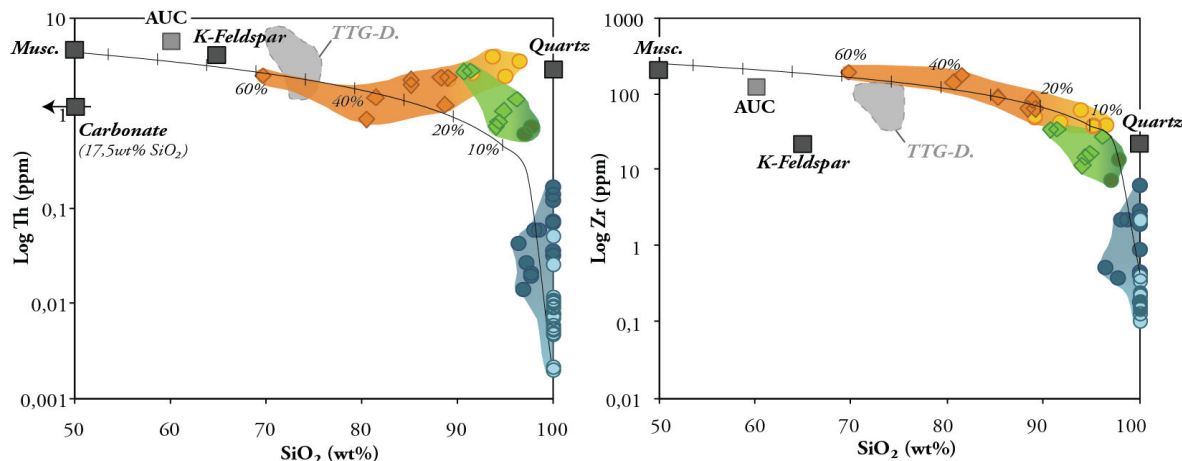
FIGURE 4.18 – *Harker diagrams for Zr and Hf for Barberton cherts from the Komati River (orange shades), Barite Valley (green shades) and Buck Reef (blue shades) sites. Solid lines are mixing curves between the purest withe chert from Buck Reef and the Archean Upper Crust (Condie 1993). Symbols are similar to Figure 4.6.*

selected for analysis were generally free of secondary veins and obvious alteration fronts.

The purity of Buck Reef cherts.

The chemical composition of Buck Reef cherts is in agreement with the silica-dominated mineralogy : the white cherts have the highest silica content of the whole sample set (Fig. 4.6), with SiO_2 concentrations very near $100wt\%$ and most other major elements being below the detection limit (Table 4.2). Black cherts also contain very low aluminum ($<0.2wt\%$) and potassium ($<0.07wt\%$) contents that may be inherited from the rare rounded detrital grains preserved as ghosts in the matrix. Significant iron contents are recorded in both the black and white facies, ranging from 0.15 to $0.33wt\%$. The iron is probably hosted in the minute disseminated oxides : although they are $<2\mu m$ in size, they are abundant in the siliceous matrix.

As expected from the major elements, the trace element concentrations are extremely low (Fig.4.14). The ΣREE in white cherts is below $1ppm$ ($<0.5ppm$ in average) but can reach $6.4ppm$ in the black cherts, especially those with non-zero Al_2O_3 and K_2O contents. The LILE content of the white cherts is below $50ppm$ and the HFSE
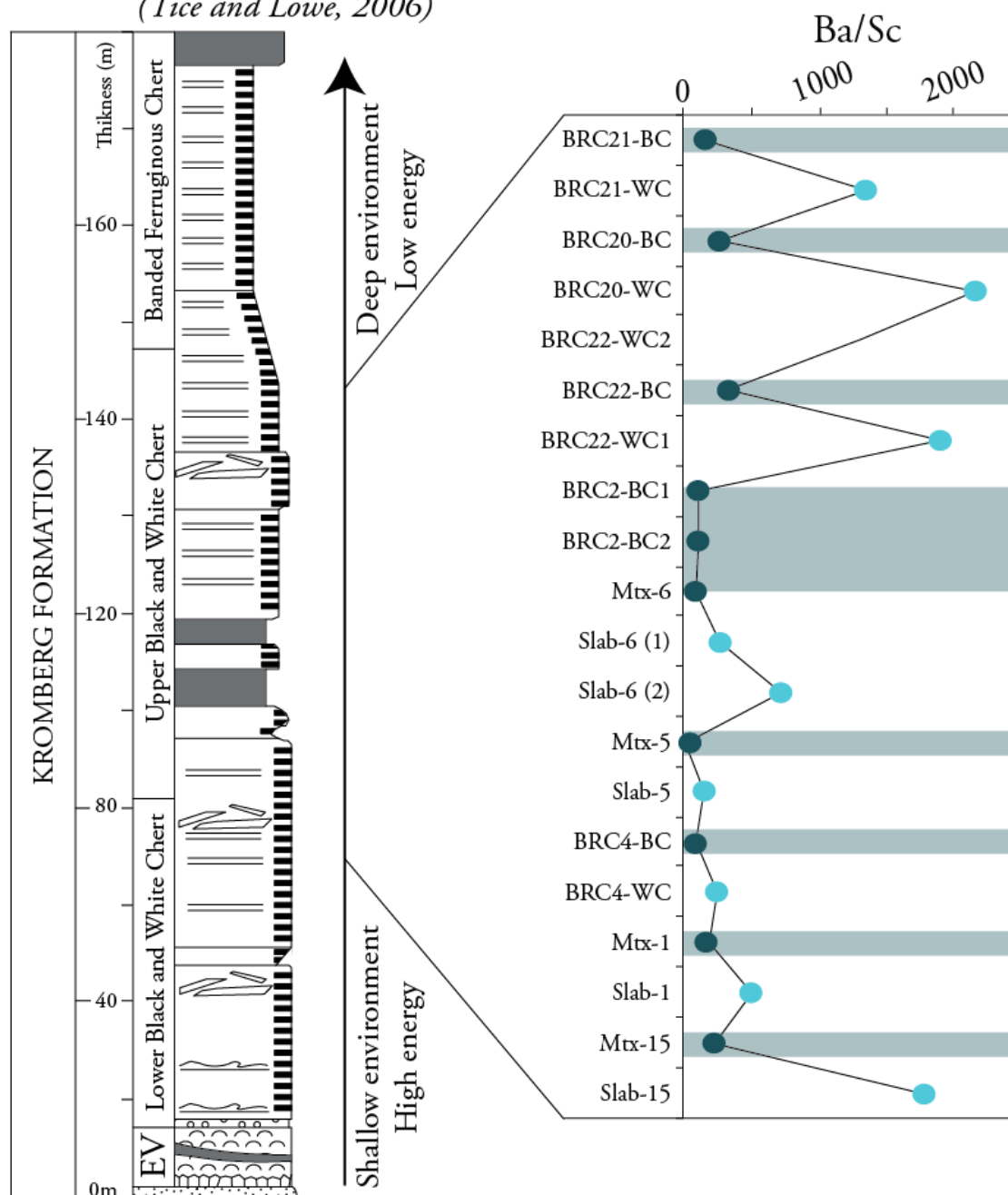
FIGURE 4.19 – *Evolution of the Ba/Sc ratio across the Buck Reef sequence. Stratigraphy is modified from* Tice et Lowe *(2006). Ba/Sc strongly differs from one layer to another, especially in black and white chert facies sampled in adjacent layers. Thus, the mobile elements (here Ba) might not have been significantly remobilized during secondary fluid circulations. Dark bands represent black layers. When samples have "Mtx" (matrix) of "Slab" in their name, they are from conglomerate layers. Otherwise they are from massive layers.*

concentrations do not exceed $10ppm$ for Zr and $1ppm$ for Th (Fig.4.18; Table 4.2). In the black cherts the LILE and HFSE contents are 2 to 10 times higher.

In the previous sections, we showed that the presence of even a small amount of contaminant (*e.g.* detrital particles, phyllosilicates, carbonates) dominates the bulk chemical signature whereas the silica contribution is difficult, if not impossible, to recognize. In the Buck Reef Chert samples, the black cherts may contain a certain amount of contaminant, as shown by the Al and K enrichment in some samples. However, the massive white chert layers, with their spectacularly low concentrations and almost pure silica mineralogy, provide the best chance to estimate the chemical signature of pure, oceanic, silica deposits. The minute iron oxides do not contribute significantly to their bulk chemistry as no correlation was found between iron concentrations and the trace element contents.

Because the whole Buck Reef section underwent significant secondary fluid circulation (see previous section), their bulk composition could have been significantly disturbed depending on the fluid characteristics (*i.e.* temperature, pH, dissolved species; Michard et Albarède 1986, Michard 1989, Seyfried 1987, Bau 1991, Bignall et Browne 1994, Seyfried et al. 1998, Elderfield et al. 1999, Douville et al. 1999). However, as shown in Figure 4.19, adjacent black and white chert layers display distinct and specific trace element characteristics that would have been averaged if the fluid had exchanged with surrounding layers. Mobile elements, such as Pb, Sr, Ba, U and Li, would have been leached or mobilized, but instead their concentrations vary strongly between layers collected at the same place, and from black to white units. Although it is possible that the carbonaceous matter or another component of the black chert fixed a certain proportion of the trace elements, we take the parallel patterns to indicate that the difference in concentration of the trace elements is due to the dilution effect of silica. Thus, one may assume that the composition of Buck Reef cherts remained unchanged and reflect the primarily deposited, oceanic silica composition.

Silica signal and the use of seawater proxies.

The trace element patterns of Buck Reef cherts are shown in Figure 4.20, which dramatically illustrates the extremely low concentrations we are dealing with.
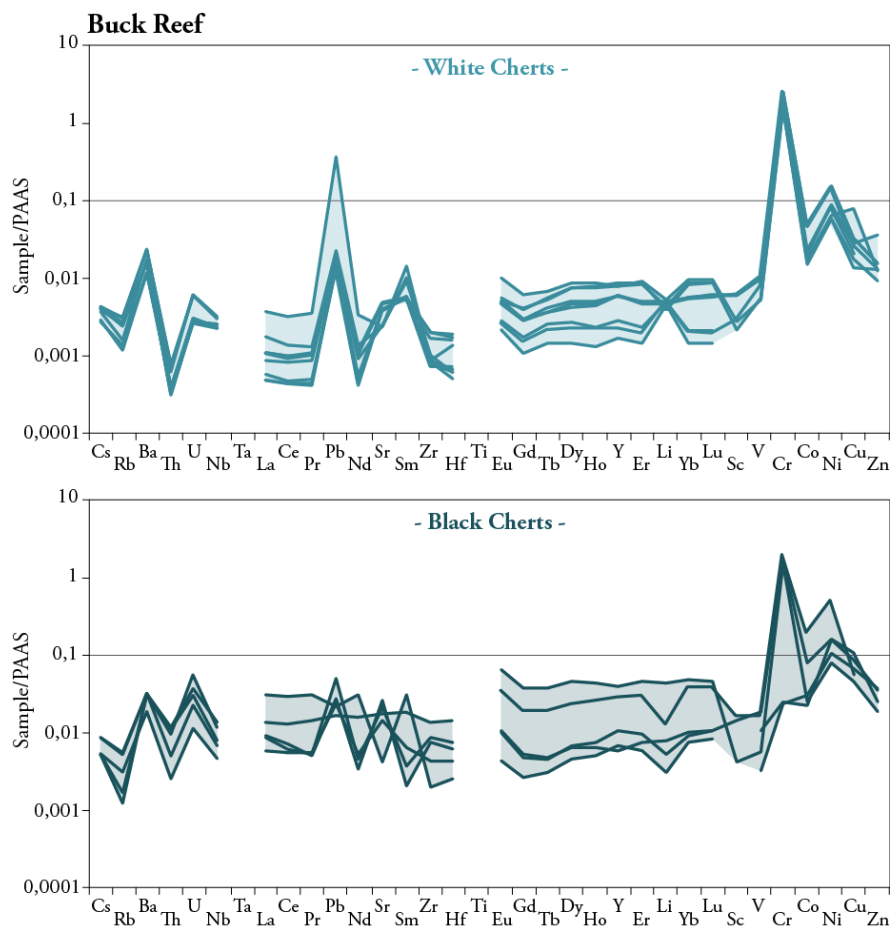
FIGURE 4.20 – *Shale-normalized trace element patterns of Buck Reef cherts showing the homogeneity of white cherts (upper graph) compared to black cherts (lower graph). The*

From this figure, and from Figures 4.18 and 4.21, the white cherts are characterized by strong enrichments in Ba, Pb, Cr and Ni. As previously noticed, the HFSE are extremely low. The black cherts are much more variable and, in average, have lower Ba enrichment but higher U contents. Other elements have a wide range of concentrations, which we believe is representative of the presence of variable amount of contaminant in the black chert (*i.e.* carbonaceous matter and detrital grains). Mass balance calculations like those described in the previous sections indicate that the amount of contaminant is probably less than 1-2% (Fig.4.18).

The variability of the black chert facies, either in massive or conglomerate layers, is similarly observed in the REE patterns of Figure 4.22 : the LREE are either flat or strongly depleted (Pr/Yb_{SN} = 0.09-1.00), the lanthanum and cerium anomalies are either absent or weakly to strongly positive (La/La^* = 1.0-7.8 ; Ce/Ce^* = 0.98-2.15), the europium anomaly is strongly positive and ranges from 1.36 to 2.43, and
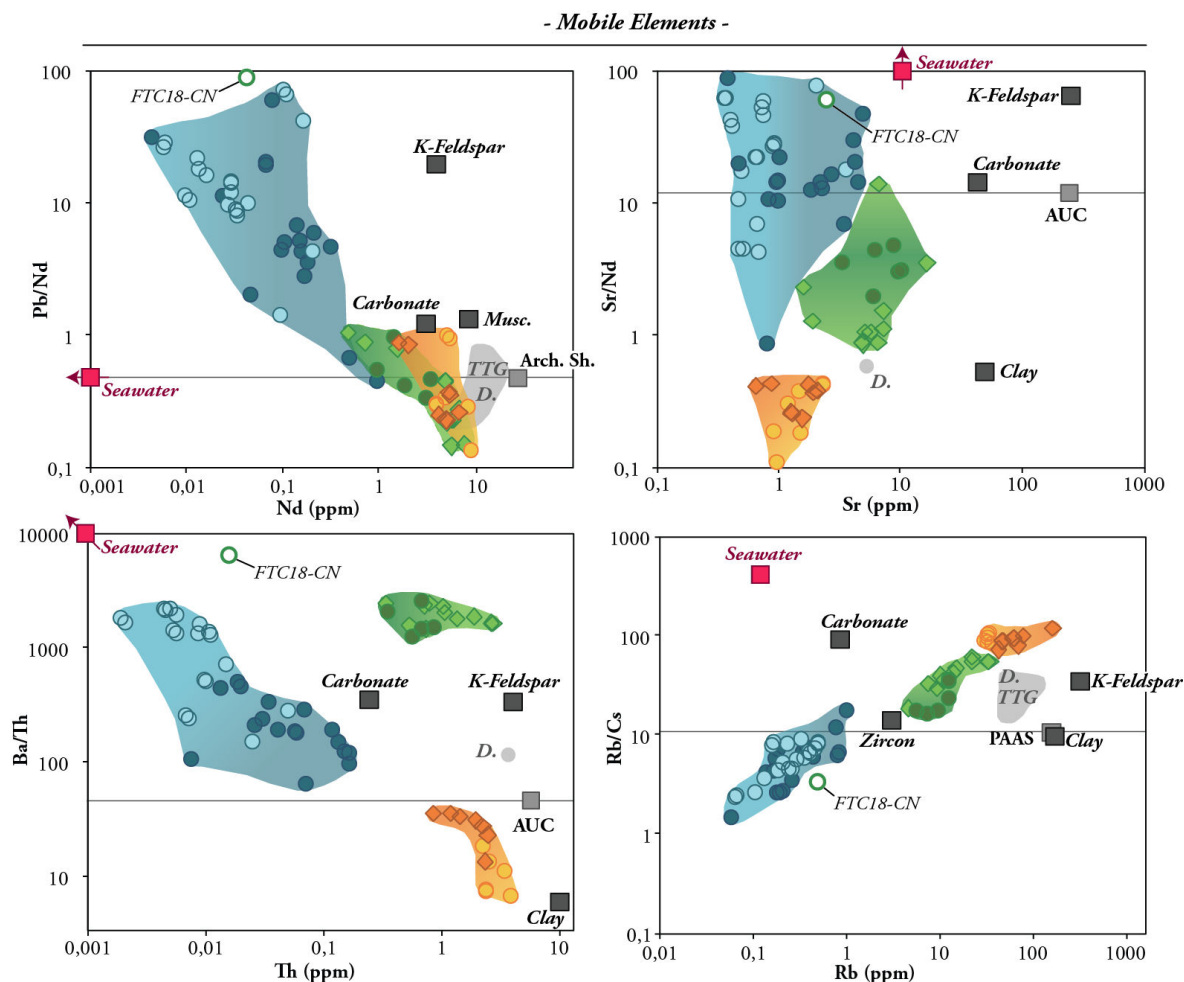
FIGURE 4.21 – *Selected ratio vs. element diagrams for Komati River (orange), Barite Valley (green) and Buck Reef (blue) cherts. Symbols are detailed in Fig.4.6. Horizontal lines represent AUC ratio. Archean Upper Crust (AUC) is from Condie (1993); Dacite (D.) from Hofmann et Harris (2008); Modern Pacific seawater from Alibo et Nozaki (1999). Carbonate = Sample KRC5; Other mineral compositions are from Garçon et al. (2011).*

the Y/Ho ratio ranges from subchondritic to superchondritic values, from 24.7 to 45.9. The presence of some contaminant is again advocated to explain such a range of compositions.

In contrast, the purity of the white chert facies allows us to consider their REE composition as representative of pure siliceous deposits. The massive layers have highly fractionated REE patterns characterized by strong LREE depletion (Pr/Yb_{SN} = 0.10-0.59) and nearly flat HREE. The lanthanum and europium anomalies are either slightly negative or positive, with La/La^* ranging from 0.87 to 1.57 and Eu/Eu^* from 0.82 to 1.29, whereas a cerium anomaly is absent (Ce/Ce^* = 0.81-
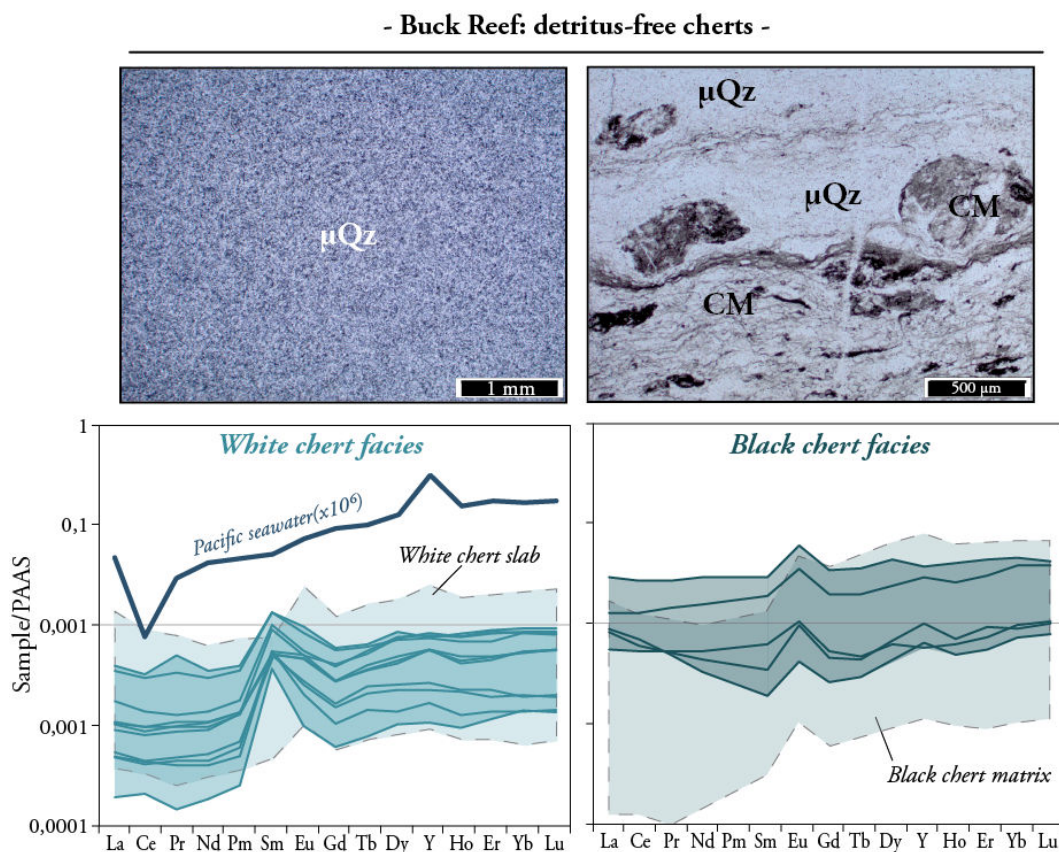
FIGURE 4.22 – *PAAS-normalized REE+Y patterns for Buck Reef Chert samples in relation with their respective mineralogy. The composition of modern Pacific seawater from Taylor et McLennan (1985) is shown form comparison. The massive white chert layers display strong positive samarium anomalies that are barely explainable.*

1.12). Yttrium is variably enriched, producing chondritic to superchondritic Y/Ho ratios of 25 up to 36.6. The white chert slabs in conglomerates are interpreted as disrupted layers of massive white chert. Indeed, they show REE patterns similar to those found in previous massive layers, although slight differences are observed : the lanthanum and europium anomalies are much more positive ($La/La^* = 1.00$-1.7 ; $Eu/Eu^* = 1.38$-2.51) and the Y/Ho ratio is even more superchondritic, ranging from 30.3 to 43.4.

Such REE characteristics approach those of modern seawater as shown in Figure 4.10, although the lack of Ce-anomaly and the variable Eu-anomalies are evidence for specific environmental conditions, *i.e.* more reducing conditions (*e.g.* Sverjensky 1984, Danielson et al. 1992, Shields et al. 1997, Bau et al. 1998, Yang et al. 1999).

The seawater-like characteristics found in the white cherts (*i.e.* LREE depletion, La and Y enrichment) could have been inherited from Archean seawater if we ac-

cept that seawater proxies are reliable indicators of oceanic contribution. However, in Figure 4.23, we show that the Buck Reef white cherts fall within the field of modern hydrothermal, magmatic and metamorphic quartz (Monecke et al. 2000, Götze et al. 2004) that did not precipitated from oceanic fluids. Thus, we can be confident that the chert precipitated on the seafloor using the field and petrographic approach of Chapter 2, but we cannot distinguish the various oceanic and hydrothermal contributions to the ambient fluids on a geochemical basis.

The mysterious samarium anomaly

A spectacular and unexpected feature is the presence of strong positive samarium anomalies in all the sampled massive white chert layers. Such anomaly is particularly of interest, as it has never been observed in any terrestrial rock. We believe that the anomaly is neither an analytical artifact, nor due to contamination during the digestion procedure or within the ICP-MS analysis (see Appendix A for analytical details). We repeated the analysis three times with variable dilution factors and reproduced the anomaly in each case. Black and white samples from both massive and disrupted layers were randomly placed in the analytical sequence. For two of the three series, the samples underwent the same procedure, from the digestion until the analysis. We systematically obtained the Sm enrichment in the white cherts but not in the black cherts, confirming the reality of the anomaly.

The Sm-anomaly is expressed as Sm/Sm^* and calculated from the equation 4.4 : it corresponds to the ratio between the measured value and that expected by the slope defined by the closest neighbors that are not affected by anomalous enrichment or depletion.

Samarium anomaly :

$$Sm/Sm* = Sm_{SN}/[(Pr_{SN} + Gd_{SN})/2] \qquad (4.4)$$

The anomaly ranges from 2.80 to 7.77 in white cherts, but is lacking or even negative in black cherts ($Sm/Sm^* = 0.53$-1.18) (Table 4.2). Because the total REE content is higher in the latter, we argue that the samarium enrichment might have
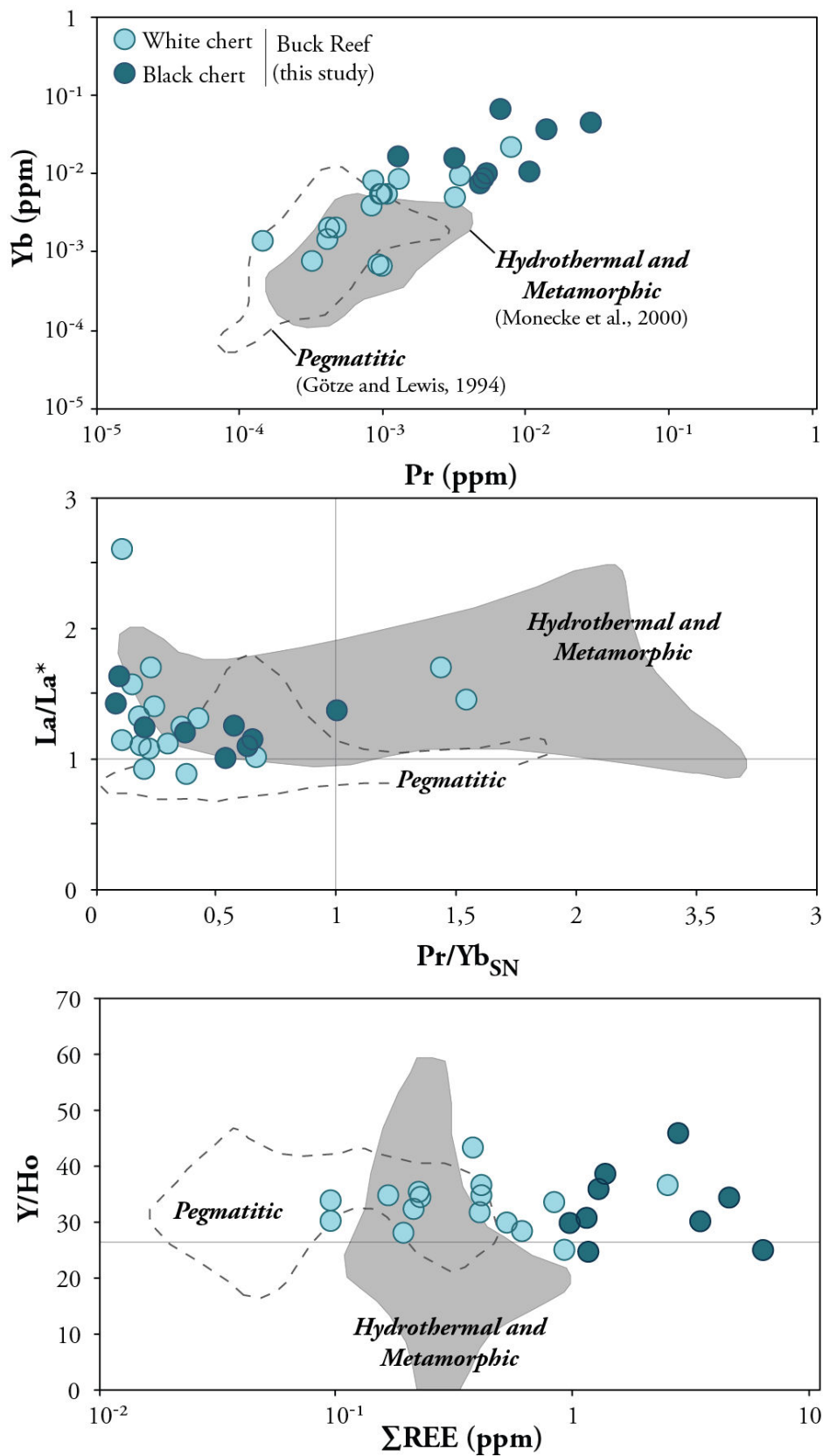
FIGURE 4.23 – *Selected diagrams showing the superposition of Buck Reef chert compositions with those of pegmatitic, hydrothermal and metamorphic quartz. Various quartz types cannot be distinguished on the basis of their REE content. Pegmatitic quartz compositions are from Götze et Lewis (1994) and hydrothermal and metamorphic quartz are from Monecke et al. (2000).*

been obscured in these samples. Only one slab sample (BRC15-Slab) has a positive Sm anomaly whereas other slabs have normal patterns. Thus, either the specific condition that fractionated samarium was not constant through time, or the anomaly was obscured during the disruption and reworking of most of the slabs.

We found only one study reporting anomalous Sm behavior : Pack et al. (2004) observed distinct *negative* Sm anomalies in ordinary chondrite chondrules, probably inherited from the REE gas-solid fractionation in nebular environments. However, such conditions are obviously unlikely on the primitive Earth, and we propose here several other possibilities for the fractionation of samarium.

(1) The complexation of REE with dissolved phosphate can fractionate Sm because it is preferentially removed from seawater (Byrne et al. 1996). Thus, it is not inconceivable that similar Sm-phosphates exist in the Buck Reef white cherts. However, the P_2O_5 contents are below the detection limits in these samples and we failed to identify phosphates in chemical maps.

(2) Minute oxides are the only other minerals found in the microquartzitic matrix. Thus, we envisage that samarium could have been preferentially retained in these oxides during the chert formation. Such fractionation could have been rendered possible by the specific magnetic moment of samarium, especially that of [147]Sm and [149]Sm (Lock 1957, Benz et Martin 1970, Taylor 1971, Danebrock et al. 1996, Malaman et al. 1997, Wolff et al. 2001). The way the samarium is used in the industry to produce powerful magnets could provide further information on the way it might fractionate under specific conditions.

(3) Although we recognized the cherts as oceanic precipitates, we cannot entirely rule out a possible hydrothermal contribution to the basin on the basis of their composition. Indeed, Archean hydrothermal systems may have been very different from modern equivalent, especially in terms of the fluid composition and deep fluid-rock interactions (Isley 1995, de Vries et Touret 2007, Shibuya et al. 2010). Following the model of Shibuya et al. (2010), we envisage the precipitation of the white layers from a mixture of seawater and a hydrothermal plume. The plume could have been enriched in Sm within the crust, especially if it interacted with ultramafic rocks that are known, in some cases, to be preferentially enriched in samarium (*e.g.* Sharma et al. 1995). However, modern systems with ultramafic basements do

not produce such Sm-rich fluids (Logatchev and Rainbow fields Batuyev et al. 1994, Bogdanov et al. 1995, German et al. 1996, Charlou et al. 1998, Douville et al. 2002). We speculate that and Archean fluid may have had chemical characteristics (*i.e.* T°, salinity, acidity and the nature of dissolved and particulate species) that could have promote the fractionation of samarium.

We can also envisage specific fission reactions, or the fractionation of samarium during the precipitation of amorphous silica. None of these hypotheses is convincing, and additional investigations are needed. In the future, we plan to measure the Nd isotopic composition of these cherts, in the hope that the enormous range of Sm-Nd ratios of the white and black cherts will allow us to place constraints on the timing of the fractionation.

PART II
-
The geochemistry of fracture-filling cherts

In this section, we focus on the silicified shales (S-chert) that comprises the sedimentary sequence of the Barite Valley locality, and on the black chert dykes (F-chert) that cross-cut these units. The composition of both chert types are discussed in terms of mineral compositions. By this approach, we investigate the origin of the silica that now fills the fractures and the effect of dyke emplacement on the country rock chemistry.

4.2.8 The silicified shales from the Barite Valley site.

S-chert characteristics.

The shales from the Barite Valley site comprises two distinct facies.

The first facies corresponds to the laminated, more or less ferruginous, carbonate-rich shales described in Part I (Section 4.2.6). Their mineralogy is summarized in Figure 4.24-f. These shales are characterized by abundant grains of micro-carbonaceous matter associated with isolated and slightly less abundant carbonate grains. Phyllosilicates in this facies are limited to fine grains less than 5-10μm in size. Both these phases are enclosed in a microquartzitic matrix whose dark color is attributed to the presence of diffuse carbonaceous matter. In the following sections, we will referred to this facies as "carbonate-shale".

The second facies is enriched in detrital grains and consists of a mixture of microquartz and phyllosilicates in roughly equal proportions, in which iron oxides may be abundant (Fig. 4.24-d). The coarser phyllosilicates (typically 50μm in size) display well-defined zoning (Fig. 4.25) whereas the finest grains are homogeneous. The elongated shapes and rounded edges of phyllosilicates suggest that these are primary detrital particles rather than secondary material produced during diagenesis. From the microprobe analyzes of Table 4.3, the phyllosilicates have sericite composition and we will thus referred to this facies as "sericite-shale".
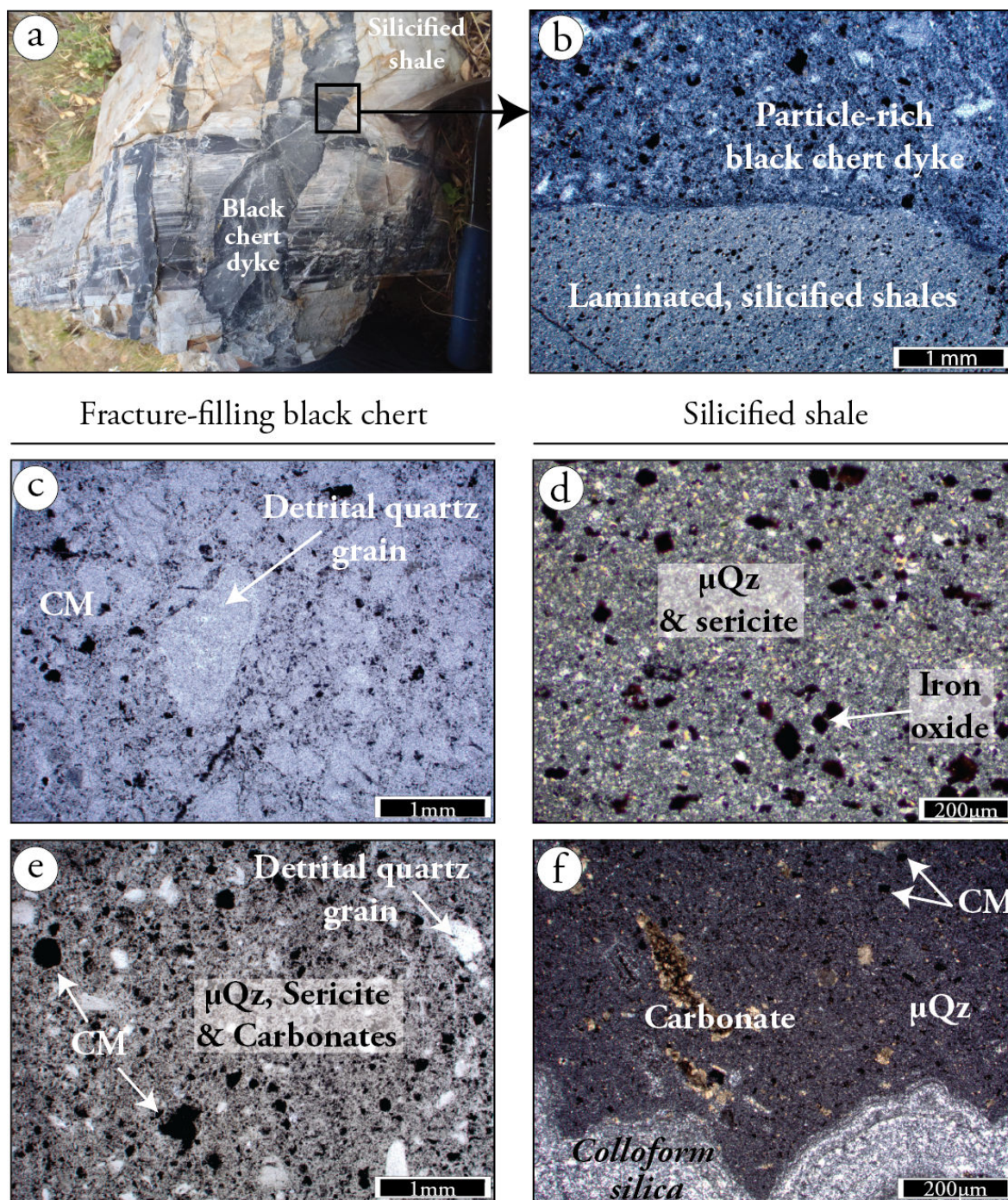
FIGURE 4.24 – *Selected photomicrographs of Barite Valley dyke-filling black cherts (c, e) and silicified country rocks. The photo (a) shows the relationship between the dyke and shales. The silicified shales are either (d) sericite- or (f) carbonate-rich according to their stratigraphic levels, the former being older and deposited under deeper marine conditions (Lowe 1999; in press.). The fracture-filling cherts are characterized by the abundance of rounded particles of microquartz and carbonaceous matter enclosed in a microquartzitic matrix. μQz = microquartz ; CM = carbonaceous matter.*
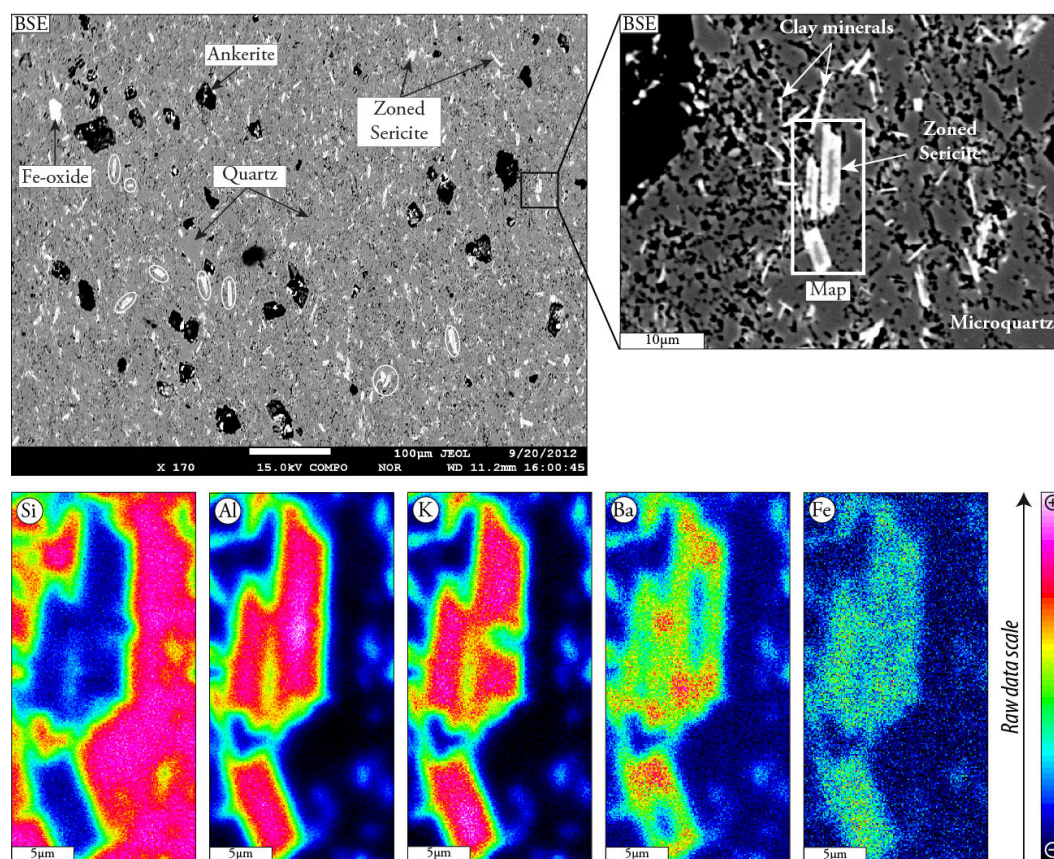
FIGURE 4.25 – *BSE photos of Barite Valley shales, and in situ, high resolution microprobe maps of zoned sericite grains showing the preferential location of barium in sericite rims. Note that the rim is relatively thick compared to the central, narrow zone, and that the thin, green aureole around the grain is an artifact due to the color scale. Quantitative analyzes are given in Table 4.3.*

Composition of sericite-shales.

Compared to the clastic-rich, turbiditic samples of Komati River , the sericite-shales are significantly enriched in SiO_2 whereas major and trace element concentrations are lower (Fig. 4.6 and 4.14). Aluminum is the most enriched element, with concentrations up to $3.86wt\%$, whereas other major elements are below $1wt\%$ (Fig. 4.6), which is consistent with the siliceous, phyllosilicate-dominated mineralogy that lacks coarse, clastic particles and heavy minerals. The SiO_2 content ($>90wt\%$) represents the amount of siliceous matrix around detrital clays as no detrital quartz is observed. Other elements are thus more or less diluted according to samples, which provides the negative correlations curves of Fig. 4.6, a dilution effect already observed at Komati River.

As shown in Figure 4.26, Al_2O_3, K_2O, Zr and Ti concentrations correlate po-
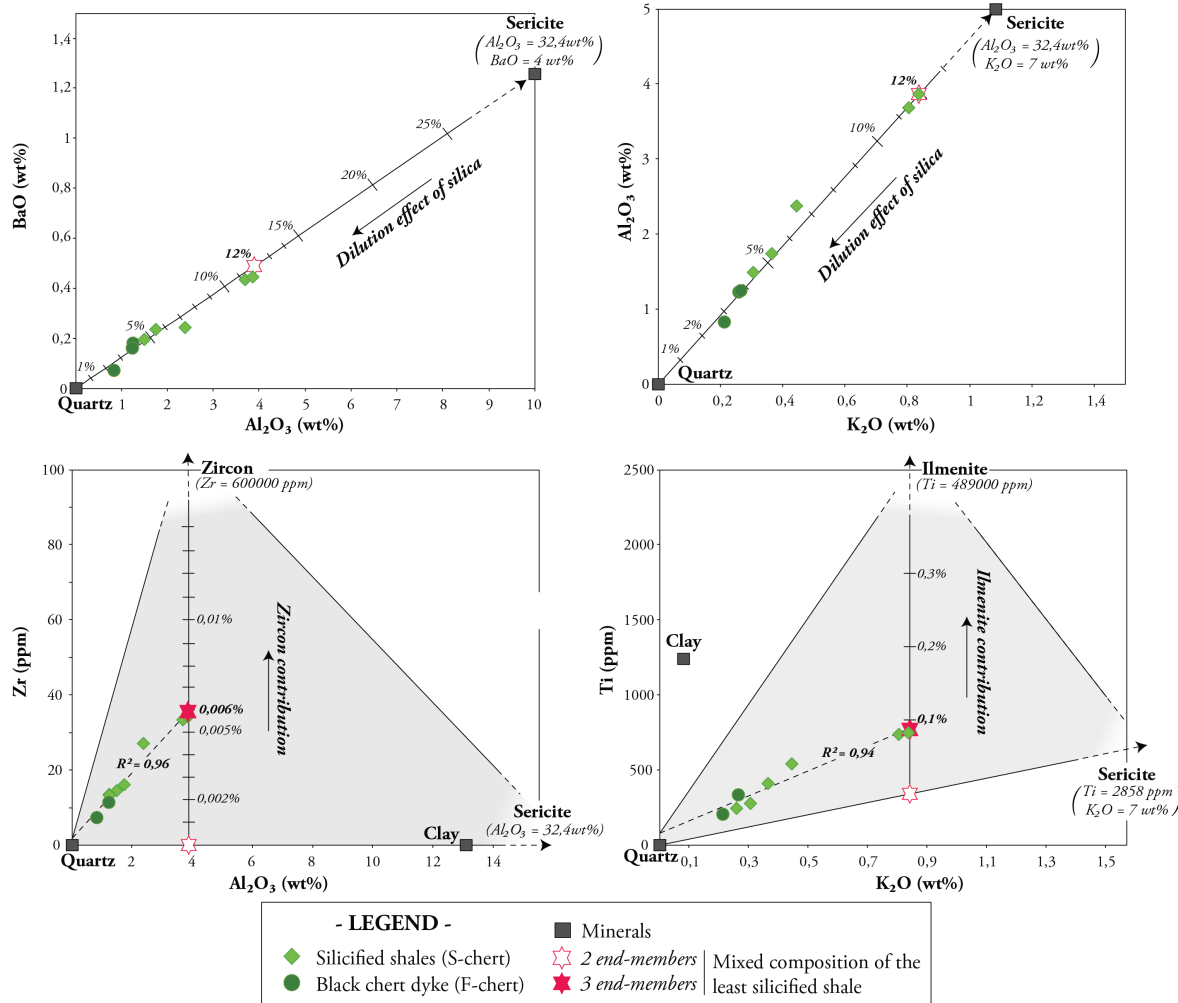
FIGURE 4.26 – *Barite Valley major element correlation diagrams. The well-defined positive correlations are consistent with the location of Al, K, Zr, Ba and Ti in the fine-grained fraction. We can model the bulk shale composition with* 12% *sericite,* 0.2% *ilmenite and less than* 0.01% *zircon, the rest being microquartz.*

sitively with each other, suggesting that the detrital fraction preserves a similar composition across the sampled sericite-shales. As we did in Section 4.2.5 for Komati River siltstones , the major element content of the sericite-shales can be linked to specific minerals species, and the bulk composition can thus be expressed as a mixture of mineral compositions.

The mineralogy is homogeneous and dominated by the mixture of phyllosilicates and microquartz. As shown in Table 4.3, the zoned, coarser phyllosilicates found in most of the samples have sericite-like compositions similar to those in Komati River samples. (SiO_2=50wt%, Al_2O_3=32-34wt% and K_2O=7wt%). The rim
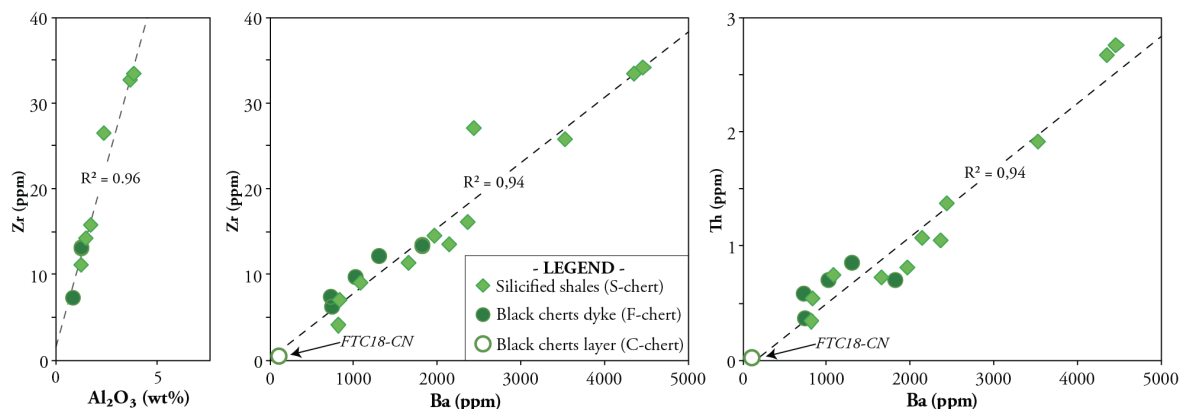
FIGURE 4.27 – *Element vs. element diagrams showing positive correlations between the continental-derived elements Zr and Al. The correlation with barium indicates that this element is exclusively located in the clastic fraction. Samples FTC18 corresponds to the massive, black chert layers deposited as C-chert in the carbonate-shales.*

is enriched in barium ($4wt\%$), and to a lesser extent in heavy elements (*Cr, Ti, Fe*) and MgO, whereas Na_2O is depleted. Iron is most probably located in siderite that can be abundant in some layers (up to 5%).

In Figure 4.26, we model the major element composition of Barite Valley sericite-shales using the composition of the mineral components. From this figure, the Al_2O_3 and K_2O contents of sericite-shale samples can be modeled using a mixture of 88% quartz and 12% sericite. Similarly, we estimate that $\sim$ 0.1% of ilmenite and less than 0.006% zircon are required to account for the *Ti* and *Zr* concentrations observed in our samples.

The well-defined positive correlation between BaO and the continent-derived elements Al_2O_3 (Fig.4.27), Zr and Th (Fig.4.27) suggest that barium is located in the clastic fraction. In Table 4.3 and Figure 4.25, we see that the sericite grains have high Ba contents, particularly the rims. It is uncertain whether the Ba is part of the detrital component or introduced during diagenesis or later alteration. The mixing calculation of Figure 4.26 shows that 12% of sericite can account for the barium content.

As previously noticed for Komati River cherts, the silica acts as a diluent in these silicified shales but, otherwise, seems contribute only SiO_2 to the bulk composition. The trace and rare-earth element patterns of Barite Valley sericite-shales may thus
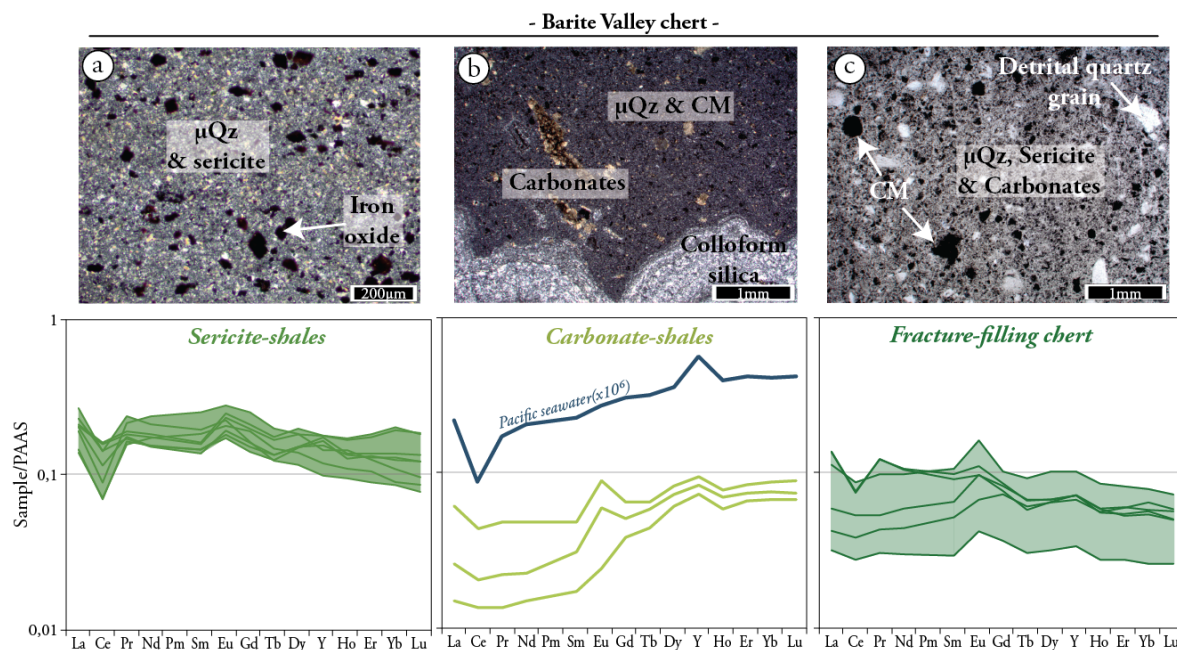
FIGURE 4.28 – *Barite Valley PAAS-normalized REE patterns for the silicified shales (S-chert) and fracture-filling cherts (F-chert). The silicified shales are further divided into Carbonate- and sericite-shales according to their mineralogy. The composition of modern Pacific seawater (Alibo et Nozaki 1999) is shown for comparison.*

be representative of their phyllosilicates-dominated fraction. The carbonate-shale have much lower REE contents, as seen in Figure 4.28.

REE composition and the contaminant signal.

The REE patterns for the two shale types are shown in Figure 4.28. The sericite-shales have total REE contents of $\sim$ 24-38ppm and form an homogeneous group characterized by relatively flat LREE whereas the HREE are more variable, being either flat or strongly depleted with Pr/Yb_{SN} ranging from 0.94 to 2.8. These samples display weak to strong negative cerium anomalies ($Ce/Ce* = $ 0.80-0.41), chondritic to superchondritic Y/Ho ratios ($Y/Ho = $ 27.2-34.9), and absent to weak, positive Eu-anomalies, with $Eu/Eu*$ of 1.1 to 1.3. These features are somehow similar to those of Komati River clastic samples and are characteristics of their respective detrital components.

The carbonate-shales are very different as they contain much lower REE contents ($\sim$ 5-12ppm) and display highly fractionated REE patterns, with strong LREE depletion and relatively flat HREE ($Pr/Yb_{SN} = $ 0.2-0.54). They lack cerium

anomalies ($Ce/Ce* = 0.92$-1.11) and lanthanum is slightly enriched with $La/La*$ of 1.18-1.35. Y/Ho ratios are superchondritic 32.7 to 33.9, and europium is strongly enriched for the least LREE-depleted samples ($Eu/Eu* = 0.95$-1.61). These characteristics, and especially the LREE depletion, and La and Y enrichments,approach those obtained in the reference carbonate KRC5 (see Fig.4.16) and resemble modern seawater characteristics, despite the presence of low amount of phyllosilicates.

These results are in good agreement with the previous conclusions reached for Komati River samples : the sericite-shale chemistry is controlled by its phyllosilicate fraction whereas the carbonate-shales have a composition that approaches that of the Buck Reef cherts. In both cases, the silica dilute the detrital fraction composition and contribute to the average low concentrations in these samples.

Silicification process.

A key question is wether these rocks were primarily silicified during early to late diagenesis, or secondarily modified during the black chert dyke emplacement. Figure 4.29 represents a X-ray microfluorescence map of the interface between a black chert dyke and surrounding sericite-shales. Whereas the dyke is almost entirely composed of silica, with rare, isolated carbonate grains, the shale preserves chemical and mineralogical variations in agreement with its primary layering. The variable clay/microquartz ratio from band to band is responsible for the color variations of the rock, and the organization seems undisturbed by the proximity of the fracture.

However, pervasive silicification has been reported tens of meters below chert horizons in more resistant mafic and ultramafic magmatic rocks (Paris et al. 1985, Lowe et Byerly 1986a, Duchac et Hanor 1987, Hanor et Duchac 1990, Hofmann et Harris 2008). Thus, why was the Si-metasomatism so limited in the Barite Valley shales ?

In Figures 4.27 and 4.26, we showed that barium is located in the fine-grained, clastic fraction as it correlates positively with the HFSE and Al_2O_3 content. From the microprobe analyses of Table 4.3 and microprobe maps of Figure 4.25, we showed that it is highly concentrated in sericite rims ($\sim 4wt\%$), less in their core ($0.67wt\%$) and otherwise absent from other phases.
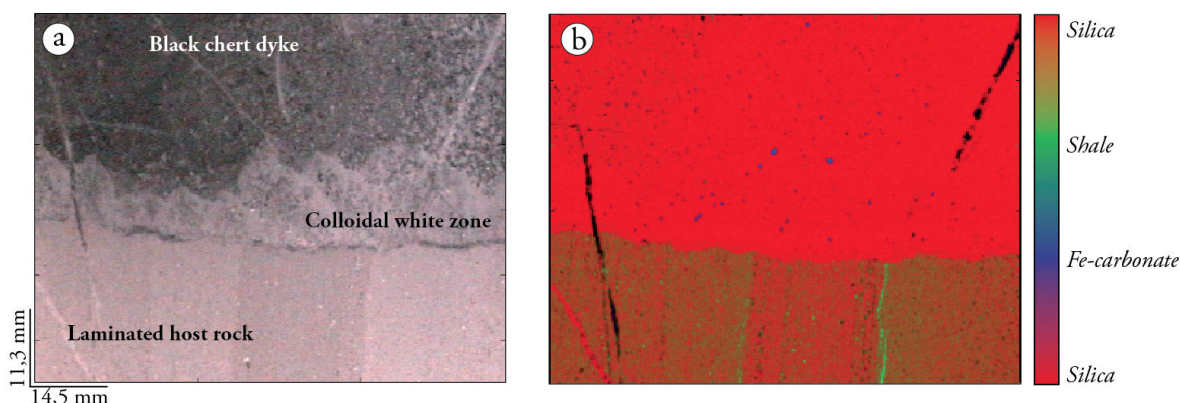
FIGURE 4.29 – *In situ X-ray microfluorescence map at the interface between a fracture-filling black chert and surrounding laminated and silicified shales in the Barite Valley area. (a) Photo of the selected area. The primary layering of the shale is preserved despite its contact with the black chert dyke.*

Such specific location could be easily explained by the transfer of Ba (together with K and Si) from the circulating fluid through to the country rock during the dyke emplacement and subsequent Si-metasomatism Hofmann et Harris (*e.g.* 2008), and preferential incorporation of Ba in phyllosilicates (*e.g.* Eylem et al. 1990, Zhang et al. 2001). However, based on the following evidence, we argue that the shales were silicified prior to dyke emplacement : (1) other mineral phases, and especially carbonates, do not contain Ba enrichment as shown in Table 4.3 ; (2) the primary layering in shales is preserved even close to the fracture wall.

Previous studies on massive barite deposits (Heinrichs et Reimer 1977, Reimer 1980) and Fig Tree greywackes (Hofmann 2005) argued that the area was a geothermally active zone during shale deposition. Hofmann (2005) proposed that ascending Ba-rich hydrothermal fluids could have been responsible for the metasomatic alteration of the Mendon Formation along major upflow zones.

Following their idea, we propose that the shales were silicified very early, during or shortly after deposition. However, we depart from their interpretation as we believe that the Ba and Si enrichments could be inherited from hydrothermally-influenced bottom seawater, rather than from shallow circulating hydrothermal fluids. We argue that Si and Ba sorption onto clays, either during their deposition or subsequent pervasive seawater infiltrations, can account for both the early silicification (*e.g.* Rouchon et al. 2009) and the specific location of Ba in sericite

rims (*e.g.* Eylem et al. 1990, Zhang et al. 2001). The early metasomatism of shales and following diagenetic compaction could have sufficiently reduced their average porosity to prevent further silicification when the fracture-filling chert emplaced.

4.2.9 The fracture-filling cherts from the Barite Valley site.

Fracture-filling chert (F-chert) are found in large dykes that cross cut the previously described silicified shales in the Barite Valley site. The fractures are perpendicular to the bedding, as shown in Figure 4.24-a, and can reach a few meters in thickness with variable intensities of fracturation. As discussed in Chapter 3, they may have originate either from oceanic crust fracturation triggered by meteorite impact (Lowe et Byerly 2003, Lowe in press.) or from hydraulic fracturation triggered by overpressured hydrothermal fluids (Hofmann et Bolhar 2007). The petrographic characteristics of the chert are described in Chapter 3 : it is composed of quartz and carbonaceous matter rounded grains in a matrix of microquartz, as shown in Figure 4.12. Phyllosilicates are a minor component as shown by the diffraction analysis of Figure A.3.

Major element composition.

Two samples (FTC2-BC and FTC4-BC) having sericite-shales as country rocks were analyzed for major element compositions (Fig.4.2). They display relatively high concentrations in Al_2O_3 ($\sim 1wt\%$), K_2O ($\sim 0.25wt\%$) and Fe_2O_3 ($\sim 0.2wt\%$) given their high silica content (97-97$wt\%$) (Fig.4.6). Sample FTC4-BC has low MnO (0.01$wt\%$), Na_2O (0.02$wt\%$) and significant CaO of 0.25$wt\%$ (Table 4.2).

In Figure 4.26, these samples plot on the correlation curves previously obtained from the Barite Valley shales. From this, we can infer that their compositions are controlled by the presence of non-silica phases, *i.e.* the phyllosilicates described in Chapter 3 and seen in diffraction spectra of Figure A.3.
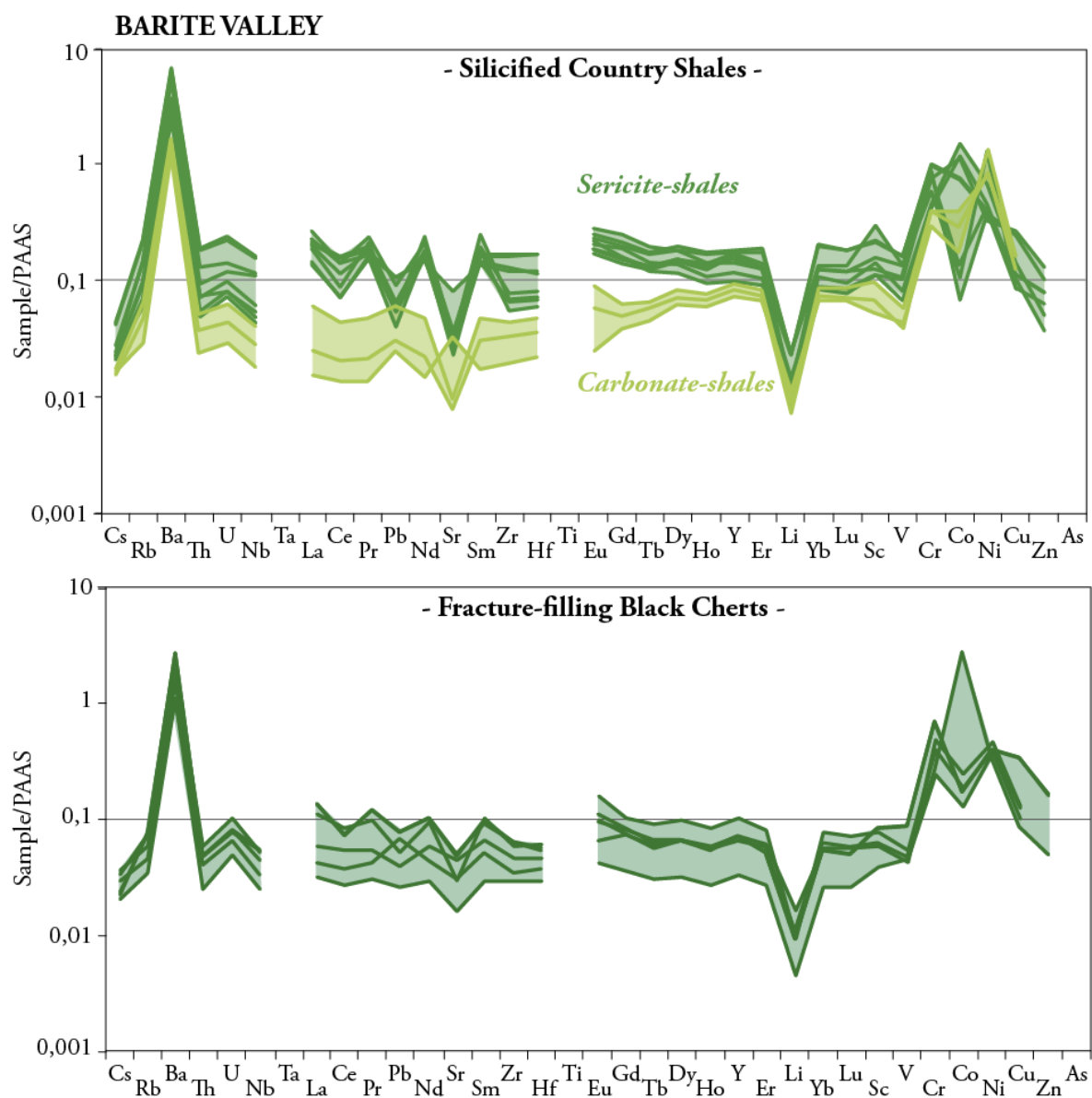
FIGURE 4.30 – *PAAS-normalized trace element patterns of Barite Valley chert dykes and associated host rocks. Associated REE patterns are shown in Fig.4.28.*
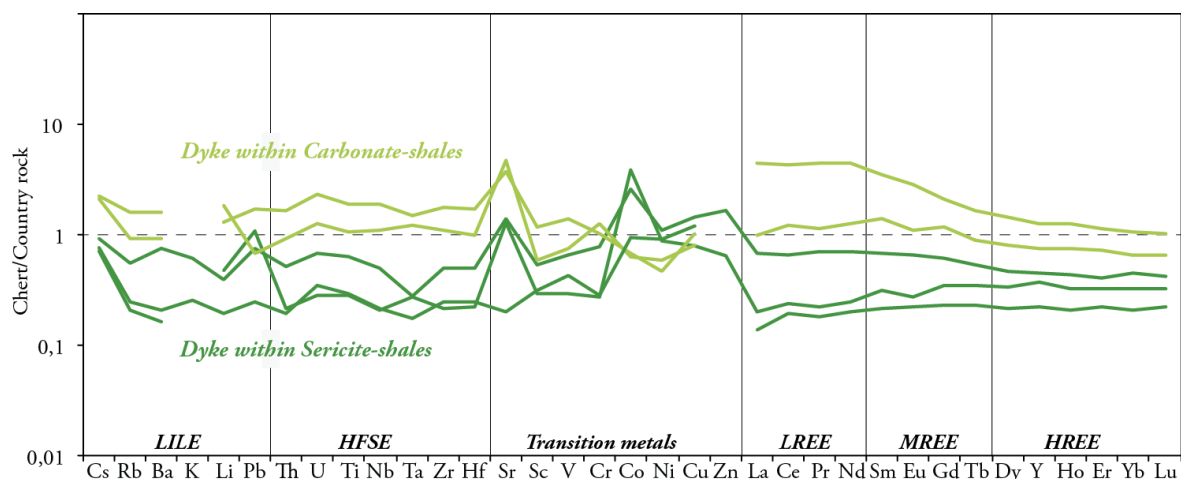
FIGURE 4.31 – *Composition of the fracture-filling black cherts from Barite Valley, normalized to the composition of adjacent country rocks.*

Trace element composition.

In good agreement with the above observations, the fracture-filling cherts display trace element patterns very similar to those of surrounding shales (Fig.4.30) (REE patterns are shown in Fig.4.28). Common features include the strong enrichment in Ba, Cr and Ni, and more variably in Co, and the strong Li depletions in both facies.

However, key differences can be observed in Figure 4.31, where the composition of F-cherts is normalized to that of adjacent country rock. In this graph, we can see which elements in the chert are controlled by the particles from the adjacent country rock, and which others are inherited from a different source. All samples display relatively flat patterns, especially for the HFSE and REE that are depleted (or even enriched) to equal amounts within the same sample. Because it is unlikely that these immobile elements where gained or lost during water-host rock interaction, they represent the shale fraction of the chert. Accordingly, for each sample, elements falling within the HFSE/REE range may be inherited from the shale fraction, while elements that depart from the general flat pattern may be controlled either (1) by the primary fluid itself, or (2) by eroded particles from other parts of the dyke complex.

The F-cherts sampled within the sericite-shales (dark green in Fig.4.31) have

trace element concentrations systematically lower that the host rock shale, except for significant enrichment in Co, and to a lesser extent in Cu and Zn. The elements are known to be significantly leached during the Si-metasomatism of volcanic rocks and associated erosion products (*e.g.* Hofmann 2005). Although we showed that the shales were silicified prior to dyke emplacement, we do not exclude secondary fluid-rock interactions, and the trace metal enrichment in the dyke could well be attributed to such chemical exchange.

The F-cherts from carbonate-shales zones show similar or even higher concentrations compared to surrounding host rocks, whereas one may expect lower concentrations given the higher silica content in the dyke. Sr and the LREE especially are enriched whereas part of the trace metals (Sc, Co, Ni) are slightly depleted. Because neither the surrounding shales nor the hypothetical primary fluid can account for the higher concentrations in the vein, we argue that additional host rock fragments could have been added to the chert during previous fluid circulations within other parts of the Barite Valley section.

According to the above observations, the chemical differences between the cherts and surrounding shales are limited, supporting the idea that the F-chert composition is essentially controlled by the nature and amount of fragments eroded while the fluid was circulating through the sedimentary pile.

PART III
-
Discussion and Conclusions

4.2.10 Identification of fluid compositions in Archean cherts : the effect of contamination.

In the previous Part I and II, we showed that the trace element composition of the silica phase in cherts is rapidly obscured by the addition of various components. We observed that clastic particles and carbonates easily masks the siliceous signal whereas carbonaceous matter has a limited effect on the bulk chert chemistry. Here, we quantify the fraction of contaminant required to totally obscure the signal hosted by the silica.

In the Figures 4.32 and 4.33, we consider the average composition of Buck Reef white cherts as representative of a pure silica precipitate. To estimate the contaminant capacity of the various phases encountered in the three sites, we used the following compositions :

(1) The silicified sericite-shales from Barite Valley have trace element contents controlled by their sericite fraction. Their average composition can thus be used to estimate the contaminant capacity of phyllosilicates, providing we apply a correction to rule out the dilution effect of silica. Here, we calculated the REE concentrations expected for unsilicified rocks using the average SiO_2 of cratonic Archean shales as a reference ($\sim$ 60%, data from Condie 1993).

(2) Similarly, the silicified siltstones from Komati River can be used to represent a mixed contaminant of K-feldspar and sericite. Their average composition is corrected from their excess SiO_2 using the average SiO_2 of Archean siltstones ($\sim$ 60%, data from Condie 1993).

(3) The composition of the Komati River KRC5 reference layer is used to estimate the contaminant capacity of carbonates. Because the $18wt\%$ SiO_2 of the rock is exclusively linked to the siliceous matrix, and because ankerite is free of silica (Deer et al. 1966), we applied the same correction as before using a SiO_2 content of $0wt\%$.

(4) The Buck Reef black cherts contain significant amount of carbonaceous matter as well as possible other minor detrital phases. Both these contributions may account for the variability of black chert composition, but may have a limited effect given the very low trace element concentrations in these samples. Because of the high silica content, the composition of the carbonaceous matter contaminant cannot
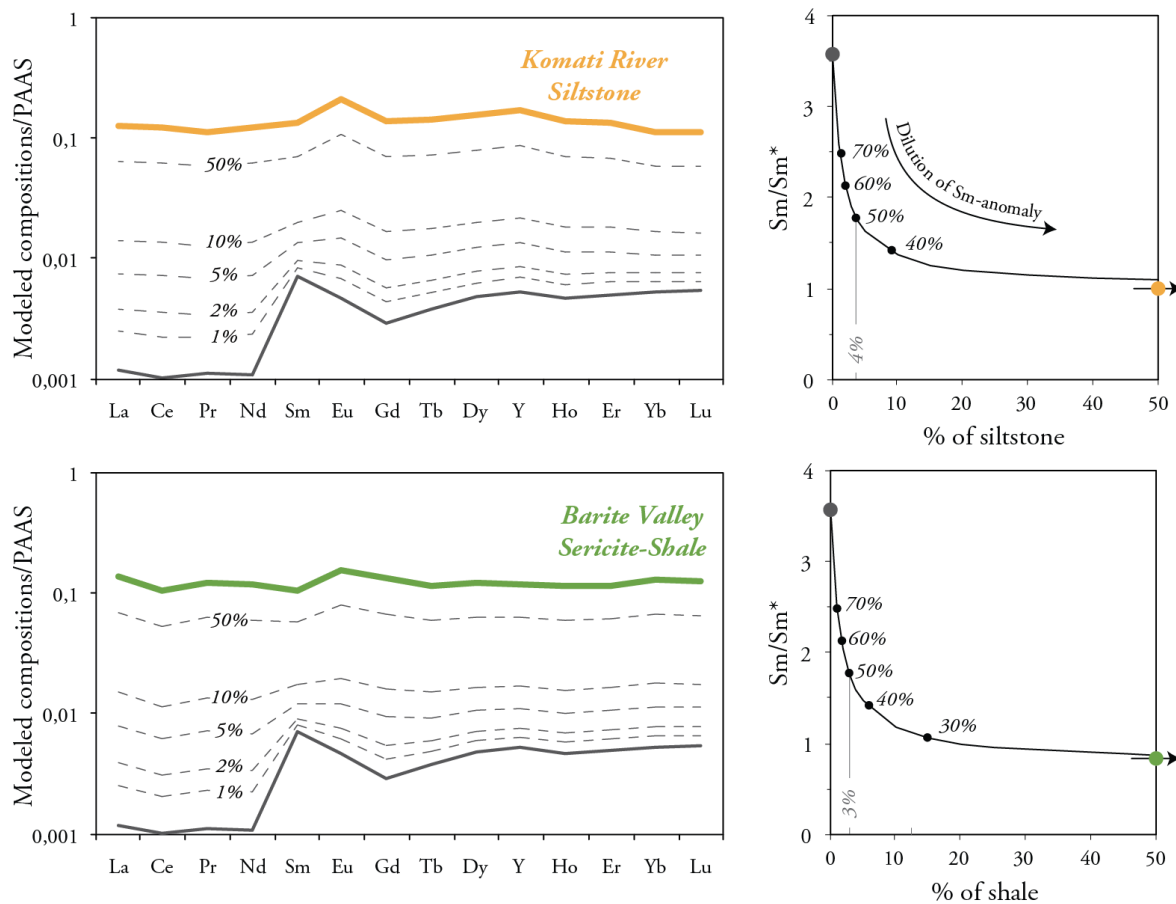
FIGURE 4.32 – *PAAS-normalized REE models of average Buck Reef white chert composition conta-minated by increasing fractions of Komati River siltstone and Barite Valley shale. The composition of siltstone and shale is corrected from the dilution effect of silica (see text for explanation). The Sm anomaly, expressed as Sm/Sm*, is used to monitor the preservation of white chert signature while contaminated. Only 3 to 4% of continentally-derived contaminant can obscure the silica composi-tion.*

be isolated and corrected from the silica dilution. Thus, we use the average composition of black cherts as the contaminant, knowing that this will overerestimate the carbonaceous matter fraction required to disturb the silica composition.

In the Figures 4.32 and 4.33, the chemical signal of each phase is added to that of the pure Buck Reef chert, and we quantify their efficiency as contaminant by monitoring the disappearance of the primary positive Sm-anomaly.

We show that only 3 to 4% of continental-derived particles, *i.e.* shale and silts-tone, are required to lower the Sm-anomaly by a factor of 2. Carbonates are even more efficient as only 2% is enough for similar results. On the contrary, carbo-
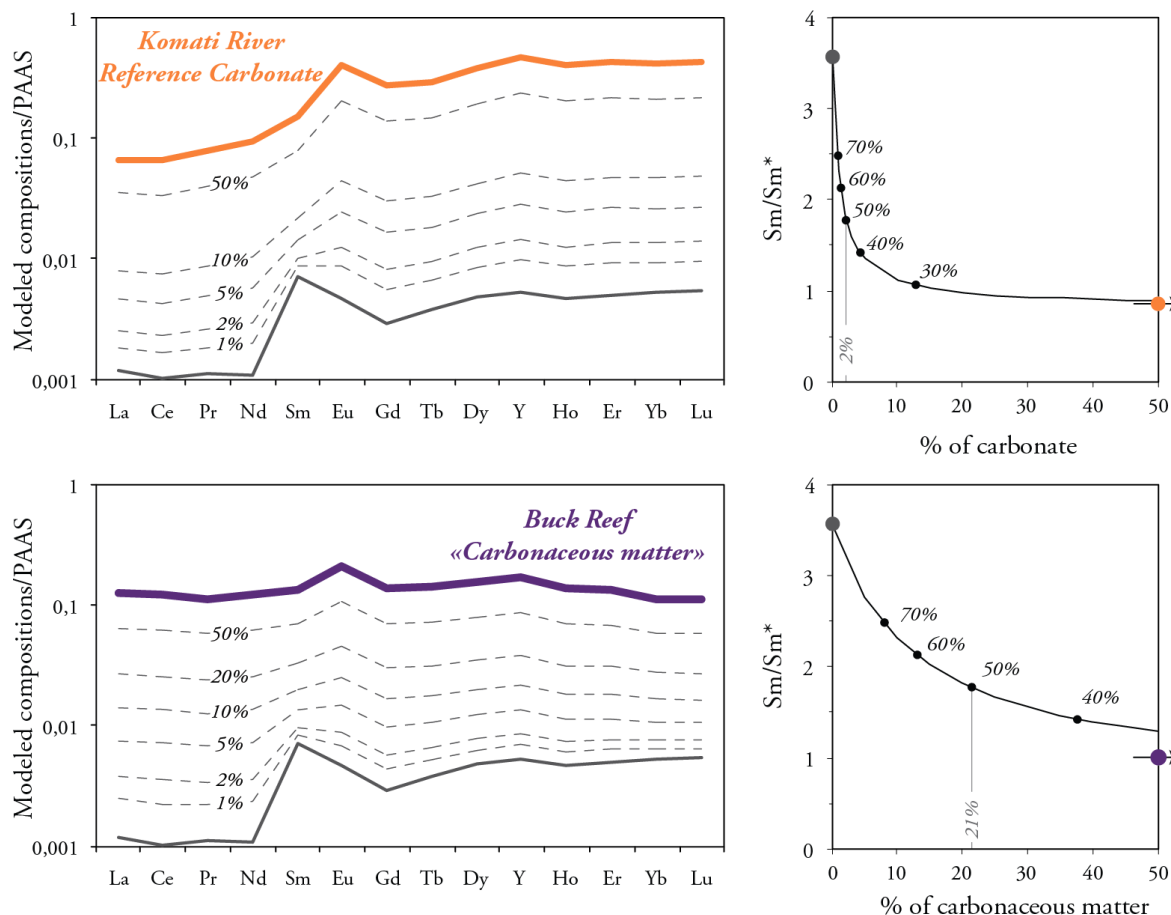
FIGURE 4.33 – *PAAS-normalized REE models of average Buck Reef white chert composition contaminated by increasing fractions of Komati River carbonate and Buck Reef cabonaceous-matter-rich black chert (see text for explanation). The Sm anomaly, expressed as Sm/Sm^*, is used to monitor the preservation of white chert signature while contaminated. Carbonates hide the silica composition after 2% of contamination whereas carbonaceous matter requires about 21%.*

naceous matter seems to have a limited effect, which we attribute to lower trace elements in this material.

Thus, the cherts are very easily contaminated by the presence of clastic particles, and such contribution needs to be ruled out before any attempt is made to use the chert chemistry as paleo-environment proxy. Careful petrographic observations are of crucial importance, and we recommend that chert used for this purpose display extremely low trace element concentrations. Especially the sum of REE and HFSE must not exceed $1ppm$, whereas SiO_2 must approach $100wt\%$ and other major elements must be close to or below the detection limit. Al_2O_3 especially is a useful indicator to estimate the presence of phyllosilicates in cherts.

In these very conditions, we can be confident that the chert chemistry represents that of the siliceous phase. However, because the trace element contents are extremely low and because we do not know how trace elements are distributed between fluid and the silica phase, we believe that the composition of these cherts are unlikely to provide useful information about the composition and chemical characteristics of Archean seawater.

Although carbonates appeared to be the most efficient contaminants, they nonetheless provide key information as these minerals are able to retain the chemical composition of the fluid from which they precipitated (Veizer et al. 1989, Lee et Byrne 1992, Kamber et Webb 2001, Van Kranendonk et al. 2003, Nothdurft et al. 2004, Bau et Alexander 2006, Allwood et al. 2010). If the carbonates were co-precipitated with the siliceous phase, and if they represent at least 2% of the chert while continental contributions are lacking, then the bulk chemistry could represent the fossilized composition of the ambient fluid from which the chert formed.

In conclusion, the use of silica in cherts for past environment reconstructions is strongly limited by the very common presence of additional phases. We believe that part of the studies that recognized seawater-signatures in Archean cherts and BIFs may have, in fact, record the chemistry of the carbonate fraction. Thanks to the Buck Reef cherts, we provide here the only known Archean sample that can be undoubtedly considered as pure, marine precipitates, and whose composition represents the trace element content hosted by the silica phase. The next step for past environment reconstructions would be to put constrains on the fractionation of the various elements during the precipitation of silica. Such investigations are still lacking today whereas they are of crucial importance to retrieve the primary fluid composition from that of the precipitated silica.

4.2.11   Conclusions

The compositions of cherts from the three sites studied here are highly variable. These compositions reflect mainly the environment in which they formed, regardless of the formation process.

The cherts can be interpreted as a mixture of two main components : (1) silica, which contains extremely low concentrations of trace elements and contributes only SiO_2 to the bulk composition of the chert, and (2) another phase that dominates the trace element composition and varies from site to site.

At the Komati River site, the second component is detrital and consists of K-feldspar, clay and very minor amount of a Ti-phase (probably ilmenite), zircon and other heavy minerals. The clastic particles were derived mainly from the dacitic volcanics that stratigraphically underlie the cherts, with an additional component from granitic rocks. The proportion of different detrital phases was influenced by sorting during transport and deposition. The total amount of detrital component in our samples varies from <10% to about 30% and we estimated that 4% is enough to dominate the trace element composition of the chert.

At Barite Valley, there are three types of cherts.

(1) A concordant layer which we interpret as a *primary chemical precipitate* deposited on the seabed from hydrothermally-influenced, bottom seawater. Its composition retains some key characteristics of modern oceans, but the chemistry is controlled by the presence of <2-5% of carbonate.

(2) *Silicified shales*. We showed that these are secondary cherts that were silicified very early after deposition. Their major element compositions reflect a binary mixture of microquartz with 4 to 13% of sericite. Whereas the former acts as a diluent, the later exclusively controls the trace element composition.

(3) *Cherts precipitated in large dykes* that cross cut through the silicified units. Despite the high amount of siliceous fraction, at least 96%, their composition is controlled by the 3-4% of particles inherited from the erosion of fracture walls. The presence of high Ba is explained by its enrichment in the eroded, phyllosilicate fraction. Its location in sericite rims is interpreted as evidence for hydrothermal fluid contribution, at least during the early diagenesis of surrounding shales.

The Buck Reef cherts were identified as chemical precipitates from seawater and

are characterized by remarkably low concentrations of almost all trace elements. The black cherts contain a significant amount of carbonaceous matter in various forms, one of which is of detrital origin. Accordingly, they are enriched in trace elements compared to the white cherts, and their composition is much more variable. Varying contributions of carbonaceous matter or other micro-detrital particles (less than 0.5%) can account for the compositions.

The white cherts have near 100% SiO_2 and their trace element content is exclusively controlled by the siliceous fraction. We recognized some of the characteristic REE anomalies of modern seawater, including strong LREE depletion and positive La and Y anomalies. An unusual feature are the Sm anomalies that have never been observed in any terrestrial rocks. We envisage several possible explanations : (1) the possible existence of Sm-phosphates ; (2) the magnetic retention of Sm onto Fe- and/or Cr-oxides ; (3) the contribution of hydrothermal fluids that interacted with ultramafic rocks ; (4) specific fission processes ; (5) the fractionation of samarium during the precipitation of amorphous silica.

In conclusion, the geochemistry does not allow the recognition of various chert types as their composition is independent from their formation processes. For example, the primary cherts (C-chert) from the three sites have very different compositions, while S-cherts and F-cherts from the Barite Valley site have similar compositions.

The chert chemistry is strongly influenced by the presence of even minor amounts of detrital or other components and provides little direct evidence about the composition of the fluid from which they precipitated. Thus, only very pure cherts with extremely low trace element contents can be interpreted as pure siliceous precipitates. Additional petrographic and field evidence is needed to distinguish seafloor-deposited cherts from cherts of other origins (*i.e.* hydrothermal, magmatic, metamorphic).

To interpret the chert composition in terms of paleo-seawater chemistry, we lack the partition coefficients between the fluid and the siliceous, colloidal phase that precipitated at or near the sea floor. Until we can improve our knowledge of REE fractionation by silica, Archean cherts cannot be used as reliable paleo-seawater proxies, except if their composition is dominated by carbonates. Some informations

can still be derived from Si and O isotopes, which will be hosted in the dominant silica component.

Acknowledgments

5 | Composition isotopique des cherts Archéens.

Dans ce chapitre, j'utilise les compositions isotopiques de cherts de Barberton (Si et O) afin d'identifier la nature et l'origine des fluides impliqués dans leur formation.

——————————————————————

In this chapter, I use the Si and O isotopic composition of Barberton cherts in order to identify the nature and origin of the fluids from which they formed.

5.1   Avant-propos.

Dans le chapitre précédent, nous avons vu que les compositions géochimiques des cherts Archéens est largement contrôlée par les différentes phases non-siliceuses qu'ils contiennent. Cette caractéristique, imputable aux concentrations extrêmement faibles portées par la silice, limite sérieusement l'utilisation de la géochimie des cherts pour les reconstructions paléo-environnementales. Nos résultats montrent en outre qu'une telle composition est indépendante des processus qui ont vu leur formation, et qu'il n'est donc pas possible de distinguer par cette approche les trois types de chert définis dans ces travaux.

Nous avons montré que seuls les cherts les plus purs sont susceptibles d'avoir enregistré la composition du fluide dont ils sont issus. Une minéralogie exclusivement siliceuse (*i.e.* microquartz pur pour les C-cherts, quartz, calcédoine et/ou microquartz pour les F-cherts) et des concentrations extrêmement faibles en éléments majeurs et traces (*i.e.* REE, HFSE, Al, K) sont ainsi le seul critère fiable existant à ce jour pour reconnaître un précipité chimique pur, et dont la composition représente effectivement celle de la phase siliceuse primaire.

Cependant, même dans ces cas extrêmes, les proxys océaniques couramment utilisés pour identifier un signal d'eau de mer dans les cherts n'en sont pas fiables pour autant puisqu'ils ont été identifiés dans des quartz d'origines variées, à savoir dans les cherts océaniques de Buck Reef, mais aussi dans des quartz hydrothermaux, métamorphiques et pegmatitiques.

Si ces contraintes limitent l'utilisation des éléments majeurs et traces, la composition isotopique des cherts, elle, peut s'avérer un outil puissant. Un grand nombre de travaux utilise les isotopes de l'oxygène et du silicium dans les sédiments chimiques anciens afin de retrouver les températures ambiantes au moment de leur mise en place. Les récents travaux de Johanna Marin-Carbonne et collaborateurs montrent en outre qu'il est possible par cette approche de déterminer le degré de préservation des compositions isotopiques primaires et d'identifier les différents fluides ayant contribué à la formation des cherts.

Dans ce chapitre, je présente les compositions isotopiques du silicium et de l'oxygène de six échantillons précédemment caractérisés en termes de contexte de mise en place et composition géochimique. Ces analyses ont été réalisées sur la SIMS (*Secondary Ion Mass Spectrometer*) du CRPG de Nancy sous la direction de Marc Chaussidon et Claire Rollion-Bard que je remercie. Une première partie est dédiée à la préservation du signal primaire dans ces échantillons et une deuxième partie s'attache à comprendre l'origine des fluides dont ils sont issus, afin d'apporter plus de contraintes aux modèles développés dans le Chapitre 2 quand à la formation des cherts de Barberton.

Nos résultats nous font douter des critères de préservation proposés par Marin-Carbonne et al. (2012), mais offrent une vision relativement claire des conditions de mise en place des cherts de Komati River et Barite Valley, les premiers en tant que C-chert en environnement clastique et les seconds en tant que F-chert dans un paleo-système hydrothermal de basse température. Les cherts de Buck Reef sont quand à eux toujours ambigus et montrent des compositions isotopiques en parfaite opposition dans deux échantillons de chert blanc prélevés à quelques mètres d'intervalle, pourtant identiques en termes de composition chimique et minéralogique.

5.2 The use of isotopes for chert recognition and paleo-seawater temperature estimations.

As emphasized in this manuscript, Precambrian cherts have been extensively studied for paleo-environment reconstructions. Their trace element composition is commonly used as proxies for the recognition of Archean fluid chemistry and their isotopic composition is used to infer the temperature and origin of these fluids (*e.g.* Perry 1967, Knauth et Epstein 1976, Knauth et Lowe 1978, Karhu et Epstein 1986, Sugitani 1992, Winter et Knauth 1992, Sugitani et al. 2002, Knauth et Lowe 2003, Perry et Lefticariu 2003, Robert et Chaussidon 2006).

Oxygen isotopes in particular have been used to assess the temperature of Archean seawater, and provide evidence for a decrease of about $50°C$ from the Precambrian until today according to Knauth et Lowe (2003). Coupled or not with silicon, the oxygen isotopic composition in cherts indicate a range of Archean seawater temperatures. Although high temperature of about $90\text{-}160°C$ had been proposed by Paris et al. (1985) and de Wit et al. (1987a), most studies converge on lower temperatures, *i.e.* $\sim 70°C$ for Knauth et Lowe (1978), Knauth (2005) and Robert et Chaussidon (2006), $55\text{-}85°C$ for Knauth et Lowe (2003), $55°C$ for Van den Boorn et al. (2010), down to $40°C$ for De Ronde et de Wit (1994) and more recently $\sim 37\text{-}52°C$ for Marin et al. (2010).

All these studies rely on the temperature dependance of oxygen and silicon fractionation in natural systems. Fractionation equations for oxygen are shown in Table 5.1 between a fluid and quartz (Matsuhisa et al. 1979), amorphous silica (Kita et al. 1985) or chert (Knauth et Epstein 1975). De La Rocha et al. (1997) reported fractionation of silicon in diatoms in the 12 to $22°C$ temperature range, but no other study has yet been conducted on the temperature dependance of silicon fractionation.

Oxygen fractionation between fluid and various silica phases			
Minerals	**1000 ln α**	**T (°C)**	**Références**
Quartz - H_2O	3,34 x $(10^6/T^2)$-3,31	250-500	Matsuhisa et al., 1979
Amorphous silica - H_2O	3,52 x $(10^6/T^2)$-4,35	34-93	Kita et al., 1985
Chert - H_2O	3,09 x $(10^6/T^2)$-3,29		Knauth et Epstein, 1975

TABLE 5.1 – *Temperature-dependant fractionation equations between a fluid and various forms of silica.*

However, before using isotopic compositions of Archean cherts for estimating paleo-seawater temperature, several constraints need to be considered :

(1) The isotopic composition of paleo-seawater must be estimated. It has been concluded that Precambrian seawater does not depart from modern value by more than 2‰ (see Muehlenbachs 1998, for a review), a consistency that is probably inherited from buffering processes during hydrothermal interaction between seawater and the oceanic crust (Muehlenbachs et Clayton 1976, Gregory et Taylor 1981, Muehlenbachs 1998, Lécuyer et Allemand 1999, Gregory et al. 2008). Thus, Precambrian seawater is generally assumed to have a $\delta^{30}Si$ at $\sim$ 0‰ although an upper limit of +1.3‰ has been proposed by Van den Boorn et al. (2010).

(2) The chert isotopic composition must be related to that of seawater, *i.e.* the chert must have formed, at least in part, from oceanic fluids.

(3) The isotopic composition must have been preserved from secondary isotopic resetting (Becker et Clayton 1976, Perry et Lefticariu 2007), especially for oxygen isotopes which are sensitive to secondary fluid circulations (*e.g.* Perry et Lefticariu 2003, Marin-Carbonne et al. 2012) whereas silicon isotopes are thought the be unaffected by metamorphic or hydrothermal fluid circulations (*e.g.* André et al. 2006).

The use of isotopic compositions of cherts thus depends essentially on our capability to recognize the origin of the studied cherts and on the preservation of their primary compositions from secondary changes during diagenesis and associated fluid circulations.

Major advances have been made on these questions by Johanna Marin-Carbonne and co-workers who provided three major papers, Marin et al. (2010), Marin-Carbonne et al. (2011) and Marin-Carbonne et al. (2012), in which they discuss high-resolution, *in situ* oxygen and silicon isotopic data down to a micrometer scale in cherts from various ages (from 1.88 to 3.5Ga).

One of the most important finding of these studies is that the isotopic composition of cherts is much more heterogeneous at a fine scale, as revealed by ion probe analyses with a 2μm spatial resolution (*i.e.* which corresponds to individual microquartz grain analyses) as opposed to bulk analyses (André et al. 2006, Van den Boorn et al. 2007; 2010, Abraham et al. 2011) or *in situ* ion probe or LA-ICP-MS analyses at larger scales (typically 25μm and more; Robert et Chaussidon 2006, Steinhoefel et al. 2010).

Three key issues emerge from their data : (1) the origin of the microquartz, which could be formed by the diagenesis of an amorphous silica precursor (C-chert), by precipitation from hydrothermal fluids (F-chert) or by the replacement of sedimentary of volcanic precursors (S-chert); (2) the effect of diagenesis and subsequent metamorphic fluid circulation on the chert isotopic composition; and (3) the preservation of the primary isotopic signal inherited from diagenesis.

Marin-Carbonne et al. (2012) proposed five criteria which can be used to recognize cherts that preserved their primary isotopic composition.

Criterion (1) : the chert must be essentially composed of microquartz and free of detrital and other components (Knauth 1994), a prerequisite that is not self-sufficient for oceanic cherts, but that can be reinforced by field evidence such as those developed in Chapter 2 (*i.e.* layering, sedimentary structures, field relationship with surrounding units, etc). The lack of evident replacement of carbonate or silicate minerals is also required.
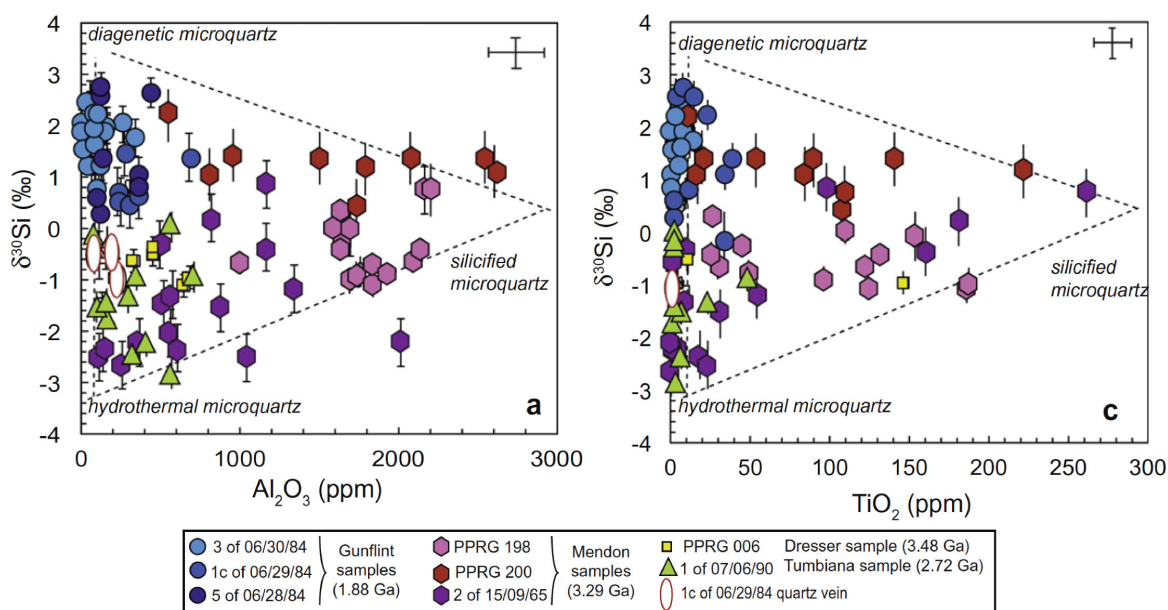
FigurE 5.1 – *Silicon isotopic composition vs. Al₂O₃ and TiO₂ diagrams showing the three possible microquartz end members : diagenetic with positive δ³⁰Si and low trace element content, hydrothermal with negative δ³⁰Si and low trace element content and silicified with near-zero δ³⁰Si and high trace element content. This figure is from Marin-Carbonne et al. (2012) and shows the repartition of Gunflint (1.88Ga), Mendon (3.29Ga), Dresser (3.48Ga) and Tumbiana cherts (2.72Ga) between these end members. Quartz veins are shown in circles.*

Criterion (2) : the bulk $\delta^{18}O$ must be close to the maximum $\delta^{18}O$ value measured in other cherts from the same age (Knauth et Lowe 1978). This condition relies on the contrasting low $\delta^{18}O$ of meteoric fluids compared to seawater and on the temperature dependance of quartz-water fractionation (decreasing with T°) (Knauth et Lowe 2003).

Criterion (3) : the range of $\delta^{18}O$ in the chert must be large at the micrometer scale, *i.e.* ~ 10‰ at $2\mu m$. This criterion emerged from the inferred formation of oceanic cherts : the idea is that an amorphous silica precursor transformed to chert by successive dissolution-precipitation processes (Knauth 1994). In a closed system, each precipitating microquartz grain will record the $\delta^{18}O$ of the remaining fluid, leading to highly heterogeneous isotopic compositions at the single-grain scale if the primary values are preserved from secondary resetting (Marin et al. 2010).

Criterion (4) : similar to the above criterion, the range of $\delta^{30}Si$ must be large in pure diagenetic microquartz, *e.g.* 1.7-4.5‰ in Marin-Carbonne et al. (2012) as a

result of the successive dissolution-precipitation processes and distillation of the fluid in a closed system. Marin et al. (2010) reported that the range of $\delta^{30}Si$ should be similar to that observed for $\delta^{18}O$.

Criterion (5) : trace elements (Al_2O_3, K_2O and TiO_2), coupled with $\delta^{30}Si$ help to unravel the origin of the microquartz as shown in Figure 5.1 (*i.e.* diagenetic, hydrothermal or secondarily produced by silicification) (Van den Boorn et al. 2007; 2010, Marin-Carbonne et al. 2012). Marin-Carbonne et al. (2012) proposed three distinct components that can account for the $\delta^{30}Si$ range in Archean cherts : (a) *silicified microquartz* (S-chert) enriched in Al_2O_3, K_2O or TiO_2 and having $\delta^{30}Si$ close to 0‰ (*e.g.* Mendon samples in Fig.5.1) ; (b) *hydrothermal microquartz* with low trace elements and negative $\delta^{30}Si$ (*e.g.* Tumbiana samples in Fig.5.1) ; and (c) *diagenetic microquartz* with similar low trace elements but positive $\delta^{30}Si$ (*e.g.* Gunflint samples in Fig.5.1).

If the above criteria are realized, then the isotopic composition of the chert is preserved and can be used to assess both the nature and temperature of the fluid from which they formed.

In this chapter, we use the approach of Marin-Carbonne et al. (2012) in order to characterize a selection of cherts from the Barberton belt, and to test the various hypotheses we developed in Chapter 2 and 3 for their origin and formation. Each site is discussed in terms of chert composition, chemical preservation and origin of the primary fluid. Attempt is made to propose temperature estimations, either for the primary depositional environment or the secondary diagenetic conditions.

Miocene Quartz			NL615		
Analysis #	δ ³⁰Si /²⁸Si	Error (1σ)	Analysis #	δ ¹⁸O /¹⁶O	Error (1σ)
1	-33,157	0,15	1	7,009	0,10
2	-31,913	0,18	2	7	0,13
3	-33,129	0,18	3	7,217	0,10
4	-32,564	0,23	4	6,973	0,10
5	-32,256	0,24	5	7,274	0,09
6	-32,192	0,24	6	7,435	0,11
7	-32,184	0,24	7	7,315	0,11
8	-32,22	0,23	8	7,439	0,09
9	-31,703	0,19	9	6,9	0,11
10	-31,383	0,19	10	6,935	0,08
11	-32,145	0,18	11	6,25	0,06
12	-31,117	0,19	12	6,269	0,08
13	-32,017	0,21	13	6,697	0,07
14	-31,658	0,21			
15	-30,635	0,20			
16	-31,256	0,21			
17	-30,866	0,23			
18	-30,759	0,22			
19	-30,598	0,19			

TABLE 5.2 – *Analytical results for standards used for Si and O estimations. Estimated uncertainties (1σ) are ±0.24‰ for oxygen and ±0.13‰ for silicon.*

5.3   Method and studied samples.

Six samples from the Barberton Belt were selected for *in situ* Si and O isotopic analyses, and all but one have been described in terms of petrography and chemical composition in the previous Chapters 2 and 3.

Two black chert layers (KRC8, KRC11) are from the top of Komati River turbiditic layers. They represent C-cherts formed by the chemical precipitation of silica on suspended clay particles and forming, at first, a siliceous ooze on the seafloor (Chapter 2).

Two white chert layers (BRC20 and BRC22) were selected from the Buck Reef black-and-white banded chert unit. They were also chemically precipitated on the seafloor (C-chert), probably as amorphous silica, but they lack detrital contributions (Chapter 2).

Two fracture-filling black cherts (FTC4 and FTC17) are from the Barite Valley dykes . Both formed by the precipitation of silica from Si-rich fluids circulating through the sedimentary pile (Chapter 3). Sample FTC17 was not included in previous chapters and some of its geochemical characteristics will be presented here.

These samples were chosen (1) because they contain only few secondary veins, or no vein at all, which guarantee their preservation, at least at the macroscopic scale, and (2) because they were not secondarily produced, *i.e.* they are not S-chert issued from the silicification of any carbonate or other protolith, although some of our samples contain significant clastic components : K-feldspar and sericite at Komati River, and sericites at Barite Valley (FTC4 only). Buck Reef samples are exclusively composed of microquartz.For the six, we intended to unravel their origin and the nature of the fluid that precipitated.

Analyses were performed on the Cameca IMS 1270 ion microprobe at CRPG (Nancy, France) and supervised by Marc Chaussidon and Claire Rollion-Bard. The procedure follows the method described in Robert et Chaussidon (2006), Marin et al. (2010), Marin-Carbonne et al. (2011) and Marin-Carbonne et al. (2012) and is detailed in Annexe A.4.

The beam diameter was less than $5\mu m$, which limited the number of grain analysed at the same time as microquartz is typicall 2 to $20\mu m$ in size. Between 15 and 62 measurements were obtained for each sample for both silicon and oxygen isotopes.

A summary of the results is listed in Table 5.3 and full data are available in Annexe A.4. The results are expressed as per mil deviations from the reference standards Miocene quartz for oxygen and NL615 for silicon ($\delta^{18}O_{NL615} = +18.4\text{‰}$; $\delta^{30}Si_{QuartzMiocene} = -0.69\text{‰}$), using the delta notation of Equations 5.1 and 5.2 :

$$\delta^{18}O = \left[\frac{(^{18}O/^{16}O)_{Ech.}}{(^{18}O/^{16}O)_{Std.}} - 1\right] \times 1000 \qquad (5.1)$$

$$\delta^{30}Si = \left[\frac{(^{30}Si/^{28}Si)_{Ech.}}{(^{30}Si/^{28}Si)_{Std.}} - 1\right] \times 1000 \qquad (5.2)$$

Standard analyses are given in Table 5.2 where the precision of the data is at least $\pm0.24\text{‰}$ and $\pm0.13\text{‰}$ for oxygen and silicon composition respectively.

Age	Site	Sample	$\delta^{18}O$ (‰)				
			Minimum	Maximum	Mean value		Range
3432 Ma	Komat River	KRC8	16,25	17,48	17.13 ± 0.17	*(n = 16)*	1.23
		KRC11	18,60	20,17	19.35 ± 0.34	*(n = 62)*	1.57
		KRC8, vein	16,25	17,31	16.83 ± 0.17	*(n = 5)*	1,06
3416 Ma	Buck Reef	BRC20	19,93	21,09	20.58 ± 0.34	*(n = 20)*	1.15
		BRC22	19,44	20,67	20.01 ± 0.34	*(n = 28)*	1.23
3260 Ma	Barite Valley	FTC4	20,67	21,35	20.97 ± 0.11	*(n =15)*	0.68
		FTC17	23,35	24,26	23.68 ± 0.34	*(n = 20)*	0.92

Age	Site	Sample	$\delta^{30}Si$ (‰)				
			Minimum	Maximum	Mean value		Range
3432 Ma	Komat River	KRC8	-0.69	+1.61	$+0.13 \pm 0.23$	*(n = 41)*	2.30
		KRC11	-1.89	+3.89	$+0.76 \pm 0.31$	*(n = 29)*	5.78
		KRC8, vein			*not analysed*		
3416 Ma	Buck Reef	BRC20	-3.10	-1.4	-2.23 ± 0.29	*(n = 20)*	1.70
		BRC22	+0.55	+1.58	$+1.13 \pm 0.28$	*(n = 20)*	1.03
3260 Ma	Barite Valley	FTC4	-4.50	-0.19	-1.37 ± 0.22	*(n = 60)*	4.31
		FTC17	-1.89	+0.22	-0.91 ± 0.32	*(n = 20)*	2.11

TABLE 5.3 – $\delta^{30}Si$ and $\delta^{18}O$ compositions of microquartz in Komati River black cherts from the top of turbidite units. Each sample is presented as a probability density function F(X). Vertical solid lines show the mean value of each sample and the dotted lines show additional peaks representative of multiple distribution of the silicon data whereas oxygen displays an unimodal distribution.

5.4 Description of isotopic compositions.

Results are summarized in Table 5.3 and shown as probability density functions in Figures 5.2, 5.4 and 5.5. The calculation of such function takes into account the uncertainty of each measurement and is calculated following the method of Marin et al. (2010) and Marin-Carbonne et al. (2012). The following text is taken from these papers and adapted here to inform the reader about the method.

Each measurement is replaced by a gaussian curve $f_{\delta^{30}Si,\sigma}$ as defined by Equation 5.3.

$$f_{\delta^{30}Si,\sigma} = \left[\frac{1}{\sigma \times \sqrt{2\pi}}\right] \times exp\left[\frac{-(x - \delta^{30}Si)^2}{2\sigma^2}\right] \tag{5.3}$$

The integral of $f_{\delta^{30}Si,\sigma}$ between x_1 and x_2 gives the probability that the true $\delta^{30}Si$ of the chert is between x_1 and x_2 (Equation 5.4). $F(x)$ is the density probability function describing the variations of $\delta^{30}Si$ in the sample, and is calculated from Equation 5.5. It is defined as the sum of individual $f_{\delta^{30}Si,\sigma}$ divided by the number N of measurements.

$$P(x) = \int_{-\infty}^{+\infty} F(x) \times dx = 1 \tag{5.4}$$

$$\text{with } F(x) = \sum_{j=1}^{j=N} \frac{f_{\delta^{30}Si_j,\sigma_j}}{N} \tag{5.5}$$

The use of $F(x)$ allows the comparison between data sets obtained in different sessions when the precision may have varied. We note that the limited number of analyses in some of the samples (*i.e.* for 15 single points) renders less accurate the probability density function calculation, but such approach still allows the characterization of the distribution of $\delta^{30}Si$ and $\delta^{18}O$ in these samples.

5.4.1 Komati River.

Sample KRC8 has $\delta^{30}Si$ values ranging from $-0.69‰$ to $+1.6‰$, corresponding to a relatively large range of $2.3‰$ (Table 5.3). The probability density function of Figure 5.2 shows a bimodal distribution : the first peak, at $+0.1‰$, is close to the mean value of $+0.13 \pm 0.23‰$ in this sample, and the second peak is more positive at $+1.5‰$.

Sample KRC11 is much more heterogeneous and its range of $\delta^{30}Si$ of $5.78‰$ is the largest of the whole sample set. $\delta^{30}Si$ varies from negative to strongly positive values ($-1.89‰$ to $+3.89‰$) with an heterogeneous distribution where several peaks can be identified on the basis of Figure 5.2 : only one peak is in the negative field at $\delta^{30}Si = -1.9‰$ whereas three peaks can be distinguished at $+0.2‰$, $+0.8‰$ and $+2.2‰$ respectively. The $+0.8‰$ peak is the largest and is close to the mean value of $+0.76 \pm 0.31‰$ in this sample.

Both KRC8 and KRC11 have very narrow $\delta^{18}O$ variations of $1.23‰$ and $1.57‰$ respectively, but depart from each other when considering their mean values : $\delta^{18}O$ is $+17.13 \pm 0.17‰$ for KRC8 and $+19.35 \pm 0.34‰$ for KRC11.
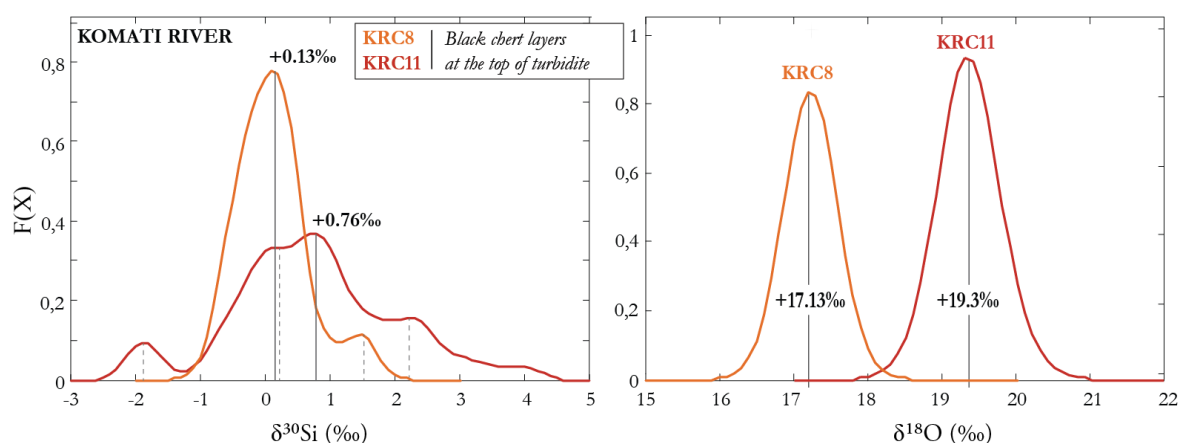
FIGURE 5.2 – $\delta^{30}Si$ and $\delta^{18}O$ compositions of microquartz in Komati River black cherts from the top of turbidite units. The analyses of each sample are presented as a probability density function F(X). Vertical solid lines show the mean value of each sample and the dotted lines show additional peaks representative of multiple distribution of the silicon data whereas oxygen displays an unimodal distribution.
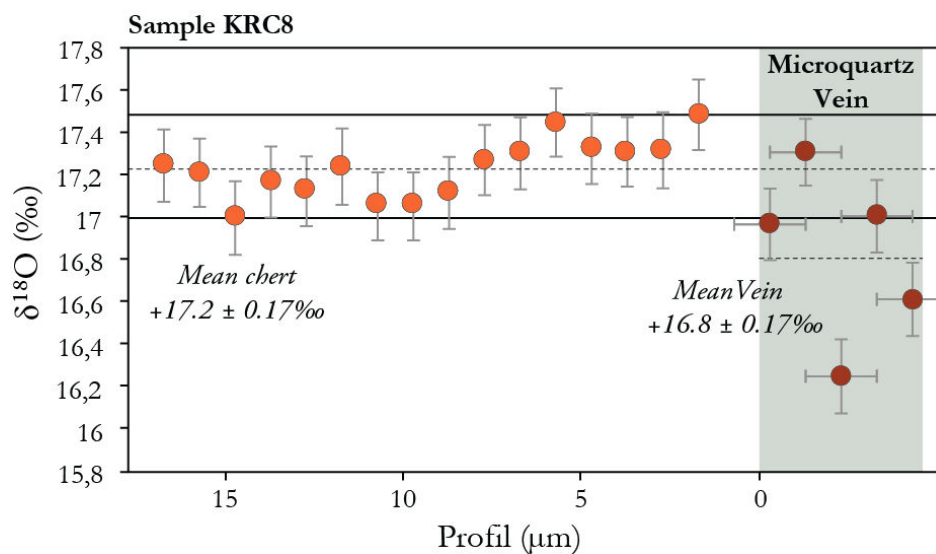
FIGURE 5.3 – *Microscale profile at proximity of a microquartzitic vein in sample KRC8 from Komati River. The vein has a lower $\delta^{18}O$ that seems not to affect the average isotopic composition of surrounding microquartz from the massive chert. Instead, a slight increase of $\delta^{18}O$ above KRC8 average value is observed in microquartz within 8µm of the vein.*

A microquartzitic vein analysed in sample KRC8 gives a lower mean $\delta^{18}O$ value of 16.83 ± 0.17‰. Adjacent to the vein, the $\delta^{18}O$ of the chert seems unaffected, and, instead, slightly increases above its average value within the last 7-8μm to the contact (Fig.5.3).

5.4.2 Barite Valley.

Unlike the Komati River samples, the fracture-filling black cherts from Barite Valley have distinctive negative silicon isotopic compositions as shown in Figure 5.4.

$\delta^{30}Si$ in sample FTC4 varies from -4.50‰ to -0.19‰ corresponding to a very large range of 4.31‰ close to that observed in KRC8 (Table 5.3). Similarly, its distribution is highly heterogeneous around a mean value of -1.37 ± 0.22‰. Two main peaks are observed at -2‰ and -1‰, and two minor peaks are visible at much lower values of -4.5‰ and -3.3‰.

The range is more restricted in sample FTC17, but still significant as it covers 2.11‰. The $\delta^{30}Si$ in this sample ranges from a less negative value of -1.89‰ up to a positive value of $+0.22$‰. However, the positive $\delta^{30}Si$ is limited to one analysis and the mean $\delta^{30}Si$ remains negative at -0.91 ± 0.32‰.
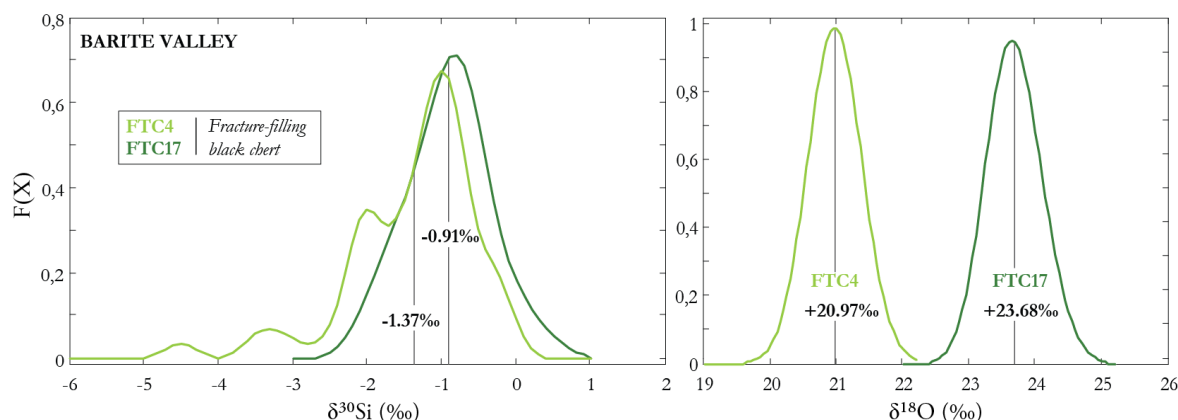
FIGURE 5.4 – $\delta^{30}Si$ and $\delta^{18}O$ compositions of microquartz in fracture-filling black cherts from the Barite Valley site. Each sample is presented as a probability density function F(X). Vertical solid lines show the mean value of each sample. Note the presence of multiple peaks in the $\delta^{30}Si$ composition of sample FTC4 whereas FTC17 is homogeneously distributed around its mean composition. Oxygen values have unimodal distribution in both samples.

The $\delta^{18}O$ in these samples have a very narrow range of less than 1‰, which is the lowest found in this study. FTC17 differs strongly from FTC4 by showing a surprisingly high mean $\delta^{18}O$ of 23.68 ± 0.34‰ whereas the latter has a mean value at 20.97 ± 0.11‰.

5.4.3   Buck Reef.

The Buck Reef white cherts display very narrow ranges of $\delta^{18}O$ similar to those found at Komati River, being restricted to 1.15‰ for BRC20 and 1.23‰ for BRC22 (Table 5.3). The mean $\delta^{18}O$ composition of BRC20 and BRC22 are very similar with values of 20.58 ± 0.34‰ and 20.01 ± 0.34‰ respectively.

Both samples have a $\delta^{30}Si$ range smaller than other samples, being 1.70‰ for BRC20 and 1.03‰ for BRC22, with well-defined unimodal distributions in Figure 5.5. However, given the inferred similar origin for both these samples (*i.e.* C-cherts), we are surprised by their contrasting silicon isotopic compositions. Indeed, BRC20 is strongly negative with a mean $\delta^{30}Si$ of -2.23 ± 0.29‰ (minimum -3.10‰) whereas BRC22 is the most positive of our samples with an average $\delta^{30}Si$ of 1.13 ± 0.28‰ (maximum $+1.58$‰).
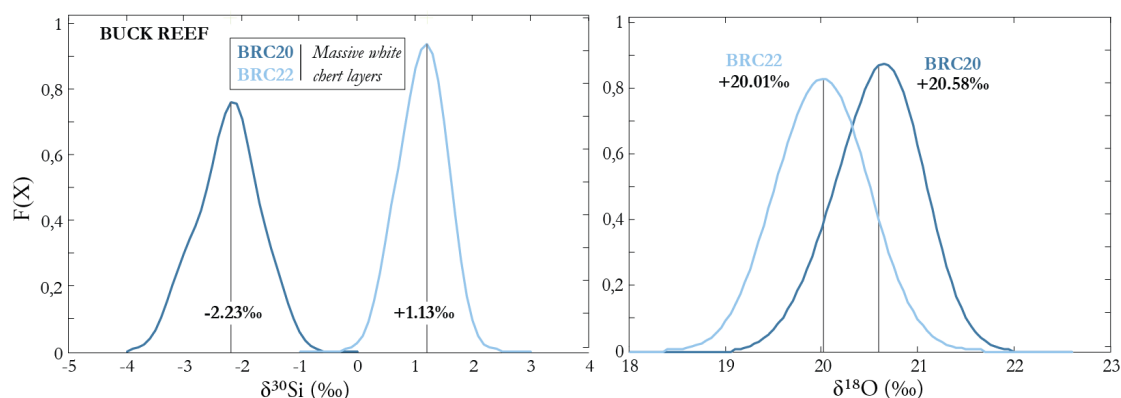
FIGURE 5.5 – $\delta^{30}Si$ and $\delta^{18}O$ compositions of microquartz in massive white chert layers from Buck Reef. Each sample is presented as a probability density function F(X). Vertical solid lines show the mean value of each sample. Both the silicon and oxygen isotopic composition of these samples have unimodal distributions.

5.5 Discussion.

5.5.1 Questioning the reliability of preservation criterion.

According to Marin et al. (2010) and Marin-Carbonne et al. (2012), a large range of $\delta^{18}O$ and $\delta^{30}Si$ represents an heritage from the diagenesis of a primary amorphous precursors. In their models, shown in Figure 5.6, the transformation to chert is thought to occur by successive stages of dissolution-precipitation of this precursor. Each step of microquartz precipitation results in an increase of $\delta^{18}O$ and $\delta^{30}Si$ in the remaining fluid, assuming a closed system, and thus in a similar increase of $\delta^{18}O$ and $\delta^{30}Si$ for each, newly formed, microquartz grain until the chert is fully indurated. This Rayleigh distillation-like process implies evolving isotopic compositions during chert formation and results in a large range of isotopic values at the microscopic scale. The criteria 3 and 4 previously described assumes that if such ranges are observed in a chert, thus its primary isotopic composition is preserved and can be used for studying the nature and temperature of the primary fluid.

A feature common to the six samples studied here is the uniformity of their $\delta^{18}O$ compositions (Fig.5.7). The very narrow ranges observed in individual samples, varying from 0.68‰ to 1.57‰, are far from the 12‰ to 14‰ intra sample variations reported by Marin et al. (2010) for the Gunflint cherts (1.88Ga), which are mostly
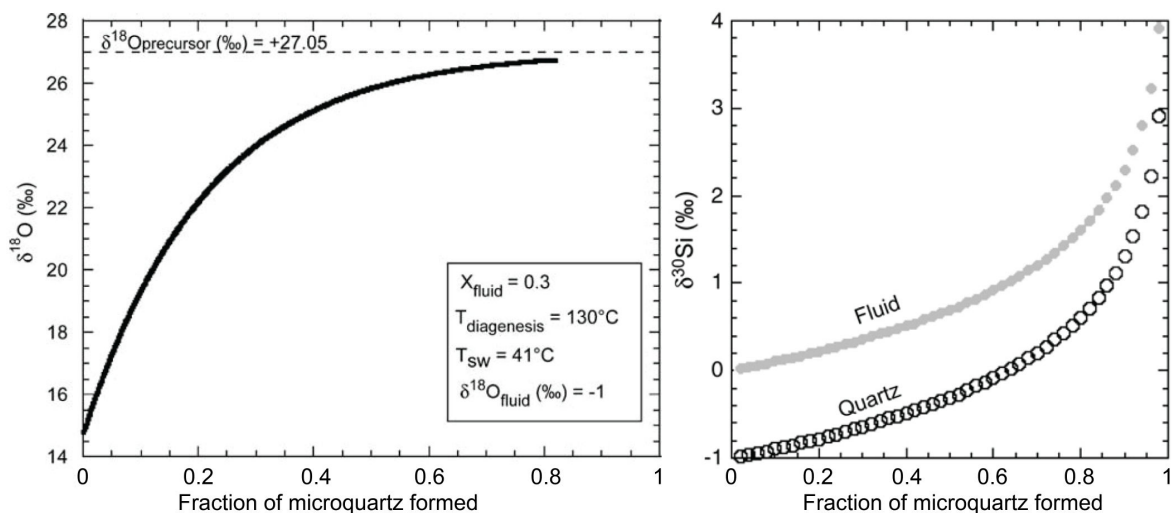
FIGURE 5.6 – *Models from the isotopic evolution of microquartz that precipitates after the dissolution of an amorphous silica precursor in a closed system. (left) Model for $\delta^{18}O$ evolution from Marin et al. (2010) assuming an initial $\delta^{18}O$ of $+27.05‰$ for the silica precursor and $-1‰$ for seawater, fractions of fluid and amorphous silica of 0.3 and 0.7 respectively, and temperatures of 41°C for seawater and 130°C for diagenetic conditions. A difference of 11.9‰ is obtained for $\delta^{18}O$ between the first and last microquartz formed. (right) Model for $\delta^{30}Si$ evolution from Marin-Carbonne et al. (2011) assuming an initial and final $\delta^{30}Si$ of 0‰ and $+4‰$ respectively and a fractionation of $-1‰$ between the dissolved and precipitated silica. Note that we could not find any explanation for the respective convex and concave shapes of these models.*

composed of diagenetic quartz and were preserved from secondary isotopic modifications.

Contrarily to oxygen isotopic data, silicon isotopes display large variations in Figure 5.8, where reference terrestrial reservoir compositions are plotted for comparison. Especially the Komati River and Fig Tree samples have large $\delta^{30}Si$ ranges of 2.11‰ (FTC17) up to 5.78‰ (KRC11). The range is narrower in the Buck Reef cherts, being $\sim 1‰$ and 1.7‰ for BRC22 and BRC20 respectively. Marin-Carbonne et al. (2012) reported a similar range of 1.7‰ in the Gunflint cherts and concluded that this range is directly inherited from the amorphous silica precursor.

Both the narrow $\delta^{18}O$ and large $\delta^{30}Si$ ranges in all the studied samples can be compared to some extent to those observed in cherts from the Mendon Formation (Uppermost Onverwacht Group), which are dated at 3.29Ga and composed essentially of silicified microquartz. Marin-Carbonne et al. (2011) reported a narrow $\delta^{18}O$ range of 3.4‰ and a large range of 3.5‰ for $\delta^{30}Si$. These variations were
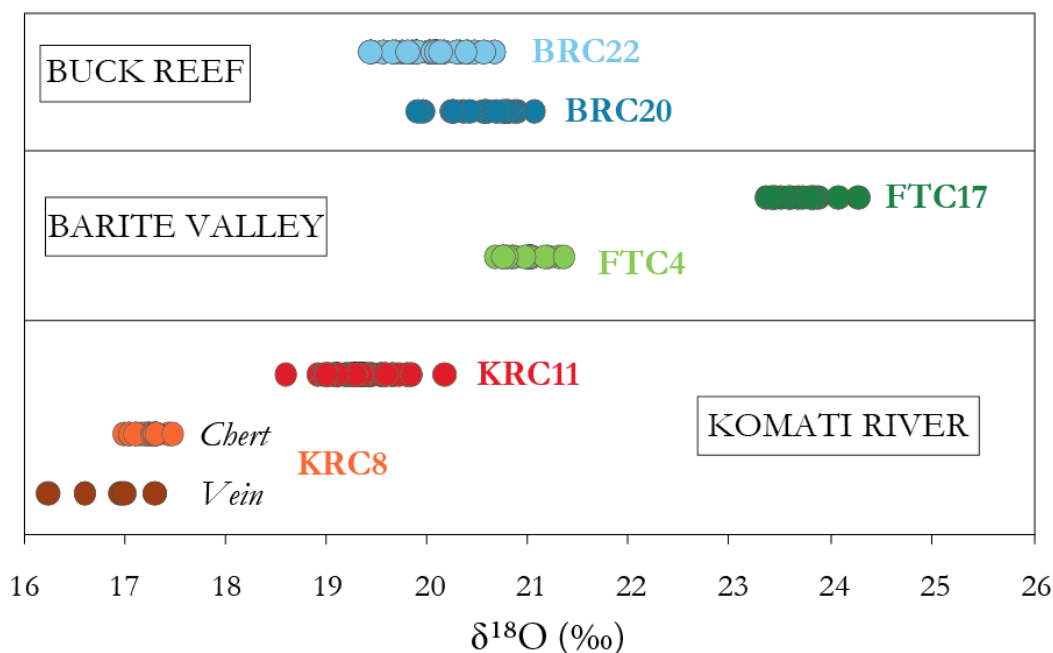
FIGURE 5.7 – *Variations of $\delta^{18}O$ in Barberton chert samples and of a vein from the Komati River site. All samples have very narrow $\delta^{18}O$ ranges, which could result from circulating fluid-induced resetting of isotopic compositions as proposed by Marin-Carbonne et al. (2012). See text for a discussion of such preservation criterion.*

interpreted by the authors as evidence for a reset of the oxygen isotopic system whereas silicon isotopic compositions were preserved during circulations of gold-bearing fluids at temperature of 200-300°C ca. 3230*Ma*. Other evidence for fluid circulations and oxygen isotopic reset across the Onverwacht Group of the Barberton Belt are the abundance of quartz veins and the very low $\delta^{18}O$ of +16‰ to +19‰ observed in a variety of cherts according to Knauth et Lowe (1978).

Thus, according to the criteria proposed by Marin-Carbonne et al. (2012), the lack of large $\delta^{18}O$ range in each of our individual sample would indicate that the primary heterogeneity of individual microquartz has not been preserved and that the oxygen isotopic system was reset by secondary hydrothermal or metamorphic fluid circulations. On the other hand, the silicon isotopes, from the same range-size criterion, would be unaffected, even if fluids circulated at temperature below 300°C.
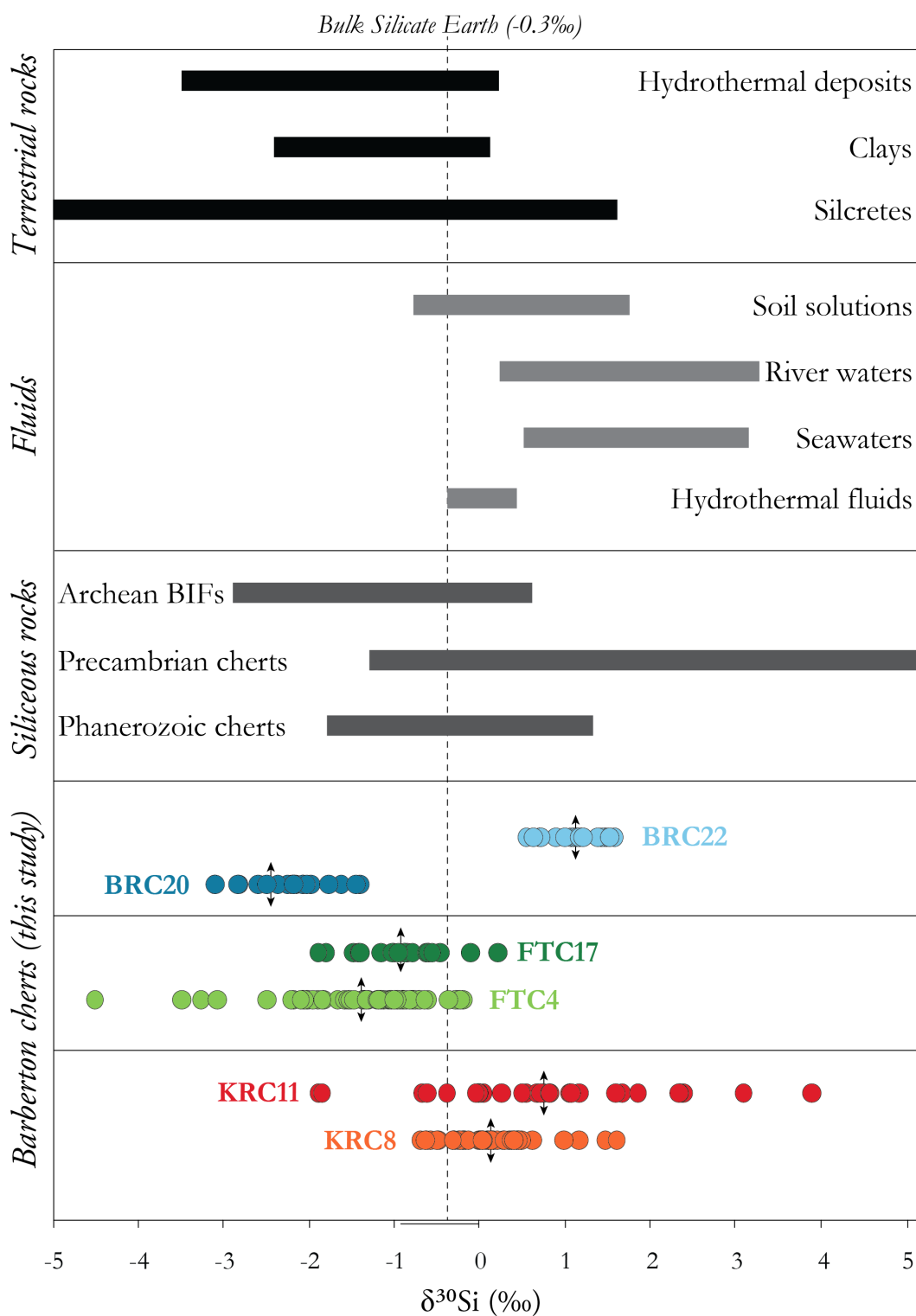
FIGURE 5.8 – *Variations of $\delta^{30}Si$ in Barberton chert samples and ranges of composition of selected terrestrial reservoirs, including terrestrial rocks, waters and siliceous deposits. Reference data are from Douthitt (1982), Ding et al. (1996; 2004), De La Rocha et al. (2000), Alleman et al. (2005), Cardinal et al. (2005), Basile-Doelsch et al. (2005), Ziegler et al. (2005), Reynolds et al. (2006), Robert et Chaussidon (2006), André et al. (2006) and Van den Boorn et al. (2007). Black arrows represent the mean $\delta^{30}Si$ of each sample.*

However, we doubt of the approach and of the reliability of the preservation criterion (*i.e.* the largeness of isotopic ranges). The distillation models developed by Marin et al. (2010) ($\delta^{18}O$) and Marin-Carbonne et al. (2011) ($\delta^{30}Si$) are defined for a closed system where the composition of ambient fluids evolves as a response to microquartz precipitation. Such assumption is questionable for seafloor-deposited cherts because the transformation of colloidal silica to microquartz occurred at, or just below, the seafloor. Evidence for rapid induration of C-cherts at surface conditions were observed in Chapter 2, especially from the slab conglomerates in the Buck Reef site. In these units, the white chert slabs were interpreted as the disrupted equivalent of massive layers, showing that these were already brittle when present at the top of the sedimentary pile.

Thus, we argue that C-cherts precipitated from large, uniform oceanic reservoirs (with or without hydrothermal influxes) and that ambient fluids were able to circulate through the siliceous material, at least until the porosity is sufficiently reduced to prevent such circulation. Until the pores in the silica network disconnected, no closed-system fractionation took place and the fluids would have precipitated microquartz with similar isotopic composition. Rayleigh distillation would be limited to the very final stages of diagenesis, thus limiting the number of microquartz grains with different isotopic compositions. This hypothesis is also relevant for F-cherts, because they precipitated in fractures or veins where long- to short-term circulations of fluids maintain open the system, at least until the precipitated quartz crystals sealed the structure (Chapter 3).

We do not deny that some Rayleigh-type distillation may have occurred in chert during the very last stages of their formation, *i.e.* when it loosed its interconnected porosity. However, we strongly believe that the narrowness of isotopic variations is not a self-sufficient preservation criterion and needs to be reinforced by combining with other local evidence, as will be discussed for each site in the following section.

5.5.2 Recognition of silica sources.

In this section, we will use the terminology of Marin-Carbonne et al. (2012) to described the various types of microquartz that can be encountered in our samples,
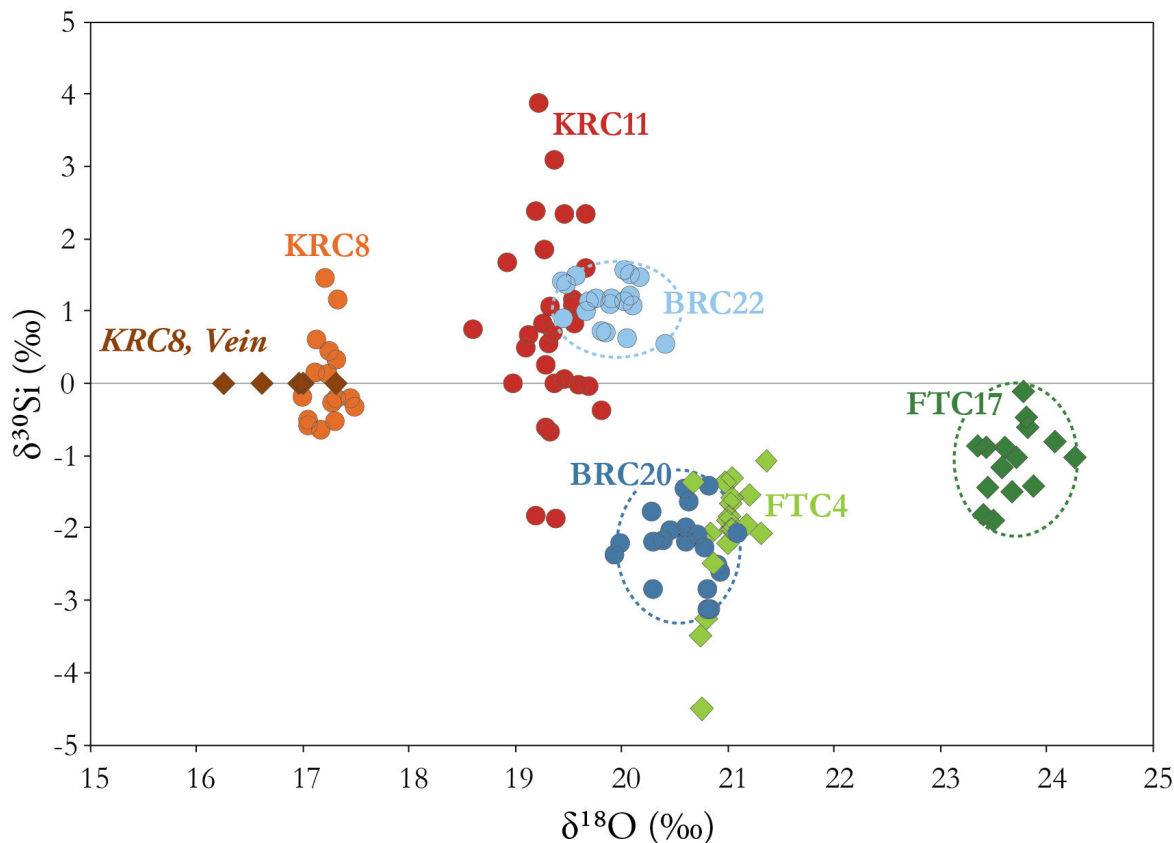
FIGURE 5.9 – $\delta^{18}O$ vs. $\delta^{30}Si$ diagram for the Barberton chert samples and for the vein in sample KRC8 from the Komati River site. $\delta^{30}Si$ composition of each microquartz grain is plotted as a function of the $\delta^{18}O$ obtain at a very short distance ((within <50-100μm). Given the heterogeneity of $\delta^{30}Si$ at the microquartz grain scale, we admit that such correlation diagram is biased as each point samples a different quartz crystal. The aim of this figure is to highlight the distribution of Barberton chert compositions and we consider the beam-sampling bias negligible. The vein is plotted at $\delta^{30}Si$ = 0‰ but it is arbitrary as no data for its silicon isotopic composition was obtained. The observed variations from sample to sample are attributed to variable fluid contributions at the time the chert formed or during subsequent diagenesis as discussed in the text.

each type being linked to the nomenclature we defined in Chapter 2 for Archean cherts.

According to Marin-Carbonne et al. (2012), and following the previous idea proposed by Van den Boorn et al. (2010), three types of microquartz are defined and can be distinguished in cherts based on trace element-silicon isotope systematics :

(1) "Diagenetic" microquartz (C-chert) formed from an amorphous precursor at the seafloor or under shallow burial conditions. It is characterized by low Al_2O_3, TiO_2 and K_2O contents, and have positive $\delta^{30}Si$ compositions.
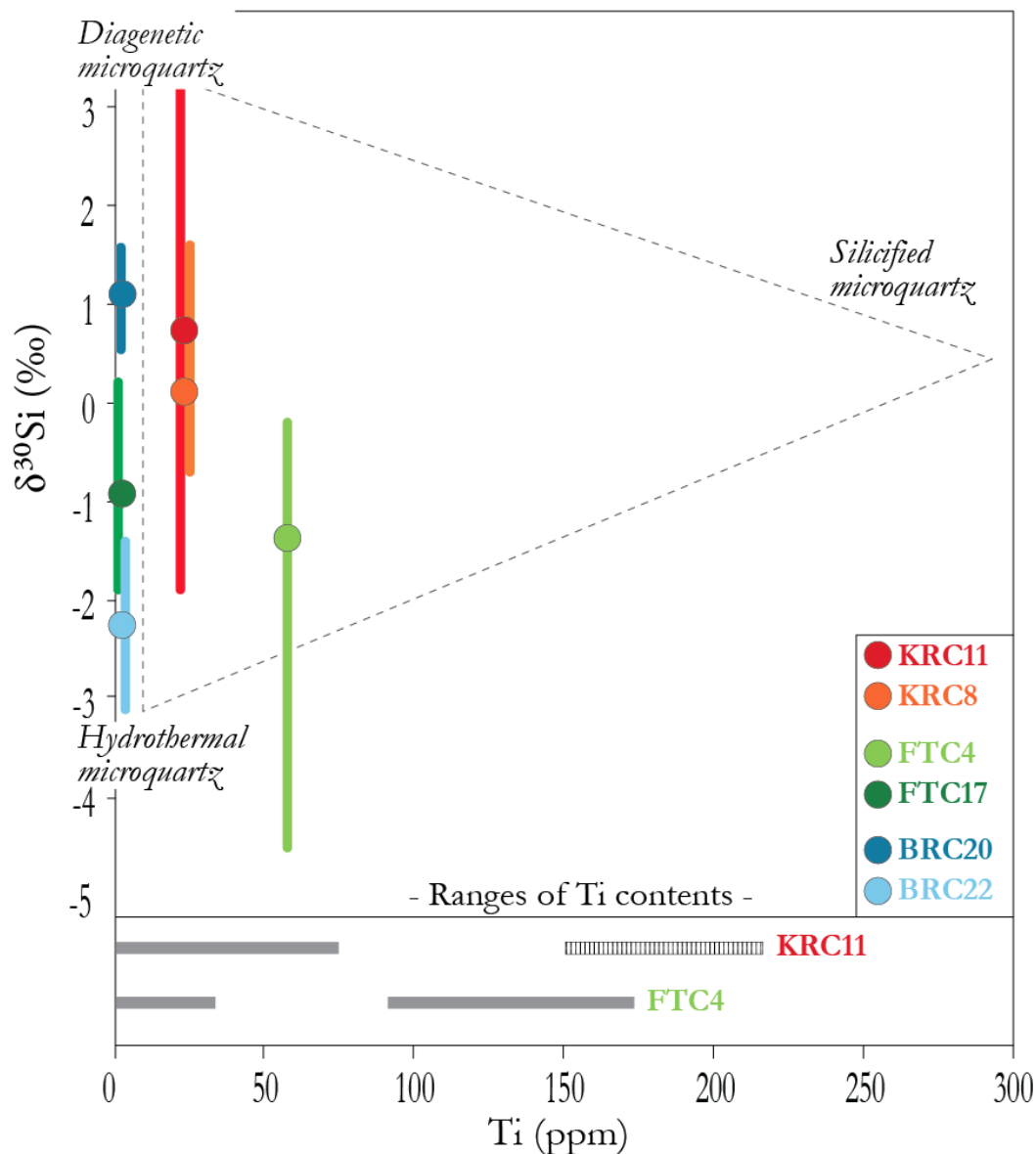
FIGURE 5.10 – *Titanium concentrations vs. $\delta^{30}Si$ of Barberton cherts. Dots are mean $\delta^{30}Si$ whereas vertical lines cover the range of $\delta^{30}Si$ values of each sample. Komati River is in red, Barite Valley in green and Buck Reef in blue. Fields for the three microquartz types are from Marin-Carbonne et al. (2012). Horizontal grey lines represent the range of Ti concentrations measured by microprobe in samples KRC8 and FTC4. The hatched value for KRC8 are those excluded from the data set because they displayed Al/Ti ratio typical of surrounding clay, meaning the beam sampled a mixture of both quartz and phyllosilicate and that the Ti content is no more representative of that in the microquartz.*

(2) *Hydrothermal quartz* (F-chert) precipitated from percolating hydrothermal fluids and has similarly low Al_2O_3, TiO_2 and K_2O contents, but negative $\delta^{30}Si$ values.

(3) *Silicified microquartz* (S-chert) results from the replacement of a sedimentary or volcanic precursor. It has the highest trace element content and has either a negative $\delta^{30}Si$ if silicified from hydrothermal fluids (Van den Boorn et al. 2010) or positive values if the silicification was triggered by seawater percolation (Marin-Carbonne et al. 2012).

In the Figure 5.10, we plot $\delta^{30}Si$ as a function of titanium to allow for microquartz type recognition and the end members are those of Marin-Carbonne et al. (2012). Titanium was chosen because we lack reliable Al_2O_3 and K_2O measurements in the Buck Reef cherts (below the detection limits using ICP-AES analyses). Single-point microprobe analyses were not performed in these samples because the bulk trace element content was demonstrated to be representative of the microquartz composition (see previous Chapter 4). Thus, we use the *Ti* concentrations of 2.1ppm and 1.4ppm obtained by ICP-MS for BRC20 and BRC22 respectively. Similarly, we use a *Ti* concentration of 0.54ppm for microquartz in sample FTC17 because the total REE and HFSE contents in this sample are 0.53 and 0.64ppm respectively, which fit the criterion of purity defined in Chapter 4.

For the Komati River and Barite Valley cherts, trace element compositions are controlled by the detrital fraction they host (see Chapter 3) and the *Ti* content is thus estimated using high-resolution microprobe analyses on single microquartz grains. Microquartz in both sample types have a bimodal titanium composition represented on Figure 5.10 by the thick horizontal, grey lines : one fraction of microquartz shows *Ti* contents below 90ppm for Komati River and 40ppm for Barite Valley, and another fraction is enriched, being 180-260ppm and 110-210ppm respectively for these cherts. No intermediate data were observed.

For Komati River cherts, Al/Ti ratios of some microquartz are within the range of Al/Ti in surrounding phyllosilicates (56-69), especially for grains with the highest *Ti* contents ($>$90ppm ; $Al/Ti = $ 54-65). These microquartz are excluded from the data set as the beam probably sampled a mixture of quartz and clay. A mean
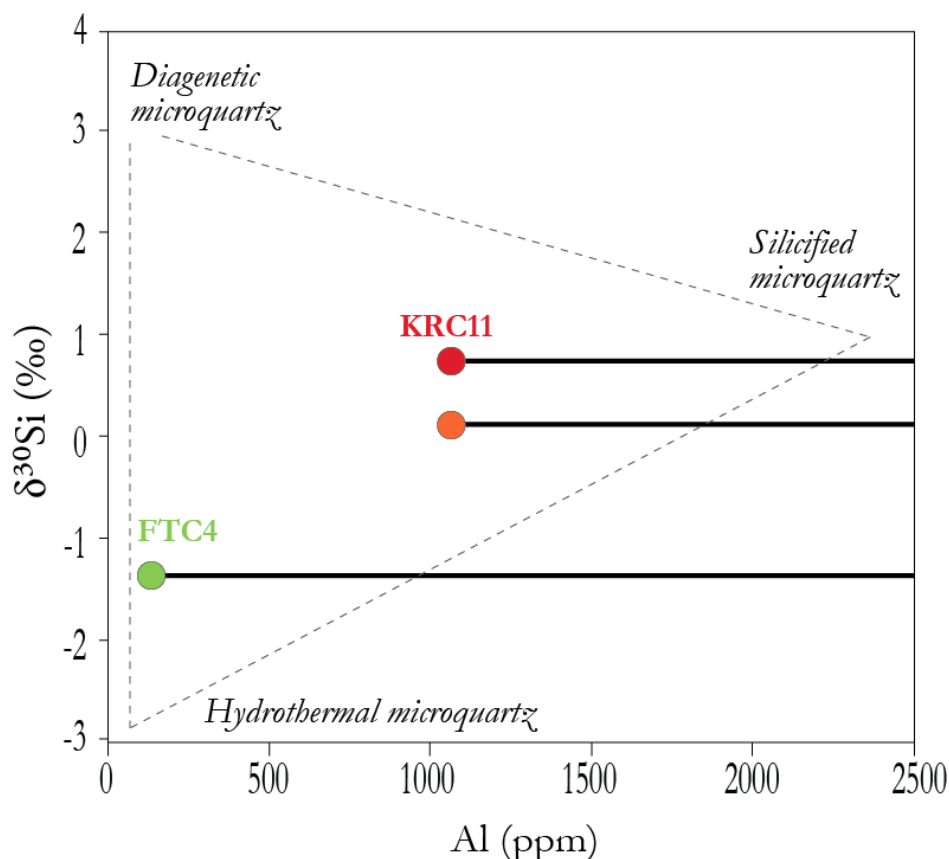
FIGURE 5.11 – *Aluminum concentrations vs. $\delta^{30}Si$ for samples KRC8, KRC11 and FTC4. Dots are the mean $\delta^{30}Si$ and horizontal lines represent the range of aluminum content measured by microprobe in these samples. Microquartz end members are from* Marin-Carbonne et al. (2012). *Al extent to* $9650ppm$ *for KRC8 and KRC11, and to* $4400ppm$ *for FTC4. The range of Al is consistent here with the presence of silicified microquartz in these samples, whereas is is not observed using titanium concentrations in Figure* 5.10.

value of 23.3*ppm* is thus obtain for the *Ti* content in Komati River microquartz grains. In Barite Valley samples, clay and carbonates are present in the chert, but the *Al/Ti* and *Ca/Ti* ratios in microquartz are strongly different from these non-siliceous phases and all data are conserved, leading to a mean *Ti* content of 58*ppm* in these samples.

According to the Figure 5.10, and following the criteria of Marin-Carbonne et al. (2012), all our samples seem to lack significant silicified component because of the very low titanium contents hosted by the microquartz. Instead, they all plot close to the diagenetic-hydrothermal field and have $\delta^{30}Si$ compositions ranging between the two end members. However, a completely different scheme is observed in Figure 5.11 where aluminum is used for the same approach. Here, both the Komati River
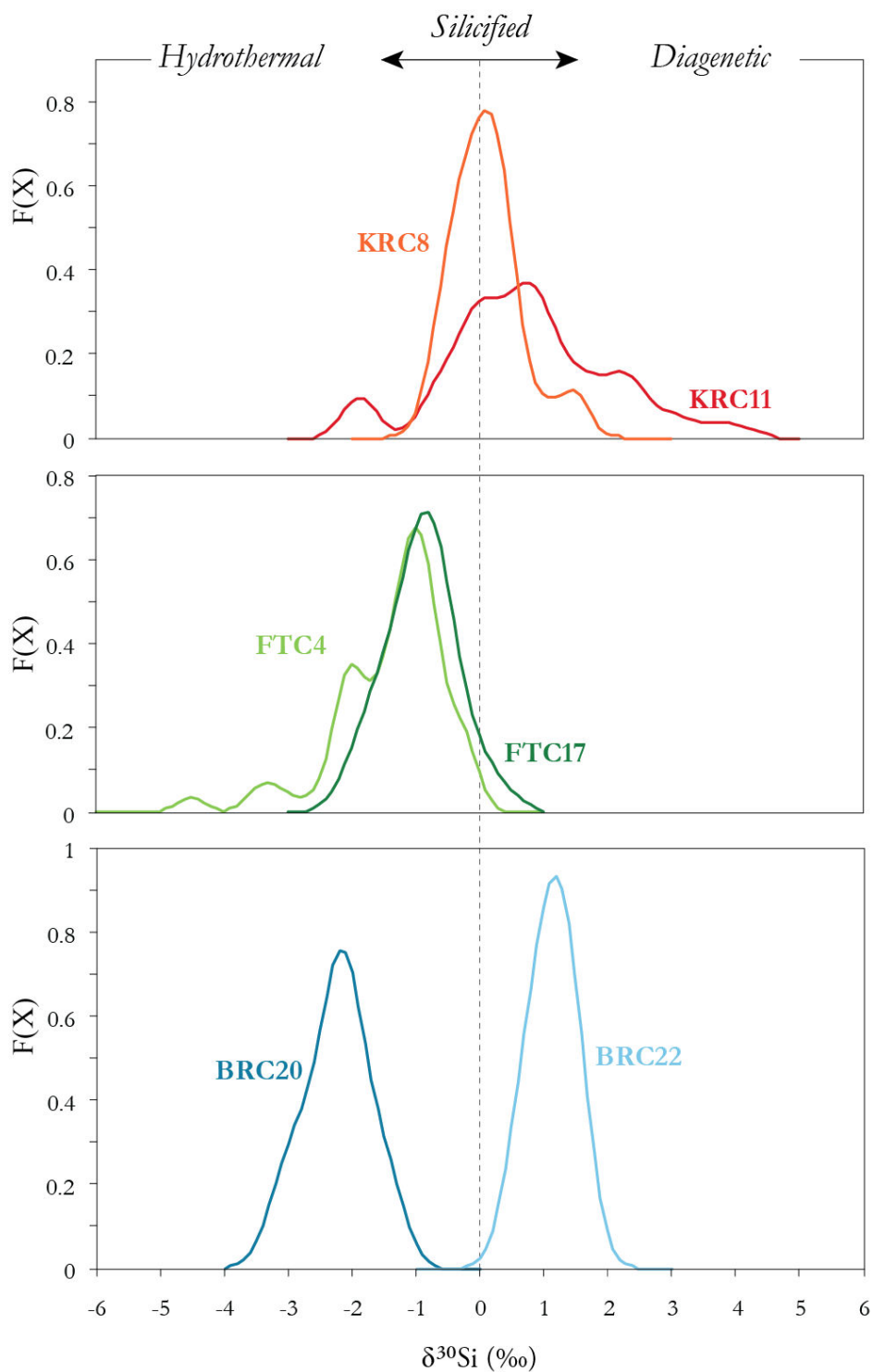
FIGURE 5.12 – *Probability density functions of microquartz $\delta^{30}Si$ compositions in Barberton cherts. Graphs are similar to Figures 5.2, 5.4 and 5.5 and are shown here together for comparison. The vertical, grey dotted line indicates the average $\delta^{30}Si$ expected for silicified microquartz (S-chert), higher, positive values represent the diagenetic end member (C-chert) and lower, negative values the hydrothermal endmember (F-chert).*

(KRC8, KRC11) and Barite Valley (FTC4) cherts, for which microprobe data are available, have high amount of aluminum in their microquartz, which would indicate a silicified component in these samples. Thus, we doubt of the reliability of the trace element-silicon isotope recognition criterion, and we argue that neither *Ti* nor *Al* can be used to monitor a silicified component. Instead, we believe that the amount of these elements depends on their availability in the fluid from which the microquartz precipitated (*e.g.* Dennen 1966, Götze et al. 2004, Rusk et al. 2008), resulting in variable amount of substitutions in the quartz lattice and producing the enormous aluminum range for example.

The distributions and mean $\delta^{30}Si$ values in each samples could be more accurate to identified the various contributions in our samples, as shown in Figure 5.12, if we agree that the $\delta^{30}Si$ solely can be used for the identification. According to Marin-Carbonne et al. (2012), positive $\delta^{30}Si$ are best representative of diagenetic microquartz (C-chert) whereas peaks at more negative values are attributed to hydrothermal microquartz (F-chert) contribution. When close to zero, $\delta^{30}Si$ best represents silicified microquartz (S-chert).

Komati River. Both KRC8 and KRC11 have heterogeneous $\delta^{30}Si$ distributions varying around mean values of +0.13‰ and +0.76‰ respectively. Sample KRC11 is the most heterogeneous and could be a mixture of all the three types of microquartz as it shows distinctive $\delta^{30}Si$ peaks at −1.9‰, +0.2-+0.8‰ and +2.2‰. Sample KRC8 seems to lack the hydrothermal component and is more consistent with a mixture of diagenetic and silicified microquartz as shown by individual $\delta^{30}Si$ peaks at +0.1‰ and +1.5‰.

Barite Valley. Both samples from the Barite Valley dykes have strong negative silicon isotopic compositions, with a mean $\delta^{30}Si$ of −1.37‰ for FTC4 and −0.91‰ for FTC17, which indicates that these cherts are essentially, if not exclusively, composed of hydrothermal microquartz. The main difference between these samples is that FTC4 has a range of $\delta^{30}Si$ (4.31‰) about twice larger than that of FTC17 (2.11‰), display several peaks representative of different sources of silica and have

negative $\delta^{30}Si$ as low as $-4.5‰$. The possible origin of such extreme values is discussed hereafter.

Buck Reef.   The unexpected feature in the Buck Reef white cherts is the opposite $\delta^{30}Si$ signatures recognized in these samples which were thought to be similar from the petrological and geochemical investigations in Chapter 2 and 4. Here, the unimodal distribution in Figure 5.12 shows that both BRC20 and BRC22 are composed of a unique type of quartz, being of hydrothermal origin for BRC20 and of oceanic (diagenetic) origin for BRC22.

5.5.3   On the origin of Barberton cherts and resetting temperatures.

Komati River C-cherts.

The Komati River cherts have puzzling features that are not easily interpretable with respect to the heterogeneous mineralogy of these samples. Here, we propose an interpretation which we believe fits at best the observed isotopic composition.

Together, KRC8 and KRC11 have $\delta^{30}Si$ varying from $-1.89‰$ to $+3.89‰$, a range that is similar to those observed by Marin-Carbonne et al. (2012) in Archean cherts from the Mendon (South Africa) and Dresser (Australia) Formation ($-2.7‰$ to $+2.5‰$) and from the Tumbiana formation (Australia) ($-3.6‰$ to $+1.2‰$). The mean $\delta^{30}Si$ values for all these samples is negative or close to zero, and Marin-Carbonne et al. (2012) interpreted these samples as a mixture essentially of hydrothermal and silicified microquartz, with minor contributions of the diagenetic endmember.

However, the positive mean $\delta^{30}Si$ of $+0.13‰$ and $+0.76‰$ in Komati River cherts are taken here as evidence that significant diagenetic microquartz is present in these samples, meaning oceanic microquartz in our sense. From the younger Gunflit chert samples (1.88Ga), Marin-Carbonne et al. (2012) proposed that the "diagenetic" end member would have a range of $\delta^{30}Si$ between $+0.82‰$ and $+2.52‰$, which is consistent with what we see in KRC8 and KRC11.

The negative $\delta^{30}Si$ peak observed at $-1.9‰$ in Sample KRC11 could be attributed to the presence of a small fraction of hydrothermal microquartz in this sample.
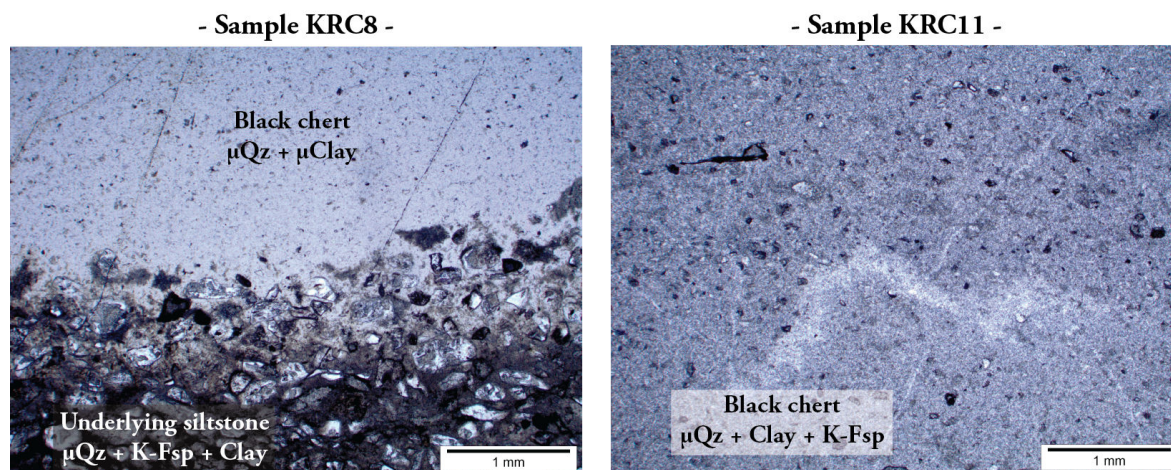
FIGURE 5.13 – *Microscopy photos of samples KRC8 and KRC11 from the Komati River site. Sample KRC11 is enriched in clastic components, comprising >20% of K-feldpar and clay, compared to KRC8, which consists essentially of pure microquartz with <10% of clay minerals. µQz = microquartz ; K-Fsp = potassium feldspar.*

An alternative explanation, which we believe is more consistent with the positive-dominated $\delta^{30}Si$ distribution, is the abundance of detrital particles in this sample. As shown in Figure 5.13, KRC11 is much more enriched in clastic components (clay and K-feldspar >20%) than KRC8 (<10% of clay). Clay minerals have $\delta^{30}Si$ ranging from −2.3‰ to +1.5‰ (*e.g.* Georg et al. 2006), but generally restricted below −0.3‰. Thus, both the heterogeneous distribution of $\delta^{30}Si$ and the negative peak could be inherited from analytical bias, meaning that the ion probe beam, even if <5μm in diameter, could have sample detrital phases in addition to microquartz.

The presence of clay in Komati River samples is important to notice because if these minerals are authigenic, *i.e.* if they formed from the fluid at the origin of the chert, they could be responsible for the positive $\delta^{30}Si$ compositions in our samples. Indeed, ^{28}Si is preferentially incorporated in phyllosilicates during weathering processes (*e.g.* Georg et al. 2006), leading to an enrichment of the fluid in ^{30}Si and an increases of its average $\delta^{30}Si$ to much more positive values. However, from the petrographic study conducted in Chapter 2, we are quite confident that the present clays are of detrital origin. Their physical and chemical preservation is evidence for us that they did not exchange sufficiently with surrounding fluids to produce the observed $\delta^{30}Si$ distribution in our samples.

Taking a value of $\sim -1‰$ for $\Delta_{Dissolved\ silica-Precipitated\ silica}$ (*i.e.* fractionation between dissolved and precipitated silica; De La Rocha et al. 1997, Ding et al. 2004, Marin-Carbonne et al. 2011), the mean $\delta^{30}Si$ composition of KRC8 and KRC11 would indicate that the majority of the silica precipitated from fluids with $\delta^{30}Si_{Fluid}$ of about $+1.63‰$ and $+2.26‰$, which is within the range of modern seawater isotopic composition, ranging from $+0.6‰$ and $+3.1‰$ (De La Rocha et al. 2000, Varela et al. 2004, Cardinal et al. 2005). Another $\Delta_{Dissolved\ silica-Precipitated\ silica}$ of $-1.5‰$ has been proposed for the fractionation of silica during inorganic processes such as silcretization, clay formation or silica sorption onto Fe-oxides (Basile-Doelsch et al. 2005, Georg et al. 2007, Delstanche et al. 2009). Because the present silica precipitated together with fine grained clay, such value could be relevant for the Komati River cherts, which gives higher values of $\delta^{30}Si_{Fluid}$ of about $+2.13‰$ and $+2.76‰$, still consistent with the contribution of oceanic fluids.

The oxygen isotopic composition is much ore homogeneous and the range of $\delta^{18}O$ is similarly narrow in both samples. However, it is evident from Figure 5.9 that they preserved very different mean compositions, with an average $\delta^{18}O$ in sample KRC11 that is 2.22‰ higher than in KRC8. Such contrasting values are hard to reconcile with cherts re-equilibrated with a circulating fluid, because these two samples were taken within a few tens of meter away from each other (*i.e.* stratigraphy distance).

Only one vein was observed here and is located in sample KRC8. One way to investigate the resetting effect and possible degree of hydrothermal alteration is to compare the composition of microquartz in the massive chert to that of the microquartz in the cross-cutting vein. The vein has a $\delta^{18}O$ of $+16.83 \pm 0.17‰$, which, considering uncertainties, is significantly lower than surrounding microquartz with a mean $\delta^{18}O$ of $+17.13 \pm 0.17‰$ (Fig.5.3, 5.7 and 5.9). This suggests that both phases did not significantly exchanged during the vein emplacement. Thus, if homogenization of $\delta^{18}O$ values occurred in this sample, it happened before the formation of the vein.

Two mutual excluding hypotheses emerge : (1) if we admit that the narrow $\delta^{18}O$ ranges are inherited from a secondary resetting, thus fluids with very different temperatures and/or isotopic compositions were involved; (2) if we refute

the criterion for resetting, thus the contrasting $\delta^{18}O$ are directly inherited from different conditions of formation and/or different sources for the silica in KRC8 and KRC11 cherts.

We can test the second hypothesis by calculating the temperature of the fluid involved in the chert formation, using the temperature-dependant fractionation equation given between chert and water in Table 5.1. The $\delta^{18}O_{SW}$ of Archean seawater is thought to have been relatively similar to present day values, at $\pm 2‰$ (*e.g.* Muehlenbachs et Clayton 1976, Karhu et Epstein 1986, Holmden et Muehlenbachs 1993, Muehlenbachs 2008), and we thus use a $\delta^{18}O_{SW}$ of $-1‰$ in the calculation (Marin et al. 2010). The corresponding temperatures, which represent the fluid involved in chert formation, are estimated at 103-107° for KRC8 and 82-94°. We believe that these values are too high to be consistent with the depositional setting and with the temperature estimations broadly accepted for Archean seawater (*i.e.* $<70°C$; Knauth et Lowe 1978, De Ronde et de Wit 1994, Knauth 2005, Robert et Chaussidon 2006, Van den Boorn et al. 2010). Thus, the second hypothesis is not relevant here and the oxygen isotopic system is most probably reset in the Komati River cherts.

To explain the different mean $\delta^{18}O$ in our samples, we can advocate either the circulation of fluids of different composition/temperature, or the re-equilibration of quartz with the surrounding low $\delta^{18}O$ clastic particles.

If KRC8 is essentially contaminated by muscovite grains, KRC11 is much more heterogeneous as previously noticed from the $\delta^{30}Si$ range and the petrography of Figure 5.13. Thus, re-equilibration of similar oceanic quartz with different mineral phases could be responsible for the different $\delta^{18}O$ of 17.13‰ and 19.45‰ in KRC8 and KRC11 respectively. Because we miss the $\delta^{18}O$ of the muscovite fraction, we can barely calculate a re-equilibration temperature from temperature-dependant fractionation equation between muscovite and quartz (Equation 5.6 from Chacko et al. 1996).

Temperature-dependant fractionation equation between muscovite and quartz from Chacko et al. (1996)

$$1000 ln\alpha = 1.350x + 0.042x^2 - 0,0086x^3 \quad \text{with} \quad x = (10^6.T^{-2}) \tag{5.6}$$

However, assuming a $\delta^{18}O_{Musc.}$ of 8.04‰, which is the mean obtain by Gottardi et al. (2011) in muscovite-bearing quartzite, we obtain a re-equilibration temperature of 415°C and 371°C for KRC8 and KRC11 respectively. These values far exceed the low metamorphic gradient recorded in the area by Grosch et al. (2012), being estimated at 140-209°C in the lowermost Kromberg Formation.

Rest the hypothesis of secondary fluid circulations. Given the metamorphism recorded by Grosch et al. (2012), we can postulate a circulating fluid of metamorphic origin with a $\delta^{18}O_{Fluid}$ of 6‰, which correspond to metamorphic fluids re-equilibrated at depth with mafic-ultramafic rocks as proposed by Lécuyer et al. (1994). From the fractionation equation of Table 5.1 between chert and water, the temperature of reset is estimated at 184-192°C and 148-168°C, which is much more consistent with the metamorphic and geological context of the area.

The above discussion helps to better constrain the model of chert formation we proposed in in Chapter 2. In this chapter, we argued that the silica precipitated together with suspended clay particles from Si-rich ambient marine fluids, a process favored by the sorption capacity of phyllosilicates. From the silicon isotopic composition of the cherts, we confirm that the resulting silica (now chert) is a mixture of diagenetic and silicified microquartz, meaning that a large fraction of the silica is indeed of oceanic origin but that a significant fraction may record the presence of the phyllosilicates. From the oxygen isotopic composition, we show that the chert probably underwent low grade metamorphic conditions, which transformed the primary detrital clay to muscovite at temperatures below 200°C. The metamorphism reset the oxygen isotopic system, leading to the observed narrow range of $\delta^{18}O$, and was heterogeneous, leading to the distinct mean $\delta^{18}O$ in both chert samples. Our model contrast with that of Rouchon et al. (2009) who advocated Si- and K-metasomatism to account for the abundance of K-micas in the Komati River turbiditic units.

Barite Valley F-cherts.

The Barite Valley cherts display the best comprehensive isotopic compositions and are in very good agreement with their formation as chemical precipitates in fractures within the shallow crust (*i.e.* $<100m$ depth) (Chapter 3).
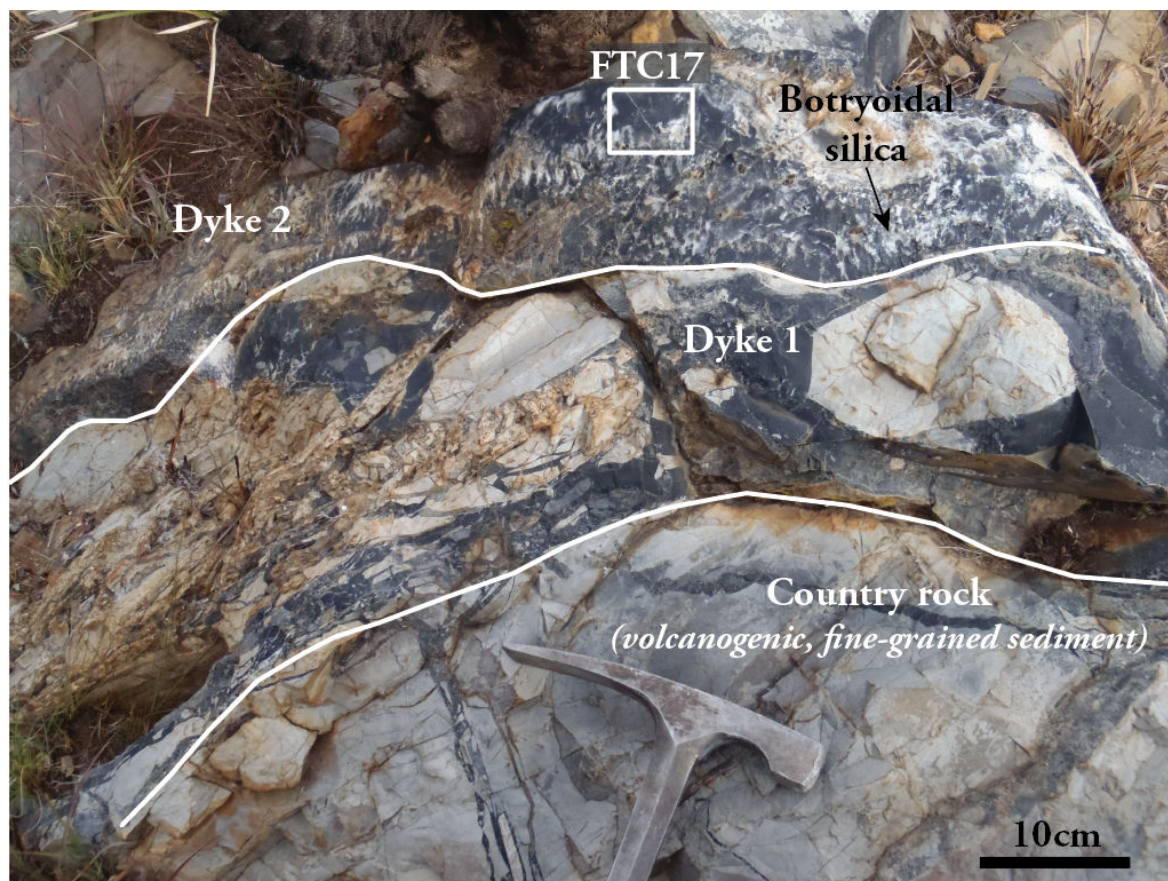
FIGURE 5.14 – *Photo of the dyke where was sampled FTC17. The dyke is filled with botryoidal silica and lack suspended host rock fragments.*

The total $\delta^{30}Si$ range of $-4.5‰$ to $+0.22‰$ covered by these samples gives a mean $\delta^{30}Si$ at $-1.25 \pm 0.24‰$ that is consistent with the silicon isotopic composition of modern hydrothermal deposits (Fig.5.8), such as opal precipitated in siliceous sinters which have a mean $\delta^{30}Si$ of about $-1.4‰$ according to Douthitt (1982). The fact that our fracture-filling cherts lack positive $\delta^{30}Si$ values, with the exception of one $+0.22‰$ measured in a single microquartz grain, is a good evidence that they are exclusively composed of hydrothermal microquartz.

Analogous, modern samples that best fit with our data are submarine sediments produced by black smoker fluids near mid-oceanic ridges. Ding et al. (1996) reported $\delta^{30}Si$ ranging from $-3.1‰$ to $-0.4‰$, with a mean value at $-1.6‰$. In average, black smoker fluids produce siliceous sediments with $\delta^{30}Si$ down to $-3.5‰$ (Jiang et al. 1997) with a mean value of $-1.56‰$ in average (n=25 ; André et al. 2006).

To explain the extreme low $\delta^{30}Si$ composition of hydrothermal deposits, Li et al. (1995) proposed that "the lower the exhalative temperature and the slower the precipitation rate of SiO_2, the lower the $\delta^{30}Si$ values will be". The high average $\delta^{18}O$ reported in our samples, being $\sim 21‰$ for FTC4 and 23.7‰ for FTC17, is in perfect agreement with such postulate. The mineralogy itself point to a slow precipitation of the silica, at least considering the internal structure of the dyke from which was sampled FTC17. As shown in Figure 5.14, the dyke is entirely filled with botryoidal silica that precipitated as columnar crystals whose remarkable large sizes ($\sim 5cm$-long in average) are consistent with slow growth rate.

Using a $\Delta_{Dissolved\ silica-Precipitated\ silica}$ of $\sim -1‰$ (De La Rocha et al. 1997, Ding et al. 2004, Marin-Carbonne et al. 2011), the primary precipitating fluid would have had a $\delta^{30}Si_{Fluid}$ of $-0.37‰$ for FTC4 and 0.09‰ for FTC17. The $-0.37‰$ value for FTC4 in particular is close to that of oceanic black smoker fluids which display $\delta^{30}Si_{Fluid}$ of $-0.3‰$ in average (De La Rocha et al. 2000). Moreover, De La Rocha et al. (2000) and André et al. (2006) proposed that hydrothermal fluids that are in equilibrium at depth with mafic to ultramafic rocks, such as komatiites, will show a mean $\delta^{30}Si_{Fluid}$ around 0‰, a value very consistent with the putative $\delta^{30}Si_{Fluid}$ of 0.09‰ inferred for the fluid that precipitated sample FTC17.

Such considerations are in perfect agreement with the model we proposed in Chapter 3 where we argued on the basis of dyke geometry that part of the fluids came from below to produce the intense fracturation of country sedimentary rocks. The dykes extent down to the komatiitic units of the Mendon Formation which could represent the reaction zone where the fluid acquired their negative to near-zero $\delta^{30}Si$.

From the silicon and oxygen isotopic compositions, it is clear that the FTC4 and FTC17 dykes did not formed from a single type of fluid, but rather represent a plumbing system where fluids of various origin and/or temperature circulated. We can barely conclude on the origin of the narrow $\delta^{18}O$ ranges in our samples, which could be of two origin : it could represent the precipitation of highly homogeneous silica in an open system where fluids were free to circulate until the fracture is sealed ; or it correspond to a reset of the oxygen isotopic system by secondary fluid circulations.

From the chert-water fractionation equation given in Table 5.1, we can calculate the temperature of the fluid that produced the very high $\delta^{18}O$ in the cherts, and we consider here that the calculated temperature represents the youngest fluid circulations saw by the fracture-filling cherts.

We constrain a putative $\delta^{18}O$ for the fluid using the $\delta^{30}Si$ data : a $\delta^{18}O_{Fluid}$ of $+6\permil$ is used for FTC17, which corresponds to the mean oxygen isotopic composition of metamorphic fluids that interacted with komatiites (Lécuyer et al. 1994) ; a minimum and a maximum $\delta^{18}O_{Fluid}$ of $+0.4\permil$ and $+2.1\permil$ respectively are used for FTC4, which corresponds to the range covered by Precambrian hydrothermal fluids derived from seawater (De Ronde et de Wit 1994, Channer et al. 1997).

Using these parameters, we obtain temperatures of 106 to 114°C for FTC4 and of 84 to 103°C for FTC17. If we use the same $\delta^{18}O_{Fluid}$ for FTC17 as that taken for FTC4, the calculated temperature drops to much lower values of 64-82°. In both cases, the dykes seem to have record low temperature fluid circulations, and the different isotopic composition in both dykes show the heterogeneity of the plumbing system. Such low temperatures are consistent (1) with the stability field of chalcedony and thus the presence of the botryoidal silica in dyke FTC17, and (2) with the maximum depth reached by the fractures, which is $\sim 100m$ according to Lowe (in press.).

However, it is less consistent with the presence of an active hydrothermal system at the base of the dyke complex, as proposed by Hofmann et Bolhar (2007), but do not contradict the model for dyke formation we proposed in Chapter 3. Instead, we reinforced our model by proposing that the impact of a large meteor advocated by Lowe (in press.) can account for most of the observe data : it could have been the triggered mechanism of the intense fracturation of the area : it increased the pressure at depth and favored the ascension of overpressured Si-rich fluids by hydraulic fracturation process, and, in the same time, it produced large fractures on the seafloor that allowed the sinking of both seawater and unconsolidated sediment down into the dykes. The low temperature we found, below 120°C, are consistent with both these types of fluids. However, we cannot exclude that the last fluid that produced the oxygen isotopic reseting circulated long after the impact.

Buck Reef C-cherts.

Among all the studied sites, Buck Reef is once again the most intriguing. The two white cherts have similar and uniform $\delta^{18}O$, within uncertainties, with a mean value of $+20.3‰$, but display very contrasting $\delta^{30}Si$, which is well seen in Figures 5.9 and 5.12. BRC20 is strongly negative, with a mean $\delta^{30}Si$ of $-2.23‰$, and exclusively composed of hydrothermal microquartz. On the other hand, BRC22 is strongly positive, with a mean $\delta^{30}Si$ of $+1.13‰$, and exclusively consists of diagenetic microquartz, meaning oceanic silica.

From the previously used $\Delta_{Dissolved\ silica-Precipitated\ silica}$ of $\sim -1‰$ (De La Rocha et al. 1997, Ding et al. 2004, Marin-Carbonne et al. 2011), and providing that the silicon isotopic system was not preserved, these two cherts precipitated from different fluids having $\delta^{30}Si_{Fluid}$ of $-1.23‰$ and $\delta^{30}Si_{Fluid}$ of $+2.13‰$ for BRC22 and BRC20 respectively. If the latter is within the range of modern seawater composition ($+0.6‰$ to $+3.1‰$; De La Rocha et al. 2000, Varela et al. 2004, Cardinal et al. 2005), the value obtained for BRC22 is far from the mean $-0.3‰$ expected for typical of hydrothermal fluids. One explanation, proposed by Marin-Carbonne et al. (2012) to account for a similar depleted $\delta^{30}Si$ in the Mendon chert, would be that the chert acquired its depleted signature from a succession of precipitation-dissolution processes, involving a primary fluid having a $\delta^{30}Si_{Fluid}$ at about $-0.3‰$.

These contrasting compositions are astonishing as both these samples were identified in previous chapters as massive silica precipitates deposited in a similar manner and in the same environment. Moreover, these samples were taken at no more than $5m$ from each other and have trace elements and REE contents very similar, both showing the same Sm/Sm* positive anomaly described in Chapter 4. Their trace element and REE compositions are shown in Figure 5.15 : each sample was analysed three times, and the only slight difference is the highest REE concentrations of sample BRC20, whereas other trace elements display similar concentrations in both samples.

If the silica originated from a hydrothermal-oceanic fluid mixture, which is one of the hypotheses proposed in Chapter 2, one would have expect a bimodal distribution between a hydrothermal negative $\delta^{30}Si$ endmember and an oceanic positive $\delta^{30}Si$ endmember, which, from Figure 5.12, is not the case. The only explanation we
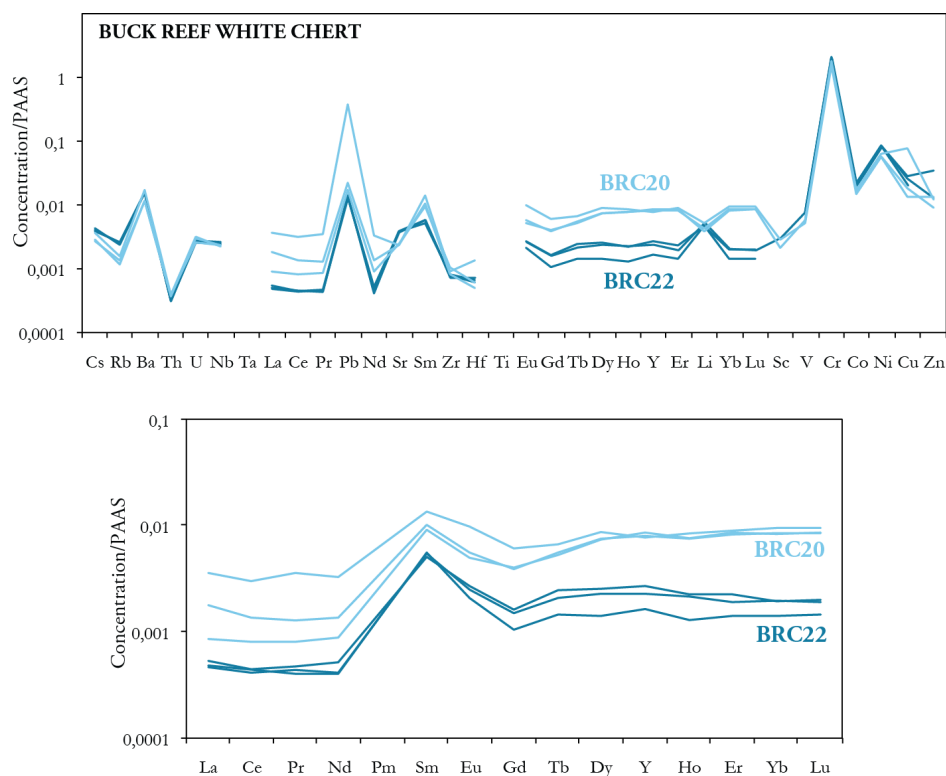
FIGURE 5.15 – *PAAS-normalized (Taylor et McLennan 1985) trace element and REE+Y patterns of Buck Reef chert samples BRC20 and BRC22. Both samples have very similar composition that contrast with their opposite average $\delta^{30}Si$ of -2.23‰ and $+1.13$‰ for BRC20 and BRC22 respectively. BRC20 has higher total REE concentrations, but both samples have similar characteristics, especially the positive Sm anomaly is meaningful as it is a unique feature of Buck Reef cherts, and it is exclusively found in the white chert facies.*

have for now would be that the fluid composition of the basin was heterogeneous through time, being once dominated by hydrothermal inputs, then evolving to a strictly oceanic reservoir. Such a change in environmental conditions is consistent with either (1) the upwelling of Si-enriched bottom seawater or (2) the contribution from oceanic hydrothermal vents and the occasional formation of Si-rich plumes that migrated laterally to reach the Buck Reef shallow basin (Chapter 2).

However, the mixing of oceanic and hydrothermal water masses cannot be the trigger mechanism for the precipitation of silica because, as previously mentioned, both isotopic signatures would be observed in the resulting precipitate, unless both masses were highly immiscible. As proposed in Chapter 2, a drop of temperature or a rise in concentration by evaporative process may be envisage to account for the precipitation.
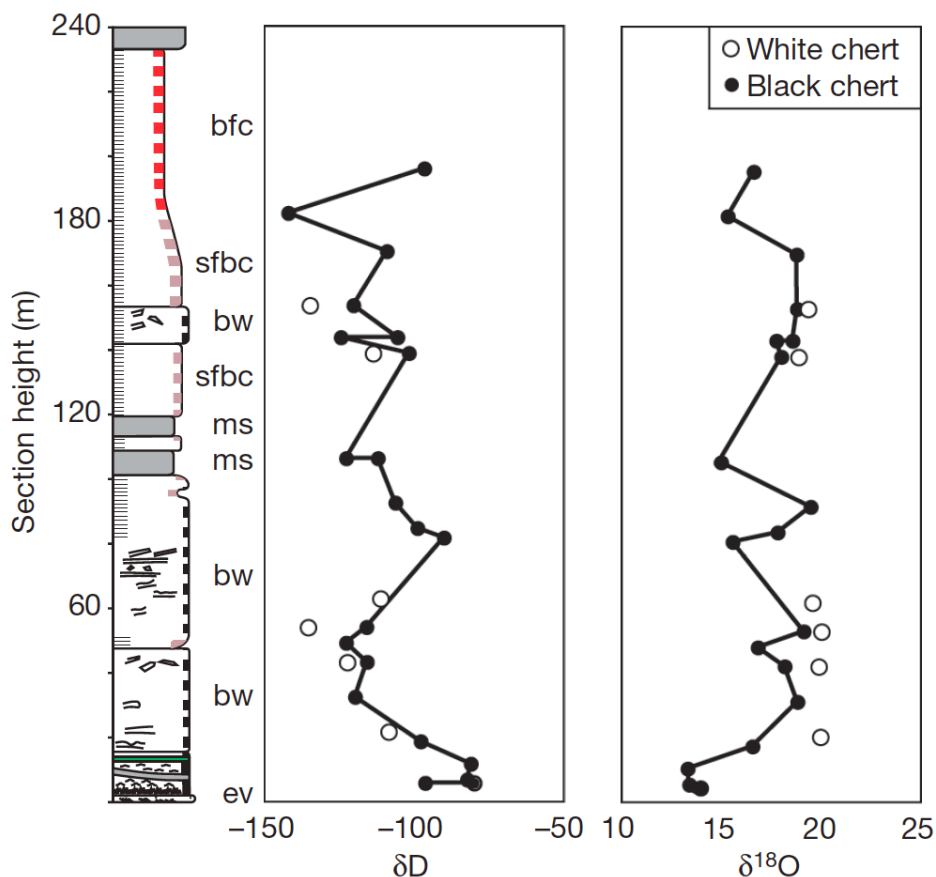
FIGURE 5.16 – $\delta^{18}O$ and δD of black and white cherts from the Buck Reef Chert unit from Hren et al. (2009). Stratigraphic is from Tice et Lowe (2006). "ev" represents black cherts deposited in shallow coastal lagoons, "bw" black-and-white banded cherts deposited on a storm-active platform, "ms" mafic sills, "sfbc" slightly ferruginous banded chert deposited on a low-energy platform/basin, "bfc" banded ferruginous chert deposited in a low-energy basin.

We will not go further in this discussion as it is evident that further isotope analyses are needed to unravel the origin of these paradoxical $\delta^{30}Si$ values, especially the comparison between black an white chert layer compositions and an isotopic transect across a black and white sequence would be useful. We note that, given the very contrasting isotopic composition find here, the comparison between both chert facies could be additionally used to test the hypothesis proposed by Lowe et Fisher Worrell (1999) and Tice et Lowe (2006) for a diagenetic origin of the banding.

We can still calculate a temperature from the oxygen isotopic composition, which will represent the temperature of secondary circulating fluids : because $\delta^{18}O$ values are very consistent between the two samples while they strongly differ in silicon isotopic composition, it is obvious from this site that the oxygen isotopic

system was reset while silicon isotopic compositions were preserved, a conclusion which contradict that of Hren et al. (2009).

These authors provided an isotopic profile across the Buck Reef cherts, shown in Figure 5.16, and reported $\delta^{18}O$ ranging from +13.7‰ up to 20‰ for both the black and white facies. Based on the large variations they saw across the stratigraphic and on the consistency between silicon and oxygen isotopes, they argued for a primary origin of the $\delta^{18}O$ and calculated a paleo-temperature between 32 and 65°C. However, in fact, they did not analysed the $\delta^{30}Si$ in the Buck Reef cherts, but instead, based their argument on those previously advocated by Robert et Chaussidon (2006) for a compilation of cherts from the Barberton belt. Moreover, using the δD analyses, they estimated a $\delta^{18}O$ between -18‰ and -8‰ for the seawater that would have produced the cherts, a value far from the assumption that Archean seawater was closed to modern values (*e.g.* Muehlenbachs et Clayton 1976, Karhu et Epstein 1986, Holmden et Muehlenbachs 1993, Muehlenbachs 2008).

Both these limitations make us doubt of the reliability of their conclusions, although we do not contest the reliability of their data. Thus, we still argue that the cherts from Buck Reef were reset with respect to their oxygen isotopic compositions. Given the variations seen by Hren et al. (2009) across the sequence, the reset must have been heterogenous thorough, which could indicate that it is not a regional reset, but instead a reset produced by local fluid circulations within the upper part of the siliceous sedimentary pile.

The problem for us now is to postulate the nature of the fluid that pervaded through the cherts, because its composition could well have been very different from both the pure seawater or hydrothermal fluids advocated as the primary source of the silica.

We will thus consider here two hypotheses, one involving permeation of seawater at shallow diagenetic conditions, the other involving hydrothermal fluids as the negative $\delta^{30}Si$ proves they were present to some extent in the area. Two $\delta^{18}O$ of +19.44‰ and +21.09‰ represents respectively the lowermost and uppermost values recorded in BRC20 and BRC22. Using these values allow us to obtain the extremum temperatures recorded in our samples.

When using a $\delta^{18}O_{SW}$ for Archean seawater of -10‰, as proposed by Hren

et al. (2009), the calculated temperature for the circulating fluid is between 26 and 33°C. Such low temperatures are unlikely given the reset of the oxygen isotopic system. As previously mentioned for the Komati River calculations, the $\delta^{18}O_{SW}$ of Archean seawater is more likely within ±2‰ of present day values, and we thus use a $\delta^{18}O_{SW}$ of −1‰ in the calculation (Marin et al. 2010). For the hydrothermal fluid hypothesis, we use a $\delta^{18}O_{Hydro}$ range of +0.4‰ and +2.1‰, as previously described for Barite Valley samples, which represent Precambrian hydrothermal fluids derived from seawater (De Ronde et de Wit 1994, Channer et al. 1997).

If seawater was responsible for the reset, it would have circulated at temperatures of 76-88°C through the massive white chert layers. These temperatures are significantly lower than those calculated for the contribution of hydrothermal fluid, which give temperatures of 86-99°C using the minimum $\delta^{18}O_{Hydro}$ and of 100-114°C using the maximum $\delta^{18}O_{Hydro}$. Both hypothesis are likely, but we prefer the involvement of seawater heated at shallow depth because of the lack of major hydrothermal structures in the area. Whatever the fluid was, we can conclude that the Buck Reef samples saw the circulation of fluid with temperatures <100°C after their emplacement, which is significantly lower than the 150°C reported by Hofmann et Harris (2008) in the silicified dacitic volcanic rocks which underlie the Buck Reef cherts.

Mean $\delta^{18}O$ similar to our samples have already been reported for other cherts from the Onverwacht Group (*e.g.* Knauth et Lowe 1978), and the reset was then attributed to fluid circulations at temperatures below 300°C, a conclusion consistent with the present data. Our temperatures are also consistent with the low metamorphic conditions reported in the area, which are known to have not exceed the greenshist facies (Button 1973, Miyano et Beukes 1984, Ward 1995, Toulkeridis et al. 1998, Tice et al. 2004, Rouchon et Orberger 2008, Grosch et al. 2012).

5.6 Conclusions

Silicon and oxygen isotopic compositions of various Archean cherts from the Barberton Greenstone Belt were presented and discussed (1) to assess the possible reseting of isotopic systems, (2) to recognize the origin of the silica and (3) to propose temperature estimations for the various fluids involved in the chert isotopic composition.

We attempted to use the preservation and recognition criteria available in the literature and found that two of these are doubtful. (1) The narrowness of isotopic variations at a microscopic scale, which is thought to represent a reseting of isotopic compositions, is certainly relevant for closed systems but may be irrelevant for natural systems, especially for cherts that formed and indurated at or close to the surface. However, combining with the silicon isotopic compositions and with the local geological and environmental settings of chert emplacement, this criterion can be more confidently used and appeared applicable in all the three sites studied here. (2) The trace element content in microquartz, used to recognize silicified material, showed contradictory results in our samples using Ti and Al as tracers. Thus either Al or Ti (or both) are not efficient to distinguish silicified microquartz from diagenetic and hydrothermal origins.

The sole use of silicon isotopic compositions gave very good results that allowed us to recognize the origin of the studied cherts and to test the model proposed for their formation in Chapter 2 and 4. The figure 5.17 summarizes the inferred origin of the various encountered cherts.

The Komati River black cherts formed by the precipitation of silica at the surface (C-chert) together with suspended clay minerals during the waning stage of turbidite emplacement. Such a formation process is consistent with both the positive $\delta^{30}Si$ and and the near-zero values in these samples, representing an oceanic origin for the primary silica and minor porosity fluid contributions respectively. The large range of $\delta^{30}Si$ may be inherited, at least in part, from the abundance of detrital particles, which acts in two ways : minor depleted $\delta^{30}Si$ values may result from clay analyses together with microquartz grains, and some of the positive $\delta^{30}Si$
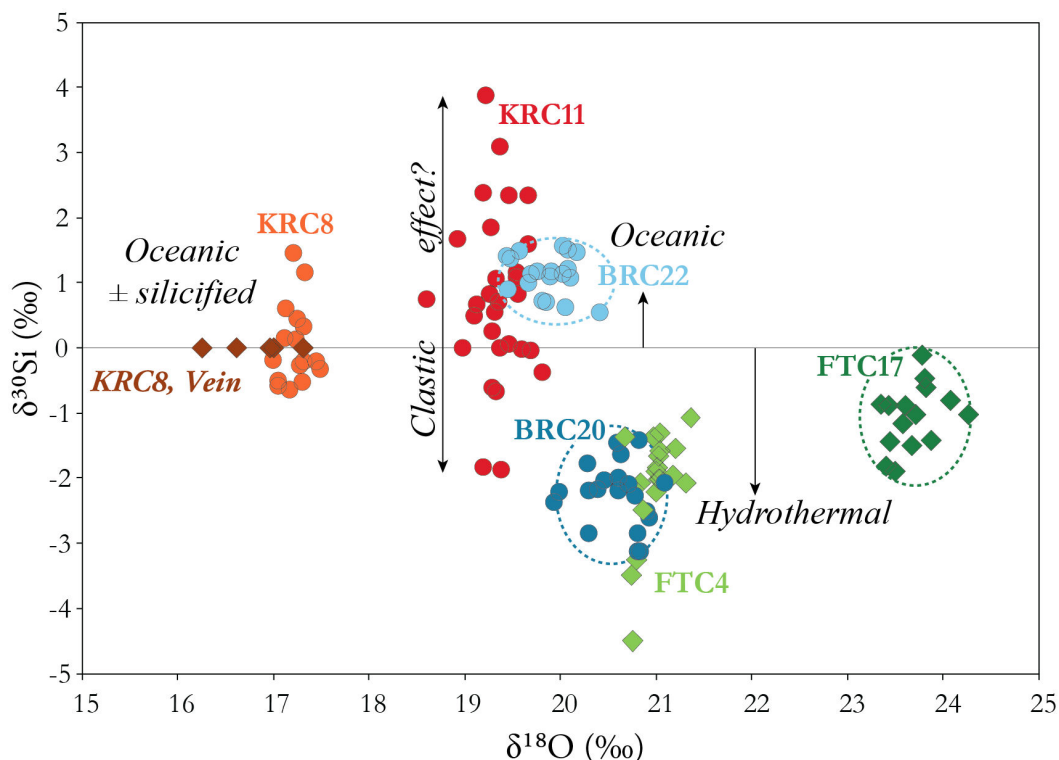
FIGURE 5.17 – $\delta^{18}O$ vs. $\delta^{30}Si$ diagram summarizing principal conclusions reached for the Barberton chert origin. The legend is the same as Figure 5.9.

may come from minor authigenic clay formation. Oxygen isotopic compositions were rest during the low grade metamorphism recorded in the area that produced the transformation of detrital clay to muscovite at temperatures below $200°C$.

The fracture-filling cherts (F-chert) from the Barite Valley site display strongly negative $\delta^{30}Si$ that highlight their formation by the precipitation of "hydrothermal" fluids. The different compositions in individual dykes shows the heterogeneity of the plumbing system. The circulating fluids probably equilibrated at depth with the komatiitic units of the Mendon Formation. We take the low temperature estimated in these samples, below $120°C$, as evidence that the area was not a real hydrothermally active zone with strong heat gradient, and propose instead that the fluid migrated upward as a result of the overpressure induced by a large meteorite impact. The heated fluids were confined below the silicified sedimentary cap formed by upper Mendon units, and the impact induced their migration by hydraulic fracturation, a model that is in perfect agreement with tht proposed in Chapter 3.

The Buck Reef cherts remain obscure for now as the two white cherts were deposited in a similar setting and show similar chemical compositions but strongly differ with respect to their $\delta^{30}Si$: one layer is depleted and of hydrothermal origin while the other is enriched and of oceanic origin. These puzzling characteristics imply the involvement of different water masses at the time these cherts formed, but we can barely explain the lack of hydrothermal-oceanic mixing evidence expected in such an environment. Oxygen isotopic compositions were reset in the area as a result of secondary fluids circulations at temperatures below $100°C$.

Conclusion générale et perspectives

6

_____

6.1 Conclusion.

L'étude de cherts archéens de la ceinture de roches vertes de Barberton, m'a permise de poser de nouvelles contraintes quand à l'origine de ces roches emblématiques. Un premier effort a été de rassembler l'ensemble des faciès rencontrés sous une nomenclature commune, axée sur trois processus de formation distincts qui ont servi de base à l'ensemble de ces travaux.

Les C-cherts, ou cherts primaires, se forment par la précipitation chimique de la silice dissoute dans l'eau de mer, soit sous la forme d'une boue siliceuse (ou gel) sur le plancher océanique, soit en ciment dans les sédiments meubles. Les F-cherts, ou cherts de fracture, précipitent depuis les fluides circulant dans la croûte, au sein de veines concordantes ou recoupant les unités en place. Les S-cherts, ou cherts secondaires, sont le produit du métasomatisme (silicification) de roches préexistantes lié à la percolation de fluides enrichis en silice.

Les sites de Komati River, Buck Reef et Barite Valley ont été sélectionnés afin de réaliser une étude détaillée de ces différents types de chert, avec une attention plus particulière donnée aux cherts océaniques, les plus prometteurs pour les reconstructions paléo-environnementales. Pour chacun de ces sites, j'ai collecté un ensemble d'observations de terrain, de descriptions pétrologiques et d'analyses géochimiques et isotopiques qui m'ont permis de contraindre (1) le contexte environnemental et géologique de mise en place, (2) l'origine de la silice et la nature des fluides impliqués, (3) le processus de formation et (4) les caractéristiques de la phase précipitante.

Des processus de mise en place contrôlés par l'environnement.

Les cherts océaniques en milieu clastique, le cas de Komati River.

Les cherts de Komati River se sont mis en place il y a $3432 Ma$ au sein de sédiments volcanoclastiques dérivés de sources magmatiques felsiques. Proches du continent, ces sédiments se sont déposés par écoulement gravitaire dans un delta à faible profondeur. Le sommet de plusieurs lits dans la série turbiditique correspond à un horizon de chert noir de type C-chert.

Ces niveaux siliceux constituent le faciès terminal des séquences de Bouma. Les structures sédimentaires et de déformation préservées dans ces cherts sont la preuve de leur présence à la surface, tandis que la préservation physique et chimique des particules détritiques qu'ils contiennent (feldspaths, argiles) est un argument fort contre une origine de type S-chert.

La composition chimique du chert représente un mélange entre ses composantes détritiques et siliceuses. Les caractéristiques géochimiques et les fortes concentrations dans ces niveaux indiquent que la composition est essentiellement contrôlée par la fraction clastique, me permettant de reconnaître une source dacitique pour les particules détritiques, à laquelle s'ajoute une certaine composante granitique.

Le signal géochimique contenu dans la silice est masqué par la présence des argiles et feldspaths dans le chert et la fraction siliceuse ne joue qu'un rôle de dilution sur les concentrations totales. La composition isotopique en silicium du microquartz ($\delta^{30}Si > 0$) renforce cependant l'idée d'une origine essentiellement océanique pour la silice.

Les isotopes de l'oxygène sont plus ambigus et semblent avoir enregistré la circulation de fluides métamorphiques à basse température ($< 200°$C), probablement associés à une phase d'obduction tardive à 3227-3230Ma.

Je propose un modèle de formation pour ces cherts où la précipitation de silice, d'abord en tant que ciment, puis en tant que boue siliceuse, est déclenchée par l'arrivée massive des particules argileuses maintenues en suspension dans le nuage turbiditique. L'adsorption de la silice sur ces nuclei permettrait alors la formation de flocules hétérogènes qui sédimentent sur le plancher océanique pour produire un mélange de silice colloïdale et phyllosilicates à comportement visqueux. Un tel processus ne nécessite pas un état de saturation élevé de la silice dans le paléo-bassin, et la formation du chert est contrôlée ici par les flux clastiques.

Ce site est particulièrement intéressant car il illustre l'importance des approches pétrologiques et géochimiques et des données de terrain dans la différenciation des cherts primaires et secondaires.

Les séries litées de cherts océaniques, le cas de Buck Reef.

Les cherts de Buck Reef se sont déposés ~ 16 millions d'années plus tard, mais dans un environnement préservé de contributions continentales. Cette unité épaisse de cherts lités noirs et blancs marque l'accumulation de plusieurs centaines de mètres de sédiments chimiques, d'abord en conditions lagunaires, puis en conditions plus profondes ($> 200m$) lors de la subsidence d'une plateforme continentale.

Les concentrations extrêmement faibles en éléments majeurs et traces montrent l'absence totale de contribution clastique dans les cherts blancs et se traduit par une composition chimique exclusivement contrôlée par la silice. A ce signal siliceux s'ajoute une légère composante clastique dans les cherts noirs ($<< 1\%$), attribuée à la présence de matière carbonée et reliquats de grains détritiques.

Si les structures sédimentaires, la pétrologie, et la géochimie convergent vers une origine océanique pour ces niveaux de chert pur, les données isotopiques et certains éléments traces (Ba, Pb, Cr, Ni) montrent que la chimie du bassin était en partie contrôlée par l'apport de fluides hydrothermaux. Une caractéristique chimique des niveaux blancs reste inexpliquée : la présence d'une anomalie positive en samarium a été découverte dans ces roches et ne trouve aucune comparaison dans les roches et environnements modernes ou anciens. Le principe même d'un fractionnement du samarium des autres terres rares en milieu naturel est un mystère.

La faible profondeur, les conditions d'évaporation favorables et l'absence de flux clastiques majeurs ont permis la colonisation de ce milieu par des organismes primitifs. Une alternance saisonnière semble être préservée dans les tapis microbiens : les conditions estivales sont favorables à l'activité biologique et à la croissance des tapis sur un substrat siliceux plus ou moins riche en particules détritiques ; les refroidissements hivernaux marquent une phase de quiescence microbienne et favorisent la précipitation de silice pure. L'accumulation de ces paleo-varves forme les niveaux de cherts noirs.

Les niveaux de chert blancs représentent les précipités chimiques les plus purs rencontrés dans cette étude et alternent avec les faciès noirs avec une régularité remarquable. Ils se retrouvent fréquemment sous la forme de fragments au coeur de niveaux conglomératiques éparpillés dans la séquence, un argument fort qui

soutient la mise en place de ces cherts à la surface du plancher archéen. Lors d'épisodes occasionnels à plus haute énergie, l'action de vagues puissantes générées par des tempêtes provoque la rupture de ces niveaux et leur remaniement au sein d'une matrice de chert noir pour former des "slab conglomerates" (conglomérats à tablettes de chert). Le contraste rhéologique entre ces deux faciès est la preuve d'une induration extrêmement rapide des cherts blancs en conditions de surface ou sub-surface. Leur minéralogie, exclusivement formée de microquartz, est considérée comme une caractéristique typique des C-cherts formés à partir d'un gel colloidal précipité sur le plancher d'un bassin saturé en silice.

L'origine du litage reste également ouvert à la discussion. Je montre qu'une origine diagénétique est peu probable, surtout aux vues des contacts francs entre les différents niveaux et de la préservation des tapis microbiens et reliquats de grains détritiques non déformés dans les cherts noirs. Je propose une alternative où les niveaux blancs sont considérés comme des phases de précipitation intense, produites par la déstabilisation de masses d'eaux enrichies en silice dans un océan archéen stratifié. Ces précipitations catastrophiques se répètent avec une périodicité compatible avec des alternances glaciaires/inter-glaciaires (type cycle de Milankovitch) et la température pourrait alors être le facteur principal ayant contrôlé la mise en place du litage de Buck Reef.

Les cherts de fracture et leur encaissant silicifié, le cas de Barite Valley.

Les dykes de chert de Barite Valley, mis en place il y a $3260 Ma$, offrent une vision relativement claire des processus de circulation de fluides enrichis en silice dans la croûte archéenne.

A l'image des C-cherts de Komati River, la composition chimique des cherts de fracture est essentiellement contrôlée par la présence en abondance de fragments d'encaissant sédimentaire érodés et embarqués par le fluide siliceux initial lors de sa mise en place. A nouveau, la silice n'a qu'un rôle de diluant sur les concentrations totales.

Une approche essentiellement axée sur les structures de fracturation et sur la pétrologie des cherts remplissant les dykes me permet de proposer un modèle de

mise en place réconciliant les modèles envisagés par Hofmann et Bolhar (2007) et Lowe (in press.).

Sous l'effet d'un impact météorique, de larges fractures s'ouvrent dans le plancher océanique et se remplissent d'eau de mer et de sédiments meubles présents à la surface. L'onde de pression générée par l'impact produit une surpression dans les fluides stockés sous les unités silicifiées et imperméables qui constituent la couverture sédimentaire du plancher. Le confinement, couplé à la surpression, provoque la remontée des fluides par un processus de fracturation hydraulique intense, qui se traduit aujourd'hui par l'abondance de fragments d'encaissant sédimentaire anguleux et peu déplacés au coeur des dykes. D'après ce modèle, le complexe de Barite Valley se serait formé à des températures plus faibles que dans le cas d'un paléo-système hydrothermal actif. Ce postulat est étayé par les données isotopiques de l'oxygène qui indiquent que les dernières phases de circulations impliquaient des fluides chauffés à moins de 120°C. Les compositions isotopiques en silicium sont quant à elles en accord avec des fluides ré-équilibrés en profondeur, probablement au sein des unités komatiitiques de la formation Mendon.

Un des résultats majeurs pour ce site est la reconnaissance d'un comportement thixotrope pour les fluides à l'origine des cherts. Lors de la fracturation, le matériel siliceux présente une viscosité faible et se comporte comme un fluide tandis que l'arrêt du fluage provoque une augmentation des interactions internes et une augmentation drastique de la viscosité. Un tel comportement est imputé à une organisation interne du chert de type "suspension colloidale", où des particules fines de silice et matière carbonée flottent dans une matrice siliceuse. Cette caractéristique thixotropique pourrait s'appliquer aux C-cherts précipités sur le plancher océanique aux vues des nombreuses déformations ductiles préservées dans ces roches.

Les séries sédimentaires volcanoclastiques formant l'encaissant des dykes semblent peu affectées par la mise en place des cherts de fracture. Les données géochimiques et pétrologiques indiquent une silicification précoce de ces unités, probablement dans un environnement profond sous influence hydrothermale. Ce processus pourrait les avoir préservées d'un métasomatisme tardif lors de la circulation des fluides. Certains niveaux concordants et massifs de chert noir océa-

nique ont été identifiés dans ces unités. Malgré une minéralogie dominée par le microquartz (> 95%), leur composition chimique semble contrôlée par les 5% de carbonates qu'ils contiennent.

La chimie des cherts et les reconstructions paléo-environnementales.

A mon sens, le message le plus important à retenir de ces travaux concerne l'utilisation de la chimie des cherts archéens pour les reconstructions paléo-environnementales.

La composition chimique des cherts reflète essentiellement leur environnement de formation et n'apporte pas de réel critère pour différencier leur mode de formation. Cette limitation tient au fait que leur composition représente un mélange entre une phase siliceuse et une phase contaminante, indépendamment des processus qui ont précipité la silice.

Les contaminants identifiés dans ces travaux sont d'origine clastique (argiles, feldspaths, minéraux lourds) ou chimique (carbonates), et chacun d'eux exerce un contrôle majeur sur la composition moyenne du chert, une caractéristique imputable aux concentrations extrêmement faibles portées par la phase siliceuse. J'estime qu'une contribution d'à peine 2% de carbonates et 3-4% de matériel continental est suffisante pour masquer le signal chimique porté par la silice.

Dans ces conditions, seuls les cherts les plus purs sont susceptibles d'avoir enregistré la composition chimique du fluide initial, encore faut-il que la silice soit effectivement capable de retenir cette composition.

Les critères à utiliser pour s'affranchir d'une potentielle contamination sont :

(1) une minéralogie exclusivement siliceuse, en sachant qu'un assemblage dominé par le microquartz favorise une origine océanique tandis qu'un assemblage de calcédoine, quartz et microquartz reflètera plutôt une précipitation au sein de veines et cavités depuis des fluides circulants.

(2) une composition en éléments majeurs où SiO_2 représente plus de $99wt\%$ du chert.

(3) des concentrations extrêmement faibles en éléments traces, plus particulièrement en terres rares, et ne dépassant pas quelques ppm pour les éléments dérivés des produits continentaux (*e.g.* REE, Th, Zr, Hf).

Ces conditions ont été rencontrées dans les cherts blancs de Buck Reef tandis que les autres cherts se sont tous avérés plus ou moins contaminés. Grâce à ces échantillons, j'ai pu tester les proxys océaniques couramment utilisés pour identifier un signal océanique dans les précipités chimiques anciens. Certains critères sont effectivement remplis par les cherts blancs, notamment un appauvrissement fort en terres rares légères et un enrichissement en La and Y. Cependant, ces caractéristiques se retrouvent également dans des quartz hydrothermaux, magmatiques et pegmatitiques, me faisant sérieusement douter de la fiabilité de ces proxys.

Dans ces conditions, les isotopes de la silice offrent une solution efficace au problème. Ils m'ont permis de distinguer les C-cherts des F-cherts par leur composition respectivement positive et négative en $\delta^{30}Si$. La contribution de particules clastiques rend plus délicate l'interprétation des isotopes en raison (1) d'un biais analytique qui résulte de l'analyse à la fois du quartz et des particules connexes sous un même faisceau, (2) des échanges isotopiques durant la diagenèse, et (3) de la précipitation éventuelle de minéraux autogéniques qui modifient la composition du fluide initial.

L'homogénéisation des compositions isotopiques de l'oxygène est une sérieuse contrainte pour retrouver la température des océans archéens, mais s'avère autrement utile pour estimer les températures enregistrées dans les cherts lors de circulations fluides secondaires.

The "take home message".

1. Je montre qu'il est possible de retrouver des indices d'une sédimentation chimique sur le plancher des océans archéens, malgré l'abondance de circulations fluides et malgré les processus de recristallisations diagénétiques et/ou métamorphiques.

2. Une approche de terrain, couplée à une caractérisation pétrologique et géochimique détaillée des cherts, est indispensable pour reconnaitre leur environnement et mode de formation.

3. La composition chimique des cherts est largement contrôlée par les phases contaminantes qu'ils contiennent et ne semble pas adaptée pour étudier la chimie des océans archéens, sauf en présence de carbonates et dans le cas des cherts les plus purs. Elle n'en reste pas moins un outil efficace pour toute autre investigation, notamment sur les processus de surface, d'altération, de sédimentation, etc.

4. Même appliquée aux échantillons les plus purs, l'utilisation des proxys océaniques modernes dans les cherts Archéens n'est pas une approche fiable pour identifier un signal d'eau de mer, et seuls les isotopes du silicium semblent efficaces.

5. Les compositions isotopiques du silicium du microquartz sont un outil puissant pour caractériser l'origine de la silice, et la nature des fluides impliqués dans la formation des cherts.

6. Les compositions isotopiques de l'oxygène sont rarement préservées et leur utilisation est restreinte à la caractérisation des températures de reset du système isotopique lors de circulations fluides précoces à tardives.

7. L'étude des structures sédimentaires et de déformation dans les cherts montre qu'il est possible de contraindre la nature et le comportement rhéologique précoce du précurseur siliceux dont ils sont issus. Les traces d'un comportement de type gel colloidal sur le plancher et d'un comportement thixotropique dans les fractures de la croûte ont été identifiés.

6.2 Perspectives

Nombres de questions restent ouvertes malgré le degré de détail et l'étendue des méthodes utilisées dans mes travaux, et il reste encore beaucoup à faire pour comprendre l'origine des cherts et les conditions qui ont vu leur formation.

• Bien que conséquente, la base de donnée collectée ne représente qu'une gamme restreinte de cherts mis en place dans un même environnement. Utiliser l'approche développée ici sur une collection d'échantillons plus étendue permettrait de renforcer les modèles proposés dans chacun des sites étudiés, et offrirait une vision plus complète des processus de formation des cherts à l'Archéen. Les échantillons promis par le forage du groupe d'AEON de l'Université du Cap à Komati River et d'ICPD dans les sites de Buck Reef et Barite Valley (débuté en été 2011), constituent une matériel prometteur, préservé des altérations de surface, et promettant une continuité d'échantillonnage que ne permettent pas les affleurements de surface. Une partie des carottes de Buck Reef est déjà en cours d'analyse.

• Si l'approche géochimique adoptée dans le Chapitre 4 a sérieusement remis en question la validité des proxys océaniques modernes, elle a surtout mis à jour le potentiel des cherts à préserver la chimie de son environnement. J'ai montré que la compositions des cherts est essentiellement contrôlée par les différentes phases contaminantes qu'ils contiennent, sauf pour les rares exceptions où le chert est pur et entièrement formé de silice. En isolant le signal chimique porté par le contaminant, il devient alors possible d'obtenir un certain nombre d'informations sur sa provenance, sur les processus qui ont vu sa formation et sur le lien qui l'uni à la fraction siliceuse.

• Dans le cas de Komati River, en montrant que la composition des cherts représente celle des particules détritiques, j'ai pu mettre à jour la contribution d'une source granitique en plus de la source dacitique généralement proposée pour les turbidites. Sachant que la fraction argileuse est souvent considérée comme la plus représentative de la source, la reconnaissance d'un tel signal dans les cherts, exclusivement contaminés par cette fraction, devient un outil puissant dans l'étude des contextes géologiques archéennes.

Une des particularités de Komati River est la composition remarquablement homogène de la fraction détritique d'un niveau turbiditique à l'autre. En utilisant cette approche géochimique aux cherts de chacun des niveaux clastiques que comprend la séquence de Komati River, il sera possible de tracer l'évolution des sources, le cas échéant. A l'image des études tectono-sédimentaires appliquées aux roches plus récentes, il serait alors possible de corréler l'apparition des différentes sources à une évolution des processus tectoniques qui les ont mises à l'érosion.

• Certains problèmes persistent quant à la nature des sources identifiées à Komati River. Si la minéralogie des dacites est compatible avec l'absence notable de quartz détritique dans les cherts, la reconnaissance d'une source granitique est nettement plus problématique compte-tenu de la richesse en quartz de ces roches. Une des hypothèses serait une concentration préférentielle des quartz détritiques dans les niveaux plus grossiers de la séquence de Bouma, mais les études pétrologiques de Rouchon et al. (2009) ne montrent qu'une faible proportion de tels grains dans ces niveaux. Une autre possibilité serait la recristallisation totale du quartz sous une forme microquartzitique désormais partie intégrante de la matrice siliceuse, hypothèse peu probable aux vues de la préservation physique des autres particules clastiques. Pour résoudre ce paradoxe, un début de solution serait de comparer les sources identifiées par la composition chimique dans les niveaux de Komati River à des sources potentielles n'étant plus présentes à l'affleurement aujourd'hui. Les syénites en particuliers, seraient de bon candidats, malgré leur absence notable des enregistrement archéens vers $3Ga$.

• Un dernier résultat majeur révélé grâce aux cherts de Komati River est le lien étroit existant entre la présence des argiles en suspension et la floculation de la silice en solution. S'il semble évident que la sédimentation clastique a joué un rôle essentiel dans la formation de ces cherts, une question reste importante à poser concernant la nature et la quantité des argiles effectivement impliquées dans la précipitation de la silice. En utilisant la composition chimique des cherts pour déterminer les rapports argiles/quartz dans l'ensemble des cherts de la séquence (par un rapport simple du type Al_2O_3/SiO_2) il sera possible de poser certaines contraintes sur le processus même de floculation : existe-t-il, par exemple, une

limite de concentration en argiles à partir de laquelle le processus n'est plus effi-cace ? Ou encore, quelle quantité de silice sont capables d'absorber ces argiles dans cet environnement précis ? Résoudre ces questions est largement abordable par l'approche géochimique développée ici. A plus grande échelle, une telle approche pourrait aboutir à une vision toute nouvelle de la mise en place des cherts en lien étroit avec la sédimentation clastique archéenne. L'analyse isotopique du silicium et de l'oxygène des argiles sera nécessaire pour ces travaux, afin de bien différencier les argiles effectivement détritiques des argiles potentiellement néoformées lors des processus diagénétiques précoces.

• Le contrôle exercé par les fragments d'encaissant sédimentaire sur la compo-sition des cherts de fracture de Barite Valley offre également de nouvelles perspec-tives. En utilisant la composition chimique des cherts, il serait possible de tracer la source de ces fragments, de retrouver à quelles unités lithologiques ils appar-tiennent et ainsi de contraindre l'origine des fluides qui les ont embarqués. Pour aller encore plus loin, il est également possible de contraindre le degré d'altéra-tion subit pas les fragments lors de leur transport au sein des fluides circulants. Dans ce cas, cette approche serait un excellent moyen de comparer des processus de silicification dynamiques, aux sein des réseaux de fracture, à des processus de silicification passifs, par simple percolation de fluides sur le plancher océanique.

• Une étude comparée entre les cherts de fractures et leur encaissant mafique en profondeur formerait également une approche solide pour étayer ou non une ori-gine profonde pour les fluides à l'origine des cherts. Les interactions chimiques, les transformations minéralogiques et le ré-équilibrage isotopique dans cette zone de réaction sont autant d'indices qui peuvent être révélés par l'approche géochimique et isotopique proposée dans cette thèse.

• Une méthode particulièrement intéressante pour distinguer les contributions océaniques des contributions hydrothermales dans les dykes serait la réalisation de profils isotopiques au sein des fractures, depuis ces zones profondes de ré-équilibrage jusqu'à leur terminaison sommitale au niveau du paleo-plancher océa-nique. En couplant ces données à l'évolution des structures de fracturation le long du profil, on peut s'attendre à voir ressortir un schéma de mise en place des dykes,

soit par des remontées actives de fluides hydrothermaux chauds, soit par la descente passive de fluides océaniques froids, soit les deux.

• Lors des campagnes de terrain de 2010 et 2011, je n'ai pu m'octroyer que 2 journées à décrire les structures de fracturation et à chercher les traces du comportement rhéologique des fluides siliceux lors de leur mise en place. Il parait évident qu'une campagne plus longue et dédiée à cette approche fournirait de précieux indices pour contraindre au mieux le (ou les) mécanisme(s) ayant produit la fracturation hydraulique et l'ouverture des dykes. Les indices d'un comportement initialement thixotrope dans les cherts de fracture sont quand à eux relativement clairs, bien que les raisons physiques et chimiques d'un tel comportement restent obscures. La mise en place de modèles analogiques et/ou numériques impliquant des solutions colloidales siliceuses et dopées en particules détritiques fines pourrait aider à comprendre le phénomène.

• L'étude systématique des structures de déformation et des structures sédimentaires dans les cherts océaniques, comme je l'ai fait dans le Chapitre 2, devrait aider à mieux contraindre la rhéologie de ces sédiments chimiques en condition de surface. Cette volonté de comprendre le comportement initial des cherts n'est pas anodine puisque cette approche offre de précieuses informations sur la forme même de précipitation de la silice (gel de silice, boue siliceuse, croissance cristalline), autrement masquée par les processus de recristallisation et circulation fluides tardifs. *In fine*, une telle approche renseignera sur les processus de précipitation et sur les conditions environnementales au moment de la formation, notamment grâce aux analogies possibles avec les structures sédimentaires modernes et grâce à notre compréhension du comportement de la silice en solution.

• Dans le site de Buck Reef, l'approche géochimique a confirmé la pureté des niveaux de cherts blancs déjà observée en pétrologie, et m'a permise de proposer des critères fiables pour identifier de tels précipités. Les cherts noirs en revanche semblent contaminés par une phase difficilement identifiable, attribuée soit à la présence de matière carbonée, soit aux rares reliquats détritiques qu'ils contiennent. Isoler la composante contaminante dans ces niveaux est un vrai challenge compte-tenu des concentrations globalement très faibles dans ces roches, à peine plus éle-

vées que dans dans les niveaux blancs. Peut-être faut-il envisager ici une approche plus localisée que les analyses sur roche totale et plus précise que les analyses microsondes. Je suspecte que seules des analyses par spectromètre de masse à ablation laser sur le microquartz et sur les contaminants potentiels pourraient offrir la précision nécessaire pour résoudre ce problème.

• L'origine du litage reste globalement obscure malgré les preuves tangibles que j'ai développé en faveur d'une origine sédimentaire, et non diagénétique. Le site de Buck Reef a souffert d'une lacune dans l'échantillonnage, et la réalisation de profils à petite échelle (quelques mètres) à différentes niveaux stratigraphiques de la séquence (environnement peu profond à profond) semble indispensable pour mieux comprendre la mise en place de ces unités de chert lité. Compte tenu des résultats obtenus ici, les relations pétrologiques, géochimiques et isotopiques entre les cherts noirs et blancs à travers de tels profils devraient fournir une base solide pour comprendre les mécanismes à l'origine du litage. Cette approche devrait intervenir à l'échelle micrométrique dans les cherts noirs, pour étayer l'hypothèse des alternances saisonnières, et à l'échelle de l'affleurement, pour distinguer des variations glaciaire/inter-glaciaire ou l'implication de masses d'eaux différentes dans la formation des cherts blancs.

• Dans cette optique, les analyses isotopiques constituent un outil potentiellement puissant pour tracer l'origine de la silice et les variations possibles des sources au cours du temps. Les analyses présentées ici ont été faites à très haute résolution et sur un nombre d'échantillons très restreint, et il est clair qu'appliquer la méthode à un plus grand nombre d'échantillons serait un cas idéal aux vues des résultats prometteurs mis en avant dans le Chapitre 5. Cependant, compte tenu de la réalité des coûts analytiques, une approche par analyse isotopique sur roche totale serait un bon début pour étoffer le set de données et contraindre au mieux les différences entre les niveaux de cherts et blancs.

• Les cherts blancs en particulier sont devenus une cible majeurs pour de futures recherches, notamment en raison de cette anomalie positive en samarium qui nous laisse perplexe quand aux processus physico-chimiques en place à l'Archéen. En ce moment, je suis en train de développer une méthode analytique avec Cathe-

rine Chauvel dans le but d'analyser les rapports isotopiques du samarium et du néodyme dans ces roches, une approche nécessaire pour identifier lequel des isotopes du samarium est responsable de l'anomalie. Les concentrations extrêmement faibles rendent difficiles, mais pas impossible, de telles analyses par ICP-MS. Les résultats sont attendus dans les mois qui viennent et espérés avant la soutenance.

Les méthodes et approches décrites ici ne se limitent pas aux sites choisis pour cette étude et offrent une base solide pour l'étude des cherts archéens en général. Nombre de questions à plus grande échelle restent à élucider, notamment en ce qui concerne l'implication des cherts dans le cycle global de la silice à l'Archéen.

(1) Comment expliquer la quantité phénoménale de silice précipitant à Barberton ? Est-ce réellement la preuve d'un environnement océanique particulièrement chaud et sans biota médiateur du cycle de la silice à cette époque ? Ou n'est-ce pas un effet de site, limité aux ceintures préservées de Pilbara et Barberton, et qui ne reflète pas la Terre primitive dans son ensemble ? De telles questions sont légitimées par la décroissance significative des dépôts siliceux dès $2.7 Ga$, et par les quantités différentes de silice accumulées dans les ceintures de roches vertes de par le monde. Seule une approche comparative par bilans de masse entre les différentes ceintures archéennes et la Terre moderne pourraient apporter un début de réponse à ces questions.

(2) Est-ce que l'accumulation massive de silice au coeur des croûtes océaniques primitives peut jouer un rôle dans l'évolution de la croûte continentale vers une composition felsique ? La quantité de sédiments siliceux (primaires ou secondaires) et le métasomatisme (silicification) systématique des roches magmatiques du plancher archéen montrent que des quantités considérables de silice sont stockées dans le croûte océanique. Il est alors raisonnable de penser que la fusion de ces matériaux dans les zones de subduction a contribué à l'extraction d'une croûte continentale felsique, et là encore une approche par bilans de masse serait un premier outil à envisager pour traiter la question.

Bibliographie

Abbott D H et Hoffman S E. 1984. Archean plate tectonics revisited. 1. Heat flow, spreading rate, and the age of subducting oceanic lithosphere and their effect on the origin and evolution of continents. *Tectonics*, 3 : 429–448. (Cité page 86.)

Abraham K, Hofmann A, Foley S F, Cardinal D, Harris C, Barth M G, et André L. 2011. Coupled silicon-oxygen isotope fractionation traces Archaean silicification. *Earth and Planetary Science Letters*, 301(1-2) : 222–230. (Cité page 217.)

Alexander Brian W, Bau Michael, et Andersson Per. 2009. Neodymium isotopes in Archean seawater and implications for the marine Nd cycle in Earth's early oceans. *Earth and Planetary Science Letters*, 283(1-4) : 144–155. (Cité page 91.)

Alexander Brian W, Bau Michael, Andersson Per, et Dulski Peter. 2008. Continentally-derived solutes in shallow Archean seawater : Rare earth element and Nd isotope evidence in iron formation from the 2.9Ga Pongola Supergroup, South Africa. *Geochimica et Cosmochimica Acta*, 72(2) : 378–394. (Cité pages 91 et 140.)

Alfimova N A et Matrenichev V A. 2006. Continental weathering in the early Precambrian : Specific features of mineral transformations and composition of supergene solutions. *Lithology and Mineral Resources*, 41 : 518–529. (Cité page 51.)

Alibert C et McCulloch M T. 1993. REE and Nd isotopic compositions of the banded iron-formations and associated shales from Hamersley, Western Australia. *Geochimica et Cosmochimica Acta*, 57 : 187–204. (Cité pages 87 et 140.)

Alibo Dia Sotto et Nozaki Yoshiyuki. 1998. Rare earth elements in seawater : particle association, shale normalization, and Ce oxidation. *Geochimica et Cosmochimica Acta*, 63 : 363–372. (Cité page 174.)

Alibo Dia Sotto et Nozaki Yoshiyuki. 1999. Rare earth elements in seawater : particle association, shale-normalization, and Ce oxidation. *Geochimica et Cosmochimica Acta*, 63 (3–4) : 363–372. (Cité pages 137, 139, 165, 181 et 194.)

Alleman L Y, Cardinal D, Cocquyt C, Plisnier P D, Descy J P, Kimirei I, Sinyinza D, et André L. 2005. Silicon isotopic fractionation in Lake Tanganyika and its main tributaries. *Journal of Great Lakes Research*, 31(4) : 509–519. (Cité page 230.)

Allen J R L. 1982. Sedimentary Structures : Their Character and Physical Basis. *Developments in Sedimentology, 30, Elsevier, Amsterdam*, 2 : 663. (Cité page 78.)

Allwood A C, Walter M R, Burch I W, et Kamber B S. 2007. 3.43 billion-year-old stromatolite reef from the Pilbara Craton of Western Australia : ecosystem-scale insights to early life on Earth. *Precambrian Research*, 158 : 198–227. (Cité pages 10, 92 et 135.)

Allwood A C et al. 2006. Stromatolite reef from the early Archean era of Australia. *Nature*, 441 : 714–718. (Cité pages 10, 92 et 135.)

Allwood Abigail C, Kamber Balz S, Walter Malcolm R, Burch Ian W, et Kanik Isik. 2010. Trace elements record depositional history of an Early Archean stromatolitic carbonate platform. *Chemical Geology*, 270(1–4) : 148–163. (Cité pages 12, 92, 135, 172 et 206.)

Ambrose H. a. et Loomis a. G. 1933. Fluidities of Thixotropic Gels : Bentonite Suspensions. *Physics*, 4(8) : 265. (Cité page 79.)

Andersson P S, Porcelli D, Frank M, Björk G, Dahlqvist R, et Gustafsson Ö. 2008. Neodymium isotopes in seawater from the Barents Sea and Fram Strait Arctic– Atlantic gateways. *Geochimica et Cosmochimica Acta*, 72 : 2854–2867. (Cité pages 10 et 136.)

André L, Cardinal D, Alleman L Y, et Moorbath S. 2006. Silicon isotopes in 3.8 Ga West Greenland rocks as clues to the Eoarchaean supracrustal Si cycle. *Earth and Planetary Science Letters*, 245 : 162–173. (Cité pages 216, 217, 230, 243 et 244.)

Armstrong R A, Compston W, de Wit Maarten J, et Williams I S. 1990. The Stratigraphy of the 3.5-3.2 Ga Barberton greenstone belt revisited : a single zircon microprobe study. *Earth and Planetary Science Letters*, 101(1) : 90–106. (Cité pages 30, 32, 106 et 108.)

Awramik S M, Schopf J W, et Walter M R. 1983. Filamentous fossil bacteria 3.5 Gy old from the Archean of Western Australia. *Precambrian Research*, 20 : 357–374. (Cité pages 10 et 135.)

Ayres M et Harris N. 1997. REE fractionation and Nd-isotope disequilibrium during crustal anatexis : constraints from Himalayan leucogranites. *Chemical Geology*, 139 : 249–269. (Cité page 163.)

Baker E T. 1990. Hydrothermal plume prospecting ; hydrographic and geochemical techniques. *In : Gorda Ridge (Eds. McMurray, G.R.), Springer, Berlin Heidelberg New York*, pages 155–167. (Cité page 88.)

Baker E T, Lavelle J W, et Massoth G J. 1985. Hydrothermal particle plumes over the southern Juan de Fuca Ridge. *Nature*, 316 : 342– 344. (Cité page 88.)

Baker E T et Massoth G J. 1986. Hydrothermal plume measurements ; a regional perspective. *Science*, 234 : 980–982. (Cité page 88.)

Baker E T, Massoth G J, et Feely R A. 1987. Cataclysmic hydrothermal venting on the Juan de Fuca Ridge. *Nature*, 329 : 149–151. (Cité page 88.)

Bao Huiming, Rumble Iii Douglas, et Lowe Donald R. 2007. The five stable isotope compositions of Fig Tree barites : Implications on sulfur cycle in ca. 3.2 Ga oceans. *Geochimica et Cosmochimica Acta*, 71(20) : 4868–4879. (Cité page 172.)

Bao Shen-Xu, Zhou Huai-Yang, Peng Xiao-Tong, Ji Fu-Wu, et Yao Hui-Qiang. 2008. Geochemistry of REE and yttrium in hydrothermal fluids from the Endeavour segment, Juan de Fuca Ridge. *Geochemical Journal*, 42 : 359–370. (Cité pages 139 et 174.)

Barley M E, Pickard A L, et Sylvester P J. 1997. Emplacement of a large igneous province as a possible cause of banded iron formation 2.45 billion years ago. *Nature*, 385 : 55–58. (Cité pages 83, 89 et 90.)

Barnes Haward A. 1997. Thixotropy - a review. *Journal of Non-Newtonian Fluid Mechanics*, 70 : 1–33. (Cité pages 79, 121 et 122.)

Barton J M et al. 1983. Geochronological and Sr-isotopic studies of certain units in the Barberton granite-greenstone terrane, South Africa. *Special Publication of the Geological Society of South Africa*, 9 : 63–72. (Cité page 50.)

Basile-Doelsch I, Meunier J D, et Parron C. 2005. Another continental pool in the terrestrial silicon cycle. *Nature*, 433 : 399– 402. (Cité pages 91, 230 et 240.)

Batuyev B N, Krotov A G, Markov V F, Cherkashev G A, Krasnov S G, et Lisitsyn Y D. 1994. Massive sulfide deposits discovered and sampled at 1445VN, Mid-Atlantic Ridge. *BRIDGE Newslett. 6, 6– 10.*, 6 : 6–10. (Cité page 186.)

Bau M, Beukes N J, et Romer R L. 1998. Increase of oxygen in the Earth's atmosphere and hydrosphere between y2.5 and y2.4 GA B.P. *Mineral. Mag.*, 62A : 127–128. (Cité pages 9, 139 et 182.)

Bau M et Dulski P. 1992. Small-scale variations of the rare-earth element distribution in Precambrian iron formations. *European Journal of Mineralogy*, 4 : 1429–1433. (Cité page 138.)

Bau M, Dulski P, et Möller Peter. 1995. Yttrium and holmium in South Pacific seawater : vertical distribution and possible fractionation behavior. *Chem. Erde*, 55 : 1–15. (Cité pages 136 et 138.)

Bau Michael. 1991. Rare-earth element mobility during hydrothermal and metamorphic fluid-rock interaction and the significance of the oxidation state of europium. *Chemical Geology*, 93(3–4) : 219–230. (Cité pages 140 et 179.)

Bau Michael. 1996. Controls on the fractionation of isovalent trace elements in magmatic and aqueous systems : evidence from Y/Ho, Zr/Hf, and lanthanide tetrad effect. *Contributions to Mineralogy and Petrology*, 123(3) : 323–333. (Cité page 140.)

Bau Michael. 1999. Scavenging of dissolved yttrium and rare earths by precipitating iron oxyhydroxide : experimental evidence for Ce oxidation, Y-Ho fractionation, and lanthanide tetrad effect. *Geochimica et Cosmochimica Acta*, 63(1) : 67–77. (Cité pages 9, 136, 138 et 139.)

Bau Michael et Alexander Brian. 2006. Preservation of primary REE patterns without Ce anomaly during dolomitization of Mid-Paleoproterozoic limestone and the potential reestablishment of marine anoxia immediately after the "Great Oxidation Event". *South African Journal of Geology*, 109(1-2) : 81–86. (Cité page 206.)

Bau Michael et Dulski Peter. 1996. Distribution of yttrium and rare-earth elements in the Penge and Kuruman iron-formations, Transvaal Supergroup, South Africa. *Precambrian Research*, 79(1–2) : 37–55. (Cité pages 138, 139 et 163.)

Bau Michael et Dulski Peter. 1999. Comparing yttrium and rare earths in hydrothermal fluids from the Mid-Atlantic Ridge : implications for Y and REE behaviour during nearvent mixing and for the Y/Ho ratio of Proterozoic seawater. *Chemical Geology*, 155(1–2) : 77–90. (Cité page 172.)

Bau Michael, Dulski Peter, et Brantley Susan. 2000. Estuarine Origin of the Positive La Anomaly and Super-chondritic Y/Ho Ratio of Seawater : Evidence from Mixing Experiments. *Journal of Conference Abstracts*, 5(2) : 199. (Cité pages 136, 138 et 173.)

Bau Michael et Koschinsky Andrea. 2009. Oxidative scavenging of cerium on hydrous Fe oxide : Evidence from the distribution of REE and Y between Fe oxides and Mn oxides in hydrogenetic ferromanganese crusts. *Geochemical Journal*, 43 : 37–47. (Cité pages 9, 136, 138, 139 et 174.)

Bau Michael, Koschinsky Andrea, Dulski Peter, et Hein James R. 1996. Comparison of the partitioning behaviours of yttrium, rare earth elements, and titanium between hydrogenetic marine ferromanganese crusts and seawater. *Geochimica et Cosmochimica Acta*, 60 (10) : 1709–1725. (Cité pages 9, 136, 138 et 139.)

Bau Michael et Möller P. 1993. Rare earth element systematics of the chemically precipitated component in early Precambrian iron formations and the evolution of terrestrial atmosphere-hydrosphere-lithosphere system. . *Geochimica et Cosmochimica Acta*, 57 : 2239–2249. (Cité pages 140 et 163.)

Bau Michael, Möller Peter, et Dulski Peter. 1997. Yttrium and lanthanides in eastern Mediterranean seawater and their fractionation during redox-cycling. *Marine Chemistry*, 56 (1–2) : 123–131. (Cité page 138.)

Bauer W H et Collins E A. 1967. Chapter 8, in F.R. Eirich (Ed.), Rheology : Theory and Applications. *Academic Press, New York*, 4. (Cité page 121.)

Becker Richard H et Clayton Robert N. 1976. Oxygen isotope study of a Precambrian banded iron-formation, Hamersley Range, Western Australia. *Geochimica et Cosmochimica Acta*, 40(10) : 1153–1165. (Cité page 216.)

Bennett P C. 1991. Quartz dissolution in organic-rich aqueous systems. *Geochimia et Cosmochimia Acta*, 55 : 1781–1797. (Cité page 91.)

Benz M G et Martin D L. 1970. COBALTâSAMARIUM PERMANENT MAGNETS PREPARED BY LIQUID PHASE SINTERING. *Appl. Phys. Lett.*, 176(17). (Cité page 185.)

Berelson W M, Corsetti F a, Pepe-Ranney C, Hammond D E, Beaumont W, et Spear J R. 2011. Hot spring siliceous stromatolites from Yellowstone National Park : assessing growth rate and laminae formation. *Geobiology*, 9(5) : 411–24. (Cité page 89.)

Bergna H E. 1994. Colloidal chemistry of silica : An overview. In : The colloidal chemistry of silica. Eds. Bergna, H.E. *American Chemical Society, Advances in Chemistry series*, 234 : 1–47. (Cité page 123.)

Berner R A. 2004. The Phanerozoic carbon cycle : CO2 and O2. *Oxford University Press.* (Cité page 4.)

Berner R A, Lasaga A C, et Garrels R M. 1983. The carbonate–silicate geochemical cycle and its effect on atmospheric carbon dioxide over the past 100 million years. *American Journal of Science*, 283 : 641–683. (Cité page 4.)

Besq A, Monnet P, et Pantet A. 2000. Flow Situations of drilling muds – Effects of thixotropic property. *Flucome Euro*. (Cité pages 79 et 122.)

Bhat M I et Gosh S K. 2001. Geochemistry of the 2.1 Ga old Rampur group pelites, western Himalayas : implications for their provenance and weathering. *Precambrian Research*, 108 : 1–16. (Cité page 6.)

Bialik A, Trammer J, et Zapasnik T. 1972. Synsedimentary disturbances in Middle Triassic carbonates of the Holy Cross Mts. *Acta Geologica Polonica*, 22(2) : 265–279. (Cité page 80.)

Biggin A J, de Wit Maarten J, Langereis C G, Zegers T E, Voûte S, Dekkers M J, et Drost K. 2011. Palaeomagnetism of Archaean rocks of the Onverwacht Group, Barberton Greenstone Belt (southern Africa) : Evidence for a stable and potentially reversing geomagnetic field at ca. 3.5 Ga. . *Earth and Planetary Science Letters*, 303 : 314–328. (Cité page 32.)

Bignall G et Browne Patrick R.L. 1994. Surface hydrothermal alteration and evolution of the Te Kopia thermal area, New Zealand. *Geothermics*, 23(5/6) : 645–658. (Cité page 179.)

Bishop R S. 1977. Shale diapir emplacement in south texas : Laward and Sherriff examples. *Gulf Coast Association of Geological Societies Transactions*, 27 : 20–31. (Cité page 78.)

Bogdanov Y A, Sagalevitch A M, Chernyaev E S, Ashadze A M, Gurvich E G, Lukashin V N, Ivanov G V, et Peresypkin V N. 1995. A study of the hydrothermal field at 1445VN on the Mid- Atlantic Ridge using the "Mir" submersibles. *BRIDGE Newslett*, 9 : 9–13. (Cité page 186.)

Bolhar Robert, Kamber Balz S, Moorbath Stephen, Fedo Christopher M, et Whitehouse Martin J. 2004. Characterization of early Archaean chemical sediments by trace element signatures. *Earth and Planetary Science Letters*, 222 : 43–60. (Cité pages 12, 135, 137, 140 et 163.)

Bolhar Robert, Van Kranendonk Martin J, et Kamber Balz S. 2005. A trace element study of siderite-jasper banded iron formation in the 3.45 Ga Warrawoona Group, Pilbara Craton - Formation from hydrothermal fluids and shallow water. . *Precambrian Research*, 137 : 93–114. (Cité pages 25, 29 et 87.)

Boswell P G H. 1948. A preliminary examination of the thixotropy of sedimentary rocks. *Quarterly Journal of the Geological Society*, 104 : 499–526. (Cité page 122.)

Bouma Arnold H. 1962. Sedimentology of some Flysch deposits. *A graphic approach to facies interpretation, Elsevier., 1962, 168 pp.*, pp. 168. (Cité pages 35, 82 et 155.)

Brady Patrick V et Walther John V. 1990. Kinetics of quartz dissolution at low temperatures. *Chemical Geology*, 82(0) : 253–264. (Cité page 91.)

Brandl G, Cloete M, et Anaeusser C R. 2006. Archaean greenstone belts. *The Geology of South Africa (Eds. Johnson, M.R., Anhaeusser, C.R. and Thomas, R.J.)*, Geological Society of South Africa, Council for Geosciences, Pretoria : 9–15. (Cité page 30.)

Brasier Martin D, Green Owen R, Jephcoat Andrew P, Kleppe Annette K, Van Kranendonk Martin J, Lindsay John F, Steele Andrew, et Grassineau Nathalie V. 2002. Questioning the evidence for Earth's oldest fossils. *Nature*, 416(6876) : 76–81. (Cité page 87.)

Braun Jean-Jacques, Pagel Maurice, Muller Jean-Pierre, Bilong Paul, Michard Annie, et Guillet Bernard. 1990. Cerium anomalies in lateritic profiles. *Geochimica et Cosmochimica Acta*, 54(3) : 781–795. (Cité page 138.)

Braun M et Friedman G M. 1969. Carbonate lithofacies and environments of the Tribes Hill Formation (Lower Ordovician) of the Mohawk Valley, New York. *Journal of Sedimentary Petrology*, 39(1) : 113–135. (Cité pages 80 et 81.)

Brocks J J, Logan G A, Buick R, et Summons R E. 1999. Archean molecular fossils and the early rise of eukaryotes. *Science*, 285 : 1033– 1036. (Cité page 10.)

Buick R et Dunlop J S R. 1990. Evaporitic sediments of early Archean age from the Warrawoona Group, North Pole, Western Australia. *Sedimentology*, 37 : 247–277. (Cité page 135.)

Butterfield D A, Jonasson I R, Massoth G J, Feely R A, Roe K K, Embley R E, Holden J F, McDuff R E, Lilley M D, et Delaney J R. 1997. Seafloor eruptions and evolution of hydrothermal fluid chemistry. *Philosophical Transactions of the Royal Society of London. Series A : Mathematical, Physical and Engineering Sciences*, 355(1723) : 369–386. (Cité page 174.)

Button A. 1973. The stratigraphic history of the Malmani dolomite in the eastern and north-eastern Transvaal. *Geological Society of South Africa Transactions*, 76 : 229–247. (Cité pages 30 et 250.)

Byerly G R, Lowe D R, Wooden J L, et Xie X. 2002. An Archean impact layer from the Pilbara and Kaapvaal Cratons. *Science*, 297 : 1325–1327. (Cité page 15.)

Byerly Gary R, Kröner Alfred, Lowe Don R, et Walsh Maud M. 1993. Sequential magmatic evolution of the early Archean Onverwacht Group : evidence from the upper formations. . *Eos, Transactions, American Geophysical Union*, 74 : 660. (Cité pages 30, 106, 108 et 167.)

Byerly Gary R, Kröner Alfred, Lowe Donald R, Todt W, et Walsh Maud M. 1996. Prolonged magmatism and time constraints for sediment deposition in the early Archean Barberton greenstone belt : evidence from the Upper Onverwacht and Fig Tree groups. *Precambrian Research*, 78(1-3) : 125–138. (Cité pages 13, 15, 30, 106, 108 et 167.)

Byrne R H et Kim K. 1990. Rare earth element scavenging in seawater. *Geochimica et Cosmochimica Acta*, 54 : 2645–2656. (Cité page 137.)

Byrne R H et Lee J H. 1993. Comparative yttrium and rare earth element chemistries in seawater. *Marine Chemistry*, 44 : 121–130. (Cité pages 137 et 138.)

Byrne R H, Liu X, et Schijf J. 1996. The influence of phosphate coprecipitation on rare earth distributions in natural waters. *Geochimia et Cosmochimia Acta*, 60(17) : 3341–3346. (Cité page 185.)

Cady S L, Wenk H-R, et Sintubin M. 1998. Microfibrous quartz varieties : Characterization by quantitative X-ray texture analysis and transmission electron microscopy. *Contributions to Mineralogy and Petrology*, 130(3-4) : 320–335. (Cité page 77.)

Cardinal D, Alleman L Y, Dehairs F, Savoye N, Trull T W, et Andre L. 2005. Relevance of silicon isotopes to Si-nutrient utilization and Si-source assessment in Antarctic waters. *Global Biogeochem. Cycles*, 19 : 1–13. (Cité pages 230, 240 et 246.)

Chacko T, Hu X, Mayeda T K, Clayton R N, et Goldsmith J R. 1996. Oxygen isotope fractionations in muscovite, phlogopite, and rutile. *Geochimia et Cosmochimia Acta*, 60 (14) : 2595–2608. (Cité page 241.)

Chandler F W. 1988. Quartz arenites : review and interpretation. . *Sedimentary Geology*, 58 : 105–126. (Cité page 6.)

Channer D M D, deRonde C E J, et Spooner E T C. 1997. The Cl-Br-I composition of similar to 3.23 Ga modified seawater : implications for the geological evolution of ocean halide chemistry. *Earth and Planetary Science Letters*, 150(3-4) : 325–335. (Cité pages 245 et 250.)

Channing A, Edwards D, et Sturtevant S. 2004. A geothermally influenced wetland containing unconsolidated geochemical sediments. *Canadian Journal of Earth Sciences*, 41 : 809–827. (Cité page 123.)

Chanson H, Jarny S, et Coussot P. 2006. Dam break wave of thixotropic fluid. *Journal of Hydraulic Engineering*, 132(3) : 280–293. (Cité page 123.)

Charlou J L, Fouquet Y, Bougault H, Donval J P, Etoubleau J, Jean-Baptiste P, Dapoigny A, Appriou P, et Rona P A. 1998. Intense CH4 plumes generated by serpentinization of ultra-mafic rocks at the intersection of the 15°20VN Fracture Zone and the Mid-Atlantic Ridge. *Geochimica Et Cosmochimica Acta*, 62(12) : 2323–2333. (Cité page 186.)

Chauvel Catherine, Bureau Sarah, et Poggi Christèle. 2011. Comprehensive Chemical and Isotopic Analyses of Basalt and Sediment Reference Materials. *Geostandards and Geoanalytical Research*, 35(1) : 125–143. (Cité pages 145 et 329.)

Chen Chen-Tung A et Marshall William L. 1982. Amorphous silica solubilities IV. Behavior in pure water and aqueous sodium chloride, sodium sulfate, magnesium chloride, and magnesium sulfate solutions up to 350 °C. *Geochimica et Cosmochimica Acta*, 46 : 279–287. (Cité page 123.)

Cloud Preston. 1973. Paleoecological Significance of the Banded Iron-Formation. *Economic Geology*, 68(7) : 1135–1143. (Cité page 91.)

Condie K C. 1997. Plate Tectonics and Crustal Evolution. *Butterworth Heinemann, Oxford.*, (4th ed.). (Cité pages 8 et 9.)

Condie K C, DesMarais D J, et Abbott D. 2001. Precambrian superplumes and supercontinents : a record in black shales, carbon isotopes, and paleoclimates ? *Precambrian Research*, 106 : 239–260. (Cité pages 6 et 8.)

Condie Kent C. 1993. Chemical composition and evolution of the upper continental crust : Contrasting results from surface samples and shales. *Chemical Geology*, 104(1–4) : 1–37. (Cité pages 157, 159, 165, 177, 181, 203 et 333.)

Condie Kent C, Macke J E, et Reimer T O. 1970. Petrology and geochemistry of early Precambrian graywackes from the Fig Tree Group, south Africa. *GSA Bulletin*, 81(2759-2776). (Cité page 15.)

Connolly James R. 2009. Introduction to X-Ray Powder Diffraction. *EPS400-001*. (Cité page 315.)

Cook H E et Mullins H T. 1983. Basin margin environment. In : Scholle, P.A., et al. (Eds.), Carbonate Depositional Environments. *American Association of Petroleum Geologists Memoirs*, 33 : 540–617. (Cité page 80.)

Coppin F, Berger G, Bauer A, Castet S, et Loubet M. 2002. Sorption of lanthanides on smectite and kaolinite. *Chemical Geology*, 182(1) : 57–68. (Cité pages 163 et 165.)

Corcoran P L, Mueller W U, et Chown E H. 1998. Climatic and tectonic influences on fan deltas and wave- to tide-controlled shoreface deposits : evidence from the Archean Keskarrah Formation, Slave Province, Canada. *Sedimentary Geology*, 120 : 125–152. (Cité page 6.)

Coussot P., Nguyen Q. D., Huynh H. T., et Bonn D. 2002. Viscosity bifurcation in thixotropic, yielding fluids. *Journal of Rheology*, 46(3) : 573. (Cité page 79.)

Dandurand J L, Schott J L, et Tardy Y. 1982. Solubilité de la silice dans des solutions aqueuses très concentrées de formamide et chlorure de lithium. Détermination du coefficient d'activité de la silice en solution. *Bulletin of Mineralogy*, 105 : 357–363. (Cité page 123.)

Danebrock M E, Evers C B H, et Jeitschko W. 1996. Magnetic properties of alkaline earth and lanthanoid iron antimonides AFe4Sb12 (A = Ca, Sr, Ba, La, Nd, Sm, Eu) with the LaFe4P12 structure. *Journal of Physics and Chemistry of Solids*, 57(4) : 381–387. (Cité page 185.)

Danielson A, Möller Peter, et Dulski Peter. 1992. The europium anomalies in banded iron formations and the thermal history of oceanic crust. *Chemical Geology*, 97 : 89–100. (Cité pages 87, 139, 140, 174 et 182.)

Davies R D. 1971. Geochronology and isotope evolution of the early Precambrian crustal rocks in Swaziland. *PhD Thesis, Univ. Witwatersrand, Johannesburg*, pp. 135. (Cité page 50.)

Dawson A G, Long D, Smith D E, Shi S, et Foster I D L. 1991. Tsunamis in the Norwegian Sea and the North Sea caused by the Storegga submarine landslides. *Proc. Symp. Tsunamis, Inter. Union Geodesy Geophysics, Vienna.* (Cité page 81.)

De Baar Hein J W. 1991. On cerium anomalies in the Sargasso Sea. *Geochimica et Cosmochimica Acta*, 55(10) : 2981–2983. (Cité pages 138 et 174.)

De Baar Hein J W, Bacon Michael P, Brewer Peter G, et Bruland Kenneth W. 1985. Rare earth elements in the Pacific and Atlantic Oceans. *Geochimica et Cosmochimica Acta*, 49 (9) : 1943–1959. (Cité pages 137 et 138.)

De Baar Hein J W, Schijf R H, et Byrne R H. 1991. Solution chemistry of the rare earth elements in seawater. *European Journal of Solid State and Inorganic Chemistry*, 28 : 357–373. (Cité page 138.)

De Carlo E H, Wen X Y, et Irving M. 1998. The influence of redox reactions on the uptake of dissolved Ce by suspended Fe and Mn oxide particles. *Aquatic Geochemistry*, 3 : 357–389. (Cité pages 9 et 139.)

de Kretser R G et Boger D V. 2001. A structural model for the time-dependent recovery of mineral suspensions. *Rheologica Acta*, 40(6) : 582–590. (Cité page 122.)

De La Rocha C L, Brzezinski M A, et DeNiro M J. 1997. Fractionation of silicon isotopes by marine diatoms during biogenic silica formation. *Geochimica et Cosmochimica Acta*, 61 : 5051–5056. (Cité pages 215, 240, 244 et 246.)

De La Rocha C L, Brzezinski M A, et DeNiro M J. 2000. A first look at the distribution of the stable isotopes of silicon in natural waters. *Geochimica et Cosmochimica Acta*, 64 : 2467–2477. (Cité pages 230, 240, 244 et 246.)

De Ronde C E J et de Wit M J. 1994. Tectonic history of the Barberton greenstone belt, South Africa : 490 million years of Archean crustal evolution. *Tectonics*, 13 : 983–1005. (Cité pages 6, 215, 241, 245 et 250.)

de Vries S T. 2004. Early Archaean sedimentary basins : depositional environment and hydrothermal systems. *Geologica Ultraiectina*, 244 : 1–160. (Cité pages 25, 29, 54, 74 et 174.)

de Vries S T. 2010. Sedimentary geology of the Palaeoarchean Buck Ridge (South Africa) and Kittys Gap (Western Australia) volcano-sedimentary complexes. *Precambrian Research*, 183 : 749–769. (Cité pages 34, 53 et 54.)

de Vries S T, Nijman W, et Armstrong R A. 2006. Growth-fault structure and stratigraphic architecture of the Buck Ridge volcano-sedimentary complex, upper Hooggenoeg Formation, Barberton Greenstone Belt, South Africa. *Precambrian Research*, 149 : 77–98. (Cité pages 34, 53, 54, 74, 105 et 174.)

de Vries Sjoukje T et Touret Jacques L R. 2007. Early Archaean hydrothermal fluids ; a study of inclusions from the 3.4 Ga Buck Ridge Chert, Barberton Greenstone Belt, South Africa. *Chemical Geology*, 237(3–4) : 289–302. (Cité pages 12 et 185.)

de Wit M J. 1982. Archean abiogenic and probable biogenic structures associated with mineralized hydrothermal vent systems and regional metasomatism, with implications for greenstone belt studies. *Economic Geology*, 77 : 1783–1802. (Cité pages 25, 32, 74 et 87.)

de Wit M J, Armstrong R A, Hart R J, et Wilson A H. 1987a. Felsic igneous rocks within the 3.3-3.5 Ga Barberton greenstone belt : High crustal level equivalents of the surrounding tonalite-trondhjemite terrain, emplaced during thrusting. *Tectonics*, 6 : 529–549. (Cité pages 8, 12, 32 et 215.)

de Wit M J, Furnes H, et Robins B. 2011. Geology and Tectonostratigraphy of the Onverwacht Suite, Barberton Greenstone Belt, South Africa. . *Precambrian Research*, 186 : 1–27. (Cité pages 30, 32, 53 et 105.)

de Wit M J et Hart R. 1993. Earth's earliest continental lithosphere, hydrothermal flux and crustal recycling. *Lithos*, 30 : 309–335. (Cité page 25.)

de Wit M J, Hart R A, et Hart R J. 1987b. The Jamestown ophiolite complex, Barberton mountain belt ; a section through 3.5 Ga oceanic crust. . *Journal of African Earth Sciences*, 6 : 681–730. (Cité page 32.)

Deer W A, Howie R A, et Zussman J. 1966. An introduction to the rock-forming minerals. *Second edition.* (Cité pages 166, 169 et 203.)

Degens E T et Stoffers P. 1976. Stratified waters as a key to the past. *Nature*, 263 : 22–27. (Cité page 93.)

Delstanche S, Opfergelt S, Cardinal D, Elsass F, Andre L, et Delvaux B. 2009. Silicon isotopic fractionation during adsorption of aqueous monosilicic acid onto iron oxide. *Geochimia et Cosmochimia Acta*, 73 : 923–934. (Cité page 240.)

Dennen W H. 1966. Stoichiometric substitution in natural quartz. *Geochimia et Cosmochimia Acta*, 30(12) : 1235–1241. (Cité page 237.)

Derry Louis A et Jacobsen Stein B. 1990. The chemical evolution of Precambrian seawater : Evidence from REEs in banded iron formations. *Geochimica et Cosmochimica Acta*, 54(11) : 2965–2977. (Cité pages 25, 26, 87, 139 et 140.)

Dezileau L, Ulloa O, Hebbeln D, Lamy F, Reyss J L, et Fontugne M. 2004. Iron control of past productivity in the coastal upwelling system off the Atacama Desert, Chile. *Paleoceanography*, 19 : PA3012. (Cité page 94.)

Diergaardt B N, Stevens G, et Moyen Jean-Francois. Janvier 2011. 3.45 Ga potassic rhyolites of the Hooggenoeg formation : Barberton Greenstone Belt. *23rd Congress of African Geology, Johannesburg*. (Cité page 50.)

Dietzel M. 2000. Dissolution of silicates and the stability of polysilicic acid. *Geochimia et Cosmochimia Acta*, 64(19) : 3275–3281. (Cité page 123.)

Ding T, Jiang S, Wang D, Li Y, Li J, Song H, et Lao X. 1996. Silicon isotope geochemistry. *Beijing, Geological Publishing House*, pages 50–64. (Cité pages 230 et 243.)

Ding T, Wan D, Wang C, et Zhang F. 2004. Silicon isotope compositions of dissolved silicon and suspended matter in the Yangtze river, China. *Geochimica et Cosmochimica Acta*, 68 : 205–216. (Cité pages 230, 240, 244 et 246.)

Donaldson J A et de Kemp E A. 1998. Archean quartz arenites in the Canadian Shield : examples from the Superior and Churchill Provinces. *Sedimentary Geology*, 120 : 153–176. (Cité page 6.)

Douthitt C B. 1982. The geochemistry of the stable isotopes of silicon. *Geochimica et Cosmochimica Acta*, 46 : 1449–1458. (Cité pages 230 et 243.)

Douville E, Charlou J L, Oelkers E H, Bienvenu P, Jove Colon C F, Donval J P, Fouquet Y, Prieur D, et Appriou P. 2002. The rainbow vent fluids ($36°14â^2N, MAR$) : $the influence of ultramafic rocks and phase separation on trace metal content in Mid-Atlantic Ridge hydrothermal fluids. Chemical Geology, 184(1--2) : 37--48. (Cit pages 11 et 186.$)

Douville Eric, Bienvenu Philippe, Charlou Jean Luc, Donval Jean Pierre, Fouquet Yves, Appriou Pierre, et Gamo Toshitaka. 1999. Yttrium and rare earth elements in fluids from various deep-sea hydrothermal systems. *Geochimica et Cosmochimica Acta*, 63(5) : 627–643. (Cité pages 139 et 179.)

Dove Patricia M. 1994. The dissolution kinetics of quartz in sodium chloride solutions at 25 degrees to 300 degrees C. *American Journal of Science*, 294(6) : 665–712. (Cité page 91.)

Drever J I. 1974. Geochemical model for the origin of Precambrian banded iron formations. *Geological Society of America Bulletin*, 35 : 1099–1106. (Cité page 93.)

Duchac K C et Hanor J S. 1987. Origin and timing of the metasomatic silicification of an early archean komatiite sequence, barberton mountain land, South Africa. . *Precambrian Research*, 37(2) : 125–146. (Cité pages 12, 25, 29, 108, 135 et 195.)

Dymek R F et Klein C. 1988. Chemistry, petrology and origin of banded iron-formation lithologies from the 3800 Ma Isua supracrustal belt, west Greenland. *Precambrian Research*, 39 : 247–302. (Cité page 87.)

Dymond J et Roth S. 1988. Plume dispersed hydrothermal particles : a time-series record of settling flux from the Endeavour Ridge using moored sensors. *Geochimica Et Cosmochimica Acta*, 52 : 2525–2536. (Cité page 88.)

Eglington B M, Talma A S, Marais S, Matthews P E, et Dixon J G P. 2003. Isotopic composition of Pangola Supergroup limestones from the Buffalo River Gorge, South Africa : constrains on their regional depositional setting. *South African Journal of Geology*, 106 : 1–10. (Cité page 87.)

Elderfield H et Greaves M J. 1981. Negative cerium anomalies in the rare earth element patterns of oceanic ferromanganese nodules. *Earth and Planetary Science Letters*, 55(1) : 163–170. (Cité pages 9, 138 et 139.)

Elderfield H et Pagett R. 1986. Rare earth elements in ichthyoliths : variations with redox conditions and depositional environment. *Sci. Total Environ.*, 49 : 175–197. (Cité page 140.)

Elderfield H, Upstill-Goddard R, et Sholkovitz E R. 1990. The rare earth elements in rivers, estuaries, and coastal seas and their significance to the composition of ocean waters. *Geochimica et Cosmochimica Acta*, 54(4) : 971–991. (Cité pages 136 et 137.)

Elderfield H, Wheat C G, Mottl M J, Monnin C, et Spiro B. 1999. Fluid and geochemical transport through oceanic crust : a transect across the eastern flank of the Juan de Fuca Ridge. *Earth and Planetary Science Letters*, 172(1–2) : 151–165. (Cité pages 11 et 179.)

Elderfield H, Whitfield M, Burton J D, Bacon M P, et Liss P S. 1988. The Oceanic Chemistry of the Rare-Earth Elements [and Discussion]. *Philosophical Transactions of the Royal Society A : Mathematical, Physical and Engineering Sciences*, 325(1583) : 105–126. (Cité pages 136 et 137.)

Elderfield Henry et Schultz A. 1996. Mid-ocean ridge hydrothermal fluxes and the chemical composition of the ocean. *Annual Review of Earth and Planetary Sciences*, 24 : 191–224. (Cité page 136.)

Eriksson P G, Condie K C, Tirsgaard H, Mueller W U, Altermann W, Miall A D, Aspler L B, Catuneanu O, et Chiarenzelli J R. 1998. Precambrian clastic sedimentation systems. *Sedimentary Geology*, 120(1–4) : 5–53. (Cité pages 3, 6 et 92.)

Eugster H P. 1966. Sodium carbonate-bicarbonate minerals as indicators of PCO2. . *Journal of Geophysical Research*, 71 : 3369–3378. (Cité page 3.)

Ewers W E. 1983. Chemical factors in the deposition and diagenesis of banded iron-formation. In : Trendall, A.F., Morris, R.C. (Eds.), Iron-Formation : Facts and Problems. *Elseviers Science Publishers*, pages 491–512. (Cité page 93.)

Ewers W E et Morris R C. 1981. Studies of the Dales Gorge Member of the Brockman Iron Formation, Western Australia. *Economic Geology*, 76 : 1929–1953. (Cité page 93.)

Eylem C, Erten H N, et Göktürk H. 1990. Sorption-desorption behaviour of barium on clays . *Journal of Environmental Radioactivity*, 11(2) : 183–200. (Cité pages 163, 165, 196 et 197.)

Farquhar J et Wing B A. 2003. Multiple sulfur isotopes and the evolution of the atmosphere. *Earth and Planetary Science Letters*, 213 : 1–13. (Cité page 5.)

Farquhar James, Bao Huiming, et Thiemens Mark. 2000. Atmospheric Influence of Earth's Earliest Sulfur Cycle. *Science*, 289(5480) : 756–758. (Cité page 5.)

Fedo Christopher M, Eriksson Kenneth A, et Krogstad E J. 1996. Geochemistry of shales from the Archean (3.0 Ga) Buhwa Greenstone Belt, Zimbabwe : implications for the provenance and source§area weathering. *Geochimica Et Cosmochimica Acta*, 60 : 1751–1763. (Cité page 6.)

Feely R A, Baker E T, Marumo K, Urabe T, Ishibashi J, Gendron J, Lebon G T, et Okamura K. 1996. Hydrothermal plume particles and dissolved phosphate over the superfast-spreading southern East Pacific Rise. *Geochimica Et Cosmochimica Acta*, 60 : 2297–2323. (Cité page 88.)

Feely R A, Gendron J F, Baker E T, et Lebon G T. 1994a. Hydrothermal plumes along the East Pacific Rise, 840' to 1150'N : particle distribution and composition. *Earth and Planetary Science Letters*, 128 : 19–36. (Cité page 88.)

Feely R A, Massoth G J, Trefry J H, Baker E T, Paulson A J, et Lebon G T. 1994b. Composition and sedimentation of hydrothermal plume particles from North Cleft segment, Juan de Fuca Ridge. *Journal of Geophysical Research*, 99(B) : 4985–5006. (Cité page 88.)

Fournier Robert O. 1985. The behavior of silica in hydrothermal solutions. In : Geology and geochemistry of epithermal systems. Eds. Berger, B.R. and Bethke, P.M. *Reviews in Economic Geology*, 2 : 45–61. (Cité pages 11 et 123.)

Frei Robert et Polat Ali. 2007. Source heterogeneity for the major components of 3.7 Ga Banded Iron Formations (Isua Greenstone Belt, Western Greenland) : Tracing the nature of interacting water masses in BIF formation. *Earth and Planetary Science Letters*, 253 (1–2) : 266–281. (Cité pages 26 et 172.)

Freundlich H. 1935. Thixotropy. *The Colloidal State, Hermann*, 267. (Cité page 122.)

Fryer B J. 1977. Rare earth evidence in iron formations for changing Precambrian oxidation states. *Geochimica et Cosmochimica Acta*, Acta 41, 361–367. : 361–367. (Cité page 174.)

Fryer B J, Fyfe W S, et Kerrich Robert. 1979. Archean volcanogenic oceans. *Chemical Geology*, 24 : 25–33. (Cité pages 87 et 139.)

Furnes H, De Wit M J, Robins B, et Sandståd N R. 2011. Volcanic evolution of the upper Onverwacht Suite, Barberton Greenstone Belt, South Africa. *Precambrian Research*, 186 : 28–50. (Cité pages 30, 32 et 53.)

Galer S J C. 1991. Interrelationships between continental freeboard, tectonics and mantle temperature. *Earth and Planetary Science Letters*, 105 : 214–228. (Cité pages 4 et 11.)

Gamo Toshitaka, Chiba Hitoshi, Yamanaka Toshiro, Okudaira Takamoto, Hashimoto Jun, Tsuchida Shinji, Ishibashi Jun-ichiro, Kataoka Satoshi, Tsunogai Urumu, Okamura Kei, Sano Yuji, et Shinjo Ryuichi. 2001. Chemical characteristics of newly discovered black smoker fluids and associated hydrothermal plumes at the Rodriguez Triple Junction, Central Indian Ridge. *Earth and Planetary Science Letters*, 193(3–4) : 371–379. (Cité page 11.)

Garçon M, Chauvel C, et Bureau S. 2011. Beach placer, a proxy for the average Nd and Hf isotopic composition of a continental area. *Chemical Geology*, 287 : 182–192. (Cité pages 161, 163, 165 et 181.)

Gehlen M et Van Raaphorst W. 2002. The role of adsorption–desorption surface reactions in controlling interstitial Si(OH)(4) concentrations and enhancing Si(OH)(4) turn-over in shallow shelf seas. *Continental Shelf Research*, 22(10) : 1529–1547. (Cité page 84.)

Georg R B, Reynolds B C, Frank M, et Halliday A N. 2006. Mechanisms controlling the silicon isotopic composition of river waters. *Earth and Planetary Science Letters*, 249 : 290–306. (Cité page 239.)

Georg R B, Reynolds B C, West A J, Burton K W, et Halliday A N. 2007. Silicon isotope variations accompanying basalt weathering Iceland. *Earth and Planetary Science Letters*, 261 : 476–490. (Cité page 240.)

German C R, Holliday B P, et Elderfield H. 1991. Redox cycling of rare earth elements in the suboxic zone of the Black Sea. *Geochimica et Cosmochimica Acta*, 55 : 3535–3558. (Cité page 137.)

German C R, Klinkhammer G P, et Rudnicki M D. 1996. The Rainbow hydrothermal plume, 3615VN—MAR. *Geophysical Research Letters*, 23 : 2979–2982. (Cité page 186.)

German Christopher R et Elderfield Henry. 1989. Rare earth elements in Saanich Inlet, British Columbia, a seasonally anoxic basin. *Geochimica et Cosmochimica Acta*, 53 : 2561–2571. (Cité page 137.)

Gibbs R J, Meathews M D, et Link D A. 1971. The relationship between sphere size and settling velocity. *Journal of Sedimentary Petrology*, 41 : 7–18. (Cité pages 84 et 163.)

Gilliland R L. 1989. Solar Evolution. *Global and Planetary Change*, 1(1-2) : 35–55. (Cité page 3.)

Göktürk H, Eylem C, Hatipoĝlu S, et Erten H N. 1995. Radiochemical studies of the sorption behavior of strontium and barium. *Journal of Radioanalytical and Nuclear Chemistry*, 198(December, Volume, Issue 2, pp) : 449–456. (Cité page 163.)

Goldberg E D, Koide M, Schmitt R A, et Smith R H. 1963. Rare-earth distributions in the marine environment. *Journal of Geophysical Research*, 68 : 4209–4217. (Cité pages 9 et 139.)

Goldblatt C, Lenton T M, et Watson A J. 2006. Bistability of atmospheric oxygen and the Great Oxidation. *Nature*, 443 : 683–686. (Cité page 4.)

Goldblatt C et Zahnle K J. 2011. Faint young Sun paradox remains. *Nature*, 474(7349) : E3–4 ; discussion E4–5. (Cité page 3.)

Goldstein S J et Jacobsen S B. 1987. The Nd and Sr isotopic systematics of river-water dissolved material : implications for the sources of Nd and Sr in seawater. *Chemical Geology*, 66 : 245–272. (Cité page 137.)

Goscombe B D, Passchier C W, et Hand M. 2004. Boudinage classification : end-member boudin types and modified boudin structures. *Journal of Structural Geology*, 26(4) : 739–763. (Cité page 60.)

Gottardi R, Teyssier C, Mulch A, Vennemann T W, et Wells M L. 2011. Preservation of an extreme transient geotherm in the Raft River detachment shear zone. *Geology*, 8 : 759–762. (Cité page 242.)

Götze J et Lewis R. 1994. Distribution of REE and trace elements in size and mineral fractions of high-purity quartz sands. *Chemical Geology*, 114 : 43–57. (Cité pages 163, 165 et 184.)

Götze J, Plötze M, Graupner T, Hallbauer D K, et Bray C J. 2004. Trace element incorporation into quartz : A combined study by ICP-MS, electron spin resonance, cathodoluminescence, capillary ion analysis, and gas chromatography. *Geochimica et Cosmochimica Acta*, 68(18) : 3741–3759. (Cité pages 183 et 237.)

Gough D O. 1981. Solar interior structure and luminosity variations. *Solar Physics*, 74 : 21–34. (Cité page 3.)

Grandstaff D E. 1980. Origin of uraniferous conglomerates at Elliot Lake, Canada and Witwatersrand South Africa ; implications for oxygen in the Precambrian atmosphere. *Precambrian Research*, 13(1) : 1–26. (Cité page 5.)

Gregory R T, Richards I J, Fergusson K M, et Banerjee S. 2008. Coupled oxygen and hydrogen isotope exchange in Archean igneous rocks : constraints on the seawater and the hydrosphere. *Geochimia et Cosmochimia Acta*, 72(A327). (Cité page 216.)

Gregory R T et Taylor H P. 1981. An Oxygen Isotope Profile in a Section of Cretaceous Oceanic-Crust, Samail Ophiolite, Oman - Evidence for Delta-18-O Buffering of the Oceans by Deep (Less-Than 5 Km) Seawater-Hydrothermal Circulation at Mid-Ocean Ridges. *Journal of Geophysical Research*, 86 : 2737–2755. (Cité page 216.)

Grenne T et Slack J F. 2003. Paleozoic and mesozoic silica-rich seawater : evidence from hematitic chert (jasper) deposits. *Geology*, 31(4) : 319–322. (Cité pages 84 et 123.)

Grosch E G, Kosler J, McLoughing N, Drost K, Slama J, et Pedersen R B. 2011. Paleoarchean detrital zircon ages from the earliest tectonic basin in the Barberton Greenstone Belt, Kaapvaal craton, South Africa. *Precambrian Research, 191 (1-2), pp.85-99.*, 191(1-2) : 85–99. (Cité pages 31, 32, 33, 39, 49, 82, 141 et 155.)

Grosch E G, McLoughing N, de Wit M J, et Furnes H. 2009a. Deciphering Earth's Deep History : Drilling in Africa's Oldest Greenstone Belt. *Eos, Transactions, American Geophysical Union*, 90 : 350–351. (Cité page 32.)

Grosch E G, McLoughing N, de Wit MJ, et Furnes H. 2009b. Drilling for the Archean Roots of Life and Tectonic Earth in the Barberton Mountains. *Scientific Drilling, 8, pp.24-28.*, 8 : 24–28. (Cité page 32.)

Grosch Eugene G, Vidal Olivier, Abu-Alam Tamer, et McLoughlin Nicola. 2012. P-T Constraints on the Metamorphic Evolution of the Paleoarchean Kromberg Type-Section, Barberton Greenstone Belt, South Africa. *Journal of Petrology*, 53(3) : 513–545. (Cité pages 15, 30, 51, 157, 242 et 250.)

Guidry Sean A et Chafetz Henry S. 2002. Factors governing subaqueous siliceous sinter precipitation in hot springs : examples from Yellowstone National Park, USA. *Sedimentology*, 49(6) : 1253–1267. (Cité page 123.)

Guidry Sean a et Chafetz Henry S. 2003. Anatomy of siliceous hot springs : examples from Yellowstone National Park, Wyoming, USA. *Sedimentary Geology*, 157(1-2) : 71–106. (Cité page 123.)

Haas Johnson R, Shock Everett L, et Sassani David C. 1995. Rare earth elements in hydrothermal systems : Estimates of standard partial molal thermodynamic properties of aqueous complexes of the rare earth elements at high pressures and temperatures. *Geochimica et Cosmochimica Acta*, 59(21) : 4329–4350. (Cité page 11.)

Hamade Tristan, Konhauser Kurt O, Raiswell Rob, Goldsmith Sarah, et Morris Richard C. 2003. Using Ge/Si ratios to decouple iron and silica fluxes in Precambrian banded iron formations. *Geology*, 31(1) : 35–38. (Cité pages 87 et 91.)

Hanor J S et Duchac K C. 1990. Isovolumetric silicification of early Archean Komatites : geochemical mass balances and constraints on origin. *Journal of Geology*, 98 : 863–877. (Cité pages 12, 108, 135 et 195.)

Harland W B. 1981. The Late Archean (?) Witwatersand conglomerate, South Africa. In : Earth's Pre-Pleistocene Glacial Record, eds. Hambrey, M.J. and Harland, W.B. *Cambridge University Press*, pages 185–187. (Cité pages 3 et 93.)

Hawkesworth C J et al. 1975. Age relationships between greenstone belts and "granites" in the Rhodesian Archaean craton. *Earth and Planetary Science Letters*, 25 : 251–262. (Cité page 50.)

Hayashi Takamasa, Tanimizu Masaharu, et Tanaka Tsuyoshi. 2004. Origin of negative Ce anomalies in Barberton sedimentary rocks, deduced from La–Ce and Sm–Nd isotope systematics. *Precambrian Research*, 135(4) : 345–357. (Cité page 174.)

Heinrichs T. 1980. Lithostratigraphische Untersuchungen in der Fig Tree Gruppe des Barberton Greenstone Belt zwischen Umsoli und Lomati (Südafrika). *Göttinger Arbeiten zur Geologie und Paläontologie*, 22 : 118. (Cité pages 15 et 108.)

Heinrichs T K et Reimer T O. 1977. A sedimentary barite deposit from the Archean Fig Tree Group of the Barberton Mountain Land (South africa). *Economic Geology*, 72 : 1426–1441. (Cité pages 172 et 196.)

Herzig P M, Becker K P, Stoffers P, Backer H, et Blum N. 1988. Hydrothermal silica chimney fields in the Galapagos spreading center at 86 degrees W. *Earth and Planetary Science Letters*, 89 : 261–272. (Cité page 11.)

Hesse R. 1989. Silica diagenesis : origin of inorganic and replacement cherts. *Earth-Science Reviews*, 26(C) : 253–284. (Cité pages 26 et 29.)

Hessler A M et al. 2004. A lower limit for atmospheric carbon dioxide levels 3.2 billion years ago. . *Nature*, 428 : 736–738. (Cité page 4.)

Hessler Angela M et Lowe Donald R. 2006. Weathering and sediment generation in the Archean : An integrated study of the evolution of siliciclastic sedimentary rocks of the 3.2Ga Moodies Group, Barberton Greenstone Belt, South Africa. *Precambrian Research*, 151(3-4) : 185–210. (Cité pages 6, 7, 51 et 92.)

Hofmann A et Bolhar R. 2007. The origin of carbonaceous cherts in the Barberton greenstone belt and their significance for the study of early life in mid-Archaean rocks. *Astrobiology*, 7 : 355–388. (Cité pages 10, 27, 29, 55, 103, 105, 118, 119, 122, 124, 125, 135, 197, 245 et 261.)

Hofmann A et Wilson A H. 2007. Silicified basalts, bedded cherts and other sea floor alteration phenomena of the 3.4 Ga Nondweni greenstone belt, South Africa. *Developments in Precambrian Geology, Earth's Oldest Rocks. (Eds. Van Kranendonk, M.J., Smithies, R.H. and Bennett, V.)*, 15 : 571–605. (Cité pages 12, 25, 29 et 32.)

Hofmann Axel. 2005. The geochemistry of sedimentary rocks from the Fig Tree Group, Barberton greenstone belt : Implications for tectonic, hydrothermal and surface processes during mid- Archaean times. *Precambrian Research 143(1-4), 23-49.*, 143(1-4) : 23–49. (Cité pages 13, 14, 15, 25, 26, 27, 28, 30, 31, 106, 142, 196 et 200.)

Hofmann Axel et Harris Chris. 2008. Silica alteration zones in the Barberton greenstone belt : A window into subseafloor processes 3.5-3.3 Ga ago. *Chemical Geology*, 257(3-4) : 221–239. (Cité pages 13, 15, 25, 30, 32, 55, 106, 108, 165, 181, 195, 196 et 250.)

Hofmann H J. 1976. Precambrian microflora, Belcher Islands, Canada : Significance and systematics. *Journal of Paleontology*, 50 : 1040–1073. (Cité page 5.)

Hofmann H J et al. 1999. Origin of 3.45 Ga coniform stromatolites in Warrawoona Group, Western Australia. *Geological Society of America Bulletin*, 111 : 1256–1262. (Cité page 92.)

Hogdahl O T, Bowen B T, et Melson S. 1968. Neutron activation analysis of lanthanide elements in seawater. *Advances in Chemical Series*, 73 : 308–325. (Cité page 138.)

Holland H D. 1973. The oceans : A possible source of iron in iron formations. *Economic Geology*, 68 : 1169–1172. (Cité page 87.)

Holland H D. 1994. Early Proterozoic atmospheric change. *Early Life on Earth (Eds. Bengston, S.), Nobel Symposium, Columbia Univ. Press*, 84 : 237–244. (Cité page 5.)

Holland Heinrich D. 2006. The oxygenation of the atmosphere and oceans. *Philosophical transactions of the Royal Society of London. Series B, Biological sciences*, 361(1470) : 903–15. (Cité page 5.)

Holmden C et Muehlenbachs K. 1993. The 18O/16O ratio of 2-billion-year-old seawater inferred from ancient oceanic crust. *Science*, 259 : 1733–1736. (Cité pages 241 et 249.)

Holser William T. 1997. Evaluation of the application of rare-earth elements to paleoceanography. *Palaeogeography, Palaeoclimatology, Palaeoecology*, 132(1–4) : 309–323. (Cité pages 9 et 139.)

Hongo Yayoi, Obata Hajime, Gamo Toshitaka, Nakaseama Miwako, Ishibashi Junichiro, Konno Uta, Saegusa Shunsuke, Ohkubo Satoru, et Tsunogai Urumu. 2007. Rare Earth Elements in the hydrothermal system at Okinawa Trough back-arc basin. *Geochemical Journal*, 41 : 1–15. (Cité page 139.)

Hoskin P W O et Schaltegger U. 2003. The composition of zircon and igneous and metamorphic petrogenesis. *Reviews in Mineralogy and Geochemistry*, 53 : 27–62. (Cité page 163.)

Hren M T, Tice M M, et Chamberlain C P. 2009. Oxygen and hydrogen isotope evidence for a temperate climate 3.42 billion years ago. *Nature*, 462(7270) : 205–208. (Cité pages 248 et 249.)

Iler R K. 1979. The chemistry of silica : Solubility, polymerization, Colloid and surface properties, and biochemistry. *John Wiley and Sons Inc., New York*. (Cité page 123.)

Isley A E. 1995. Hydrothermal plumes and the delivery of iron to banded iron formation. *Journal of Geology*, 103 : 169–185. (Cité pages 88 et 185.)

Jaffres J B D, Shields G, et Wallman K. 2007. The oxygen isotope evolution of seawater : A critical review of a long-standing controversy and an improved geological water cycle model for the past 3.4 billion years. . *Earth-Science Reviews*, 83 : 83–122. (Cité page 25.)

James H L. 1992. Precambrian iron-formations : Nature, origin, and metamorphic evolution from sedimentation to metamorphism. In : Wolf, K.H., Chilingarian, G.V. (Eds.), Developments in Sedimentology 47. Diagenesis. *Elsevier Science Publishers*, 111 : 543–589. (Cité page 93.)

James M P. 1984. Shallowing-upward sequences in carbonates. In : Facies Models (Ed. R.G. Walker), 2nd edn. *Geological Association of Canada, Toronto.*, pages 213– 228. (Cité page 80.)

James R H, Elderfield H, et Palmer M R. 1995. The chemistry of hydrothermal fluids from the Broken Spur site, 29 °N Mid-Atlantic ridge. *Geochimica et Cosmochimica Acta*, 59(4) : 651–659. (Cité pages 11 et 139.)

Jansa L F et Fischbuch N R. 1974. Evolution of a Middle and Upper Devonian sequence from a clastic coastal plain-deltaic complex into overlying carbonate reef complexes and banks, Sturgeon-Mitsue area, Alberta. *Geological Survey Canada Bulletin*, 234 : 1–103. (Cité page 81.)

Jenkins G S. 1995. Early Earth's climate : cloud feedback from reduced land fraction and ozone concentrations. *Geophysical Research Letters*, 22 : 1513–1516. (Cité pages 4 et 11.)

Jenkins G S, Marshall H G, et Kuhn W R. 1993. Precambrian climate : The effects of land area and Earth's rotation rate. *Geophysical Research Letters*, 98 : 8785–8791. (Cité page 4.)

Jiang S Y, Palmer M R, Peng Q M, et Yang J H. 1997. Chemical and stable isotopic compositions of Proterozoic metamorphosed evaporites and associated tourmalines from Houxianyu borate deposit, eastern Liaoning, China. *Chemical Geology*, 135 : 189—211. (Cité page 243.)

Johannesson Karen H., Hawkins Doyle L., et Cortés Alejandra. 2006. Do Archean chemical sediments record ancient seawater rare earth element patterns ? *Geochimica et Cosmochimica Acta*, 70(4) : 871–890. (Cité page 140.)

Jones B et Dixon O A. 1976. Storm deposits in the Read Bay Formation (Upper Silurian), Somerset Island, Artic Canada (an application of Markov Chain analysis). *Journal of Sedimentary Petrology*, 46(2) : 393–401. (Cité page 81.)

Kamber Balz S, Greig Alan, et Collerson Kenneth D. 2005. A new estimate for the composition of weathered young upper continental crust from alluvial sediments, Queensland, Australia. *Geochimica et Cosmochimica Acta*, 69(4) : 1041–1058. (Cité page 333.)

Kamber Balz S et Webb Gregory E. 2001. The geochemistry of late Archaean microbial carbonate : Implications for ocean chemistry and continental erosion history. *Geochimica et Cosmochimica Acta*, 65(15) : 2509–2525. (Cité pages 87, 139, 140, 172 et 206.)

Kamineni D C, Rao A T, et Bonardi M. 1991. The geochemistry of monazite types from the Eastern Ghats granulite terrain, India. *Mineralogy and Petrology*, 45 : 119–130. (Cité page 163.)

Kamo S L et Davis D W. 1994. Reassessment of Archean crustal development in the Barberton Mountain Land, South Africa, based on U-Pb dating. . *Tectonics*, 13(1) : 167–192. (Cité pages 15, 30, 106 et 108.)

Karhu J et Epstein S. 1986. The implication of the oxygen isotope records in coexisting cherts and phosphates. *Geochimica et Cosmochimica Acta*, 50 : 1745–1756. (Cité pages 215, 241 et 249.)

Kasting J F. 1987. Theoretical constraints on oxygen and carbon dioxide concentrations in the Precambrian atmosphere. *Precambrian Research*, 34 : 205–229. (Cité page 3.)

Kasting J F. 1991. Box models for the evolution of atmospheric oxygen : An update. *Palaeogeogr., Palaeoclimatol., Palaeoecol.*, 97 : 125–131. (Cité page 4.)

Kasting J F. 2001. Earth history : The rise of atmospheric oxygen. *Science*, 293 : 819–820. (Cité pages 3 et 5.)

Kasting J F. 2005. Methane and climate during the Precambrian era. *Precambrian Research*, 137(3-4) : 119–129. (Cité page 4.)

Kasting J F. 2010. Faint young sun paradox. *Nature*, 464 : 687–689. (Cité page 3.)

Kasting J F, Zahnle K J, et Walker J C G. 1983. Photochemistry of methane in the Earth's early atmosphere. *Precambrian Research*, 20 : 121–148. (Cité page 4.)

Kasting James F. 1993. Earth's Early Atmosphere. *Science*, 259 : 920–926. (Cité pages 3, 4 et 6.)

Kasting James F et Pavlov A A. 2002. Methane Greenhouses and the Anti-Greenhouses During the Archean Era. *American Geophysical Union, Fall Meeting 2002*. (Cité page 4.)

Kato Y et Nakamura K. 2003. Origin and global tectonic significance of early Archean cherts from the Marble Bar greenstone belt, Pilbara Craton, Western Australia. *Precambrian Research*, 125 : 191–243. (Cité pages 25, 29 et 135.)

Kato Yasuhiro, Ohta Izumi, Tsunematsu Tomoki, Watanabe Yoshio, Isozaki Yukio, et Maruyama Shigenori. 1998. Rare earth element variations in mid-Archean banded iron formations : Implications for the chemistry of ocean and continent and plate tectonics. *Geochimica et Cosmochimica Acta*, 62(21/22) : 3475–3497. (Cité page 87.)

Kazmierczak Józef et Goldring R. 1978. Subtidal flat-pebble conglomerate from the Upper Devonian of Poland : a multiprovenant high-energy product. *Geological Magazine*, 115 (05) : 359–366. (Cité page 81.)

Kelley Deborah S, Karson Jeffrey A, Blackman Donna K, Fruh-Green Gretchen L, Butterfield David A, Lilley Marvin D, Olson Eric J, Schrenk Matthew O, Roe Kevin K, Lebon Geoff T, Rivizzigno Pete, et The A T Shipboard Party. 2001. An off-axis hydrothermal vent field near the Mid-Atlantic Ridge at 30[deg] N. *Nature*, 412(6843) : 145–149. (Cité pages 11 et 94.)

Kern A. et Eysel W. 1993. Mineralogish-Petrograph. *Inst., Univ. Heidelberg, Germany*. (Cité pages 146, 314, 315 et 316.)

Kiehl J T et Dickinson R E. 1987. A study of the radiative effects of enhanced atmospheric CO2 and CH4 on early Earth surface temperatures. *Journal of Geophysical Research*, 92 : 2991–2998. (Cité page 4.)

Kita I, Taguchi S, et Matsubaya O. 1985. Oxygen isotope fractionation between amorphous silica and water at 34-93 °C. *Nature*, 314(6006) : 83–84. (Cité page 215.)

Klein B et Hallbom D. 2002. Modifying the Rheology of Nickel Laterite Suspensions. *Minerals Engineering*, 15(10) : 745–749. (Cité page 122.)

Klein Cornelis et Beukes Nicolas J. 1989. Geochemistry and sedimentology of a facies transition from limestone to iron-formation in the Early Proterozoic Transvaal Supergroup, South Africa. *African Economic Journal*, 84 : 1733–1774. (Cité pages 88, 93, 94 et 139.)

Klemme S, Günther D, Hametner K, Prowatke S, et Zack T. 2006. The partitioning of trace elements between ilmenite, ulvospinel, armalcolite and silicate melts with implications for the early differentiation of the moon. *Chemical Geology*, 234 : 251–263. (Cité page 163.)

Klinkhammer G P, Elderfield H, Edmond J M, et Mitra A. 1994. Geochemical implications of rare earth element patterns in hydrothermal fluids from midocean ridges. *Geochimica et Cosmochimica Acta*, 58 : 5105–5113. (Cité page 172.)

Knauss Kevin G et Wolery Thomas J. 1988. The dissolution kinetics of quartz as a function of pH and time at 70 °C. *Geochimica et Cosmochimica Acta*, 52(1) : 43–53. (Cité page 91.)

Knauth L P. 1973. Oxygen and hydrogen isotope ratios in cherts and related rocks. *PhD Thesis, Californian Institute of Technology.*, pp. 369. (Cité page 25.)

Knauth L P. 1994. Petrogenesis of Chert. . *In Silica : Physical Behavior, Geochemistry and In : Silica : Physical Behavior, Geochemistry and Materials Applications. Reviews of Mineralogy*, 29 : 233–258. (Cité pages 12, 25, 29, 217 et 218.)

Knauth L Paul. 2005. Temperature and salinity history of the Precambrian ocean : implications for the course of microbial evolution. *Palaeogeography, Palaeoclimatology, Palaeoecology*, 219(1–2) : 53–69. (Cité pages 6, 8, 9, 12, 26, 215 et 241.)

Knauth L Paul et Epstein Samuel. 1976. Hydrogen and oxygen isotope ratios in nodular and bedded cherts. *Geochimica et Cosmochimica Acta*, 40(9) : 1095–1108. (Cité page 215.)

Knauth L Paul et Lowe Donald R. 1978. Oxygen isotope geochemistry of cherts from the Onverwacht Group (3.4 billion years), Transvaal, South Africa, with implications for secular variations in the isotopic composition of cherts. *Earth and Planetary Science Letters*, 41(2) : 209–222. (Cité pages 6, 8, 12, 25, 26, 92, 215, 218, 229, 241 et 250.)

Knauth L Paul et Lowe Donald R. 2003. High Archean climatic temperature inferred from oxygen isotope geochemistry of cherts in the 3.5 Ga Swaziland Supergroup, South Africa. *Geological Society of America Bulletin*, 115(5) : 566–580. (Cité pages 6, 9, 12, 25, 27, 29, 75, 92, 135, 215 et 218.)

Knauth P L et Epstein S. 1975. Hydrogen and oxygen isotope ratios in silica from the JOIDES Deep Sea Drilling Project. *Earth and Planetary Science Letters*, 25(1) : 1–10. (Cité page 215.)

Knoll A H et al. 2006. Eukaryotic organisms in Proterozoic oceans. *Philosophical Transactions of the Royal Society B : Biological Sciences*, 361 : 1023–1038. (Cité page 5.)

Konhauser Kurt O, Newman D K, et Kappler Andreas. 2005. The potential significance of microbial Fe (III) reduction during deposition of Precambrian banded iron formations. *Geobiology*, 3 : 167–177. (Cité pages 83, 89 et 90.)

Konhauser Kurt O, Phoenix Vernon R, Bottrell Simon H, Adams David G, et Head Ian M. 2001. Microbial–silica interactions in Icelandic hot spring sinter : possible analogues for some Precambrian siliceous stromatolites. *Sedimentology*, 48(2) : 415–433. (Cité pages 89 et 90.)

Kozub P. 1997. The Origin of Flat-Pebble Conglomerates in the Upper Cambrian of the Clarks Fork Region, Park County Wyoming. *Keck Symposium Volum*, 10. (Cité page 81.)

Krapez B, Barley M E, et Pickard A L. 2003. Hydrothermal and resedimented origins of the precursor sediments to banded iron formation : sedimentological evidence from the Early Palaeoproterozoic Brockman Supersequence of Western Australia. *Sedimentology*, 50 : 979–1011. (Cité page 85.)

Kröner A, Byerly G, et Lowe D R. 1991. Chronology of Early Archean granite-greenstone evolution in the Barberton Mountain Land, South Africa, based on precise dating by signle zircon evaporation. *Earth and Planetary Science Letters*, 103(1-4) : 41–54. (Cité pages 30, 53, 88, 106, 108, 167 et 174.)

Kröner A et Compston W. 1988. Ion microprobe ages of zircons from early Archaean granite pebbles and greywacke, Barberton greenstone belt, southern Africa. *Precambrian Research*, 38 : 367–380. (Cité page 50.)

Kröner A, Hegner E, Wendt J I, et Byerly G R. 1996. The oldest part of the Barberton granitoid-greenstone terrain, South Africa : evidence for crust formation between 3.5 and 3.7 Ga. *Precambrian Research*, 78(1–3) : 105–124. (Cité page 13.)

Krüner A, Byerly G R, et Lowe D R. 1991. Chronology of early Archaean granite– greenstone evolution in the BarbertonMountain Land, South Africa, based on precise dating by single zircon evaporation. *Earth and Planetary Science Letters*, 103(1-4) : 41–54. (Cité page 13.)

Krupp R, Oberthuer T, et Hirdes W. 1994. The early Precambrian atmosphere and hydrosphere : thermodynamic constraints from mineral deposits. *Economic Geology*, 89(7) : 1581–1598. (Cité page 5.)

Kulaksiz S et Bau M. 2007. Contrasting behaviour of anthropogenic gadolinium and natural rare earth elements in estuaries and the gadolinium input into the North Sea. *Earth and Planetary Science Letters.*, 260 : 361–371. (Cité page 137.)

Kullberg J C, Oloriz F, Marques B, Caetano P S, et Rocha R B. 2001. Flat-pebble conglomerates : a local marker for Early Jurassic seismicity related to syn-rift tectonics in the Sesimbra area (Lusitanian Basin, Portugal). *Sedimentary Geology*, 139 : 49–70. (Cité page 81.)

Labanda Jordi et Llorens Joan. 2006. A structural model for thixotropy of colloidal dispersions. *Rheologica Acta*, 45(3) : 305–314. (Cité page 79.)

Lascelles D F. 2007. Black smokers and density currents : A uniformitarian model for the genesis of banded iron-formations. *Ore Geology Reviews*, 32 : 381–411. (Cité page 85.)

Laschet Christoph. 1984. On the origin of cherts. *Facies*, 10(1) : 257–289. (Cité page 91.)

Lawrence M G et Kamber B S. 2006. Behaviour of the rare earth elements during estuarine mixing — revisited. *Marine Chemistry*, 100 : 147–161. (Cité pages 136 et 137.)

Lécuyer C, Gruau G, Anhaeusser C R, et Fourcade S. 1994. The origin of fluids and the effects of metamorphism on the primary chemical compositions of Barberton komatiites : new evidence from geochemical (REE) and isotopic (Nd, O, H,) data. *Geochimica et Cosmochimica Acta*, 58(2) : 969–984. (Cité pages 242 et 245.)

Lécuyer Christophe et Allemand Pascal. 1999. Modelling of the oxygen isotope evolution of seawater : implications for the climate interpretation of the δ18O of marine sediments. *Geochimica et Cosmochimica Acta*, 63(3–4) : 351–361. (Cité page 216.)

Ledevin Morgane, Arndt Nicholas, Simionovici Alexandre, et Ulrich Marc. in prep.a. Chert recognition and new insights in formation process based on field and petrological approaches, Barberton Greenstone Belt, 3.5 - 3.2Ga, South Africa. *To be submitted to Precambrian Research*. (Cité pages 125, 135, 155 et 175.)

Ledevin Morgane, Arndt Nicholas, Simionovici Alexandre, et Ulrich Marc. in prep.b. Rheology : a new tool for investigating the formation of Archean cherts. *To be submitted to Precambrian Research*. (Cité page 141.)

Lee J H et Byrne R H. 1992. Complexation of trivalent rare earth elements (Ce, Eu, Gd, Tb, Yb) by carbonate ions. *Geochimica et Cosmochimica Acta*, 57 : 295–302. (Cité pages 137, 172 et 206.)

Li Y, Ding T, et Wan D. 1995. Experimental stdy of silicon isotope dynamic fractionation and its application in geology. *Chinese Journal of Geochemistry*, 14(3) : 212–219. (Cité page 244.)

Lindsay J F, Brasier M D, McLoughlin N, Green O R, Fogel M, Steele A, et Mertzman S A. 2005. The problem of deep carbon-An Archean paradox. *Precambrian Research*, 143(1-4) : 1–22. (Cité page 29.)

Liu Y G, Miah M R U, et Schmitt R A. 1988. Cerium : A chemical tracer for paleo-oceanic redox conditions. *Geochimica Et Cosmochimica Acta*, 52 : 1361–1371. (Cité page 138.)

Lock J M. 1957. The Magnetic Susceptibilities of Lanthanum, Cerium, Praseodymium, Neodymium and Samarium, from 1.5 °K to 300 °K. *Proceedings of the Physical Society. Section B.*, 70(6) : 556. (Cité page 185.)

Lowe D R. 1975. Water escape structures in coarse-grained sediments. *Sedimentology*, 22 (2) : 157–204. (Cité page 78.)

Lowe D R et Byerly G R. 1986a. Archaean flow-top alteration zones formed initially in a low temperature sulphate-rich environment. *Nature*, 324 : 245–248. (Cité pages 32, 135 et 195.)

Lowe D R et Byerly G R. 1986b. Early Archean silicate spherules of probable impact origin, South Africa and Western Australia. *Geology*, 14 : 83–86. (Cité pages 25, 106, 108 et 119.)

Lowe D R et Byerly G R. 1999. Stratigraphy of the west-central part of the Barberton Greenstone Belt, SouthAfrica. *Geological Society of America Special Papers*, 329 : 1–36. (Cité pages 30, 32, 55 et 106.)

Lowe D R et Byerly G R. 2003. Field Guide to the Geology of the 3.5–3.2 Ga Barberton Greenstone Belt, South Africa. *Guidebook prepared for Field Conference : Archean Surface Processes*, pp. 184. (Cité pages 15, 105, 118 et 197.)

Lowe D R et Nocita B W. 1999. Foreland basin sedimentation in the Mapepe Formation, southern-facies Fig Tree Group. *Geological Society of America Special Paper 329*, 329 : 233–258. (Cité pages 30, 106, 108 et 141.)

Lowe Don R. 1980. Archean Sedimentation. *Annual Review of Earth and Planetary Sciences*, 8 : 145–167. (Cité page 25.)

Lowe Don R. 1999. Petrology and sedimentology of cherts and related silicified sedimentary rocks in the Swaziland Supergroup. *Geological Society of America Special Papers*, 329 : 83–114. (Cité pages 12, 25, 27, 34, 51, 74, 108, 135, 143, 155, 174 et 190.)

Lowe Don R et Byerly Gary R. 2007. An overview of the geology of the Barberton Greenstone Belt : implications for early crustal development. *Developments in Precambrian Geology*, 15 : 481–526. (Cité pages 53, 54 et 174.)

Lowe Don R et Knauth L Paul. 1977. Sedimentology of the Onverwacht Group (3.4 billion years), Transvaal, South Africa, and its bearing on the characteristics and evolution of the early Earth. *Journal of Geology*, 85(6) : 699–723. (Cité pages 25, 27, 32, 33, 80, 105, 155, 172 et 174.)

Lowe Donald R. in press. Crustal fracturing and chert dike formation triggered by large meteorite impacts, ca. 3.260 Ga, Barberton greenstone belt, South Africa. *Geological Society of America Bulletin*, pages 1–19. (Cité pages 105, 106, 107, 108, 111, 119, 120, 122, 124, 141, 167, 190, 197, 245 et 261.)

Lowe Donald R et Braunstein Deena. 2003. Microstructure of high-temperature (>73 °C) siliceous sinter deposited around hot springs and geysers, Yellowstone National Park : the role of biological and abiological processes in sedimentation. *Canadian Journal of Earth Sciences*, 40 : 1611–1642. (Cité page 108.)

Lowe Donald R, Byerly Gary R, Kyte Frank T, Shukolyukov Alexander, Asaro Frank, et Krull Alexandra. 2003. Spherule Beds 3.47-3.24 Billion Years Old in the Barberton Greenstone Belt, South Africa : A Record of Large Meteorite Impacts and Their Influence on Early Crustal and Biological Evolution. *Astrobiology*, 3(1) : 7–48. (Cité pages 14, 105, 108 et 142.)

Lowe Donald R et Fisher Worrell G. 1999. Sedimentology, mineralogy, and implications of silicified evaporites in the Kromberg Formation, Barbeton Greenstone Belt, South Africa. *Geological Society of America Special Paper*, 329 : 167–188. (Cité pages 25, 27, 54, 74, 75, 85, 92, 135 et 248.)

Lowe Donald R et Tice Michael M. 2004. Geologic evidence for Archean atmospheric and climatic evolution : Fluctuating levels of CO_2, CH_4, and O_2 with an overriding tectonic control. *Geology*, 32(6) : 493–496. (Cité page 92.)

Lowe Donald R et Tice Michael M. 2007. Tectonic controls on atmospheric, climatic, and biological evolution 3.5-2.4Ga. *Precambrian Research*, 158(3-4) : 177–197. (Cité page 92.)

Ludwig Kristin A, Kelley Deborah S, Butterfield David A, Nelson Bruce K, et Früh-Green Gretchen. 2006. Formation and evolution of carbonate chimneys at the Lost City Hydrothermal Field. *Geochimica et Cosmochimica Acta*, 70(14) : 3625–3645. (Cité page 11.)

Lupton J E. 1995. Hydrothermal plumes : near and far field. In : Humphris, S.E., Zierenberg, R.A., Mullineaux, L.S., Thomson, R.E. (Eds.), Seafloor Hydrothermal Systems : Physical,

Chemical, Biological, and Geological Interactions. *Geophysical Monograph*, 91 : 317–346. (Cité page 94.)

Lupton J E, Delaney J R, Johnson H P, et Tivey M K. 1985. Entrainment and vertical transport of deep-ocean water by buoyant hydrothermal plumes. *Nature*, 316 : 621–623. (Cité pages 88 et 94.)

Macfarlane A W, Danielson A, et Holland H D. 1994. Geology and major trace element chemistry of late Archean weathering profiles in the Fortescue Group Western Australia : implications for atmospheric po2. *Precambrian Research*, 65 : 297–317. (Cité page 5.)

Malaman B, Venturini G, Chafik El Idrissi B, et Ressouche E. 1997. Magnetic properties of NdMn6Sn6 and SmMn6Sn6 compounds from susceptibility measurements and neutron diffraction study. *Journal of alloys and coumpounds*, 252 : 41–49. (Cité page 185.)

Maliva Robert G, Knoll Andrew H., et Simonson Bruce M. 2005. Secular change in the Precambrian silica cycle : Insights from chert petrology. *Geological Society of America Bulletin*, 117(7/8) : 835–845. (Cité pages 11, 25, 29 et 83.)

Maltman A J et Bolton A. 2003. How sediments become mobilized. *Geological Society of London Special Publication*, 216 : 9–20. (Cité page 78.)

Mantler M. et Kawahara N. 21. How accurate are modern fundamental parameter methods ? *Rigaku Journal*, 2(17-25). (Cité page 319.)

Marin J, Chaussidon M, et Robert F. 2010. Microscale oxygen isotope variations in 1.9 Ga Gunflint cherts : Assessments of diagenesis effects and implications for oceanic paleotemperature reconstructions. *Geochimica et Cosmochimica Acta*, 74(1) : 116–130. (Cité pages 6, 9, 12, 29, 215, 217, 218, 219, 221, 223, 227, 228, 231, 241 et 250.)

Marin-Carbonne J, Chaussidon M, et Robert F. 2012. Micrometer-scale chemical and isotopic criteria (O and Si) on the origin and history of Precambrian cherts : Implications for paleo-temperature reconstructions. *Geochimia et Cosmochimia Acta*, 92 : 129–147. (Cité pages 26, 29, 214, 216, 217, 218, 219, 221, 223, 227, 228, 229, 231, 232, 233, 234, 235, 237, 238, 246 et 335.)

Marin-Carbonne Johanna, Chaussidon Marc, Boiron Marie-Christine, et Robert François. 2011. A combined in situ oxygen, silicon isotopic and fluid inclusion study of a chert sample from Onverwacht Group (3.35Ga, South Africa) : New constraints on fluid circulation. *Chemical Geology*, 286(3–4) : 59–71. (Cité pages 29, 217, 221, 228, 231, 240, 244 et 246.)

Marr J G, Harf P A, Shanmugam G, et Parker G. 2001. Experiments on subaqueous sandy gravity flows : The role of clay and water content in flow dynamics and depositional structures. *Geological Society of America Bulletin*, 113(11) : 1377–1386. (Cité page 79.)

Marshall W L et Warakomski J M. 1980. Amorphous silica solubilities - II. Effect of aqueous salt solutions at 25°C. *Geochimica et Cosmochimica Acta*, 44 : 915–924. (Cité page 123.)

Marshall William L. et Chen Chen-Tung A. 1982. Amorphous silica soluhilities V . Predictions of soluhility behavior in aqueous mixed electrolyte solutions to 300 ° C. *Geochimica et Cosmochimica Acta*, 46 : 289–291. (Cité page 123.)

Martin H, Albarède F, Claeys P, Gargaud M, Marty B, Morbidelli A, et Pinti D L. 2006. Building of a habitable planet. *Earth, Moon and Planets*, 98(1-4) : 97–151. (Cité page 11.)

Martin W, Baross J, Kelley D, et Russell M J. 2008. Hydrothermal vents and the origin of life. *Nature Reviews Microbiology*, 6 : 805–814. (Cité page 94.)

Matsuhisa Y, Goldsmith J R, et Clayton R N. 1979. Oxygen isotopic fractionation in the system quartz–albite–anorthite–water. *Geochimica et Cosmochimica Acta*, 43(7) : 1131–1140. (Cité page 215.)

McKee E D et Goldberg M. 1969. Experiments on formation of contorted structures in mud. *Geological Society of America Bulletin*, 80(2) : 231–244. (Cité page 78.)

McKenzie D et Weiss D. 1975. Speculations on the thermal and tectonic history of the Earth. *Geophys. J. R. Astr. Soc.*, 42 : 131–174. (Cité page 86.)

McLaughlin P L et Brett C E. 2006. Widespread soft-sediment deformation horizons in Lower Silurian strata of the Appalachian basin : distal signature of orogeny. *GFF*, 128 : 169–172. (Cité pages 58 et 80.)

Mewis Jan et Wagner Norman J. 2009. Thixotropy. *Advances in Colloid and Interface Science*, 147–148(0) : 214–227. (Cité pages 121 et 122.)

Michard Annie. 1989. Rare earth element systematics in hydrothermal fluids. *Geochimica et Cosmochimica Acta*, 53(3) : 745–750. (Cité pages 136 et 179.)

Michard Annie et Albarède Francis. 1986. The REE content of some hydrothermal fluids. *Chemical Geology*, 55(1–2) : 51–60. (Cité pages 136 et 179.)

Mills P C. 1983. Genesis and diagnostic value of soft-sediment deformation structures—A review. *Sedimentary Geology*, 35 : 83–104. (Cité page 78.)

Mills Rachel A et Elderfield Henry. 1995. Rare earth element geochemistry of hydrothermal deposits from the active TAG Mound, 26 °N Mid-Atlantic Ridge. *Geochimica et Cosmochimica Acta*, 59(17) : 3511–3524. (Cité page 139.)

Miyano T et Beukes N J. 1984. Phase relations of stilpnomelane, ferri-annite, and riebeckite in very low grade metamorphosed iron formations. *Transaction Geological Society of South Africa*, 87 : 111–124. (Cité pages 30 et 250.)

Mojzsis S J, Harrison T M, et Pidgeon R T. 2001. Oxygen-isotope evidence from ancient zircons for liquid water at the Earth's surface 4,300 Myr ago. *Nature*, 409(6817) : 178–181. (Cité page 8.)

Mojzsis S L, Arrhenius G, et Friend C R L. 1996. Evidence for life onEarth before 3,800 million years ago. *Nature*, 384 : 55–57. (Cité page 10.)

Monecke T, Bombach G, Klemm W, Kempe U, Götze J, et Wolf D. 2000. Determination of trace elements in the quartz reference material UNS-SpS and in natural quartz samples by ICP-MS. *Geostandards Newsletter*, 24(1) : 73–81. (Cité pages 183 et 184.)

Morris R C. 1993. Genetic modeling for banded iron-formation of the Hamersley Group, Pilbara Craton, Western Australia. *Precambrian Research*, 60 : 243–286. (Cité page 93.)

Morris RC et Horwitz R C. 1983. The origin of the iron-formation-rich Hamersley Group of Western Australia — deposition on a platform. *Precambrian Research*, 21(3-4) : 273–297. (Cité page 93.)

Muehlenbachs K. 2008. Revisiting the oxygen isotopic composition of Archean ocean. *Geochimica et Cosmochimica Acta*, 72 : A659. (Cité pages 241 et 249.)

Muehlenbachs K et Clayton R N. 1976. Oxygen isotope composition of the oceanic crust and its bearing on seawater. *Journal of Geophysical Research*, 81 : 4365–4369. (Cité pages 216, 241 et 249.)

Muehlenbachs Karlis. 1998. The oxygen isotopic composition of the oceans, sediments and the seafloor. *Chemical Geology*, 145(3–4) : 263–273. (Cité page 216.)

Mueller W U et Corcoran P L. 1998. Characteristics of pre-vegetational, late-orogenic basins : examples from the Archean Superior Province, Canada.. *Sedimentary Geology*, 120 : 177–204. (Cité pages 6 et 92.)

Muñoz M. et al. 2008. Hyperspectral Î¼-XANES mapping in the diamond-anvil cell : analytical procedure applied to the decomposition of (Mg, Fe)-ringwoodite at the upper/lower mantle boundary. *High Pressure Research*, 4(665-673). (Cité page 321.)

Murray Richard W, Buchholtz Ten Brink Marilyn R, Gerlach David C, Price Russ III G, et Jones David L. 1992a. Rare earth, major, and trace element composition of Monterey and DSDP chert and associated host sediment : Assessing the influence of chemical fractionation during diagenesis. *Geochimica et Cosmochimica Acta*, 56 : 2657–2671. (Cité page 140.)

Murray Richard W, Buchholtz Ten Brink Marilyn R, Gerlach David C, Russ Iii G Price, et Jones David L. 1991. Rare earth, major, and trace elements in chert from the Franciscan Complex and Monterey Group, California : Assessing REE sources to fine-grained marine sediments. *Geochimica et Cosmochimica Acta*, 55(7) : 1875–1895. (Cité page 140.)

Murray Richard W, Buchholtz ten Brink Marilyn R, Gerlach David C, Russ Iii G Price, et Jones David L. 1992b. Interoceanic variation in the rare earth, major, and trace element depositional chemistry of chert : Perspectives gained from the DSDP and ODP record. *Geochimica et Cosmochimica Acta*, 56(5) : 1897–1913. (Cité pages 12 et 135.)

Myrow P M, Fisher W, et Goodge J W. 2002. WAVE-MODIFIED TURBIDITES : COMBINED-FLOW SHORELINE AND SHELF DEPOSITS, CAMBRIAN, ANTARCTICA. *Journal of Sedimentary Research*, 72(5) : 641–656. (Cité page 78.)

Myrow P M, Tice L, Archuleta B, Clark B, Taylor J F, et Ripperdan R L. 2004. Flat-pebble conglomerate : its multiple origins and relationship to metre-scale depositional cycles. *Sedimentology*, 51 : 973–996. (Cité page 81.)

Nagy G, Draganits E, Demeny A, Panto G, et Arkai P. 2002. Genesis and transformations of monazite, florencite and rhabdophane during medium grade metamorphism : examples from the Sopron Hills, Eastern Alps. *Chemical Geology*, 191 : 25–46. (Cité page 163.)

Nesbitt H W, Markovics G, et price R C. 1980. Chemical processes affecting alkalis and alkaline earths during continental weathering. *Geochimica et Cosmochimica Acta*, 44(11) : 1659–1666. (Cité page 163.)

Newman M J et Rood R T. 1977. Implications of solar evolution for the Earth's early atmosphere. *Science*, 198 : 1035–1067. (Cité page 3.)

Nguyen Q D et Boger D V. 1985. Thixotropic behaviour of concentrated bauxite residue suspensions. *Rheologica Acta*, 24(4) : 427–437. (Cité page 122.)

Nichols R J. 1955. The liquefaction and remobilization of sandy sediments. In : Hartley, A.J., Prosser, D.J. (Eds.), Characterization of Deep Marine Clastic Systems. *Geological Society, London, Special Publications*, 94 : 63–76. (Cité page 78.)

Nijman W, de Bruijne K C, et Valkering M E. 1998. Growth fault control of Early Archaean cherts, barite mounds and chert-barite veins, North Pole Dome, Eastern Pilbara, Western Australia. *Precambrian Research*, 88 : 25–52. (Cité page 105.)

Nijman W, de Bruijne K H, et Valkering M E. 1999. Growth fault control of Early Archean cherts, barite mounds et chert-barite veins, North Pole Dome, Eastern Pilbara, Western Australia. *Precambrian Research*, 95(3) : 247–274. (Cité pages 29 et 135.)

Nisbet E G et Sleep N H. 2001. The habitat and nature of early life. *Nature*, 409 : 1083–1091. (Cité page 8.)

Norton D L. 1984. Theory of Hydrothermal Systems. *Annual Review of Earth and Planetary Sciences*, 12(1) : 155–177. (Cité page 10.)

Nothdurft G E, Webb Gregory E G, et Kamber Balz S. 2004. Rare earth element geochemistry of Late Devonian reefal carbonates, Canning basin, Western Australia : confirmation of a seawater REE proxy in ancient limestones. *Geochimica et Cosmochimica Acta*, 68 : 263–283. (Cité pages 140, 163, 172 et 206.)

Nozaki Y, Zhang J, et Amakawa H. 1997. The fractionation between Y and Ho in the marine environment. *Earth and Planetary Science Letters*, 148 : 329–340. (Cité pages 138 et 173.)

Nutman A P, Mojzsis S J, et Friend C R L. 1997. Recognition of â¥ 850Ma water-lain sediments in West Greenland and their significance for the early Archean Earth. *Geochimia et Cosmochimia Acta*, 61 : 2575–2484. (Cité page 8.)

Obermeier S F. 1998. Liquefaction evidence for strong earthquakes of Holocene and latest Pleistocene ages in the states of Indiana and Illinois, USA. *Engineering Geology*, 50 : 227–254. (Cité pages 58 et 80.)

Obermeier S F et Pond E C. 1999. Issues in using liquefaction features for paleoseismic analysis. *Seismol. Res. Lett.*, 70 : 34–58. (Cité pages 58 et 80.)

Ohmoto H. 2004. Archean atmosphere, hydrosphere, and biosphere. In : Eriksson, P.A., Altermann, D.R., Nelson, D.R., Mueller,W.U., Catuneanu, O. (Eds.), The Precambrian Earth : Tempos and Events. *Elsevier, Amsterdam*, pages 361–387. (Cité page 92.)

Oleksy M, Heneczkowski M, et Galina H. 2007. Thixotropic compositions : unsaturated polyester resins/ modified bentonites. *Polimery*, 5 : 345. (Cité page 122.)

Olivarez Annette M et Owen Robert M. 1989. REE/Fe variations in hydrothermal sediments : Implications for the REE content of seawater. *Geochimica et Cosmochimica Acta*, 53 (3) : 757–762. (Cité page 136.)

Olivarez Annette M et Owen Robert M. 1991. The europium anomaly of seawater : implications for fluvial versus hydrothermal REE inputs to the oceans. *Chemical Geology*, 92 (4) : 317–328. (Cité page 174.)

Oliveira C M, Hodgson D M, et Flint S S. 2011. Distribution of soft-sediment deformation structures in clinoform successions of the Permian Ecca Group, Karoo Basin, South Africa. *Sedimentary Geology*, 235 : 314–330. (Cité pages 78 et 79.)

Oliveira C M M, Hodgson D M, et Flint S S. 2009. Aseismic controls on in situ softsediment deformation processes and products in submarine slope deposits of the Karoo Basin, South Africa. *Sedimentology*, 56 : 1201–1225. (Cité page 79.)

Ono S, Eigenbrode J L, Pavlov A A, Kharecha P, Rumble III D, Kasting J F, et Freeman K H. 2003. New insights into Archean sulfur cycle from mass-independent sulfur isotope records from the Hamersley Basin Australia. *Earth and Planetary Science Letters*, 213 : 15–30. (Cité page 5.)

Orberger Beate, Rouchon Virgile, Westall Frances, de Vries Sjoukje T, Pinti Daniele L, Wagner Christiane, Wirth Richard, et Hashizume Ko. 2006. Microfacies and origin of some Archean cherts (Pilbara, Australia). *Geological Society of America Special Papers*, 405 : 133–156. (Cité pages 12 et 29.)

Owen G. 1987. Deformation processes in unconsolidated sands. In : Jones, M.E., Preston, R.M.F. (Eds.), Deformation of Sediments and Sedimentary Rocks. *Geological Society, London, Special Publications*, 29 : 11–24. (Cité page 78.)

Owen G. 1996. Experimental soft-sediment deformation : structures formed by the liquefaction of unconsolidated sands and some ancient examples. *Sedimentology*, 43 : 279–293. (Cité pages 58 et 80.)

Pack A, Shelley J Michael G, et Palme H. 2004. Chondrules with Peculiar REE Patterns : Implications for Solar Nebular Condensation at High C/O. *Science*, 303(5660) : 997–1000. (Cité page 185.)

Pack Andreas, Russell Sara S, Shelley J Michael G, et van Zuilen Mark A. 2007. Geo- and cosmochemistry of the twin elements yttrium and holmium. *Geochimica et Cosmochimica Acta*, 71(18) : 4592–4608. (Cité pages 138, 164 et 173.)

Palmer M R. 1985. Rare earth elements in foraminifera tests. *Earth and Planetary Science Letters*, 73 : 285–298. (Cité page 140.)

Palmer M R et Elderfield H. 1986. Rare earth elements and neodymium isotopes in ferro-manganese oxide coatings pf Cenozoic foraminifera from the Atlantic Ocean. *Geochimica Et Cosmochimica Acta*, 50 : 409–417. (Cité page 140.)

Panahi Alireza, Young Grant M., et Rainbird Robert H. 2000. Behavior of major and trace elements (including REE) during Paleoproterozoic pedogenesis and diagenetic alteration of an Archean granite near Ville Marie, Québec, Canada. *Geochimica et Cosmochimica Acta*, 64(13) : 2199–2220. (Cité page 140.)

Paris Isabelle, Stanistreet Ian G, et Hughes Martin J. 1985. Cherts of the Barberton Greenstone Belt Interpreted as Products of Submarine Exhalative Activity. *The Journal of Geology*, 93(2) : 111–129. (Cité pages 8, 12, 25, 26, 29, 87, 195 et 215.)

Pavlov A A, Hurtgen M T, Kasting J F, et Arthur M A. 2003. Methane-rich Proterozoic atmosphere ? *Geology*, 31 : 87–90. (Cité page 4.)

Pavlov A A et Kasting J F. 2002. Mass-independent fractionation of sulfur isotopes in Archean sediments : Strong evidence for an anoxic Archean atmosphere. *Astrobiology*, 2 : 27–41. (Cité page 5.)

Pavlov A A, Kasting J F, Brown L L, Rages K A, et Freedman R. 2000. Greenhouse warming by CH4 in the atmosphere of early Earth. *Journal of Geophysical Research*, 105 : 11 981–11 990. (Cité page 4.)

Peck W H, Valley J W, Wilde S A, et Graham C M. 2001. Oxygen isotope ratios and rare earth elements in 3.3 to 4.4 Ga zircons : Ion microprobe evidence for high Î´18O continental crust and oceans in the Early Archean. *Geochimia et Cosmochimia Acta*, 65 : 4215– 4229. (Cité page 8.)

Perret A, Locat P, et Martignoni P. 1996. Thixotropic behavior during shear of a fine-grained mud from Eastern Canada. *Engineering Geology*, 43(1) : 31–44. (Cité page 79.)

Perry E C. 1967. The oxygen isotopes chemistry of ancient cherts. *Earth and Planetary Science Letters*, 3 : 62–66. (Cité page 215.)

Perry E C et Lefticariu L. 2003. Formation and Geochemistry of Precambrian cherts. *Treatise of geochemistry, Vol. 7, pp. 99-113.*, 7 : 99–113. (Cité pages 11, 12, 25, 26, 135, 215 et 216.)

Perry E C et Lefticariu L. 2006. The oxygen isotopic composition of Precambrian cherts. *Geochimica Et Cosmochimica Acta*, 70(18) : A483–A483. (Cité page 25.)

Perry E C et Lefticariu L. 2007. Formation and geochemistry of Precambrian cherts. *Treatise of geochemistry*, 7 : 99–113. (Cité page 216.)

Pichler Thomas, Veizer Jan, et Hall Gwendy E M. 1999. The chemical composition of shallow-water hydrothermal fluids in Tutum Bay, Ambitle Island, Papua New Guinea and their effect on ambient seawater. *Marine Chemistry*, 64(3) : 229–252. (Cité page 140.)

Pickard A L. 2002. SHRIMP U-Pb zircon ages of tuffaceous mudrocks in the Brockman Iron Formation of the Hamersley Range, Western Australia. *Australian Journal of Earth Sciences*, 49 : 491–507. (Cité pages 83, 89 et 90.)

Piepgras D J et Wasseburg G J. 1980. Neodymium isotopic variations in seawater. *Earth and Planetary Science Letters*, 50 : 128–138. (Cité pages 10 et 136.)

Pignon Frédéric, Magnin Albert, et Piau Jean-michel. 1998. Thixotropic behavior of clay dispersions : Combinations of scattering and rheometric techniques. *Journal of Rheology*, 42(6) : 1349–1373. (Cité page 79.)

Pinti Daniele L, Mineau Raymond, et Clement Valentin. 2009. Hydrothermal alteration and microfossil artefacts of the 3,465-million-year-old Apex chert. *Nature Geocience*, 2 : 640–643. (Cité page 135.)

Pope M C, Read J F, Bambach R, et Hofmann J J. 1997. Late Middle to Late Ordovician seismites of Kentucky, southwest Ohio and Virginia : sedimentary recorders of earthquakes in the Appalachian basin. *Geological Society of America Bulletin*, 109 : 489–503. (Cité pages 58 et 80.)

Posth Nicole R., Hegler Florian, Konhauser Kurt O., et Kappler Andreas. Septembre 2008. Alternating Si and Fe deposition caused by temperature fluctuations in Precambrian oceans. *Nature Geoscience*, 1(10) : 703–708. (Cité pages 87 et 93.)

Potter P E et Pettijohn F J. 1963. Palaeocurrents and Basin Analysis. *Springer, Berlin*, pp. 296. (Cité pages 58 et 80.)

Pratt B R. 2002. Storms versus tsunamis : Dynamic interplay of sedimentary diagenesic, and tectonic processes in the Cambrian of Montana. *Geology*, 30(5) : 423–426. (Cité page 81.)

Radulescu I G, Rubatto D, Gregory C, et Compagnoni R. 2009. The age of HP metamorphism in the Gran Paradiso Massif, Western Alps : a petrological and geochronological study of "silvery micaschists". *Lithos*, 110 : 95–108. (Cité page 163.)

Ramberg H. 1955. Natural and experimental boudinage and pinch-and-swell structures. *Journal of Geology*, 63(6) : 512–526. (Cité page 80.)

Rasmussen B et Buick R. 1999. Redox state of the Archean atmosphere : Evidence from detrital heavy minerals in ca. 3250–2750 Ma sandstones from the Pilbara Craton, Australia. *Geology*, 27 : 115–118. (Cité page 5.)

Reimer T O. 1980. Archean sedimentary baryte deposits of the Swaziland Supergroup (Barberton Mountain Land, South Africa). *Precambrian Research*, 12 : 393–410. (Cité page 196.)

Renaut R W, Jones B, Tiercelin J J, et Tarits C. 2002. Sublacustrine precipitation of hydrothermal silica in rift lakes : evidence from Lake Baringo, centra Kenya Rift Valley. *Sedimentary Geology*, 148 : 235–257. (Cité page 123.)

Renaut Robin W et Jones Brian. 2003. Sedimentology of hot spring systems. *Canadian Journal of Earth Sciences*, 40 : 1439–1442. (Cité page 123.)

Reynard B, Lécuyer C, et Grandjean P. 1999. Crystal-chemical controls on rare earth element concentrations in fossil biogenic apatite and implications for paleoenvironmental reconstructions. *Chemical Geology*, 155 : 233–242. (Cité page 140.)

Reynolds B C, Frank M, et Halliday A N. 2006. Silicon isotope fractionation during nutrient utilization in the North Pacific. *Earth and Planetary Science Letters*, 244 : 431–443. (Cité page 230.)

Rimstidt J D et Barnes H L. 1980. The kinetics of silica-water interaction. *Geochimia et Cosmochimia Acta*, 44 : 1683–1699. (Cité pages 83 et 123.)

Rimstidt J Donald et Cole D R. 1983. Geothermal mineralization 1 : The mechanism of formation of the Beowawe, Nevada, siliceous sinter deposit. *American Journal of Science*, 283 : 861–875. (Cité page 123.)

Robert Francois et Chaussidon Marc. 2006. A palaeotemperature curve for the Precambrian oceans based on silicon isotopes in cherts. *Nature*, 443(7114) : 969–972. (Cité pages 6, 8, 12, 25, 92, 215, 217, 221, 230, 241 et 249.)

Rosing M T. 1999. C-13-depleted carbon microparticles in N3700- Ma sea-floor sedimentary rocks from west Greenland. *Science*, 283 : 674– 676. (Cité page 10.)

Rosing M T, Bird D K, Sleep N H, et Bjerrum C J. 2010. No climate paradox under the faint early Sun. *Nature*, 464 : 744–747. (Cité pages 3 et 4.)

Rosing M T et Frei R. 2004. U-rich Archaean sea-floor sediments from Greenland—indications of N3700 Ma oxygenic photosynthesis. *Earth and Planetary Science Letters*, 217 : 237–244. (Cité page 10.)

Rosing M T, Rose N M, Bridgwater D, et Thomsen H S. 1996. Earliest part of Earth's stratigraphic record : A reappraisal of the > 3.7Ga Isua (Greenland) supracrustal sequence. *Geology*, 24 : 43–46. (Cité page 8.)

Rouchon Virgile et Orberger Beate. 2008. Origin and mechanisms of K–Si-metasomatism of ca. 3.4–3.3 Ga volcaniclastic deposits and implications for Archean seawater evolution : Examples from cherts of Kittys Gap (Pilbara craton, Australia) and Msauli (Barberton Greenstone Belt, South Africa). *Precambrian Research*, 165(3–4) : 169–189. (Cité pages 25, 30, 83, 84, 123 et 250.)

Rouchon Virgile, Orberger Beate, Hofmann Axel, et Pinti Daniele L. 2009. Diagenetic Fe-carbonates in Paleoarchean felsic sedimentary rocks (Hooggenoeg Formation, Barberton greenstone belt, South Africa) : Implications for CO2 sequestration and the chemical budget of seawater. *Precambrian Research*, 172(3–4) : 255–278. (Cité pages 34, 42, 50, 51, 83, 84, 155, 162, 164, 165, 196, 242 et 266.)

Runnegar B. 1982. The Cambrian explosion—animals or fossils. *J. Geol. Soc. Aust.*, 29 : 395–411. (Cité page 10.)

Rusk B G, Lowers H A, et Reed M H. 2008. Trace elements in hydrothermal quartz : Relationships to cathodoluminescent textures and insights into vein formation. *Geology*, 36(7) : 547–550. (Cité page 237.)

Russell M J, Daniel R M, et Hall A J. 1993. On the emergence of life via catalytic iron-sulphide membranes. *Terra Nova*, 5 : 343–347. (Cité page 94.)

Rye R et Holland H. 1998. Paleosols and the evolution of atmospheric oxygen ; a critical review. *American Journal of Science*, 298(8) : 621–672. (Cité page 5.)

Rye R, Kuo P H, et Holland H D. 1995. Atmospheric carbon dioxide concentrations before 2.2 billion years ago. *Nature*, 378 : 603–605. (Cité page 4.)

Sagan C et Chyba C. 1997. The early faint Sun paradox : Organic shielding of ultraviolet-labile greenhouse gases. *Science*, 276 : 1217–1221. (Cité pages 3 et 4.)

Sagan C et Mullen G. 1972. Earth and Mars : evolution of atmospheres and surface temperatures. *Science*, 177 : 52–56. (Cité page 3.)

Sanchez-Garrido Cynthia, Stevens Gary, Armstrong Richard A, Moyen Jean-François, Martin Hervé, et Doucelance Régis. September 2011. Diversity in Earth's early felsic crust : Paleoarchean peraluminous granites of the Barberton Greenstone Belt. *Geology*, 39(10) : 963–966. (Cité page 50.)

Sanderson D J. 1974. Patterns of boudinage and apparent stretching lineation developed in folded rocks. *Journal of Geology*, 82 : 651–661. (Cité page 80.)

Schopf J W. 1993. Microfossils of the early Archean Apex chert : new evidence of the antiquity of life. *Science*, 260 : 640–645. (Cité pages 10 et 135.)

Schopf J William, Kudryavtsev Anatoliy B, Czaja Andrew D, et Tripathi Abhishek B. 2007. Evidence of Archean life : Stromatolites and microfossils. *Precambrian Research*, 158(3–4) : 141–155. (Cité pages 10 et 135.)

Seilacher A. 1991. Events and their signatures - an overview. In : Einsele, G. (Ed.). Cycles and Events in Stratigraphy. *Springer, Berlin*, pages 222–226. (Cité page 81.)

Sepkoski Jr J J, Bambach R K, et Droser M L. 1991. Secular changes in Phanerozoic event bedding and the biological overprint. In : Einsele, G. (Ed.). Cycles and Events in Stratigraphy. *Springer, Berlin*, pages 298–312. (Cité page 81.)

Seyfried W E. 1987. Experimental and Theoretical Constraints on Hydrothermal Alteration Processes at Mid-Ocean Ridges. *Annual Review of Earth and Planetary Sciences*, 15(1) : 317–335. (Cité pages 11 et 179.)

Seyfried W E, Chen Xian, et Chan Lui-Heung. 1998. Trace Element Mobility and Lithium Isotope Exchange During Hydrothermal Alteration of Seafloor Weathered Basalt : An Experimental Study at 350 °C, 500 Bars. *Geochimica et Cosmochimica Acta*, 62(6) : 949–960. (Cité pages 10 et 179.)

Seyfried Jr. W E, Seewald J S, Berndt M E, Ding Kang, et Foustoukos D I. 2003. Chemistry of hydrothermal vent fluids from the Main Endeavour Field, northern Juan de Fuca Ridge : Geochemical controls in the aftermath of June 1999 seismic events. *J. Geophys. Res.*, 108 (B9) : 2429. (Cité page 174.)

Shahwan T, Sayan S, Erten H N, Black L, Hallam K R, et Allen G C. 2000. Surface spectroscopic studies of Cs^+, and Ba^{2+} sorption on chlorite-illite mixed clay. *Radiochimica Acta*, 88(9-11) : 681. (Cité page 163.)

Shannon R D. 1976. Revised effective ionic radii and systematic studies of interatomic distances in halides and chalcogenides. *Acta Crystallographica*, A32 : 751–767. (Cité page 138.)

Sharma N, Wasserburg G J, Papanastassiou D A, Quick J E, Sharkov E V, et Laz'ko E E. 1995. High 143Nd/144Nd in extremly depleted mantle rocks. *Earth and Planetary Science Letters*, 135 : 101–114. (Cité page 185.)

Shaw George H. 2008. Earth's atmosphere – Hadean to early Proterozoic. *Chemie der Erde - Geochemistry*, 68(3) : 235–264. (Cité page 92.)

Shibuya Takazo, Komiya Tsuyoshi, Nakamura Kentaro, Takai Ken, et Maruyama Shigenori. 2010. Highly alkaline, high-temperature hydrothermal fluids in the early Archean ocean. *Precambrian Research*, 182(3) : 230–238. (Cité pages 11, 88, 93 et 185.)

Shields G, Stille P, Brasier M D, et Atudorei N V. 1997. Stratified oceans and oxygenation of the late Proterozoic environment : a post glacial geochemical record from the Neoproterozoic of W Mongolia. *Terra Nova*, 9 : 218–222. (Cité pages 9, 139 et 182.)

Shields Graham et Stille Peter. 2001. Diagenetic constraints on the use of cerium anomalies as palaeoseawater redox proxies : an isotopic and REE study of Cambrian phosphorites. *Chemical Geology*, 175(1–2) : 29–48. (Cité pages 138, 140, 163 et 174.)

Shields Graham A et Webb Gregory E. 2004. Has the REE composition of seawater changed over geological time ? *Chemical Geology*, 204(1–2) : 103–107. (Cité pages 138, 140 et 163.)

Shimizu H, Umemoto N, Masuda A, et Appel P W U. 1990. Source of iron-formations in the Archean Isua and Malene supracrustals, West Greenland : evidence from La-Ce and Sm-Nd isotopic data and REE. *Geochimica et Cosmochimica Acta*, 54 : 1147–1154. (Cité page 139.)

Sholkovitz E R et Shen G T. 1995. The incorporation of rare earth elements in modern coral. *Geochimica Et Cosmochimica Acta*, 59 : 2749–2756. (Cité page 140.)

Sholkovitz Edward R, Landing W M, et Lewis B L. 1994. Ocean particle chemistry : The fractionation of rare earth elements between suspended particles and seawater. *Geochimica et Cosmochimica Acta*, 58 : 1567–1579. (Cité pages 137 et 138.)

Siever R et Woodford N. 1973. Sorption of silica by clay minerals. *Geochimica et Cosmochimica Acta*, 37 : 1851–1880. (Cité pages 84 et 165.)

Siever Raymond. 1992. The silica cycle in the Precambrian. *Geochimica et Cosmochimica Acta*, 56(8) : 3265–3272. (Cité pages 11, 25, 83 et 90.)

Sleep N H, Zahnle K J, Kasting J F, et Morowitz H J. 1989. Annihilation of ecosystems by large asteroid impacts on the early Earth. *Nature*, 342 : 139–142. (Cité page 8.)

Sleep Norman H. et Hessler Angela M. 2006. Weathering of quartz as an Archean climatic indicator. *Earth and Planetary Science Letters*, 241(3-4) : 594–602. (Cité page 51.)

Smith R B. 1975. Unified theory of the onset of folding, boudinage, and mullion structure. *Geological Society of America Bulletin*, 86(11) : 1601–1609. (Cité page 80.)

Smith R B. 1977. Formation of folds, boudinage, and mullions in non-Newtonian materials. *Geological Society of America Bulletin*, 88(2) : 312–320. (Cité page 80.)

Stade H et Wicker W. 1971. *Anorg. Allg. Chem.*, 384(53). (Cité page 123.)

Steinhoefel G, von Blanckenburg F, Horn I, Konhauser K O, Beukes N J, et Gutzmer J. 2010. Deciphering formation processes of banded iron formations from the Transvaal and the Hamersley successions by combined Si and Fe isotope analysis using UV femtosecond laser ablation. *Geochimia et Cosmochimia Acta*, 74 : 2677–2696. (Cité page 217.)

Sugitani K, Yamamoto K, Adachi M, Kawabe I, et Sugisaki R. 1998. Archean cherts derived from chemical, biogenic and clastic sedimentation in a shallow restricted basin : examples from the Gorge Creek Group in the Pilbara Block. *Sedimentology*, 45(6) : 1045–1062. (Cité pages 12, 25 et 26.)

Sugitani Kenichiro. 1992. Geochemical characteristics of Archean cherts and other sedimentary rocks in the Pilbara Block, Western Australia : evidence for Archean seawater enriched in hydrothermally-derived iron and silica. *Precambrian Research*, 57(1–2) : 21–47. (Cité pages 12, 25, 26, 27, 29, 135, 140 et 215.)

Sugitani Kenichiro, Horiuchi Yoshikuni, Adachi Mamoru, et Sugisaki Ryuichi. 1996. Anomalously low Al2O3/TiO2 values for Archean cherts from the Pilbara Block, Western Australia - possible evidence for extensive chemical weathering on the early earth. *Precambrian Research*, 80 : 49–76. (Cité pages 6, 12, 25 et 51.)

Sugitani Kenichiro, Mimura Koichi, Suzuki Kazuhiro, Nagamine Koichiro, et Sugisaki Ryuichi. 2003. Stratigraphy and sedimentary petrology of an Archean volcanic–sedimentary succession at Mt. Goldsworthy in the Pilbara Block, Western Australia : implications of evaporite (nahcolite) and barite deposition. *Precambrian Research*, 120 (1–2) : 55–79. (Cité pages 4 et 92.)

Sugitani Kenichiro, Yamamoto Koshi, Wada Hideki, Binu-Lal S S, et Yoneshige Masakazu. 2002. Geochemistry of Archean carbonaceous cherts deposited at immature island-arc setting in the Pilbara Block, Western Australia. *Sedimentary Geology*, 151(1–2) : 45–66. (Cité page 215.)

Sverjensky Dimitri A. 1984. Europium redox equilibria in aqueous solution. *Earth and Planetary Science Letters*, 67(1) : 70–78. (Cité page 182.)

Szulczewski M. 1968. Slump structures and turbidites in Upper Devonian limestones of the Holy Cross Mts. *Acta Geologica Polonica*, 18 : 304–326. (Cité pages 80 et 81.)

Tanner L H et Lucas S G. 2010. Deposition and deformation of fluvial–lacustrine sediments of the Upper Triassic–Lower Jurassic Whitmore Point Member, Moenave Formation, northern Arizona. *Sedimentary Geology*, 223 : 180–191. (Cité page 79.)

Taylor K N R. 1971. INTERMETALLIC RARE-EARTH COMPOUNDS. *Advances in Physics*, 20(87) : 551–660. (Cité page 185.)

Taylor S R et McLennan S M. 1985. The Continental Crust : its composition and evolution. *Blackwell Scientific Publications, (Eds. A. Hallam)*, pp. 312. (Cité pages 137, 161, 162, 182, 247 et 333.)

Taylor S R et McLennan S M. 1995. The geochemical evolution of the continental crust. *Reviews of Geophysics*, 33 : 241–265. (Cité page 11.)

Thomsen V. 2007. Basic Fundamental Parameters in X-Ray Fluorescence. *Spectroscopy*, 5 : 46–58. (Cité page 319.)

Thöni M, Miller C, Zanetti A, Habler G, et Goessler W. 2008. Sm–Nd isotope systematics of high-REE accessory minerals and major phases : ID-TIMS, LA-ICP-MS and EPMA data constrain multiple Permian–Triassic pegmatite emplacement in the Koralpe, Eastern Alps. *Chemical Geology*, 254 : 216–237. (Cité page 163.)

Tice Michael M, Bostick Benjamin C, et Lowe Donald R. 2004. Thermal history of the 3.5-3.2 Ga Onverwacht and Fig Tree Groups, Barberton greenstone belt, South Africa, inferred by Raman microspectroscopy of carbonaceous material. *Geology*, 32(1) : 37–40. (Cité pages 30, 174 et 250.)

Tice Michael M et Lowe Donald R. 2004. Photosynthetic microbial mats in the 3,416-Myr-old ocean. *Nature*, 431(7008) : 549–552. (Cité pages 30 et 55.)

Tice Michael M et Lowe Donald R. 2006. The origin of carbonaceous matter in pre-3.0 Ga greenstone terrains : A review and new evidence from the 3.42 Ga Buck Reef Chert. *Earth-Science Reviews*, 76(3–4) : 259–300. (Cité pages 25, 26, 27, 31, 54, 55, 74, 75, 85, 87, 88, 92, 143, 174, 175, 178 et 248.)

Tobler Dominique J, Stefánsson Andri, et Benning Liane G. 2008. In-situ grown silica sinters in Icelandic geothermal areas. *Geobiology*, 6(5) : 481–502. (Cité page 123.)

Tosca N H, Johnston D T, Mushegian A A, Rothman D H, Summons R E, et Knoll A H. 2012. Clay mineralogy, organic carbon burial, and redox evolution in the Proterozoic oceans. *Geochimica Et Cosmochimica Acta*, 75(5) : 1579–1592. (Cité page 6.)

Toulkeridis Theofilos, Goldstein Steve L, Clauer Norbert, Kröner Alfred, Todt Wolfgang, et Schidlowski Manfred. 1998. Sm–Nd, Rb–Sr and Pb–Pb dating of silicic carbonates from the early Archaean Barberton Greenstone Belt, South Africa : Evidence for post-depositional isotopic resetting at low temperature. *Precambrian Research*, 92(2) : 129–144. (Cité pages 30 et 250.)

Towe K M. 1996. Environmental oxygen conditions during the origin and early evolution of life. *Advances in Space Research*, 18(12) : 7–15. (Cité page 5.)

Trainer M G et al. 2006. Organic haze on Titan and the early Earth. . *Proceedings of the National Academy of Sciences of the United States of America*, 103 : 18035–18042. (Cité page 4.)

Treguer P, Nelson D M, Van Bennekom A J, DeMaster D J, Leynaert A, et Queguiner B. 1995. The silica balance in the world ocean : a reestimate. *Science*, 268 : 375–379. (Cité pages 11 et 25.)

Ueno Yuichiro, Yamada Keita, Yoshida Naohiro, Maruyama Shigenori, et Isozaki Yukio. 2006. Evidence from fluid inclusions for microbial methanogenesis in the early Archaean era. *Nature*, 440 : 516–519. (Cité page 4.)

Ulrich M, Munoz E, Guillot S, Cathelineau M, Picard C, Quesnel B, et Boulvais P. submitted. Dissolution-precipitation processes governing the carbonation and subsequent silicification of the serpentine sole from the New Caledonia Ophiolite. *Economic Geology*. (Cité pages 46, 146 et 320.)

Ulrich Marc. 2010. Péridotites et serpentinites du complexe ophiolitique de la Nouvelle-Calédonieridotites et serpentinites du complexe ophiolitique de la Nouvelle-Calédonie. *PhD manuscript ; Université de la Nouvelle-Calédonie et Université Joseph Fourier de Grenoble*, pages 1–272. (Cité page 320.)

Valley J W. 2006. Early Earth. *Elements*, 2 : 201–204. (Cité page 14.)

Van den Boorn H J M, van Bergen M J J, Vroon P Z Z, de Vries S T T, et Nijman W. 2010. Silicon isotope and trace element constraints on the origin of 3.5 Ga cherts : Implications for Early Archaean marine environments. *Geochimica et Cosmochimica Acta*, 74(3) : 1077–1103. (Cité pages 6, 9, 12, 26, 29, 135, 215, 216, 217, 219, 232, 234 et 241.)

Van den Boorn Sander H J M, van Bergen Manfred J, Nijman Wouter, et Vroon Pieter Z. 2007. Dual role of seawater and hydrothermal fluids in Early Archean chert formation : Evidence from silicon isotopes. *The Geological Society of America*, 35(10) : 939–942. (Cité pages 12, 26, 27, 29, 135, 217, 219 et 230.)

van Kranendonk M J. 2006. Volcanic degassing, hydrothermal circulation and the flourishing of early life onEarth : a review of the evidence from c. 3490–3240 Ma rocks of the Pilbara Supergroup, Pilbara Craton,Western Australia. *Earth-Science Reviews*, 74 : 197–240. (Cité page 135.)

van Kranendonk M J. 2007. A review of the evidence for putative Paleoarchean life in the Pilbara Craton, Western Australia. *Earth's Oldest Rocks (Ed. MJ van Kranendonk, RH Smithies, VC Bennett)*, Amsterdam : Elsevier : 855– 77. (Cité pages 10 et 135.)

Van Kranendonk M J et Pirajno F. 2004. Geochemistry of metabasalts and hydrothermal alteration zones associated with c. 3.45 Ga chert and barite deposits : implication for the geological setting of the Warrawoona Group, Pilbara Craton, Australia. *Geochem. Expl. Env. Anal.*, 4 : 253–278. (Cité pages 12 et 25.)

Van Kranendonk Martin J, Webb Gregory E, et Kamber Balz S. 2003. Geological and trace element evidence for a marine sedimentary environment of deposition and biogenicity of 3.45 Ga stromatolitic carbonates in the Pilbara Craton, and support for a reducing Archaean ocean. *Geobiology*, 1(2) : 91–108. (Cité pages 25, 87, 92, 140, 172 et 206.)

van Sprang H. A. 2000. Fundamental Parameter Methods in XRF Spectroscopy. *Advances in X-ray Analysis*, 42 : 1–10. (Cité page 319.)

Varela D E, Pride C J, et Brzezinski M A. 2004. Biological fractionation of silicon isotopes in Southern Ocean surface waters. *Global Biogeochem. Cycles*, 18 : 1041–1048. (Cité pages 240 et 246.)

Veizer J, Hoefs Jochen, Lowe D R, et Thurston Phillips C. 1989. Geochemistry of Precambrian carbonates : II. Archean greenstone belts and Archean seawater. *Geochimica et Cosmochimica Acta*, 53(859-871). (Cité pages 87, 172 et 206.)

Vierek A. 2010. Flat-pebble conglomerate : its multiple origins and relationship to metrescale depositional cycles. *Geologos*, 16(3) : 153–168. (Cité page 81.)

Viezer J et Jansen S L. 1985. Basement and sedimentary recycling - 2 : Time dimension to global tectonics. *The Journal of Geology*, 93(6) : 625–643. (Cité page 4.)

Viljoen M J et Viljoen R P. 1969a. An introduction to the geology of the Barberton, granite-greenstone terrain. *Geological Society of south Africa Special Publication*, 9 : 1–20. (Cité pages 30, 32, 53 et 106.)

Viljoen M J et Viljoen R P. 1969b. The geological and geochemical significance of the upper formations of the Onverwacht Group. Upper Mantle Project Special. *Publications of the Geological Society of South Africa*, 2 : 113–151. (Cité pages 30 et 106.)

Viljoen M J et Viljoen R P. 1969c. The geology and geochemistry of the lower ultramafic unit of the Onverwacht Group and a proposed new class of igneous rocks. . *Geological Society of south Africa Special Publication*, 2 : 55–86. (Cité pages 30, 53 et 106.)

Von Brunn V et Gold D J D. 1993. Diamictite in the Archean Pongola sequence of southern Africa. *Journal of African Earth Sciences*, 16 : 367–374. (Cité pages 3 et 93.)

Von Damm K L. 1990. Seafloor Hydrothermal Activity : Black Smoker Chemistry and Chimneys. *Annual Review of Earth and Planetary Sciences*, 18(1) : 173–204. (Cité page 174.)

Wacey D. 2010. Stromatolites in the â¼3400 Ma Strelley Pool Formation, Western Australia : examining biogenicity from the macro- to the nano-scale. *Astrobiology*, 10 : 381–95. (Cité pages 10 et 135.)

Walker J C G, Hays P B, et Kasting J F. 1981. A negative feedback mechanism for the long-term stabilization of Earth's surface temperature. *Journal of Geophysical Research*, 86 : 9776–9782. (Cité pages 3, 4 et 6.)

Walsh Maud M. 1992. Microfossils and possible microfossils from the Early Archean Onverwacht Group, Barberton Mountain Land, South Africa. *Precambrian Research*, 54 : 271–292. (Cité pages 55 et 174.)

Walsh Maud M et Lowe Don R. 1999. Modes of accumulation of carbonaceous matter in the early Archean : A petrographic and geochemical study of the carbonaceous cherts of the Swaziland Supergroup. *Geological Society of America Special Paper 329, p.115–132.*, 329 : 115–132. (Cité page 27.)

Walter M R, Bauld J, et Brock T D. 1972. Siliceous algal and bacterial stromatolites in hot spring and geyser effluents of Yellowstone National Park. *Science*, 178 : 402–405. (Cité page 89.)

Wang Y, Xu H, Merino E, et Konishi H. 2009. Generation of banded iron formations by internal dynamics and leaching of oceanic crust. *Nature Geoscience*, 2 : 781–784. (Cité page 94.)

Ward J M.H. 1995. Geology and metallogeny of the Barberton Greenstone Belt : a survey. . *Journal of African Earth Sciences*, 21(2) : 213–240. (Cité pages 30 et 250.)

Webb Gregory E et Kamber Balz S. 2000. Rare earth elements in Holocene reefal microbialites : a shallow seawater proxy. *Geochimica et Cosmochimica Acta*, 64 : 1557–1565. (Cité pages 138, 140, 163 et 173.)

Wefer G, Berger W H, Richter C, et Party Shipboard Scientific. 1998. Facies patterns and authigenic minerals of upwelling deposits off Southwest Africa. *Proceedings of the Ocean Drilling Program, Initial Reports*, 175 : 487–504. (Cité page 94.)

Weis D et Wasserburg G J. 1987. Rb-Sr and Sm-Nd isotope geochemistry of cherts from the Onverwacht Group (3.5 AE), South Africa. *Geochimica et Cosmochimica Acta*, 51 : 973–984. (Cité page 25.)

Westall Frances. 2005. Life on the Early Earth : A Sedimentary View. *Science*, 308(5720) : 366–367. (Cité pages 55 et 174.)

Westall Frances, de Wit Maarten J, Dann Jesse, van der Gaast Sjerry, de Ronde Cornel E J, et Gerneke Dane. 2001. Early Archean fossil bacteria and biofilms in hydrothermally-influenced sediments from the Barberton greenstone belt, South Africa. *Precambrian Research*, 106(1–2) : 93–116. (Cité pages 10, 74, 135 et 174.)

Wheat C Geoffrey, Mottl Michael J, et Rudnicki Mark. 2002. Trace element and REE composition of a low-temperature ridge-flank hydrothermal spring. *Geochimica et Cosmochimica Acta*, 66(21) : 3693–3705. (Cité pages 11, 140 et 174.)

Wiebols J H. 1955. A Suggested Glacial Origin for the Witwatersrand Conglomerates. *Geological Society of South Africa*, 58 : 21. (Cité pages 3 et 93.)

Wilde S A, Valley J W, Peck W H, et Graham C M. 2001. Evidence from detrital zircons for the existence of continental crust and oceans on Earth 4.4 Gyr ago. *Nature*, 409 : 175–178. (Cité page 8.)

Williams George E. 1998. Precambrian tidal and glacial clastic deposits : implications for Precambrian Earth–Moon dynamics and palaeoclimate. *Sedimentary Geology*, 120(1-4) : 55–74. (Cité page 4.)

Williams L A, Parks G A, et Crerar D A. 1985. Silica diagenesis, I. Solubility controls. *Journal of Sedimentary Petrology*, 55 : 301–311. (Cité pages 83, 84 et 123.)

Williams Loretta Ann et Crerar David A. 1985. Silica diagenesis ; II, General mechanisms. *Journal of Sedimentary Research*, 55(3) : 312–321. (Cité pages 83, 84 et 123.)

Winter Bryce L et Knauth L Paul. 1992. Stable isotope geochemistry of cherts and carbonates from the 2.0 Ga gunflint iron formation : implications for the depositional setting, and the effects of diagenesis and metamorphism. *Precambrian Research*, 59(3–4) : 283–313. (Cité page 215.)

Wolff M W, Niemann S, Ebel T, et Jeitschko W. 2001. Magnetic properties of rare-earth transition metal aluminides R6T4Al43 with Ho6Mo4Al43-type structure. *Journal of magnetism and magnetic materials*, 223(1) : 1–15. (Cité page 185.)

Wood Scott A. 1990. The aqueous geochemistry of the rare-earth elements and yttrium : 1. Review of available low-temperature data for inorganic complexes and the inorganic REE speciation of natural waters. *Chemical Geology*, 82(0) : 159–186. (Cité page 136.)

Wright J, Schrader H, et Holser W T. 1987. Paleoredox variations in ancient oceans recorded by rare earth elements in fossil apatite. *Geochimica Et Cosmochimica Acta*, 51 : 631–644. (Cité pages 9 et 139.)

Xie X, Byerly G R, et Ferrell R E. 1997. IIb trioctahedral chlorite from the Barberton Greenstone Belt : crystal structure and rock composition constraints with implications to geothermometry. *Contributions to Mineralogy and Petrology*, 126 : 275–291. (Cité page 15.)

Yang J, Sun W, Wang Z, Xue Y, et Tao X. 1999. Variations in Sr and C isotopes and Ce anomalies in successions from China : evidence for the oxygenation of Neoproterozoic seawater. *Precambrian Research*, 93 : 215–233. (Cité pages 9, 139 et 182.)

Yates D M, Joyce K J, et Heaney P J. 1998. Complexation of copper with polymeric silica in aqueous solution. *Applied Geochemistry*, 13(2) : 235–241. (Cité page 123.)

Young G M et Gostin V A. 1991. Late Proterozoic (Sturtian) succession of the North Flinders Basin, South Australia ; An example of temperate glaciation in an active rift setting. In : Anderson, J.B., Ashley, G.M. (Eds.), Glacial Marine Sedimentation ; Paleoclimatic Significance. . *Geological Society of America Special Paper*, 261 : 207–222. (Cité pages 3 et 93.)

Zahnle J, Arndt N T, Cockell C, Halliday A, Nisbet E, Selsis F, et Sleep N H. 2007. Emergence of a habitable planet. *Space Science Reviews*, 129 : 35–78. (Cité page 8.)

Zhang J et Nozaki Y. 1998. Behavior of rare earth elements in seawater at the ocean margin : A study along the slopes of Sagami and Nankai Troughs near Japan. *Geochimica et Cosmochimica Acta*, 62 : 1307–1317. (Cité page 136.)

Zhang Jing et Nozaki Yoshiyuki. 1996. Rare earth elements and yttrium in seawater : ICP-MS determinations in the East Caroline, Coral Sea, and South Fiji basins of the western South Pacific Ocean. *Geochimica et Cosmochimica Acta*, 60(23) : 4631–4644. (Cité pages 137 et 138.)

Zhang P C, Brady P V, Arthur S E, Zhou W Q, Sawyer D, et Hesterberg D A. 2001. Adsorption of barium(II) on montmorillonite : an EXAFS study. *Colloids and Surfaces - A : Physicochemical and Engineering Aspects*, 190(3) : 239–249. (Cité pages 196 et 197.)

Zhang Y S, Amakawa H, et Nozaki Y. 1994. The comparative behaviours of yttrium and lanthanides in the seawater of the North Pacific. *Geophysical Research Letters*, 21(24) : 2677–2680. (Cité page 138.)

Zhu X K et O'Nions R K. 1999. Monazite chemical composition : some implications for monazite geochronology. *Contributions to Mineralogy and Petrology*, 137 : 351–363. (Cité page 163.)

Ziegler K, Chadwick O A, Brzezinski M A, et Kelly E F. 2005. Natural variations of 30Si ratios during progressive basalt weathering, Hawaiian Islands. *Geochimica et Cosmochimica Acta*, 19 : 4597–4610. (Cité page 230.)

ANNEXES

A.1   Microfluorescence X et Diffraction X

A.1.1   Equipement et paramètres analytiques

Les cartographies élémentaires *in situ* par microfluorescence X ont pour but de caractériser les différentes phases minérales contenues dans les cherts de Barberton, et d'évaluer le degré de préservation de ces phases de part leur composition chimique. Cette approche a le grand avantage de permettre une acquisition de données relativement rapide et peu coûteuse. Les cartographies élémentaires sont complétées par les analyses ponctuelles par microsonde décrites en Annexe A.2. Les analyses par diffraction X sont présentées ici car elles ont permis de résoudre certains biais analytiques observés dans les spectres de microfluorescence X.

Les analyses par microfluorescence X sont réalisées sur un EDAX Eagle III et avec le support technique Vision 32 XRF. Les paramètres techniques de la machine sont optimisés pour chaque échantillon et répertoriés dans la Table A.1.

L'utilisation de lames polies plutôt que de fragments de roches permet de limiter les phénomènes de diffraction liés à la rugosité de surface. Les lames ont été réalisées soit à Montpellier par Christophe Nevado (Université Montpellier 2), soit à Chambéry par Fayçal Soufi (Université de Savoie).

Les éléments analysés sont choisis en fonction des concentrations obtenues lors des analyses chimiques sur roche totale, à savoir Si, Al, K, Fe, Ti, Cr, Ni, Ca, Mg. Le magnésium se situant dans les énergies basses, les résultats sont peu représentatifs et ne sont pas traités lors de l'analyse des résultats. La précision du détecteur et les temps d'acquisition choisis offrent une limite de détection supérieure à quelques centaines de *ppm* (typiquement $> 500 ppm$).

Les données ne sont pas corrigées à l'aide de standards de référence (Mode d'acquisition Standardless) et les cartes de répartition élémentaires sont exprimées en données brutes (*i.e.* nombre de coups sur le détecteur). La précision absolue de ce mode d'acquisition est estimée entre 2 et 3% sur les éléments majeurs. L'avantage d'une telle approche non quantitative est qu'elle ne nécessite pas une connaissance parfaite de chaque phase minérale présente et permet une exploration plus libre des échantillons les plus hétérogènes, en particulier pour ce qui est des phases mineures et accessoires parfois difficiles à identifier en microscopie optique.

Paramètres		Voltage (kV)	Ampérage (µA)	Taille (µm)	Matrice (pixels)	Tps/point (ms)	Gamme d'énergie (kV)
Komati River							
KRC8	1	25	350	30	256x200	1000	0-20
	2	25	295	30	512x400	1000	0-20
	3	25	350	30	128x100	5000	0-20
KRC11		25	400	30	256x200	4000	0-20
KRC13		25	350	30	512x400	1000	0-20
Buck Reef							
BRC12		25	350	30	512x400	700	0-20
BRC21		25	400	30	128x100	3500	0-20
BRC22		25	350	30	512x400	800	0-20
Fig Tree							
FTC2B		25	400	30	256x200	1000	0-20
FTC4A		25	400	30	256x200	1000	0-20
FTC4B		25	350	30	256x200	1000	0-20
FTC9		25	350	30	256x200	900	0-20
Josefsdal							
JC2		20	350	30	256x200	1200	0-20
JC4		20	350	30	256x200	1200	0-20

TABLE A.1 – *Paramètres analytiques des analyses par microfluorescence X pour les différents échantillons*

A.1.2 Traitement des données : PyMCA

Le logiciel libre d'accès PyMCA (version 4.5.0) a été développé par le "Software Group" de l'ESRF (European Synchrotron Radiation Facility) et a pour but de visualiser et analyser les données de microfluorescence X en termes de spectres énergétiques. Ce logiciel offre des outils performants de calibration, comparaison et compilation des spectres bruts permettant d'obtenir des cartographies élémentaires complémentaires entre les différents éléments. Nous avons utilisé cette interface dans le but d'observer les caractéristiques des spectres énergétiques, tandis que la section A.1.3 décrit les approches quantitatives basées sur un logiciel différent.

Grâce au logiciel PyMCA, la plupart des pics observés peuvent être associés aux $K\alpha$ des principaux éléments majeurs (*e.g.* Al, Si, Fe, K). Cependant, indépendamment de la nature des cherts et du site d'échantillonnage, les spectres montrent systématiquement plusieurs pics à des énergies spécifiques ne correspondant à aucune $K\alpha$ des éléments majeurs. Ces pics se retrouvent pour des énergies de 4.26, 4.76, 5.18 et 5.50 keV (Fig.A.1), ce qui pourrait correspondre aux raies L de certains éléments traces et terres rares (notamment Cs, Ba, La, Ce, Pr, Nd). Cependant, les analyses géochimiques sur roche totale montrent que les concentrations de ces éléments sont inférieures à 60ppm et ne peuvent donc être responsables des pics observés. Seul le baryum peut atteindre plusieurs centaines de ppm, mais uniquement dans les échantillons de la Barite Valley.

L'hypothèse la plus probable est un phénomène de diffraction systématique lié à la microcristallinité du quartz, présent dans l'ensemble des échantillons. Pour tester cette hypothèse, nous calculons les distances interréticulaires d (équation A.3), correspondant à chacune des énergies des pics observés, en combinant la loi de Bragg (équation A.1) et l'équation des longueurs d'onde (équation A.2).

$$2dsin\theta = n.\lambda \tag{A.1}$$

$$\lambda = hcE \tag{A.2}$$

$$d = 2Ehcsin\theta \tag{A.3}$$

avec θ l'angle de Bragg (27.5°), h la constante de Planck (4.14.10$^{-15}eV.s$) et c la vitesse de la lumière (2.99.10$^8 m/s$).
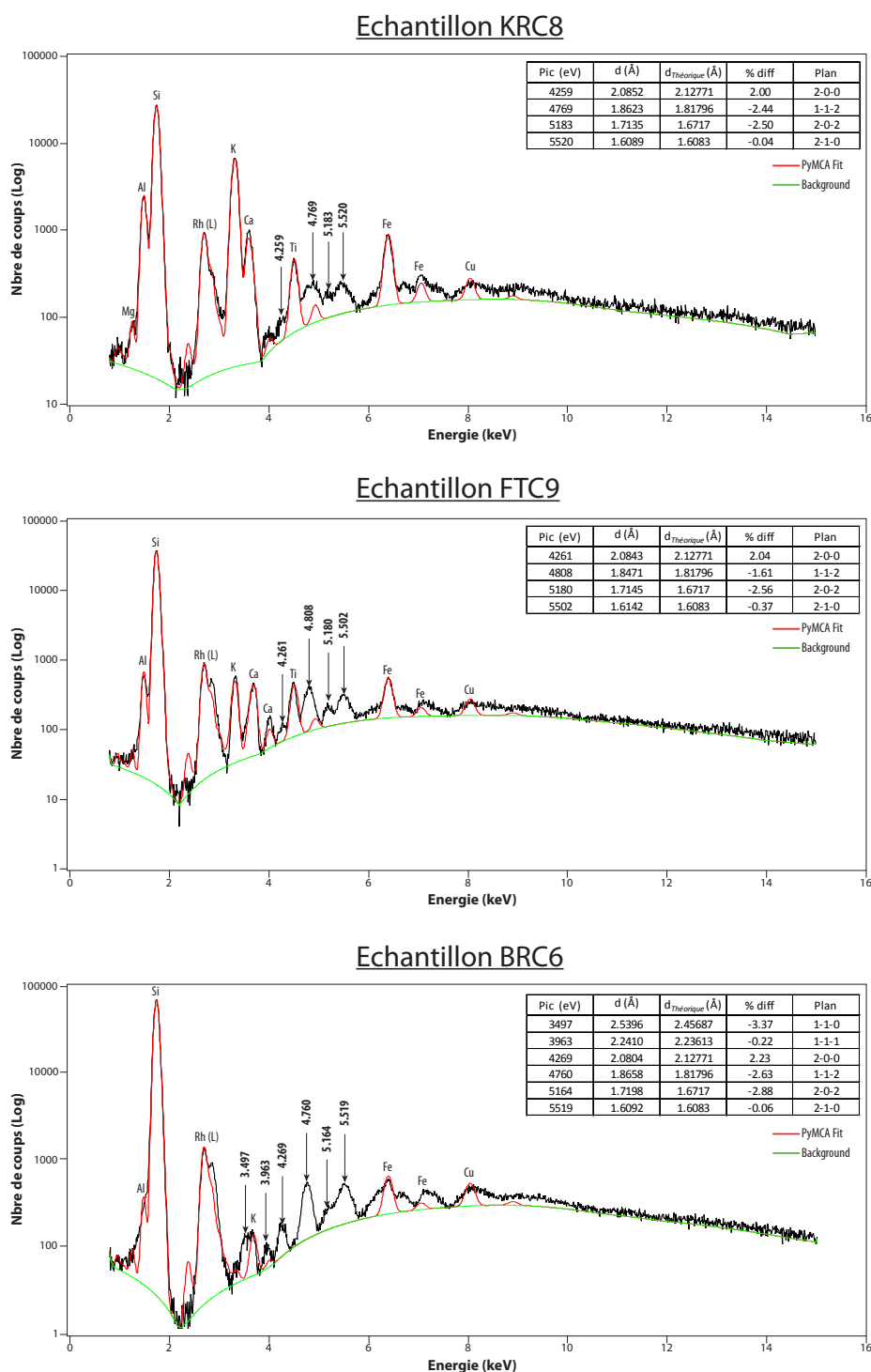
Figure A.1 – *Etude des spectres de microfluoresence X pour trois échantillons de Komati River (haut), Fig Tree (centre) et Buck Reef (bas). Les courbes noires représentent les spectres moyennés sur l'ensemble des cartographies acquises. Les courbes rouges représentent le meilleur fit obtenu grâce au logiciel PyMCA et en imposant pour chaque pic l'élément majeur associé. Les pics non identifiés représentent des éléments improbables (concentrations trop faibles) et sont donc utilisés dans les calculs de plan réticulaires associés. Les tableaux associés à chaque échantillon montrent : l'énergie de chaque pic, le calcul de la distance d associée, la valeur théorique de la distance réticulaire du standard de quartz 00 − 046 − 1045 de Kern et Eysel (1993), la déviation entre ces deux dernières valeurs, et enfin le nom du plan réticulaire associé à chaque pic. Malgré une déviation systématique des trois premiers plans, les pics non-fittés semblent correspondre à un phénomène de diffraction lié au quartz présent dans les échantillons.*

La Figure A.1 montre trois exemples de spectres traités grâce au logiciel PyMCA. La courbe noire représente le spectre moyenné sur l'ensemble de l'échantillon et la courbe rouge représente le meilleur *fit* obtenu en identifiant les éléments majeurs responsables des pics principaux. Les distances réticulaires d sont calculées pour les pics non identifiés et données dans les tableaux associés à chaque échantillon. Les valeurs obtenues sont comparées aux valeurs de référence issues des bases de données de la diffraction X de plusieurs minéraux. La meilleure correspondance pour l'ensemble des plans est observée pour le quartz de référence $00 - 046 - 1045$ décrit par Kern et Eysel (1993). Un décalage en énergie est tout de même visible : il est minime pour les pics associés au plan réticulaire $2 - 1 - 0$ ($< 0.06\%$) mais varie systématiquement de 1.61 à 3.37% pour les autres pics et plans associés. D'après ces observations, les pics non-identifiés sont effectivement liés à la diffraction systématique du faisceau par le microquartz constitutif de nos échantillons.

Pour plus de fiabilité, nous avons réalisé des analyses par diffraction X sur les trois échantillons présentés en Figure A.1. Les échantillons sont réduits en poudre ($\varnothing=63\mu m$) et tamisés pour favoriser une orientation aléatoire des minéraux. Les analyses sont réalisées à ISTerre (Grenoble) sur le diffractomètre Bruker D5000/D8 équipé d'un détecteur SolX Si(Li) et utilisant les radiations Kα 1 du cuivre. Les intensités sont enregistrées sur des intervalles de $0.04°$ entre 19.5 à $58.06°$ avec un temps de comptage de $3s$. par pas.

Les résultats comparés des trois échantillons sont présentés en Figure A.2. Les spectres sont tous quasiment identiques et parfaitement alignés avec le spectre de référence du quartz $00 - 046 - 1045$ (lignes verticales rouges), confirmant que les pics non identifiés dans les données de fluorescence X sont dus à un phénomène de diffraction porté par la phase microquartzitique. De plus, aucun pic de diffraction ne manque par rapport au spectre de référence et les intensité sont comparables, traduisant un comportement de type "poudre homogène" pour nos échantillons. Un tel comportement montre que la taille des grains de quartz ne dépasse pas $5\mu m$ (voir par exemple Connolly 2009) et qu'il n'y a pas d'orientation préférentielle du quartz (*i.e.* tamisage efficace). Si le faisceau de rayon X rencontrait une fraction cris-
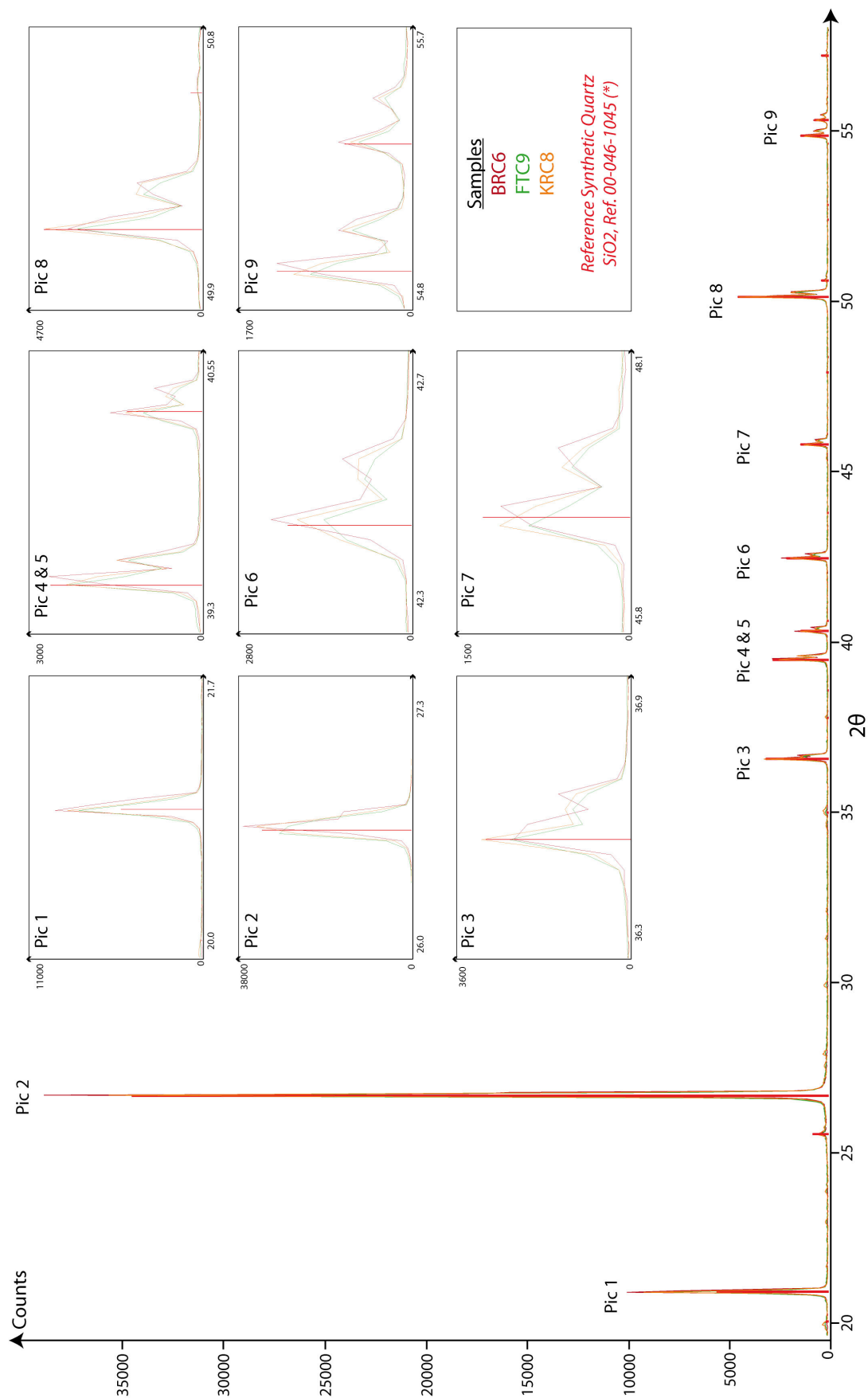
FIGURE A.2 – *Spectres de diffraction des échantillons de Komati River (jaune), Buck Reef (rouge) et Barite Valley (vert). Pour chaque échantillon, tous les pics observés sont alignés sur les pics du quartz de référence* 00 − 046 − 1045 *(barres verticales) de Kern et Eysel (1993)*

talline de plus forte taille, ou si le tamisage avait créé une orientation préférentielle des grains, certains plans réticulaires seraient mieux représentés et les intensités des pics de diffraction correspondants seraient nettement supérieures au spectre de référence du quartz.

La largeur des pics de diffraction des trois échantillons montre tout de même de légères différences : les pics de BRC6 (Buck Reef) sont systématiquement les plus larges, avec une position intermédiaire pour KRC8 (Komati River) et des pics plus étroits pour FTC9 (Barite Valley). La largeur est corrélée de manière indirecte à la taille des grains qui diffractent, ce qui traduit une cristallinité légèrement plus forte pour les échantillons de Buck Reef.

Dans le cas de la fluorescence X, le faisceau est calibré pour un diamètre de $30\mu m$, ce qui représente un diamètre effectif d'environ $50\mu m$ en raison des incertitudes paramétriques. La profondeur de pénétration du faisceau étant de $20\mu m$ aux basses énergies, et $100\mu m$ aux hautes énergies ($\sim 1.2 keV$ dans notre cas), le volume échantillonné lors de l'analyse varie entre $39000\mu m^3$ et $1960000\mu m^3$. Un calcul simple montre alors que pour une taille maximale de $5\mu m$, le faisceau balaye jusqu'à 39000 grains, ce qui est largement suffisant pour expliquer le nombre important de pics de Bragg reconnus dans les spectres et supporte l'idée d'une orientation aléatoire du microquartz dans nos échantillons.

D'après ces tests, nous pouvons conclure que (1) tous les échantillons de cherts, qu'ils soient formés de quartz pur ou de protolithe silicifié contiennent une proportion majoritaire de microquartz de granulométrie inférieure ou égale à $5\mu m$, (2) que cette phase ne présente pas d'orientation préférentielle quelque soit le degré de diagenèse, compaction, circulations fluides ou métamorphisme rencontrés, (3) et que les échantillons de Buck Reef semblent mieux cristallisés que ceux de Komati River et Barite Valley.

Les analyses par diffraction X ont également permis d'identifier les phases minérales présentes en plus de la silice dans les différents échantillons. La Figure A.3 met en avant la composition de chaque échantillon : le chert de Komati River est le plus hétérogène et représente un mélange entre le microquartz, l'orthoclase et la muscovite. A l'inverse, le chert de Buck Reef est le plus homogène et est exclusivement formé de microquartz. Le chert de Barite Valley est également majoritaire-
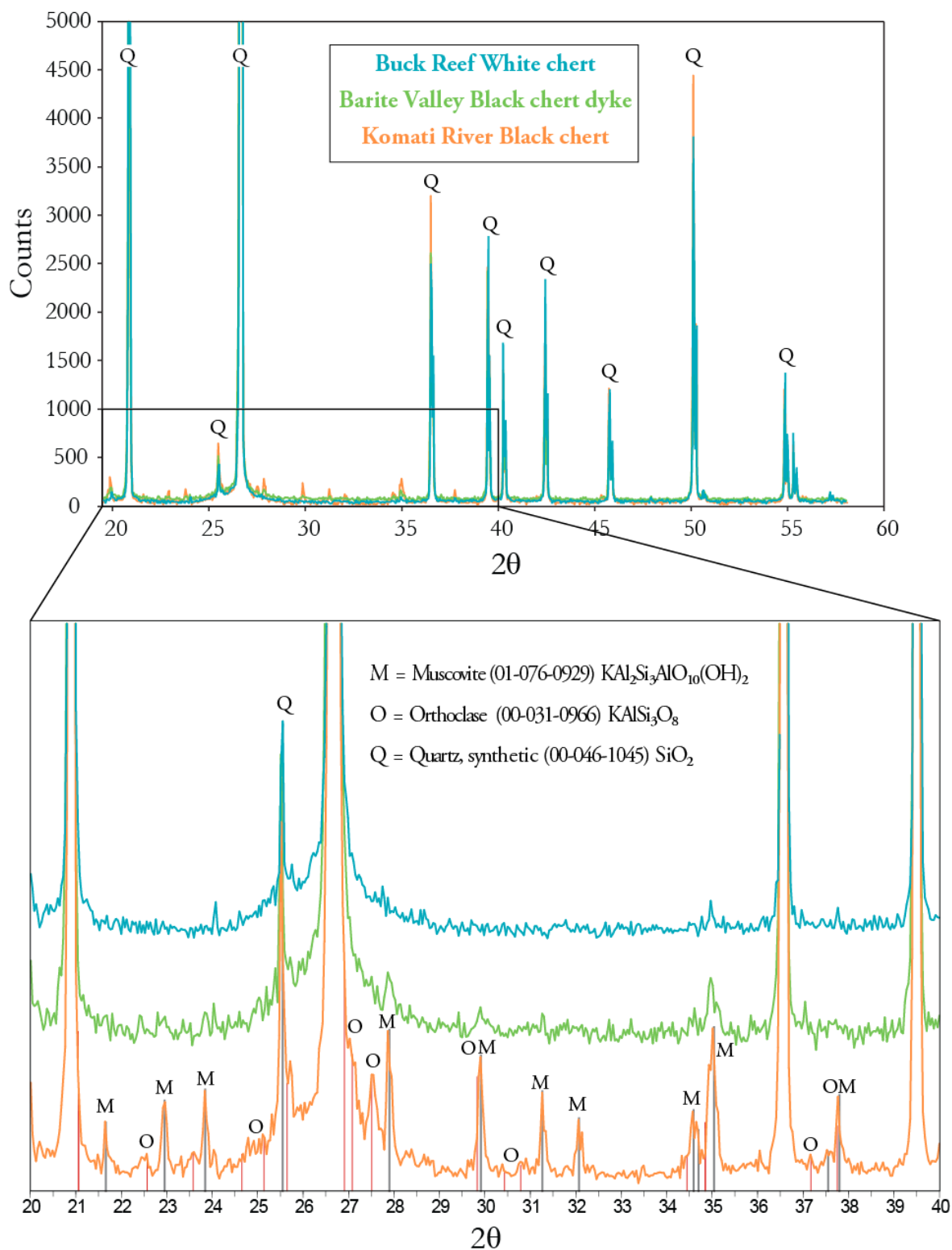
Figure A.3 – *Spectres de diffraction des échantillons de Komati River, Buck Reef et Barite Valley mettant en avant la nature des phases minérales. L'échantillon de Buck Reef est exclusivement constitué de microquartz tandis que le chert de Komati River est un mélange de microquartz, orthoclase et muscovite. Le chert de Barite Valley est relativement pur, essentiellement composé de microquartz, mais pourrait contenir des traces de muscovite aux vues de certains pics, ce qui est confirmé par les observations microscopiques (Chap.3 et 4).*

ment constitué de microquartz, mais la présence de muscovite est soupçonnée aux vues de certains pics, certes de petite taille, mais significatifs. Toutes ces observations concordent avec les descriptions microscopiques des présentées dans les chapitres 2 à 4.

A.1.3 Traitement des données : SuperMaps

Les cartographies élémentaires brutes (*i.e.* données en nombre de coups) obtenues par microfluorescence X sont traitées en deux étapes : le première permet une quantification des éléments en pourcentage de poids d'oxyde, et la seconde permet d'exprimer les cartographies en pourcentage de phases minérales.

Quantification : $wt\%$

Le logiciel de contrôle Vision 32 de l'EAGLE III permet de réaliser un calcul itératif des cartes ROI prenant en compte les paramètres fondamentaux de la matrice minérale (van Sprang 2000, Thomsen 2007, Mantler et Kawahara 21). Le passage des données brutes en pourcentage de poids d'oxydes se basent sur des valeurs imposées de standards préalablement mis en place. Dans cette étude, nous utilisons les standards développés par Emmanuel Muñoz (*comm.pers.*). Les calculs ne sont pas forcés pour boucler les concentrations à $100wt\%$ de telle sorte que les phases non mesurées (*e.g.* H_2O) correspondent à 1-$\Sigma quantifications$.

Les cartes quantifiées fournissent une première estimation de la composition chimique de certaines phases minérales (précision de quelques $wt\%$). En fonction des résultats, certains échantillons sont sélectionnés pour des analyses ponctuelles *in situ* plus précises par microsonde (*cf.* Annexe A.2).

Par ailleurs, les cartes sont couplées aux observations par microscopie optique afin de repérer les phases les plus pures présentes dans nos échantillons. Cette étape est essentielle pour le traitement des données en termes de pourcentage de phase comme décrit ci-après.
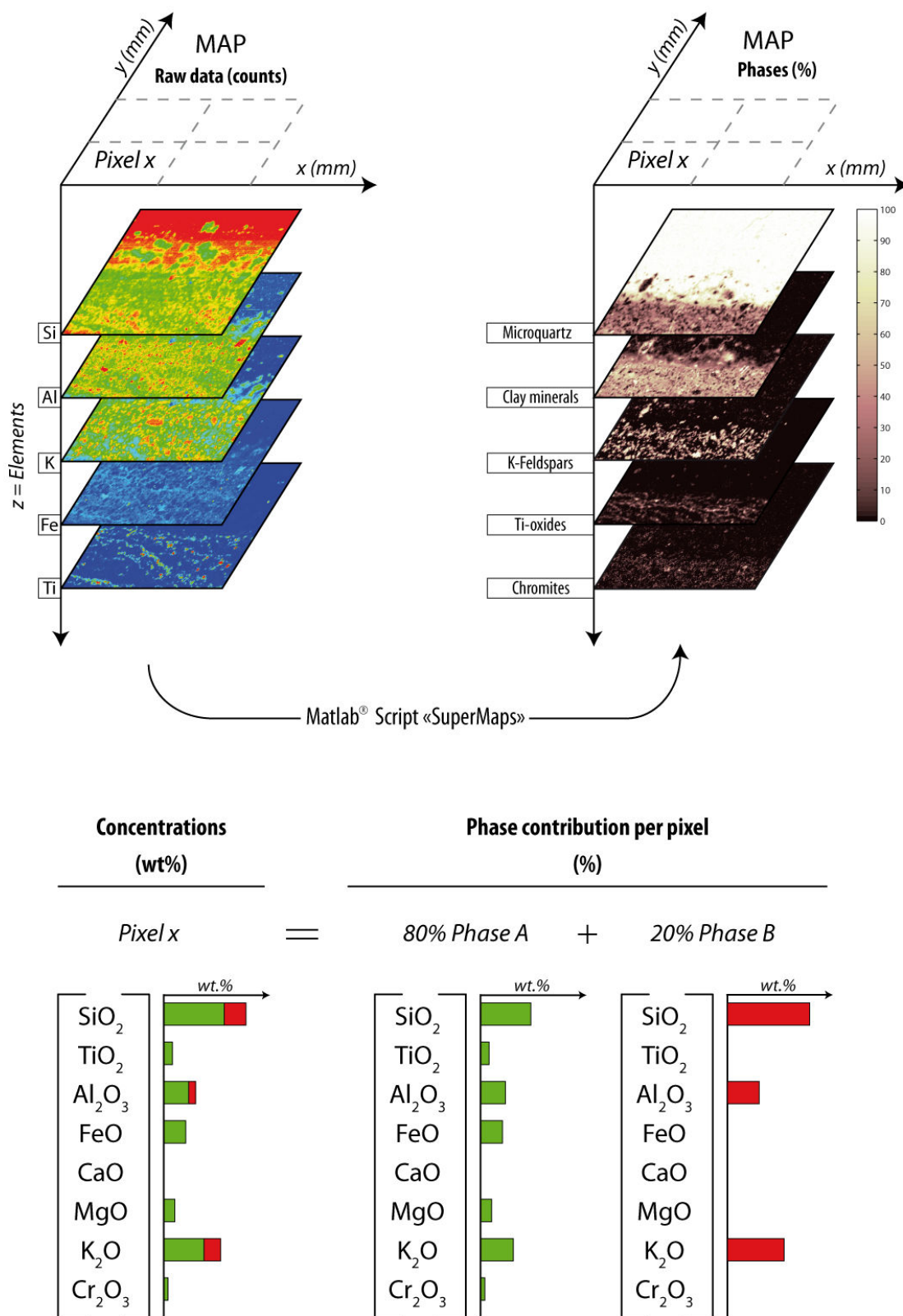
Figure A.4 – *Schéma simplifié inspiré de* Ulrich (*2010*) *et rprésentant la conversion des cartographies élémentaires en cartographies de phases. Méthode basée sur le script Matlab "Supermaps" développé par Emmanuel Muñoz et Marc Ulrich à ISTerre, Grenoble (voir la description de la méthode dans* Ulrich et al. submitted*). Les données brutes sont préalablement converties en concentrations de poids d'oxydes grâce au logiciel Vision 32.*

Quantification : *%phase*

Le but de cette étape est d'obtenir des cartographies en pourcentages de phases minérales plutôt qu'en concentrations élémentaires. La Figure A.4 est une représentation schématique de la méthode employée.

Cette méthode repose sur les travaux de Muñoz (2008). Elle était préalablement appliquée aux cartographies XANEX (analyses synchrotron), et a été développée récemment par Emmanuel Muñoz et Marc Ulrich pour une application en microfluorescence X. Ils sont les auteurs d'un script *Matlab* qui compile les cartographies élémentaires quantifiées sous la forme d'une matrice *3D* (X, Y, Z), où X et Y correspondent aux coordonnées de chaque pixel sur la carte et Z correspond à la concentration chimique en *wt%* de chaque élément analysé. Chaque pixel est ensuite interprété par le script comme résultant d'un mélange entre *n* phases minérales dont les caractéristiques sont définies manuellement.

Une bonne connaissance de la minéralogie des échantillons est essentielle pour cette étape : sur les cartographies en *wt%*, l'utilisateur définit quelles zones de la carte correspondent aux phases minérales pures identifiées préalablement en microscopie optique. Par exemple, une zone à $100wt\%$ de SiO_2 sera utilisée comme "pôle pur" du quartz. Le logiciel interprète ensuite chaque pixel de la carte comme étant un mélange de ces pôles purs et fournit une nouvelle carte en pourcentage pour chaque phase identifiée par l'utilisateur.

Cette approche offre une grande liberté dans le choix des phases puisqu'elles sont définies manuellement. Par exemple, nous utilisons les pixels les plus riches en aluminium comme représentatifs d'un pôle pur "phyllosilicate". Ce choix ne prend pas en compte une éventuelle silicification des minéraux, mais ce biais est considéré comme acceptable puisque c'est la répartition des minéraux qui nous intéresse ici et non leur composition élémentaire vraie. Celle-ci sera déterminée par la suite de manière précise par les analyses ponctuelles par microsonde (*cf.* Annexe A.2).

Afin de vérifier que toutes les phases présentes dans les échantillons ont bien été identifiées, une carte de la somme des phases est compilée et utilisée comme critère de qualité des résultats.

A.2   Microsonde

Les analyses par microsonde ont été réalisées à ISTerre sous la supervision de Valentina Sobolev.

Cet outil de pointe a été choisi pour réaliser des analyses *in situ* ponctuelles et surfaciques sur les échantillons de Komati River et Barite Valley, dans le but de déterminer la composition chimique des différentes phases minérales autres que la silice dans ces échantillons (analyses ponctuelles), et pour observer la répartition des compositions chimiques en lien avec la matrice siliceuse (cartographies). Les images BSE et SEI sont utilisées pour déterminer de manière précise les cibles pour les analyses ponctuelles, et pour réaliser en parallèle une étude approfondie des structures sédimentaires, diagénétiques et morphologiques dans les échantillons choisis pour ces deux sites.

La microsonde électronique JEOL JXA-8230 est équipée de cinq spectromètres WDS (*Wavelength Dispersive Spectrometer*) permettant l'acquisition de données quantitatives pour les éléments de B^5 à U^{92}, d'un spectromètre EDS (*Energy Dispersive Spectrometer*) généralement utilisé pour une quantification rapide, et de deux détecteurs à électrons rétrodiffusés et secondaires pour l'acquisition des images TOPO, BSE et SEI.

Les échantillons se présentent sous la forme de lames minces polies et métallisées. Une zone de l'échantillon est bombardée par le faisceau d'électron généré par la microsonde (voir Figure A.5), et les spectromètres analysent le spectre de rayons X ré-émis par cette surface. Chaque spectre est constitué d'un mélange d'éléments chimiques reconnaissables à différentes raies caractéristiques.

Parmi les deux types de spectromètres à disposition (EDS et WDS), le spectromètre WDS est plus performant pour la quantification, mais demande une acquisition plus longue et se limite à un nombre restreint d'éléments. En effet, le spectromètre WDS est calibré sur une longueur d'onde particulière ce qui ne permet pas une acquisition continue du spectre et implique la quantification d'un seul élément à la fois. La microsonde étant équipée de 5 spectromètres WDS, il n'est donc pas possible de quantifier plus de 5 éléments à la fois et plusieurs passages sont alors nécessaires. A l'inverse, le spectromètre EDS permet une acquisition continue des
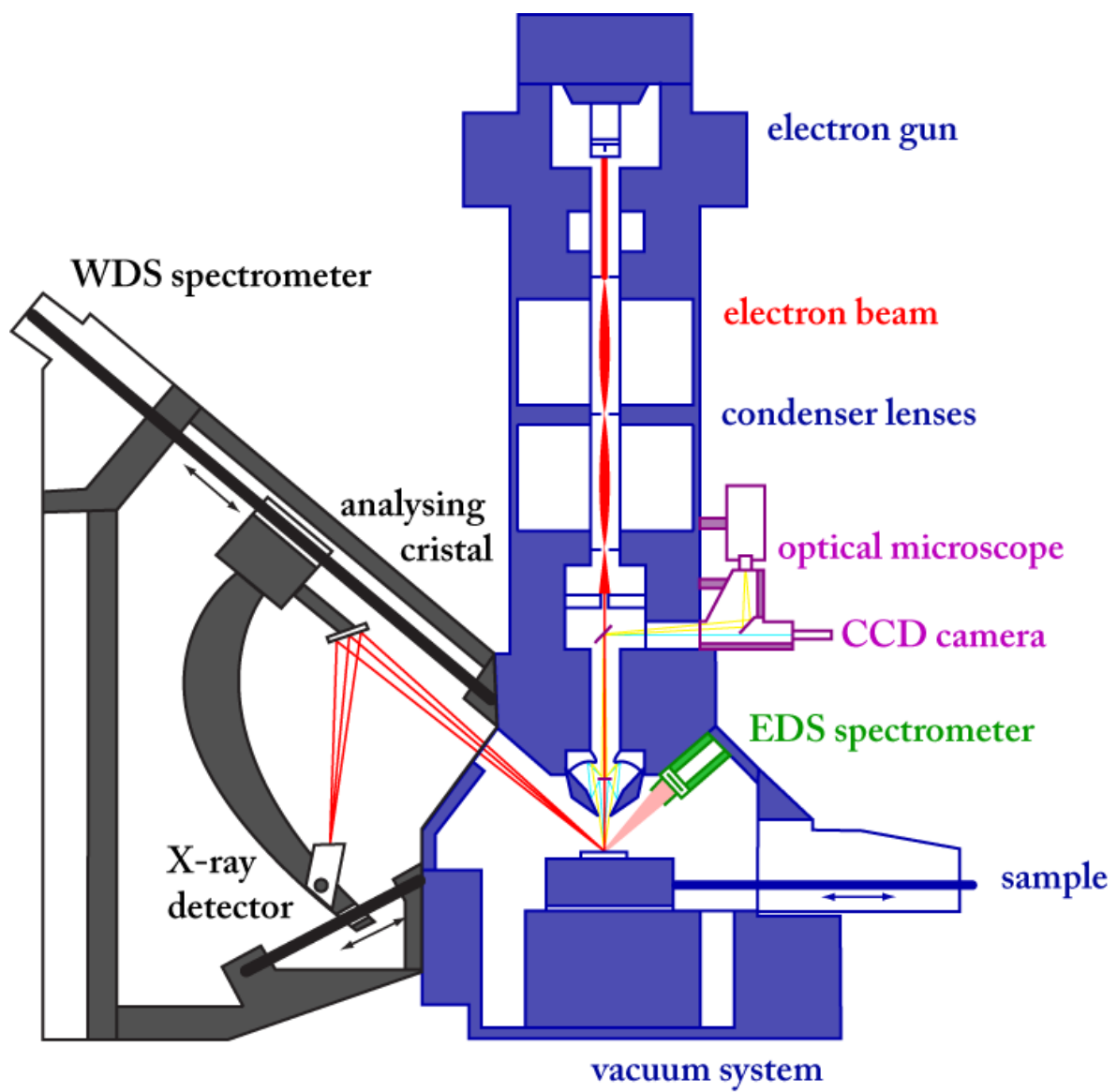
FIGURE A.5 – *Schéma simplifié d'une microsonde, d'après la thèse de Pierre Lanari (2013).*

spectres et la reconnaissance de tous les éléments présents au cours de la même analyse, mais la précision des quantifications est moins bonne.

Pour ces raisons, les éléments Si, K, Al, Fe et Ti sont quantifiés par WDS et les éléments Mg, Na, Ca, Mn, Ba sont quantifiés par EDS. Les concentrations en silice sont corrigées en utilisant un standard d'orthose cohérent avec la nature potassique des feldspaths. Cette correction est nécessaire car, à la date des analyses, une erreur systématique de 2% biaisait les données sur l'un des spectromètres. Les résultats ainsi corrigés sont précis à $\pm$2-3wt% en moyenne, généralement $< 1wt$%. Le standard d'orthose est également utilisé pour calibrer les quantifications et les valeurs obtenues lors des différentes sessions sont présentées dans la Table A.2.

Plusieurs cartographies sont couplées aux analyses ponctuelles. Ayant été réalisées de manière tardive dans ces travaux de thèse, aucun traitement des données n'est appliqué et les données sont brutes : les cartographies sont donc regardées en termes de concentrations relatives, et exprimées en variations de nombre de coups d'une phase minérale à l'autre. La quantification des cartographies sera effectuée dans les mois suivant le rendu de ces travaux en vue d'une publication ultérieure.

Les tableaux suivants regroupent l'ensemble des données acquises par analyses ponctuelles pour les standards d'orthose (Table A.2) et pour les échantillons :

- de Komati River, KRC8, Table A.3
- de Barite Valley, FTC4, Table A.4 et FTC9, Table A.5

Analyses du standard Orthose dans l'ensemble des sessions microsonde (wt%)

# analyse	SiO_2	Al_2O_3	K_2O	Na_2O	MgO	CaO	FeO	MnO	TiO_2	Cr_2O_3	P_2O_5	BaO	NiO	C	Total
Orthose 1	64,81	18,38	14,87	1,39	0,00	0,00	0,03	0,02	0,01	0,00	0,00	0,15	0,00	5,09	104,75
Orthose 2	65,08	18,54	14,79	1,36	0,00	0,00	0,04	0,00	0,00	0,00	0,02	0,17	0,00	4,80	104,79
Orthose 3	65,18	18,42	14,96	1,41	0,00	0,00	0,01	0,00	0,00	0,00	0,02	0,19	0,03	5,07	105,29
Orthose 4	65,39	18,53	14,84	1,40	0,00	0,00	0,01	0,02	0,01	0,00	0,00	0,22	0,02	5,06	105,49
Orthose 5	65,03	18,59	14,86	1,42	0,00	0,00	0,03	0,00	0,00	0,02	0,00	0,18	0,00	5,72	105,86
Orthose 6	64,82	18,54	14,89	1,39	0,00	0,00	0,00	0,00	0,00	0,01	0,00	0,15	0,00	5,04	104,85
Orthose 7	64,77	18,55	14,91	1,40	0,01	0,00	0,09	0,00	0,00	0,01	0,00	0,17	0,00	4,89	104,78
Orthose 8	65,28	18,47	14,79	1,43	0,00	0,00	0,05	0,01	0,01	0,00	0,02	0,18	0,00	5,18	105,42
Orthose 9	64,89	18,47	14,90	1,41	0,00	0,00	0,04	0,00	0,01	0,00	0,03	0,19	0,01	4,71	104,65
Orthose 10	64,84	18,52	14,77	1,41	0,02	0,00	0,03	0,01	0,00	0,01	0,00	0,19	0,01	4,86	104,64
Orthose 11	65,01	18,41	14,88	1,40	0,00	0,00	0,02	0,01	0,00	0,00	0,00	0,21	0,02	4,77	104,74
Orthose 12	65,25	18,56	14,90	1,39	0,01	0,00	0,03	0,04	0,01	0,00	0,00	0,19	0,04	5,01	105,42
Orthose 13	64,888	18,456	14,593	1,398	0	0	0,035	0,001	0,018	0	0,003	0,157	0	n.a.	99,549
Orthose 14	64,899	18,454	14,702	1,416	0	0	0,024	0	0	0,005	0	0,18	0,01	n.a.	99,69
Orthose 15	64,898	18,486	14,743	1,435	0	0	0,024	0	0,007	0	0	0,219	0,014	n.a.	99,819
Orthose 16	65,06	18,494	15,051	1,416	0	0	0,04	0	0,015	0	0	0,219	0,015	n.a.	100,302
Orthose 17	64,825	18,579	14,993	1,419	0	0	0,023	0	0	0,015	0,025	0,173	0,001	n.a.	100,068
Orthose 18	65,197	18,507	14,886	1,413	0,006	0	0,016	0	0	0	0,014	0,173	0,023	n.a.	100,235
Orthose 19	67,047	18,437	14,709	1,378	0	0	0,035	0	0,005	0	n.a.	n.a.	0	n.a.	101,611
Orthose 20	67,045	18,429	14,622	1,386	0	0	0,045	0	0,007	0	n.a.	n.a.	0	n.a.	101,534
Orthose 21	67,069	18,242	14,601	1,395	0,005	0	0,042	0	0,007	0	n.a.	n.a.	0	n.a.	101,361
Moyenne	**65,30**	**18,48**	**14,82**	**1,40**	**0,00**	**0,00**	**0,03**	**0,01**	**0,00**	**0,00**	**0,01**	**0,18**	**0,01**	**5,02**	**105,26**
Ecart-type	*0,75*	*0,08*	*0,13*	*0,02*	*0,00*	*0,00*	*0,02*	*0,01*	*0,01*	*0,01*	*0,01*	*0,02*	*0,01*	*0,27*	
Theorique	65,4	18,53	14,67	1,36											

TABLE A.2 – *Composition chimique du standard d'orthose acquises au cours des différentes sessions d'analyse. La composition théorique est en accord avec la moyenne des valeurs mesurées. Le carbone est lié à la métallisation de la lame et n'a pas été systématiquement analysé.*

KRC8

# analyse	SiO₂	Al₂O₃	K₂O	Na₂O	MgO	CaO	FeO	MnO	TiO₂	Total

Composition chimique des phases minérales de Komati River

# analyse	SiO₂	Al₂O₃	K₂O	Na₂O	MgO	CaO	FeO	MnO	TiO₂	Total
- Facies inférieur: Siltstone -										
Sericite 1	49,40	34,32	8,19	0,12	1,649	0	0,88	0,002	0,532	95,08
Sericite 2	47,99	34,25	7,85	0,10	1,752	0,023	0,86	0,001	0,52	93,34
Sericite 3	48,27	34,78	8,18	0,08	1,649	0,012	0,90	0,009	0,503	94,38
Sericite 4	48,63	34,75	8,56	0,12	1,634	0,007	0,84	0,006	0,539	95,09
Sericite 5	48,67	33,80	8,01	0,06	1,538	0	0,82	0	0,543	93,45
Sericite 6	49,11	35,14	8,56	0,10	1,739	0	0,82	0,003	0,625	96,10
Feldspath 1	64,04	18,48	15,62	0,20	0,012	0,025	0,03	0	0,002	98,40
Feldspath 2	65,33	18,16	16,16	0,16	0,004	0	0,05	0		99,86
Feldspath 3	65,26	18,03	16,28	0,14	0	0	0,00	0		99,71
Feldspath 4	65,09	18,11	16,01	0,16	0	0	0,05	0,007		99,43
Feldspath 5	66,01	17,66	15,06	0,20	0	0	0,03	0,009	0,004	98,97
Feldspath 6	65,74	17,86	15,73	0,17	0,018	0	0,03	0,024	0,001	99,57
Feldspath 7	65,86	17,77	15,39	0,16	0	0	0,01	0		99,19
Feldspath 8	65,29	18,23	16,16	0,16	0	0	0,01	0	0,002	99,86
Feldspath 9	64,91	18,17	16,04	0,22	0	0	0,02	0,002	0,022	99,38
Feldspath 10	65,35	16,75	14,02	0,22	0	0	0,00	0	0	96,35
Feldspath 11	65,76	17,88	15,49	0,19	0	0	0,00	0	0,002	99,32
Feldspath 12	65,04	18,33	15,56	0,19	0,008	0	0,02	0,009		99,16
Feldspath 13	65,91	17,92	15,90	0,17	0	0	0,05	0,009		99,95
Feldspath 14	64,91	18,58	15,99	0,15	0	0	0,01	0		99,64
Feldspath 15	64,87	18,43	16,13	0,17	0	0	0,04	0	0,006	99,66
Feldspath 16	64,74	18,59	15,90	0,17	0,008	0	0,00	0,008	0,016	99,43
Feldspath 17	65,64	17,91	15,85	0,15	0	0	0,01	0		99,57
Feldspath 18	64,57	18,42	15,66	0,17	0	0	0,05	0,004	0,035	98,91
Feldspath 19	65,92	18,07	16,21	0,16	0,002	0	0,04	0		100,39
Feldspath 20	64,95	18,47	16,22	0,18	0,007	0	0,02	0		99,84
Feldspath 21	64,69	18,64	15,54	0,17	0	0	0,03	0,004	0,002	99,07
Feldspath 22	64,52	18,54	14,75	0,18	0	0	0,04	0	0,009	98,03
Feldspath 23	65,17	18,59	15,98	0,18	0	0	0,04	0,005		99,97
Feldspath 24	64,41	18,62	16,11	0,19	0	0	0,00	0	0,025	99,35
Feldspath 25	65,00	18,17	15,76	0,14	0	0	0,01	0,003		99,09
Feldspath 26	65,41	18,28	16,39	0,17	0	0	0,00	0	0,005	100,25
Feldspath 27	65,75	18,59	16,35	0,16	0,012	0	0,04	0		100,90
Feldspath 28	65,15	18,35	15,95	0,17	0,005	0	0,01	0,006	0,003	99,64
Feldspath 29	65,82	18,25	16,19	0,17	0	0	0,03	0,003		100,45
Feldspath 30	64,28	18,30	16,45	0,16	0	0	0,03	0,002	0,009	99,23
Feldspath 31	65,26	18,14	16,21	0,14	0	0	0,01	0		99,76
Feldspath 32	64,92	18,44	16,06	0,18	0	0	0,02	0,018		99,64
Feldspath 33	64,77	18,10	16,26	0,21	0	0	0,00	0	0,003	99,34
Feldspath 34	65,98	17,92	15,61	0,20	0	0	0,04	0,009	0,011	99,76
Feldspath 35	65,00	18,37	16,08	0,15	0	0	0,01	0	0,001	99,60
Feldspath 36	64,31	18,39	15,82	0,17	0	0	0,02	0,004		98,72
Feldspath 37	65,77	18,16	15,98	0,15	0	0	0,04	0,013		100,12
Feldspath 38	64,59	18,20	16,12	0,16	0	0	0,01	0		99,08
Feldspath 39	64,64	17,75	15,50	0,13	0	0	0,05	0	0,009	98,09
- Facies supérieur: Black chert -										
Microquartz 1	95,57	1,39	0,44	0,00	0,058	0	0,06	0,018	0,026	97,56
Microquartz 2	96,38	1,17	0,40	0,00	0,045	0	0,09	0	0,018	98,10
Microquartz 3	96,59	0,97	0,35	0,07	0,039	0,016	0,03	0	0,004	98,07
Microquartz 4	97,97	0,58	0,21	0,02	0,001	0	0,07	0,012	0	98,85
Microquartz 5	97,98	0,12	0,03	0,00	0	0,001	0,04	0,006	0,007	98,18
Microquartz 6	97,98	0,56	0,19	0,00	0,009	0,004	0,05	0	0,009	98,80
Microquartz 7	98,04	0,50	0,16	0,02	0,017	0,005	0,03	0	0,003	98,77
Microquartz 8	98,30	0,45	0,13	0,04	0,02	0,001	0,03	0	0	98,97
Microquartz 9	98,78	0,73	0,19	0,01	0,017	0,002	0,04	0	0,007	99,77
Microquartz 10	98,91	0,11	0,05	0,02	0,011	0,007	0,04	0	0	99,14
Microquartz 11	98,97	0,08	0,03	0,01	0,003	0,014	0,03	0	0	99,13
Microquartz 12	99,45	0,10	0,05	0,02	0,001	0	0,01	0	0,018	99,64

TABLE A.3 – *Composition chimique des phases minérales dans l'échantillon KRC8 (Komati River). Les analyses sont réalisées à la fois dans le siltstone riche en particules détritiques et dans le chert noir sus-jacent, exclusivement constitué de microquartz et séricite.*

FTC4

Composition chimique des phases minérales de Barite Valley

# analyse	SiO$_2$	Al$_2$O$_3$	K$_2$O	Na$_2$O	MgO	CaO	FeO	MnO	TiO$_2$	Cr$_2$O$_3$	P$_2$O$_5$	BaO	NiO	C	Total
Dolomie 1	0,13	0,14	0,02	0,03	15,17	27,64	8,46	3,00	0,00	0,01	0,01	0,04	0,00	8,19	69,22
Dolomie 2	5,58	0,06	0,02	0,04	16,67	27,91	6,90	0,60	0,00	0,02	0,00	0,05	0,00	7,22	71,44
Dolomie 3	0,67	0,06	0,02	0,01	16,87	27,87	8,01	0,86	0,00	0,01	0,03	0,08	0,01	7,87	68,75
Dolomie 4	0,04	0,02	0,01	0,02	17,70	28,72	7,80	0,96	0,03	0,00	0,00	0,05	0,00	5,70	67,42
Dolomie 5	0,14	0,01	0,01	0,04	16,09	28,35	7,69	2,98	0,00	0,05	0,01	0,06	0,00	7,39	69,20
Dolomie 6	0,67	0,03	0,00	0,01	14,55	27,92	9,74	0,57	0,00	0,01	0,00	0,07	0,01	6,82	66,79
Dolomie 7	0,21	0,00	0,00	0,00	17,49	28,21	7,22	0,79	0,00	0,01	0,03	0,05	0,03	7,37	67,79
Dolomie 8	0,47	0,05	0,00	0,01	18,11	28,44	6,53	0,55	0,01	0,00	0,05	0,10	0,00	7,06	67,75
Dolomie 9	2,12	0,03	0,00	0,01	18,38	27,95	5,47	0,53	0,00	0,00	0,05	0,06	0,00	7,46	68,43
Dolomie 10	0,17	0,04	0,00	0,00	16,65	28,07	7,23	0,82	0,01	0,00	0,00	0,06	0,00	7,72	67,14
Dolomie 11	6,08	0,06	0,00	0,00	16,46	27,23	5,10	0,54	0,01	0,00	0,00	0,04	0,02	6,64	68,56
Dolomie 12	1,05	0,09	0,01	0,00	19,31	29,12	4,91	0,51	0,00	0,00	0,03	0,08	0,00	5,80	67,29
Dolomie 13	0,01	0,08	0,00	0,00	17,11	28,16	7,80	0,81	0,01	0,01	0,02	0,04	0,00	8,29	68,73
Dolomie 14	0,19	0,09	0,01	0,03	15,77	28,02	8,85	0,61	0,00	0,02	0,05	0,09	0,00	7,38	67,47
Dolomie 15	0,15	0,00	0,01	0,01	15,36	28,02	7,28	0,75	0,00	0,01	0,03	0,04	0,05	6,39	64,46
Dolomie 16	0,38	0,08	0,01	0,01	16,49	28,21	6,42	0,59	0,01	0,01	0,00	0,00	0,00	6,56	65,13
Dolomie 17	1,28	0,07	0,02	0,01	17,49	28,43	4,84	0,67	0,00	0,00	0,00	0,10	0,02	6,88	66,19
Dolomie 18	2,07	0,08	0,00	0,00	16,57	27,82	5,50	0,49	0,00	0,00	0,04	0,04	0,00	6,60	65,60
Dolomie 19	7,44	0,05	0,00	0,00	14,80	26,39	6,36	0,48	0,00	0,03	0,00	0,09	0,01	7,42	69,44
Dolomie 20	58,82	0,77	0,14	0,01	5,80	12,09	3,34	0,39	0,00	0,01	0,00	0,16	0,00	8,16	96,06
Dolomie 21	4,79	0,08	0,00	0,02	16,56	27,46	4,73	0,58	0,00	0,02	0,00	0,04	0,01	6,31	66,98
Dolomie 22	3,09	0,02	0,01	0,00	14,00	27,17	9,44	0,87	0,01	0,01	0,00	0,06	0,00	7,15	68,20
Dolomie 23	3,69	0,04	0,00	0,00	15,28	27,43	7,17	0,83	0,00	0,02	0,00	0,05	0,04	7,08	68,00
Sericite Core 1	59,24	27,57	6,87	0,21	1,05	0,01	0,85	0,02	0,12	0,06	0,00	1,81	0,02	5,80	103,62
Sericite Core 2	48,39	32,84	7,36	0,08	1,28	0,00	1,88	0,00	0,25	0,14	0,00	0,49	0,00	5,23	97,93
Sericite Core 3	48,77	34,08	8,26	0,12	1,46	0,01	1,75	0,01	0,25	0,06	0,03	0,33	0,01	6,30	101,43
Sericite Core 4	51,52	36,44	5,79	0,58	0,82	0,00	0,68	0,00	0,23	0,07	0,04	0,73	0,02	5,91	102,81
Sericite Core 5	46,48	37,60	8,19	0,94	0,41	0,00	0,55	0,00	0,27	0,06	0,01	0,54	0,00	6,45	101,49
Sericite Core 6	35,13	27,01	0,03	2,55	4,57	0,10	15,16	0,06	1,32	0,06	0,03	0,10	0,05	5,67	91,84
Sericite Core 7	36,81	33,64	0,01	1,53	4,28	0,03	8,72	0,00	0,04	0,03	0,01	0,04	0,00	6,02	91,15
Sericite Core 8	46,99	36,74	9,39	0,27	1,03	0,00	0,52	0,01	0,11	0,02	0,00	0,21	0,00	4,85	100,12
Sericite Rim 1	46,08	33,93	7,20	0,09	1,52	0,00	0,71	0,03	0,23	0,16	0,00	4,64	0,00	5,43	100,01
Sericite Rim 2	48,82	31,06	7,46	0,08	1,84	0,00	2,85	0,00	0,34	0,14	0,05	0,94	0,00	5,62	99,19
Sericite Rim 3	63,02	22,17	5,81	0,11	1,09	0,01	0,81	0,00	1,16	0,11	0,00	4,03	0,00	11,89	110,22
Sericite Rim 4	44,65	35,36	5,89	0,09	1,65	0,01	0,74	0,00	0,23	0,12	0,00	4,81	0,04	5,66	99,25
Sericite Rim 5	48,67	30,93	7,30	0,10	1,21	0,01	0,83	0,00	0,24	0,13	0,04	4,29	0,00	6,22	99,97
Sericite Rim 6	37,28	31,49	0,03	2,43	7,07	0,14	5,75	0,01	0,55	0,39	0,00	0,06	0,10	5,86	91,15
Sericite Rim 7	49,53	30,62	7,34	0,10	1,52	0,00	1,10	0,01	0,39	0,16	0,01	5,66	0,00	5,38	101,82
Quartz Shale 1	98,58	0,60	0,05	0,01	0,00	0,01	0,04	0,01	0,00	0,00	0,00	0,11	0,01	6,89	106,29
Quartz Shale 2	99,09	0,27	0,03	0,00	0,00	0,02	0,04	0,02	0,00	0,00	0,00	0,08	0,00	6,08	105,63
Quartz Shale 3	99,45	0,06	0,02	0,00	0,00	0,01	0,04	0,00	0,00	0,00	0,01	0,08	0,00	6,42	106,08
Quartz Shale 4	99,24	0,05	0,02	0,00	0,00	0,01	0,05	0,00	0,00	0,05	0,00	0,05	0,05	6,39	105,90
Quartz Shale 5	98,73	0,36	0,09	0,00	0,00	0,00	0,02	0,00	0,02	0,00	0,00	0,07	0,00	6,23	105,53
Quartz Shale 6	99,02	0,34	0,08	0,00	0,00	0,01	0,04	0,00	0,00	0,00	0,01	0,12	0,02	6,54	106,17
Quartz Dyke 1	99,64	0,06	0,01	0,00	0,00	0,00	0,05	0,00	0,00	0,02	0,01	0,06	0,00	7,00	106,84
Quartz Dyke 2	99,14	0,22	0,04	0,02	0,00	0,01	0,01	0,02	0,00	0,00	0,00	0,07	0,00	6,58	106,09
Quartz Dyke 3	99,13	0,01	0,01	0,00	0,00	0,01	0,02	0,00	0,00	0,00	0,00	0,07	0,00	7,03	106,27
Quartz Dyke 4	98,79	0,46	0,12	0,03	0,02	0,01	0,02	0,01	0,00	0,01	0,00	0,11	0,00	7,29	106,87
Quartz Dyke 5	98,95	0,21	0,02	0,01	0,00	0,01	0,00	0,02	0,17	0,00	0,00	0,08	0,01	7,12	106,61
Quartz Dyke 6	99,44	0,39	0,02	0,00	0,00	0,01	0,07	0,01	0,00	0,01	0,00	0,08	0,00	6,26	106,29
Quartz Dyke 7	99,34	0,26	0,02	0,01	0,00	0,00	0,04	0,00	0,00	0,00	0,00	0,06	0,04	6,15	105,91
Quartz Dyke 8	99,35	0,06	0,01	0,00	0,00	0,00	0,07	0,00	0,01	0,03	0,00	0,09	0,00	6,72	106,34
Quartz Dyke 9	99,40	0,15	0,00	0,00	0,00	0,01	0,04	0,03	0,00	0,01	0,00	0,07	0,01	6,29	106,00
Quartz Dyke 10	98,85	0,37	0,02	0,01	0,00	0,00	0,02	0,00	0,00	0,00	0,00	0,08	0,00	6,02	105,38
Quartz Dyke 11	99,40	0,33	0,04	0,02	0,00	0,00	0,01	0,01	0,00	0,00	0,00	0,04	0,00	6,03	105,90
Quartz Dyke 12	99,28	0,16	0,03	0,00	0,00	0,01	0,06	0,00	0,00	0,01	0,00	0,12	0,00	6,32	106,00
Quartz Dyke 13	99,05	0,30	0,09	0,01	0,00	0,01	0,00	0,00	0,00	0,00	0,00	0,08	0,00	6,31	105,84
Quartz Dyke 14	99,50	0,00	0,01	0,00	0,00	0,01	0,01	0,01	0,01	0,00	0,00	0,09	0,00	6,01	105,65
Quartz Dyke 15	99,21	0,26	0,02	0,00	0,00	0,01	0,05	0,02	0,00	0,00	0,01	0,07	0,00	6,40	106,05
Quartz Dyke 16	99,14	0,14	0,01	0,00	0,02	0,01	0,00	0,01	0,02	0,01	0,02	0,08	0,00	5,92	105,38
Quartz Dyke 17	99,49	0,42	0,01	0,02	0,00	0,00	0,03	0,00	0,00	0,01	0,01	0,09	0,01	6,21	106,29
Quartz Dyke 18	98,97	0,13	0,01	0,00	0,01	0,00	0,00	0,00	0,02	0,03	0,00	0,08	0,00	6,21	105,46
Quartz Dyke 19	98,63	0,53	0,01	0,01	0,00	0,00	0,04	0,02	0,01	0,02	0,00	0,10	0,03	6,11	105,49
Quartz Dyke 20	99,23	0,31	0,02	0,02	0,02	0,01	0,02	0,01	0,00	0,00	0,01	0,07	0,01	6,31	106,04
Quartz Dyke 21	99,85	0,00	0,00	0,00	0,00	0,02	0,02	0,00	0,00	0,01	0,00	0,04	0,00	6,39	106,34
Quartz Dyke 22	99,86	0,03	0,00	0,01	0,01	0,01	0,00	0,01	0,00	0,01	0,02	0,04	0,02	6,19	106,20
Quartz Dyke 23	99,87	0,08	0,02	0,00	0,00	0,00	0,02	0,02	0,00	0,02	0,00	0,08	0,00	6,00	106,10
Quartz Dyke 24	99,34	0,00	0,00	0,00	0,00	0,00	0,02	0,01	0,01	0,00	0,00	0,06	0,00	6,26	105,70
Quartz Dyke 25	100,00	0,00	0,00	0,00	0,00	0,03	0,04	0,00	0,00	0,01	0,04	0,06	0,01	6,37	106,56
Quartz Dyke 26	99,80	0,01	0,00	0,00	0,00	0,03	0,05	0,00	0,00	0,01	0,00	0,03	0,01	5,96	105,90
Quartz Dyke 27	99,81	0,07	0,00	0,01	0,00	0,04	0,03	0,00	0,02	0,01	0,00	0,07	0,00	6,85	106,89
Quartz Dyke 28	99,42	0,01	0,01	0,00	0,00	0,00	0,00	0,00	0,01	0,00	0,00	0,05	0,00	6,36	105,86
Quartz Dyke 29	99,29	0,01	0,00	0,01	0,01	0,01	0,00	0,00	0,00	0,00	0,02	0,07	0,01	6,19	105,60
Quartz Dyke 30	99,71	0,04	0,00	0,00	0,00	0,01	0,04	0,02	0,00	0,01	0,03	0,07	0,00	6,48	106,41

TABLE A.4 – *Composition chimique des phases minérales dans l'échantillon FTC4 (Barite Valley). Quartz Dyke correspond au microquartz dans les cherts de fracture tandis que les autres phases sont toutes situées dans les argiles encaissantes.*

FTC9

| | | | | | | Composition chimique des phases minérales de Barite Valley | | | | | | | |

# analyse	SiO₂	Al₂O₃	K₂O	Na₂O	MgO	CaO	FeO	MnO	TiO₂	Cr₂O₃	P₂O₅	BaO	NiO	Total
Dolomie 1	0,02	0,11	0,01	0,02	17,66	27,93	7,26	1,33	0,02	0,00	0,02	0,07	0,00	54,43
Dolomie 2	0,51	0,25	0,04	0,06	14,37	27,42	9,74	0,61	0,00	0,05	0,03	0,08	0,01	53,17
Dolomie 3	0,02	0,04	0,02	0,05	16,22	28,10	8,11	2,40	0,00	0,01	0,03	0,07	0,00	55,07
Dolomie 4	0,01	0,05	0,01	0,04	16,13	27,76	8,29	1,99	0,00	0,04	0,03	0,03	0,00	54,38
Dolomie 5	0,17	0,00	0,00	0,01	15,76	27,35	8,48	1,22	0,00	0,00	0,02	0,05	0,02	53,07
Dolomie 6	2,28	1,35	0,26	0,05	14,97	26,14	7,53	1,29	0,02	0,02	0,00	0,21	0,02	54,14
Dolomie 7	0,23	0,11	0,02	0,05	15,86	27,08	8,41	2,52	0,02	0,00	0,02	0,06	0,03	54,40
Dolomie 8	0,00	0,06	0,00	0,02	16,51	27,52	7,57	1,81	0,01	0,01	0,03	0,04	0,03	53,61
Dolomie 9	8,22	0,12	0,03	0,03	14,28	25,99	7,87	0,78	0,00	0,00	0,01	0,07	0,02	57,40
Dolomie 10	0,11	0,08	0,02	0,04	16,85	27,62	7,50	0,89	0,00	0,01	0,01	0,05	0,01	53,17
Dolomie 11	2,70	0,01	0,00	0,00	14,51	26,94	8,77	2,21	0,00	0,01	0,01	0,08	0,05	55,29
Dolomie 12	0,00	0,02	0,01	0,03	16,04	27,22	8,91	1,15	0,00	0,00	0,00	0,09	0,00	53,46
Dolomie 13	1,63	0,09	0,01	0,02	14,91	28,05	8,41	2,73	0,00	0,00	0,03	0,07	0,01	55,96
Dolomie 14	0,15	0,03	0,00	0,02	17,53	28,07	7,11	0,94	0,00	0,03	0,02	0,07	0,00	53,97
Dolomie 15	0,03	0,04	0,00	0,06	14,91	27,70	7,74	2,51	0,00	0,02	0,04	0,05	0,00	53,09
Dolomie 16	0,07	0,08	0,01	0,05	16,74	27,49	7,87	1,76	0,00	0,01	0,03	0,07	0,00	54,17
Dolomie 17	0,98	0,71	0,15	0,02	15,51	27,36	7,97	2,12	0,02	0,03	0,04	0,10	0,04	55,04
Quartz Dyke 1	98,57	0,08	0,02	0,00	0,00	0,00	0,02	0,00	0,02	0,00	0,01	0,07	0,00	98,79
Quartz Dyke 2	98,71	0,07	0,02	0,00	0,00	0,01	0,02	0,00	0,00	0,00	0,03	0,05	0,01	98,92
Quartz Dyke 3	98,49	0,23	0,06	0,00	0,00	0,00	0,01	0,00	0,00	0,00	0,00	0,06	0,00	98,84
Quartz Dyke 4	99,18	0,04	0,00	0,00	0,00	0,01	0,04	0,01	0,00	0,00	0,00	0,06	0,00	99,34
Quartz Dyke 5	98,96	0,01	0,01	0,00	0,00	0,02	0,03	0,00	0,00	0,01	0,00	0,09	0,01	99,14
Quartz Dyke 6	98,24	0,02	0,00	0,02	0,00	0,01	0,02	0,03	0,00	0,02	0,00	0,05	0,00	98,40
Quartz Dyke 7	97,35	0,44	0,10	0,01	0,00	0,01	0,06	0,02	0,00	0,00	0,01	0,08	0,00	98,08
Quartz Dyke 8	98,45	0,16	0,02	0,01	0,00	0,00	0,02	0,02	0,00	0,00	0,00	0,04	0,02	98,75
Quartz Dyke 9	98,22	0,09	0,02	0,01	0,00	0,01	0,03	0,02	0,01	0,00	0,00	0,09	0,00	98,49
Quartz Dyke 10	97,95	0,24	0,03	0,02	0,00	0,01	0,03	0,00	0,01	0,00	0,00	0,08	0,02	98,38
Si-sericite 1	74,16	15,11	4,52	0,09	0,58	0,00	0,36	0,00	0,14	0,01	0,00	2,41	0,01	97,40
Si-sericite 2	78,13	11,27	3,33	0,08	0,45	0,01	0,39	0,02	0,12	0,04	0,00	1,97	0,00	95,81
Si-sericite 3	79,53	10,71	3,36	0,07	0,52	0,00	0,50	0,00	0,05	0,05	0,02	1,44	0,04	96,29
Si-sericite 4	52,56	30,91	7,93	0,13	1,17	0,00	0,77	0,00	0,25	0,03	0,00	3,87	0,03	97,64
Si-sericite 5	71,24	17,33	4,84	0,07	0,73	0,00	0,51	0,00	0,14	0,09	0,00	2,38	0,02	97,34
Si-sericite 6	76,19	12,69	3,76	0,06	0,50	0,02	0,50	0,00	0,16	0,03	0,01	1,97	0,02	95,89
Si-sericite 7	77,85	11,42	3,13	0,11	0,47	0,01	0,44	0,02	0,14	0,01	0,00	1,48	0,01	95,10
Si-sericite 8	62,78	22,80	7,07	0,25	0,57	0,01	0,56	0,00	0,14	0,09	0,00	1,12	0,00	95,39
Si-sericite 9	67,63	18,42	5,43	0,08	0,79	0,00	0,64	0,00	0,17	0,08	0,00	2,68	0,01	95,94
Si-sericite 10	57,78	30,04	4,70	0,10	1,19	0,02	0,78	0,00	0,23	0,02	0,00	3,71	0,02	98,57
Sericite Core 1	47,61	32,34	7,33	0,12	1,51	0,00	0,79	0,03	0,27	0,09	0,00	4,72	0,00	94,80
Sericite Core 2	46,55	30,19	7,71	0,15	1,32	0,06	0,96	0,01	0,26	0,10	0,04	4,47	0,00	91,80
Sericite Core 3	49,31	32,87	7,25	0,08	1,33	0,02	0,89	0,01	0,21	0,13	0,01	4,14	0,01	96,26
Sericite Core 4	47,67	32,91	8,59	0,18	1,63	0,01	2,83	0,03	0,22	0,04	0,01	0,93	0,00	95,04
Sericite Core 5	48,68	34,35	8,43	0,24	0,93	0,00	1,46	0,01	0,27	0,05	0,01	1,26	0,00	95,67
Sericite Core 6	48,81	33,32	7,80	0,13	1,20	0,00	1,32	0,02	0,27	0,08	0,02	1,75	0,00	94,73
Sericite Core 7	53,36	30,05	5,44	0,10	1,34	0,00	0,85	0,02	0,15	0,16	0,00	3,31	0,04	94,80
Sericite Core 8	48,82	32,73	6,32	0,36	0,93	0,04	0,74	0,00	0,15	0,07	0,01	2,50	0,00	92,66
Sericite Core 9	47,03	36,70	9,07	0,53	0,70	0,00	0,88	0,01	0,30	0,18	0,00	0,70	0,00	96,10
Sericite Rim 1	47,84	33,13	7,31	0,09	1,43	0,00	0,80	0,02	0,27	0,10	0,03	4,98	0,05	96,04
Sericite Rim 2	48,52	34,18	7,66	0,12	1,06	0,02	1,35	0,00	0,20	0,07	0,01	1,53	0,01	94,73
Sericite Rim 3	51,26	29,80	7,02	0,12	1,31	0,00	0,91	0,00	0,18	0,05	0,00	3,42	0,01	94,08
Sericite Rim 4	46,28	33,48	6,92	0,10	1,60	0,00	0,95	0,00	0,28	0,04	0,02	5,52	0,02	95,21
Sericite Rim 5	47,59	34,34	7,95	0,15	1,38	0,02	0,85	0,00	0,13	0,13	0,02	2,05	0,00	94,60
Sericite Rim 6	48,32	36,09	7,34	0,40	0,89	0,00	0,74	0,00	0,12	0,05	0,00	1,76	0,02	95,73
Sericite Rim 7	49,56	31,24	6,63	0,15	1,37	0,00	1,15	0,00	0,20	0,09	0,02	4,30	0,00	94,71
Sericite Rim 8	52,42	29,10	7,42	0,15	1,42	0,00	0,81	0,05	0,19	0,12	0,00	4,14	0,02	95,84

TABLE A.5 – *Composition chimique des phases minérales dans l'échantillon FTC9 (Barite Valley). Quartz Dyke correspond au microquartz dans les cherts de fracture, les carbonates sont également dans le dyke tandis que les autres phases sont toutes situées dans les argiles encaissantes.*

A.3 Géochimie : éléments majeurs et traces

Le protocole de préparation des échantillons pour les analyses en éléments majeurs et traces a été détaillé dans le Chapitre 4. Ils sont représentés ici de manière schématique dans les Figures A.6 et A.7. La méthode est adaptée de Chauvel et al. (2011). La Table A.6 présente les résultats obtenus sur les standards BHVO-2, AGV-1 et RGM1 au cours des différentes sessions d'analyse. La Figure A.8 montre que le choix de la normalisation n'influence pas les valeurs des différents proxys océaniques (voir Chapitre 4).
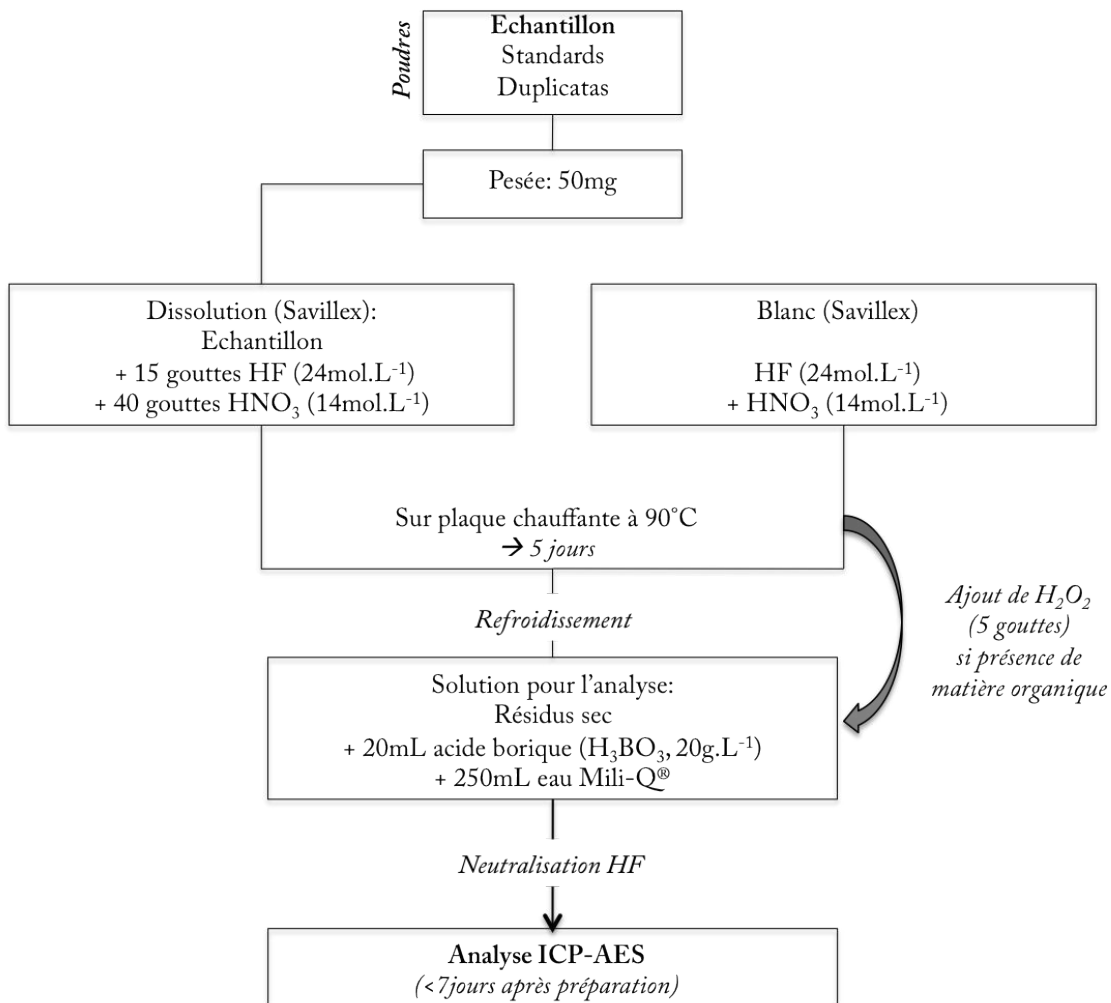
FIGURE A.6 – *Protocole expérimental : préparation des échantillons pour les analyses en éléments majeurs sur roche totale par ICP-AES.*
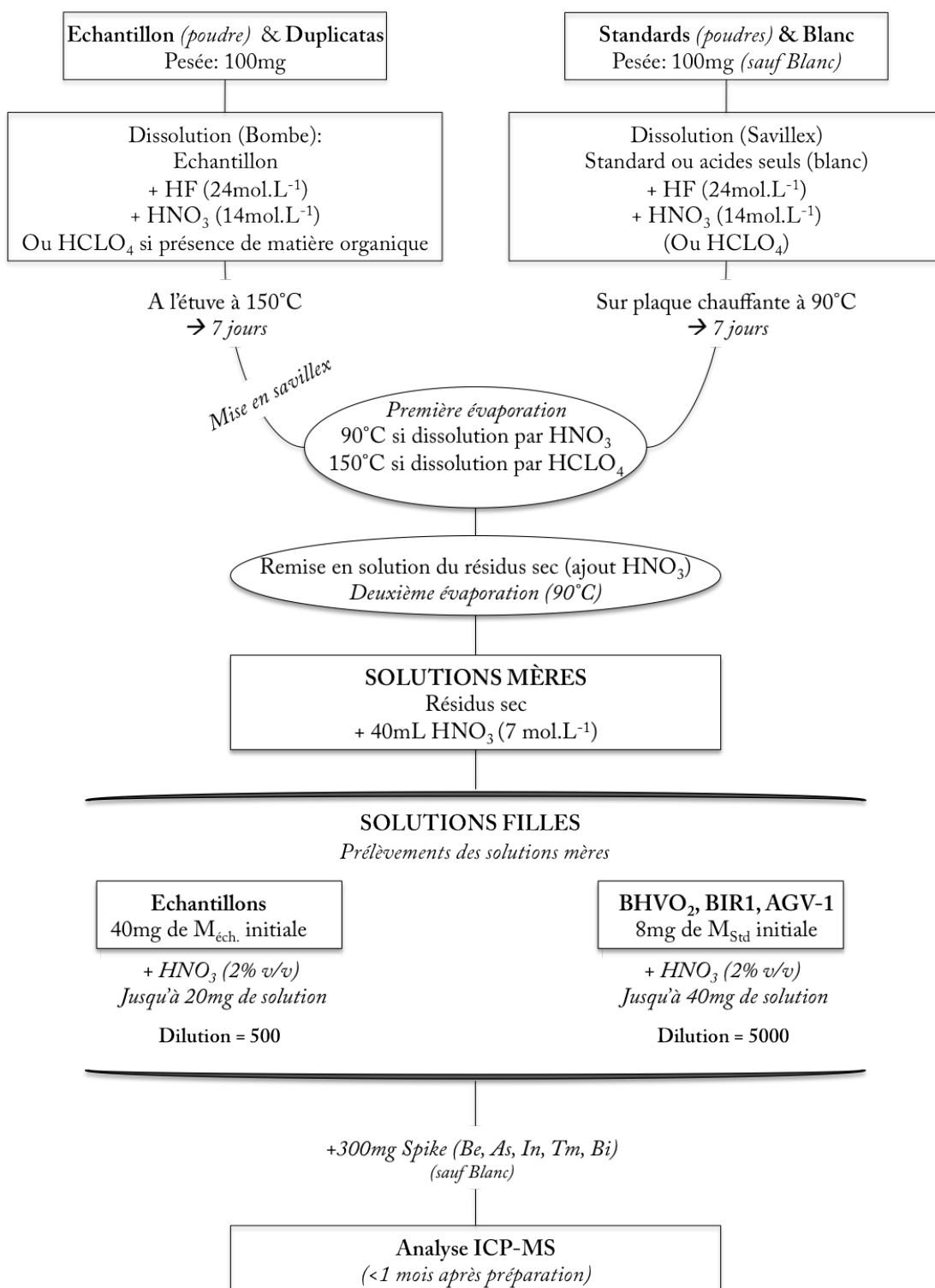
FIGURE A.7 – *Protocole expérimental : préparation des échantillons pour les analyses en éléments traces et terres rares sur roche totale par ICP-MS.*

	BHVO2				AGV1				RGM1			
(wt%)	Moyenne (n=45)	Ecart-type	Théorique	Différence (%)	Moyenne (x=3)	Ecart-type	Théorique	Différence (%)	Moyenne (n=10)	Ecart-type	Théorique	Différence (%
SiO_2	50,28	0,96	49,90	0,76	60,34	0,40	58,84	2,55	70,89	1,23	73,45	-3,49
TiO_2	2,79	0,06	2,73	2,20	1,08	0,01	1,05	2,86	0,26	0,00	0,27	-2,62
Al_2O_3	13,95	0,28	13,50	3,33	17,72	0,18	17,15	3,32	14,01	0,08	13,72	2,11
Fe_2O_3 t	12,84	0,25	12,30	4,39	6,95	0,07	6,77	2,66	1,85	0,01	1,86	-0,54
MnO	0,18	0,00	0,17	5,88	0,10	0,00	0,10	0,00	0,03	0,00	0,04	-16,67
MgO	7,62	0,26	7,23	5,39	1,44	0,02	1,53	-5,88	<LD		0,28	
CaO	11,76	0,23	11,40	3,16	5,03	0,05	4,94	1,82	1,14	0,00	1,15	-0,87
Na_2O	2,27	0,08	2,22	2,25	4,31	0,04	4,26	1,17	4,14	0,03	4,07	1,72
K_2O	0,55	0,01	0,52	5,77	2,82	0,03	2,92	-3,42	4,09	0,03	4,30	-4,88
P_2O_5	0,26	0,01	0,27	-3,70	0,51	0,01	0,49	4,08	<LD		0,05	
(ppm)												
Cs	0,10	0,00	0,10	0,02	1,28	0,06	1,29	-1,03	10,44	0,12	10,40	0,38
Rb	9,09	0,23	9,11	-0,18	69,50	1,21	66,80	4,04	160,90	9,99	153,00	5,16
Ba	131,02	0,89	131,00	0,02	1236,00	15,13	1230,00	0,49	834,40	5,42	853,00	-2,18
Th	1,22	0,02	1,22	0,05	6,33	0,03	6,35	-0,26	14,28	0,51	14,70	-2,86
U	0,40	0,01	0,40	0,03	1,85	0,01	1,83	1,09	5,18	0,36	5,39	-3,88
Nb	18,09	0,14	18,10	-0,07	14,30	0,10	13,90	2,88	9,44	0,60	9,24	2,12
Ta	1,14	0,01	1,14	0,00	0,84	0,01	0,83	1,78	0,90	0,01	0,90	0,95
La	15,21	0,09	15,20	0,06	38,13	0,15	38,00	0,35	21,82	1,28	23,20	-5,95
Ce	37,51	0,13	37,50	0,02	69,53	0,68	69,00	0,77	44,35	2,15	47,40	-6,43
Pr	5,35	0,03	5,35	0,02	8,46	0,06	8,47	-0,08	5,11	0,21	5,35	-4,45
Pb	1,53	0,04	1,54	-0,49	39,17	0,64	35,90	9,10	23,16	2,75	24,00	-3,50
Nd	24,50	0,14	24,50	0,02	31,93	0,32	31,80	0,42	18,70	0,65	19,40	-3,61
Sr	395,36	4,18	396,00	-0,16	681,67	11,59	657,00	3,75	108,60	4,27	111,00	-2,16
Sm	6,07	0,08	6,07	0,05	5,77	0,09	5,77	0,00	3,82	0,15	3,94	-3,05
Zr	171,73	1,85	172,00	-0,16	238,67	1,53	237,00	0,70	249,10	13,09	234,00	6,45
Hf	4,36	0,03	4,36	-0,05	5,07	0,01	5,05	0,40	5,89	0,05	5,93	-0,73
Ti	16325,22	223,68	16300,00	0,15	6252,00	100,16	6080,00	2,83	1542,30	51,82	1550,00	-0,50
Eu	2,07	0,02	2,07	-0,04	1,59	0,03	1,61	-1,04	0,58	0,03	0,61	-4,95
Gd	6,15	0,22	6,24	-1,44	4,42	0,31	4,69	-5,83	3,50	0,15	3,67	-4,66
Tb	0,91	0,02	0,92	-0,61	0,61	0,02	0,63	-3,27	0,56	0,03	0,59	-3,89
Dy	5,31	0,05	5,31	-0,06	3,60	0,04	3,55	1,31	3,57	0,16	3,70	-3,41
Ho	0,98	0,01	0,98	-0,05	0,68	0,00	0,68	0,35	0,74	0,02	0,77	-2,95
Y	25,96	0,26	26,00	-0,15	19,90	0,17	19,50	2,05	23,52	0,42	23,50	0,09
Er	2,54	0,02	2,54	-0,05	1,83	0,05	1,84	-0,36	2,29	0,06	2,33	-1,76
Li	4,80	0,06	4,80	0,04	10,93	0,21	10,90	0,31	62,96	0,79	65,40	-3,73
Yb	2,00	0,02	2,00	0,01	1,67	0,03	1,65	1,01	2,44	0,07	2,52	-3,33
Lu	0,27	0,00	0,27	-0,04	0,24	0,00	0,24	0,41	0,38	0,01	0,39	-2,72
Sc	32,05	0,46	32,00	0,15	12,97	0,38	12,80	1,30	5,48	0,38	5,35	2,50
V	317,38	3,06	317,00	0,12	122,00	1,73	117,00	4,27	11,20	0,38	11,00	1,82
Cr	280,47	2,64	280,00	0,17	7,95	0,36	8,05	-1,20	2,89	0,50	3,23	-10,46
Co	45,09	0,47	45,00	0,20	15,93	0,06	15,30	4,14	1,98	0,11	2,02	-1,83
Ni	119,20	1,20	119,00	0,17	15,03	0,12	14,50	3,68	2,25	0,10	2,10	7,33
Cu	127,24	1,46	127,00	0,19	59,77	1,54	57,20	4,49	11,53	1,16	11,10	3,87
Zn	103,27	1,16	103,00	0,26	94,53	1,18	91,70	3,09	33,05	0,76	36,20	-8,70

TABLE A.6 – *Récapitulatif des analyses géochimiques en éléments majeurs et traces sur les standards BHVO-2, AGV-1 et RGM-1. Les valeurs théoriques sont comparées à la moyenne des valeurs mesurées au cours de différentes sessions d'analyses. La différence est exprimée en écart-type (1σ).*

Effet du choix de la normalisation sur les anomalies en éléments traces
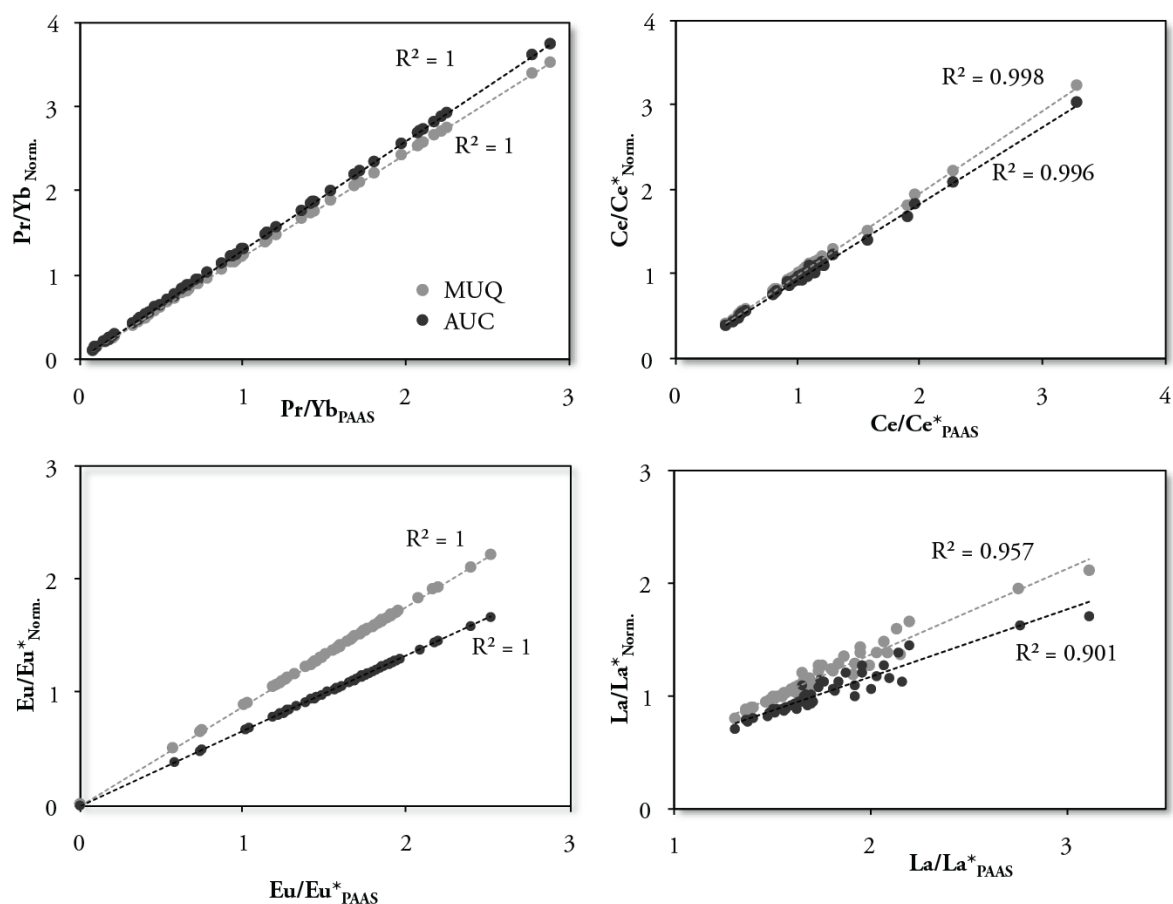
FIGURE A.8 – *Diagrammes comparant les valeurs des différents proxys océaniques utilisés dans le Chapitre 4 en fonction des différentes normalisations : Post-Archean Australian Shales (PAAS) de Taylor et McLennan (1985), Mud Of Queensland (MUQ) de Kamber et al. (2005) et Archean Upper Continental Crust (AUC) de Condie (1993). Seule l'anomalie en lanthane semble légèrement affectée par la normalisation, mais les $R^2 > 0.90$ montrent que l'effet de la normalisation est limitée. Dans le Chapitre 4, j'ai choisi d'utiliser les PAAS qui représentent la normalisation la plus couramment utilisée et permettent une comparaison plus aisée des données avec la littérature.*

A.4 Géochimie : isotopes de Si et O

Après avoir identifié les différents types de chert à notre disposition, nous avons sélectionné 6 échantillons pour effectuer des analyses *in situ* des isotopes de l'oxygène et du silicium au CRPG de Nancy, sous la direction de Marc Chaussidon et Claire Rollion-Bard. Deux échantillons correspondent aux cherts noirs des niveaux turbiditiques de Komati River, deux échantillons correspondent à des niveaux massifs de chert blanc dans la séquence litée de Buck Reef, et deux échantillons sont issus des veines de chert noir de Barite Valley. La totalité des résultats est présentée dans le seconde partie de cette annexe.

Les roches brutes sont fracturées en morceaux de 1 à 2cm et placés dans des bagues d'aluminium. L'ensemble est enrobé et maintenu par une résine de type araldite couplée à un durciceur, et placé à l'étuve (*min 2h*) pour favoriser la polymérisation. Un polissage en plusieurs étapes permet de terminer le montage et d'obtenir une surface parfaitement lisse essentielle aux analyses : quatre polissages manuels successifs sont réalisés à l'aide de papier abrasif en carbure de silicium et à granulométrie décroissante (successivement 400, 600, 1200 puis $2400 grains/cm^2$). Cette première étape permet d'atteindre une qualité de surface suffisante pour les deux polissages mécaniques suivant, sur disques de feutres et à l'aide de pâtes diamantées de granulométrie 3 puis $1\mu m$. Après contrôle du polissage au microscope, les bagues sont métallisées à l'or et prêtes pour les analyses (Fig.A.9).

Les analyses sont réalisées sur la sonde ionique Cameca ims 1270. Les éléments à analyser étant l'oxygène et le silicium, qui s'ionisent préférentiellement en anions, la source d'ions primaires doit être constituée de cations, d'où le choix de la source à césium (produit uniquement des ions Cs^+) (Fig.A.9). Le diamètre du faisceau est calibré de manière à être inférieur à $5\mu m$, ce qui permet de réaliser les analyses ponctuelles sur un nombre restreint de microquartz puisque les analyses par diffraction X (Annexe A.1) ont montré une taille de grain proche de celle du faisceau (soit $\sim 5\mu m$). Cette approche à haute résolution permet d'étudier la variabilité des compositions isotopiques au coeur de la matrice cristalline. La gamme de $\delta^{30}Si$ et $\delta^{18}O$ obtenue sur un même échantillon est un paramètre révélateur de la préserva-
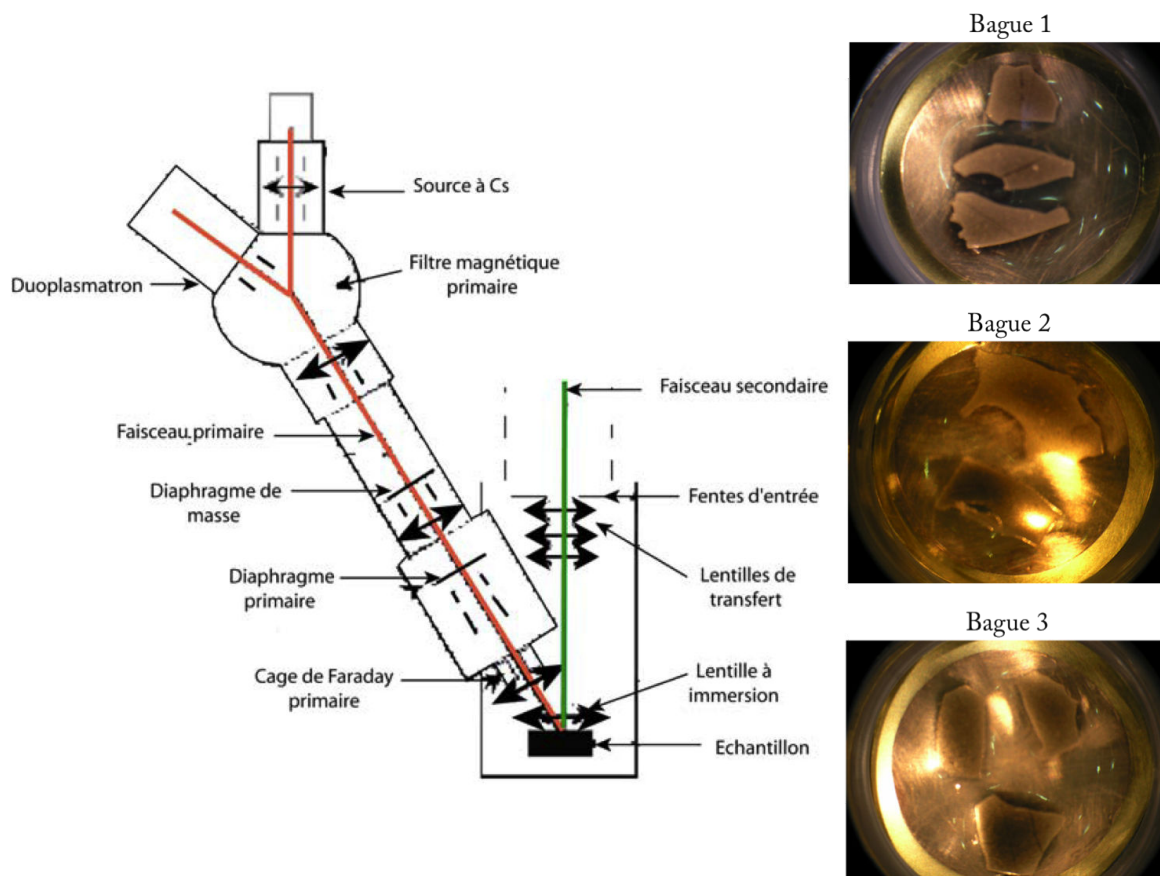
FIGURE A.9 – *Schéma simplifié du dispositif expérimental (canon ionique à source césium) et photos des supports des échantillons après métallisation à l'or. La largeur d'une bague est de 1.5cm.*

tion des cherts d'après Marin-Carbonne et al. (2012), un argument discuté dans le Chapitre 5.

Le vide analytique est établi et stabilisé à $10^{-8}torr$, valeur en deçà de laquelle l'influence des hydrures peut biaiser de manière significative les résultats. Différents standards ont été utilisés, à savoir deux références de quartz pour l'oxygène (Quartz du Brésil = +9.6‰ ; Quartz NL615 = +18.4‰) et un chert Miocène pour le silicium (Chert Miocène = −0.69‰). Les données obtenues pour ces standards sont données dans le tableau A.7.

Entre 15 et 62 analyses ponctuelles sont réalisées sur chaque échantillon et pour chaque isotope. La précision obtenue pour les données en oxygène est comprise entre ±0.28‰ et ±0.32‰. Pour le silicium, la première série d'analyse a donné d'excellents résultats à ±0.11 et ±0.17‰ en fonction des échantillons, tandis que la deuxième série est estimée à ±0.34‰.

Cette différence est interprétée comme liée aux instabilités de la machine durant la nuit séparant les deux sets d'analyses (*N.B. cette nuit là, les orages les plus violents que la région ait connu depuis des décennies ont inondé et perturbé l'ensemble de l'agglomération de Nancy, mettant à mal les onduleurs du système de sécurité de la sonde...*).

Les données obtenues sont présentées dans les Tables A.8 pour le silicium et A.9 pour l'oxygène.

Miocene Quartz				**NL615**		
Analysis #	**δ ^{30}Si /^{28}Si**	**Error (1σ)**		**Analysis #**	**δ ^{18}O /^{16}O**	**Error (1σ)**
1	-33,157	*0,15*		1	7,009	*0,10*
2	-31,913	*0,18*		2	7	*0,13*
3	-33,129	*0,18*		3	7,217	*0,10*
4	-32,564	*0,23*		4	6,973	*0,10*
5	-32,256	*0,24*		5	7,274	*0,09*
6	-32,192	*0,24*		6	7,435	*0,11*
7	-32,184	*0,24*		7	7,315	*0,11*
8	-32,22	*0,23*		8	7,439	*0,09*
9	-31,703	*0,19*		9	6,9	*0,11*
10	-31,383	*0,19*		10	6,935	*0,08*
11	-32,145	*0,18*		11	6,25	*0,06*
12	-31,117	*0,19*		12	6,269	*0,08*
13	-32,017	*0,21*		13	6,697	*0,07*
14	-31,658	*0,21*				
15	-30,635	*0,20*				
16	-31,256	*0,21*				
17	-30,866	*0,23*				
18	-30,759	*0,22*				
19	-30,598	*0,19*				

TABLE A.7 – *Analyses des isotopes de l'oxygène et du silicium pour les deux standards utilisés dans cette étude : Chert Miocène $\delta^{30}Si = -0.69$‰ ; Quartz NL615 $\delta^{18}O = +18.4$‰*

- KOMATI RIVER -				- BARITE VALLEY -				- BUCK REEF -			
KRC8		KRC11		FTCX		FTC4		BRC20		BRC22	
$\delta 30Si$ (‰)	1σ	$\delta 30Si$ (‰)	1σ	$\delta 30Si$ (‰)	1σ	$\delta 30Si$ (‰)	1σ	$\delta 30Si$ (‰)	1σ	$\delta 30Si$ (‰)	1σ
0,45	0,23	0,05	0,32	-1,48	0,31	-2,01	0,23	-1,62	0,29	0,90	0,29
1,47	0,20	1,17	0,32	-1,42	0,30	-1,82	0,23	-2,19	0,29	1,47	0,28
-0,17	0,23	0,75	0,34	-1,80	0,31	-2,49	0,24	-2,82	0,28	1,19	0,29
-0,62	0,24	-0,67	0,32	-0,87	0,30	-2,18	0,21	-2,59	0,29	1,13	0,29
0,62	0,21	0,55	0,32	-1,89	0,32	-1,30	0,24	-1,97	0,30	1,08	0,29
0,15	0,21	-0,01	0,29	-0,84	0,32	-2,07	0,22	-1,76	0,29	1,11	0,29
-0,48	0,21	0,68	0,37	-1,40	0,32	-1,66	0,22	-2,25	0,28	1,11	0,29
-0,57	0,22	1,67	0,34	-1,15	0,32	-2,21	0,20	-1,40	0,28	1,58	0,28
0,16	0,21	0,00	0,32	-0,46	0,32	-1,58	0,21	-1,45	0,29	1,49	0,28
-0,24	0,22	3,89	0,39	-0,88	0,29	-2,07	0,21	-2,15	0,29	1,15	0,29
-0,50	0,22	0,26	0,33	-0,60	0,31	-2,02	0,21	-2,36	0,28	1,00	0,28
-0,19	0,23	-0,61	0,29	-1,00	0,33	-1,54	0,20	-3,10	0,29	1,43	0,28
1,17	0,26	-1,89	0,28	-1,02	0,32	-1,89	0,22	-2,49	0,29	1,39	0,30
-0,19	0,23	-1,84	0,29	-0,79	0,33	-1,95	0,21	-3,09	0,30	0,71	0,28
0,35	0,23	2,39	0,33	-0,10	0,31	-1,36	0,21	-2,83	0,28	1,53	0,28
-0,30	0,22	0,72	0,32	-0,63	0,32	-1,06	0,21	-2,07	0,30	1,17	0,27
0,00	0,24	0,82	0,33	-0,95	0,32	-3,48	0,20	-2,17	0,28	0,72	0,28
0,01	0,23	3,09	0,31	-0,60	0,34	-1,36	0,22	-2,07	0,30	1,21	0,29
0,09	0,23	1,06	0,29	0,22	0,35	-3,26	0,24	-2,02	0,28	0,55	0,28
-0,23	0,23	1,86	0,33	-0,56	0,28	-4,50	0,20	-2,18	0,28	0,63	0,27
0,28	0,25	0,82	0,29			-1,34	0,26				
0,49	0,25	-0,38	0,30			-2,05	0,19				
0,21	0,23	-0,01	0,29			-1,12	0,21				
-0,30	0,21	2,35	0,29			-1,84	0,20				
0,11	0,21	-0,04	0,31			-1,51	0,23				
-0,69	0,22	0,50	0,31			-1,47	0,20				
0,14	0,22	1,60	0,30			-1,32	0,22				
0,03	0,25	1,07	0,29			-1,15	0,22				
0,43	0,24	2,34	0,33			-0,71	0,21				
1,61	0,20					-0,78	0,20				
0,29	0,23					-1,15	0,24				
0,99	0,24					-1,04	0,22				
0,38	0,22					-0,96	0,23				
-0,13	0,25					-0,24	0,22				
0,04	0,26					-0,89	0,23				
0,04	0,23					-0,19	0,23				
0,46	0,23					-0,90	0,21				
-0,63	0,25					-1,03	0,21				
0,40	0,23					-0,80	0,21				
0,40	0,23					-0,27	0,22				
-0,31	0,22					-1,18	0,19				
						-0,90	0,23				
						-2,09	0,25				
						-0,93	0,21				
						-0,60	0,22				
						-0,28	0,20				
						-0,86	0,24				
						-0,77	0,24				
						-0,22	0,23				
						-3,07	0,24				
						-0,75	0,21				
						-0,98	0,20				
						-1,19	0,22				
						-0,70	0,23				
						-1,18	0,19				
						-0,82	0,22				
						-0,36	0,23				
						-0,96	0,21				
						-0,64	0,20				
						-1,00	0,21				

TABLE A.8 – *Analyses des isotopes du silicium pour les échantillons de Komati River, Buck Reef et Barite Valley.*

| - KOMATI RIVER - | | | | - BARITE VALLEY - | | | | - BUCK REEF - | | | |
| KRC8 | | KRC11 | | FTCX | | FTC4 | | BRC20 | | BRC22 | |
δ18O (‰)	1σ	δ18O (‰)	1σ	δ18O (‰)	1σ	δ18O (‰)	1σ	δ18O (‰)	1σ	δ18O (‰)	1σ
17,24	0,17	19,45	0,34	23,67	0,34	21,03	0,12	20,62	0,34	19,45	0,34
17,21	0,16	19,54	0,34	23,44	0,33	21,00	0,12	19,98	0,34	20,17	0,34
17,00	0,17	18,60	0,34	23,40	0,34	20,85	0,12	20,28	0,34	19,75	0,34
17,17	0,17	19,32	0,34	23,60	0,34	20,76	0,10	20,92	0,34	20,02	0,34
17,12	0,16	19,31	0,34	23,49	0,34	21,03	0,10	20,60	0,34	20,10	0,34
17,24	0,18	19,59	0,33	23,35	0,34	21,30	0,12	20,27	0,35	19,89	0,34
17,05	0,16	19,11	0,34	23,87	0,34	21,02	0,12	20,77	0,34	19,88	0,34
17,05	0,16	18,92	0,34	23,57	0,34	20,99	0,11	20,82	0,34	20,03	0,34
17,12	0,17	18,98	0,34	23,81	0,34	21,03	0,10	20,58	0,34	19,57	0,34
17,27	0,17	19,22	0,34	23,43	0,34	20,83	0,10	20,38	0,34	19,69	0,34
17,30	0,17	19,28	0,34	23,82	0,34	21,02	0,12	19,93	0,34	19,66	0,34
17,45	0,16	19,29	0,34	23,71	0,34	21,19	0,11	20,80	0,34	19,44	0,34
17,32	0,17	19,37	0,34	24,26	0,34	20,99	0,12	20,89	0,34	19,47	0,34
17,31	0,16	19,19	0,34	24,07	0,34	21,16	0,11	20,83	0,34	19,85	0,34
17,32	0,18	19,19	0,34	23,78	0,34	20,96	0,10	20,79	0,34	20,08	0,34
17,48	0,17	19,35	0,34			21,35	0,11	21,09	0,34	19,90	0,34
16,97	**0,17**	19,25	0,34			20,74	0,11	20,60	0,34	19,81	0,34
17,31	**0,16**	19,37	0,34			20,67	0,11	20,71	0,34	20,08	0,34
16,25	**0,17**	19,33	0,34			20,79	0,11	20,45	0,34	20,41	0,34
17,01	**0,17**	19,26	0,34			20,75	0,10	20,29	0,34	20,06	0,34
16,61	**0,17**	19,55	0,34							20,32	0,34
		19,81	0,34							20,09	0,34
		19,36	0,34							20,29	0,34
		19,66	0,34							20,67	0,34
		19,68	0,34							20,47	0,34
		19,10	0,34							20,13	0,34
		19,65	0,34							20,56	0,34
		19,54	0,34							20,38	0,34
		19,46	0,33								
		19,44	0,33								
		19,58	0,34								
		19,38	0,34								
		19,41	0,34								
		19,03	0,34								
		19,07	0,34								
		19,35	0,34								
		19,30	0,33								
		19,80	0,34								
		19,37	0,34								
		19,11	0,34								
		19,34	0,34								
		19,84	0,34								
		19,34	0,34								
		19,41	0,34								
		19,72	0,34								
		20,17	0,34								
		19,23	0,34								
		19,29	0,34								
		19,84	0,33								
		19,00	0,34								
		19,38	0,34								
		19,60	0,34								
		19,27	0,34								
		19,14	0,34								
		19,35	0,34								
		19,28	0,34								
		19,09	0,34								
		19,29	0,34								
		19,11	0,34								
		19,11	0,34								
		19,02	0,34								
		19,01	0,33								

TABLE A.9 – *Analyses des isotopes de l'oxygène pour les échantillons de Komati River, Buck Reef et Barite Valley. Les données en gras dans l'échantillon KRC8 correspondent à une veine de micro-quartz.*

"J'ai rien compris, mais j'ai jamais autant rêvé..."

Lucas